Design and constructability of fabric-formed concrete elements reinforced with FRP materials

Kostova, Kaloyana

Award date:
2016

Awarding institution:
University of Bath

Design and constructability of fabric-formed concrete elements reinforced with FRP materials

Kaloyana Zdravkova Kostova

A thesis submitted for the degree of Doctor of Philosophy

University of Bath

Department of Architecture and Civil Engineering

August 2016

Table of Contents

List of Figures

List of Tables

Acknowledgements

This research project has been generously funded by the Leverhulme Trust, which awards many research grants for the development of novel and original ideas, such as fabric formwork. I gratefully thank my supervisors Tim Ibell, Antony Darby and Mark Evernden for introducing me to the concept of fabric formwork and for their continuous support throughout the years of research and writing up.

Most of the presented work in this thesis would not have been possible without the technical support of the Structures Laboratory at the Department of Architecture and Civil Engineering, especially without the help of Will Bazeley, Neil Price and Sophie Hayward who have been involved throughout the whole duration of the current project.

I would also like to thank Socrates Ioannou for helping me to develop practical skills in the design and preparation of concrete mixes, as well as for sharing his knowledge of low carbon cements through a collaborative study on the utilisation of fabric-formed concrete for improving the durability of supersulfated cement based concrete.

Another person I would like to thank is Professor Mark West for his advices on fabric-formed construction during his visits to Bath and for his inspirational works, which have motivated my research.

I may not be able to mention all of my colleagues at the Department of Architecture and Civil Engineering, who have been a part of my PhD journey, but I would like to thank Kunal Kansara, Monika Brindley, Stella Papatzani and Abbas Tajaddini.

I would also like to thank my current directors and colleagues at Tony Gee and Partners for encouraging my continuous academic relations and for providing me with opportunities for furthering my knowledge in FRP materials.

And above all, I thank my family for their support and patience.

Declaration

The author declares that, except for where specific reference is made to work done by others, or for commonly accepted and commonly understood ideas, and unless otherwise stated in the text, the content of the thesis are their own work.

This thesis has not been previously submitted, in part or whole, to any institution or university for any diploma, degree or other qualification.

The full length of this thesis is approximately 73,000 words.

Abstract

Concrete has many advantages as a low cost and sustainable material. However, more than 5% of the planet's total carbon emissions are associated with the production of cement, which, in fact, is predominantly due to the large volume of concrete used worldwide. It is known that traditionally designed concrete structures typically use more material than structurally required and, therefore, an important question is whether material demand can be reduced through structural optimisation. A major drawback from optimised design, however, is the cost and complexity of producing conventional rigid moulds.

Fabric formwork is emerging as a new method for construction, gaining popularity among architects and engineers for the opportunity to build unique forms and to shape concrete elements efficiently. Porous fabrics, acting as controlled permeability formwork, also have proven effect on the durability characteristics of concrete. While fabric formwork has a profound potential to change the appearance of concrete structures, the shapes cast in fabrics are not defined in advance and have been often created unintentionally. The design of load-bearing reinforced concrete structures, however, requires accurate form-prediction and construction methods for securing steel reinforcement inside flexible fabrics, which presents a number of constructability challenges. For example, cover formers cannot be used to ensure adequate thickness of protective cover, inevitably affecting the acceptance of such structures in practice.

This research has demonstrated that non-corrodable FRP reinforcement can be incorporated more easily than steel bars in fabric-formed concrete due to its light weight and flexibility, while it is possible to ensure ductility of such structures through confinement of concrete using FRP helices. A novel splayed anchorage system has been developed to provide end anchorage for optimised sections where standard bends or hooks cannot fit. This work also provides an experimentally verified methodology and guidance for the design and optimisation of fabric-formed elements.

List of Publications

Kostova K.Z., Ibell T.J., Darby A.P. and Evernden M.C., 2016. Using fabric to shape appropriate concrete structures, *Sustainable Construction Materials and Technologies (SCMT4)*, 7- 11 August 2016, Las Vegas.

Ioannou, S., Badr, A., Kostova K.Z., Paine, K. and Ibell T.J., 2016. Utilization of fabric formwork for improving the durability of supersulfated cement based concrete, *8th International Conference on Concrete Under Severe Conditions-Environment and Loading* (CONSEC2016),12-14 September 2016, Lecco, Lake Como, Italy.

Ibell T.J., Orr J., Kostova K.Z., Darby A.P. and Evernden M.C., 2013. Extraordinary possibilities for future concrete structures, *The IES Journal Part A: Civil & Structural Engineering*, 6 (4), pp. 239-248. doi:10.1080/19373260.2013.831380.

Kostova K.Z., Ibell T.J., Darby A.P. and Evernden M.C., 2013. Sustainable concrete construction using fabric formwork, *In Proceedings of FutureBuild 2013*, 4 - 6 September 2013, Bath.

Kostova K.Z., Ibell T.J., Darby A.P. and Evernden M.C., 2013. Behaviour of fabric-formed concrete beams reinforced with FRP bars, *In Proceedings of Advanced Composites in Construction conference (ACIC 2013)*, 10 - 12 September 2013, Belfast.

Kostova K.Z., Ibell T.J., Darby A.P. and Evernden M.C., 2013. Novel splayed anchorage system for internally reinforced concrete members, *In Proceedings of 11th International Symposium on Fiber Reinforced Polymer for Reinforced Concrete Structures (FRPRCS-11)*, 26 - 28 June 2013, Guimarães.

Kostova K.Z.,2013. A new form of architecture for concrete structures. *In Proceedings of the 15th Young Researchers' Conference*, 14 March 2013, London.

Kostova K.Z., Ibell T.J., Darby A.P. and Evernden M.C., 2012. Advanced composite reinforcement for fabric-formed structural elements, *In Proceedings of Second International Conference on Fabric Formwork (icff2012)*, 27 - 29 June 2012, Bath.

Kostova K.Z., Ibell T.J., Darby A.P. and Evernden M.C., 2012. Innovative structural systems for architecturally expressive and sustainable concrete structures, *In Proceedings of 6th International Conference on Advanced Composite Materials in Bridges and Structures (ACMBS-VI)*, 22 – 25 May 2012, Kingston.

Symbols

Latin upper case letters

A	Area of fabric-formed cross section
A_b	Area of reinforcing bar
A_{conf}	Area of confined concrete
A_e	Equivalent area of FRP reinforcement
A_{frp}	Area of FRP reinforcement
A_{fv}	Area of shear reinforcement
A_s	Area of steel reinforcement
A_{tot}	Total bond surface area
A_w	Surface area of wedge plate
B	Top breadth of a fabric-formed cross section
B_s	Width of support of a fabric-formed beam
B_{web}	Web thickness of a ‘key-hole’ fabric-formed cross section
D	Overall depth of fabric-formed cross section
D_b	Depth of bottom bulb of a ‘key-hole’ fabric-formed cross section
E_b	Modulus of elasticity of reinforcing bar
E_{cm}	Modulus of elasticity of concrete
E_{frp}	Modulus of elasticity of FRP reinforcement
E_s	Modulus of elasticity of steel reinforcement
F	Vertical force
F_b	Pull-out force in a reinforcing bar
F_c	Compressive force in concrete
F_f	Tension force in FRP reinforcement
$F_{f,h}$	Horizontal component of tension force in FRP reinforcement
$F_{f,v}$	Vertical component of tension force in FRP reinforcement

F_s Tension force in steel reinforcement

$F_{s,h}$ Horizontal component of tension force in steel reinforcement

$F_{s,v}$ Vertical component of tension force in steel reinforcement

F_{tie} Force in a tie restraining fabric formwork

G Characteristic value of permanent action

L_w Wedge length of splayed anchorage

N Normal reaction of concrete on a wedge anchor

P Perimeter of fabric-formed cross section

P^* Perimeter of fabric-formed cross section, including fabric extension

P_b Perimeter of the bottom bulb of a ‘key-hole’ fabric-formed cross section

P_b^* Perimeter of the bottom bulb, including fabric extension

Q Characteristic value of leading variable action

R Radius of curvature

T Constant value of tension force in fabric

T_s Tension force in fabric

T_x Horizontal component of tension force

T_y Vertical component of tension force

T_1 Tension force in bottom bulb of a ‘key-hole’ fabric-formed cross section

T_2 Tension force in top bulb of a ‘key-hole’ fabric-formed cross section

V_f Shear resistance of continuous FRP shear spiral

X Depth of neutral axis

Latin lower case letters

c Constant defining the curvature of fabric-formed section

c_2 Constant defining the curvature of fabric-formed section (top bulb)

d_b Diameter of reinforcing bar

d_{eff} Effective depth of reinforcement

f_{cm}	Mean compressive strength of concrete
f_{ctm}	Mean tensile strength of concrete
f_{fv}	Ultimate stress in continuous FRP shear spiral
f_s	Stress in steel reinforcement
f_u	Ultimate tensile strength of FRP reinforcement
f_y	Yield strength of steel reinforcement
g	Standard gravity
h_{bulb}	Height of fabric-formed bulb
h_m	Depth at which the maximum breadth of a fabric-formed section occurs
h_{web}	Web height of a ‘key-hole’ fabric-formed cross section
k	Parameter of the stress-strain model of concrete in EN1992-1-1:2004
l_0	Initial horizontal length
l_d	Development length of reinforcing bar
n	Constant of the splayed anchorage model in § 3
m	Bond parameter
p	Parameter defining the softening branch of the modified BEP bond-slip model
p_s	Hydrostatic pressure
s	Slip of reinforcing bar
s_r	Parameter of the CMR bond-slip model
s_v	Pitch of continuous FRP shear spiral
s_1	Slip corresponding to maximum bond strength
t_w	Thickness of slot in splayed reinforcing bar
v	Vertical deflection
v_1	Vertical upward displacement of beam end due to rotation at support
w_m	Maximum breadth of fabric-formed section
x	Coordinate in the horizontal direction
x_L	Position of cross section along the length of a fabric-formed beam
y	Coordinate in the vertical direction

z Hydrostatic height

Greek upper case letters

Δ Transverse deformation of wedge anchor

Δl Incremental length of fabric-formed section perimeter

Greek lower case letters

α Curve-fitting parameter of the BEP and CMR bond-slip models

α_w Wedge angle of splayed anchorage

α_1 Initial horizontal angle of fabric-formed profile

δ_{sw} Deflection due to selfweight

δ_{total} Total deflection for quasi-permanent combination of actions

ε Strain

ε_c Shortening strain in concrete

ε_{c1} Strain at peak stress in concrete

ε_{frp} Strain in FRP reinforcement

η Parameter of the stress-strain model of concrete in EN1992-1-1:2004

θ Angle between successive straight lines representing a fabric-formed curve

θ_h Horizontal angle at top of fabric-formed profile

θ_0 Initial angle of fabric-formed profile

κ Curvature of fabric-formed profile

μ Coefficient of friction

ρ Density of wet concrete

σ Normal stress

σ_c Compressive stress in concrete

σ_{frp} Stress in FRP reinforcement

τ Bond stress

τ_b	Bond stress in bar
τ_m	Peak bond stress
τ_w	Bond stress in wedge plate
τ_1	Maximum bond strength
τ_3	Bond friction component
φ	Rotational angle of hinged-beam blocks
ψ_2	Factor for quasi-permanent value of a variable action

1. Introduction

1.1. Fabric-formed concrete

Fabric-formed concrete is a term describing concrete cast in flexible textile membranes, known as fabric formwork. As a construction method fabric formwork offers the possibility to explore the mouldabilty of fresh concrete and create non-prismatic concrete elements of varying complex shapes without the additional costs and limitations on reusability, associated with production of non-standard rigid moulds. It can be used to form beams, columns, slabs, panels, walls, foundations, canal linings, etc., as can be seen from the large number of examples presented in § 2. There are four major distinctive areas in which fabric formwork can have a significant advantage over traditional formwork systems (Kostova et al., 2013). These include the architectural appearance of structures, the efficient use of concrete material through design of optimised structural forms, the benefits from lightweight construction and the proven durability enhancement on concrete cast in permeable textiles.

Fabric-formed concrete has been recognised and well researched by architects for the opportunity to create unconventional forms and surface textures. According to Professor Mark West, concrete elements cast in fabric formwork show a ‘kinship of form’ with all living organisms, including human bodies, which are shaped by fluid pressure applied onto their external membranes (Chandler and Pedreschi, 2007). This adds a strong associative power to fabric-formed concrete and the appeal of an organic material. Impressions on concrete left from stitches and wrinkles of fabric, intentional or not, also create unique aesthetic details not achievable through other methods of construction. Furthermore, the interaction between the process and the material in fabric formwork construction is identified by Manelius (2012) as stereogeneous architecture, in which the final form reveals the traces of the construction process.

Understanding the forming process and developing capability to predict the final concrete shapes also gives the opportunity to manipulate fabric formwork, such that structurally optimised forms can be created. Orr (2012) reviewed the data of material savings, obtained by different researchers, for fabric-formed beams compared with equivalent rectangular beams, arriving at an average value of 41%. A further investigation has shown that a similar amount of total savings can be achieved for a typical concrete frame building case study, comparing fabric formwork optimised beam construction with conventional construction systems comprising uniform rectangular beams (Orr, 2012).

Fabric formwork is an extremely lightweight form of construction, which removes the need for densely supported heavy shuttering systems. This may lead to major cost savings and improved safety conditions on site. The major advantage of fabric formwork, however, lies

in the simplicity and accessibility of the construction process. Unlike many innovative developments, fabric formwork is an intuitive low technology method, which requires traditional skills and can be easily adopted at any part of the world. This is confirmed by a number of experimental construction projects built at various locations (C.A.S.T., 2007; West and Araya, 2012; Bhooshan and El Sayed, 2012).

Concrete durability is another area where the advantages of fabric formwork can be explored and developed. Permeable textiles, used as fabric formwork material, effectively act as controlled permeability formwork, which has a known effect on improving the durability characteristics of concrete by forming a denser surface layer with a reduced water-to-cement ratio (Price, 2000). The properties of the textile materials can be controlled to achieve an optimal performance, as demonstrated by experimental investigations (Harrison, 1991; Orr et al., 2013; Lee, 2012). This could result in creating durable, aesthetically appealing exposed surfaces, which would not need to be hidden, allowing even further cost savings on finishing works.

Despite all positive aspects of fabric formwork construction, inevitably, there are challenges related to the practical application of the method in industry. From design perspective, even the simplest design problem would require solving three somewhat difficult tasks, including prediction of the unknown hardened concrete shapes, analysis of reinforced concrete elements of complex geometries and applying methods for structural optimisation. The construction challenges experienced by different researchers have also raised questions over the feasibility of structural fabric-formed concrete applications. Achieving the desired concrete shapes and the installation of steel reinforcement inside flexible membranes are common problems in fabric formwork construction. Providing shear reinforcement in beams of varying non-prismatic cross sections, as well as end anchorage of longitudinal reinforcement in sections with optimised depths present other problematic areas, which cannot directly utilise existing standard methods. However, the major drawback of using flexible formwork is the lack of appropriate methods for control of the thickness of concrete cover to steel reinforcement. Due to the role of concrete in protecting steel against corrosion, this may have a significant effect on ensuring the durability of steel reinforcement and would most likely be unacceptable in practice.

One approach to deal with the various challenges is to consider them as separate problems and develop specific solutions, which may, however, compromise some of the key advantages, such as freedom of form and simplicity of construction. For example, although it is possible to restrain the fabric membranes by external rigid supports, which pre-define the final shape more accurately, this is likely to add excessive material

requirements and complexity to the temporary works. Furthermore, seeking particular benefits on their own, such as an architectural expression only, may not lead to competitive solutions economically. Nevertheless, if simplicity and economy were perceived as leading advantages, the complications in the design and reinforcement installation again would limit the applications. Similarly, the durability enhancement could only be considered practical as an added benefit. However, the challenges can also be seen as opportunities to introduce novel materials, construction techniques and ideas for reinforced concrete detailing, which rather than being limited by the formwork flexibility, could potentially benefit from it. This may ultimately help to develop holistic solutions, which enable the profound use of fabric-formed concrete, while realising all advantages of fabric formwork and reinforced concrete as a material.

1.2. Motivation

1.2.1. Towards a carbon economy

The carbon-equivalent cost is expected to play a significant role in the businesses and decision-making processes as a result of the commitments to tackle climate change. With the Climate Change Act 2008, UK has already set a long-term target of at least 80% cut in the greenhouse gas emissions by 2050 compared to 1990, and introduced legally binding carbon budgets. According to the major review of the HMG's approach to carbon valuation conducted in 2009, the traded price of carbon will be increased from £4.48 in 2014 (Department of Energy and Climate Change, 2014) to £200 central estimate per tonne of CO_2e in 2050 (Department of Energy and Climate Change, 2009) and, therefore, would become an important economic factor for all sectors of the industry. Furthermore, the shared long-term ambitions defined by the joint government and industry partnership strategy, in Construction 2025, aim at achieving by 2025: "50% reduction in greenhouse gas emissions in the built environment", together with "33% reduction in both the initial cost of construction and the whole life cost of assets", "50% reduction in the overall time from inception to completion for new build and refurbished assets" and "50% reduction in the trade gap between total exports and total imports for construction products and materials" (HM Government, 2013).

As indicated by the emission factors of raw materials and processes associated with the production of concrete, given in *Table 1.1*, the cement has the greatest contribution to the carbon footprint of concrete. On a global scale, the cement industry alone accounts for approximately 8% of the total CO_2 emissions, half of which are generated by carbonate oxidation in the cement clinker, representing the largest non-combustion CO_2 source from the manufacturing industries (Olivier et al., 2012).

Table 1.1. CO_2 emission factors (Flower and Sanjayan, 2007)

Activity	Emission factor	Unit
Coarse aggregates – Granite/Hornfels	0.0459	t CO_2-e/tonne
Coarse aggregates – Basalt	0.0357	t CO_2-e/tonne
Fine aggregates	0.0139	t CO_2-e/tonne
Cement	0.8200	t CO_2-e/tonne
Fly ash (F-type)	0.0270	t CO_2-e/tonne
GGBFS	0.1430	t CO_2-e/tonne
Concrete batching	0.0033	t CO_2-e/m^3
Concrete transport	0.0094	t CO_2-e/m^3
On aite placement activities	0.0090	t CO_2-e/m^3

Within established limits, Portland cement can be replaced with secondary products from other production processes, which have much lower emission factors, such as ground granulated blast furnace slag (GGBS), fly ashes, silica fume, pozzolana and fillers (Sprung, 2008). The typical commercially available cement types containing 25% by weight of fly ash can reduce the carbon emissions of concrete by 15%, while cements containing 40% GGBS can magnify the reduction to 22% in comparison with concretes produced with a 100% Portland cement (Flower and Sanjayan, 2007). Although a significant proportion of Portland cement is usually required to activate any additive materials, GGBS can also be activated by sulphates and allow a much larger replacement of cement with more than 80% of GGBS and up to 15% of gypsum or anhydrite. The resulting product is known as supersulphated cement (SSC) and was invented by Hans Kühl in 1909 (Juenger et al., 2011). A more recent patent claims the invention of a cementitious binder, totally free from Portland cement, which comprises at least 90% by weight of GGBS (Ball et al. 2013) and is used for production of the commercially offered CEMFREE concrete.

Despite the benefits in terms of carbon emissions reduction, a large replacement of Portland cement content can potentially lead to poorer resistance to carbonation and affect the long-term performance of concrete. The proportion of cement replacing materials is usually limited by the requirement to maintain high pH values (above 12) in order to passivate the steel reinforcement surfaces against corrosion (Sprung, 2008). Another probable drawback of using by-products could be their availability, which depends on other carbon intensive processes such as the production of steel. Furthermore, achieving the long-term carbon reduction targets would most likely require a combination of more than one approach, such as technological innovations and optimisation of material demands. However, the need to re-use plywood formwork in traditional concrete construction is a major limitation for building materially-efficient concrete forms. Producing

moulds for bespoke concrete elements could lead to wastage of formwork material, exceeding significantly the benefit of optimising the amount of concrete material.

1.2.2. Research aim and significance

By 2050 concrete is likely to remain a key construction material for its durability and the wide availability of locally sourced aggregates. Concrete has an inherent fire resistance, good sound insulation properties; it requires little maintenance and easily meets vibration criteria. Moreover, the utilisation of thermal mass in concrete buildings can help to reduce energy demands for heating during the winter and delay the peak temperatures during the summer. The re-carbonation of concrete during its service life and after demolition has also been shown to have a significant effect on the net CO_2 emissions (Pade and Guimaraes, 2007), which adds to the definition of concrete as a sustainable material. In fact, the carbon footprint of concrete per unit weight is relatively low compared to most construction materials, which indicates that the total amount of concrete used worldwide is responsible for its high environmental impact. The data published by CEMBUREAU shows a global cement production for 2014 of 4.3 billion tonnes, increased in only four years from 3.3 billion tonnes in 2010. Therefore, there is a strong motivation to design concrete structures in a more material-efficient way, thereby reducing the environmental impact of the global production.

Recent studies quantifying and comparing the total embodied carbon of several 2012 Olympic structures, including the Olympic Stadium, Aquatics Centre and Velodrome, with the Beijing and Sydney Olympic stadia, found large differences in the absolute carbon emissions, demonstrating how the application of efficient design principles can lead to a considerable reduction of embodied carbon (Cullen et al. 2011). Likewise, Thirion (2010) investigated the role of material-efficiency in structural design and suggested, based on two case studies, that the material demand based on current design practice can be reduced by at least 27% through optimisation of structural element geometries.

Considering the future needs of embodied carbon reduction and the substantial material savings, which can be achieved through building efficient structural forms, the potential of fabric formwork in helping to bridge the existing gap between the design and constructability of structurally optimised elements may be unrivalled, in addition to the reduced requirements for transportation, heavy weight lifting on site and finishing works. For that reason, the research goal of this thesis is to establish a design and construction methodology for fabric-formed concrete elements, in order to demonstrate the feasibility and enable the application of fabric-formed concrete in practice. The specific objectives addressed during this research have been:

- To develop design methodology and guidance, including finding of the final concrete shape and structural optimisation, for fabric-formed elements.
- To resolve the existing constructability problem related to ensuring an adequate protective cover to steel reinforcement cover through use of appropriate materials and construction methods.
- To develop an end anchorage system suitable for concrete elements with relatively small optimised end cross sections.
- To develop appropriate techniques for production of shear reinforcement suitable for fabric-formed elements with varying geometry.

1.3. Research approach

As emphasised earlier, the durability of steel-reinforced concrete depends on ensuring a consistent thickness of adequate concrete cover. This requirement may present a major drawback in fabric formwork construction, precluding the wide application of flexibly-formed concrete in practice. The use of fibre-reinforced polymer (FRP) reinforcement, however, could change the nature of the problem as FRP composite materials do not rely on concrete for protection against corrosion, which also implies they can be cast in low carbon concretes with reduced alkalinity. In addition, the high strength, light weight and flexibility of FRP bars may offer further advantages. Consequently, the main focus of the current research has become the development of appropriate methods for design and construction of fabric-formed elements reinforced with FRP composites.

The adopted research approach included both analytical and experimental work aiming to develop a design methodology for fabric-formed concrete based, as much as possible, on standard design methods and material models, such as the ones defined in BS EN 1992-1-1:2004. For this purpose, a design programme capable of performing form-finding, sectional analysis and geometry optimisation of fabric-formed beams, reinforced with steel or FRP materials, was written in MATLAB and validated through physical testing. The programme was gradually extended to allow for more design options and boundary conditions, corresponding to the ideas explored in the construction of experimental beams, and can further be upgraded to allow the design of various structural elements and systems.

As it is almost impossible to consider design and construction of fabric-formed concrete separately, a carefully staged experimental programme was followed. Overall five different experimental studies were undertaken, three of which were focused on fabric-formed beams. The initial investigation of fabric-formed beams was carried out to identify

appropriate construction methods and techniques, predominantly suitable for installation of FRP reinforcement, and to define parameters required in the design, such as a range of boundary conditions. The second experimental study was performed to verify the results produced by the developed as part of this research computational design program, in terms of both shape and structural behaviour predictions. The third investigation explored methods for building ductile FRP-reinforced elements through confinement of concrete in compression and producing FRP shear spiral reinforcement for beams with varying cross-sectional shapes.

A major experimental work was undertaken to study a novel method for end anchorage of reinforcing bars, previously explored by Darby et al. (2007) at the University of Bath. The method is named splayed anchorage as it involves splaying the ends of reinforcing bars in tension to form wedges, resisting the end pull-out forces. This offers a significant advantage for the design of optimised geometries, due to minimising the need to provide non-structural depth in order to fit anchorage bends at end sections. Furthermore, the method was specifically developed for FRP reinforcement and, therefore, would provide a single solution for the identified problems, related to fabric-formed optimised beams and FRP bars.

All fabric-formed test beams were cast in flat sheets. However, this could limit the freedom of form due to excessive wrinkling of fabric, as revealed during the construction process. The last experimental study explored the application of sewn fabric formwork for building unconventional wall and column shapes, highlighting the advantages not only in terms of reducing wrinkling effects, but also demonstrating the incomparable simplicity of fabric formwork construction for creating forms of variable complexity. The fabrics were stitched using a standard heavy-duty industrial sewing machine and attached to simple lightweight timber frames, foldable during transportation and quick to install on site.

1.4. Outline of the content

The content of this document is organised in ten chapters. The next chapter provides an overview of the background in the research areas of fabric formwork and FRP composites. Chapter 3 presents the study on splayed anchorage, including experimental results and development of a theoretical anchorage model, which have been used in the subsequent chapters. Chapter 4 explains the proposed design methodology for form-finding, analysis and optimisation of fabric-formed beams. The experimental beam studies are split into the next three consecutive chapters. Chapter 5 provides results of the investigation on construction methods. Chronologically, it precedes the design approach developed in Chapter 4 and, therefore, it also discusses the limits of existing design and

form-finding methods, identifying the needs of further development. The experimental study undertaken to validate the developed computational program is described in Chapter 6, including a discussion on the achievable construction tolerances and the consequences of the deviations from predicted geometry on the structural performance of fabric-formed beams. Chapter 7 links the current research work to the real-life design of fabric-formed beams by providing practical methods for production of shear reinforcement and improving the ductility of FRP-reinforced concrete. Chapter 8 summarises all presented theoretical studies and experimental findings, related to the design and construction of fabric-formed beams, through the demonstration of a step-by-step design procedure for two case study beams. Chapter 9 expands the scope of the current work, showing the potential of sewn fabric formwork construction. Finally, Chapter 10 provides the conclusions derived from this research and discusses the possible directions of future work.

2. Research Background

2.1. Introduction

The background of the current work encompasses two major areas of research, namely fabric formwork and FRP-reinforced concrete design. However, there is little research combining the two areas. Therefore, they are presented as separate topics, including a discussion of the opportunities and the challenges, which need to be further investigated in order to realise the best opportunities for use of FRP materials in fabric formwork construction.

2.2. Fabric formwork

Even nowadays fabric-formed concrete is mainly seen as an area of research interest and has had little application in engineering design. This section provides an overview of the historical background of fabric formwork systems, tracing back the major steps in the development of such systems and helping to differentiate between the limited industrial applications and the potential for profound use of fabric formwork, which is the focus of the current research. The existing construction methods are reviewed in detail in order to explore the possibilities, identify constructability issues and establish a scope for further investigations. The existing design methods are presented next, again with the aim to recognise possible approaches to design of fabric-formed elements, identify the gaps in research and set a basis for the current work. Finally, the role of fabric formwork for enhancing the appearance and durability of concrete surfaces is discussed, highlighting the potential for future development of advanced textiles for concrete construction.

2.2.1. Historical development

While fabric formwork considered as a combination of utilising contemporary fabric materials and the vision of new applications for building structures can be defined as a novel construction method, the idea of using flexible formwork for casting concrete elements is not entirely new. Historically, a number of inventions, some of patented more than a century ago, may be regarded as early developments of fabric formwork construction. Lilienthal (1899) patented a method for building concrete slabs reinforced with wire mesh cast in impermeable fabric or paper, as illustrated in *Figure 2.1a*. Waller (1934) developed full structural systems made of cementitous materials, reinforced with woven vegetable fabrics (see *Figure 2.1b*). His patented methods were applicable to a variety of structural elements, including columns, walls, slabs and shells. Other early examples of flexibly-formed concrete were the revetment mattresses for protection of riverbanks, patented by Condie (1911). The mattresses comprised two layers of cloth, such as burlap, tied together and filled with concrete.

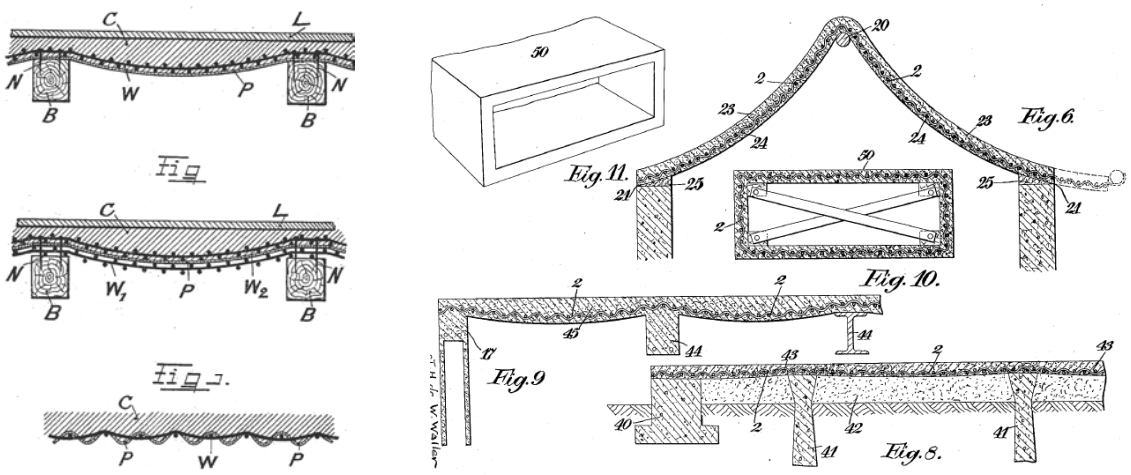

a. b.

Figure 2.1. First patents: (a) Lilienthal (1899) and (b) Waller (1934)

Overall, the early flexible formwork inventions remained isolated and distant from each other in time, which could be attributed to the lack of suitable formwork materials (Veenendaal et al., 2011b). The emergence of synthetic fibres, however, was about to change this. Although the first fully synthetic fibre produced from polyvinyl chloride was invented in 1913, the commercial production of polyester fibres was not initiated until 1950, followed by polypropylene fibres around 1958 (Fourne, 1999). The 1960s, as indicated by the graph in *Figure 2.2*, saw a rapid increase in the production of synthetic fibres, when permeable, high-strength and durable fabrics became available at a low cost, making possible the application of fabric formwork on a large industrial scale (Lamberton, 1989).

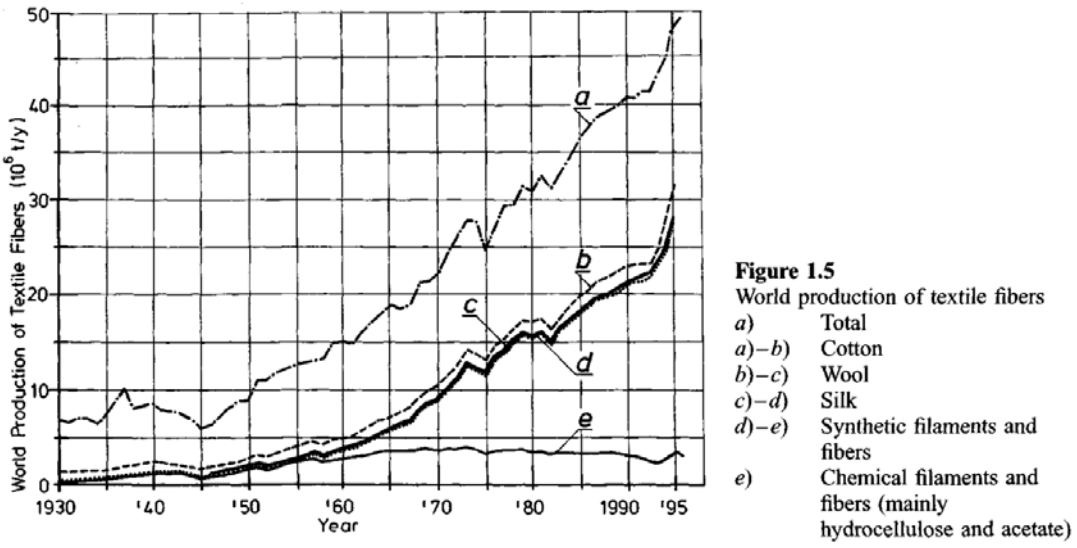

Figure 1.5
World production of textile fibers

a)	Total
a)–*b*)	Cotton
b)–*c*)	Wool
c)–*d*)	Silk
d)–*e*)	Synthetic filaments and fibers
e)	Chemical filaments and fibers (mainly hydrocellulose and acetate)

Figure 2.2. World production of textile fibres (Fourne, 1999)

Casting concrete in porous fabrics allowed the use of easily flowing high water-to-cement ratio concrete mixes and offered an economical and practical solution for jacketing of bearing piles under water, encasement of underwater structures and pipelines, as well as repairs of underwater structures (Lamberton, 1989). Numerous patents obtained by Lamberton in the late 1960s describe a variety of applications of fabric formwork, such as constructing bridge piers, caissons and tanks (Lamberton, 1968a), “filter beds” for protection of shorelines (Lamberton, 1968b) and beach protection concrete mattresses cast between three layers of fabric (Lamberton, 1969). These methods have become widely used in marine construction nowadays, as demonstrated by recent applications, shown in *Figure 2.3* (Hawkswood, 2012).

Figure 2.3. Fabric formwork for filter point mattresses (Hawkswood, 2012)

The architectural interest in fabric formwork, which has shaped the present perception of fabric-formed concrete, remained less evident before the recent three decades. One of the first examples of architectural work using fabric formwork is attributed to the architect Felix Candela who, most likely, influenced by Waller, used a burlap fabric to form two-way anticlastic arch shells for a primary school in Mexico, built in 1951 (Abdelgader et al., 2008). However, the first patented method for truly acknowledged architectural application of polyethylene film sheets as formwork, shown in *Figure 2.4*, belongs to the Spanish architect Miguel Fisac and was used for creating textured wall panels (Veenendaal et al., 2011b).

Figure 2.4. Centro de Rehabilitación para la MUPAG (1969) (Veenendaal et al., 2011b)

The foundation of the Centre for Architectural Structures and Technologies (C.A.S.T.) by Professor Mark West at the University of Manitoba in the mid-1980s presented a major historical step towards the application of fabric formwork for construction of building structures. The research work carried out at C.A.S.T. revealed the potential of fabric formwork for creating both architectural and structural elements, and provided realistic scale examples of construction. Various construction techniques were developed in order to produce concrete forms, ranging from beams and columns to slabs, thin-walled panels and vaults (C.A.S.T., 2007). During the same time period, the Japanese architect Kenzo Unno invented independently fabric formwork methods for casting walls, known as URC ('Unno Reinforced Concrete'), which combine simplicity, 'zero' construction waste and beauty (West, 2010a). A third major development of fabric formwork systems for construction of building foundations and circular columns, also independently realised at the same time as Unno and West, belongs to Rick Fearn and is commercially available in Canada and the USA via his company Fab-Form Industries (Veenendaal et al., 2011b).

At present, the idea of casting concrete in flexible fabric sheets has been embraced by architects and engineers in different parts of the world, who contribute to further development and research into new exciting aspects of fabric formwork.

2.2.2. Construction methods for fabric-formed elements

A range of synthetic textiles, including polyester, polyamide, polypropylene and polyethylene fibres, have been found suitable for fabric formwork construction. They can be applied as reusable flat sheets or cut and sewn into complex patterns (Abdelgader et al., 2008). In general, most fabrics do not adhere to concrete and are easily peeled off once the concrete has hardened, without the need for releasing agents. Based on typical values, fabrics are 50 - 70 times lighter than plywood sheets per unit area, while their cost is one tenth of that of plywood. The cost of temporary works, patterning and stitching of fabric are more difficult to determine and would vary between different projects; however, it is unlikely that it would be higher than the cost of producing and assembling traditional formwork. Considering all these factors, it can be expected that the use of fabric formwork would lead to a significant reduction in construction costs, including transportation. In addition, fabric allows concrete to be compacted effectively by external vibration methods (West, 2010b), which further adds to its advantages over conventional formwork.

According to Abdelgader et al., (2008) fabric formwork can be divided into four main groups which correspond to the construction method used: mattresses, sleeves, shuttering and the open trough group. The mattresses are usually formed by filling

concrete between two horizontal layers of fabric and are used for erosion control and protection of slopes. The sleeve group comprises cast in-situ vertical elements such as pile jackets and columns. The shuttering group is also mainly used for in-situ applications including concrete repair works and walls cast vertically. In the case of concrete repairs, fresh concrete is pumped between fabric formwork and the old concrete. The open trough group represents construction methods for concrete cast horizontally in a fabric sheet, usually flat and supported on horizontal frames or tables. These methods are suitable for pre-cast panels and columns, ribbed slabs, shells, footings and beams.

The design of fabric-formed elements depends highly on the chosen method of construction, which has to be known in advance in order to predict the final shape of the elements. An important parameter in the form finding process is the orientation of the fabric surface during the casting process. For elements cast in vertically supported fabrics, where the gravity force is predominantly parallel with the fabric surface, the hydrostatic pressure at each horizontal plane would be uniformly distributed along the perimeter enclosed by the fabric. Therefore, this construction approach is suitable for forming circular or other symmetrical cross-sectional shapes. The elements cast in horizontally supported fabric generally correspond to the open trough group. The resulting hydrostatic forms are more complex and require appropriate methods for form-finding and analysis. Producing thin shell elements by placing or spraying concrete onto fabric sheets is a third distinctive construction approach affecting the design process. Thus, another useful classification of fabric-formed elements, more directly related to the design and adopted for the discussion of existing construction methods in this section, would include three types of elements: vertically cast, horizontally cast and thin shells.

2.2.2.1. Vertically cast fabric-formed elements

Fabric formwork offers practical and cost-efficient construction methods for vertically cast insitu walls and columns. The fabric-formwork wall systems, developed by Kenzo Unno, use a flexible mesh material to form the face side of a wall, while the back side is usually supported by a rigid insulation (West, 2010b). The two sides can be connected by standard formwork ties, which also allow the installation of reinforcement (See *Figure 2.5*). This method of forming walls is known as the ‘quilt-point’ method because of the pattern created under the hydrostatic pressure of the wet concrete. The formwork ties at each ‘quilt-point’ provide full lateral restraint of the fabric sheets, removing the need of external supports. As there is practically no construction waste and the mesh can be reused a sufficiently large number of times, the method is considered ‘zero-waste’. The flexible formwork sides can also be restrained by linear elements, for example timber studs or steel pipes, supported externally or connected again by means of formwork ties, as shown

in *Figure 2.6*. This represents another method invented by Unno, called the 'frame-restraint' method, which may be used to achieve a greater variety of wall patterns, as demonstrated by Unno's built work examples, illustrated in *Figure 2.6*.

Figure 2.5. 'Quit-point' method for casting in-situ walls (Umi Architectural Atelier)

Figure 2.6. 'Frame-restraint' method for casting in-situ walls (Umi Architectural Atelier)

It should be noted that the use of the 'quilt-point' method has not been limited to the construction of concrete walls. *Figure 2.7* illustrates a successful example of a 'quilt-point' earth wall, built at the University of East London.

Figure 2.7. Rammed earth wall at UEL (Chandler and Keable, 2009)

The methods for construction of fabric-formed columns also vary depending on how the fabric is supported laterally. The commercially available system Fast-Tube™ uses single sheets, clamped between two timber studs along the full height of the column, which acts as a 'guide' post and can further be stabilised to provide a full lateral support during the concrete pour, as indicated in *Figure 2.8a*. The batch column formwork method, invented at C.A.S.T., also uses a 'guide' post to support the fabric during sequential pours of hand-mixed concrete batches (see *Figure 2.8b*).

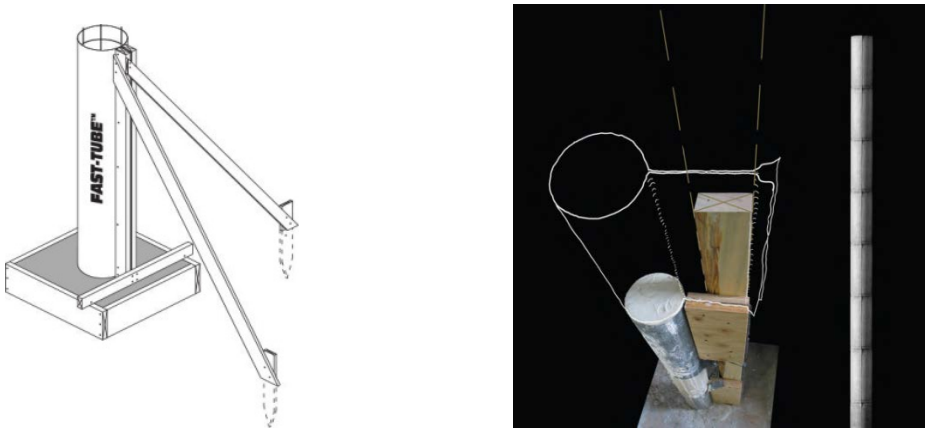

a b.

Figure 2.8. 'Guide' post column construction: (a) a single pour (Fast-Tube™) and (b) sequential pours batch column (C.A.S.T., 2007)

The 'guide' post method is particularly useful for forming circular column sections at low cost and minimum construction waste. Another method for supporting column fabric formwork, which may be able to offer more freedom in manipulating the final shapes, involves pre-tensioning the fabric sheets by stretching them vertically between a footing or

a floor slab and scaffolding at the top, as shown in *Figure 2.9*. For the illustrated project, the formwork consisted of two different layers, an inner stretch-knit liner and an outer laced polyethylene jacket, chosen to create the specific aesthetic feature of the demoulded columns.

Figure 2.9. Pre-tensioned fabric formwork for insitu cast column for a private villa in Culebra Puerto Rico (West, 2010c)

The fabric-formed columns, presented in *Figure 2.10*, further reveal the potential of the latter method for achieving unlimited variation in form. The patterns and voids were created by pinching or sewing the fabric around rigid restraints, such as steel strips or timber pieces (Chandler and Pedreschi, 2007).

Figure 2.10. Fabric-formed columns (Chandler and Pedreschi, 2007)

A workshop entitled Disruptive Technology and led by Remo Pedreschi and Chris Speed at the University of Edinburgh resulted in the creation of the intricate structure, shown in *Figure 2.11.* The structure was cast in a single stitched pre-tensioned fabric, similarly to the column construction.

Figure 2.11. Disruptive technology workshop (Edinburgh College of Art, 2010)

The fatty shell, built at University of Michigan, presents another example of a construction approach, similar to the already-discussed methods for fabric-formed walls and columns. In this case, the concrete was cast between two sheets of rubber stretched onto curved edge frames, as can be seen in *Figure 2.12*. These examples help to demonstrate the adaptability of fabric formwork, which allows casting forms of any complexity using the same basic simple processes associated with fabric formwork construction.

Figure 2.12. Fatty shell (Sturgeon et al., 2010)

2.2.2.2. Horizontally cast fabric-formed elements

Casting concrete in a horizontally placed fabric can be appropriate for in-situ beams, slabs and foundations, as well as for various precast elements. The Fastfoot® formwork system for strip foundations, shown in *Figure 2.13*, presents another industrial application of fabric formwork. In this case, the fabric is left in place. However, it is made of a high density polyethylene impermeable material and plays the role of waterproofing in the long term. The system also includes pre-fabricated standard details, such as sewn corners (illustrated in *Figure 2.13b*) and T-joints, which allow fast installation on site. This once

again demonstrates how the opportunity to stitch fabrics in advance can benefit the constructability of complex insitu details, in addition to saving time and effort on site.

a.

b.

Figure 2.13. Fast foot® strip foundations: (a) construction details and formwork installation and (b) pre-fabricated sewn corners

Figure 2.14 shows the construction of bespoke tilt-up concrete wall panels for a Guest House and Visitor's Centre for the Hanil Construction Company in Korea, designed by West and Araya (2012). The panels were cast horizontally on the ground, similarly to foundation slabs, and lifted into their final position. The unique appearance of the wall panels was created by simply draping the fabric onto PVC pipes laid along the height of the panels.

Figure 2.14. Tilt-up concrete walls (West and Araya, 2012)

Fabric-formed concrete beam elements would typically be constructed by hanging fabric from a horizontal frame support. As the depth of the formed cross-section is easily controlled by the length of the hung perimeter, it is possible to easily create structurally efficient bending moment shaped beams, as can be seen in *Figure 2.15*.

Figure 2.15. Horizontally cast bending moment shaped beams in freely hung fabric (C.A.S.T., 2007)

A more precise longitudinal beam profile can be achieved by the keel mould method, which includes an additional external support defining the underside of the beam along its length. Furthermore, as illustrated in *Figure 2.16*, the fabric can be pinched by lateral side restraints to form concrete trusses or leave voids for services. These methods may be found more appropriate for precast concrete production, due to the increased complexity of the fabric restraining supports.

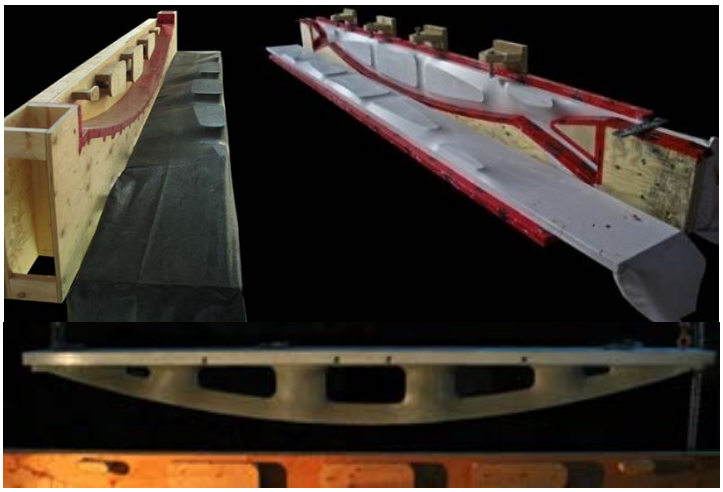

Figure 2.16. Casting a fabric-formed concrete truss using the pinch and keel mould methods (C.A.S.T., 2007)

The keel mould construction method was also successfully applied for building T-beams. For example, Lee (2010) used timber plates to form the web profile of experimental T-beams, as illustrated in *Figure 2.17a*. Orr (2012) extended the method by adding a second keel mould to create double T-beams, as explained by the detailed sketch in *Figure 2.17b*.

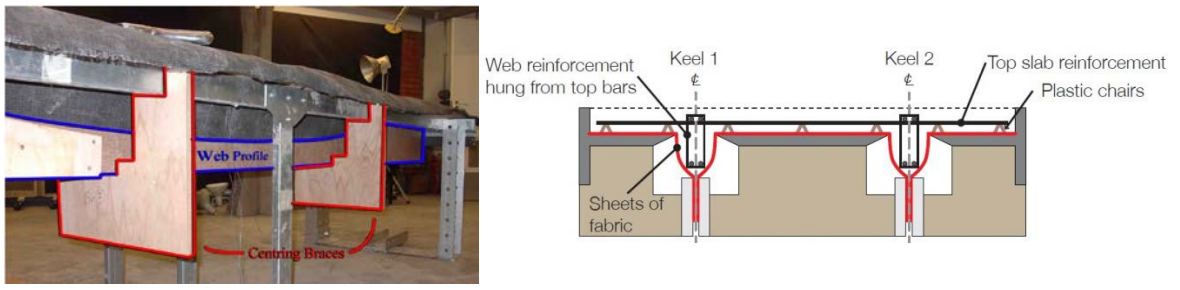

a. b.

Figure 2.17. Fabric-formed beam construction using keel method for producing: (a) T-beams (Lee, 2010) and (b) double T-beams (Orr, 2012)

In addition to forming voids, the pinch method provides an opportunity to reduce the redundant concrete volume near the neutral axis of a beam, thereby creating efficient cross-sections, such as the 'key-hole' sections developed by Garbett (2008). *Figure 2.18* illustrates the adopted construction method and the final shape of a de-moulded 'key-hole' concrete beam. The thickness of the beam webs was varied by curved web formers, made of flexible timber sheets, rigidly supported at three points. However, maintaining the position of the web formers during the concrete pour was difficult and led to deviations from the design geometry. Therefore, the use of much stiffer formers was recommended for improving the stability of the formwork during the casting process.

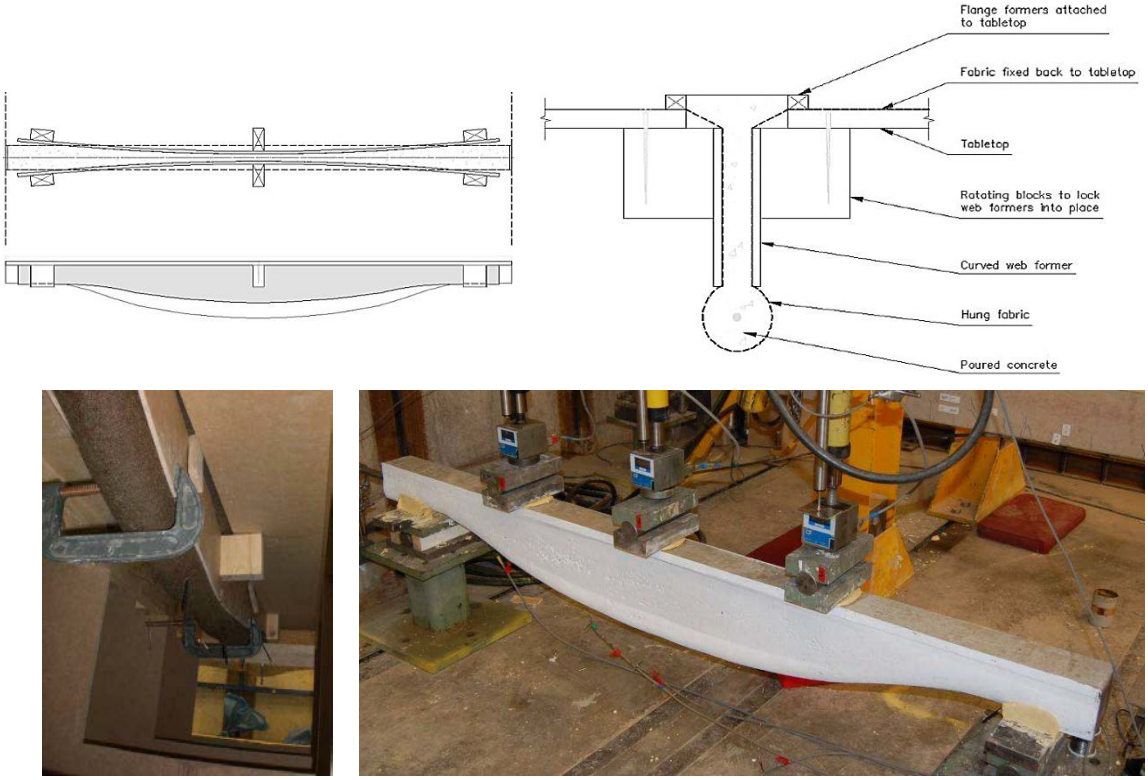

Figure 2.18. 'Key-hole' beam construction (Garbett, 2008)

Precast columns can also be cast horizontally. *Figure 2.19a* presents a plaster model of tree-like concrete columns designed to support a fabric-formed thin-shell concrete canopy

for a Women's Hospital project in Winnipeg, which would be cast in fabric held by the full scale wooden 'table' moulds, shown in *Figure 2.19b* (West and Araya, 2012). Due to the branching detail of the columns the 'tables' were constructed in such way that they could be tilted apart during de-moulding.

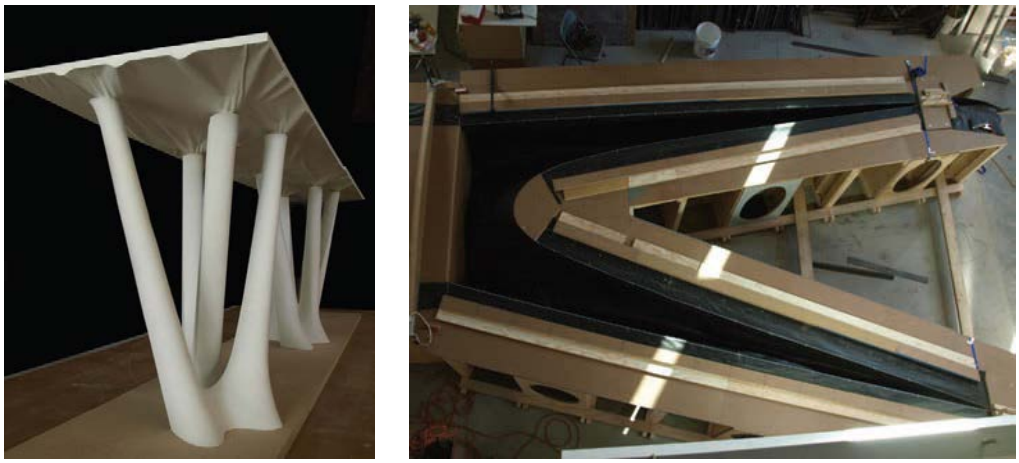

a. b.

Figure 2.19. Horizontally cast concrete columns: (a) plaster model and (b) full scale column formwork table (West and Araya, 2012)

In general, the main problem experienced during the construction of elements cast in hanging fabric was ensuring the final position of steel reinforcing bars. Lee (2010) used steel wires to hold the reinforcement from the top at the correct effective depth, while Garbett (2008) relied on welding the bars to steel plates at the ends only. Use of standard spacers was also attempted by Chawla (2010) for achieving the desired concrete cover. However, as highlighted in *Figure 2.20*, the spacers created uneven beam profile with reduced cover zones in the vicinity of spacer positions.

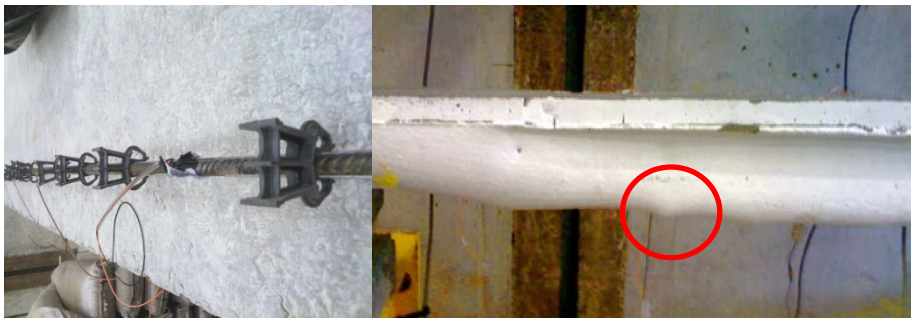

Figure 2.20. Influence of spacers on final shape (Chawla, 2010)

Considering the insufficient control of cover in all these approaches, in addition to the need to pre-deform the steel bars into a curved shape matching accurately the final fabric-formed concrete profiles, it can be concluded that the level of uncertainty in achieving a specified concrete cover may introduce an unacceptable risk of reinforcement corrosion and affect the durability performance of structural fabric-formed elements reinforced with

steel bars. Therefore, this problem presents an important area of research, a solution of which is required to advance fabric formwork construction. The use of highly resistant-to-corrosion FRP reinforcement as an alternative to conventional steel, which is the main focus of the current research, can resolve the major concern over the durability of steel and offer more flexibility in creating curved shapes, avoiding the need to pre-deform steel bars.

Another problem challenging the constructability of fabric-formed elements has been found to be the end anchorage of reinforcement. Conventional anchorage methods using bends or hooks require sufficient cross-sectional depth, which may not be available for optimised bending moment shaped beams, as can be seen from the example of the 'key-hole' beam in *Figure 2.18*. An approach adopted for the experimental construction of such beams is presented in *Figure 2.21a*. The end anchorage was achieved by welding the reinforcing bars to L-shaped steel plates bolted to the forming tables. The plates also provided an end to the concrete form and fixed the reinforcing bar into its correct position at the supports. In the case of T-beams, transverse steel bars may be welded to the main longitudinal bars in the top slab (see *Figure 2.21b)*, as proposed by Lee (2010). Both methods carry the disadvantage of introducing welded joints in reinforcing steel and of exposing steel plates to the element. Furthermore, a failure in the anchorage zone was observed during the load testing of the T-beams (Lee, 2010).

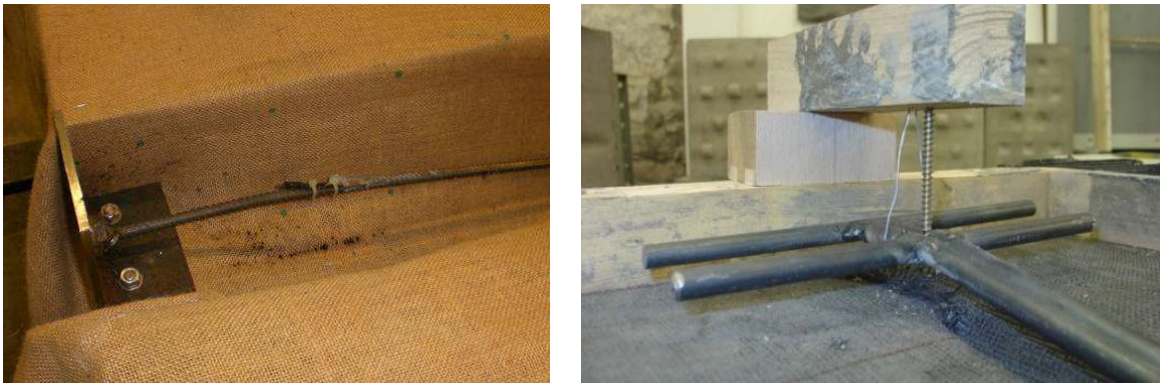

a. b.

Figure 2.21. End anchorage: (a) end plate (Garbett, 2008) and (b) welded bars (Lee, 2010)

A novel splayed anchorage, investigated at the University of Bath, which relies on the wedging action of bars splayed at the ends, could potentially offer an alternative approach suitable for thin cross sections. The method is discussed in detail in § 3 and further developed as part of the current work (see § 3).

2.2.2.3. Thin-shell fabric-formed elements

The construction of thin-shell forms differs from the construction of solid concrete volumes mainly in the process of placing concrete. In order to create thin shells, the concrete is usually sprayed or trowelled onto the fabric mould. *Figure 2.22* presents a thin lenticular shell constructed at C.A.S.T. by trowelling concrete onto two fabric sheets stretched between curved edge supports and a central keel. The shell had only 3 cm thickness and was reinforced with a carbon grid. While this is a single example of the various large scale shell prototypes built at C.A.S.T., it demonstrates the simplicity which fabric formwork adds to the process of producing complex curved surfaces. Even greater freedom of form was achieved by spraying fibre-reinforced shotcrete against suspended sheets of fabric, as illustrated in *Figure 2.23*.

Figure 2.22. Double-curvature thin shell cast onto a fabric mould (West, 2009)

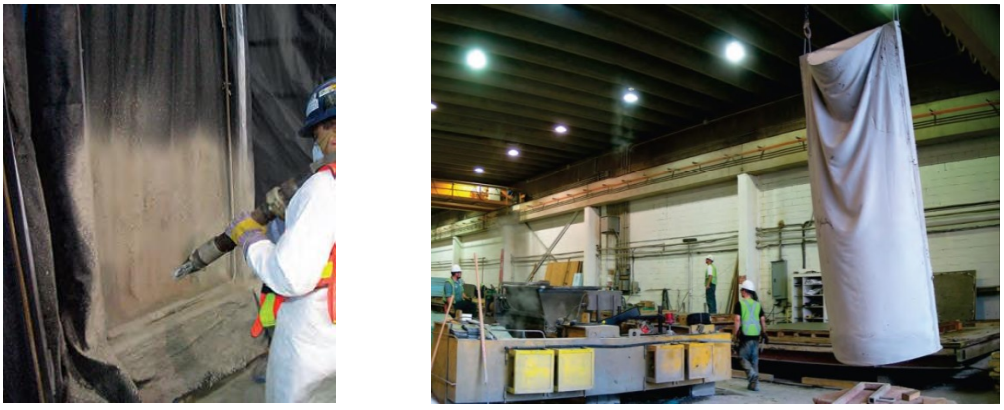

Figure 2.23. Sprayed concrete thin-shell construction (C.A.S.T.,2007)

Reinforcing fabric-formed shells with conventional steel grids may present challenges similar to those encountered in beam construction. Alternative fibre textile reinforcement for producing anticlastic shotcrete concrete thin shells was proposed by Tysmans et al. (2009). An experimental construction study also compared the preparation time before

concreting a shell reinforced with a steel grid and a second shell reinforced with fibre textile reinforcement (see *Figure 2.24*). The fibre textile reinforcement was simply cut into the design patterns in less than an hour and laid over each shotcrete layer, while shaping and installing the steel reinforcement alone required a whole day (Tysmans et al., 2009). This once again poses the question about whether steel reinforcement should be used for fabric formwork construction, and highlights the advantages of flexible reinforcement in terms of constructability and time savings.

a. b.

Figure 2.24. Double-curvature shell reinforced with: (a) steel grid and (b) fibre textile reinforcement (Tysmans et al., 2009)

Bhooshan and El Sayed (2012) built two identical hand-rendered concrete shell prototypes in order to compare the influence of different formwork methods on the design process and constructability of the desired form. The formwork for the first prototype, which was located in Mexico, represented a rigid unidirectional waffle grid made of high strength triple plywood sections. The second prototype, shown in *Figure 2.25*, was built in India using fabric formwork. The construction sites were carefully chosen, based on the available labour skills in each country. The prototype construction helped to draw a number of important conclusions concerning the two formwork methods. As could be expected, the fabric formwork was found to be less expensive, required less labour-intensive pre-fabrication and was easier to assemble on site. The cutting and stitching of fabric was completed in a day by two experienced upholstery tailors, while the installation on site was managed by 10-12 labourers in six hours, compared to over a three-day period needed for transport, cutting and assembly of the timber formwork, carried out by 8-10 full-time carpenters (Bhooshan and El Sayed, 2012). Another reported advantage of fabric formwork was the physical form-finding of the pre-tensioned fabric, which naturally took the digitally modelled form and did not rely on the accuracy of reproducing the form by rigid elements. However, the waffle grid was more stable during construction and

provided an adequate working platform, while access scaffolding was required in the case of fabric formwork. Furthermore, heavy rains and the installation of steel reinforcement caused local tears and sagging of fabric, again demonstrating the difficulties of placing steel reinforcement in fabric formwork on site.

Figure 2.25. Large scale thin shell construction built in India using fabric formwork (Bhooshan and El Sayed, 2012)

Despite any potential drawbacks, fabric formwork remains an extremely inspirational method for the creation of unique thin shell concrete forms. *Figure 2.26* shows an architectural design example of a column/skylight in the form of a bow tie, developed by Belton (2012). The shell represents a mobius strip topologically, realised by pre-tensioning fabric between two types of constraints, a fixed edge attachment and a cable inserted into an edge pocket (see *Figure 2.26*).

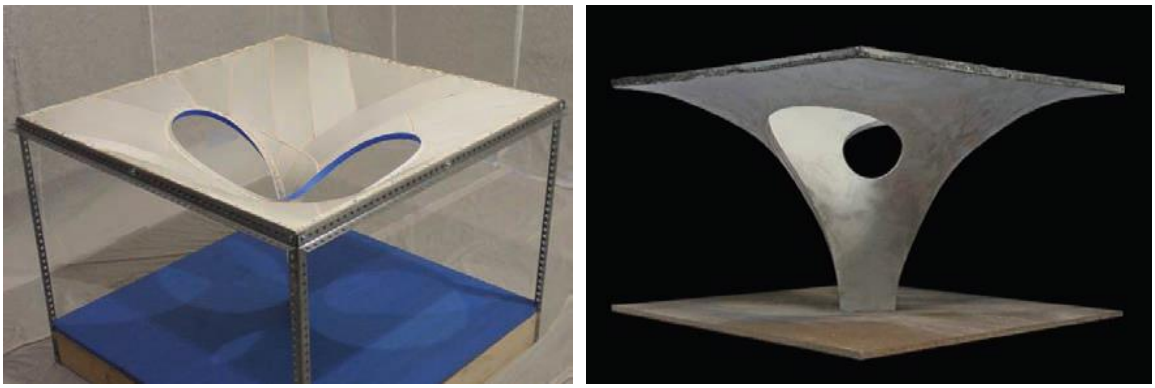

Figure 2.26. Bow-tie thin shell column formwork and gypsum mock-up (Belton, 2012)

The combination of fabric formwork and flexible cable supports can offer even wider possibilities for thin shell construction. Veenendaal and Block (2014) proposed a hybrid cable-net and fabric formwork system, which may allow the building of large span shell structures. A small-scale prototype cast in concrete using the proposed method is shown in *Figure 2.27*.

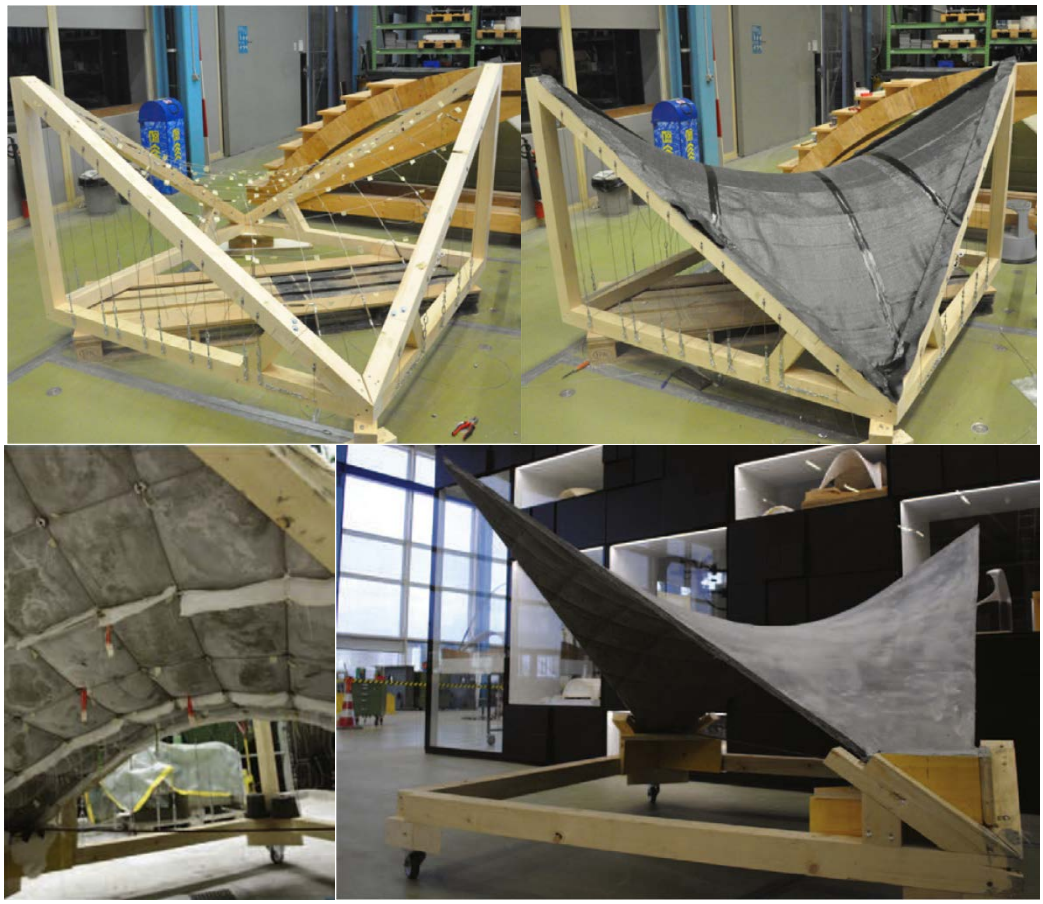

Figure 2.27.Prototype shell cast in a hybrid cable-net and fabric formwork (Veenendaal and Block, 2014)

2.2.3. Design methods for fabric-formed structures

The fundamental difference between the design of fabric-formed and conventionally-cast concrete structures lies in the initially unknown final shape. The form-finding process of determining the shape assumed by the fabric under the hydrostatic pressure exerted by the fresh concrete is closely related to the form-finding of pre-tensioned membrane structures. It depends on a number of parameters, including the characteristics of the fabric material, any applied pre-stress to the fabric and the boundary conditions defined by the methods for restraining the fabric during construction. However, there are specific differences between fabric-formed and tensioned membrane structures, as defined by Veenedaal et al. (2011a), which arise from the influence of the setting of concrete during construction, the bleeding of excessive water through permeable fabrics, the influence of 'pinch' points and the allowance for wrinkling not typical for minimal surface form-finding of pre-tensioned membranes. Therefore, although methods for form-finding and analysis of pre-tensioned fabric structures have been well investigated and developed, their applicability to fabric formwork remains a subject of research study to date.

Veenendaal and Block (2012) provide a comprehensive overview of the existing computational methods for form-finding and structural analysis of fabric-formed elements, demonstrating the limited availability of computational tools. In fact, most of the small prototypes and large scale built works at C.A.S.T. were developed based on physical form-finding methods. Lee (2010) also used a physical experimental approach in order to gradually improve the structural behaviour of fabric-formed T-beams.

Schmitz (2006) first used a finite element program (ADINA) to determine the optimum shape of a concrete wall panel cast in fabric formwork. The fabric was modelled with 2-D solid elements and the concrete material with 3-D solid slurry elements not contributing to the stiffness. The form-finding procedure involved increasing manually the thickness of the 3-D slurry elements in increments until equilibrium in the supporting fabric formwork was reached. Subsequently, the strength capacity of the panel was analysed in the finite element program and checked against the applied loads. If required, the panel geometry could have been optimised by adjusting the parameters and repeating the form-finding procedure.

A novel form-finding approach based on the force density method was proposed by Van Mele and Block (2010) for the design of thin anticlastic concrete shells built in flexible formwork. The approach offered an optimization strategy for finding an equilibrium surface closest to a given target under specified loads, and calculating the required prestress in fabric formwork.

Tysmans et al. (2011) presented a form-finding methodology, verified by case studies and applied for the design of anticlastic shell shapes made of fire-safe textile reinforced cement composite (TRC) developed by researchers at the Vrije Universiteit Brussel, which comprises fine grained cement matrix and glass fibre textiles. The form-finding strategy in this case was based on dynamic relaxation with kinetic damping, while the finite element software Abaqus was used to analyse the structural behaviour of the final shell forms under gravity loads. Due to the good tensile and compressive strength of the utilised novel composite material, steel reinforcement was not necessary. Furthermore, the studies revealed that the thickness of conventional steel-reinforced concrete shells of spans up to 15 m could be reduced up to three times with the use of TRC composite material.

Veenendaal (2008) combined evolutionary structural optimisation algorithms with dynamic relaxation methods for predicting the shape of a filled fabric membrane, and performed structural analysis of fabric-formed beams in ANSYS. The results indicated that up to 67% savings in concrete material could be achieved for a fabric-formed beam when compared with a theoretical prismatic beam of equal span, depth and stiffness (Veenendaal et al.,

2011a). Furthermore, Veenendaal and Block (2012) created a 3-D form-finding design tool capable of modelling the wrinkling behaviour of fabric, based on a combination of the natural force density method and an elastic stiffness matrix method. The tool was written in Python and connected as a toolbar to Rhino.

The customised methodology for design of optimised shapes, proposed by Bak et al. (2012), was specially developed to allow for fabric formwork construction. Topology optimisation, based on the BESO algorithm was first carried out to determine the design concrete shape. The fabric was then 'draped' over the optimised shape by using a detecting collision approach. The theoretical predictions were verified by a physical model of a slab supported on a central column. The optimised bottom surface of the slab was built by hanging fabric through cut-outs formed in a flat formwork plate, the shape of which was defined by the fabric draping procedure (Bak et al., 2012).

Several studies at the University of Bath have been focused on the structural optimisation of reinforced concrete fabric-formed beams. A 2-D sectional approach, based on beam theory, has been used for structural analysis and optimisation in these studies, as recently overviewed and summarised by Orr et al. (2014a). The form-finding approach, however, evolved from experimentally obtained empirical relations for the top breadth, depth and perimeter of sections horizontally cast in a freely hung fabric membrane (Bailiss, 2006; Garbett, 2008) to a numerical solution describing the full cross-sectional geometry for known top breadth and depth of each section (Foster, 2010). The numerical form-finding procedure is fully compatible with the adopted approach for beam optimisation and analysis and can be used for the development of a practical design tool, further discussed in § 4.

Garbett (2008) also investigated the applicability of the bone growth analogy for structural optimisation of fabric-formed beams. Although the study recognised that this approach is appropriate for modelling continuous isotropic materials and may not be directly applied to reinforced concrete (Garbett et al., 2010), options for creating more efficient fabric-formed sections were proposed. As *Figure 2.28* suggests, in addition to the possible variation of depth and width along the length of a beam already considered by Bailiss (2006), the volume of the redundant concrete material near the neutral axis can be reduced by forming hollow or pinched 'key-hole' shaped cross sections. The latter was further investigated through a physical construction and testing of the beam model illustrated in *Figure 2.18*, which showed concrete material savings of 55% compared with a rectangular section. The highest concrete savings, however, were demonstrated by Orr (2012), reaching up to 78% for double T-beams, excluding the top slab.

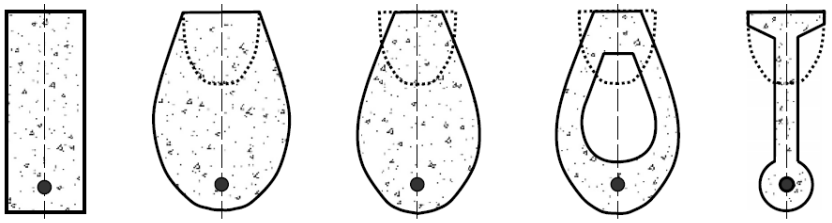

Figure 2.28. Evolution of optimal design process for fabric-formed beams (Garbett et al., 2010)

A major challenge in the optimisation of fabric-formed beams, however, remains the shear design and the provision of shear reinforcement. There is little evidence that the established standard methods for shear design can reliably predict the shear strength of beams with varying depth. Furthermore, practical methods for reinforcing non-prismatic curved cross sections are yet to be developed. Past research studies of beams with tapered cross sections could not establish a significant effect of the depth variation on the shear strength of a beam. For example, Debaiky and Elniema (1982) did not observe an appreciable difference in the ultimate shear strength of tapered beams with decreased or increased depth near the supports. It was also concluded that the inclination of the beam profile affected only the contributions of the concrete and the dowel action of the longitudinal reinforcement to the shear strength of the beams, while the nominal contribution of stirrups remained unchanged. Stefanou (1983) arrived at similar conclusions, reporting minor differences between the shear failure loads for tapered and rectangular beams, and an insignificant effect of taper on the contribution from stirrups. Nevertheless, it was found that variation in the bottom surface profile had a greater effect than sloping of the top surface.

MacLeod and Houmsi (1994) offered a method for predicting the shear strength of tapered beams without shear reinforcement. The proposed method helped to identify the depth of a cross-section which could be designed using a conventional approach, based on evaluating the contribution of the compression zone. The experimental results also revealed that increasing the angle of inclination by decreasing the depth away from a support improved the ductility of beams unreinforced in shear. Later studies demonstrated that the concrete contribution to shear strength, as well as the contributions of the longitudinal steel reinforcement and the transverse shear reinforcement, are all functions of the inclination angle of tapered beams (Tena-Colungaa et al., 2008).

Paglietti and Carta (2009) challenged the application of existing codes, which allow reduction of the shear force with the amount of force in the compression chord or the tensile force in inclined longitudinal reinforcement (BS EN 1992-1-1:2004, ACI 318M-08).

It was demonstrated that this method was valid only for cross sections of constant depth, for which the maximum shear stress occurs at the centroid of a section, assuming a parabolic distribution. However, it could considerably overestimate the shear strength of tapered beams, due to the different distribution of shear stresses and the likelihood that the maximum shear stress would exceed the shear stress at the centroid.

With the intention to offer a reliable method for shear design of fabric-formed beams, Orr et al. (2014b) compared and experimentally verified, employing digital image correlation techniques, three different design approaches for design of tapered beams, namely a truss analogy in accordance with BS EN 1992-1-1:2004, the use of the compressive force path method and a modified strut and tie model, in which the flexural tension reinforcement was not required to yield. The experimental results showed that the truss analogy may lead to unconservative design, while the last two methods were able to better predict the shear behaviour of tapered beams, as they could capture the influence of the change in direction of the compression path to the position of the critical stirrup. In addition, it was recommended to ignore the contribution of the flexural reinforcement to the shear strength of tapered beams. More recently Yang et al. (2015) used the test results obtained by Orr et al. (2014b) to further investigate the reliability of appropriate methods for tapered beam design. MATLAB models were developed to simulate the behaviour of the test beams and compare the predictions with the experimental data. A major conclusion, drawn from this study, was that the theoretical approach proposed by Paglietti and Carta (2009) did not provide satisfactory results.

Despite an improved understanding of the shear behaviour of tapered beams based on the most recent studies, the production of shear reinforcement for non-prismatic fabric-formed beams and its installation inside flexible fabric sheets still present unexplored areas of research. Furthermore, relying purely on concrete to provide the ultimate shear strength of a beam is not permitted for elements critical for the overall resistance and stability of a structure in accordance with BS EN 1992-1-1:2004. A potential manufacturing technique using flexible carbon grids, fully or partially coated with resin, as shear reinforcement was proposed and tested by Orr (2012). However, the experimental beams had rectangular cross sections and could not provide a practical example of fitting the flexible grids in non-prismatic fabric-formed sections. Similarly, Grant (2013) conducted experiments with rectangular beams containing impregnated carbon fibre-reinforced polymer (CFRP) continuous spiral reinforcement, suggesting that the adopted manufacturing process can be utilised to produce shear reinforcement for sections with non-regular shape. Previous studies demonstrated that beams reinforced with steel rectangular spirals in shear could reach higher strengths and exhibit a better, ductile

response in comparison with beams reinforced with closed stirrups (Karayannis et al., 2005). The experimental results obtained by Grant (2013) confirmed that spiral reinforcement could improve the shear performance of beams with brittle FRP reinforcement and that the existing design guidance led to conservative design. Therefore, the development of manufacturing techniques for CFRP spirals of varying geometry, suitable for reinforcing non-prismatic sections, might be able to provide a working solution for FRP-reinforced fabric-formed beams and forms a part of the current research (see § 4 and § 7 for further discussion).

The use of meshless techniques for modelling the mechanical behaviour of concrete may offer another approach for structural analysis and optimisation of fabric-formed beams. A meshfree model typically consists of individual particles or nodes, regularly arranged and connected by bars. Positioning the particles randomly, however, not only corresponds better to the physical structure of concrete but would also allow easy numerical modelling of fabric-formed concrete shapes (Williams, 2012). Although there are only limited results until now, the potential of such meshless techniques for modelling the behaviour of fabric-formed concrete could also be an important area of future research.

2.2.4. Characteristics of fabric-formed concrete surfaces

In addition to the possibility of producing unique architectural or sculptural forms, fabric formwork can have a significant impact on the concrete surfaces cast against fabrics. The texture of the fabric remains naturally imprinted on concrete, leading to a dramatic change in the material expression and the aesthetic appearance. The sculptural example in *Figure 2.29* was created by Manelius (2012) to demonstrate the exceptional capabilities of fabric formwork technology and to introduce a surprise experience in the perception of concrete as a material.

Figure 2.29. Ambiguous Chair (Manelius, 2012)

While the architectural impression of textured surfaces may alone present a vast area of exploration, fabric formwork also offers the potential to improve the surface strength and

durability characteristics of concrete. Lamberton (1969) claimed that his invention using water permeable fabric for casting concrete mattresses increased the early strength of concrete as the pressure applied on the cementious slurry during pumping of concrete forced the excessive water to escape through the pores of the fabric, thereby reducing the water-to-cement ratio. A study of ten typical pile jacketing projects, presented by Lamberton (1980), which involved casting concrete in permeable fabric, also showed an improvement of the concrete strength (see *Figure 2.30a*). Furthermore, Bindhoff (1968, cited by Lamberton, 1989) recorded the variation of the water-to-cement ratio near the concrete surface for a series of tests, demonstrating a significant reduction within 152 mm (6 in) or more from the face cast against fabric, as shown in *Figure 2.30b*.

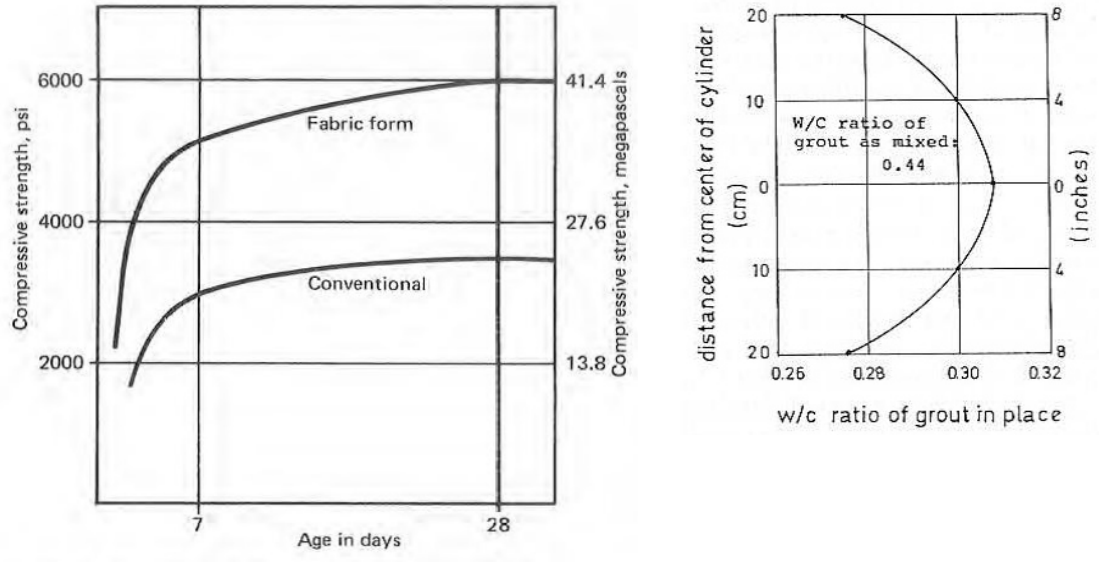

a. b.

Figure 2.30. Improvement of water-to-cement ratio of concrete cast in fabric based on: (a) compressive strength measurements (Lamberton, 1980) and (b) the distance from fabric-cast face (Bindhoff, 1968, cited by Lamberton,1989)

The reduced water-to-cement ratio in the surface layer of concrete can positively affect the durability characteristics of concrete, as previously exploited by industry through the utilisation of controlled permeability formwork. An Overseas Science and Technology Expert Mission, established in 1989, studied the controlled permeability formwork systems developed by major contractors in Japan (Harrison, 1991). The contractors reported a number of improvements including reduced rates of carbonation, chloride penetration and higher freeze thaw resistance, better surface finish and good bond characteristics for placing tiles or plaster, as well as a higher early surface strength allowing for early removal of the formwork. The two main methods used by the contractors were the textile and silk form. The textile form comprised a single textile acting as a filter and a drain, supported over a conventional formwork panel, perforated with drainage holes. The second method used two layers of fabric, polyester filter and polyethylene drainage,

tensioned over plywood formwork sheets. Fabric formwork may effectively act as controlled permeability formwork, providing all of the concrete durability advantages, without the need for additional drainage layers or perforated rigid moulds.

Orr et al. (2013) analysed the microstructure of the surface layer of concrete samples cast against fabric using scanning electron microscope (SEM) and energy dispersive X-ray spectroscopy techniques. The results demonstrated a higher density of the surface layer, indicated by the difference in the measured concentrations of Calcium and Silica concentrations. Further experiments compared the characteristics of fabric-formed and conventionally cast concrete, showing 50% lower coefficient of carbonation, based on accelerated carbonation tests, and up to 58% reduction in the chloride diffusion coefficient at 53 days for the fabric-formed surface, both confirming the positive effect of fabric formwork on the durability of concrete.

An important parameter for achieving the beneficial effects of casting concrete in fabric formwork is the pore size of the fabric material. Previous studies attempted to identify the optimum pore size based on the comparison of compressive strength of cubes cut out from fabric formed mattresses, cast in fabrics with different pore sizes (Al Awwadi Ghaib and Górski, 2001). The relationship between the fabric pore size and the concrete strength followed an increase in the comparative strength up to 570 microns pore size with a local maximum for 350 microns and a decrease for fabrics of 680 microns pore size. A more recent study carried out at the University of Bath (Lee, 2012) included a wider scope of experiments, such as accelerated carbonation, surface hardness and scanning electron microscopy to provide a comparison of the concrete durability enhancement for a range of woven and non-woven textiles. The optimum pore size for woven materials was found to be 250 microns and for non-woven materials in the region of 70 to 100 microns. Examination of the surface concrete microstructure also revealed a difference between the samples cast in woven and non-woven fabrics. It was observed that the topography of the surfaces cast against non-woven materials was less even, while the surface cast against woven materials contained smaller and more ‘flaky’ particles, in contrast to the greater indentation left by the woven fabrics reported by visual inspection.

Lee’s (2012) investigation also included a number of samples, made of cement with 70% GGBS content, demonstrating an improvement in the measured concrete characteristics of fabric-formed surfaces, similar to that for Portland cement concrete, when compared with conventionally cast samples. Furthermore, a collaborative investigation, initiated by the current research, studied the effect of fabric formwork on the durability of SSC-based concrete. The results of the study, presented in detail by Ioannou (2013), indicated that

fabric formwork can offer a practical method for a significant durability enhancement in SSC-based concrete. The experimental results showed that for fabric-formed surfaces compared with conventionally cast surfaces the carbonation depths were reduced by 35%, the absorption rates by 40% and the chloride diffusion coefficients by approximately 50% (Ioannou, 2013).

In summary, it can be concluded that carefully selected porous textiles with optimum pore size, which are widely available on the market, provide a suitable fabric formwork material. However, as previously noted, commercial products such as the formwork systems developed by Fab-Form Industries use impermeable fabrics, which can be re-used or left in place as waterproofing. Therefore, the choice of fabric formwork may vary depending on the specific requirements and conditions of application, while the future exploration of fabric formwork may offer a new range of textile materials, specifically designed for concrete construction. Brennan et al. (2013) addressed the potential of fabric formwork from the viewpoint of textile technologists and suggested areas of interest for development of advanced textiles. The discussed novel ideas included textiles with tailored anisotropic properties, such as multiple-layer geogrids and near-net-shaped reinforcements, robust free-standing textile systems and 'permanently participating' three-dimensional textile formworks. (See *Figure 2.31*).

a. b. c.

Figure 2.31. Advanced textiles for fabric formwork: (a) three-dimensional woven material, (b) free-standing woven cavity construction and (c) three-dimensional woven geogrid (Brennan et al., 2013)

2.3. FRP composite materials for structural applications

2.3.1. Advanced FRP composite materials

There are many examples of natural composite materials, such as wood, bones and plant leaves, which consist of two or more components, working together to achieve the required properties of the material. Moreover, reinforced concrete itself is a man-made composite material. Fibre-reinforced polymer composites include two material types, high-strength fibres and a matrix of a polymer material of relatively low stiffness, which became

available with the development of the petrochemical industry after the Second World War. The interface (surface interaction) between the two volumes of material provides a chemical and physical bond, allowing the transfer of stresses to the fibres (Hall et al., 2010). The major advantages of FRP composites arise from the combination of light weight, high strength and good durability performance, and have led to their wide application in the marine, wind turbine, aerospace and automotive sectors. FRP composites are also widely used in the construction industry for production of pipes, geosynthetics and cladding systems (Cripps et al., 2002). Increased research and FRP demonstration projects in the late 1980s have further encouraged the acceptance of FRP composite materials for structural applications, such as bridge decks, non-prestressed and prestressed internal FRP reinforcement, as well as externally bonded reinforcement for structural strengthening of concrete or metallic elements (Bakis et al. 2002).

2.3.1.1. Types of fibre and matrix materials

There are two major types of polymers which can be reinforced with fibres: thermoplastic polymers composed of long chain molecules held by Van der Waal's forces and thermosetting polymers composed of a three-dimensional network of polymer chains, formed by a chemical reaction. The thermoplastic matrices can be repeatedly softened and reshaped. However, due to their high viscosity during processing it is difficult to ensure contact with fibres. In construction, thermoplastic polymers are used mainly for production of fibres for geosynthetics (Hall et al., 2010). The thermosetting matrices are of three possible types: unsaturated polyesters, vinylesters and epoxies, with epoxies offering the highest performance but also being the most expensive and requiring longer curing time. The major problem of polyester resins is their water degradation. Vinylesters are the hybrid of polyester resin and epoxy molecules, combining some of the advantages of the processing of polyesters and the durability performance of epoxies (fib, 2007).

The advanced fibre–polymer composites used for structural systems are manufactured mainly by combining thermosetting polymers with carbon, glass or aramid fibres (Hall et al., 2010). The low cost and good tensile strength of E-glass fibres make them the most commonly used fibres for glass fibre-reinforced polymers (GFRP). Nevertheless, they are susceptible to alkaline environments due to the presence of silica. S-glass has better corrosion resistance and higher stiffness, while AR-glass is alkali-resistant and suitable for use in concrete, but they are both significantly more expensive. Aramid fibres have the highest strength-to-weight ratio in addition to excellent toughness and damage tolerance properties. While they are cheaper than carbon fibres, aramid fibres can suffer a significant loss in tensile strength under exposure to ultraviolet light (Hall et al., 2010). Carbon fibres for the construction industry are typically produced from polyacrylonitrile

(PAN) polymer as precursor. Being the most expensive fibres, they possess the best durability and strength characteristics, while their elastic modulus is comparable with, and can exceed, the elastic modulus of steel.

Basalt fibre-reinforced polymers (BFRP) have also been explored over the last years as an alternative to E-glass or aramid FRP composites (Crossett et al. 2015). Natural fibres are considered less practical because they can biodegrade. However, recent research in laminated bamboo fibre-reinforced composites showed good potential for using natural composites for structural applications (Sharma et al. 2015). Natural linen fibre-reinforced polymers have also been experimentally investigated for external bonding and near surface mounted applications to provide additional shear strength to concrete structures (Ngo et al., 2015).

2.3.1.2. Manufacturing techniques

The automated manufacturing methods for FRP composites used in construction can be divided into three groups: pultrusion, filament winding and resin transfer moulding processes. The pultrusion technique is suitable for production of FRP composite profiles and reinforcing bars. It involves pulling fibres, impregnated with catalysed resin, through a shaped die. The resulting continuous sections have the highest possible mechanical properties for a FRP composite material, due to the large fibre content and high degree of alignment of the fibres (Cripps et al., 2002). Although it is possible to create various complex geometries through pultrusion, the cost of the dies would usually be justified only for repeatable standard shapes. The filament winding technique is used for pipes and pressure vessels, formed by winding impregnated fibres onto mandrels (Cripps et al., 2002). A novel robotic winding technique developed at the University of Stuttgart has also demonstrated, through the construction of a series of showcase research pavilions, the possibility to build bionic fibre composite shells (Institute for Computational Design, 2012). The resin transfer moulding (RTM) process provides the most appropriate method for creating high-quality 3-D shapes of various sizes and geometries. During the RTM process, pre-catalysed resin is pumped under low pressure into a closed form containing layers of dry fibre strand mats, woven rovings or cloths. The resin-infusion process, commonly used to fabricate structural FRP elements for construction, is effectively a RTM process, in which one side of the closed form is replaced with a flexible sheet (Cripps et al., 2002).

Considering the relatively high cost of raw materials, moulds and heating required for the curing process, FRP composites for structural applications are often significantly more expensive than conventional materials. For this reason, they may offer cost-effective

solution in terms of whole-life cost only for particular projects, where there are requirements such as light selfweight, low maintenance and durability in aggressive environments (Cripps et al., 2002). However, the time savings and the lower cost for transportation and installation of FRP composites result in a competitive overall cost compared with conventional construction methods for large construction projects, with the cost of materials being 15-20% on average (Hobbs, 2015).

2.3.1.3. Durability of FRP composite materials

FRP composites are generally characterised as offering low maintenance and corrosion resistance, with excellent fatigue performance. However, they may suffer from susceptibility to moisture attack, acid, alkaline environments, thermal effects, ultraviolet radiation and fire behaviour, with the last two being less of a concern when FRP bars are used as internal reinforcement. In some instances, galvanic corrosion of carbon composites in contact with metal parts may occur if the necessary conditions are present (Böer et al. 2013).

All polymers and fibres, except carbon, can deteriorate due to moisture absorption. Moisture absorption also causes delamination of fibres from the surrounding matrix, which can be aggravated by the presence of de-icing salts and freeze–thaw cycling. The coupling of moisture and thermal effects may be particularly detrimental for the long-term performance of GFRP composites. Grammatikos et al. (2015) used various experimental techniques to study the hygrothermal aging of pultruded GFRP composites. Failures of the fibre-matrix interface were captured by SEM, while impedance spectroscopy was successfully applied as a novel method for monitoring the moisture absorption behaviour of composite materials. However, a moderate increase in temperature may have a positive effective on the post-curing of composites in some cases (Böer et al. 2013). GFRP composites are, furthermore, susceptible to both acids and alkaline solutions, although alkalinity has more severe effects on the fracture toughness of the GFRP materials. Research studies have shown that the bond and stiffness of GFRP reinforcing bars may be affected by degradation in alkaline concrete environments (Bank et al., 1998).

Micelli and Nanni (2004) studied the physico-mechanical properties of carbon and glass FRP bars subjected to simulated alkaline solution in combination with environmental effects including freeze-thaw, high relative humidity, high temperature and ultraviolet radiation. The results indicated that carbon fibres did not suffer from damage caused by alkaline solutions, while the durability of glass fibres was highly dependent on the properties of the polymer matrix, and polyester resins were not able to provide adequate

protection against alkali ingression. However, although a number of laboratory simulations have confirmed the significant degradation of glass fibres due to alkali attack, Karbhari et al. (2002) showed that the degradation could not be attributed only to high pH levels, but also to the chemistry of the simulated solution and, therefore, the actual exposure effects may not be accurately represented by accelerated laboratory tests. More recent studies of GFRP bars exposed to unsaturated concrete conditions for seven years demonstrated reduced rates of strength loss compared with results from accelerated experiments (Trejo et al., 2011). Nevertheless, it was suggested that the models used to predict the time-dependent capacity of GFRP bars in the current codes may not be appropriate and could lead to unconservative predictions.

In general, FRP composites are combustible and release smoke and heat when exposed to fire. However, their fire behaviour is determined mainly by the matrix and can be controlled by altering the resin chemical composition or by adding fillers (Hobbs, 2015). The effects due to ultraviolet radiation are also highly dependent on the type of resin, and although only the top composite layer is affected, they can cause brittleness of the matrix and contribute to moisture ingress (Böer et al. 2013).

2.3.1.4. Recycling of FRP composites

The waste management of FRP composite materials is another important area, which needs further development in the future, as currently landfill remains the easiest and cheapest method for disposal in most countries (Yazdanbakhsh and Bank, 2014). Although certain recycling technologies exist, such as fluidised bed recovery of glass fibres, re-use of mechanically recycled FRP in the production process and energy recovery through pyrolysis generating fuel gas (Conroy et al., 2006), their application cannot yet be economically justified. The use of FRP waste as fillers or aggregates in the production of cement mortars and concrete has also been investigated. However, most of the experimental results showed that recycled FRP fillers considerably reduce the strength of cementitious materials (Yazdanbakhsh and Bank, 2014).

2.3.2. FRP reinforcement for new-build concrete elements

FRP composite materials are used as reinforcement for concrete elements mainly in two forms, namely externally bonded FRP strips or sheets for strengthening of existing concrete structures and cast-in FRP bars, offering an alternative to steel reinforcement in new-build elements (Ibell et al., 2009).

FRP reinforcing bars are typically produced through the pultrusion manufacturing technique using continuous glass, carbon, aramid and potentially basalt fibres (fib, 2007).

However, a novel application of CFRP fabric laminates acting as internal reinforcement has also been investigated by Achintha et al. (2015). While steel bars have generally invariable yield strength and stiffness, the mechanical properties of FRP bars can vary significantly, depending on the different types of component materials and resin/fibre ratios. FRP bars can also be produced with different cross-sectional geometries and surface bond characteristics. Existing patents on FRP reinforcing bars can be divided into three main groups according to their cross-sectional shape and surface treatment (Portnov et al., 2013): bars with a circular cross-section and a grain-coated surface for better adhesion/friction with concrete, bars with a circular cross-section and ribs or grooves to improve mechanical interlock with concrete aggregates, and bars with non-circular cross-sections, which rely on the shape for enhancing the mechanical interlock, adhesion, and/or friction. It should also be noted that FRP bars cannot be treated as a direct substitution for steel bars due to the difference in their behaviour and failure modes, as discussed below.

2.3.2.1. Fundamental differences between FRP and steel reinforcement

In general, FRP composite materials have superior corrosion resistance and tensile strength properties than normal carbon steel, while their weight is significantly lower allowing easy installation and handling on site. However, there are a few major aspects in which FRP reinforcing bars differ from steel, which need to be considered in the design of FRP reinforced concrete structures. These include the linear elastic behaviour of FRP bars under tensile load up to failure, their high strain capacity and lower stiffness, as well as the difficulty of being bent or reshaped on site (Ibell and Burgoyne, 1999).

Avoiding catastrophic failures due to the brittle behaviour of FRP bars is normally compensated by over-reinforced design, relying on concrete crushing as the failure mode, which exhibits a certain degree of ductility (Nanni, 2003). The ductility of FRP-reinforced concrete elements is also controlled by the weaker bond mechanism of FRP bars in concrete (Oehlers et al. 2013). Further improvement in ductility of over-reinforced beams can be achieved by triaxial confinement of concrete in the compression zone (Whitehead and Ibell, 2004).

The high strain capacity of FRP bars implies that their tensile strength cannot be utilised efficiently in reinforced concrete elements (Burgoyne, 2001). Therefore, pre-stressing may offer a more rational use of FRP reinforcement and has been widely investigated. While there are examples of built FRP pre-stressed concrete structures, many aspects such as the performance of anchorage systems, the long-term behaviour of FRP tendons and serviceability remain problematic (Leung et al. 2003). Enhancing the strain capacity of

concrete can also help to develop higher strains in FRP bars. Leung and Burgoyne (2001a) demonstrated experimentally that concrete confined by aramid fibre-reinforced polymer (AFRP) spirals exhibited a significant increase in ultimate strain capacity.

Due to the relatively low modulus of elasticity, particularly of GFRP bars, FRP-reinforced structures are expected to undergo large deflections. This may imply that serviceability criteria are likely to govern design in most cases (Nanni, 2003). While the deflection limits set in the standards still need to be satisfied, it should be noted that the recommended span-to-depth ratios for steel reinforced structures would not be valid (fib, 2007). Experimental investigations have also shown that FRP reinforced concrete elements develop more and wider cracks at service load than steel reinforced concrete (Benmokrane et al. 1996).

As already discussed, thermosetting polymers provide better durability performance of FRP composites. However, unlike steel bars, once cured they cannot be re-shaped. Furthermore, forming bends in FRP bars, even in the production process, may lead to a reduction in their tensile strength of up to 40-50% due to fibre buckling and stress concentration (fib, 2007). For this reason, FRP bars are generally less efficient when used as bent stirrups and are not suitable for forming conventional end anchorage hooks or bends.

2.3.2.2. Design of FRP-reinforced concrete elements

It is possible to design under-reinforced FRP reinforced concrete structures by using a higher margin of safety against tensile failure of the FRP bars in accordance with ACI 440.1R-06. However, such structures would still fail without exhibiting any ductility. As discussed, concrete crushing failure mode may be more desirable and it is suggested that FRP reinforced concrete structures should always be over-reinforced (Burgoyne, 2001).

Abdalla (2002) observed that FRP-reinforced concrete beams behaved linearly up to and after cracking, however, the beam stiffness was significantly reduced after cracking. Therefore, it was concluded that it is appropriate to apply the design code formulations for steel reinforced concrete, modified for the reduced stiffness. The load-deflection behaviour of FRP reinforced concrete elements is also influenced by the degree of bond between an FRP bar and the concrete. Monti et al. (2000) proposed a computational model, taking into account the bond-slip of steel reinforcement, which demonstrated that the initial elastic stiffness of the bars may be reduced due to the effect of bond. The effect of bond is even more critical for FRP bars due to the lack of ductility and the theoretical risk of snapping at cracks if the bond in concrete were too strong (Burgoyne, 2001).

Furthermore, Oehlers et al. (2013) suggested that ductile FRP-reinforced concrete structures could be achieved through weak bond.

Other factors affecting the deflections of reinforced concrete elements are tension stiffening and long-term effects due to creep and shrinkage. Rafi and Nadjai (2011) showed that the current BS EN 1992-1-1:2004 method underestimates tension stiffening for FRP-reinforced beams and proposed a modification factor taking into account the relationship between tension stiffening and the relative amount of FRP reinforcing. It was also found that shear-induced deflections were insignificant and beam deflection was based on flexural curvature. Torres et al. (2012) demonstrated that the simplified empirical procedures for calculation of long-term deflections in the available codes and guidelines for FRP-reinforced concrete elements cannot account for all of the factors influencing the long-term behaviour of concrete. A new procedure, based on the BS EN 1992-1-1:2004 effective modulus method, was suggested to represent better the changes in material properties and environmental conditions.

The deflection of FRP-reinforced concrete elements can also be affected by temperature increase in a fire. Although the lack of oxygen inside concrete would prevent FRP bars from burning, the load-deflection behaviour of the structure depends on the progressive changes in the elastic modulus of FRP materials (Faruqi et al.,2012). A model, validated by available experimental results, was developed by Faruqi et al. (2012) to predict the deflection of FRP-reinforced concrete structures within a practical range of elevated temperatures.

Overall, it is generally accepted that FRP-reinforced concrete elements can be designed in flexure by modifying the formulations given in the codes for steel-reinforced concrete design. However, the simplified shear design approaches in the design codes are based on the assumption that redistribution of stresses and development of plastic failure mechanisms would occur, which cannot be relied on in the case of FRP-reinforced concrete elements, as demonstrated by Stratford and Burgoyne (2001) through a crack-based shear analysis of beams with brittle reinforcement, highlighting the need to take into account the compatibility. However, based on various pieces of experimental evidence, the methods for shear design in the current guidelines and codes for FRP reinforced concrete still suggest that the use of modified classical formulations can provide predictions with an adequate margin of safety (fib, 2007), despite question marks remaining over ductility issues.

Confinement of concrete in compression is a key approach to ensuring ductility in FRP-reinforced flexural concrete elements and an efficient use of FRP bars in tension. A

method for analysis of beams with a confined compression zone was proposed by Leung and Burgoyne (2001b), assuming that the ultimate failure of concrete was governed by snapping of the confining spiral. Experimental research at the University of Bath showed that FRP-reinforced beams confined by helical FRP reinforcement could achieve 50% higher flexural capacity (Ibell et al., 2009). Moreover, a dual-spiral system, including both confining and shear reinforcement was able to entirely prevent brittle failure, providing additional shear enhancement.

A novel mechanics-based approach for the design of reinforced concrete, which does not depend on defining pseudo material properties required for strain analysis methods (Oehlers et al. 2014), may set a new direction for FRP-reinforced concrete design in the future. The currently developed moment–rotation model for segmental analysis, based on the theories of partial-interaction and shear-friction, can simulate the effects of tension stiffening, concrete softening and concrete confinement for different types of concrete, reinforcement, and bond-slip characteristics, and, therefore, is suitable for concrete elements reinforced with FRP materials (Oehlers et al. 2013).

2.3.3. FRP-reinforced fabric-formed concrete elements

Research into fabric-formed concrete reinforced with FRP materials is fairly limited. Chawla (2010) conducted an experimental investigation into a fabric-formed beam, reinforced with a single splayed anchored CFRP bar (see *Figure 2.32a*). Although the focus of the experiment was to study the behaviour of the splayed anchorage system, a number of problematic areas were revealed throughout the construction and load-testing of the beam specimen. Weights tied by steel wires were used to form the desired curvature of an initially straight CFRP bar (see *Figure 2.32b*). The concrete profile of the beam was locally misshapen by the spacers attached to the reinforcing bars, similarly to the observation for a steel-reinforced beam shown earlier in *Figure 2.20*, which indicated that the longitudinal curves of the reinforcement and the fabric-formed concrete shape did not match well (Chawla, 2010). Therefore, future fabric-formed beam construction should either involve more accurate methods for pre-forming the reinforcement profile, defined by a highly accurate prediction of the final concrete shape, or seek a new approach, which could allow formation of the concrete and reinforcement curved profiles simultaneously, thereby minimising risk of design and construction discrepancies. The latter approach may be possible only if FRP bars are used due to their low modulus of elasticity. The technical data for the Aslan 100 GFRP bars, provided by Hughes Brothers (2011), include permissible radius for field forming of large radius curves, based on the creep rupture

stress limits in ACI 440.1R-06. Similar radius limits may be calculated for CFRP and AFRP bars.

a. b.

Figure 2.32. Fabric-formed beam CFRP reinforcing bar: (a) splayed end and (b) forming the longitudinal profile (Chawla, 2010)

The CFRP-reinforced beam tested by Chawla (2010) failed in shear, as shown in *Figure 2.33*, which was the expected failure mode, based on comparison of the predicted shear and bending moment capacities. The CFRP bar snapped outside the anchorage zone, demonstrating that the splayed anchorage could provide an appropriate solution for end anchorage of FRP bars, cast in relatively shallow sections over supports.

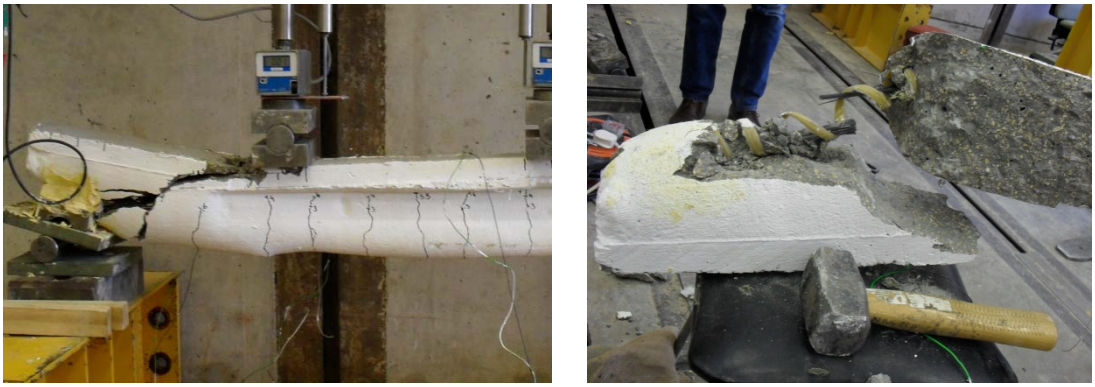

Figure 2.33. Failure of CFRP reinforced fabric-formed beam (Chawla, 2010)

While the shear failure was predictable in this case, the beam was unreinforced in shear, which is a typical problem in the construction of fabric-formed beams (Bailiss, 2006; Garbett, 2008; Lee, 2010). As already discussed, among the proposed solutions for providing shear reinforcement in beams with varying cross sections are flexible CFRP grids, shown in *Figure 2.34a*, fully or partially impregnated with resin and wrapped around the longitudinal bars to create reinforcement cages (Orr, 2012). The CFRP rectangular spirals in *Figure 2.34b*, produced by Grant (2013), can also be formed with varying shapes, and potentially offer a practical method for winding shear spiral reinforcement

directly around the longitudinal bars of a fabric-formed beam. However, further research is needed to confirm the applicability of those methods for other than rectangular cross sections.

a. *b.*

Figure 2.34.Proposed options for shear reinforcement for fabric-formed beams: (a) CFRP grids, before and after impregnation with resin (Orr, 2012) and (b) fully cured CFRP spirals (Grant, 2013)

Individual closed FRP stirrups of varying shapes may also be produced by winding a carbon fibre tow around a grooved mould. *Figure 2.35* illustrates an application of this method for forming CFRP loops made of 25 carbon tows, impregnated with epoxy resin. Fabrication of the individual moulds, however, may be less practical.

a. b.

Figure 2.35. Production of CFRP loops: (a) filament winding and (b) demoulded loops (Kiari et al., 2013)

Novel materials, such as TRC composites, applied by Tysmans et al. (2013) for building thin fabric-formed shells, present another example of fibre reinforced composites, providing a more appropriate option for fabric formwork construction than steel reinforcement. The TRC composite material uses an inorganic phosphate cement matrix. The matrix is pH neutral after hardening and, therefore, is suitable for binding the susceptible to alkali attack E-glass glass fibres. Likewise, the durability of GFRP bars may be improved by the use of low carbon concretes due to their low pH.

2.4. Concluding remarks

This chapter has presented an overview of existing research into fabric formwork. It has shown the key historical contributions responsible for the development of fabric-formed concrete. The available methods for design and construction of fabric-formed concrete elements have been discussed, as well as the suitability of materials, based on recent research aimed at identifying the optimal pore size of permeable fabrics. While the interest in using fabric formwork for building structures has been growing over the past decades, there is still a need for the development of computational tools, which can readily be used by engineers and architects. A number of constructability challenges faced by different researchers have posed the question whether it is practical to install steel reinforcement inside flexible formwork sheets. The major drawback arising from the impossibility to guarantee the protective concrete cover to steel reinforcement during construction relates directly to the durability of fabric-formed concrete, and could be a decisive factor in the acceptance of fabric formwork. As discussed, FRP bars can provide an appropriate alternative to steel for reinforcing fabric-formed concrete elements, while they may also have the potential to solve other constructability problems, such as end anchorage, shear reinforcement and simultaneous forming of matching concrete and reinforcement curved profiles.

FRP composites represent a well-studied area of research, although their use in concrete construction is often limited to structures in aggressive environments, where there is a demand for reinforcement with high resistance to corrosion. The major drawback in the use of FRP-reinforced concrete structures is their lack of ductility, which as demonstrated by research studies can be overcome by increasing the strain capacity of concrete in compression through tri-axial confinement.

Research into FRP-reinforced fabric-formed concrete is particularly limited. The suggested methods for shear reinforcement and concrete confinement have been used only for beams with rectangular cross section and cannot be applied to fabric formwork construction before the development of appropriate design methods and manufacturing techniques. The tailor-made properties of FRP reinforcement and the complexity of the design of flexibly-formed elements add a further requirement for design guidance and computational tools to be provided to designers. Furthermore, the low stiffness of FRP reinforcement would contribute to larger deformations of the potentially more deformable optimised concrete elements, exacerbating the risk of exceeding accepted serviceability limits and indicating an important area for investigation. The effects of creep, shrinkage

and temperature also remain an area for further research although they are beyond the scope of this thesis.

In conclusion, the response of the current research to the identified gaps in existing knowledge is focused on the development of a methodology for the design and optimisation of fabric-formed beams, reinforced with steel or FRP composites, development of construction methods and techniques utilising the advantages of FRP bars, development of an analytical model for the design of splayed anchorages and the development of manufacturing techniques for spiral reinforcement of varying shape. The successful application of FRP composites in fabric formwork construction would help to meet the ultimate goal of the current research in terms of demonstrating the feasibility of fabric-formed structures. In the long term it may also lead to the development of highly sustainable concrete construction, combining optimal structural forms, durable FRP reinforcement and low carbon concretes.

3. Splayed Anchorage

3.1. Introduction

This chapter presents the research background, experimental investigation and development of a model, which predicts the behaviour of a splayed anchorage. The proposed splayed anchorage system is an alternative to conventional anchorage methods for internal reinforcement, such as hooks or bends. The technique utilises the material of the bar itself by cutting a slot at the end of the bar to form a wedge (*Figure 3.1*), which provides additional mechanical anchorage. It may be applied relatively easy on site unlike other types of anchorage for FRP bars and it can be used for steel bars as well.

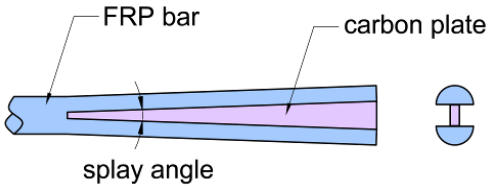

Figure 3.1. Splayed FRP bar

The main advantage of splayed anchorage in fabric formwork construction is that end sections would not require additional non-structural depth for anchoring bent bars. Furthermore, this method can provide a feasible novel anchorage for various FRP reinforced concrete applications.

3.2. Bond in concrete

3.2.1. Bond mechanisms

Bond between concrete and internal reinforcement ensures the transfer of forces and the composite action of reinforced concrete. There are three bond mechanisms: chemical adhesion acting during the initial pull out, followed by mechanical interlock and then friction (Cosenza et al., 1997). Stresses from a deformed steel bar are transferred mainly by mechanical interlock of the lugs and the surrounding concrete (Orangun et al., 1977). The radial component of the resultant force on concrete in *Figure 3.2* is balanced against tensile stress-rings as shown in *Figure 3.3*, indicating that bond strength of steel bars can be governed by the splitting failure of concrete. For steel bars the average bond stress has been found to be dependent on the tensile strength of concrete, which may be considered proportional to the square root of the concrete compressive strength (Orangun et al., 1977), while deformed FRP bars are not able to provide enough lateral confinement through rib bearing and rely on the low chemical adhesion and friction between FRP and concrete (Cosenza et al., 1997). Furthermore, deformations produced by glued spirals can lead to brittle failure caused by detachment of the spiral without crushing of concrete.

Ribbed-type and indented bars showed good bond properties and maximum average bond stresses similar to steel but larger slip (Cosenza et al., 1997).

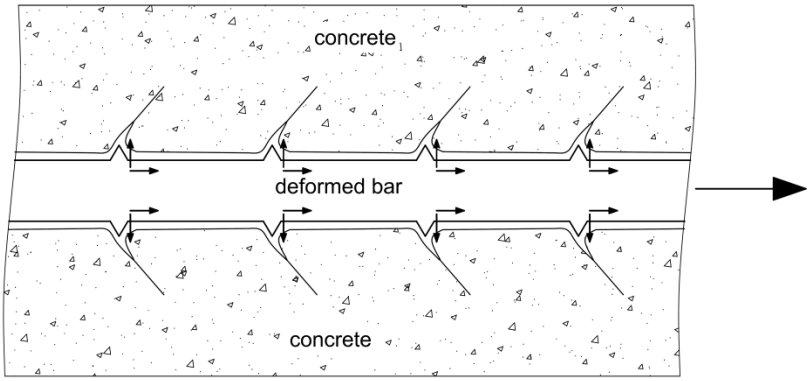

Figure 3.2. Tangential and radial components of forces acting on concrete

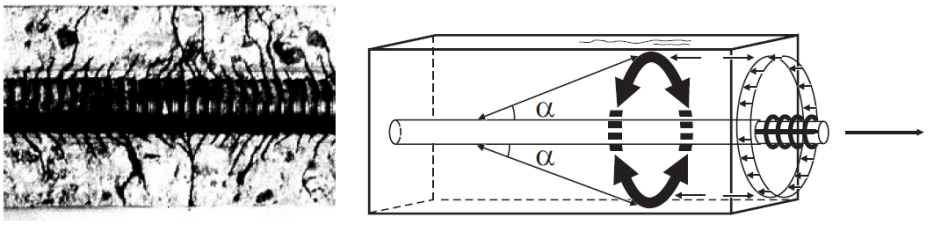

Figure 3.3. Hoop tensile stresses in concrete (Tepfers and De Lorenzis, 2003)

In general, the main parameters influencing the bond stress-slip relationship of a reinforcing bar embedded in concrete include the bar diameter, position of the bar, deformation pattern, confinement of concrete and embedment depth (Tepfers and De Lorenzis, 2003). The bond of FRP reinforcement to concrete is also controlled by the hydrostatic pressure on FRP bars due to shrinkage of concrete, swelling of FRP due to temperature change and moisture absorption (Cosenza et al., 1997). In addition, the relatively weak transverse and shear properties of FRP bars can cause additional slip mechanisms, such as inter-laminar shear failure between the fibres at the surface of a bar. The dependence of bond on fibre and resin properties as indicated in *Figure 3.4a* suggests that it could be inadequate to use smooth FRP bars in reinforced concrete structures. Furthermore, there are many types of FRP bars with different properties and bond characteristics, which unlike ordinary steel reinforcement are still far from being standardised and add to the problem of modelling the bond behaviour of FRP reinforcement in concrete (Tepfers and De Lorenzis, 2003). An increase in FRP bar diameter decreases the ultimate bond stress, while tests have indicated that the ultimate bond stress of FRP bars positioned at the top of a concrete element is 66% of that for bottom bars (Cosenza et al., 1997).

Sand coating can improve significantly the bond of FRP bars but it can also lead to brittle failure when sand grains detach as *Figure 3.4b* demonstrates. However, rough surface bars can exhibit more ductile post-peak behaviour, where the wedging of the bar surface on the surrounding concrete may alter the load-slip from slip-weakening to slip-hardening (Katz, 1999).

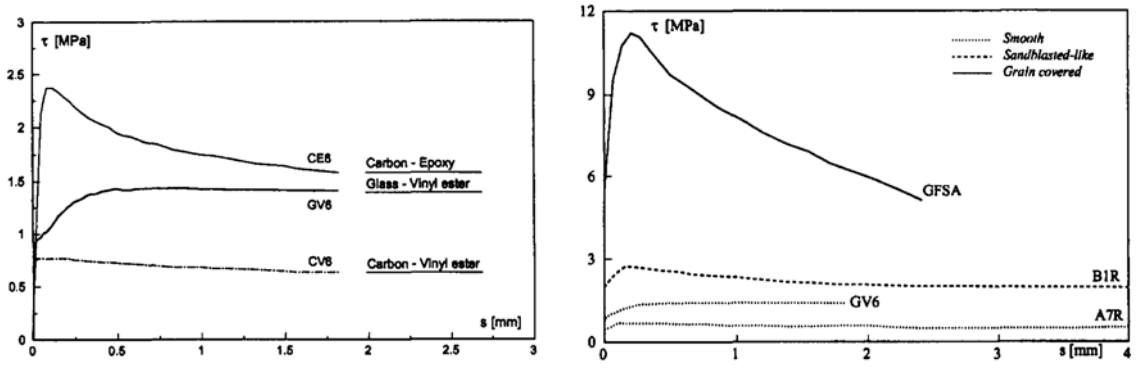

a. b.

Figure 3.4. Influence of: (a) surface smoothness and (b) surface coating on bond strength of FRP bars (Cosenza et al., 1997)

The ultimate bond stress of FRP bars with lugs was found to be similar to that of sand-coated bars (Soong at al., 2011). The sand-coated surface, however, exerts a lower splitting pressure against the surrounding concrete compared to bars with large surface deformations (fib, 2007). Twisted strands also showed larger ultimate bond stress than smooth bars and low dependency on concrete strength (Cosenza et al., 1997).

Confining reinforcement improves the ultimate bond stress due to the increased ductility of local bond failure, which allows more lugs to resist the pull-out force, leading to a more uniform distribution of bond stresses along the embedment length (Harajli et al., 2004). For steel bars the ultimate bond stress due to confinement increases in proportion to the modulus of elasticity of the transverse reinforcement, however, the effect of confinement is considered negligible for FRP bars (ACI, 2006).

Another major difference in the bond behaviour of FRP and steel bars arises from the fact that FRP bars cannot yield and allow distribution of the high strains across cracks (Burgoyne, 1993). Therefore, fully bonded FRP reinforcement will tend to snap. Partial bond produced by altering bonded and unbonded regions or by coating reinforcement with a low strength resin has been proposed, in particular, to achieve more efficient use of prestressed tendons (Lees and Burgoyne, 2000).

3.2.2. Bond-slip models

There are generally three levels of bond modelling: microscopic bond model of the relationship between local bond stress and local slip used to construct the constitutive law, macroscopic model predicting directly the relationship between the pull-out force and the displacement of bars, and intermediate or mezzo-level modelling (Shima et al., 1987).

Local bond stress-slip relationships have been developed for steel and FRP reinforcement. The first bond-slip model for FRP bars, proposed by Malvar (1994), was based on extensive testing of GFRP bars, while the Bertero-Eligehausen-Popov (BEP) model was adapted from the analytical law for deformed steel bars developed by Eligehausen et al. (1982). Cosenza at al. (1997) provides a comparison of four analytical models for FRP reinforcement including Mavlar (1994), BEP (*Figure 3.5a*), the modified BEP model (*Figure 3.5b*) and Cosenza-Manfredi-Realfonzo (CMR) model for their reliability and suitability to represent the bond-slip constitutive curve. While the Mavlar model uses a single relation to describe the entire curve, BEP and CMR models reproduce more accurately the ascending branch of the curve, most important for structural problems.

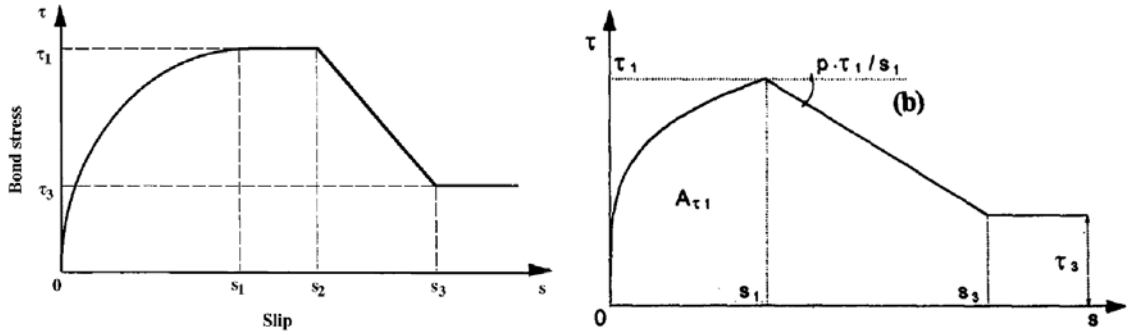

a. b.

Figure 3.5. Bond-slip models for FRP bars: (a) Bertero-Eligehausen-Popov (BEP) and (b) modified BEP (Cosenza et al., 1997)

The ascending branch of the BEP and modified BEP models is given by *Equation 3.1*:

$$\frac{\tau}{\tau_1} = \left(\frac{s}{s_1}\right)^{\alpha} \tag{3.1}$$

where τ_1 is the maximum bond strength, s_1 is the corresponding slip and $\alpha \leq 1$ is a curve-fitting parameter. The second constant bond branch of the BEP law is omitted in the modified BEP model by introducing a new parameter p defining the slope of the softening branch (*Equation 3.2*). The modified BEP model provides results closer to the

experimental data for FRP bars (Cosenza et al., 1997). The two models have a horizontal branch represented by the friction component τ_3.

$$\frac{\tau}{\tau_1} = 1 - p * \left(\frac{s}{s_1} - 1\right) \tag{3.2}$$

The CMR model is a refined model of the ascending branch, which reproduces better the adhesion phenomenon and is expressed by *Equation 3.3*, where τ_m is the peak bond stress.

$$\frac{\tau}{\tau_m} = \left(1 - e^{-\frac{s}{s_r}}\right)^{\alpha} \tag{3.3}$$

A new model for the ascending branch was proposed by Tighiouart et al. (1998) for GFRP bars, based on calibrated parameters s_r and α *(Equation 3.4)*.

$$\frac{\tau}{\tau_m} = (1 - e^{4*s})^{0.5} \tag{3.4}$$

3.2.3. Development length and end anchorage

Based on extensive experimental work, an expression for the average bond stress τ in steel reinforcement, normalised to the square root of concrete compressive strength, has been obtained accounting for the effect of bar diameter d_b, concrete cover and bar spacing (Orangun et al., 1977; Darwin et al., 1992). Since the bond stress is proportional to the stress in steel f_s, the development length l_d can be obtained from *Equation 3.5*:

$$\tau = \frac{f_s * d_b}{4 * l_d} \tag{3.5}$$

Similar methodology was used by Wambeke and Shield (2006) to find an expression, based on available experimental beam test data for FRP bars and recommended by ACI 440.1R-06 (ACI, 2006) as a conservative means to calculate the development length of FRP reinforcement in concrete.

The development length can also be obtained analytically from the actual bond-slip constitutive laws $\tau(s)$, by solving the differential equilibrium equation governing the slip (*Equation 3.6*). This approach allows definition of the development length as a function of the local bond law parameters, avoiding empirical formulations (Focacci et al., 2000).

$$\frac{d^2 s}{dx^2} = \frac{\pi * d_b}{E_b * A_b} \tau(s) \tag{3.6}$$

where E_b and A_b are the cross-sectional area and the elastic modulus of the rebar. A numerical example demonstrating the procedure for GFRP bars is given by Cosenza et al. (2002).

Hooks or bends are often used to assist in the development of tension reinforcement where a bar terminates. However, as previously discussed bending of FRP bars reduces their tensile strength, and internal FRP reinforcement is not as efficient as steel reinforcement when conventional end anchorage methods (*Figure 3.6*) are used (Ahmed et al., 2010).

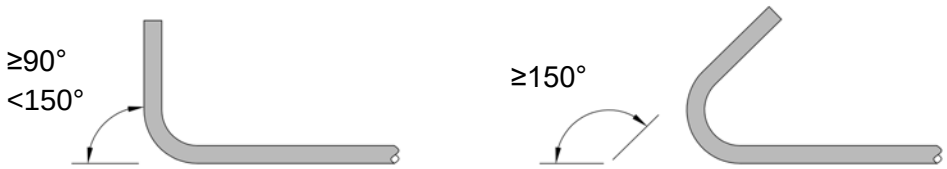

Figure 3.6. Conventional anchorage bends and hooks (BS EN 1992-1-1:2004)

Alternative end anchorage using headed GFRP bars (Trancels-Pultrall Canada Inc., 2011), illustrated in *Figure 3.7*, can provide a pull-out resistance greater than 50% of the bar strength, as demonstrated in direct pull-out tests by Ahmed and Benmokrane (2009), and perform better in comparison with bent bars under seismic loading (Hasaballa and Salakawy, 2012). However, the behaviour of such anchorage is likely to be governed by excessive slip between the bar and the attached head or by brittle failure due to head breakout.

Figure 3.7. Headed GFRP bars (Ahmed and Benmokrane, 2009)

3.2.4. Bond tests

Direct pull-out and beam test methods have been used to study the bond behaviour of reinforcing bars in concrete. An overview of different test variations can be found in (Nanni et al., 1995), including concentric pull out, cantilever beam, hinged beam, spliced reinforcement beam, notched beam and others. While direct pull-out tests are easy to conduct and a wide range of variables can be tested, they are not representative of the actual stress fields of concrete in beams subject to bending and give higher bond-slip results due to the confining action of the reaction plate. Beam type bond tests are more complex to conduct; however, they are likely to show more realistic bond performance, caused by possible longitudinal cracks in the anchorage zones (Focacci et al., 2000).

3.3. Previous pilot-study research

The bond behaviour of splayed anchorage has been previously studied through direct coupon direct and beam pull-out tests, as well as fabric-formed beam tests (Darby et al., 2007; Orr et al., 2010; Orr, 2012). The coupon tests were primarily used to demonstrate the advantage of the splayed anchorage system by comparing the behaviour of a straight bar with the behaviour of bars with different wedge geometries. The beam tests allowed identification of new failure modes and improvement in the wedge detail.

3.3.1. Coupon pull out tests

Tallis (2005) carried out nine short embedment cube pull-out tests for different combinations of wedge lengths of 50 mm, 75 mm and 100 mm and splay angles of 2°, 3° and 4°. The wedges were formed by spacers positioned as shown in *Figure 3.8*, in slots cut into the ends of circular 10 mm diameter GFRP bars. The surface of the test bars was smooth in order to separate any possible mechanical or friction effects from the effectiveness of the wedges. Both ends of the bars were cast in concrete cubes and tested by means of specially produced steel frames, holding the cubes in the testing rig (*Figure 3.9*).

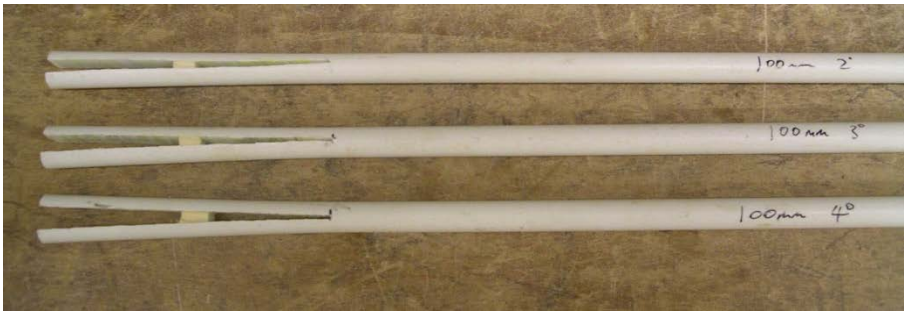

Figure 3.8. Splayed GFRP bars for coupon tests (Tallis, 2005)

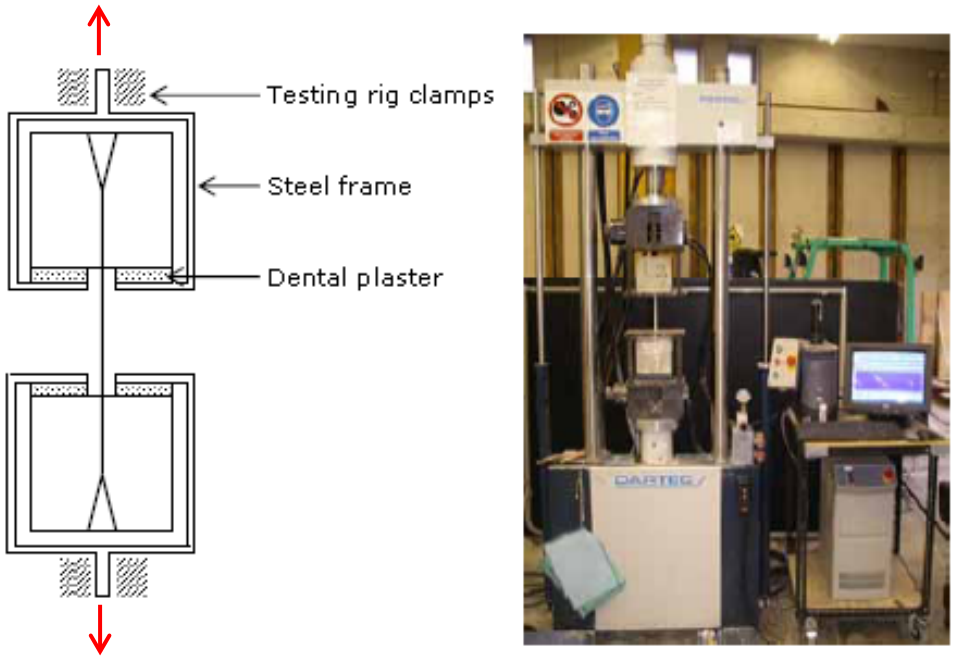

Figure 3.9. Coupon tests set-up (Tallis, 2005)

The same test set-up was used by Winkle (2005) to investigate the influence of tri-axial confinement of concrete, provided by helical AFRP reinforcement, on the anchorage bond strength of various types of straight bars. Finally, the two projects were joined and three specimens were tested for the effect of helical confinement on the bond behaviour of splayed anchorage of GFRP bars in concrete.

The average cube strength varied between 22 MPa and 30 MPa. The maximum angle of wedge opening, at which crack propagation occurred in the tested GFRP bars, was determined experimentally to be approximately 5 - 6°. Therefore, the splay angle was limited to 4°. For most specimens, the failure cracks in concrete were perpendicular to the wedge opening, as illustrated in *Figure 3.10*. The circular helices helped to maintain the integrity of the confined concrete, while cracks were formed around the helices (*Figure 3.11*).

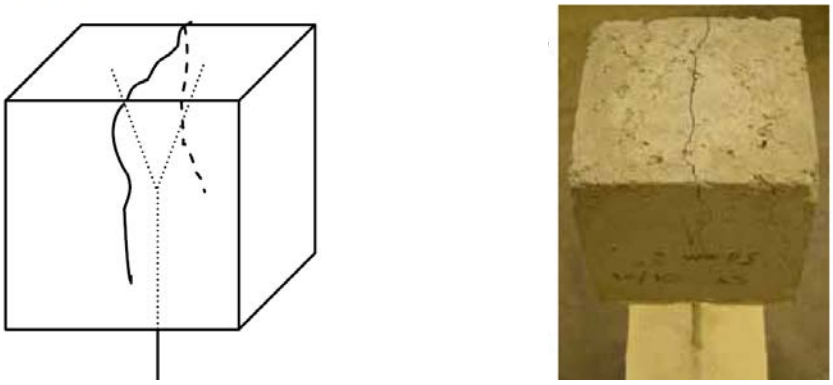

Figure 3.10. Typical failure mode of unconfined coupon test specimens (Tallis, 2005)

Figure 3.11. Confined coupon test specimen (Tallis, 2005)

Figure 3.12 presents the load-displacement results for the whole system of the concrete cubes connected by the tested bars, not confined by helices. As can be seen splayed smooth bars provide an order of magnitude increase in bond strength compared with the same type straight bar. The maximum pull-out resistance was controlled predominantly by the wedge length; however, the splay angle influenced the slope of the experimental curve. Although the main conclusion of the tests was that a small splay angle can still provide significant anchorage enhancement, the splay angle would play an important role in understanding the load-slip behaviour of splayed bars.

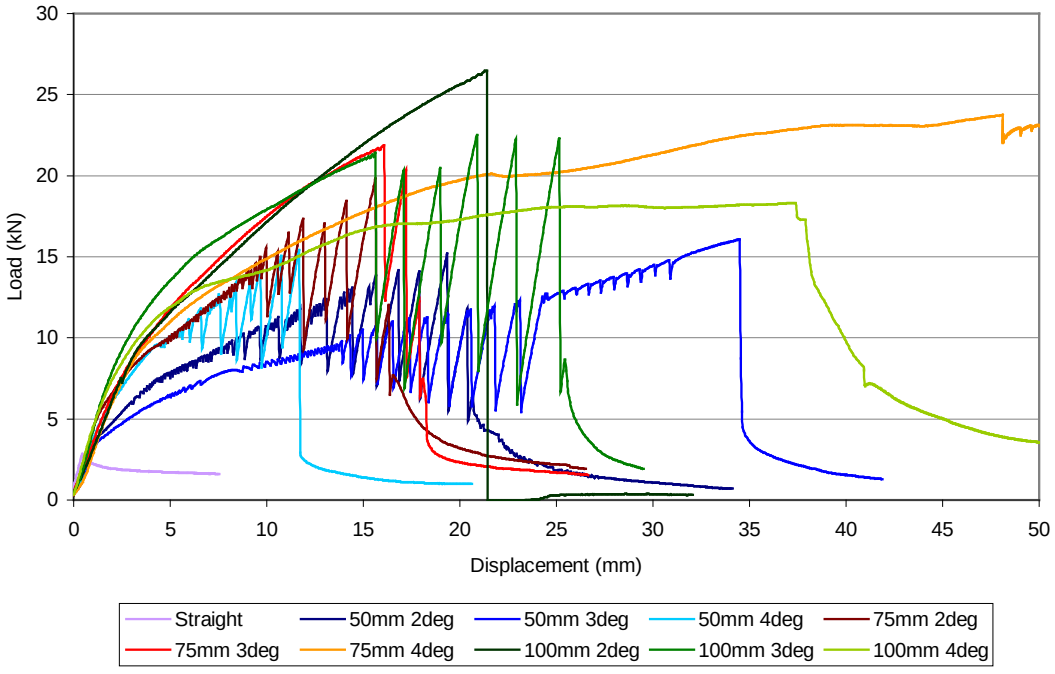

Figure 3.12. Unconfined coupon test results (Darby et al., 2007)

The helical confinement had negligible effect on the bond behavior of straight bars as indicated by the results obtained by Winkle (2005), which was not surprising since concrete splitting was not governing the bond failure. The combined wedge/helix anchorage method helped to prevent brittle failure of the surrounding concrete, while

exhibiting more ductile bond behaviour in terms of sustaining relatively high load for increased slip compared with unconfined concrete (*Figure 3.13*). However, it did not show any significant increase in the actual bond strength, as can be seen from the test curves for 100 mm 3° wedge with and without helix.

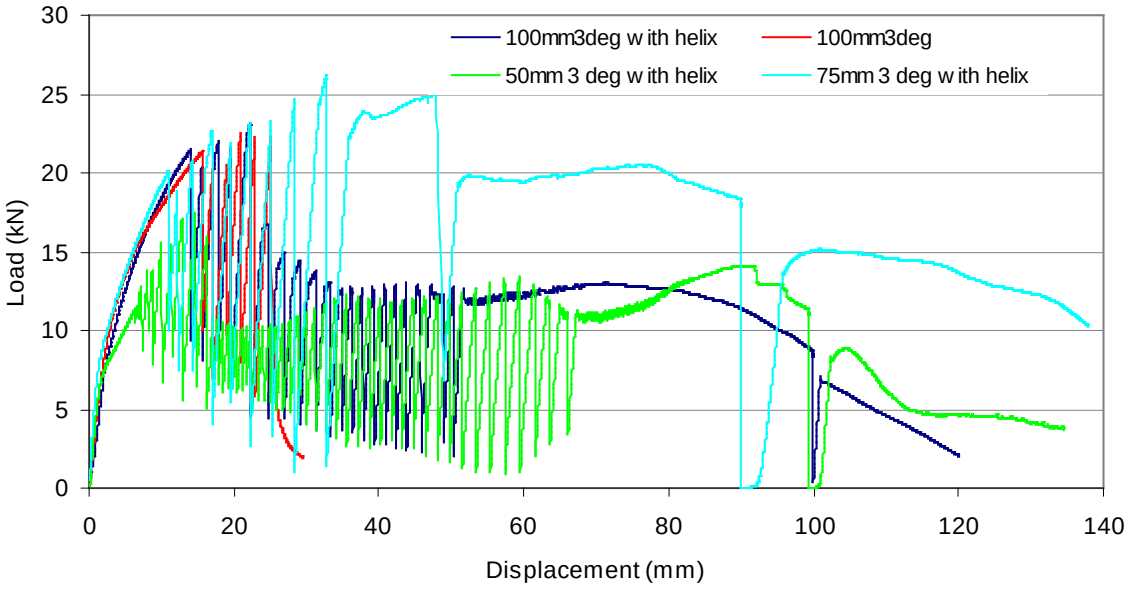

Figure 3.13. Confined coupon test results compared with unconfined concrete specimen (Darby et al., 2007)

The coupon pull-out tests were useful for demonstrating the efficacy of the proposed splayed anchorage method. A reasonable variation in the wedge geometry parameters was tested, providing a good initial assessment of their effect on the bond strength of the tested bars. However, the main drawback of these experiments was the lack of actual slip measurement. It was not possible to obtain the slip at each end of the bar needed for developing a practical analytical model. In addition, since concrete could not flow in the small wedge opening, using spacers to set the wedge angle may have resulted in geometrical inaccuracies, as well as in closing of the split ends during the pull out, as demonstrated by the experiments discussed next.

3.3.2. Improved wedge detail

Beam pull-out tests were conducted by Orr (2012) for circular 10 mm diameter CFRP sand-coated and braided bars in order to investigate further the splayed anchorage method. The adopted test set-up was similar to a cantilever beam, allowing for change in the depth of beam specimens along their length, as shown in *Figure 3.14*. Such arrangement could simulate better the behaviour of reinforcing bars in fabric-formed beams of varying section with decreasing depth near supports.

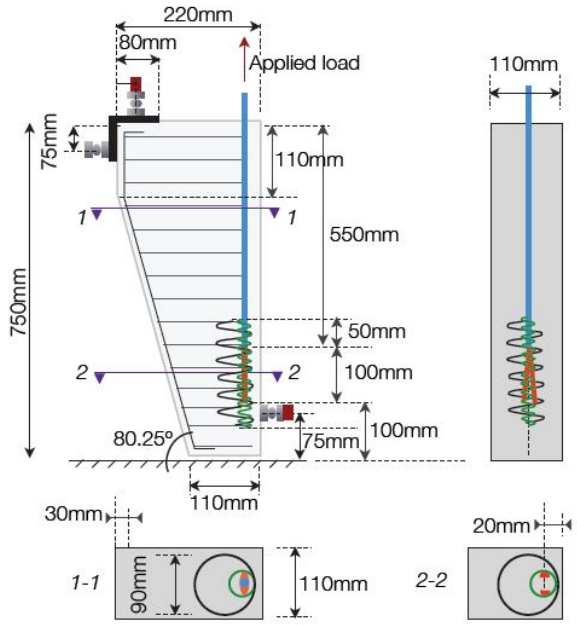

Figure 3.14. Beam pull out tests (Orr, 2012)

A post-mortem examination of the tested specimens revealed that the split ends were closed, which could have led to reduced wedging action (*Figure 3.15*). An improved 'fin splay' wedge detail was developed to achieve a more precise wedge dimension and ensure maintenance of the opening angle during the experiment. As illustrated in *Figure 3.16* the 'fin splay' comprised a triangular plate glued along the full length of the wedge.

Figure 3.15. Split bar ends closed at the end of a pull out test (Orr, 2012)

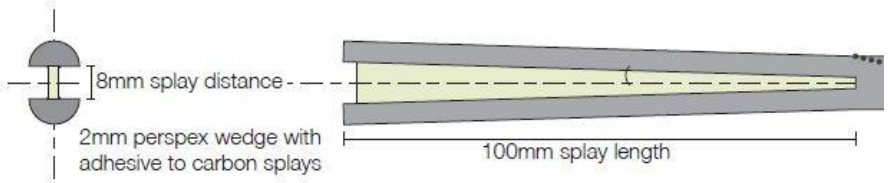

Figure 3.16. Improved 'fin splay' wedge detail (Orr, 2012)

The 'fin splay' tests, however, did not produce conclusive results because the bars failed by the grip of the machine jaws, significantly below their ultimate capacity (Orr, 2012). Furthermore, similarly to the coupon experiments, the slip at the free end of the test bar was not directly measured.

3.3.3. Fabric-formed beam tests

Two fabric formed beam tests have been carried out to compare the bond-slip behaviour of carbon FRP and steel splayed anchorage (Orr et al., 2010). The splayed ends were prepared as described in *Figure 3.17*, using glued carbon fibre plate for the FRP bar and a welded steel plate for the steel bar. Helical steel and aramid FRP reinforcement was added around the CFRP and steel splayed bars, respectively, to improve the splitting resistance of concrete. The two beams had identical geometry, shown in *Figure 3.18*.

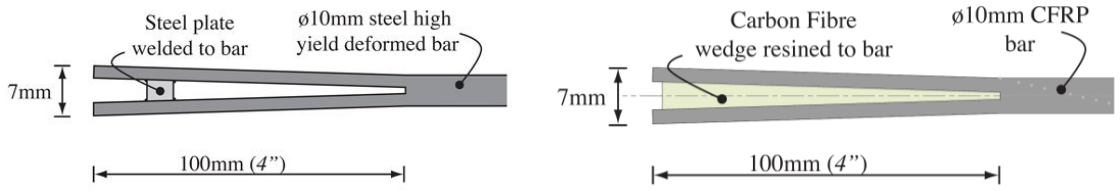

a. b.

Figure 3.17. 'Fin splay' detail for: (a) steel and (b) FRP bar (Orr et al., 2010)

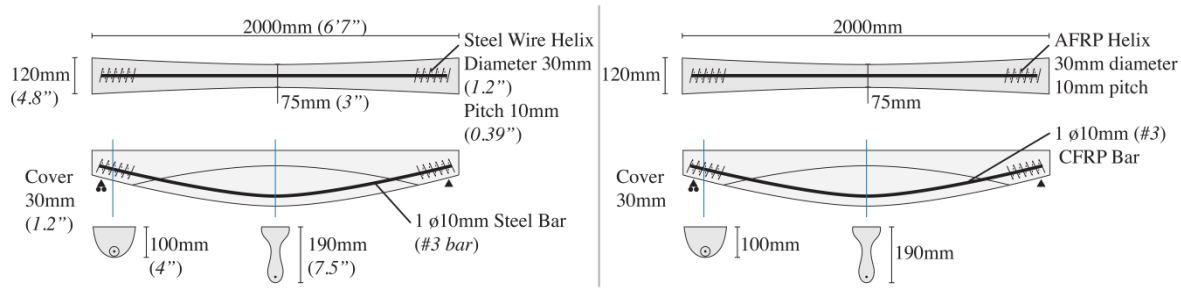

Figure 3.18. Fabric-formed beam tests containing splayed bars (Orr et al., 2010)

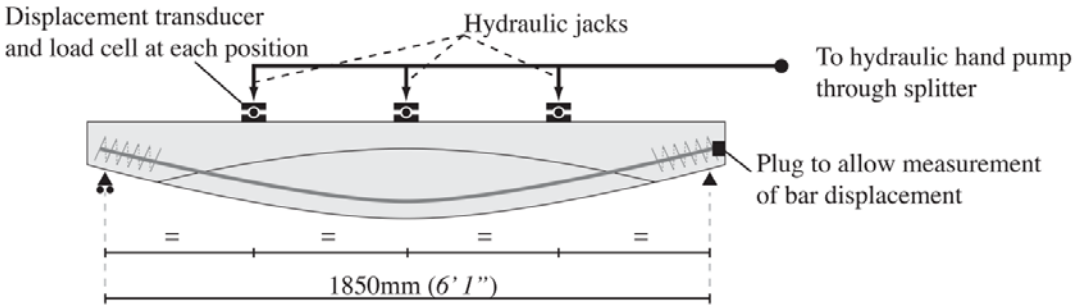

Figure 3.19. Fabric-formed beam tests set-up (Orr et al., 2010)

The fabric-formed beams were tested under five-point bending, as illustrated in *Figure 3.19*. Plugs were cast at the ends of the reinforcing bars to allow access for measurement of the final slip. Both beams failed at slip less than 1 mm. However, neither

the slip nor the force in the bar was monitored during the tests and a bond-slip relation was not established.

3.3.4. Conclusions

The previous research studies have demonstrated not only the feasibility of the splayed anchorage system but also its efficacy. However, the recorded data were insufficient to allow the development of a rigorous analytical model for the design of splayed bars. As discussed, monitoring of the bond-slip behaviour during load testing and applying high tensile force in the test bars were among the main challenges which need to be addressed in further experimental work.

3.4. Experimental programme

3.4.1. Choice of test method

The choice of test method for the new experimental programme, based on previous research findings, was influenced by the following requirements:

- a direct way of measuring the slip of the splayed end
- simulation of the real stress state of concrete in flexure
- avoiding local damage of FRP bars caused by clamping of the machine jaws

The standard hinged-beam bond test method in accordance with BS EN 10080:2005 was found to be most suitable for meeting all of the requirements (*Figure 3.20*). The hinged-beam comprises two reinforced concrete blocks, interconnected by the tested bar at the lower part of the cross section and a steel hinge at the top. The beam is loaded by simple flexure and the slip is measured at the two ends of the test bar, projecting beyond the beam ends. The mechanism for applying forces and supporting the beam specimen consists of steel rotating knife-edges or roller bearings. The beam dimensions and auxiliary reinforcement are standardised for various diameters of steel test bars.

The hinged-beam bond test has also been used for bond-slip measurement of straight FRP bars (Maji, 2005; Tighiouart et al.,1998). However, two major differences between testing straight bars and splayed anchorages should be considered. Firstly, the anchorage would be capable of resisting pull-out forces approaching the tensile strength of FRP bars and the applied vertical forces during the test would be much higher than those typical for the standard bond test, causing large rotations at the supports and high compressive stresses within the concrete around the steel hinges. Replacing the steel hinge with continuous steel bars could help to avoid high stress concentration in this case, while still

allowing sufficient rotation of the concrete blocks. Secondly, the ends of the tested bars have to be cast-in and, therefore, the slip should be measured inside specifically provided access gaps. In addition to these modifications, the force in the anchorage need to be accurately determined by strain gauges positioned near the splayed ends.

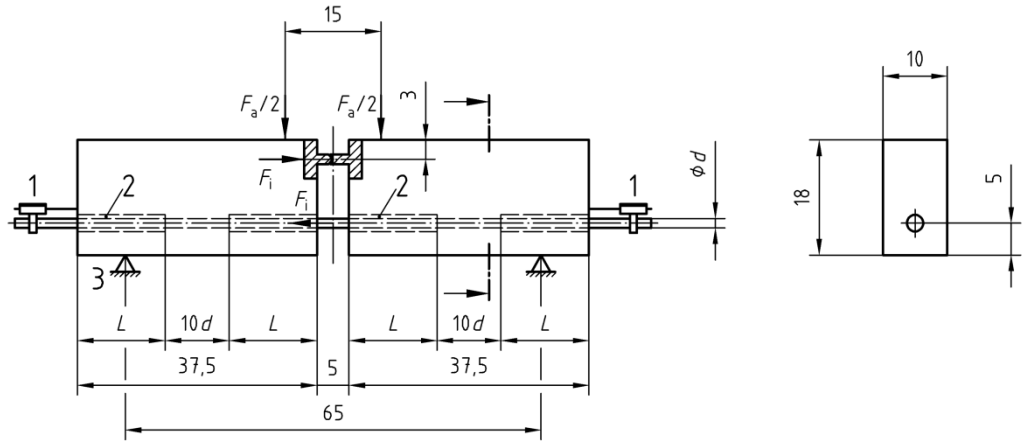

Key

1 slip measuring device
2 plastic sleeves
3 movable support

All dimensions in cm.

Figure 3.20. Standard hinged-beam test to BS EN 10080:2005

3.4.2. Test parameters

The factors influencing bond in concrete have been discussed in § 3.2. Additional parameters affecting the bond of splayed bars are the wedge length and angle. Furthermore, the tensile reinforcement in fabric formed elements will not be positioned horizontally and the inclination of the reinforcing bar presents another parameter to be investigated. The test matrix (*Table 3.1*) was designed to study the effect of the following seven parameters:

- Wedge length
- Wedge angle
- Reinforcement material (glass FRP, carbon FRP and steel)
- Reinforcement diameter
- Reinforcement surface treatment (smooth and sand-coated)
- Confinement of concrete by aramid FRP helices
- Inclination of the test bar

Selected combinations of wedge lengths and angles, used in the previous cube pull-out tests, were repeated to allow comparison between the new and the previous results. The effect of the wedge was isolated by the low friction of smooth bars in concrete. The wedge

angle was limited to 4° angle to avoid splitting of fibres, as previously studied by Tallis (2005). Three of the tests (Tests 9, 11 and 17), presented in *Table 3.1*, although still providing useful data, were repeated due to failed slip or strain measurements. Therefore, the repeat tests (Tests 10, 12 and 18) had the same parameters.

Table 3.1. Test matrix

Test ID	Wedge		Surface coating	AFRP helix	Concrete grade, MPa	Bar		Other
	Length, mm	Angle				Type	Dia, mm	
1	straight		smooth		40	glass FRP	10	
2	50	4°	smooth		40	glass FRP	10	
3	50 (+50)	4°	smooth		40	glass FRP	10	
4	100	2°	smooth		40	glass FRP	10	
5	100	4°	smooth		40	glass FRP	10	
6	straight		sand-coated		40	glass FRP	10	
7	100	4°	sand-coated		40	glass FRP	10	
8	100	4°	sand-coated	yes	40	glass FRP	10	
9	straight		smooth		40	glass FRP	12	
10	straight		smooth		40	glass FRP	12	
11	100	4°	smooth		40	glass FRP	12	
12	100	4°	smooth		40	glass FRP	12	
13	straight		sand-coated		40	glass FRP	12	
14	100	4°	sand-coated	yes	40	glass FRP	12	
15	straight		sand-coated		40	carbon FRP	12	
16	100	4°	sand-coated		40	carbon FRP	12	
17	100	4°	sand-coated	yes	40	carbon FRP	12	
18	100	4°	sand-coated	yes	40	carbon FRP	12	
19	100	4°	smooth		40	glass FRP	12	tapered
20	100	4°	sand-coated		40	glass FRP	10	tapered
21	100	4°	sand-coated		40	carbon FRP	12	tapered
22	straight		sand-coated		40	glass FRP	12	V-Rod
23	100	2°	sand-coated		40	glass FRP	12	V-Rod
24	100	4°	deformed	yes	40	steel	12	

Figure 3.21 shows the wedge details and the positions of strain gauges, used to determine the tensile forces in the anchored ends. Only the wedge length was assumed to be bonded in concrete, although Test 3 included partially a straight bonded length to study the combined effect. The final three tests contained V-Rod HM GFRP bars, which were used for the fabric-formed beam tests described in § 7, and a steel bar.

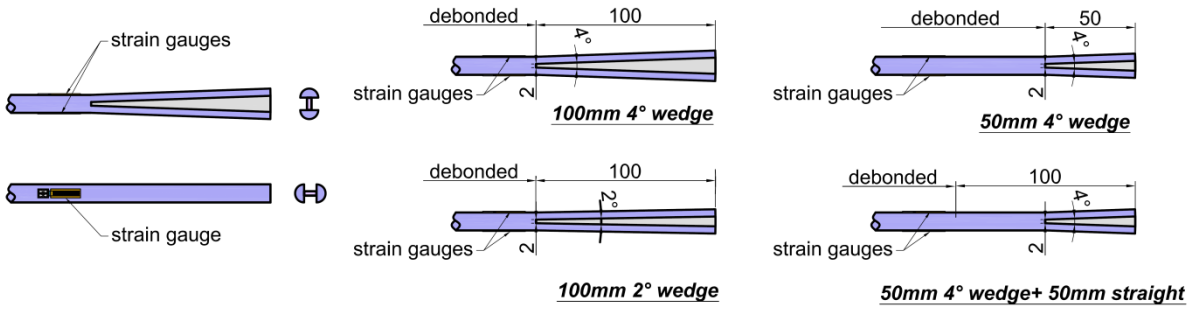

Figure 3.21. Wedge details

3.4.3. Preliminary test

A preliminary test was carried out to check the suitability of the test instrumentation and loading system, to assess the limits of the proposed test method and to consider further improvements. The preliminary test specimen was designed to allow high pull-out force and to reveal potential problems with the specimen behaviour or the measurement methods. For this purpose, the test bar was bonded along its full length in high grade concrete and anchored by the previously proposed maximum size confined wedge (100 mm 4°). The test set-up is illustrated in *Figure 3.22*, showing the position of the strain gauges on the test bars.

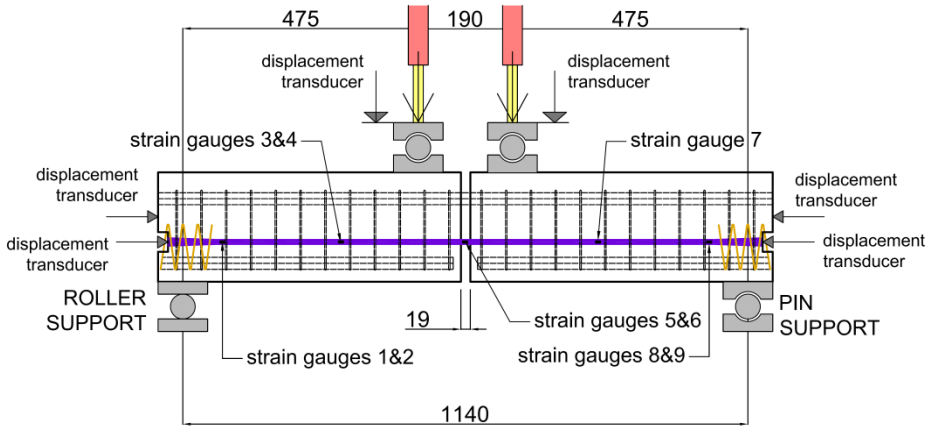

Figure 3.22. Preliminary test set-up (all dimensions are in millimetres)

The beam specimen was cast in a standard steel beam mould. The auxiliary reinforcement comprised 12 mm deformed steel bars and 3 mm smooth steel shear links, designed to resist the shear force and bending moment applied to the reinforced concrete blocks. A helical AFRP reinforcement of 90 mm diameter at 30 mm pitch, similar to the one used for the previous cube pull-out tests, was positioned in the anchorage zone over a length of 120 mm. The helix was manually produced by winding aramid fibre tow impregnated with resin. *Figure 3.23* shows the test beams cross section and

reinforcement details. The concrete used for the preliminary test beam was a laboratory designed C50/60 grade mix (water 234 l/m^3, Portland-fly ash cement CEM II/B-V 32.5 721 kg/m^3, fine sand 145 kg/m^3, fine (0-5 mm) aggregates 650 kg/m^3, coarse (5-10 mm) aggregates 650 kg/m^3 and plasticiser 1 l/m^3). The compressive cube strength at testing was 52.8 MPa.

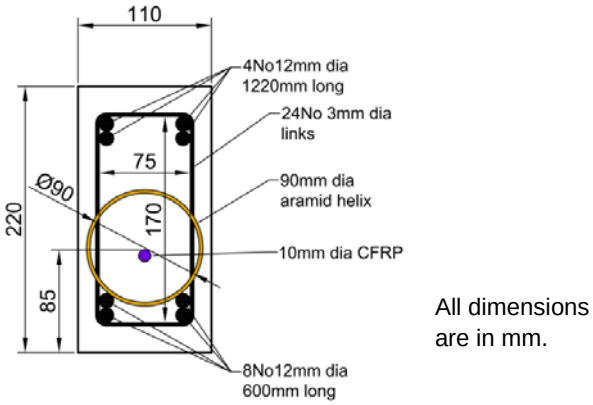

Figure 3.23. Preliminary test hinged-beam cross section

The test bar was CFRP CARBOPREE 10 mm diameter, containing carbon fibres impregnated with vinyl ester resin and surface-coated with quartz sand. It had tensile strength of 2300 MPa, modulus of elasticity of 130 GPa, ultimate load of 180 kN and ultimate deformation of 1.8%, as provided by the manufacturer. The elastic modulus of the CFRP bar was additionally tested by direct tension, using strain gauges to determine the strain in the bar. The bar failed prematurely due to interlaminar shear caused by clamping of the ends, however, the recorded data shown in *Figure 3.24*, were sufficient to confirm the manufacturer's data sheet value. The triangular wedge plate was cut out from 2 mm CFRP strip and glued with Araldite. The wedge preparation process is described in *Figure 3.25*.

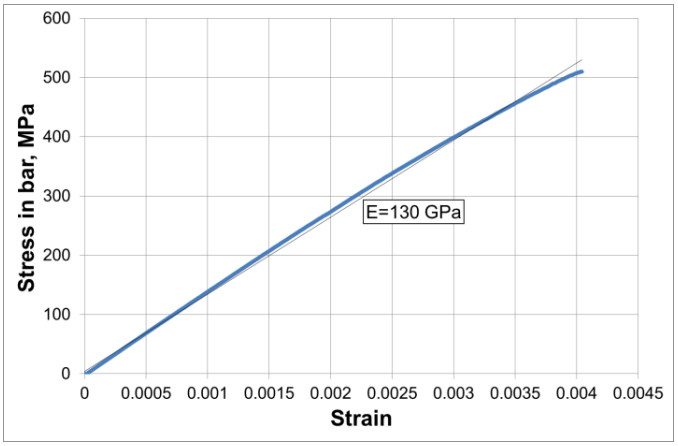

Figure 3.24. Stress-strain curve for 10 mm CARBOPREE bar

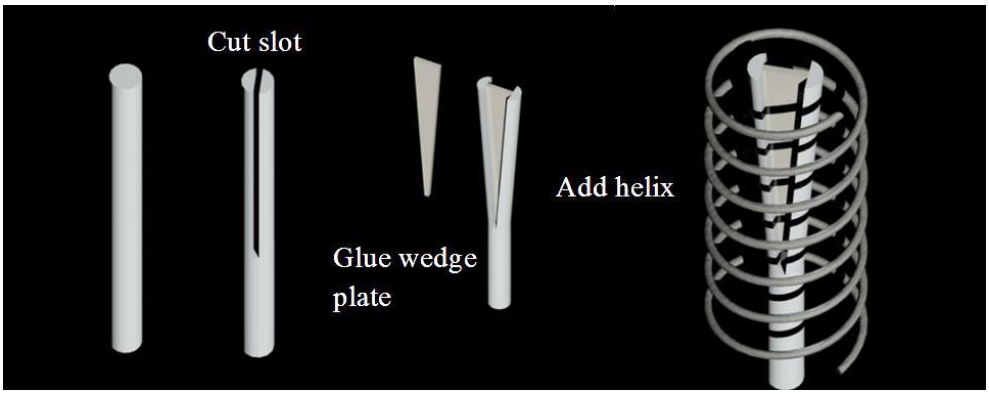

Figure 3.25. Wedge preparation procedure

The initially adopted approach for measurement of slip as a relative horizontal displacement of the test bar end and the concrete face can be seen in *Figure 3.26*. *Figure 3.27* shows the beam rotation, immediately before a sudden loss of the roller support, caused by excessive rotation. However, at that stage splitting cracks in the concrete were already present in the left anchorage zone, while the test bar had failed by interlaminar shear.

Figure 3.26. Preliminary hinged-beam test – measurement of slip

Figure 3.27. Preliminary hinged-beam failures

The measurement of slip was unsuccessful due to the large rotations, and force-slip plots could not be obtained. However, the results presented in *Figure 3.28* provided useful information regarding the maximum vertical loads and deflections that could be expected during the future hinged-beam tests. It was attempted to predict the force at the middle of the bar, as shown in *Figure 3.28*, based on the lever arm between the test bar and the steel bars in compression, after taking into account the moment resisted by the steel bars

prior to yielding. Although, the comparison with the test data from strain gauges 5 and 6 shows relatively accurate results up to 60 kN, the force in the test bar is overestimated for higher loads. This may be due to local damage of concrete and change of the lever arm. Therefore, the analytical prediction of the forces in the test bars had to be refined. However, due to the significant difference between the tensile force at the middle of the bar and near the splayed anchorages, it was concluded that the experimental results would be highly dependent on the strain gauge readings, and the use of a minimum of two gauges near the anchored ends was considered necessary for the main experimentation.

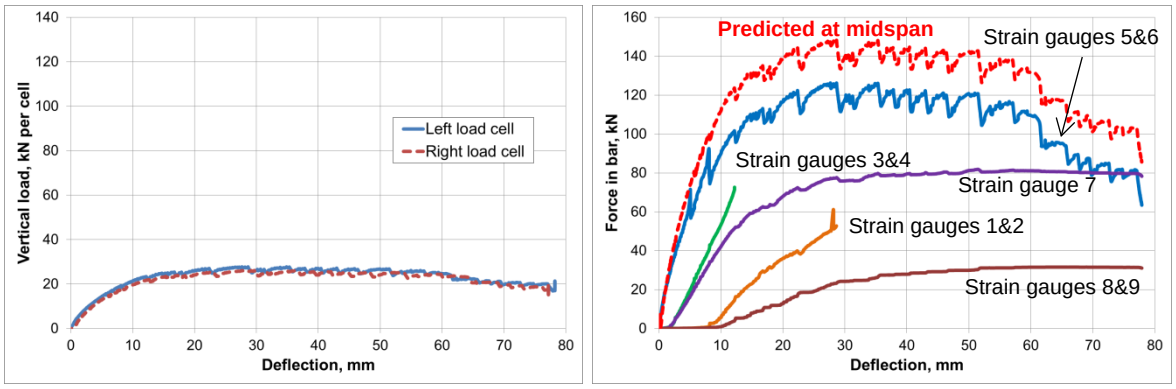

a. b.

Figure 3.28. Preliminary hinged-beam test: (a) vertical load-deflection curves and (b) force in bar-deflection curves.

The main problems to be resolved after the preliminary test included:

- The method used for supporting the beam and applying the loads was not adequate. The loading pins rotated and moved longitudinally, while the left support failed due to excessive rotation.
- The method used for measurement of the slip was not reliable and needed to be adjusted to measure the slip in the direction of the rotated beam end.
- The test bar was subject to high concentrated transverse forces at the internal faces of the concrete blocks in the middle, causing interlaminar shear failure. Therefore, sharp bends had to be avoided in order to reduce premature failure of the FRP test bars.
- The concrete mix was very stiff and difficult to compact in the anchorage zones where the helical reinforcement was placed. Therefore, design of concrete mix with improved workability was needed.
- The foil-epoxy strain gauges were found to be reliable only up to 8000 με or 0.8%, which would not be adequate for testing glass FRP with ultimate strain capacity above 1.5%. Therefore, post-yield gauges were required in order to measure higher strains.

An improved hinged-beam set-up, illustrated in *Figure 3.29*, was considered. Soft polystyrene wedges, placed over the test bar at the two sides of gap in the middle, were expected to reduce the risk of premature failure of FRP bars, caused by interlaminar shear. It was also proposed to ensure failure at one end only by debonding half of the test bar length. This could allow measurement of greater slip for the same rotation at the beam supports.

Figure 3.30 shows the new welded loading pins and non-movable cylindrical supports used for the further tests. It was also decided to use a single horizontal transducer, attached to the beam end face, for slip measurement in the direction of the moving bar. The timber plugs were replaced by polystyrene blocks attached directly to the wedge, thereby ensuring more accurate position of the access hole.

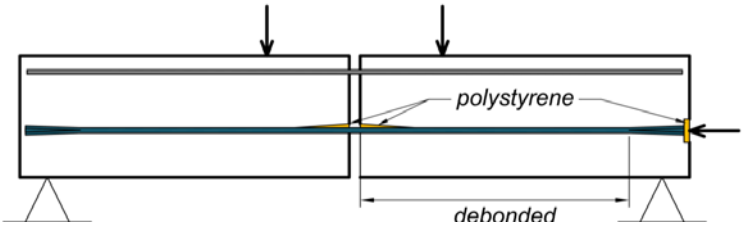

Figure 3.29. Improved hinged-beam set-up

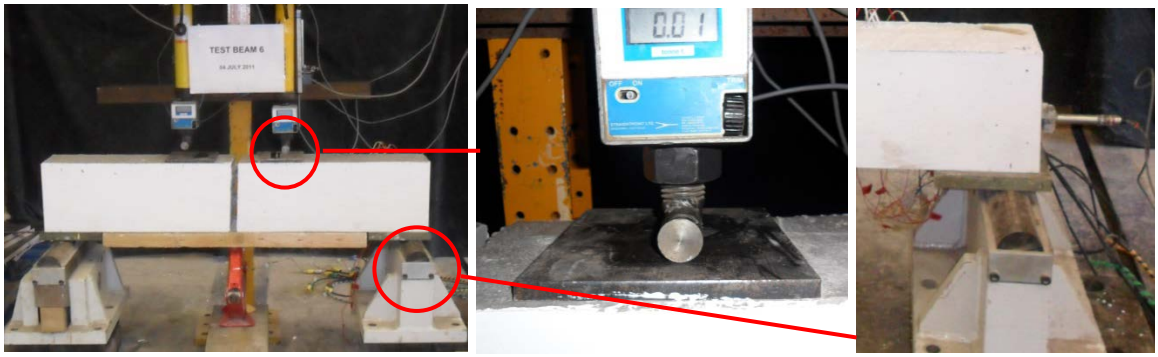

Figure 3.30. Change of loading pins and beam supports

3.4.4. Design of experiments

3.4.4.1. Materials

The concrete mix design was carried out in accordance with the recommendation given in Teychenné et al. (1997) for grade C40/50. Trial mixes were also produced to assess the fresh concrete workability and the development of early concrete strength. The design mix proportions are given in *Table 3.2*. Furthermore, in order to improve the workability of the mix 3 l/m^3 of plasticiser was added.

Table 3.2. Concrete mix proportions

Water	Cement	W/C ratio	Fine aggregates	Coarse aggregates
190 l/m^3	422 kg/m^3	0.45	800 kg/m^3	980 kg/m^3

The binder was Portland cement CEM II/B-V 32.5. Crushed limestone 4/10 mm (*Table 3.3)* was used as a coarse aggregate, while the fine aggregates consisted of 25% fine sand and 75% Marlborough grit. The maximum aggregate size was limited by the dense reinforcement details, including steel shear links, helices and three layers of longitudinal reinforcement near the specimens' ends.

Table 3.3. Characteristics of aggregates

	Crushed limestone	Marlborough grit	Fine sand
Type	carboniferous	carboniferous	alluvial
Size	4/10 mm	0/4 mm	0/0.5 mm
Shape	angular	flaky	flaky
Surface texture	rough	smooth	smooth
Specific gravity	2.7	2.65	2.65
Water absorption	0.6	0.6	0.6

The recorded development of compressive strength, shown in *Figure 3.31*, was used to define a suitable age of the concrete specimens for testing. As indicated, the 40 MPa cube strength was reached after 11 days.

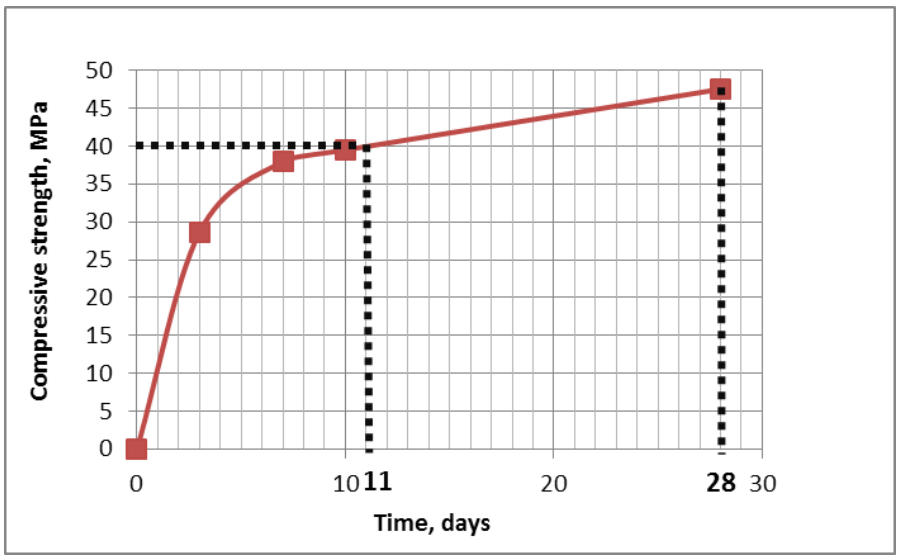

Figure 3.31. Compressive cube strength of concrete trial mixes

The hinged-beam specimens were cast in separate concrete batches. The compressive cube strength and cylinder tensile splitting strength were tested in accordance with BS EN 12390-3:2009-3 for 100 mm cubes and BS EN 12390-3:2009-6 for 100 mm x 200 mm cylinders, respectively. The compressive strength was monitored during the first days after casting to ensure the concrete quality and consistency of strength development for the different batches. *Table 3.4* presents the average concrete strengths reached at the time of testing, indicating deviation from the target compressive strength within +/-5 MPa.

Table 3.4. Concrete strengths

Test ID	Cement type	Concrete strength, MPa		
		Compressive (design)	Compressive (at testing)	Tensile (at testing)
1	PC	40	38.0	2.65
2	PC	40	35.6	3.27
3	PC	40	46.1	3.82
4	PC	40	46.1	3.07
5	PC	40	42.3	2.62
6	PC	40	36.3	3.01
7	PC	40	42.1	2.83
8	PC	40	41.1	2.23
9	PC	40	48.7	2.41
10	PC	40	39.7	3.56
11	PC	40	40.8	3.21
12	PC	40	38.6	3.11
13	PC	40	39.6	2.17
14	PC	40	37.4	2.54
15	PC	40	37.2	2.32
16	PC	40	40.1	2.31
17	PC	40	42.7	2.73
18	PC	40	41.4	3.18
19	PC	40	42.3	3.18
20	PC	40	38.4	3.26
21	PC	40	40.3	2.29
22	PC	40	43.8	N/A
23	PC	40	40.6	N/A
24	PC	40	39.9	2.43

The experiments covered three types of FRP bars. These included 10 mm and 12 mm smooth glass FRP, and 12 mm sand-coated braided carbon FRP. The 10 mm glass FRP bars, supplied by Engineered Composites Ltd (Engineered Composites), were chosen to study the effect of the wedge length and wedge angle in order to obtain results comparable with the previous cube pull-out tests. The 12 mm glass and carbon FRP bars were supplied by Sireg S.p.A. (Sireg, 2011) and the 12 mm V-Rod HM bars were produced by Pultrall Inc (Pultrall, 2011). The manufacturer's characteristics of the test

bars are presented in *Table 3.5*. In addition, a 12 mm steel bar was used to demonstrate that the technique can be successfully applied to steel bars. All bars were tested under cyclic loading to confirm their modulus of elasticity (*Figure 3.32*), which was then used to calculate the forces in test bars based on the measured strains. The sand-coating of glass FRP bars was produced manually using resin (Aradur 5052), as shown in *Figure 3.33*. The fully bonded side of all GFRP bars was also sand-coated to ensure failure only at the instrumented end.

Table 3.5. Test bars for hinged-beam tests

Nominal diameter	**10 mm**	**12 mm**	**12 mm**	**12 mm**	**12 mm**
Material	glass	glass	carbon	steel	glass
Tensile strength, MPa	550	750	2300	500	1312
Nominal cross-sectional area, mm^2	71.3	127	113	113	127
Modulus of elasticity, Gpa	30	40	130	200	63÷68
Tensile strain, %	>3	>3	1.8	-	2
Surface treatment	smooth	smooth	sand	ribbed	sand

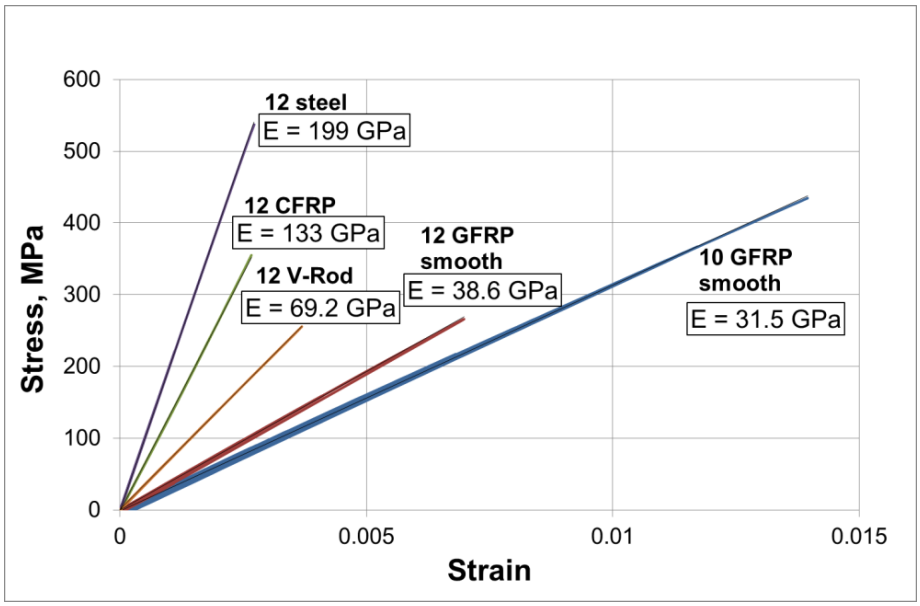

Figure 3.32. Stress-strain curves of test bars

Figure 3.33. Manual sand-coating of smooth splayed GFRP bars

Similarly to the previous experiments of combined wedge/helix anchorage described in § 3.3, helical reinforcement was used to confine the concrete in the anchorage zone. It was made of Parafil rope (Kevlar 49), containing 24 aramid yarns, manually impregnated with resin (Aradur 5052). The fibres, while freshly soaked, were wound onto a plastic tube of 90 mm diameter at 30 mm pitch, as shown in *Figure 3.34*. The hardened helices were then cut into lengths of 120 mm and positioned symmetrically around the splayed ends.

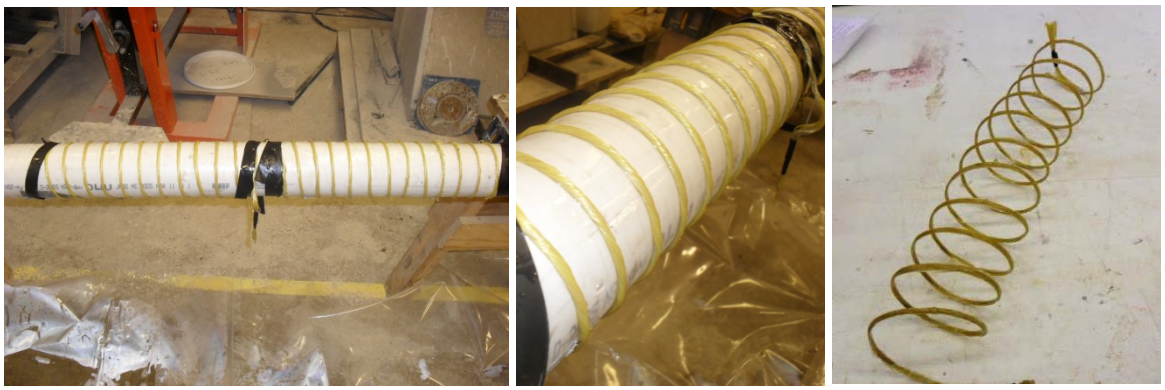

Figure 3.34. Helical AFRP reinforcement

A wet cutting disk saw was used to create slots in the ends of the FRP bars, parallel to the fibres (see *Figure 3.35*). The process was easy and could have been done manually. In a similar manner, wedge plates were cut from 2 mm x 10 mm carbon fibre strips.

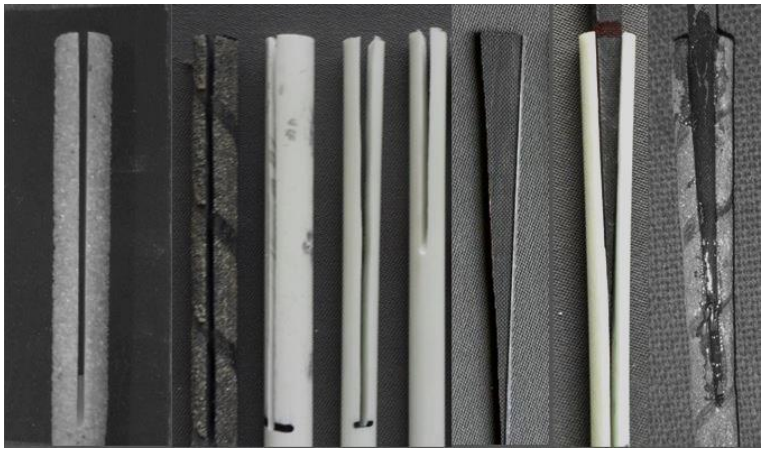

Figure 3.35. Split FRP bars and wedge plates

Two types of resin were used to glue the wedges to the test bars. *Figure 3.36a* shows the preparation of wedges using thick resin grout Sikadur-32, which was able to fully fill the openings, creating an oblong shape, shown in *Figure 3.37a*. However, the thick resin required a longer time to set. An alternative fast-setting Araldite or Aradur 5052 resin was also used (see *Figure 3.36b* and *Figure 3.37b*). The manual sand-coating of smooth bars was done after the plate was fixed inside the slot using Sikadur-32, as illustrated in *Figure 3.37c*, which resulted in a third type of wedge, having uniform surface characteristics along its perimeter. The preparation of the steel wedge, shown in

Figure 3.38, was less practical and, therefore, only a single demonstration test was carried out.

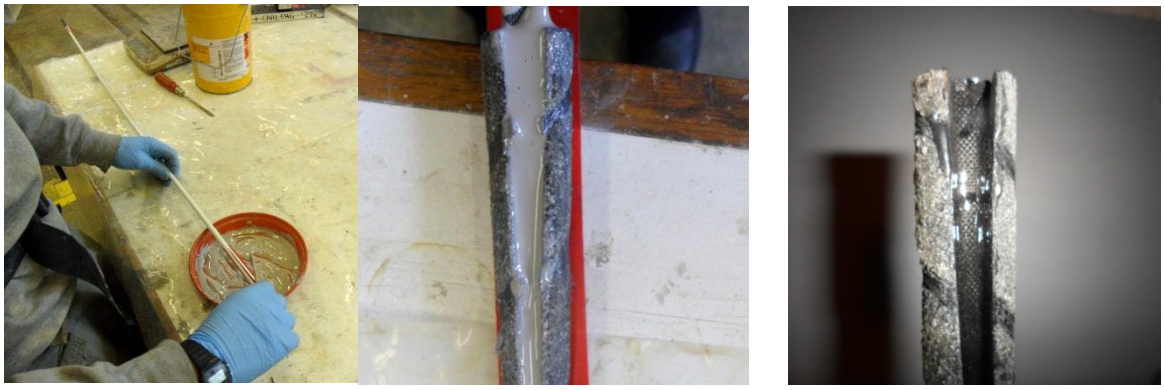

a. b.

Figure 3.36. Fixing carbon plate with: (a) Sikadur-32 and (b) Araldite or Aradur 5052

a. b. c.

Figure 3.37. Wedge types: (a) glued using Sikadur-32, (b) glued using Araldite/Aradur 5052 and (c) fully sand-coated over Sikadur-32

Figure 3.38. Steel bar wedge filled with welding material

3.4.4.2. Design of test specimens

As described in § 3.4.1, the hinged-beam specimens consisted of two reinforced concrete blocks connected by compression steel reinforcement near the top and the single test bar near the bottom. In addition to the standard constant depth beam, a tapered hinged-beam was designed to investigate the effect of anchoring reinforcing bars at an angle in fabric-formed elements of varying depth. The beams were loaded by four-point bending, indicated in *Figure 3.39*, in accordance with the standard hinged-beam test to BS EN

10080:2005. Auxiliary steel reinforcement was designed for the bending moment and shear force effects due to the vertical load, $2F$.

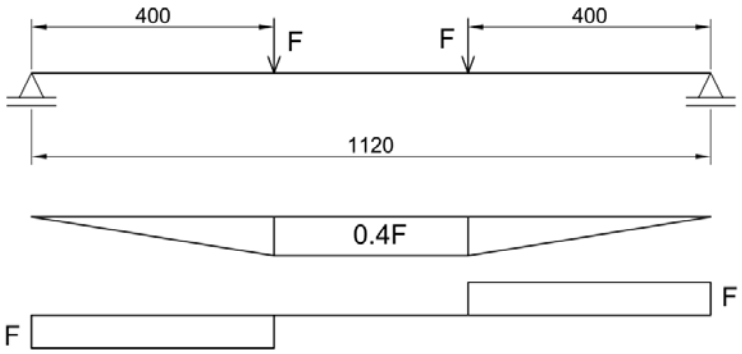

Figure 3.39.Applied loads and load effects (all dimensions are in mm)

All auxiliary steel reinforcement was sized according to the capacity of the tensile test bar. The tensile strengths of the different test bars are summarised in *Table 3.6*. The test bending moment was calculated assuming a lever arm equal to the distance between the centres of the top steel bar and the test bar. An allowance for the losses due to the bending moment of resistance of the top bars, prior to yielding, was made based on maximum yield strength of 650 MPa, confirmed by previous testing. The diameter of the top bars for all hinged beams containing GFRP or steel test bars was 16 mm, while 20 mm diameter top bars were provided for the test beams containing CFRP bars. In addition, the final vertical force, F, was limited by the capacity of the testing rig in the case of CFRP test bars. However, the theoretically predicted force in the bars would still reach almost 60% of their ultimate tensile strength, which was considered adequate for the purpose of the current investigation.

Table 3.6. Design loads

Test bar	Tensile strength, kN	Test bending moment, kNm	Applied force F before losses, kN	Applied force F after losses, kN
10 GFRP	40	4.68	11.7	14.2
12 GFRP	110	12.9	32.2	34.7
12 CFRP	260 (150*)	29.3 (17.6*)	73.1 (44.9*)	78.1 (48.9*)
12 Steel	57	6.67	16.7	19.2

* Reduced force based on capacity of the testing rig of 100 kN.

The geometry and reinforcement arrangement for the two types of hinged-beam specimens are presented in *Figure 3.40* and *Figure 3.41*. Both specimen types had the same width of 170 mm, and the test bar position was maintained at the same height from the bottom surface throughout all experiments (*Figure 3.42*).

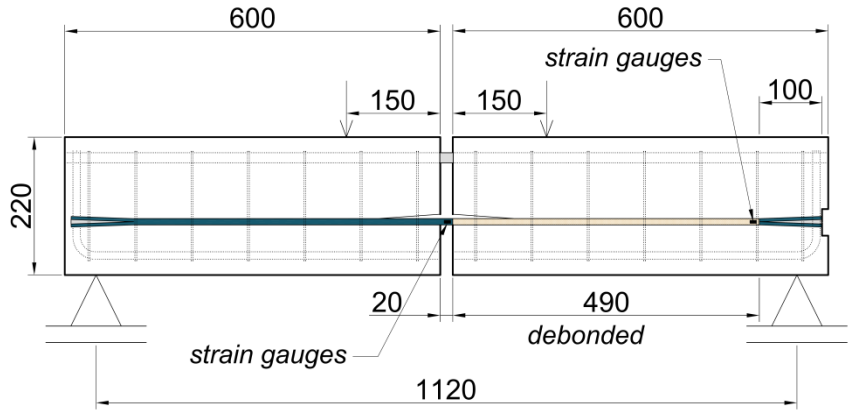

Figure 3.40. Rectangular hinged-beam specimen (all dimensions are in mm)

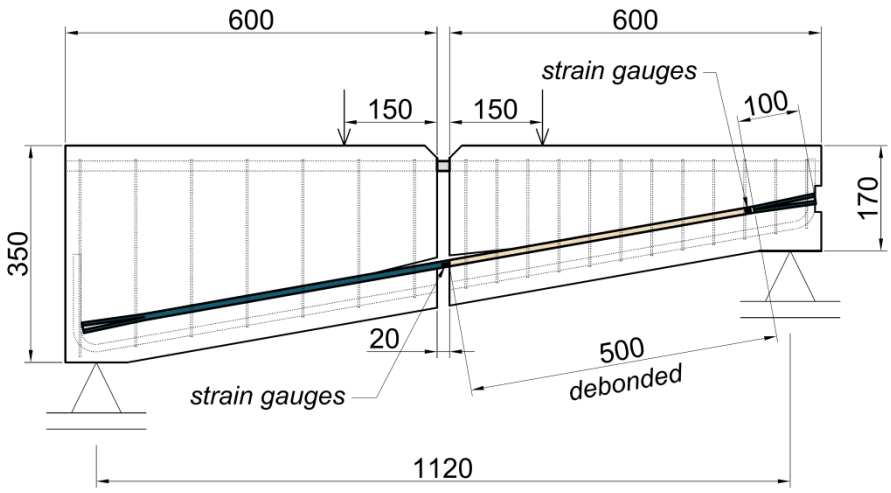

Figure 3.41. Tapered hinged-beam specimen (all dimensions are in mm)

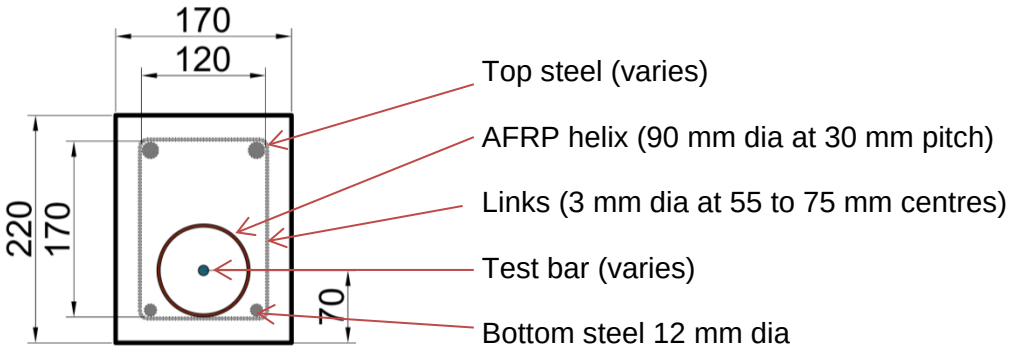

Figure 3.42. Constant hinged-beam cross section (all dimensions are in mm)

3.4.5. Construction of test specimens

The hinged-beam specimens were cast in specially produced moulds, made of high quality phenolic plywood, suitable for repeated use (*Figure 3.43*). The two halves of each beam were separated by a 20 mm polystyrene block. Polystyrene 100 mm 4° wedges were cast on the top of the test bars in the middle, as shown in *Figure 3.44*. The position of the test bar was additionally secured by plastic wire tied to the steel cage. The polystyrene end plugs were attached to the test bars (*Figure 3.45*), and then fixed to the sides of the formwork by pins pushed through holes pre-drilled in the plywood.

Figure 3.43. Hinged-beam formwork

Figure 3.44. Hinged-beam reinforcement cages

Figure 3.45. Hinged-beam end details

3.5. Test results

The presented results are based on the following recorded test data: vertical loads, vertical displacements at points of force application, slip of test bars at the instrumented end and strains in the test bars. The photographs in *Figure 3.46* illustrate the typical test set-up and instrumentation. All wedges were oriented as shown in *Figure 3.47*, and the slip was measured by a displacement transducer, positioned at the exposed end.

Two types of strain gauges were used, general purpose foil-epoxy gauges FLA-10-11 and foil-plastic YFLA-10-11 large strain (15-20%) post-yield gauges. The post-yield gauges were used mostly near the anchored ends and were able to record strains of up to 1.5% prior to their failure. Two gauges were placed on the sides of each bar near the tested wedge end, outside the bonded area, and, in some cases, a third gauge was positioned on the top or bottom side of the bar. However, the measurements of the third gauge were useful only at very low strains in the bars and, therefore, it was omitted for the later tests. In addition, control strain measurements were taken at the middle of the tested bars. They were used to enhance the confidence in the strain gauge readings by comparison with theoretically predicted values, as described in Appendix A.

The test results, based on the strain measurements near the bonded wedges, provided useful data for modelling the bond-slip behaviour of the different splayed bars. However, a number of FRP test bars failed by rupture of the extreme tensile fibres, due to excessive bending (*Figure 3.48*), without any visible damage of the surrounding concrete and, therefore, the final anchorage resistance could not be determined. Furthermore, the test results were often limited by premature failure of the strain gauges caused by movement of the bars inside concrete. Three tests were repeated due to bad readings of strain gauges or unsuccessful measurement of end slip.

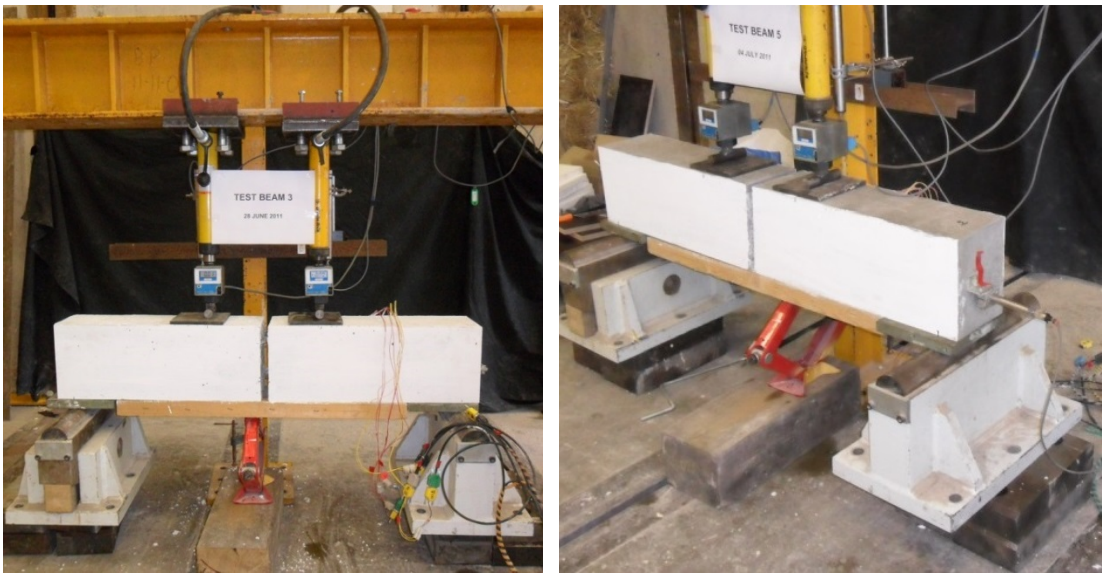

Figure 3.46. Hinged-beam test set-up for main experiments

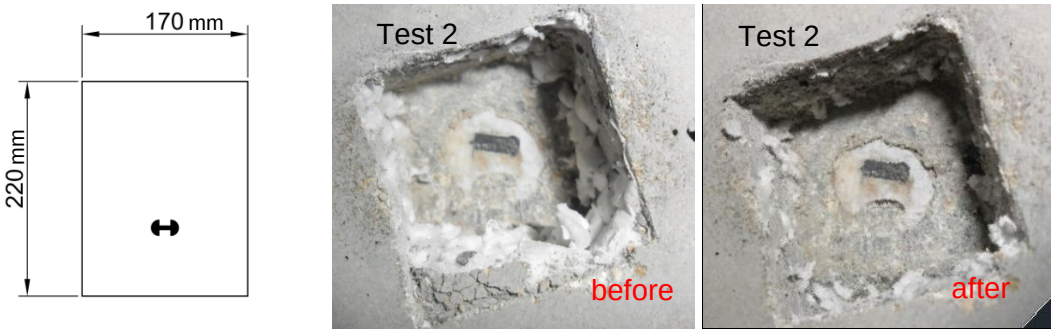

Figure 3.47. Orientation of wedge and exposed ends before and after testing

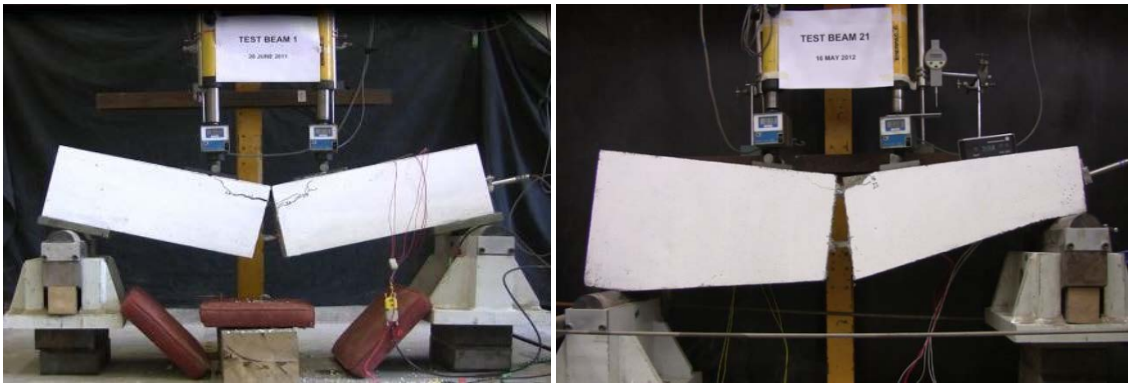

Figure 3.48. Typical rotation of the hinged beams during testing

3.5.1. Grouping of test results

The test results are summarised in *Table 3.7* for each specimen defined in the test matrix (*Table 3.1*). The maximum anchorage forces, presented in the table, were calculated from the average strains, measured near the bonded splayed ends. The maximum forces are then expressed as a percentage of the tensile capacity for each test bar. However, as pointed out these forces do not necessarily represent the maximum anchorage resistance due to premature gauge or bar failure. They simply indicate the minimum recorded anchorage strength.

Table 3.7. Hinged-beam test results

Test ID	Group	Failure type	Number of strain gauges	Maximum measured force, kN	Slip at maximum force, mm	% of tensile capacity, kN
1	I	pull out	3	2.92	0.732	7.5*
2	I	bar	3	15.4	0.127	39.6
3	I	bar	3	14.1	0.258	36.2
4	I	bar	3	25	0.616	64.1
5	I	bar	3	27.7	0.384	70.9
6	II	bar	2	24.2	0	62.1*
7	II	bar	3	25	0	64.1
8	II	bar	3	26.7	0	68.5
9	III	pull out	2	N/A	N/A	N/A*
10	III	pull out	2	5	2.2	4.5*
11	III	concrete/bar	2	64	4.5	58.2
12	III	concrete	2	71	6.6	64.5
13	IV	pull out	2	53.5	0.329	48.6*
14	IV	bar	3	78	0.067	70.6
15	V	pull out	2	25.9	0.474	10.4*
16	V	concrete	2	67.5	5.63	27
17	V	concrete	2	100	9.4	40
18	V	concrete	2	69.5	2.77	27.8
19	VI	bar	2	67	2.78	60.9
20	VI	concrete	2	60	10	24
21	VI	bar	3	25	0	64.1
22	VII	pull out	2	N/A	0	N/A*
23	VII	pull out	2	88.2	N/A	53
24	VIII	bar	2	37.6	0.06	66.5

*straight bar reference test

As can be seen from *Table 3.7*, three types of failure were observed. Pull-out failure without any damage to concrete or tested bar was typical for the reference tests of straight bars, while the splayed bar tests would generally fail by rupture of the reinforcing bar and/or tensile splitting of concrete in the anchorage zone. However, the end of the tests was mainly controlled by large rotations at the supports, which resulted in horizontal

forces acting on the hydraulic jacks. For this reason, in order to prevent damage to the loading mechanism, Test 23 was terminated prematurely. No indication of bond failure of the fully bonded hinged-beam side was present.

The test results for FRP bars can be divided into seven groups, as indicated in *Table 3.7*, according to the specific failure type and/or the effects they demonstrate, as follows:

I. **10 mm smooth GFRP bars**

This group demonstrates the effect of wedge geometry. It is characterised by failure of the test bars due to interlaminar shear. No splitting failure of concrete was observed.

II. **10 mm sand-coated GFRP bars**

This group is also characterised by failure of the test bars due to interlaminar shear. However, no slip occurred during the experiments and bond-slip relations were not recorded.

III. **12 mm smooth GFRP bars**

This group demonstrates the effect of bar size. During the experiments, splitting failure of concrete was reached before or at the same time as rupture of FRP bars.

IV. **12 mm sand-coated GFRP bars**

This group demonstrates the effect of surface treatment. Tensile failure of the FRP bar was reached without visual damage of concrete.

V. **12 mm braided sand-coated CFRP bars**

This group also demonstrates the effect of surface treatment. However, in this case splitting failure of concrete occurred before rupture of FRP bars.

VI. **Tapered beams**

This group demonstrates the effect of inclined bars for different types of FRP bars.

VII. **12 mm sand-coated V-Rod GFRP bars**

This group mainly demonstrates the effect of surface treatment. Furthermore, it demonstrates how splayed anchorage could alter the brittle failure of straight sand-coated bars.

3.5.2. Test results for 10 mm GFRP bars

The two groups comprising 10 mm GFRP bars are presented in *Table 3.8* and *Table 3.9*.

Table 3.8. Test results Group I (smooth surface)

Test 1	straight
Test 2	50 mm 4° wedge
Test 3	50 mm 4° wedge + 50 mm straight length
Test 4	100 mm 2° wedge
Test 5	100 mm 4° wedge

Table 3.9. Test results Group II (sand-coated surface)

Test 6	straight
Test 7	100 mm 4° wedge (unconfined)
Test 8	100 mm 4° wedge (confined)

Only the wedge length was assumed to be bonded in concrete, although Test 3 included partially a straight bonded length to study the combined effect. However, most likely due to the very low-bond characteristics of smooth bars, no significant difference with the results of Test 2 was observed. Failure type by rupture of the FRP bars and similar vertical load-deflection behaviour was observed for all tests with splayed bars, as *Figure 3.49* suggests, where *F* is the vertical force applied on the instrumented side of a specimen, plotted against the corresponding vertical deflection at the same point. The ultimate capacity of Test beam 2 and Test beam 3 was slightly lower compared with other splayed anchorage specimens; however it was still significantly higher than the maximum vertical load reached for the straight smooth bar.

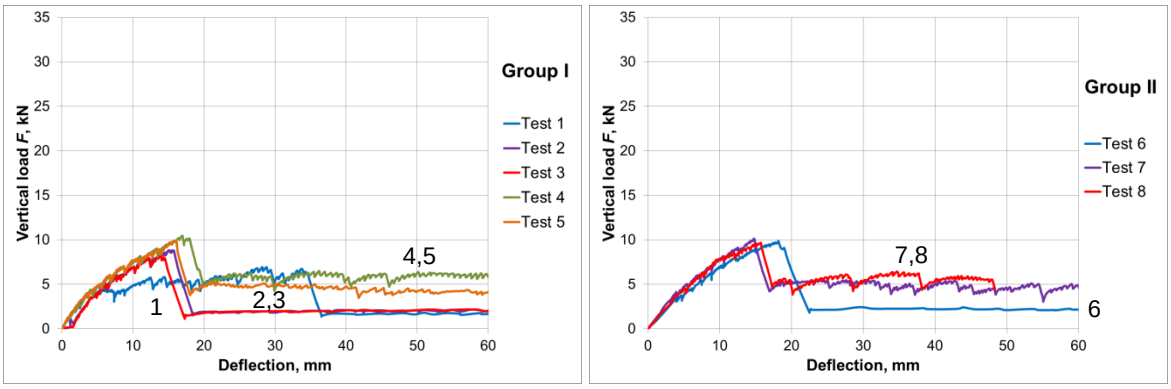

Figure 3.49. Vertical load-deflection curves (10 mm GFRP bars)

The force-deflection curves show the influence of wedge geometry on the slope of the curves for Group I, while the bars in Group II failed without recording any slip (see *Figure 3.50)*. The response for smooth 100 mm 4° wedge is identical to the 'no slip' tests, indicating that this wedge size is adequate for this type of bars.

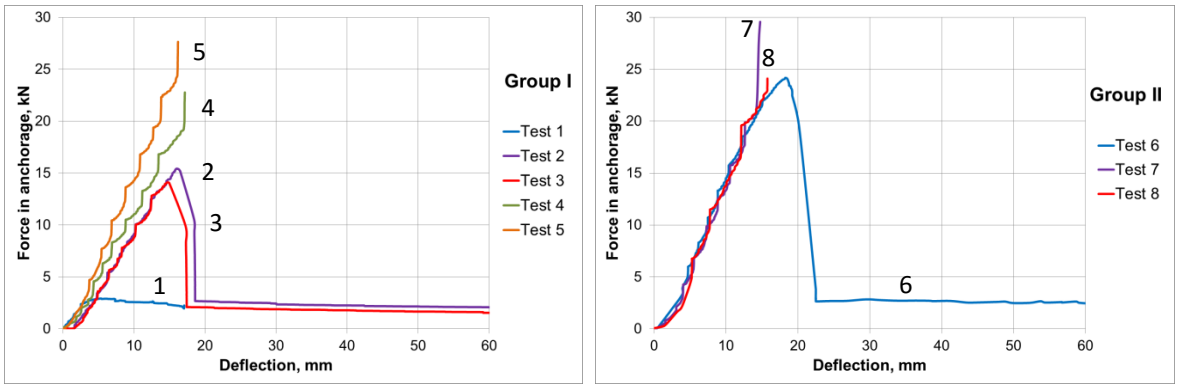

Figure 3.50. Force-deflection curves (10 mm GFRP bars)

The tests with sand-coated bars successfully demonstrated 'no-slip' behaviour of splayed anchorage. However, the force measured in the FRP bars before failure was below the expected ultimate tensile capacity of 39 kN. As can be seen from *Figure 3.51*, the typical failure of 10 mm GFRP bars was caused by interlaminar shear and longitudinal splitting along the fibres. Furthermore, the initial assumption of bond strength for straight sand-coated bars was based on previous coupon test results (*Figure 3.52*), which suggested pull-out failure at approximately 23 kN, while the hinged-beam reference test reached an anchorage force of 24 kN with no slip. Therefore, the results for the sand-coated 10 mm GFRP splayed bars were considered inconclusive and more experiments with larger size bars were conducted.

Figure 3.51. Typical failure of 10 mm GFRP bar

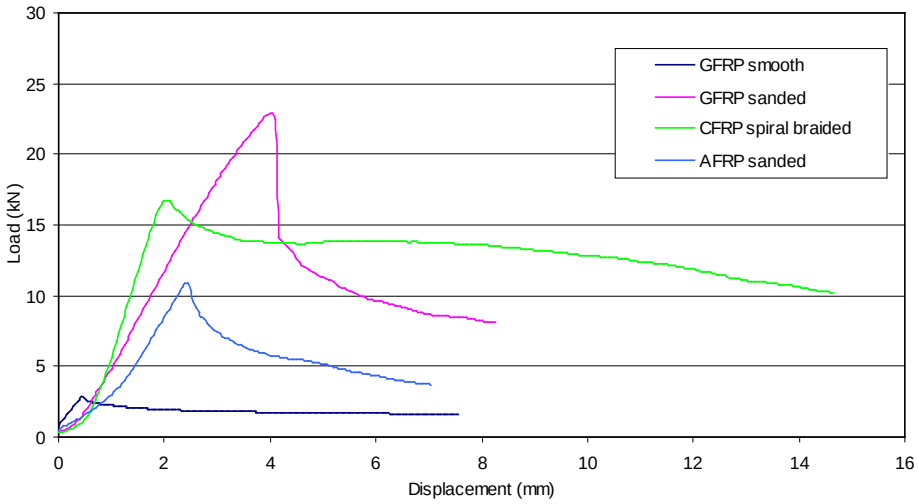

Figure 3.52. Bond strength of straight bars (Darby et al., 2007)

Figure 3.53 presents the bond-slip curves for Group I tests. Both plots indicate a tendency of wedge interlocking at low slip levels. Therefore, it can be assumed that if a bar is pulled out without damaging the surrounding concrete, the wedge may reach a state of equilibrium and interlock. However, this phenomenon was not observed for any other type of bar and including its effect was not considered safe for practical design purposes.

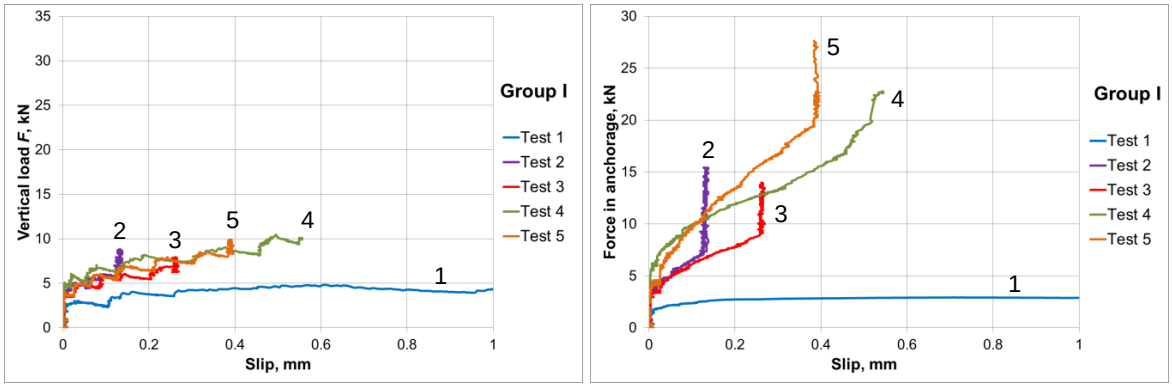

a. b.

Figure 3.53. Bond-slip curves (10 mm GFRP bars): (a) vertical load-slip and (b) force in anchorage-slip

The force-slip curves provide a useful insight into the actual bond-slip behaviour of a wedge anchor. The slope of the experimental curves is clearly controlled by the wedge size, a relation similarly suggested by the coupon test results in *Figure 3.12*. However, it was previously concluded that the splay angle had negligible influence on the bond strength of a splayed anchorage, while the new results demonstrate that the end slip for the same wedge length indeed depends on the splay angle. In fact, the difference in the anchorage capacity reaches 5 kN (or 13% of the ultimate tensile strength) for 0.4 mm slip (*Figure 3.53b*). Therefore, a model able to predict the bond-slip of splayed anchorage should take into account both the wedge length and angle.

3.5.3. Test results for 12 mm GFRP bars

The results for the 12 mm GFRP bars are also presented together, similarly including tests with smooth and sand-coated bars of the same type (see *Table 3.10* and *Table 3.11*).

Table 3.10. Test results Group III (smooth surface)

Test 9	straight (failed measurement of slip)
Test 10	straight (repeat test)
Test 11	100 mm 4° wedge (failed strain gauges)
Test 12	100 mm 4° wedge (repeat test)

Table 3.11. Test results Group IV (sand-coated surface)

Test 13	straight
Test 14	100 mm 4° wedge (confined)

Although the plots in *Figure 3.54a* show slightly different load-deflection behaviour of the initial (Test 11) and the repeat test (Test 12) with splayed smooth bars, *Figure 3.54b* confirms that the forces in the anchorage were similar. Furthermore, the capacity of the smooth splayed anchorage was close to the capacity of sand-coated anchorage, demonstrating the efficiency of pure wedging action. The peak loads reached in Test 11 and Test 12 were controlled by the splitting failure of concrete, as can be seen in *Figure 3.55* and *Figure 3.56*. However, the FRP bar failed by rupture at 4.5 mm final slip for Test 11, while Test 12 allowed recording a post-peak load equal to 50% of the maximum value for a slip larger than 20 mm.

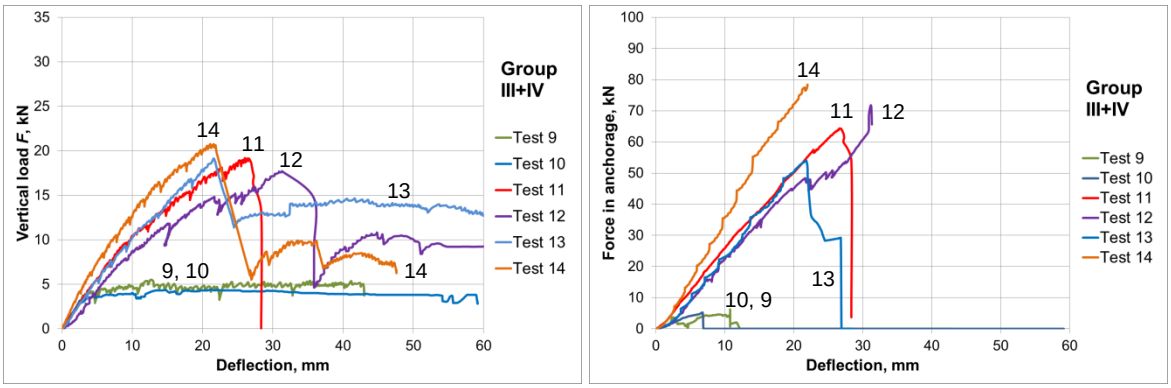

a. b.

Figure 3.54. Load-deflection curves (12 mm GFRP bars): (a) vertical load-deflection and (b) force in anchorage-deflection

Figure 3.55. Test 11

Figure 3.56. Test 12

The specimen containing sand-coated splayed anchorage failed by a tensile rupture of the FRP bar near the wedge (*Figure 3.57*) at almost negligible slip at the end, and no cracks in the concrete. Although the reference bond test of a straight sand-coated bar showed a high peak bond, the splayed end practically doubled the value and provided full anchorage resistance for this type of bar. The maximum recorded force in the anchorage, prior to failure of the gauges, was nearly 80 kN. *Figure 3.58* and *Figure 3.59* show the bond-slip curves in two different scales, plotted for the vertical load and the force in the anchorage. As can be seen, the sand-coating increased

significantly the initial stiffness of the bond-slip curve and, therefore, could play an important role in determining the bond strength of splayed bars.

Figure 3.57. Tensile failure of sand-coated splayed GFRP bar

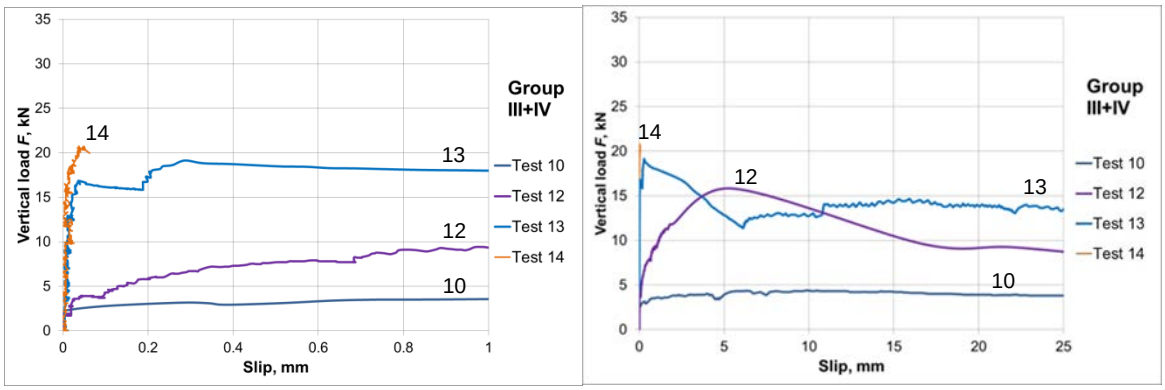

a. b.

Figure 3.58. Vertical load-slip curves (12 mm GFRP bars): (a) for 0-1 mm slip and (b) for 0-25 mm slip

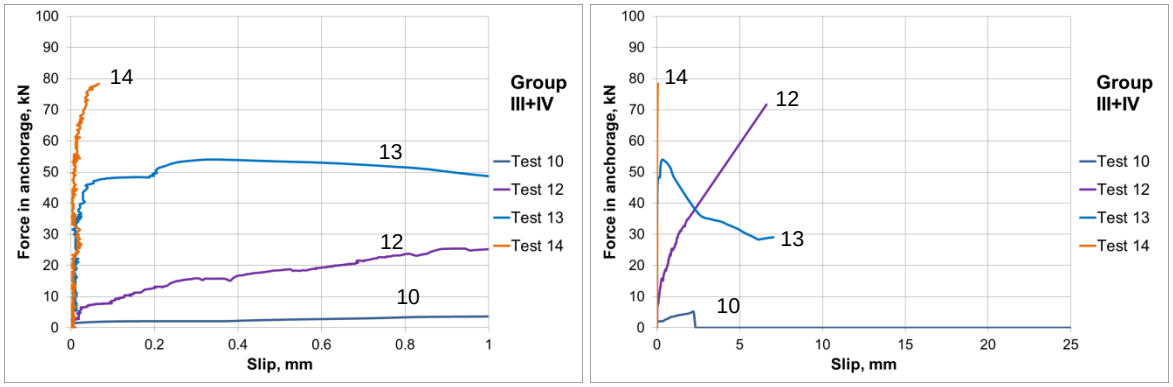

a. b.

Figure 3.59. Force in anchorage-slip (12 mm GFRP bars): (a) for 0-1 mm slip and (b) for 0-25 mm slip

3.5.4. Test results for 12 mm CFRP bars

Table 3.12 summarises the experiments carried out using 12 mm CFRP bars, shown in *Figure 3.60*.

Table 3.12. Test results Group V (CFRP)

Test 15	straight
Test 16	100 mm 4° wedge (unconfined)
Test 17	100 mm 4° wedge (confined) – failed measurement of slip
Test 18	100 mm 4° wedge (confined) – repeat test

Figure 3.60. CARBOPREE 12 mm CFRP test bar

As can be seen from the load-deflection plots in *Figure 3.61a*, the repeat test beam (Test 18) had lower stiffness and reached a lower peak load than those of Test 17, while the ascending branch of the initial two tests was similar. The only difference between Test 18 and the earlier experiments was the wedge preparation method, as explained in § 3.4.4.1. Although the effect on the ultimate load capacity appears to be significant, *Figure 3.62* suggests that the major reason for this variation is the difference in the initial bond.

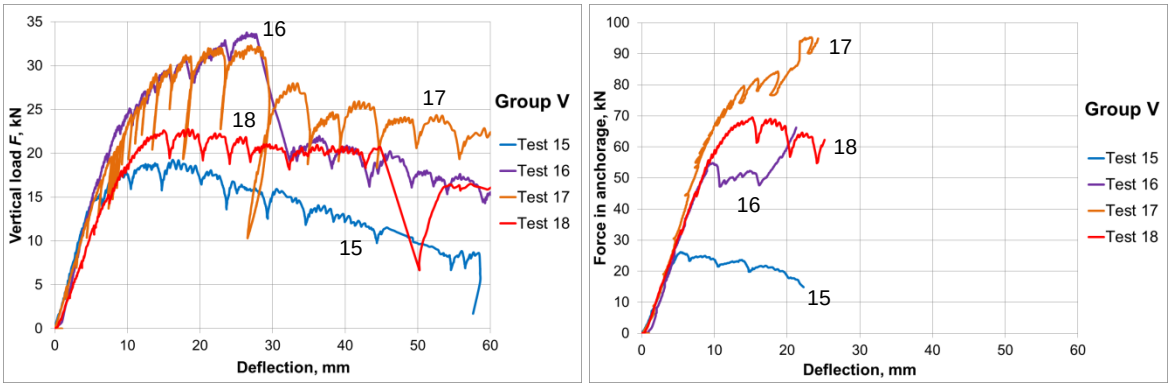

a. b.

Figure 3.61. Load-deflection curves (12 mm CFRP bars): (a) vertical load-deflection and (b) force in anchorage-deflection

Figure 3.61b indicates a problem with the strain measurement for Test 16, however, the obtained results are useful for analysing the '0-1 mm' experimental curves (*Figure 3.63a*). As can be seen from *Figure 3.63*, the increase in the anchorage bond for this type of CFRP bar is relatively low with maximum values reached at slip greater than 3 mm. In this respect, their bond-slip behaviour is closer to the smooth than to the sand-coated GFRP bars in *Figure 3.59*.

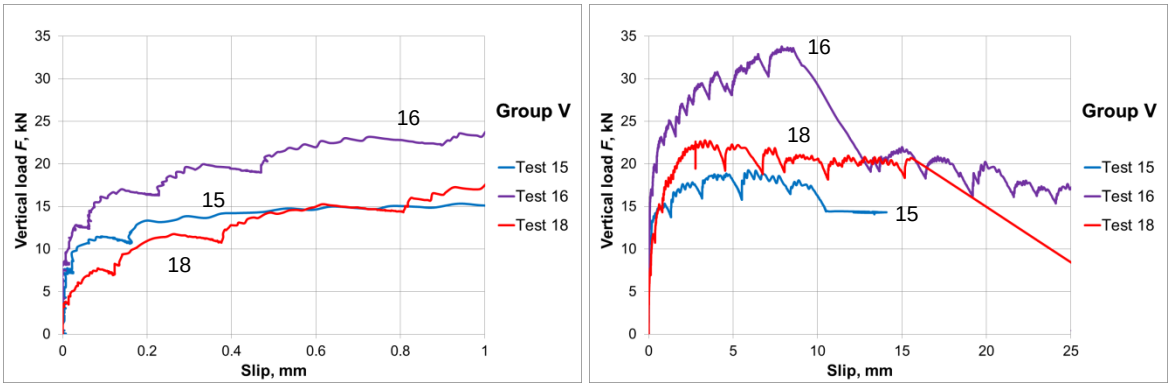

Figure 3.62. Vertical load-slip curves (12 mm CFRP bars): (a) for 0-1 mm slip and (b) for 0-25 mm slip

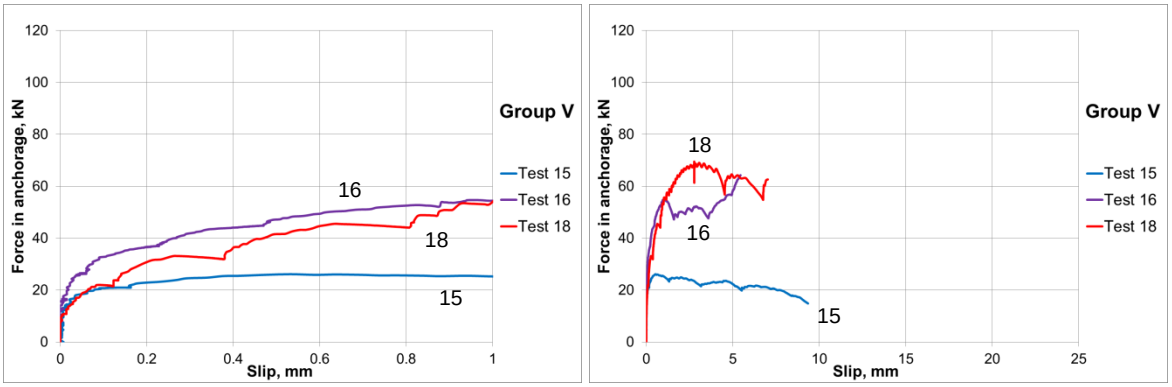

Figure 3.63. Force in anchorage-slip (12 mm CFRP bars): (a) for 0-1 mm slip and (b) for 0-25 mm slip

Similarly to previous conclusions, the wedge/helix combination did not increase the ultimate load resistance. The confined anchorage, however, exhibited more ductile behaviour. *Figure 3.64* and *Figure 3.65* present the differences between the crack patterns of confined and unconfined test specimens. Test 16 failed in a similar manner to the other unconfined test beams, exhibiting a wide single crack across the depth of the end cross section. The concrete inside the helix in Test 17 remained intact, while the failure cracks were smaller and dispersed.

Figure 3.64. Unconfined anchorage failure (Test 16)

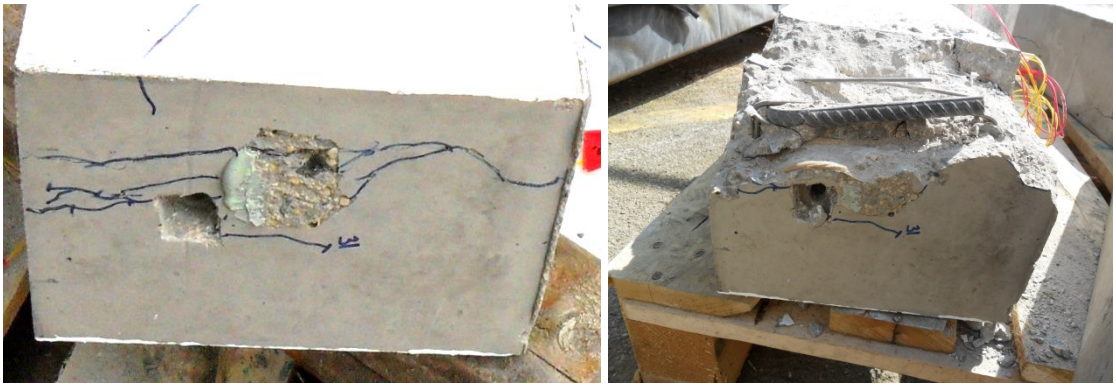

Figure 3.65. Confined anchorage failure (Test 17)

3.5.5. Test results for tapered beams

Three tapered beams were included in the test program, one representative of each type of the FRP test bars, as summarised in *Table 3.13*.

Table 3.13. Test results Group VI (tapered)

Test 19	100 mm 4° wedge 12 mm smooth GFRP
Test 20	100 mm 4° wedge 12 mm sand-coated (braided) CFRP
Test 21	100 mm 4° wedge 10 mm sand-coated GFRP (confined)

The failure modes varied across the three tests. As can be expected, based on the results already presented, the sand-coated 10 mm GFRP bar failed by rupture at zero slip. The 12 mm GFRP and CFRP bars resisted similar pull-out forces. While the GFRP bar failed prior to observing any cracks in the concrete, a sudden crack at the anchorage zone of test specimen 20 caused a brittle concrete failure (*Figure 3.66*). The load/force-deflection curves of all three tests are shown in *Figure 3.67*.

Figure 3.66. Test 20 failure

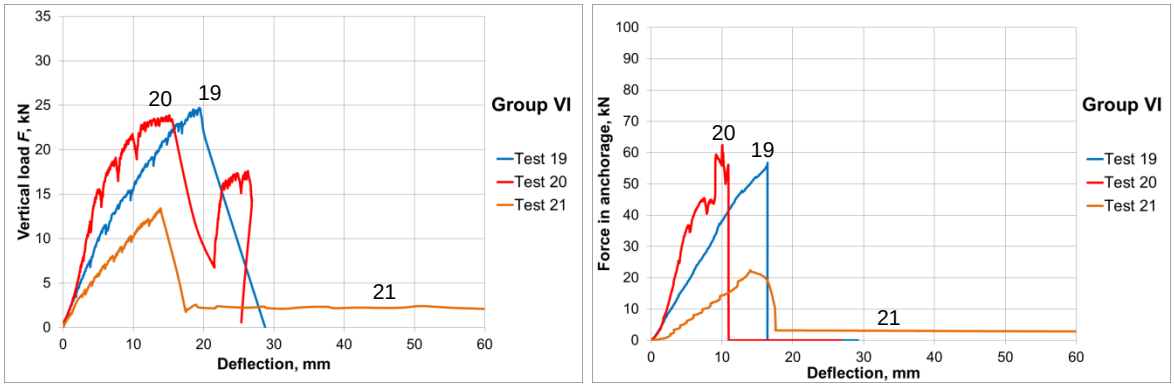

a. b.

Figure 3.67. Tapered beams: (a) vertical load-deflection curves and (b) force-deflection curves

The wedges for Test 19 and Test 20 were formed using the same resin type, resulting in an I-shaped cross section, shown in *Figure 3.37b*. However, the initial bond appears to be higher for the smooth bar, as indicated by *Figure 3.68* and *Figure 3.69*, which may be due to concrete wedging inside the slot.

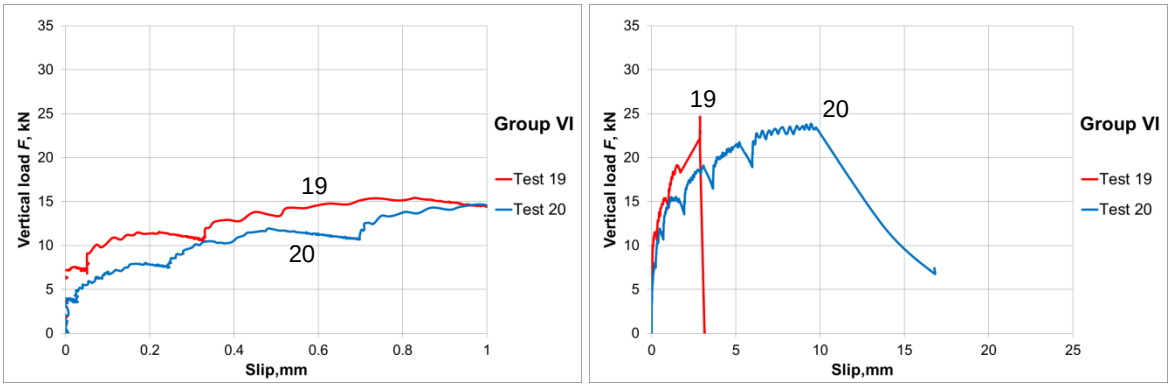

a. b.

Figure 3.68. Vertical load-slip curves (tapered beams 12 mm bars): (a) for 0-1 mm slip and (b) for 0-25 mm slip

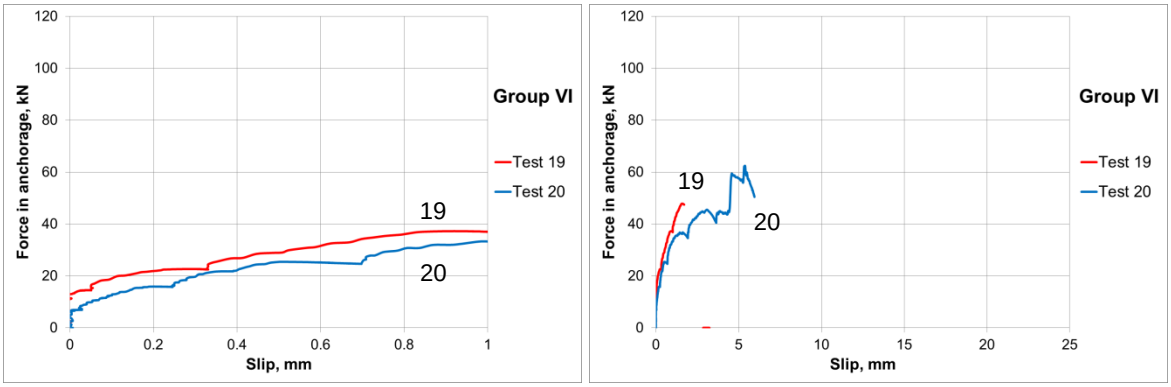

a. b.

Figure 3.69. Force in anchorage-slip (tapered beams 12 mm bars): (a) for 0-1 mm slip and (b) for 0-25 mm slip

3.5.6. Test results for V-Rod HM GFRP and steel bars

The experiments, summarised in *Table 3.14*, were carried out to investigate the behaviour of fabricated sand-coated GFRP bars, V-Rod HM (*Figure 3.70*).

Table 3.14. Test results Group VII

Test 22	straight V-Rod
Test 23	100 mm 2° wedge 12 mm V-Rod

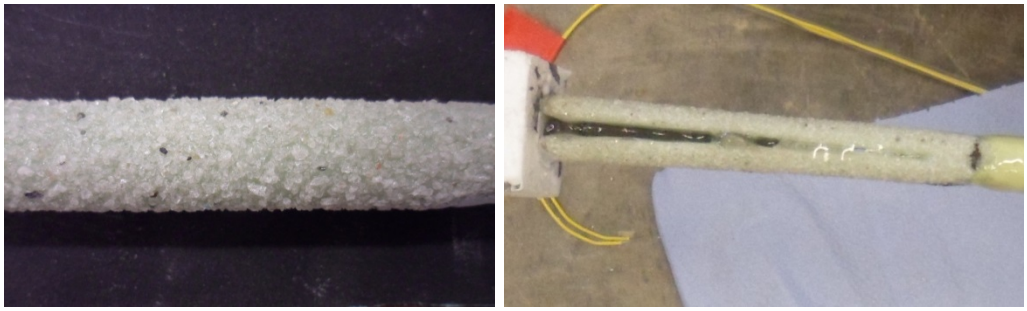

Figure 3.70. V-Rod HM test bars

The V-Rod reference test, Test 22, failed by a sudden loss of bond. The bar moved instantaneously 20 mm inside the concrete. However, the peak vertical load for the reference specimen was higher than the load resisted by the wedged anchor (*Figure 3.71*). Both strain gauges attached to the straight bar did not work during the reference test and the actual force in the bar was not determined. Furthermore, although the anchorage force for the splayed bar was measured successfully, by inspection, it was concluded that the slip was not recorded accurately. Therefore, a force-slip plot is not

presented. Nevertheless, the test results revealed the possibility of catastrophic bond failure of straight reference bars, whereas the bond-slip behaviour of the splayed V-Rod bar was similar to that of the rest of the tested splayed bars. Therefore, the splayed anchorage could be used to improve the brittle bond failure of V-Rod straight bars. As previously highlighted, the test was ended due to high rotation of the concrete blocks, prior to failure of the test bar. Splitting failure of concrete was also not present at final slip of 40 mm.

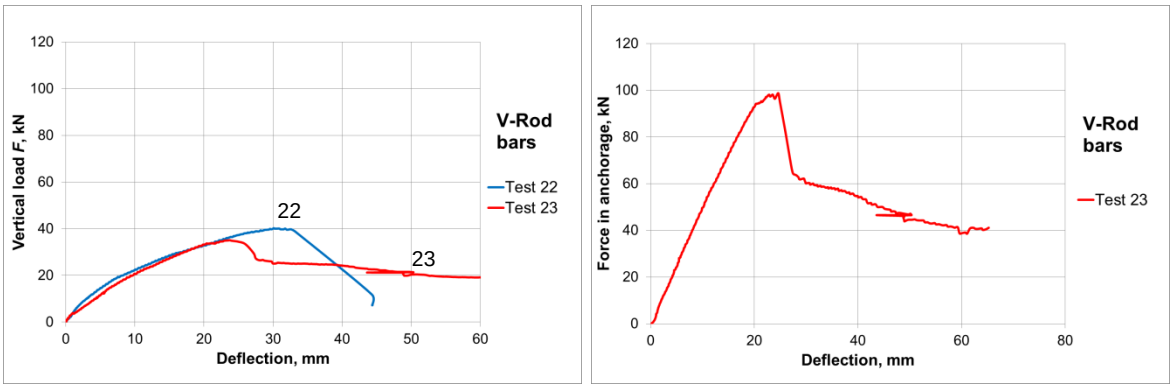

a. b.

Figure 3.71. V-Rod bars: (a) vertical load-deflection curves and (b) force-deflection curves

It may be argued that the splayed anchorage, as proposed, may not be appropriate for steel bars. However, subject to developing a practical method for creating the wedge, it would provide the same advantages when used in fabric-formed elements. The steel test bar failed in tension at 0.06 mm end slip (see *Figure 3.72*). Although the failure of the test bar and the control measurements, presented in Appendix A, confirm that the bar has reached its yield strength at the middle, the maximum force in the anchorage was measured to be 68% of the ultimate tensile capacity of the bar. Nevertheless, the spayed anchorage has still almost doubled the theoretical bond strength, corresponding to a 100 mm straight embedment length.

a. b.

Figure 3.72. Steel test bar: (a) tensile failure in the middle and (b) end slip

3.6. Discussion of results

3.6.1. General force-slip curve

A general force-slip curve can be produced based on the experimental results for splayed bars. Four main stages can be defined to describe the bond-slip, as illustrated in *Figure 3.73*, chemical adhesion (no slip), initial steep curve, followed by a potential wedge interlocking or increase of slip until the peak load is reached and a post-peak branch, dependent on the type of failure. Unconfined concrete splitting and FRP bar rupture, as exhibited in some of the experimental load-deflection plots, can be very brittle. The confined anchorage, however, showed a pronounced ductile behaviour. While the experimental data may not be sufficient to describe the full curve, the effect of all significant parameters is discussed and a model predicting the initial bond-slip curve for low slip levels is developed.

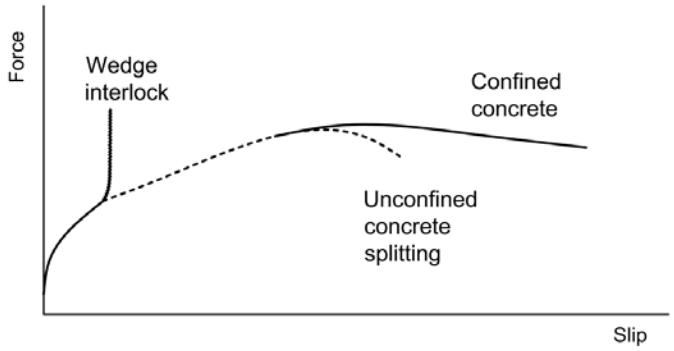

Figure 3.73. General force-slip curve

3.6.2. Reference bond tests of straight bars

The reference tests provide a basis for comparison and help in demonstrating the contribution of the wedging action to the bond strength of splay ended bars. Furthermore, the straight bar tests can be used to define the bond characteristics of the different test bars. The experimental bond stress-slip curves, presented in *Figure 3.74*, have been used to determine the curve fitting parameters of the modified BEP model and produce analytical bond-slip expressions for all types of test bars.

The ascending branch of the bond-slip curve for 10 mm smooth GFRP is given by *Equation 3.7*, and the descending branch by *Equation 3.8*:

$$\frac{\tau}{0.978} = \left(\frac{s}{0.732}\right)^{0.1} \tag{3.7}$$

$$\frac{\tau}{0.978} = 1 - 0.0404 \cdot \left(\frac{s}{0.732} - 1\right) \tag{3.8}$$

The 12 mm smooth GFRP bond-slip curve is described by *Equation 3.9* and *Equation 3.10:*

$$\frac{\tau}{0.939} = \left(\frac{s}{0.5}\right)^{0.1} \tag{3.9}$$

$$\frac{\tau}{0.939} = 1 - 0.0463 \cdot \left(\frac{s}{0.5} - 1\right) \tag{3.10}$$

Equation 3.11 and *Equation 3.12* correspond to the 12 mm sand-coated GFRP:

$$\frac{\tau}{13.5} = \left(\frac{s}{0.329}\right)^{0.1} \tag{3.11}$$

$$\frac{\tau}{13.5} = 1 - 0.023 \cdot \left(\frac{s}{0.329} - 1\right) \tag{3.12}$$

Finally, the bond-slip law for the 12 mm sand-coated CFRP is expressed by *Equation 3.13* and *Equation 3.14*:

$$\frac{\tau}{7.06} = \left(\frac{s}{0.532}\right)^{0.13} \tag{3.13}$$

$$\frac{\tau}{7.06} = 1 - 0.026 \cdot \left(\frac{s}{0.532} - 1\right) \tag{3.14}$$

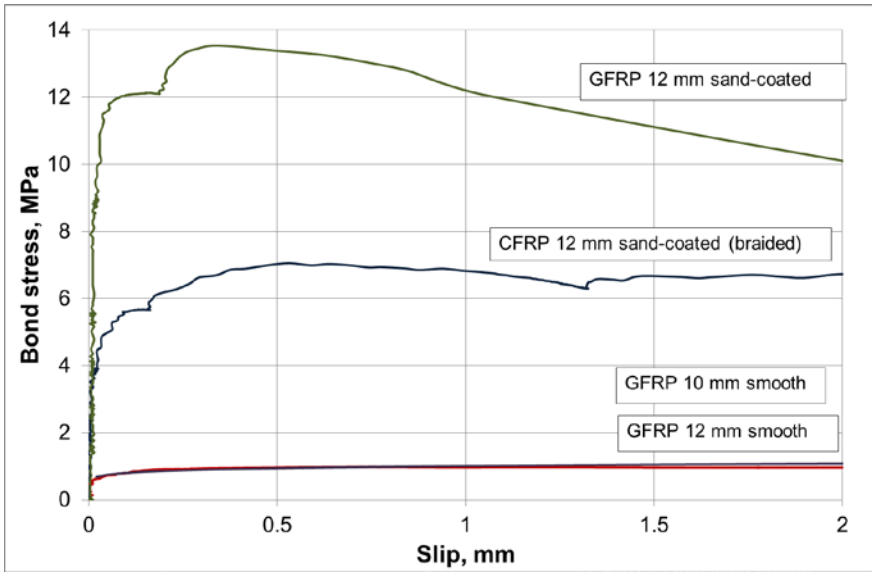

Figure 3.74. Experimental bond stress-slip curves for straight FRP test bars

3.6.3. Chemical bond

The chemical bond between splayed bars and concrete was generally higher than that recorded for straight bars. The results presented in *Table 3.15* are grouped according to the test bar size and bond characteristics. The chemical bond of splayed bars is divided into two components: bond of FRP bar and bond of wedge plate. The former is calculated from the bond stress of straight bars, taking into account the reduced bond area after cutting a slot. The remaining bond force is then divided by the bond area of the wedge plate.

Table 3.15. Chemical bond

	Test ID	Type of wedge	Bond, kN	Straight bar		Straight bar with slot		Wedge plate		
				Bond area, mm^2	Bond stress, MPa	Bond area, mm^2	Bond force, kN	Bond force, kN	Bond area, mm^2	Bond stress, MPa
10 mm GFRP	Test 1	straight	1.7	2985	0.578					
	Test 2	1	3.5			2785	1.61	1.89	375	5.05
	Test 3	1	3.4			2785	1.61	1.79	375	4.78
	Test 4	1	5.3			2585	1.49	3.81	749	5.08
	Test 5	1	4			2585	1.49	2.51	1098	2.28
12 mm GFRP	Test 13	straight	34.5	3990	8.647					
	Test 14	2	40			3590	31.0	8.96	1098	8.16
	Test 10	straight	2.3	3990	0.576					
	Test 11	3	5			3590	2.07	2.93	1098	2.67
	Test 12	3	2.8			3590	2.07	0.73	1098	0.665
	Test 19	3	12.9			3590	2.07	10.83	1098	9.86
12 mm CFRP	Test 15	straight	13.2	3707	3.561					
	Test 16	1	17.5			3307	11.8	5.72	1098	5.21
	Test 17	1	17.9			3307	11.8	6.12	1098	5.58
	Test 18	3	10.8			3307	9.92	0.92	1098	0.836
	Test 20	3	6.9			3307	6.28	0.62	1098	0.561

The results are also related to the type of adhesive used to prepare each wedge. The three types, illustrated in *Figure 3.75*, include:

- Type 1 wedge, solid section filled with Sikadur 32 epoxy bonding agent
- Type 2 wedge, formed as Type 1 and sand-coated over the total surface area
- Type 3 wedge, I-section glued with Araldite/ Aradur 5052 adhesive

Type 1 wedge shows consistent results of the chemical bond stress for five out of six specimens in *Table 3.15*. As can be expected, the bond stress for wedge Type 2 is close to the bond stress of straight sand-coated bars. The bond stress for Type 3 wedge varies significantly, possibly depending on the ability of concrete to flow inside the openings.

a. b. c.

Figure 3.75. Wedge bond types: (a) Type 1, (b) Type 2 and (c) Type 3

The theoretical bond-slip curves for straight bars based on the calibrated bond-slip expressions (*Equation 3.7* to *Equation 3.14*) are plotted in *Figure 3.76*. The bond-slip curve for Type 2 wedge is assumed to be similar to the bond-slip curve for straight sand-coated GFRP bars. A theoretical bond-slip curve describing Type 1 wedge bond is proposed by scaling up the bond-slip law for smooth bars. Conservatively, the bond-slip curve for smooth bars is adopted for Type 3 wedge, as indicated in *Figure 3.76*.

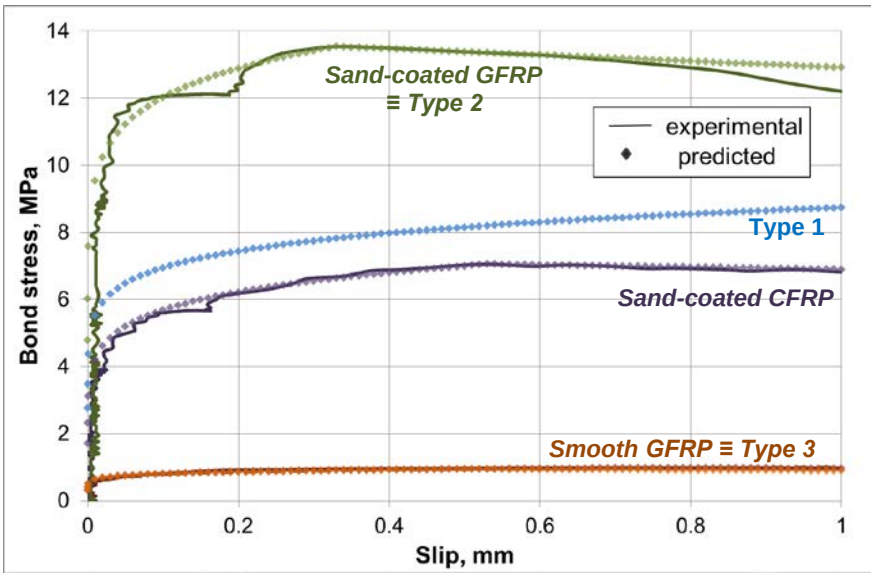

Figure 3.76. Theoretical bond stress-slip curves for straight bars and wedges

3.6.4. Effect of wedge geometry

The bond-slip behaviour of splayed bars, as previously noted, depends both on the embedded wedge length and the splay angle. Although limited in number, the hinged-beam test results show similar bond-slip relations to the ones obtained from coupon tests. All curves in *Figure 3.77* have almost linear branches, the slopes of which appear to be defined by the combination of wedge length and angle.

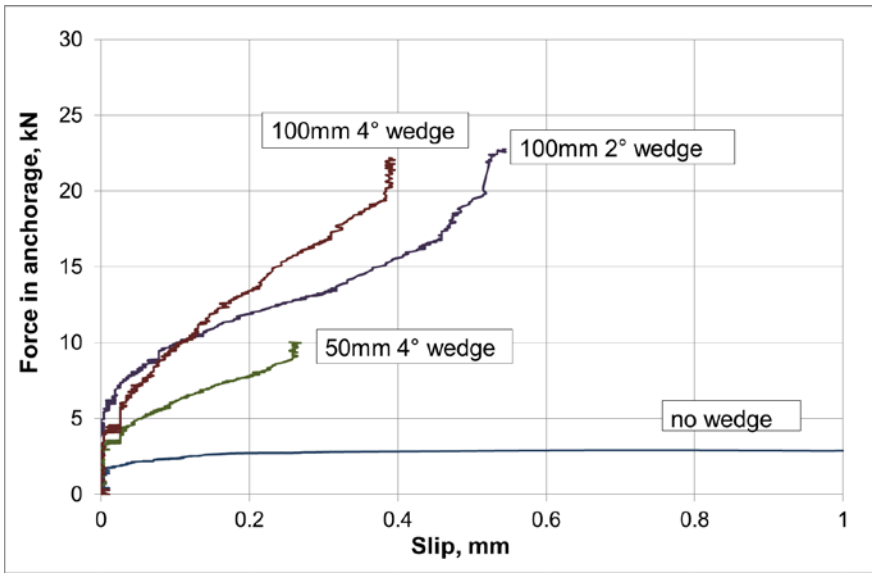

Figure 3.77. Force-slip curve for 10 mm smooth GFRP bars

3.6.5. Effect of bar size

The bar size would affect the surface bond stress of splayed bars, which is governed by the bond-slip laws, discussed in § 3.6.2 and § 3.6.3. The effect, however, would be minimal for smooth bars. Therefore, the results for two sizes of smooth GFRP bars are compared in *Figure 3.78* to determine the extent of bar size effect on wedging action. As can be seen, the two plots overlap, suggesting that the wedging action alone does not depend on the bar diameter. This may be explained with the two-dimensional nature of the proposed wedge.

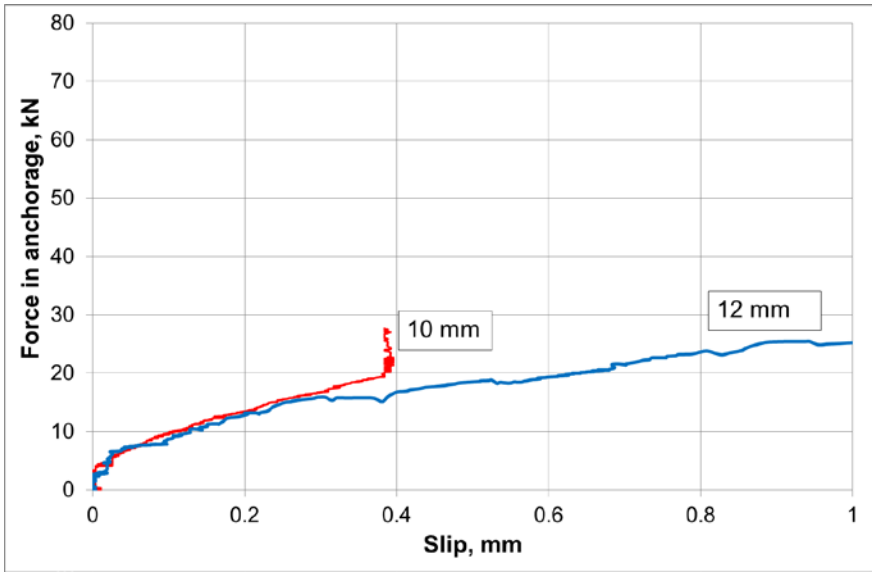

Figure 3.78. Force-slip curve for smooth GFRP bars

3.6.6. Effect of surface treatment

The surface bond characteristics of a bar can have a significant influence on the resistance of splayed anchorage. Comparing bars with the same wedge size and bar diameter demonstrates an increase in bond strength across the three different types of test bars, shown in *Figure 3.79*. Based on the experimental plots, it may be concluded that only the chemical adhesion and the initial slope of bond-slip curves depend upon the surface bond. Once the splay ended bar moves inside the concrete, it may be more appropriate to treat all wedges as smooth. For bars with brittle bond failure, the effect of surface bond may need to be ignored completely for design purposes, based on the observations from the tests with V-Rod sand-coated GFRP bars.

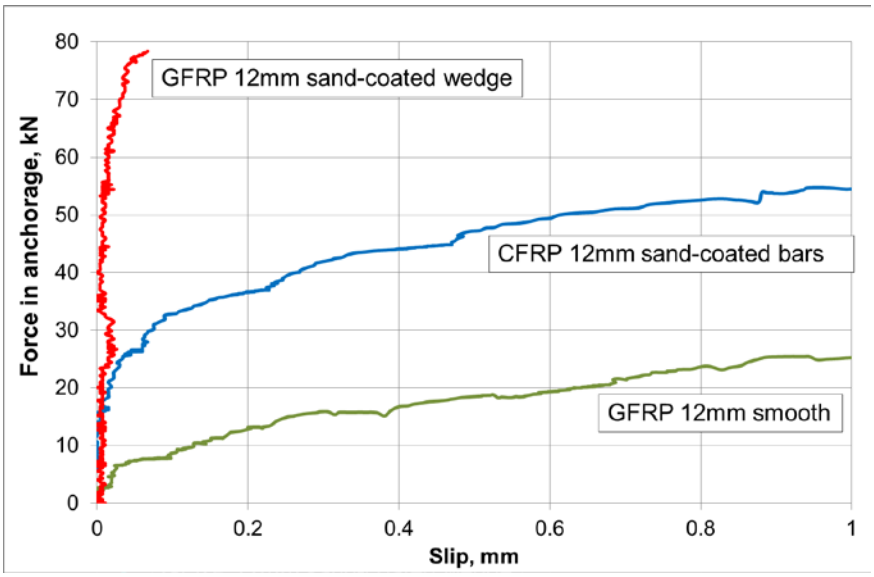

Figure 3.79. Force-slip curve for 12 mm bars with different surface treatment

3.6.7. Effect of concrete confinement

As previously suggested, confinement may not be able to influence the ascending branch of a splayed anchorage bond-slip curve and to increase the ultimate strength; nevertheless it ensures a ductile behaviour of the anchorage, as confirmed by the force-slip curve for 12 mm CFRP splayed bars with helical confinement in *Figure 3.80*, and should be recommended for structural applications.

Due to the typically large slip of bars at peak loads, the strain gauges installed near the anchored ends were usually damaged by friction against concrete, and post-peak strains were difficult to record. For this reason, the effect of confinement is demonstrated by comparing the vertical loads sustained by a confined and an unconfined hinged-beam specimen, containing bars with the same geometrical and surface properties (Test 16 and

Test 17), shown in *Figure 3.81*. A difference of approximately 5 kN is maintained after the peak load, while the final slip of the confined anchorage was nearly 10 mm less than that of the unconfined anchorage.

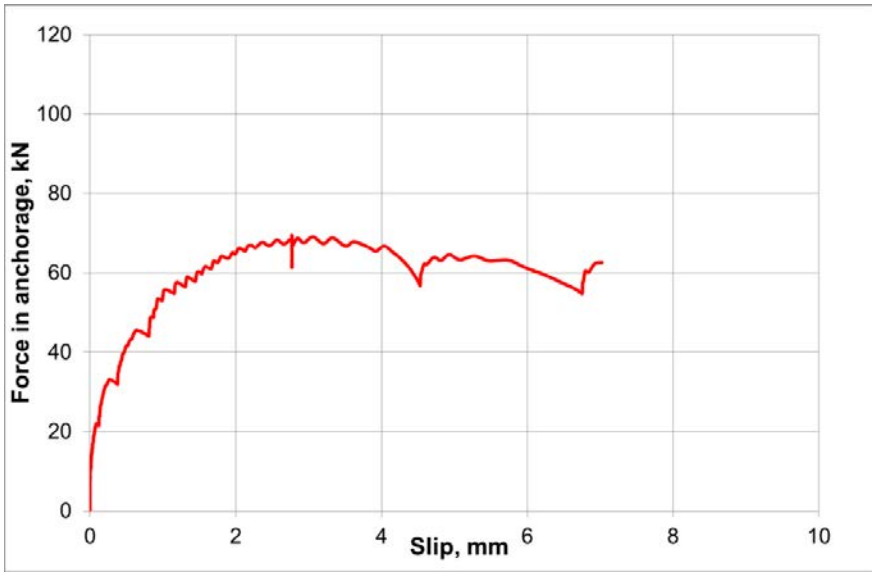

Figure 3.80. Ductile behaviour of confined splayed anchorage (Test 18)

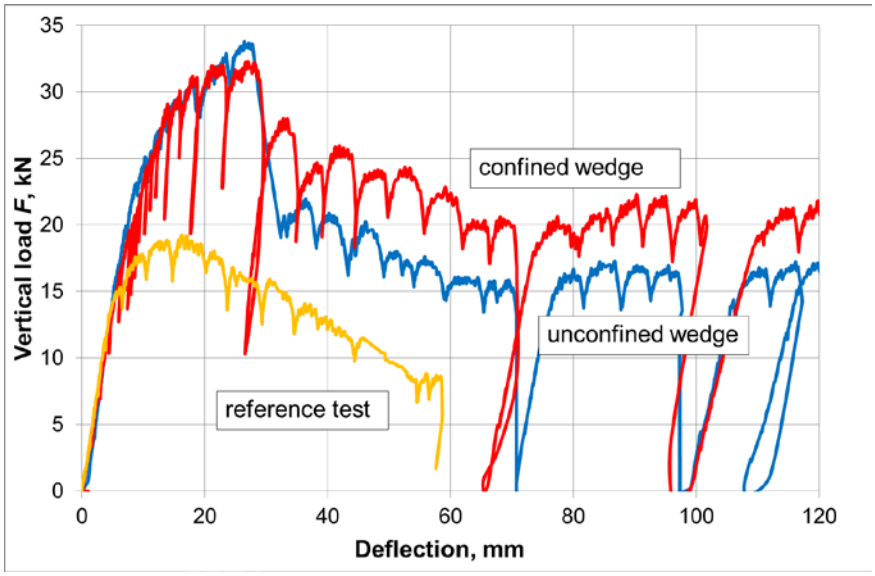

Figure 3.81. Vertical load-deflection curves for 12 mm CFRP bars

3.6.8. Effect of bar inclination

Only in two of the three tapered beam tests did the end anchorages slip. The results from those tests, presented as force-slip curves in the direction of the anchored bar, are compared with the results for similar horizontal bars in *Figure 3.82* and *Figure 3.83*. The difference between inclined and horizontal anchorages of smooth GFRP bars arises mainly from the differences in the chemical bond. However, as discussed, this may be due

to different compaction of concrete around the wedge. A similar explanation could be valid for the CFRP bars in *Figure 3.83*. Therefore, the results are insufficient to demonstrate any significant effect of the bar inclination on bond strength and behaviour of splayed bars. At present, it is concluded that such an effect can be ignored. Nevertheless, due to the small number of test specimens, further investigation may be required.

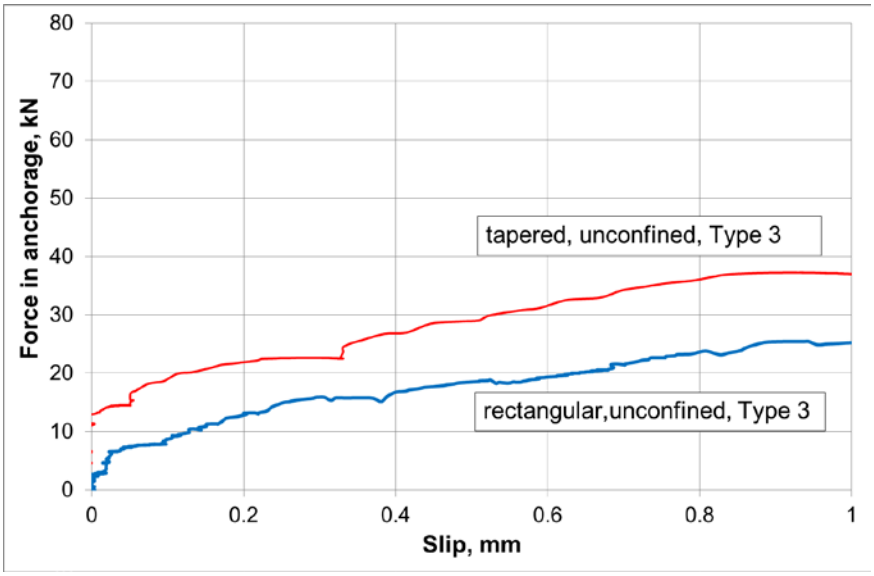

Figure 3.82. Force-slip curves for 12 mm smooth GFRP bars

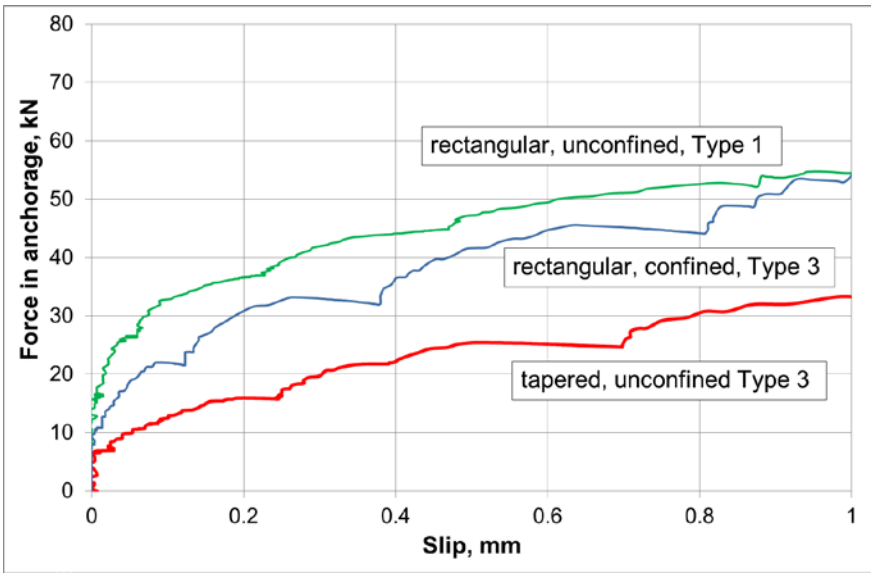

Figure 3.83. Force-slip curves for 12 mm sand-coated CFRP bars

3.7. Anchorage model

3.7.1. Forces in a wedge

For a wedge with length L_w and angle α_w, the forces acting, taking friction into account, are illustrated in *Figure 3.84*, where F_b is the pull-out force in the reinforcing bar, N is the

normal reaction from concrete, μ is the coefficient of friction between the bar surface and concrete, and τ is the bond stress over the total bond surface area A_{tot}.

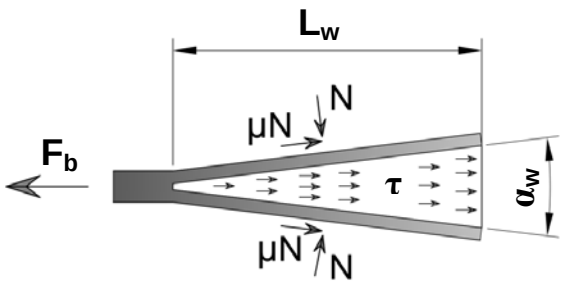

Figure 3.84. Wedge forces

From equilibrium, the pull-out force can be expressed as:

$$F_b = 2 * N * sin\left(\frac{\alpha_w}{2}\right) + 2 * \mu * N \cdot cos\left(\frac{\alpha_w}{2}\right) + \tau * A_{tot} \tag{3.15}$$

Furthermore, the following geometrical relationship can be used to relate the acting forces to the slip s:

$$\Delta = s * sin\left(\frac{\alpha_w}{2}\right) \tag{3.16}$$

where Δ is the transverse deformation (see *Figure 3.85*).

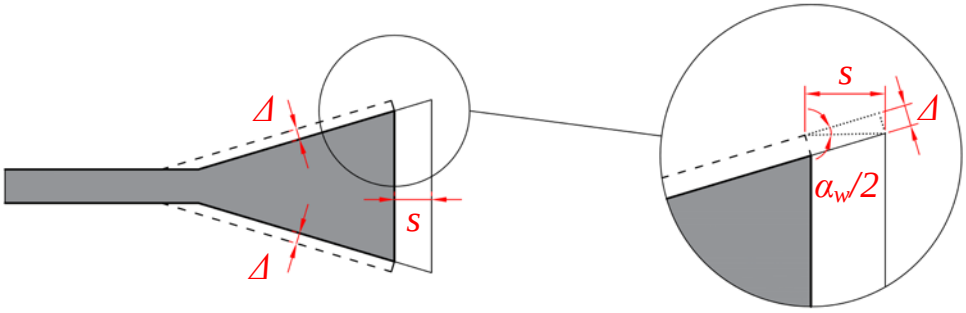

Figure 3.85. Transverse deformation

3.7.2. Assumptions

Two main assumptions are made in order to develop a theoretical anchorage model. It is assumed that N is equally distributed along the wedge length and that the transverse deformation is proportional only to N/L_w, i.e. independent of the bar diameter. The latter is based on the experimental results and would be valid for elastic behaviour of the contact materials.

Hence,

$$N = n * s * L_w * sin\left(\frac{\alpha_w}{2}\right) \tag{3.17}$$

where n is an unknown constant. By substituting *Equation 3.17* in *Equation 3.15*, the force-slip expression is obtained:

$$F_b = 2 * n * s * L_w * sin^2\left(\frac{\alpha_w}{2}\right) + \mu * n * s * L_w * sin(\alpha_w) + \tau * A_{tot} \tag{3.18}$$

The last component can be divided into two resultant forces, representing the surface bonds of the reinforcing bar and the wedge plate. If A_w is the two-sided area of the wedge plate, given by *Equation 3.20*, $\tau_w = \tau_w(s)$ and $\tau_b = \tau_b(s)$ are the bond stresses in the wedge plate and bar, respectively, and t_w is thickness of the slot, the final force-slip expression will be:

$$F_b = 2 * n * s * L_w \cdot sin^2\left(\frac{\alpha_w}{2}\right) + \mu * n * s * L_w * sin(\alpha_w) + \tau_w * A_w +$$

$$+\tau_b * (\pi * d_b - 2 * t_w) * L_w \tag{3.19}$$

where

$$A_w = L_w * \left[t_w + L_w * tan\left(\frac{\alpha_w}{2}\right)\right] \tag{3.20}$$

3.7.3. Expression for smooth bars

The constant n and the coefficient of friction μ in *Equation 3.19* are unknown. From the experimentally obtained gradients of bond-slip curves for smooth GFRP bars with known wedge geometry the parameters can be obtained from the following equations:

$\alpha_w = 4°,\ L_w = 50\ mm$

$$2 \cdot n \cdot 0.0609 + \mu \cdot n \cdot 3.49 = 18.6 * 10^3 \tag{3.21}$$

$\alpha_w = 2°,\ L_w = 100\ mm$

$$2 \cdot n \cdot 0.0304 + \mu \cdot n \cdot 3.49 = 18 * 10^3 \tag{3.22}$$

$\alpha_w = 4°,\ L_w = 100\ mm$

$$2 \cdot n \cdot 0.122 + \mu \cdot n \cdot 6.98 = 37 * 10^3 \tag{3.23}$$

giving best-fit values of n=20000 and μ=0.25 (with errors 0.3%, 0.3% and 0.9% for *Equation 3.21*, *Equation 3.22* and *Equation 3.23*, respectively). The constant *n* may be interpreted physically as stiffness, with a value between the stiffness of resin and stiffness of concrete. Therefore, the final equation for smooth FRP is:

$$F_b = 40000 * s * L_w * sin^2\left(\frac{\alpha_w}{2}\right) + 5000 * s * L_w * sin(\alpha_w) + \tau_w * A_w + \\ +\tau_b * (\pi * d_b - 2 * t_w) * L_w \quad (3.24)$$

where F_b is in [N], A_w in [mm^2], L_w and d_b in [mm] and the bond stresses, τ_b and τ_w in [N/mm^2].

3.7.4. General expression

In order to formulate a general expression, a bond parameter *m*, accounting for the different bond surface characteristics, is introduced. The parameter is expressed as a function equal to the bond-slip law for straight bars with any surface treatment divided by the bond-slip law for smooth straight bars, as defined in § 3.6.2. As previously discussed, the surface bond affects only the chemical adhesion and the initial slope of the force-slip curve and, therefore, may need to be ignored for larger slips. The general expression is given in *Equation 3.25.*

$$F_b = 40000 * L_w * sin^2\left(\frac{\alpha_w}{2}\right) + 5000 * m * L_w * sin(\alpha_w) + \tau_w * A_w + \\ +\tau_b * (\pi * d_b - 2 * t_w) * L_w \quad (3.25)$$

3.7.5. Comparison of predicted and experimental results

The obtained force-slip expressions are compared with the experimental plots to assess the extent of their validity. The predicted results for 10 mm smooth GFRP bars describe fully the experimental curves, if the mechanical interlocking is ignored (see *Figure 3.86*). However, the specimens' failure was governed by the strength of the FRP bars and the validity of predicted curves for larger pull-out forces cannot be examined.

Figure 3.87 presents the results from the general force-slip expression for the various types of bars and wedges. The bond parameter, m, was found to be applicable up to the tensile failure of the sand-coated GFRP bar, corresponding to an end slip of 0.06 mm. However, for the braided sand-coated CFRP bars the bond parameter is applicable only

up to 0.02 mm slip. As can be seen from *Figure 3.87*, the proposed model is valid approximately up to 0.3 mm slip, which could be set as a safe design limit.

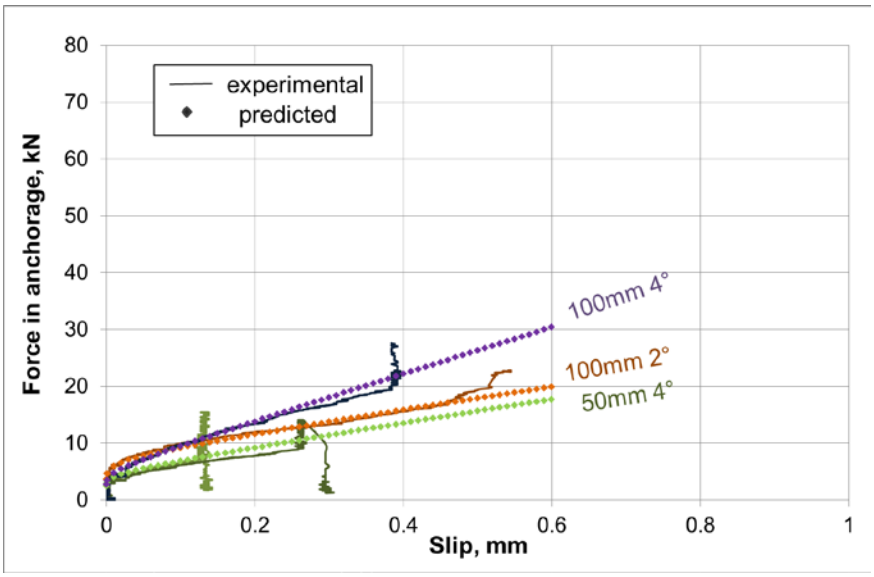

Figure 3.86. Predicted force-slip curves for 10 mm smooth GFRP bars

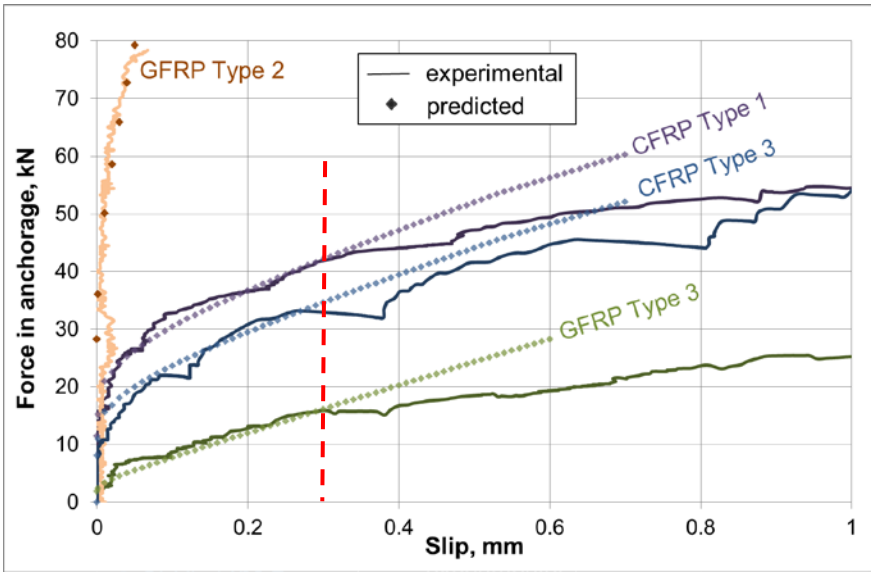

Figure 3.87. Predicted force-slip curves for 12 mm FRP bars

3.7.6. Limitations of model

The proposed model is applicable only to splayed anchorage of FRP bars. The final parameters, included in the model, are the splay angle, the wedge length, the reinforcing bar diameter and surface bond. The unknown parameters n and μ were calibrated for smooth GFRP bars. It is assumed that the parameter n depends predominantly on the stiffness of the resin used to produce the FRP bars and on the stiffness of the surrounding

concrete. Therefore, the value of n may vary for different concrete grades and types of resin. However, this could not be confirmed by the current research. The bond parameter m, which allows for use of bars with different surface bond characteristics, was not calibrated based on the test results. Instead, it was assumed that the parameter can be represented as a ratio of the bond-slip curves for straight bars, i.e. m is equal to 1 for smooth bars. This assumption may also need to be confirmed by further investigation.

It has been shown that the developed model is valid up to 0.3 mm slip. For larger slips, the behaviour of the anchorage is likely to be governed by micro-cracking and the tensile strength of concrete. Therefore, it is proposed to apply 0.3 mm slip as a conservative failure criterion for design of splayed anchorage, using the general bond-slip expression given in *Equation 3.25.*

3.8. Pull-out tests

3.8.1. Aim and test method

A new test set-up representing a simple wedge mechanism was considered to investigate further the effect of surface bond characteristics of different FRP bars on the wedging action. The aim of the test was to verify the values of the parameters μ and m, which define the bond between the FRP bar surface and the surrounding concrete, by measuring the actual transverse force in the wedge, thereby excluding the parameter n from the equilibrium *Equation 3.17.* This could be achieved by casting the splayed end of a test bar in an externally confined split concrete specimen. A schematic illustration of the test in *Figure 3.88* describes the idea, where the spring symbols represent the stiffness of the confining material. Roller supports are used to maintain horizontal sliding of the two concrete halves, while the transverse force can be obtained from the strains in the confining material.

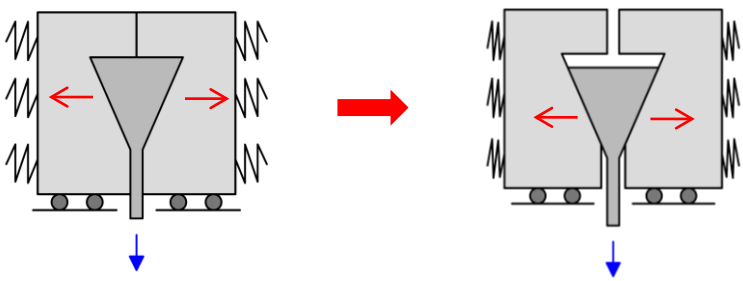

Figure 3.88. Split specimen pull-out test

The pull-out force was applied to double-ended specimens, as shown in *Figure 3.89*, using the coupon test frames described in § 3.3.1. The test-up was modified to allow

measurement of the anchorage slip. In addition, strain gauges were installed near the wedge and at the middle of the test bars to compare the calculated forces and the machine loading data. Two methods for confinement were used, FRP wrapping of split cylinders and split prisms confined by metal frames (see *Figure 3.90* and *Figure 3.91*). However, due to the generally unsuccessful strain gauge readings, the split prisms results are not presented.

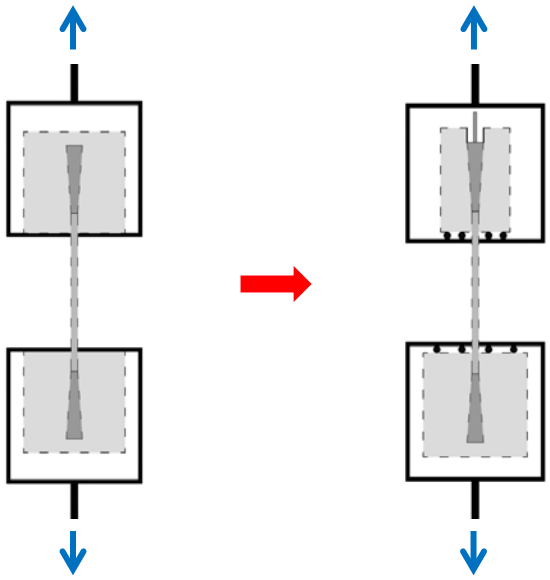

Figure 3.89. Modified coupon test set-up

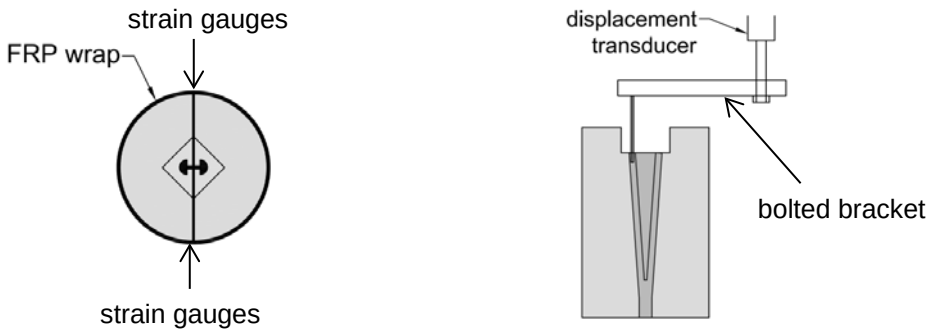

Figure 3.90. Split cylinder test specimen: (a) top view and (b) slip measurement

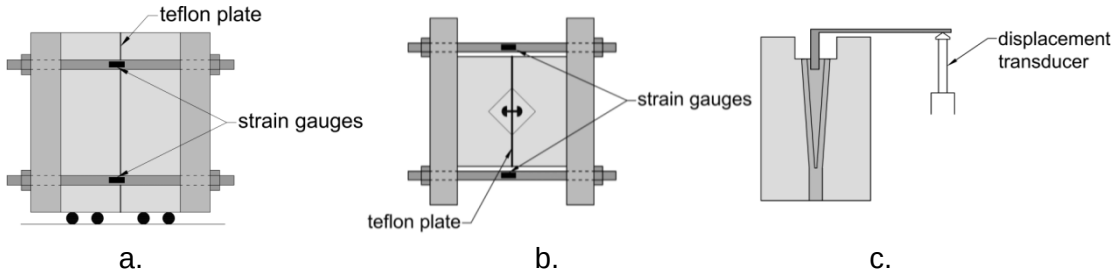

Figure 3.91. Split prism test specimen: (a) side view, (b) top view and (c) slip measurement

3.8.2. Split cylinder tests

The cylinder specimens were 100 mm in diameter and 150 mm in length, cast using the same concrete mix as for the main hinged-beam tests. The details of test bars and wedges are given in *Table 3.16.* The selected confining material was unidirectional carbon fabric Tyfo SCH-41 with dry fibre tensile modulus 230 GPa. The fabric was wrapped around the cylinder and joined with Tyfo S Epoxy two-component epoxy matrix, used for externally bonded strengthening applications with typical elastic modulus 95.8 GPa. As illustrated in *Figure 3.90b* and *Figure 3.92*, the anchorage slip was measured at the end of a steel rod, drilled and fixed into the test bar.

Table 3.16. Split cylinder test matrix

Test ID	Test bar	Wedge	
		Length, mm	Angle, °
P1	10 mm GFRP smooth	50	4
P2	10 mm GFRP smooth	100	4
P3	12 mm GFRP smooth	100	4
P4	12 mm GFRP sand-coated	100	4
P5	12 mm CFRP sand-coated	100	4

a. b. c.

Figure 3.92. Test bars: (a) preparation of wedges, (b) non-tested ends and (c) steel rods for measurement of slip

The total length of each test bar was 560 mm. The non-tested ends were also slayed and fully sand-coated before being cast in 150 mm by 150 mm high-grade concrete cubes in order to avoid slip (see *Figure 3.92*). The split cylinders were cast in two stages, as illustrated in *Figure 3.93*. An insulating tape greased with release agent for concrete

formwork was used to split the specimen in halves, after the first half was cast horizontally in a standard cylinder mould. The second half was cast in a vertical position. Any cast-in length of a bar outside of the wedge was also debonded. *Figure 3.94* shows the wrapping process. Again insulating tape was used to avoid bonding of the joint area to concrete. The overall test set-up can be seen in *Figure 3.95*. The slip measuring transducer was attached to the top frame using a bolted perpendicular extension.

Figure 3.93. Split cylinders cast

Figure 3.94. FRP wrapping of cylinders

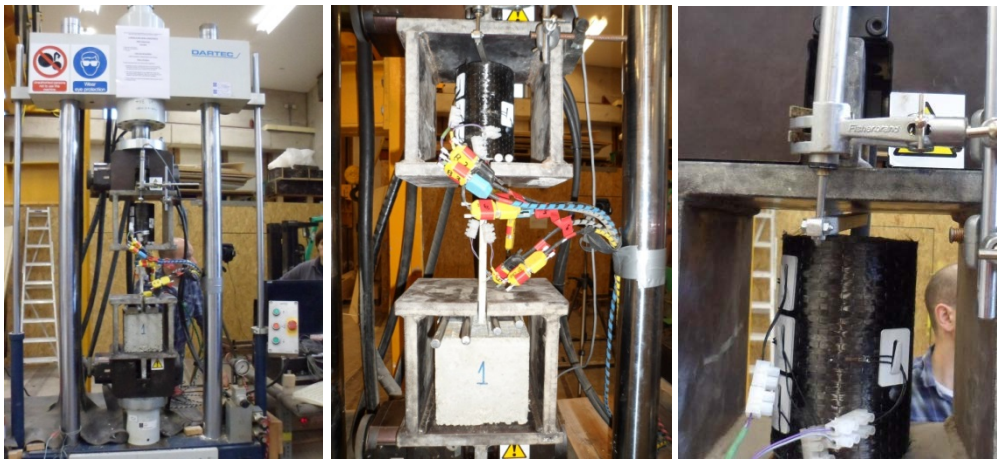

a. b. c.

Figure 3.95. Split cylinder test set-up: (a) loading machine, (b) holding frames and (c) slip measurement

A minimum of three unidirectional strain gauges for composite materials were installed along each split line of the cylinder specimens. Nevertheless, consistent readings were obtained only for Test P5. The results for the rest of the specimen were averaged for the readings of all working gauges. Furthermore, one specimen was tilted during the experiment, while unsuccessful measurement affected the results of a second experiment. Therefore, *Figure 3.96* presents results only for three (Test P3, Test P4 and Test P5) out of the five specimens. The transverse forces in the wedges, calculated from the measured strains, are compared with the theoretical predictions, based on the applied pull-out force and the values of the parameters μ and m, defined in § 3.7, used to produce the theoretical curves in *Figure 3.87*.

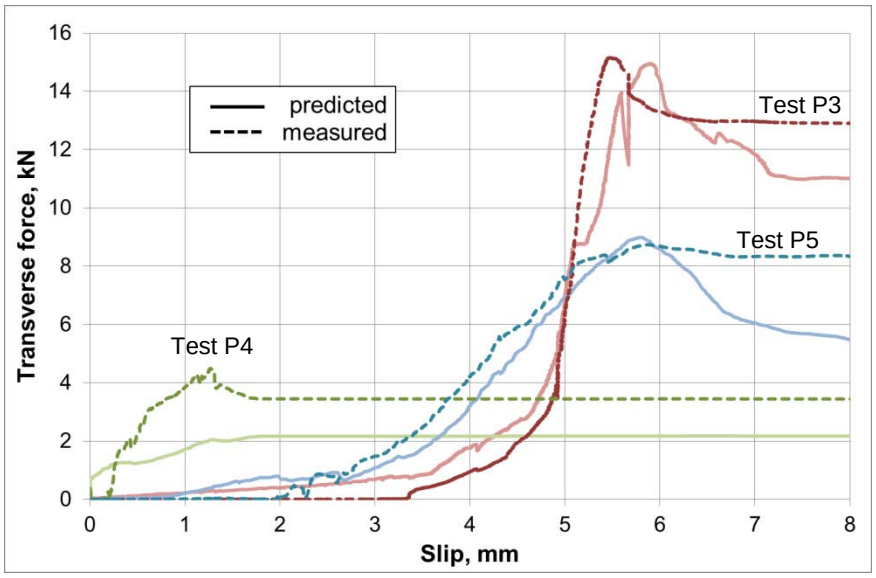

Figure 3.96. Split cylinder test results

The transverse force for smooth bars (Test P3) is greater than that for sand-coated bars, as can be expected. The measured results confirmed that the full sand-coated wedge developed the lowest transverse force, which agrees with the predictions. The larger difference between the theoretical and experimental values in this case can be explained with the interlaminar shear failure between the fibres at the surface of the bars, shown in *Figure 3.97*, affecting the assumed surface bond parameters. Such a type of failure was not observed during the hinged-beam tests, due to the greater confinement provided by concrete and the much lower end slip values. Although direct comparison of the pull-out and hinged-beam tests is not possible, the higher measured transverse forces compared with the predicted beyond 6 mm slip, for Test P5 in *Figure 3.96*, may indicate that the bond parameter m does not affect the wedging action after the initial slip, as previously concluded.

Figure 3.97. Bond failure of a sand-coated wedge

3.9. Concluding remarks

This chapter has presented an investigation of the behaviour of splayed bars carried out through a series of hinged-beam bond tests. A number of parameters have been discussed, amongst which the following were identified as most significant: size of the end wedge, FRP type, bar size, bar surface and confinement of concrete. An empirical model based on engineering principles has been developed to describe the initial behaviour of the tested bars. The proposed general expression could potentially be applied to any type of bar with known local bond-slip law. It has been shown that the model is valid up to 0.3 mm slip and, therefore, is unable to predict the anchorage strength for larger slips, governed by concrete behaviour. While the pull-out tests aimed to measure directly the transverse force in splayed ends and confirm the proposed bond parameters in the model, provided very limited results, it was possible to observe pull-out failure of splayed anchorages at lower loads and examine the failure surface of the splayed ends.

In summary, the following conclusions can be drawn based on the experimental results:

- Splayed anchorage of reinforcing bars improves significantly their anchorage strength over short embedment lengths even for small wedge angles.
- The wedging action of splayed bars overcomes the risk of brittle surface bond failure, which may occur for straight bars with same surface characteristics.
- Confinement of concrete in the anchorage zone prevents brittle failure and improves the behaviour of splayed anchorage.
- The proposed expression is able to predict the initial force-slip behaviour of FRP bars while the normal reaction in the concrete remains small and the slip is governed by the transverse deformation.
- An increase in frictional resistance due to sand-coating of FRP bars can reduce the normal force transferred to the concrete, and prevent concrete failure.
- Forming wedges in bars larger than 12 mm was not studied; however, the splay angles may need to be reduced to avoid longitudinal splitting of larger size bars. An alternative, which could be considered in future research, may explore the feasibility and performance of a three-dimensional wedge, created by cutting two perpendicular slots
- Re-writing *Equation 3.25* for 0.3 mm slip may be used as a design formula for FRP splayed bars, where m can be conservatively taken as 1 for wedges, which are not fully sand-coated:

$$F_b = 1200 * L_w * sin^2\left(\frac{\alpha_w}{2}\right) + 1500 * m * L_w * sin(\alpha_w) + \tau_w * A_w + \\ +\tau_b * (\pi * d_b - 2 * t_w) * L_w \tag{3.26}$$

4. Design of Fabric-formed Beam Elements

4.1. Introduction

The feasibility of fabric-formed structures depends predominantly on the capability to accurately predict and design the final complex concrete shapes cast in flexible formwork, while integrating structural optimisation in the process. This chapter presents a proposed design methodology, comprising form-finding, structural analysis and optimisation of horizontally cast fabric-formed elements, subject to transverse loads.

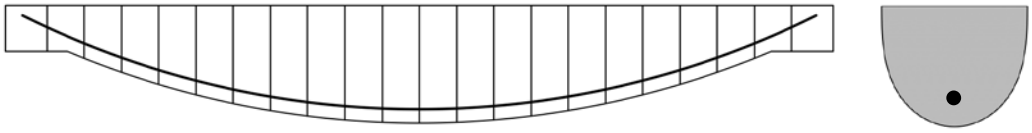

Figure 4.1. Beam modelled as a sequence of transverse sections

As introduced in § 2, there are different approaches to find the shape assumed by a hanging fabric under the hydrostatic pressure exerted from fresh concrete. Although the general problem is three-dimensional, linear structural elements, such as beam and columns, can be modelled as a sequence of two-dimensional transverse sections (*Figure 4.1*), assuming that a sufficiently large number of sections is used. This simplified approach allows rapid optimisation and design of each cross section by means of conventional methods. However, an extensive experimental investigation is required to demonstrate the accuracy of shape prediction and expected structural behaviour, and to define the limits of its application.

4.2. Form-finding

The two-dimensional shape of fabric filled with a viscous liquid, also called “lintearia”, fundamentally is an “elastic curve” and, therefore, is related to the theory of elliptic integrals and elliptic functions (Sridharan, 2004). The analytical solution of elliptic integrals, however, can be impractical for engineering applications. Therefore, empirical formulae and numerical methods have also been proposed to find the shape of fabric-formed cross-sections.

4.2.1. Background research

Bailiss (2006) used physical models to derive non-dimensional relations for the perimeter P *(Equation 4.1)* and the cross-sectional area A *(Equation 4.2)* of two-dimensional sectional profiles, as functions of the depth D and breadth B. The obtained expressions, however, are not able to describe the full cross-sectional profile, and may lead to unreliable design of fabric-formed elements.

$$P = \frac{-(0.212 * B - D) + \sqrt{(0.212 * B - D)^2 - 4 * 0.396 * (-0.49 * B^2)}}{2 * 0.396} \quad (4.1)$$

$$A = \left\{ \left[\frac{\left(\frac{B}{P}\right) - 0.05}{0.65} \right]^{-0.3} - 0.34 \right\} * B * D \quad (4.2)$$

Garbett (2008) revisited Bailiss's experimental data in order to determine important cross-sectional characteristics, including the maximum breadth w_m *(Equation 4.3)* and the depth at which it occurred h_m *(Equation 4.4).* Moreover, Garbett (2008) also concluded that sections formed in a freely hung fabric may not be efficient in terms of material use and proposed improved designs, such as hollow and 'key-hole' sections, discussed in § 2.

$$w_m = \left[3.20 * \left(\frac{B}{D}\right)^2 - 5.77 * \left(\frac{B}{D}\right) + 3.61 \right] * B \quad (4.3)$$

$$h_m = \left[-0.326 * \left(\frac{B}{D}\right) + 0.666 \right] * D \quad (4.4)$$

An analytical solution of incomplete elliptical integrals, describing the shape of a soft container under hydrostatic load, was provided by Iosilevskii (2010). The output, presented as relationships between the main parameters, established a useful basis for comparison with numerical methods. In addition, it was demonstrated mathematically that the tension force in the fabric, $T_s(t)$, is constant along the whole sectional perimeter (see *Figure 4.2*).

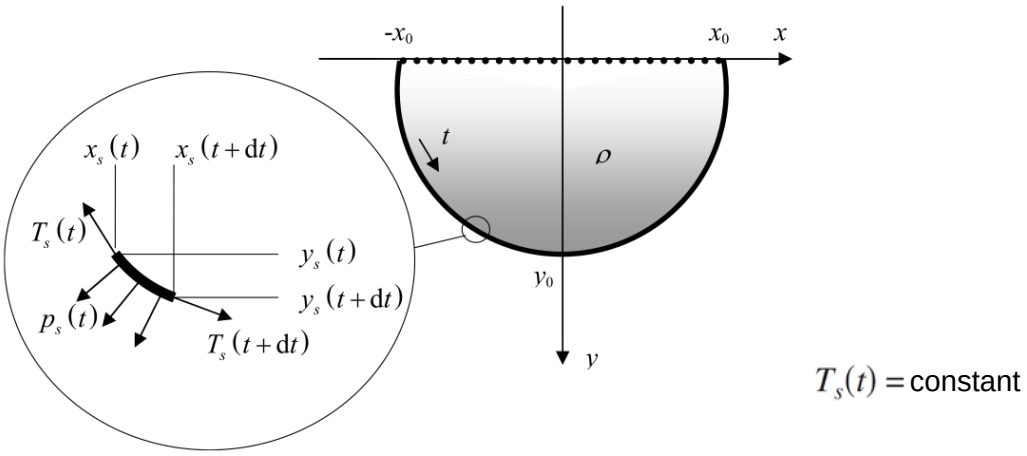

Figure 4.2. Coordinate system and model proposed by Iosilevskii (2010)

Foster (2010) developed an iterative spreadsheet-based procedure, which involves 'walking out' a cross-sectional perimeter by expressing all successive coordinates as functions of the preceding coordinates and the relation between the curvature and hydrostatic height, assuming inextensible fabric. The obtained profiles achieved good agreement against test results, provided by Bailiss (2006) and Iosilevskii (2010). Furthermore, while Iosilevskii (2010) considered only a container with a fluid surface levelled with the opening, the 'walking out' procedure was applied to over-full and part-full cases, as illustrated in *Figure 4.3*. The part-full scenario may have limited applications, possibly for creating concrete forms cast in stages. The over-full case, however, allows for modelling cross-sections with top parts, positioned above the fabric-formed bulb, such as top slabs in T-beam construction.

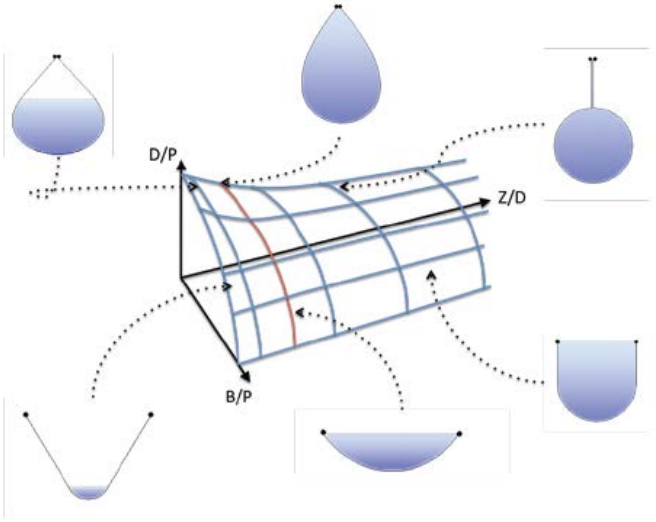

Figure 4.3. 'Walking out' procedure and physical interpretations of non-dimensional surface (Foster, 2010)

The form-finding algorithm developed in the current research is based on the numerical procedure implemented by Foster (2010). The original procedure, presented in § 4.2.2 has been improved and coded in MATLAB to allow faster and more robust design of multiple sections. In addition, the program has been extended to solve complex geometries, formed in horizontally or vertically restrained fabrics. The output of the program provides the length of the fabric perimeter at each cross section and creates patterns for construction. The theoretical perimeter may need to be adjusted to allow for the extension of fabric, depending on the fabric properties, the warp and weft orientation of woven fabrics, bias and cross grain, and potentially the shear modulus of fabric. However, it is unlikely that highly extensible fabrics would be used for casting concrete and the patterns for inextensible fabric may be reasonably accurate for construction purposes, as highlighted in the next three chapters.

4.2.2. Form-finding algorithm

The proposed iterative procedure finds the coordinates of points equally spaced along the perimeter of an inextensible fabric membrane, which is fixed at both ends and subjected to hydrostatic pressure p_s. The selfweight and out-of-plane stiffness of fabric are assumed to be negligible and, therefore, the curvature of the profile perimeter is solely dependent on the hydrostatic pressure. As indicated in *Figure 4.4*, the pressure has intensity defined by the density of fresh concrete ρ and the hydrostatic height z_i at each point. It acts perpendicular to the fabric surface, creating a constant tension force T.

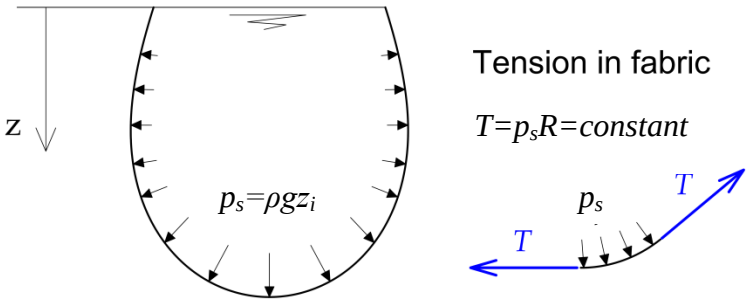

Figure 4.4. Forces acting on a fabric membrane

If the cross-sectional perimeter is represented by a large number of straight lines of equal lengths Δl, as illustrated in *Figure 4.5*, the following relationship can be derived:

$$R_i = \frac{\Delta l}{\theta_i} = \frac{T}{\rho * g * z_i} \tag{4.5}$$

where R_i is the radius of curvature.

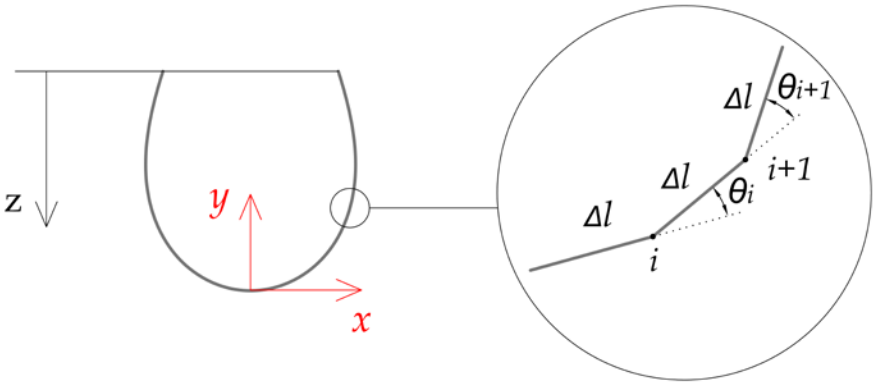

Figure 4.5. Approximation of a curved profile with straight lines

The 'walking out' starts at point *(0,0)* of a global coordinate system *(x,y)* with the origin being at the lowest point of the cross section. Due to the symmetry of the hydrostatic shape, only half of the hung perimeter is considered. By 'walking out' the curve in

increments of length Δl, every set of coordinates (x_i+1, y_i+1) at point $i+1$ is obtained from the coordinates at point i:

$$x_{i+1} = x_i + \Delta l * \cos\left(\sum_{j=0}^{i} \theta_j\right) \tag{4.6}$$

$$y_{i+1} = y_i + \Delta l * \sin\left(\sum_{j=0}^{i} \theta_j\right) \tag{4.7}$$

The sum $\Sigma\theta_j$ represents the angle of segment $(i,\ i+1)$ with the horizontal axis. Furthermore, from *Equation 4.5*, it follows that the angles θ_i are proportional to the hydrostatic heights z_i:

$$\theta_i = c * z_i, \tag{4.8}$$

where

$$c = \frac{\rho * g * \Delta l}{T} = constant. \tag{4.9}$$

Or

$$\theta_i = c * (D - y_i), \tag{4.10}$$

where D is the depth of cross section. Therefore, the angle θ_0 at $y_0=0$ will be:

$$\theta_0 = c * D. \tag{4.11}$$

In the original form-finding algorithm, θ_0 is taken equal to the initial horizontal angle by introducing an initial horizontal segment l_0, as indicated in *Figure 4.6*a, thereby allowing for the design of 'flat-bottom' sections. However, if l_0 is zero, the initial horizontal angle is half of θ_0 due to symmetry, as can be seen in *Figure 4.6b*. Therefore, it has been proposed to define the initial horizontal angle depending on the actual condition, i.e. θ_0 for 'flat-bottom' and $\theta_0/2$ for freely hung sections.

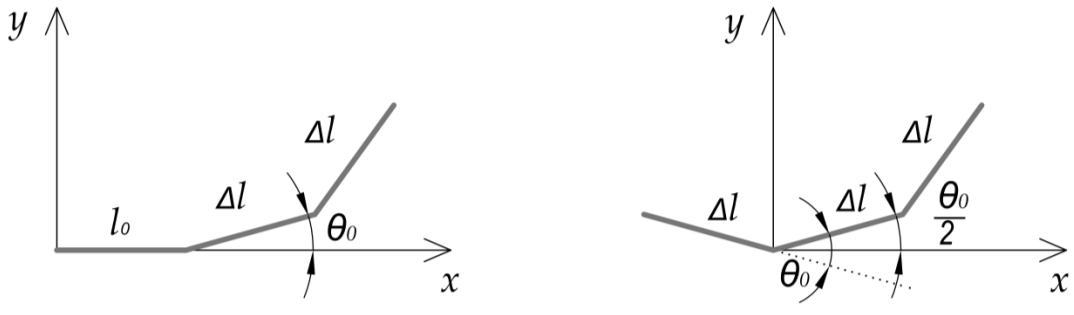

a. b.

Figure 4.6. Initial horizontal angle: (a) 'flat-bottom' and (b) freely hung section

The spreadsheet-based program uses a standard goal-seeking algorithm to vary the constant c for a sufficiently large pre-defined number of coordinates (x, y), calculated using *Equation 4.6* and *Equation 4.7*, until a set of coordinates $(B/2, D)$ is obtained by minimising the sum of the square of residuals $\sqrt{\left(x_i - {}^{B}/_{2}\right)^2 + (y_i - D)^2}$. The success of finding a solution depends upon three initial guesses: the initial value of c, the step Δl and the number of coordinates (x, y). As illustrated in *Figure 4.7*, the initial guess of constant c is most critical, particularly for deeper sections, for which loops may be formed in the initial profile and the algorithm cannot converge to a solution. In order to eliminate this problem, two control statements for the coordinate y_i have been introduced in the MATLAB program to find the profile of a typical cross section, shown in *Figure 4.8a*, thereby avoiding loops in the calculated profiles and minimising the error for coordinate x_i only by changing the constant c (see *Figure 4.8b* and *Figure 4.8c*). The new approach allows for a fast solution of multiple sections and a better control of the accuracy of each parameter. Furthermore, the final curves can easily be reproduced from the obtained constant c.

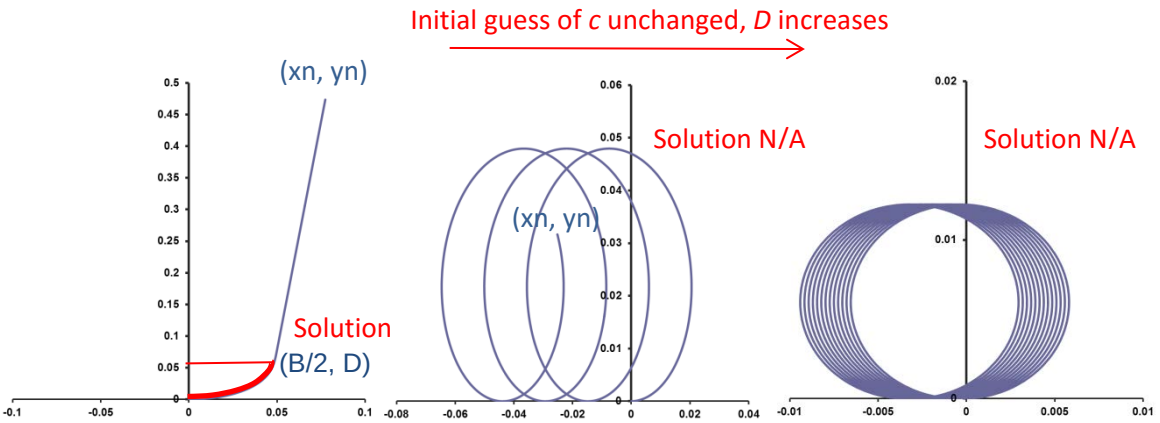

Figure 4.7. Initial curve profile for same constant c and increasing depth (using form-finding spreadsheet program, (Foster, 2010))

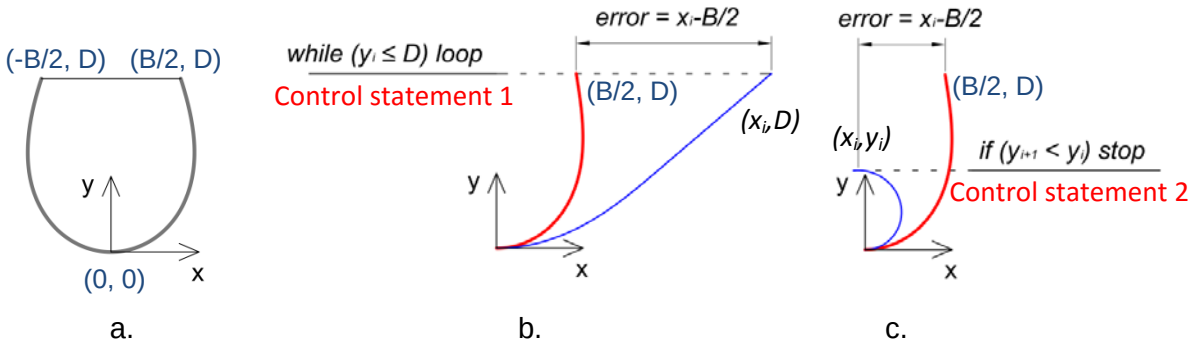

Figure 4.8. Improved form-finding algorithm: (a) final profile, (b) control statement 1 and (c) control statement 2

Figure 4.9 presents plots from the MATLAB program for sections with variable B/D ratio. As can be seen, creating deep and narrow sections in freely hung fabric is not possible, due to the pronounced bulging effect. The fabric-formed sections of flexural members with B/D ratio less than 0.8 are, in fact, less efficient than rectangular sections of the same breadth and width (*Figure 4.10*), since the additional material is concentrated near the neutral axis and has little contribution to the structural capacity.

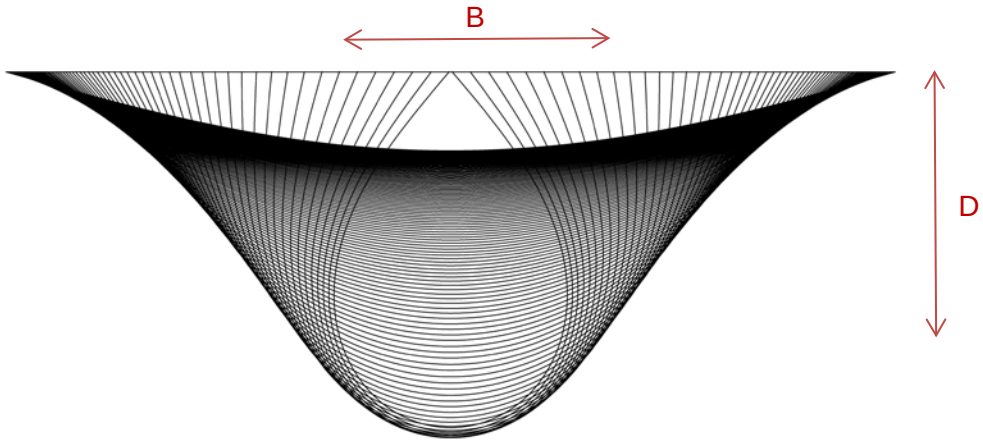

Figure 4.9. Full range of hydrostatic cross-sectional profiles

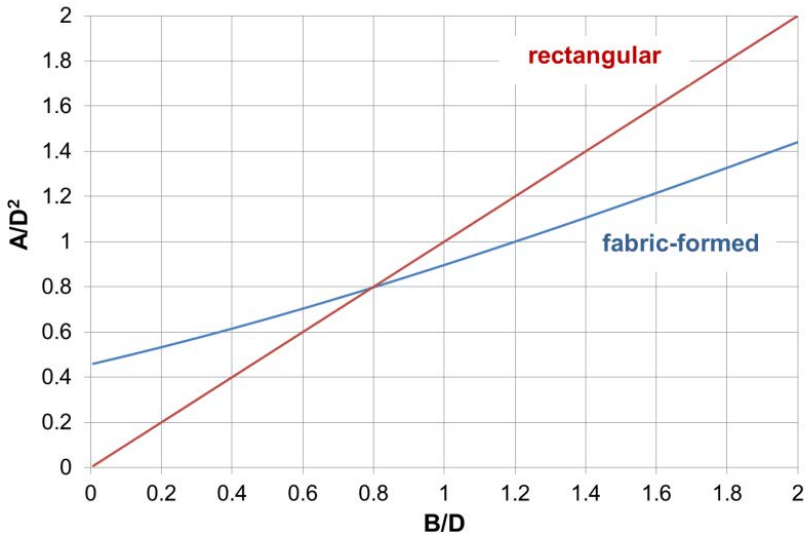

Figure 4.10. Reduced material efficiency of fabric-formed sections under a decrease in the B/D ratio

The bulging effect can also be gauged from the non-dimensional relationship between the breadth B and depth D in *Figure 4.11*. The obtained curve is compared with the analytical solution, given by Iosilevskii (2010). In addition to the good agreement of results, the curve shows a decline in depth with decrease in the opening. These observations provide useful relationships between parameters defining the efficiency of fabric-formed cross sections and encourage the development of appropriate construction methods, which can

help to avoid undesired bulging. Possible approaches, adopting the use of internally restrained fabric for sections with B/D ratios less than 0.8, are described in detail in § 5, while the theoretical basis for form-finding of the resulting cross-sectional profiles is discussed in § 4.2.3.

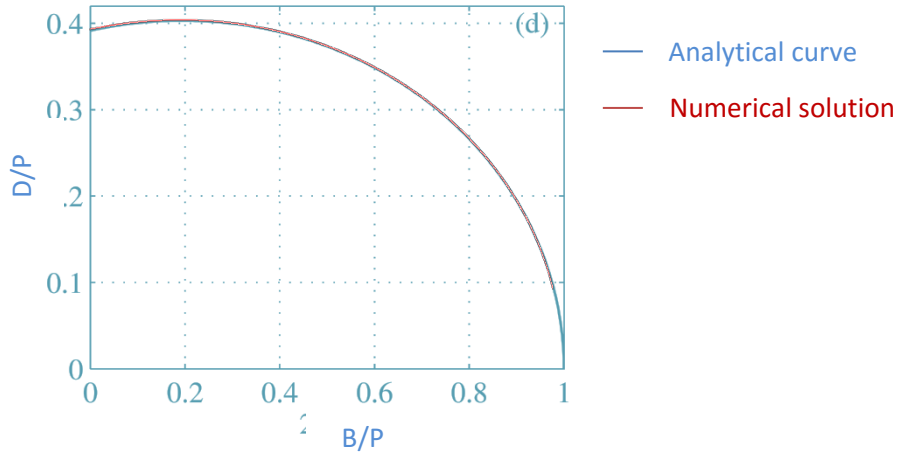

Figure 4.11. Comparison of maximum draft with analytical results of Iosilevskii (2010)

Fabric-formed sections partially restrained by rigid formwork, including T-beams and 'key-hole' sections, may have height of the bulb h_{bulb} smaller than the overall sectional depth, as illustrated in *Figure 4.12*. The curved profile of such sections can still be obtained using the described procedure and equations by evaluating the constant c at y_i coordinate equal to h_{bulb}, for the corresponding width of the section at the same level.

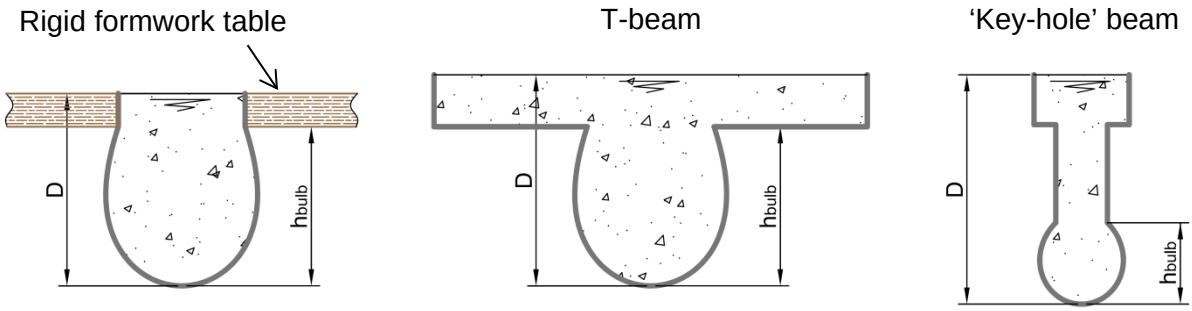

Figure 4.12. Height of bulb $\boldsymbol{h_{bulb}}$ and overall height $\boldsymbol{D}$

4.2.3. Internally restrained fabric

The shape of fabric-formed sections can easily be controlled by means of internal ties in order to avoid the need for additional external supports. While such a method is well-known and successfully used for construction of 'quilt-point' walls, as described in § 2, its application to beam sections requires further development of the form-finding algorithm to allow for prediction of the final shapes.

Figure 4.13 shows the forces due to hydrostatic pressure in a fabric, tied in the horizontal direction. The algorithm described in § 4.2.3 can predict the shape of the lower part and the force T_1. The curve profile above the restraint point, however, depends upon the angle α_1, which is unknown initially but which can be found from equilibrium of the forces (See *Figure 4.13*).

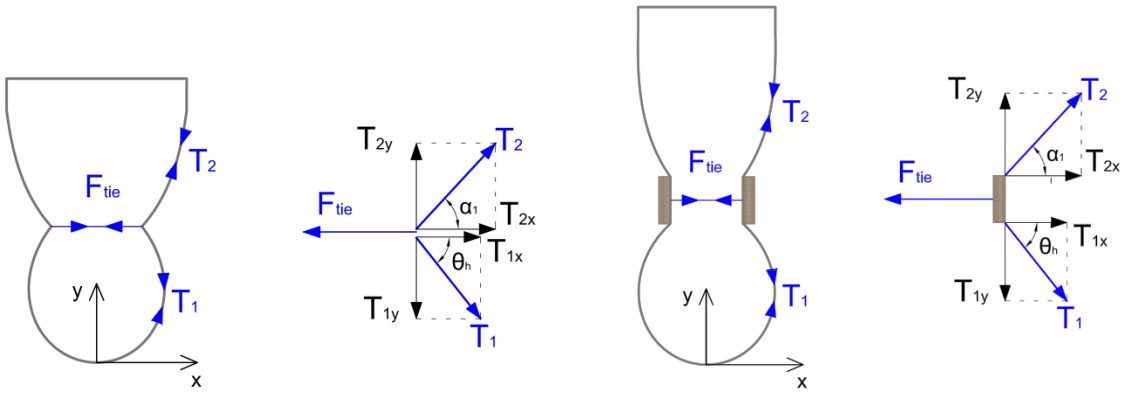

Figure 4.13. Forces acting on horizontally restrained fabric: (a) tie at a single point and (b) tie connecting rigid formers

From equilibrium in the vertical direction at the point of restraint, it follows that:

$$T_{2y} = T_{1y} \tag{4.12}$$

where T_{2y} and T_{1y} are the vertical components of the tension forces T_2 and T_1 at the upper and lower bulbs of the section, respectively. However, based on *Equation 4.9*, T_{2y} can also be expressed as:

$$T_{2y} = T_2 * sin(\alpha_1) = \frac{\rho * g * \Delta l}{c_2} \cdot sin(\alpha_1) \tag{4.13}$$

Similarly,

$$T_{1y} = T_1 * sin(\theta_h), \tag{4.14}$$

where

$$\theta_h = \pi - \sum_{i=0} \theta_i \tag{4.15}$$

The angle θ_h is obtained from the sum of angles θ_i for the lower part. Therefore, the angle α_1 is determined by solving *Equation 4.16* at each iteration for c_2.

$$sin(\alpha_1) = \frac{c_2 * T_{2y}}{\rho * g * \Delta l} \tag{4.16}$$

Once T_2 is obtained, the force in the tie can be determined from equilibrium in the horizontal direction:

$$F_{tie} = T_{1x} + T_{2x} \tag{4.17}$$

A similar approach may also be applied to sections cast in vertically restrained fabric, such as the section shown in *Figure 4.14*. Although not practical for achieving efficient geometries, a possible application of a construction method described in § 5 suggests that the design profile of longitudinal FRP reinforcement can be formed under the weight of fresh concrete, if straight bars are attached to the fabric formwork by means of vertical ties of length equal to the concrete cover.

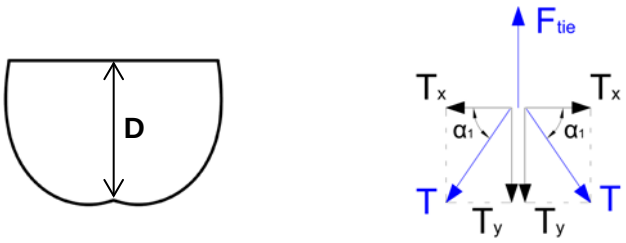

Figure 4.14. Forces acting on vertically restrained fabric

Similarly to *Equation 4.16*, the initial horizontal angle α_1 can be expressed from equilibrium of the forces at the point of restraint:

$$sin(\alpha_1) = \frac{c * F_{tie}}{2 * \rho * g * \Delta l} \tag{4.18}$$

In a design situation, the force F_{tie}, required to bend a straight FRP bar, and the minimum depth, D, would be defined, while the curved profile and perimeter need to be determined, following the described algorithm for iteration of the constant c. The curved profile and the force in the vertical tie F_{tie} can be obtained for a known maximum depth or perimeter of the section. The latter is useful mainly for assessing as-built geometries by overlapping actual profiles with shape predictions, having the same overall dimensions.

4.3. Flexural design

This section presents the theory, constitutive material models and main assumptions, used for the flexural design of fabric-formed elements throughout the current study.

Standard design methods and, where possible, material models, defined in BS EN 1992-1-1:2004 are employed. A computer program, written in MATLAB, has combined the form-finding algorithm, described in § 4.2, with sectional analysis and design presented herein.

4.3.1. Concrete model

The constitutive model for unconfined concrete in compression is based on the BS EN 1992-1-1:2004 stress-strain relation for non-linear structural analysis, illustrated in *Figure 4.15*. All parameters, including the mean strength f_{cm}, the modulus of elasticity E_{cm}, the strain at peak stress ε_{c1} and the nominal ultimate strain ε_{cu1} are defined in accordance with BS EN 1992-1-1:2004.

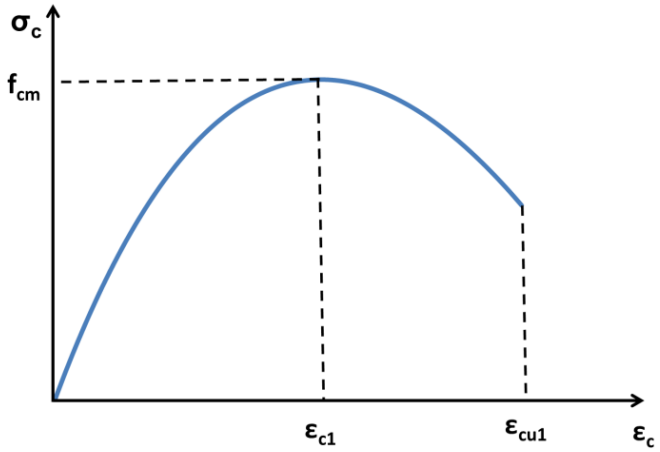

Figure 4.15. Stress-strain model for unconfined concrete in compression

The stress-strain curve is described by the expression, given in *Equation 4.17*:

$$\frac{\sigma_c}{f_{cm}} = \frac{k * \eta - \eta^2}{1 + (k - 2) * \eta} \tag{4.19}$$

where

$$\eta = \frac{\varepsilon_c}{\varepsilon_{c1}} \tag{4.20}$$

and

$$k = 1.05 * E_{cm} * \frac{|\varepsilon_{c1}|}{f_{cm}} \tag{4.21}$$

An additional stress-strain model is required to describe the behaviour of concrete, confined by helical reinforcement in the compression zone. Leung and Burgoyne (2005) obtained experimentally the uniaxial strain-stress relationship for helically confined concrete for a range of concrete strengths and confining reinforcement. Since the helical reinforcement provides passive confinement, arising from the lateral expansion of

concrete, the experiments demonstrated that for stiffer high-grade concrete, the beneficial effect of confinement is reduced significantly, as expected. Based on the published results (Leung and Burgoyne, 2005), it was concluded that for concrete strengths up to 30 MPa and confining AFRP helical reinforcement of 90 mm diameter and 30 mm pitch, the post-peak branch of the stress-strain curve can be assumed to be horizontal, while the ascending branch follows the relationship for unconfined concrete, as shown in *Figure 4.16*. For this type of confining reinforcement, the ultimate strain capacity of concrete, according to Whitehead (2002), may reach values of up to 1%, providing sufficient deformability to avoid brittle failure of concrete elements, reinforced with FRP tension reinforcement.

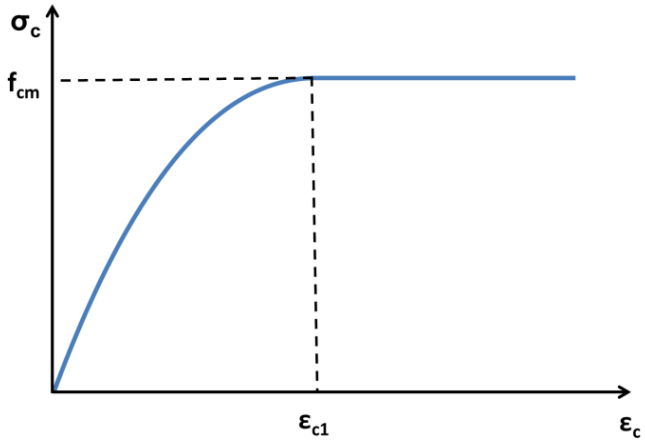

Figure 4.16. Stress-strain model for confined concrete in compression

The behaviour of concrete in tension is assumed linear-elastic until failure at ultimate tensile strain f_{ctm}/E_{cm}, where f_{ctm} is the mean tensile strength of concrete.

4.3.2. Reinforcement

While the experimental part of this research was focused entirely on FRP-reinforced elements, steel reinforcement has also been considered and included as an option in the design program. The bi-linear stress-strain relation, shown in *Figure 4.17*, is adopted for the steel reinforcement, where E_s is the modulus of elasticity of steel bars, typically taken as 200 GPa, and f_y is the material yield strength. The linear-elastic behaviour of FRP reinforcement is represented by the model given in *Figure 4.18*, with modulus of elasticity E_{frp} and ultimate tensile strength f_u, provided by the manufacturers of different types of FRP bars. For the design of experiments, E_{frp} was confirmed through testing as well.

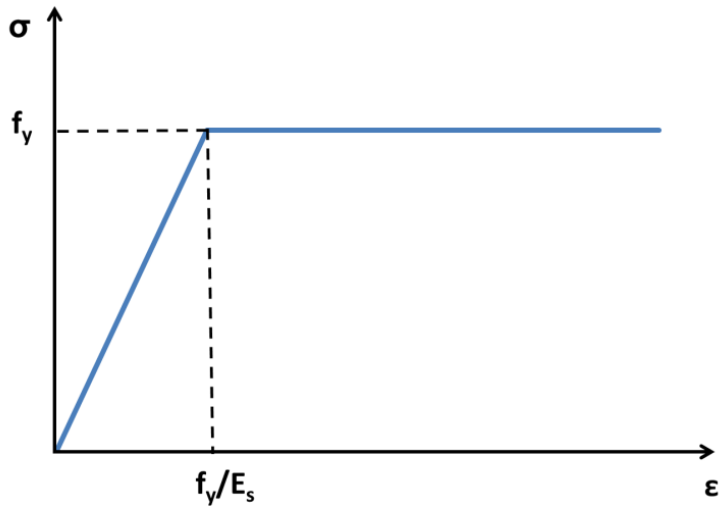

Figure 4.17. Bi-linear stress-strain model for steel reinforcement

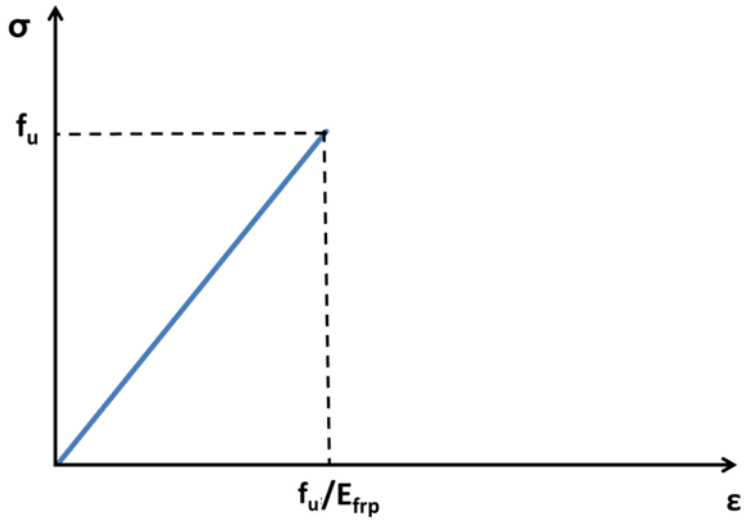

Figure 4.18. Stress-strain model for FRP reinforcement

4.3.3. Sectional analysis and design

The analysis and design of fabric-formed sections is generally based on the BS EN 1991-2-1-1:2004 design approach and assumptions. The stresses in the concrete and the reinforcement are derived from the stress-strain relationships, defined in § 4.3.1 and § 4.3.2, respectively. Perfect bond is assumed between the reinforcing bars and the surrounding concrete, while the strains are assumed to be linearly distributed along the sectional depth, i.e. assuming that plane sections remain plane. The ultimate moment of resistance is obtained from equilibrium of the forces in the concrete and the reinforcing bars, for strain at the extreme concrete fibre equal to ε_{cu1} (*Figure 4.19*).

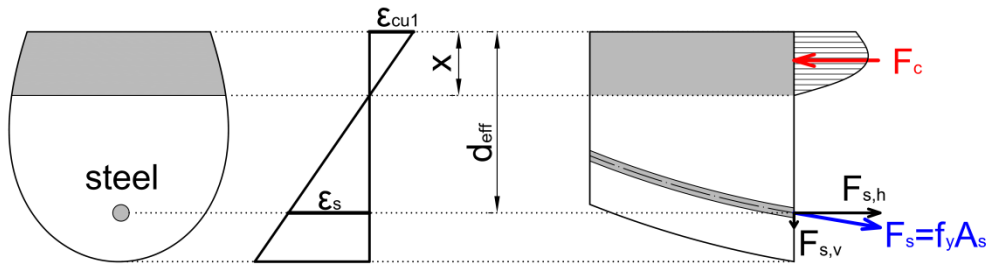

Figure 4.19. Section reinforced with steel

Whereas it is preferred that the steel reinforcement should reach its yield stress prior to concrete failure, the stress in the FRP reinforcement is found from the actual strain and increases until the concrete in compression crushes or the FRP bars snap (*Figure 4.20*). Therefore, the over-reinforced design of FRP-reinforced sections is crucial to avoid a sudden snapping failure of the FRP bars, as explained in § 2.

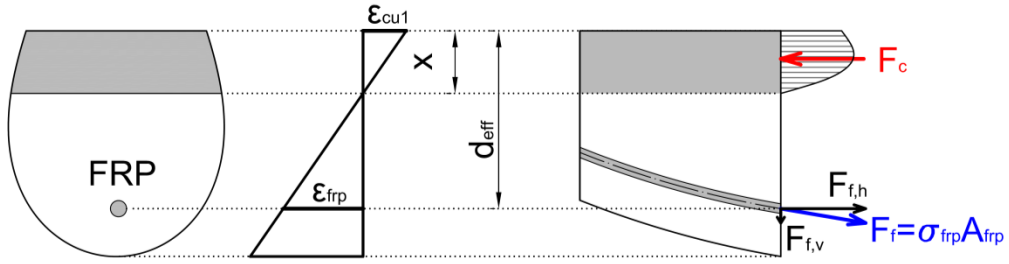

Figure 4.20. Section reinforced with FRP

Similarly to the form-finding approach, the variation of moment of resistance along the length of a beam with non-uniform depth is found by dividing the beam into transverse sections, as indicated in Figure 4.21. The output from the MATLAB form-finding program provides direct input for the beam analysis of fabric-formed beams. Optional input of pre-defined sectional profiles, such as data from as-built measurements, is included in the design program for assessing the capacities of constructed sections.

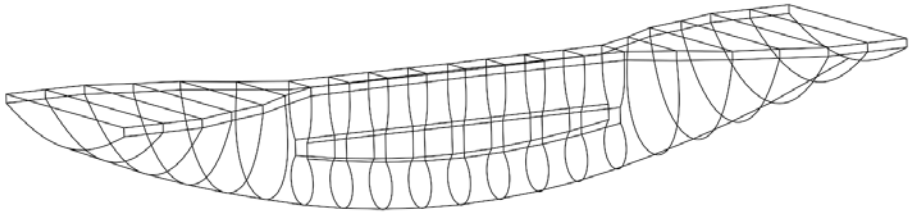

Figure 4.21. 3-D view of cross sections along the length of a typical fabric-formed beam

A layer-by-layer approach is employed in order to obtain the forces in the concrete for an assumed strain profile and concrete strain at the extreme fibres. A numerical root finding algorithm is then implemented to find the depth of the neutral axis from equilibrium of all forces acting on the cross-section under consideration (See *Figure 4.22*). In addition, the procedure has been modified by further horizontal subdivision of the layers and use of

different concrete models for deriving the stresses in the confined and unconfined concrete areas, as shown in *Figure 4.22*. The size and number of layers can be related to the division of the fabric perimeter, used for form-finding, to allow for direct transfer of data between the two computational processes.

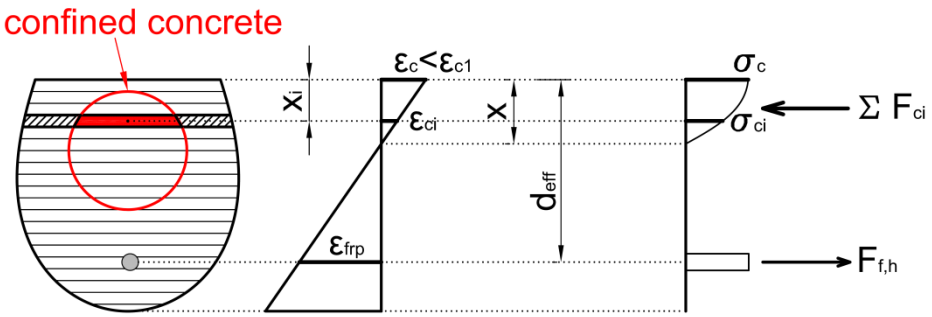

Figure 4.22. Initial stresses in section with confined compression zone

Figure 4.22 and *Figure 4.23* illustrate a typically shaped fabric-formed section with helically confined concrete in the compression zone. Based on the adopted stress-strain model of confined concrete in compression, the effect of confinement is not realised during the initial loading stages, when the stresses in the concrete are below ε_{c1} (*Figure 4.22*). Furthermore, as *Figure 4.23* suggests, the increased stresses in the confined concrete are unlikely to contribute to a significant increase in the ultimate moment of resistance.

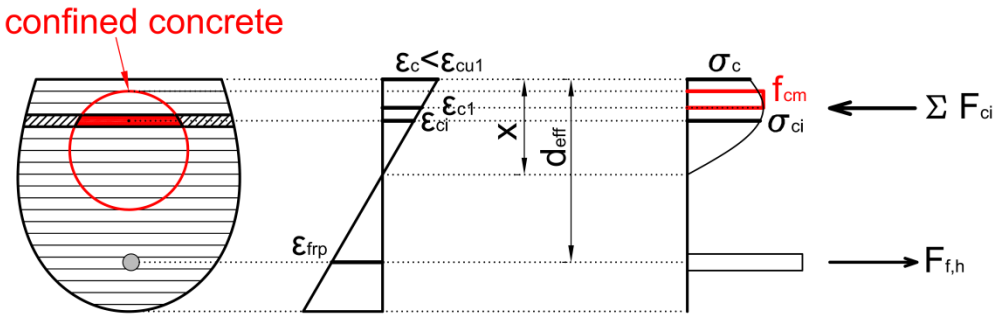

Figure 4.23. Increased stresses in section with confined compression zone

The major difference occurs when the unconfined concrete reaches its ultimate strain capacity and loses integrity. Beyond this stage the contribution of the concrete surrounding the confined area reduces progressively. *Figure 4.24* captures two moments in time, which describe the process. When the strains across the total confined area, A_{conf}, exceed the strain at peak stress ε_{c1}, the force in the confined concrete becomes equal to $f_{cm}\ A_{conf}$, and is applied at the centroid of the confined area, while the force in the unconfined concrete eventually becomes negligible.

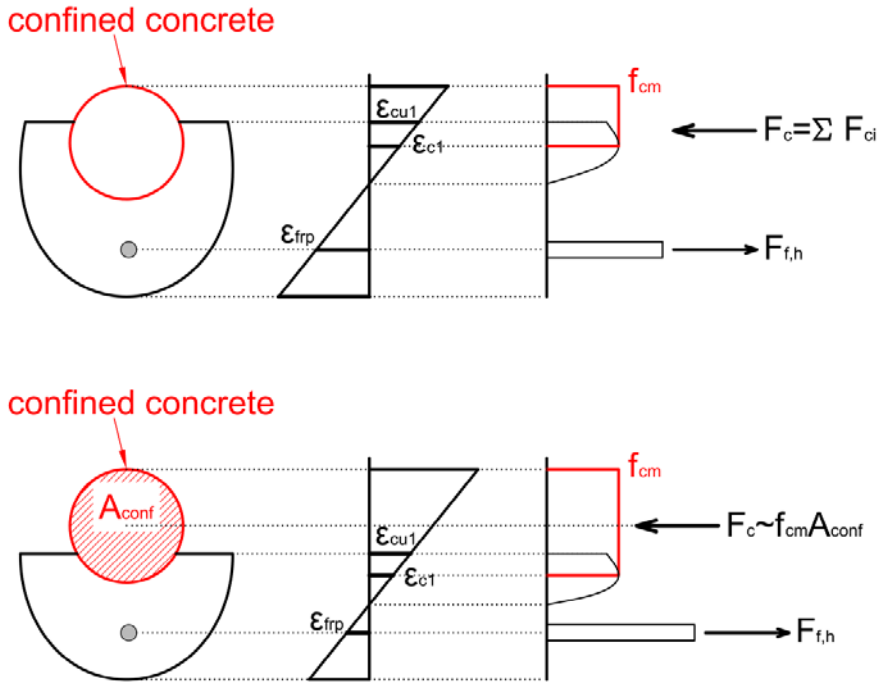

Figure 4.24. Post-peak stresses in section with confined compression zone

The proposed layer-by-layer approach allows sectional analysis to be undertaken over the full loading cycle and allows determination of the post-peak moment of resistance of sections with confined compression zones. As suggested earlier, the failure criterion in this case may be considered to be 1% ultimate strain at the extreme fibre of confined concrete.

4.3.4. Load-deflection analysis

For design purposes, the deflections of a beam element normally need to be estimated only under serviceability loads. For this reason, modelling the full load-deflection behaviour of fabric-formed beams through to the ultimate condition is not pursued as part of the current research and the adopted approach for analysis of beam cross sections, as coded in MATLAB, is utilised to predict the ascending branch of the load-deflection curve to cover the serviceability condition. In detail, the procedure involved obtaining the curvatures at each cross section from known bending moment profiles, corresponding to incrementally increasing vertical loads from zero to the maximum load at failure. The curvature κ at a section is expressed as:

$$\kappa = \frac{\varepsilon_c}{X} \tag{4.22}$$

where ε_c is the concrete strain at the extreme compression fibre and X is the depth to the neutral axis. The curvature profile at each load step is then integrated numerically twice to produce the deflection profile along the beam length.

4.3.4.1. Prismatic beams

The output from the MATLAB program has been initially verified against published experimental data for beams with rectangular sections. In order to illustrate the accuracy of the predicted load-deflection curves, two examples of steel reinforced concrete beams, singly and doubly reinforced, are presented herein, as well as three examples of FRP reinforced beams, comprising bars with different material properties and reinforcement ratios.

The first example is a singly reinforced concrete beam test carried out by Buckhouse (1997), cited and previously analysed by Wolanski (2004) and Al-Janabi et al. (2008). The beam cross section was 254 mm wide and 457 mm deep, reinforced with 3 bars #5, providing total area of steel 594 mm^2 with yield strength 414 MPa. The concrete cover was 50.8 mm and the recorded compressive cylinder strength of concrete was 33 MPa. The beam had a single span of 4572 mm and was tested under 4-point bending, as shown in *Figure 4.25*.

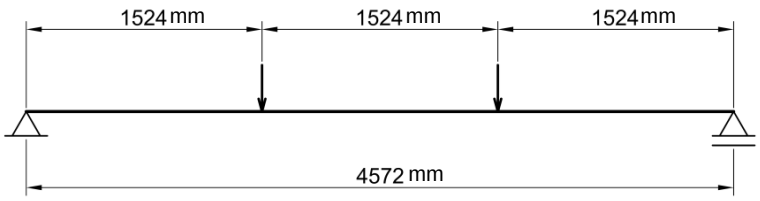

Figure 4.25. Test loading arrangement (Buckhouse, 1997, cited by Wolanski, 2004)

The dimensions of the beam were defined as an as-built input into the MATLAB program to avoid executing the form-finding algorithm. The results, presented in *Figure 4.26*, demonstrate a relatively good correlation between the experimental and the theoretical load-deflection curves, as well as an accurate prediction of the yield moment capacity.

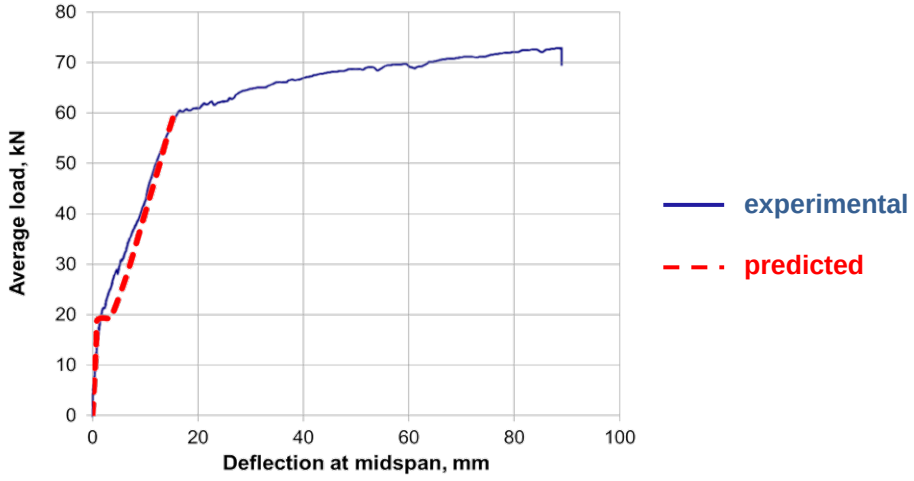

Figure 4.26. Load-deflection relation for steel singly reinforced concrete beam (Buckhouse, 1997, cited by Wolanski, 2004)

As an example of a doubly reinforced concrete beam, the results of an experimental study conducted by Rafi and Nadjai (2011) were used. The cross section of the test beam had 120 mm width and 200 mm depth, including 20 mm cover to the reinforcing bars. The tension reinforcement comprised 2 bars of 10 mm diameter each with yield strength of 530 MPa, while the compression reinforcement consisted of 2 bars of 8 mm diameter with yield strength of 566 MPa. The measured cylinder compressive strength of concrete was 46.5 MPa. Similarly to the previous example, the beam was tested under 4-point bending, indicated in *Figure 4.27*, and the comparison of results is shown in *Figure 4.28*.

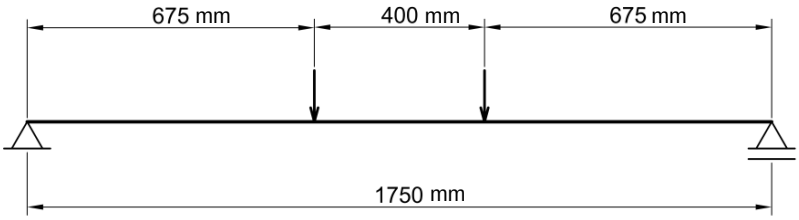

Figure 4.27. Test loading arrangement (Rafi and Nadjai, 2011)

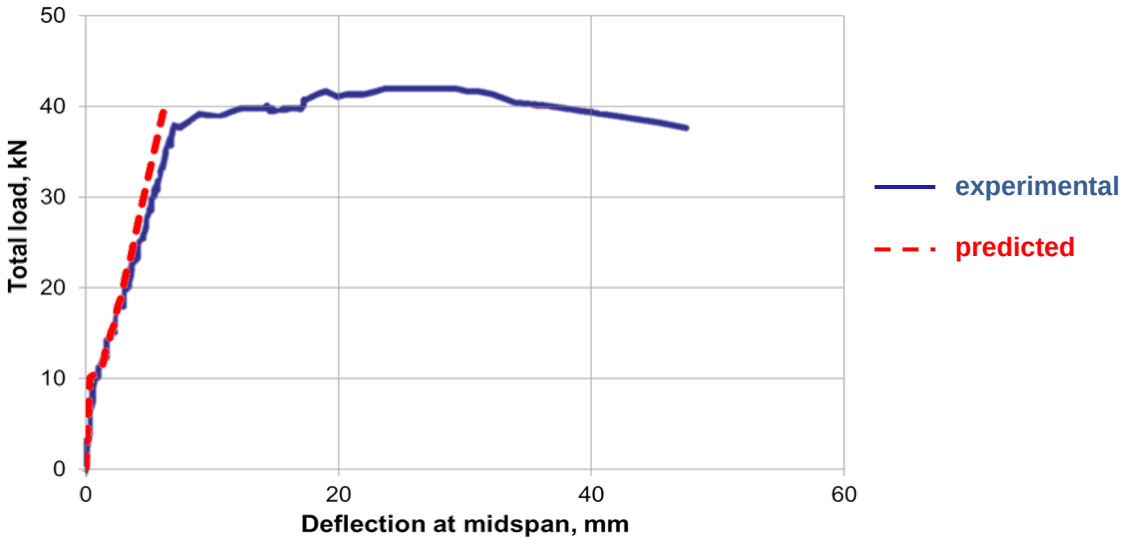

Figure 4.28. Load-deflection relation for steel doubly reinforced concrete beam (Rafi and Nadjai, 2011)

Abdalla (2002) tested a number of concrete beams, reinforced with different types of FRP bars and reinforcement ratios. The span and loading arrangement for all presented experiments can be seen in *Figure 4.29*. The beams had 500 mm width, 250 mm depth and concrete cover to the reinforcement 38 mm. The compressive concrete strength varied between 30 and 35 MPa. *Figure 4.30* presents the predicted and experimental load-deflection curves for a beam reinforced with CFRP (Leadline) bars with modulus of elasticity 147 GPa and 0.2% reinforcement ratio. The results demonstrate that the MATLAB programme can predict, with equal success, the serviceability behaviour of concrete beams reinforced with carbon FRP and steel bars.

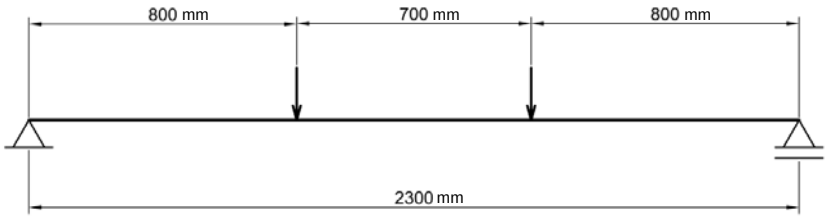

Figure 4.29. Test loading arrangement (Abdalla, 2002)

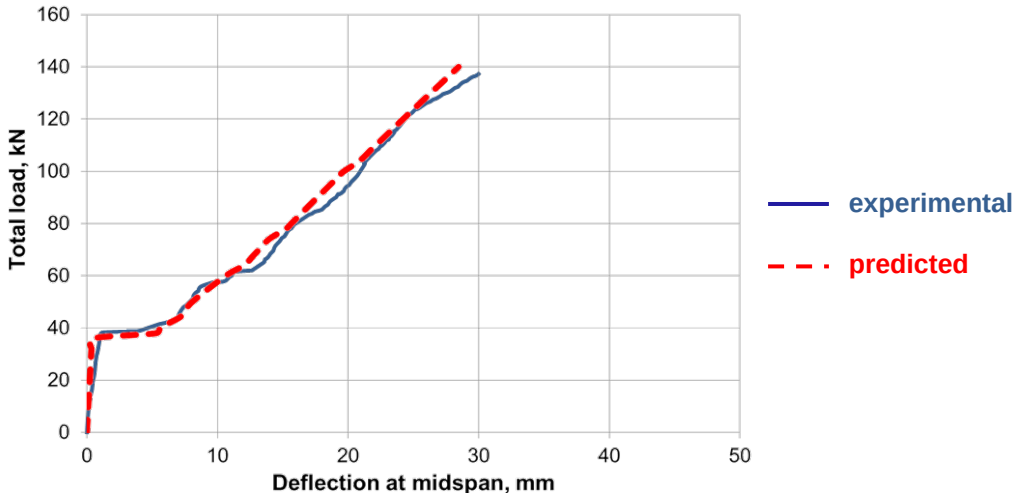

Figure 4.30. Load-deflection relation for CFRP (Leadline, 0.2%) beam (Abdalla, 2002)

Beams, containing two types of GFRP bars, C-bar and Isorod, were tested. The modulus of elasticity of both types was 42 GPa, however the reinforcement ratios were 0.45% for C-bar and 1.5% for Isorod. The comparisons of experimental results with theoretical predictions of the current program are presented in *Figure 4.31* and *Figure 4.32*. As can be seen, *Figure 4.32* indicates that the program tends to overestimate the beam stiffness under increasing reinforcement ratio. However, this problem is observed only for loads above 50% of the ultimate capacity, which may suggest that the proposed method of analysis would still be adequate under serviceability loads.

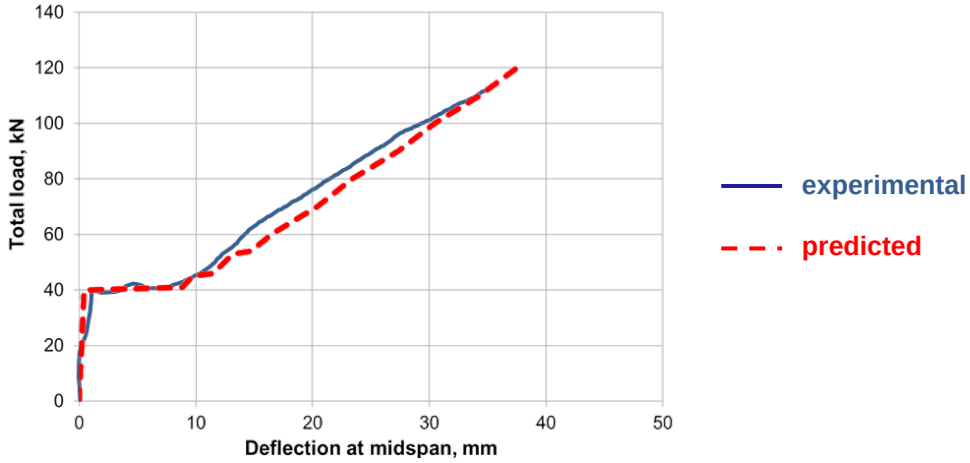

Figure 4.31. Load-deflection relation for GFRP (C-bar, 0.45%) reinforced beam (Abdalla, 2002)

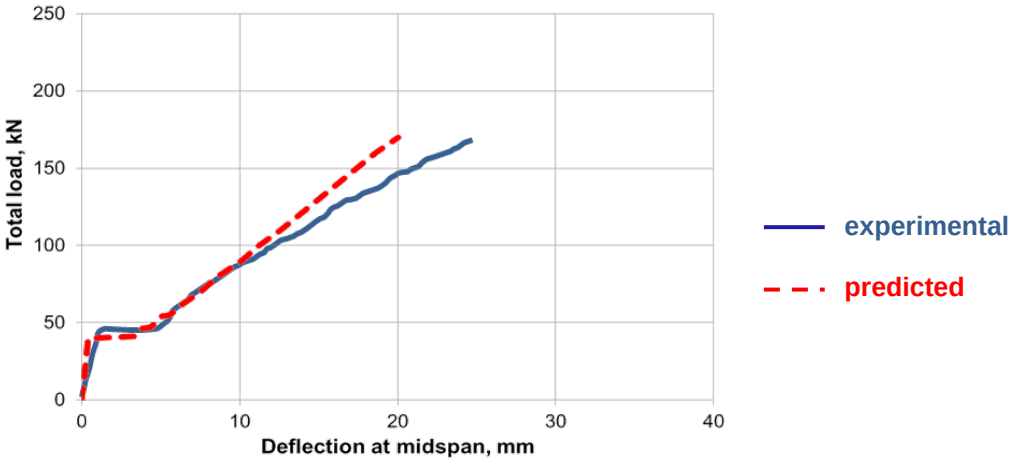

Figure 4.32. Load-deflection relation for GFRP (Isorod 1.5%) reinforced beam (Abdalla, 2002)

4.3.4.2. Fabric-formed beams

The limited available data from previous fabric-formed beam load tests have been reviewed; however, it was found that most records of the design details were insufficient to provide a reliable source for comparison between experimental and analytical results. For example, although Bailiss (2006) described the boundary conditions and loading arrangement for optimisation of the test beams, the final depth profiles were not reported. Similarly, Garbett (2008) and Chawla (2010) only indicated that 'key-hole' sections were designed and constructed by means of rigid formers but details of the extent and dimensions of beam webs were not presented. Furthermore, no thorough investigation of the as-built concrete geometries and the actual position of reinforcement was undertaken.

The most complete design detail of a fabric-formed beam test, shown in *Figure 4.33*, was provided by Garbett (2008). The beam was cast in a freely hung fabric and had overall dimensions given in *Table 4.1*. For design purposes, the 2000 mm span was divided into 20 segments of equal lengths, symmetrical about the midspan. The effective depth, d_{eff}, was calculated for 30 mm concrete cover to a single 8 mm diameter reinforcing bar with yield strength of 500 MPa. No construction errors were reported and it was observed that the reinforcement remained in its design position during the concrete pour.

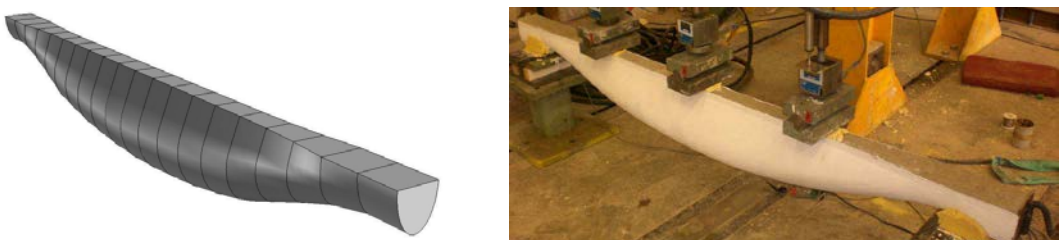

Figure 4.33. Fabric-formed beam test (Garbett, 2008)

Figure 4.34 presents the experimental results from the 5-point bending test consisting of equally spaced point loads undertaken on the above beam. The load-deflection prediction, performed by the current program, is based on assumed concrete cylinder strength of 80% of the recorded cube compressive strength of 36.4 MPa. The predicted load capacity from the MATLAB program is 16.2 kN. However, the test beam failed in shear at 12.5 kN, compared to a prediction of 12 kN, estimated following the procedure described in § 4.4.

Table 4.1. Beam details (Garbett, 2008)

Section No.	Distance from end support, mm	B, mm	D, mm	d_{eff}, m
1	0	98	92	58
2	100	98	92	58
3	200	98	112	78
4	300	76	138	104
5	400	64	171	137
6	500	62	204	170
7	600	62	222	188
8	700	62	237	203
9	800	62	246	212
10	900	62	253	219
11	1000	62	257	223

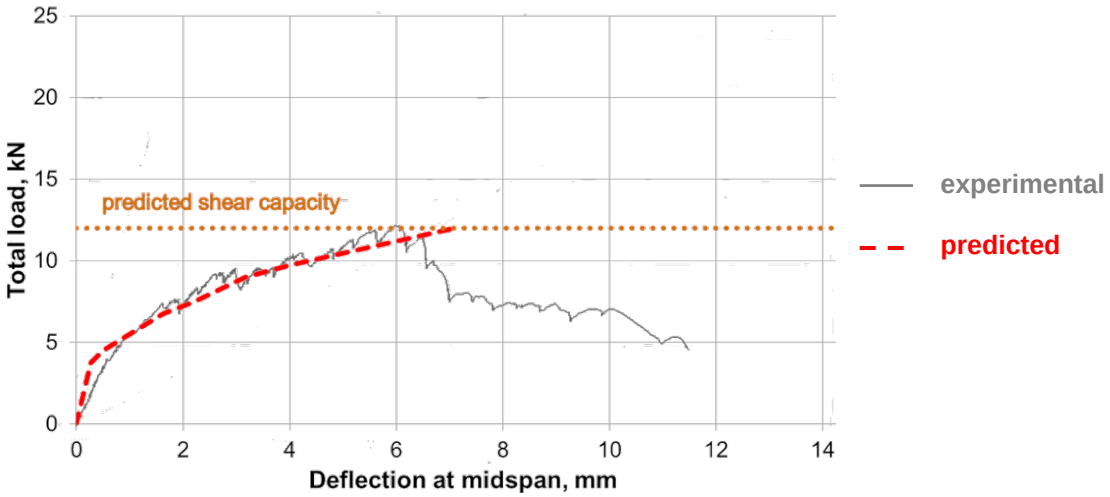

Figure 4.34. Load-deflection relation for steel reinforced fabric-formed beam (Garbett, 2008)

4.4. Shear design

The approach proposed for shear design in the current study is based on codified methods. However, more appropriate methods may need to be considered, as revealed by the findings of tapered beam studies (Orr, 2012) and discussed in detail in § 2. Furthermore, the implications of using brittle FRP tensile reinforcement in addition to the

difficulty of producing shear reinforcement for non-regular cross-sectional shapes are likely to become a subject of further research.

4.4.1. Beams without shear reinforcement

Empirically derived expressions, associated with the load at which the first shear crack occurs, are normally provided in design codes for obtaining the shear capacity of beams without stirrups (Stratford and Burgoyne, 2003). Although the validity of such expressions is questionable in the case of non-prismatic beams with non-uniform longitudinal profiles, they could be useful for preliminary design and are well suited for the sectional design approach, already implemented for form-finding and flexural design of fabric-formed beam elements.

The provisions in BS EN 1991-2-1-1:2004 for slender beams not requiring shear reinforcement are used to determine the shear resistance of concrete sections, comprising steel flexural reinforcement. For beams reinforced with FRP materials, an equivalent area of the tensile reinforcement is defined following the equivalent 'strain approach' widely accepted in existing design recommendations (fib, 2007). The approach assumes that the forces and strains in a concrete section are independent of the flexural reinforcement material, as long as adequate bond between concrete and FRP reinforcement can be achieved. Then, the equivalent area of FRP reinforcement A_e, in steel units, can be calculated based on the modular ratio of FRP and steel:

$$A_e = A_{frp} \frac{E_{frp}}{E_s} \tag{4.23}$$

Garbett (2008) applied a shape correction factor to account for the unknown irregular shape of hydrostatically formed sections when determining the nominal shear area, in order to reduce the risk of overestimating the shear capacity of sections when the breadth reduces noticeably over the depth. As a reasonable approximation, an equivalent breadth, proportional to the maximum breadth, w_m, calculated using *Equation 4.3*, was assumed (Garbett, 2008). The current approach, however, allows for direct computation of the cross-sectional area above the centroid of the tensile reinforcement. In addition, a more conservative method for 'bulging' sections is applied by finding an equivalent rectangular section of the same effective depth and moment of resistance. The shear resistance of concrete is then determined based on the lesser of the actual or the equivalent rectangular section shear area. This approach has been used to predict fairly successfully the shear failure load for the example presented previously in *Figure 4.34*.

While the capability to predict the shear capacity of concrete in fabric-formed beams is a key requirement for providing a safe design methodology, relying merely on the concrete to resist shear may not be possible for the majority of structural elements. Thus, in accordance with BS EN 1991-2-1-1:2004, shear reinforcement cannot be omitted for elements contributing to the overall resistance unless transverse redistribution of loads is possible, such as in slab members.

4.4.2. Beams with shear reinforcement

Studying the shear behaviour of fabric-formed beams has not been a primary objective of the current research. Nevertheless, a method for fabrication and installation of shear reinforcement, which could be particularly attractive from a constructability point of view, has been investigated experimentally. The proposed method uses shear spiral reinforcement, made of a continuous tow of carbon fibre, impregnated with resin (refer to *Figure 4.35*), which may be wound directly onto pre-assembled longitudinal reinforcement to form cages of varying shapes.

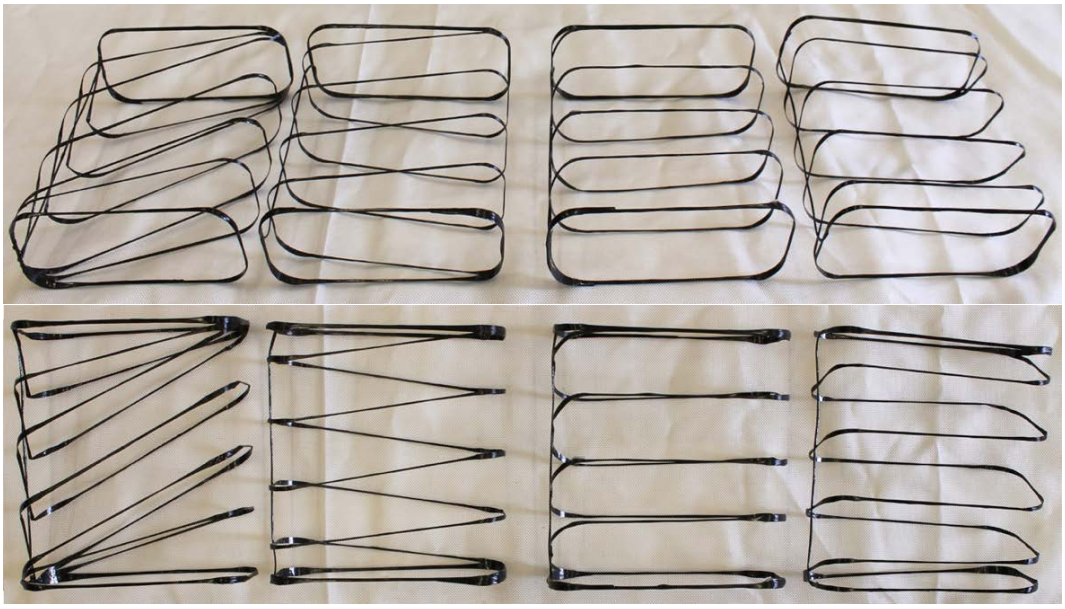

Figure 4.35. Configurations of CFRP spirals studied by Grant (2013)

Grant (2013) conducted an experimental study of concrete beams containing rectangular CFRP spirals, which demonstrated that spirals with vertical legs provide a greater contribution to the shear capacity of rectangular concrete sections than spirals with inclined legs (see *Figure 4.35*). Comparison of the experimental results with theoretical shear strengths, calculated in accordance with ACI 440.1R (2006), indicated that the guidelines tend to underestimate the contribution of spiral reinforcement with vertical legs significantly, even before applying the permissible strain limit of 0.4% (Grant, 2013).

Based on these findings, it was expected that the provisions in ACI 440.1R-06 would lead to a conservative design for spirals with vertical legs for the purpose of the current research study. The shear resistance of the continuous CFRP spirals, V_f, is obtained from *Equation 4.24,* according to the shear reinforcement area A_{vf} , pitch of the spiral s_v and ultimate stress in the FRP spiral f_{fv}:

$$V_f = \frac{A_{fv} f_{fv} d_{eff}}{s_v} \tag{4.24}$$

4.5. Shape optimisation

The main variable parameters, which define the shape of a hydrostatic section, as described in § 4.2, are the depth D and the top breadth B. By using the adopted form-finding algorithm and sectional design approach, it is possible to minimise the concrete volume of a beam for defined constraints, such as minimum and maximum dimensions and applied loading. However, as has been demonstrated in *Figure 4.10*, pure hydrostatic shapes with low breadth-to-depth ratio would not be efficient for the design of flexural elements unless some form of restraint, such as externally supported web formers or internal ties, is provided to reduce the 'bulging' effect. However, the installation of restraints may incur additional construction costs, due to the extra time, extra materials, more difficult compaction of concrete and control of construction tolerances. Alternatively, setting a limit on the breadth-to-depth ratio of sections cast in a freely hung fabric could lead to a somewhat less economical design, while maintaining a significantly simpler construction process.

Overall, the choice of construction method and constraints would depend on the specific project requirements and functionality of the optimised elements. Other factors to be taken into account may be the smoothness of the longitudinal profiles, the aesthetics, as well as any limits on the radius of curvature of the longitudinal reinforcement. Hence, applying fully automated mathematical optimisation methods for fabric-formed elements is not entirely feasible and an 'iterative-intuitive' approach is still required as part of the process. Furthermore, while some optimisation theories, such as the bone growth analogy, are not applicable to reinforced concrete, due to its anisotropic and cracking properties, previously performed optimisation of cross sections subjected to coexistent moment and shear along the beam, and designed to appropriate limit state criteria, provided a successful practical method (Garbett et al., 2010).

Following Bailiss (2006) and Garbett et al. (2010), the optimisation of fabric-formed beams has been defined as finding the optimal design depth and top breadth profiles along the

beam length to cover the applied moment and shear force envelope diagrams. *Figure 4.36* illustrates the input geometry parameters required to perform form-finding and structural analysis for sections cast in a freely hung fabric, and for sections cast in fabric with a single horizontal restraint, provided by web formers with height h_{web} or 'quilt-point' ties, if h_{web} is set to zero.

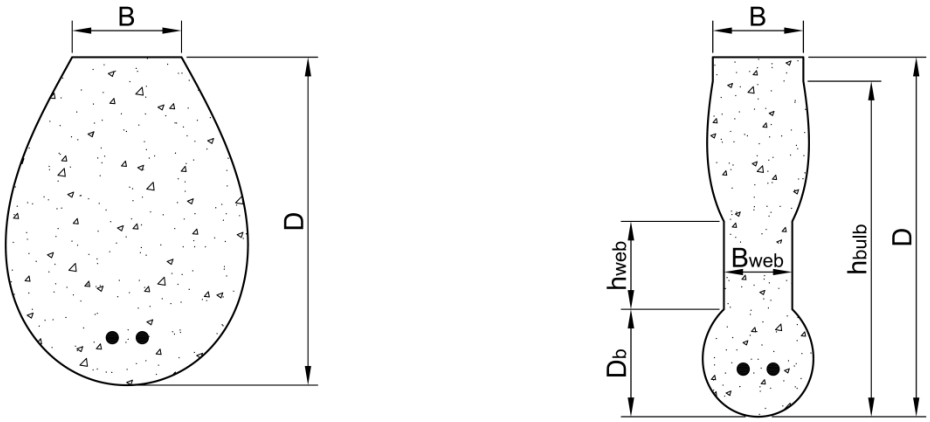

a. b.

Figure 4.36. Input parameters: (a) freely hung fabric and (b) horizontally restrained fabric

Theoretically, all parameters in *Figure 4.36b* could vary independently. However, in most cases the overall dimensions would dictate the rest of the parameters for practical or aesthetic reasons. For example, the thickness of a forming table edge would be the difference between D and h_{bulb}. Moreover, it could be most economical to maintain a minimum constant depth D_b, determined by the height of the concrete cover zone, surrounding the bottom reinforcement (*Figure 4.37*). Similarly, the web thickness, B_{web}, can be defined as constant or set to follow the change of the B-profile. The top of the web can be assumed to be a straight line, connecting points at height D_b above the beam soffit between sections with B/D ratio equal to 0.8.

Figure 4.37. Position of horizontal restraint dictated by the concrete cover zone

Initial input parameters, including B, D and reinforcement details, are required to start the optimisation process. They can be assumed the same as for a rectangular section, designed for the maximum applied moment. Furthermore, the optimisation problem has

been broken down into four simple tasks, summarised in *Table 4.2* and written as separate functions in MATLAB. An additional case for fixed B/D ratio is also considered. *Figure 4.38* explains the optimisation process of the depth profile for bending moment effects. The process is similar for the rest of the optimisation functions.

Table 4.2. Optimisation functions

Variable parameter	For applied bending moment	For applied shear force
Depth D	Minimise D for fixed B-profile	Minimise D for fixed B-profile
Breadth B	Minimise B for fixed D-profile	Minimise B for fixed D-profile

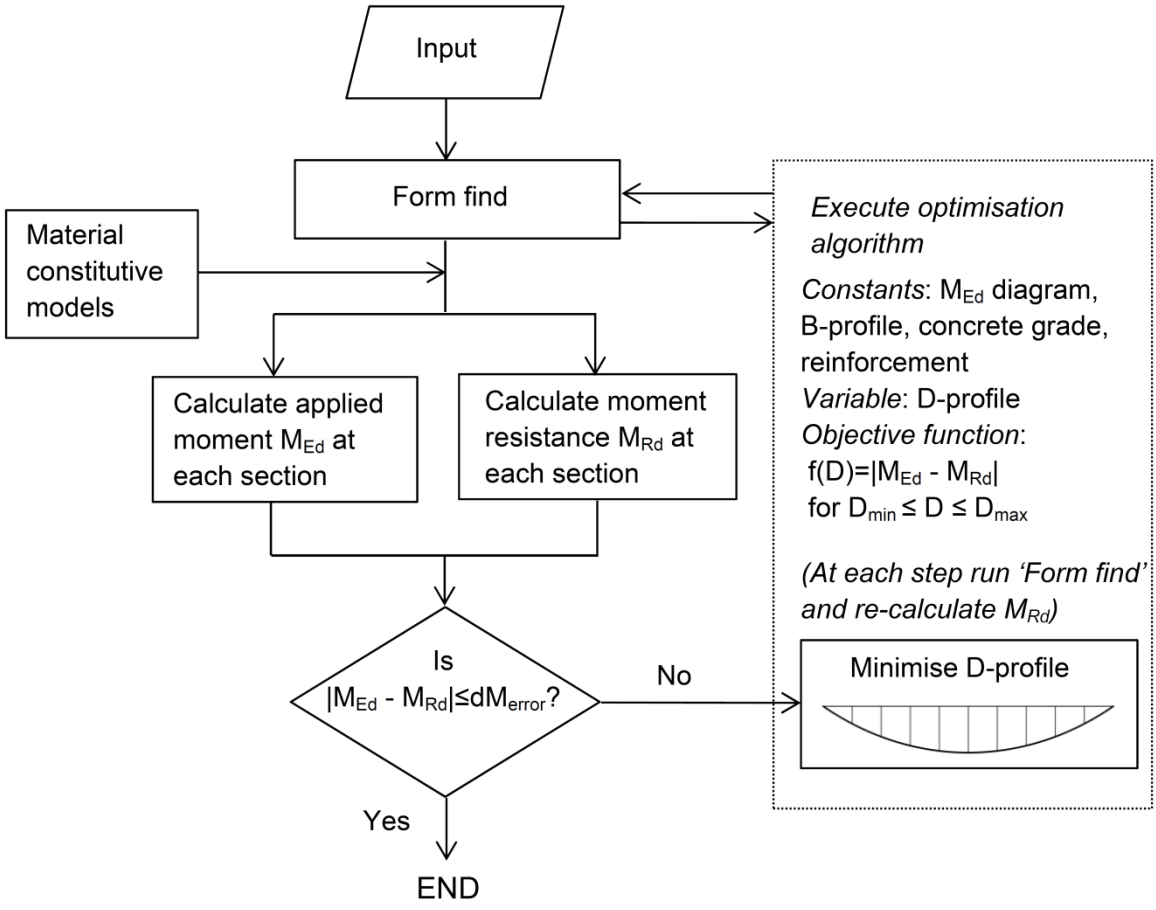

Figure 4.38. Optimisation of beam depth profile for bending moment

The functions can be combined and executed in a particular order to create optimisation algorithms. By applying basic engineering judgement, the depth profiles of flexural elements would normally be optimised for the applied bending moment at each section. The obtained profiles can be adjusted to provide the required shear resistance of a beam with a uniform top breadth, or the top breadth profile can be varied along the beam length instead. A schematic representation of this strategy is shown in *Figure 4.39*. Once the final B/D ratios are known, it can be identified which sections need restraint against

'bulging', and the whole procedure can be repeated using appropriate geometry parameters for the restrained sections. However, if the B/D ratio is set to be greater than or equal to 0.8, the last step may be avoided.

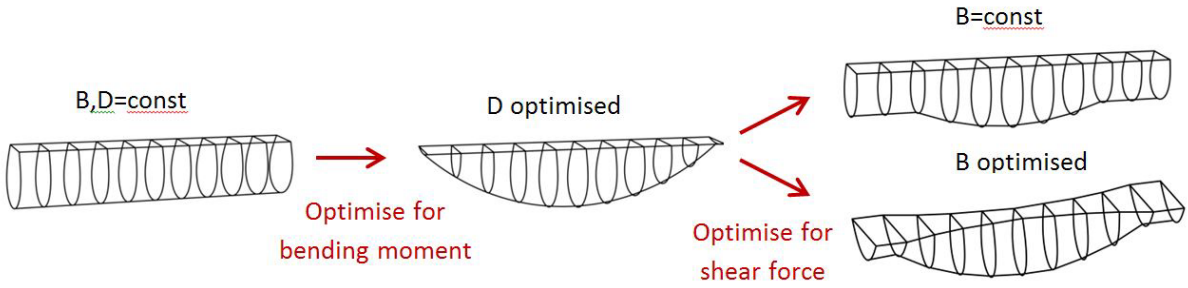

Figure 4.39. Typical optimisation strategy for fabric-formed beams

The input data is stored in the form of a matrix, which is updated each time the optimisation functions from *Table 4.2* are performed. All dependent variable parameters are re-calculated and the new cross-sectional profiles obtained from the form-finding algorithm in order to update the resistances and load effects at each section. The basic format of the input matrix is illustrated in *Figure 4.40*. This approach allows for fast optimisation using one or more of the functions in *Table 4.2*, run in a pre-selected order. Consequently, for more than one variable input parameter, it may be difficult to find a single optimal solution. However, it is easy to produce a range of efficient designs, which can be assessed against other criteria, as discussed earlier. Different examples of optimised fabric-formed beams are presented in § 6.

x_L	B	D	h_{bulb}	D_b	B_{web}	h_{web}	d_{eff}	E_{frp}	Bar dia	Load
0 : L_{beam}										

Figure 4.40. Input matrix

Although optimisation of beams containing shear reinforcement has not been discussed explicitly, it would generally follow the approach in *Figure 4.39*. The major difference, however, could arise from limitations on geometry due to the method of shear reinforcement fabrication. Furthermore, if possible, fabric-formed beams should be optimised for bending moment, while the shear reinforcement should be designed to provide full shear resistance.

It is essential to note that the described optimisation method is based on ultimate capacity design, followed by checking for serviceability criteria, such as permissible deflections. While this is a commonly accepted practice, there may be cases where stiffness governs

the design of optimised elements and needs to be considered as part of the optimisation process. A further discussion on the stiffness of optimised fabric-formed beams and experimental results can be found in § 5, § 6 and § 7.

4.6. Concluding remarks

The work presented in this chapter has aimed to provide a practical methodology for the design of horizontally cast fabric-formed elements. An appropriate form-finding algorithm and methods for flexural and shear design based on conventional two-dimensional sectional analysis have been proposed. In addition, an optimisation strategy linking construction possibilities with adopted methods for design has been discussed. A programme has been written in MATLAB to perform design and optimisation of multiple sections, as well as load-deflection beam analysis. The load-deflection results have been verified against available experimental data from literature; however, the majority of presented examples comprised prismatic test specimens, due to the lack of detailed description and limited extent of experimental work on beams of varying cross section. The outputs of the programme provide all the parameters necessary for construction, including fabric patterns and 3-D visualisation of the design beam geometries.

It is recognised that the shear behaviour of fabric-formed beams remains a problematic area of research, both in terms of design and constructability. In this respect, an experimental investigation into novel spiral shear reinforcement for fabric-formed elements is presented in § 7. Furthermore, the current design methodology for horizontally cast fabric-formed concrete has been limited to elements, subjected to transverse loads only. Although axially loaded elements can be precast in a horizontal position, casting concrete in vertically supported fabrics is a natural way of producing symmetrical sections and, therefore, could be more appropriate. Further discussion on construction methods for vertically cast columns and walls is provided in § 9.

The experimental work described in the next three chapters has been motivated by the need to demonstrate the validity of the proposed methodology. Based on findings from the physical investigation and conclusions from the comparison of analytical and test results, two case studies have been developed and are presented in § 8 in order to provide a step-by-step and easy-to-follow design procedure for fabric-formed beam elements.

5. Constructability of Fabric-formed Beams

5.1. Introduction

The design of fabric-formed concrete elements, as already discussed, is greatly dependent on the construction possibilities. Although the final concrete shapes can be found by using appropriate form-finding methods, it must be ensured that any assumed boundary conditions are feasible and practical. Therefore, studying the constructability of fabric-formed elements and establishing successful methods for achieving geometries within acceptable tolerance limits repeatedly is an extremely important step towards developing capabilities to design fabric-formed structures with predictable behaviour and long-term performance.

The fundamental construction challenges, identified in § 2, such as end anchorage of bars and concrete cover to steel reinforcement have already been addressed through the development of the splayed anchorage system, described in § 3, and introducing FRP reinforcement in the design of fabric-formed concrete elements for its superior resistance to corrosion compared to steel. However, a number of remaining problems, including the installation of reinforcement inside flexible fabric sheets and forming beam ends or connections, require more investigation in addition to the major question of how to create efficient fabric-formed beam cross sections without compromising the simplicity and economy of fabric formwork construction. This chapter describes an experimental investigation, aimed to provide practical solutions and novel methods, oriented predominantly to the construction of FRP reinforced fabric-formed beam elements, cast in flat fabric sheets.

5.2. Design of test specimens

Four test specimens (Series 1) were designed and built to explore the constructability of fabric-formed beams. In addition, all beams were tested under vertical loading until failure. The main design parameters of each test are presented in *Table 5.1*. Beams with different support conditions, reinforcement types and span arrangement were chosen to investigate a greater variety of construction details. No shear reinforcement was provided due to the lack of appropriate manufacturing methods at this stage. The last specimen, FFB4, was built during a demonstration conference workshop on fabric formwork.

Table 5.1. Test beam design parameters (Series 1)

Beam ID	No of spans	Span, m	Total length, m	Flexural reinforcement	Concrete cylinder strength, MPa
FFB 1	2	1.8	4	4 No GFRP bars	16
FFB 2	1	1.8	2	1 No GFRP bar	16
FFB 3	1	1.8	2	1 No CFRP bar	16
FFB 4	1	2	3	3 No GFRP bars	16

The optimised design of all beam specimens included in this initial investigation was carried out using the simplified approach based on equivalent breadth, proposed by Garbett (2008), and the form-finding spreadsheet programme, adopted previously by Foster (2010). The fabric was considered freely hung without any applied prestress. The design loads used for optimisation were determined by preliminary calculations taking into account the pre-defined reinforcement type and size, any construction constraints such as the capacity of laboratory concrete mixers and the limitations of the load testing equipment. This approach was necessary to ensure that the final sizes of the test specimens, obtained through optimisation, would be appropriate for construction, handling and testing in laboratory conditions.

5.2.1. Materials

5.2.1.1. Concrete

In general, for all experiments, where the development of compressive strength was not determined by trial mixes, the concrete mix design was based on a 28-day strength, corresponding to the required early compressive strength at the test age, calculated in accordance with BS EN 1992-1-1:2004. The pre-defined test age of FFB 1 beam was four days, and seven days for the rest of the specimens, dictated mainly by the laboratory storage capacity.

The concrete mixes were designed following Teychenné et al. (1997). The binder was Portland cement CEM II/B-V 32 and all of the aggregates described in § 3.4.4 were used, maintaining the same proportion of 25% fine sand and 75% Marlborough grit of the total fine aggregate content. The maximum coarse aggregate size was limited to 10 mm and it was intended to achieve adequate workability without the addition of concrete plasticisers. However, as can be presumed from the mix proportions given in *Table 5.2*, despite its relatively high water-to-cement ratio, the workability of the first mix was found unsatisfactory during the concrete pour and, consequently, a significantly higher water-to-cement ratio was chosen for FFB 2 and FFB 3 mixes. Furthermore, in order to ensure good concrete workability for the demonstration beam, FFB 4, the total water content of the concrete mix was increased and a trial mix was assessed in advance.

Table 5.2. Concrete mixes (Series 1)

Beam ID	Water	Cement	W/C ratio	Fine aggregates	Coarse aggregates
FFB 1	205 l/m^3	375 kg/m^3	0.55	880 kg/m^3	960 kg/m^3
FFB 2&3	205 l/m^3	273 kg/m^3	0.75	1070 kg/m^3	870 kg/m^3
FFB 4	230 l/m^3	383 kg/m^3	0.6	916 kg/m^3	846 kg/m^3

5.2.1.2. Reinforcement

The reinforcement bar types described in § 3 were used, as summarised again in *Table 5.3*. This allowed the design of splayed end anchorages, based on the experimental data and the anchorage model developed in § 3. AFRP helices were provided around the anchorages to prevent concrete splitting unless the design forces in the reinforcement anchorage zones were sufficiently low. The reinforcement arrangement for each test beam is presented in § 5.2.3.

The tension reinforcement comprised straight bars field-bent to produce longitudinal curves, following the optimal beam profiles. In order to prevent excessive sustained stresses in the FRP reinforcement, a minimum allowable radius for the different types of field curved bars was specified, based on the stress limits recommended in ACI 440.1R-06. The values, provided in *Table 5.3* allow for 20% sustained stresses in the GFRP bars and 55% in CFRP bars. Field bending of CFRP bars, however, is likely to be less practical due to their high stiffness and was considered only for completeness of the current investigation.

Table 5.3. Reinforcing bars properties (Series 1)

Nominal diameter	**10 mm**	**12 mm**	**12 mm**
Fibre type	glass	glass	carbon
Tensile strength, MPa	550	750	2300
Nominal cross-sectional area, mm^2	71.3	126.7	113
Modulus of elasticity, Gpa	30	40	130
Tensile strain, %	>3	>3	1.8
Surface treatment	smooth	smooth	sand
Minimum allowable radius, mm	1300	1693	620

5.2.1.3. Fabric formwork

The chosen fabric was a single layer polypropylene woven geotextile with pore opening size 0.25 mm and selfweight of 220 g/m^2, supplied by Proserve Ltd. As discussed in § 2, this pore opening size was found to be the most optimal for improving the durability characteristics of concrete in the surface zone (Lee, 2012). The strength characteristics of fabric, given in *Table 5.4*, would be adequate for casting fabric-formed sections up to 1000 mm top breadth and 2500 mm depth.

Table 5.4. Properties of single layer polypropylene fabric (Proserve)

	Tensile strength	**Extension at break**	**Tear strength**
Warp	3000 N/ 50 mm	35%	900 N
Weft	2700 N/ 50 mm	35%	900 N

Although the extension of fabric at breakage can reach 35%, for small specimen sizes with cross-sectional perimeters of around 600 mm and tension force in the fabric up to 1000 N/m, based on the supplier's stress-strain test data, the estimated extension would not exceed 0.35% or 2 mm. This would have a negligible effect on the overall cross-sectional height. Moreover, the achievable or required construction tolerance is unlikely to be less than 2 mm. Therefore, the extension of fabric was generally ignored for actual tension forces at each cross section not exceeding 1000 N/m.

5.2.2. Geometry details

The geometry of each beam was designed for a pre-defined loading arrangement and construction constraints, as described below. The reinforcement details are presented in § 5.2.3. Furthermore, detailed dimensions required for construction are given in § 5.3.2.

5.2.2.1. Beam FFB 1

The geometry of beam FFB 1 was optimised for loads applied over the first span only. As can be seen from *Figure 5.1*, the minimum cross-sectional horizontal and vertical dimensions at the end supports were set to 100 mm in order to accommodate 90 mm diameter helices at the end anchorage zones. The top breadth over the internal support was fixed to 150 mm and all other dimensions were varied. The aim was to create an unsymmetrical longitudinal beam profile with substantial variation in the cross-sectional geometry.

For design purposes, the beam was divided into 40 segments of equal lengths. The obtained geometry corresponded to the requirement to resist a total applied load of 19.5 kN, equally distributed amongst the three load points (*Figure 5.1a*). The value of the design load was dictated mainly by the concrete volume, suitable for casting in laboratory conditions. The longitudinal beam profile was firstly optimised to follow the bending moment diagram and then refined to ensure the adequate shear capacity of sections with fixed top breadth dimension. The top breadth profile was optimised for the shear force effects only, allowing a minimum top breadth of 75 mm. The first span of the beam was reinforced with 10 mm field-bent GFRP bars and, therefore, the final shape of the beam in the first span was checked against the minimum permissible curve radius.

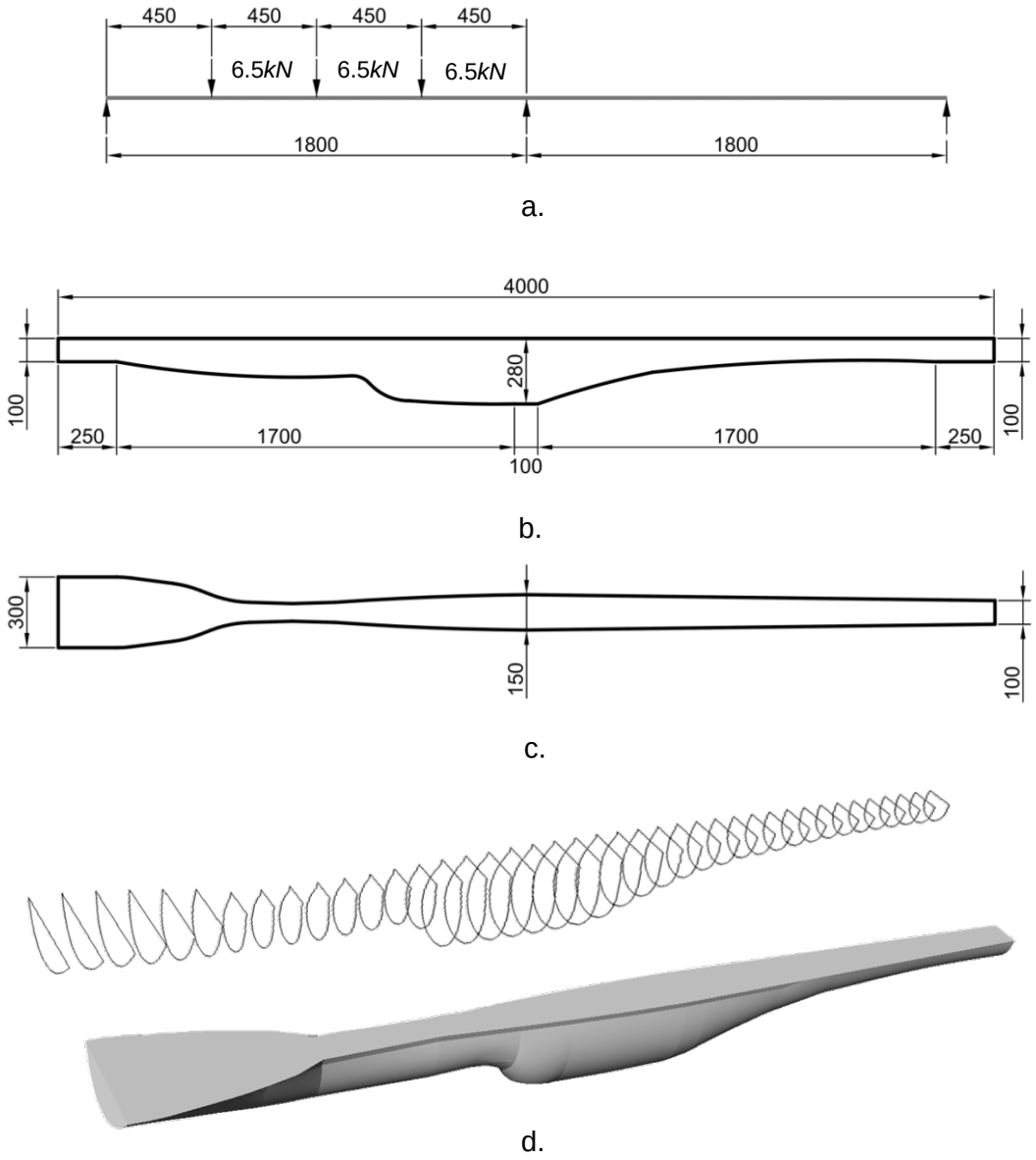

Figure 5.1. Beam FFB 1 geometry details: (a) loading arrangement, (b) elevation, (c) plan and (d) perspective view (all dimensions are in mm)

The shape of the sections at beam support locations was found by assigning an initial horizontal length equal to half of the width of the support, when defining the input parameters for form-finding of sections cast in a freely hung fabric (refer to *Figure 4.6*). The resulting 'flat-bottom' shapes illustrated in *Figure 5.2*, however, appear to be less efficient for reduced B/D ratios and may need to be controlled by appropriate construction restraints. Such methods are considered in § 6 and § 7.

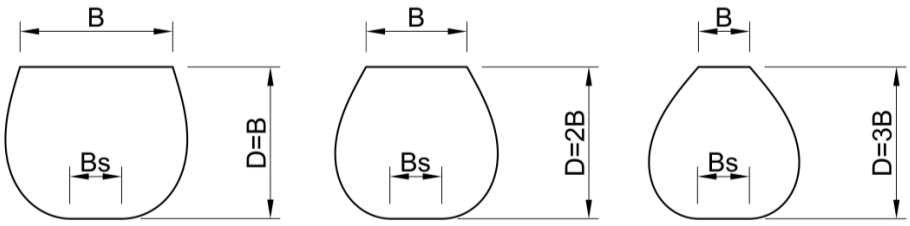

Figure 5.2. 'Flat-bottom' sections for various B/D ratios and width of support B_s

5.2.2.2. Beam FFB 2

Beam FFB 2 was designed to be simply supported and constructed using the 'quilt-point' method over the midspan region. The utilised spreadsheet-based form-finding programme, however, could not provide a solution for fabric-formed sections restrained by internal ties, as explained in § 4, and a physical model was built in order to determine the required perimeter of fabric for 'quilt-point' cross sections (see *Figure 5.3*).

Figure 5.3. 'Quilt-point' trial beam segment

The model was 400 mm long and had a uniform top breadth of 75 mm. The construction perimeter of fabric was approximated by using the form-finding algorithm for the bottom bulb and assuming that the quilt points and the top horizontal restraints were connected by a straight line. The measured-at-the-'quilt-point'-locations as-built depth of 205 mm was then set as a maximum depth for optimisation of the FFB 2 beam profile, and the final perimeters were adjusted accordingly to allow for the measured bulging effect above the quilt points.

Figure 5.4 indicates the main beam dimensions and design loading arrangement. The total design load was 22.5 kN, defined again by the maximum concrete volume, assuming that beams FFB 2 and FFB 3 would be cast together. The length of the beam was divided into 20 segments and the longitudinal profile was optimised for the applied bending moments at each section, assuming a constant top breadth of 75 mm. The depth of the sections near supports was defined as 120 mm, based on preliminary design allowing a

maximum top breadth of 500 mm. The final top breadth profile was then optimised for the shear force effects and the obtained longitudinal profile.

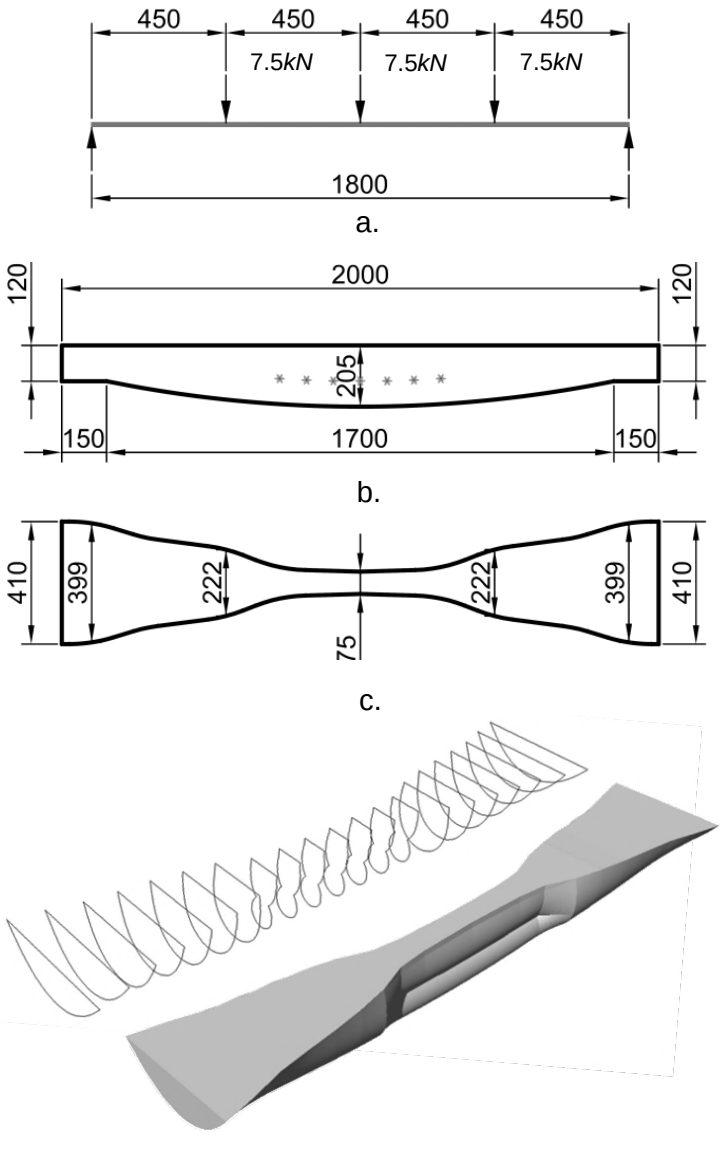

Figure 5.4. Beam FFB 2 geometry details: (a) loading arrangement, (b) elevation, (c) plan and (d) perspective view (all dimensions are in mm)

5.2.2.3. Beam FFB 3

Beam FFB 3 had a fairly simple geometry, optimised for a uniform top breadth of 100 mm, defined by the minimum dimensions at supports, required to install confinement reinforcement around the anchorages, as previously described. Unlike the first two test beams, beam FFB 3 was reinforced with a straight 12 mm CFRP bar (refer to *Table 5.3*). Trials to field bend the selected reinforcing bar demonstrated that it would not be practical to design curved profiles with radius smaller than 10 m. Therefore, the difference between the beam depth at midspan and at supports was limited to only 36 mm.

The longitudinal profile, shown in *Figure 5.5*, was obtained by optimisation for bending moment and shear force effects at each section of the beam, divided into 20 segments. The somewhat unexpected geometry for a simply supported beam was due to the high moment capacity of the CFRP reinforced sections at and near midspan, which required smaller structural depths compared to the sections providing the required shear capacity near the supports. The total design load was 18 kN.

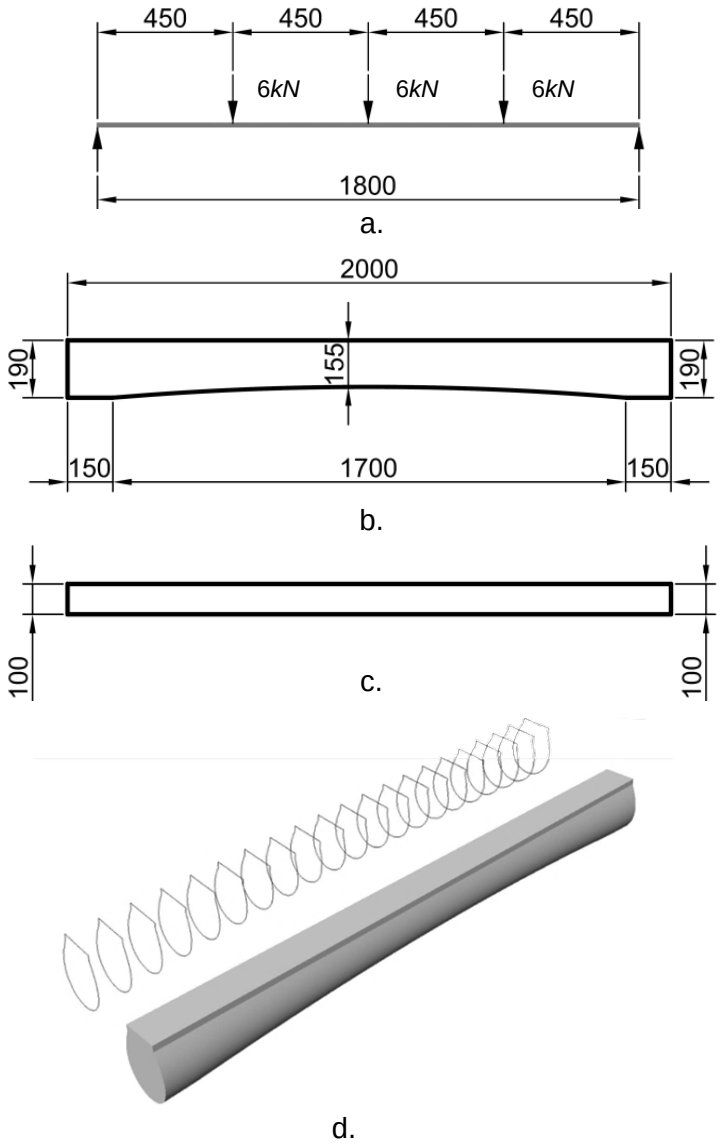

Figure 5.5. Beam FFB 3 geometry details: (a) loading arrangement, (b) elevation, (c) plan and (d) perspective view (all dimensions are in mm)

5.2.2.4. Beam FFB 4

The design of the demonstration beam, FFB 4, aimed to show a variety of construction aspects and possibilities to produce elegant and efficient reinforced concrete forms. The beam was simply supported with end cantilevers, optimised for a uniformly distributed

vertical load of 10 kN/m, represented by six concentrated forces positioned as shown in *Figure 5.6*. The beam was divided into 30 segments. The top breadth varied between 75 mm and 400 mm. Helical reinforcement was not required at the tip of the end cantilevers due to low stresses at the end anchorages and the minimum cross-sectional depth was defined by the cover to the reinforcement. In order to increase the efficiency of the cross-sections at and near midspan, web formers held in place by means of formwork ties were used to create 'key-hole' internally restrained sections, as described in § 4.

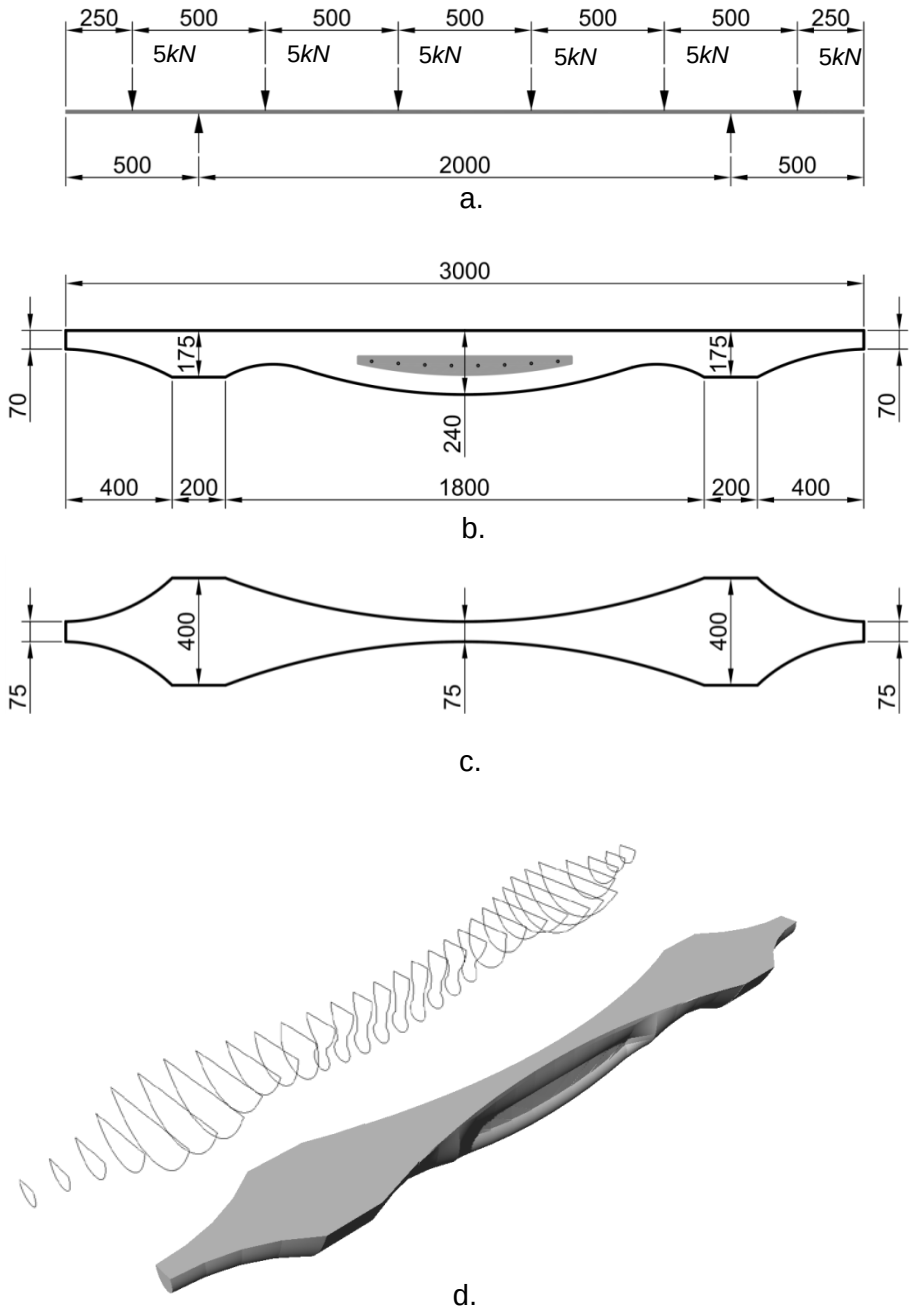

Figure 5.6. Beam FFB4 geometry details: (a) Loading arrangement, (b) Elevation, (c) Plan and (d) Perspective view (all dimensions are in mm)

Improving the efficiency of the 'flat-bottom' sections at supports was also considered. The construction perimeter was determined as the perimeter of a cross-section cast in a freely hung fabric, for which the length of fabric below the required cross-sectional depth is equal to the width of the flat support. *Figure 5.7* illustrates the approach for a 100 m width of the support.

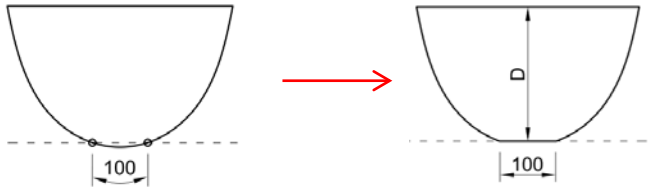

Figure 5.7. Efficient 'flat-bottom' section cast in a freely hung fabric (all dimensions are in mm)

5.2.3. Reinforcement details

The reinforcement details, shown in *Figure 5.8*, indicate the type and diameter of reinforcing bars for each test specimen, including the helical reinforcement around the splayed anchorages. The concrete cover for beams FFB 1, FFB 2 and FFB 3 was 25 mm or approximately twice the largest bar diameter. However, for beam FFB 4 the cover was increased to 30 mm to allow the concrete to flow more easily around the bar during the demonstration pour.

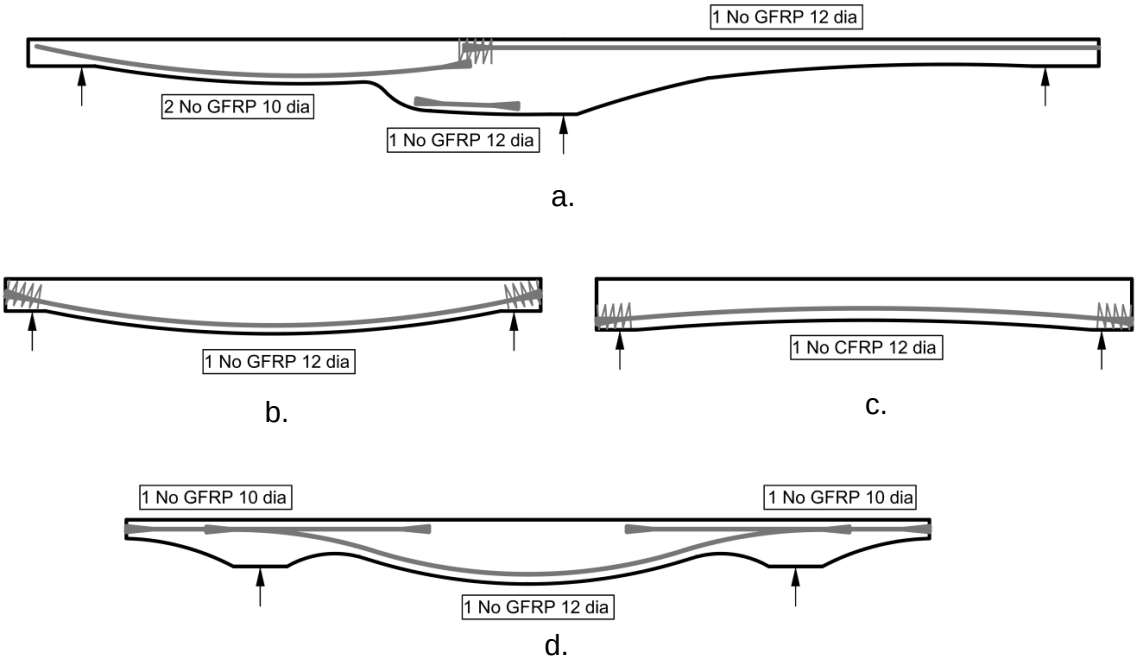

Figure 5.8. Reinforcement details (Series 1): (a) FFB 1, (b) FFB 2, (c) FFB 3 and (d) FFB 4

Due to the more complex shape and reinforcement details of beam FFB 1, *Figure 5.9* shows the position of the bars in relation to the design bending moment and shear force

diagrams. The bend radius of the curved 10 mm diameter GFRP bars at beam FFB 1 was 4452 mm compared to a minimum permissible radius of 1300 mm (refer to *Table 5.3*). Similarly, FFB 2 and FFB 3 had large curve radii of 4262 mm and 10160 mm, respectively, well above the minimum value of 1693 mm for 12 mm bars (refer to *Table 5.3*). The reinforcement bend radius at midspan for beam FFB 4 was 1950 mm, reduced to 1800 mm for the concave part of the curve near the supports but still above the safe minimum.

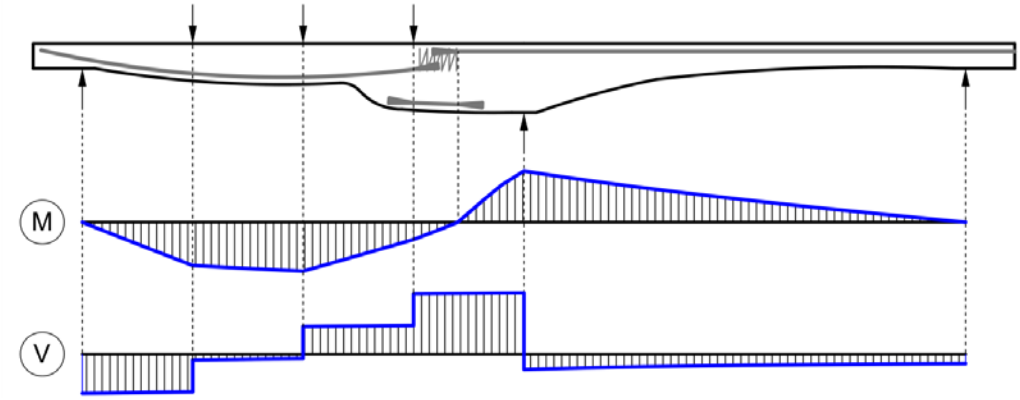

Figure 5.9. Bending moment and shear force diagram envelopes for FFB 1

5.2.4. Utilisation and material savings

An important measurement of the design efficiency is the capacity utilisation of each section along the beam length. The plots in *Figure 5.10* present the utilisation of shear and moment capacities for all of the test specimens. The load effects were calculated for the externally applied concentrated forces and the test beam selfweight. As can be seen, beam FFB 1 shows good utilisation along the loaded span, while the profile of the unloaded span was determined to a greater extent by the transition of geometry. An estimate of the material savings achieved through optimisation can be made by comparison with an equivalent rectangular section of the same peak strength capacity. However, due to the variation of the cross-sectional depth and top breadth of the fabric-formed beam, finding equivalent uniform dimensions would not be possible without defining appropriate constraints. It was proposed to follow the main steps of the procedure applied for optimisation, using the same minimum and maximum limits. Therefore, the equivalent rectangular section in the first span of beam FFB 1 was found by starting with a 75 mm breadth in order to obtain the required depth for the maximum applied bending moment. The breadth was then increased to ensure the maximum shear capacity and the final overall dimensions of B=239 mm and D=174 mm corresponded to material savings of 46%. The equivalent rectangular cross section at the internal support, however, was obtained for a fixed breadth of 150 mm, which resulted in a bigger section with B=150 mm

and D=397 mm and final considerable savings of 62%. The savings value may be considered slightly unrealistic due to the unloaded second span and would drop to approximately 49% for symmetrically loaded spans.

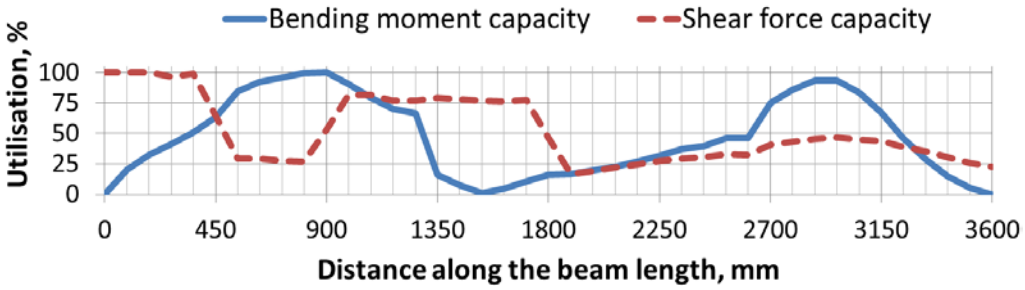

a.

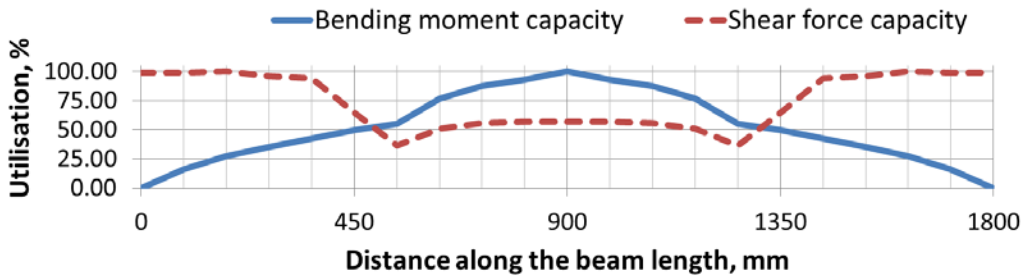

b.

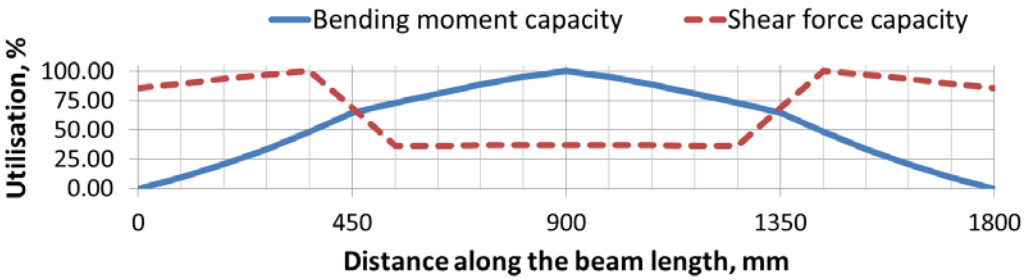

c.

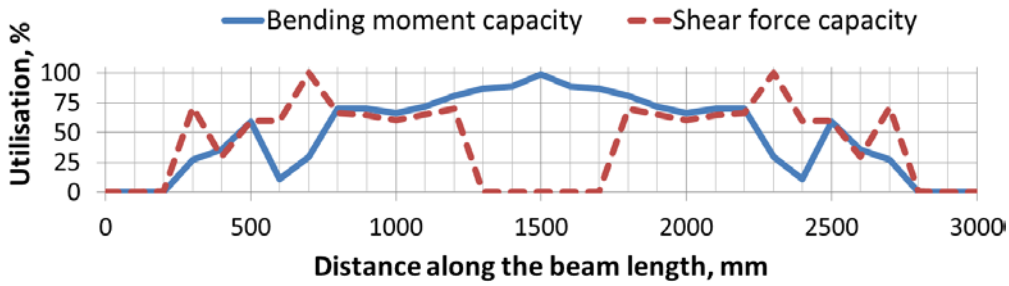

d.

Figure 5.10. Capacity utilisation: (a) FFB 1, (b) FFB 2, (c) FFB 3 and (d) FFB 4

The material savings for beam FFB 2 were calculated for an equivalent section with dimensions B=184 mm and D=210 mm. The overall depth was obtained from the required bending moment capacity for a minimum breadth of 75 mm, while the breadth

was adjusted for the shear capacity, following the rules applied for optimisation. The material savings of 30% indicate a less efficient design than for beam FFB 1, which could partially be attributed to the non-coinciding locations of maximum bending moment and shear force effects in simply supported beams.

Lower material savings, equal to 18%, were achieved for beam FFB 3. The value corresponded to an equivalent rectangular section of B=100 mm and D=235 mm. However, as stated previously, the limitations on the curved beam profile, imposed by field bending of CFRP bars, were not expected to provide an efficient design. Furthermore, no form of fabric restraint was considered for reducing any undesired bulging effects.

Beam FFB 4 was designed to be the most efficient of all test specimens included in the constructability study. The reduced bulging of the cross sections at supports and the design of 'key-hole' cross sections at midspan contributed to total material savings of 58% in comparison with an equivalent rectangular section with B=400 mm and D=147 mm, based on the maximum breadth over the supports. The equivalent section based on the minimum breadth of 75 mm indicates even greater savings of 66%. Clearly, the design of FFB 4 provided the best advantages in terms of reduced concrete material use; however, it also assumed the most challenging construction approach, hiding risks associated with achieving acceptable quality and construction tolerances.

5.2.5. Instrumentation and test set-up

The load testing was typically accompanied by measurement of vertical displacements and strains in the reinforcing bars. The horizontal displacement at the ends of the reinforcing bars of beam FFB 4 were also monitored in order to demonstrate that no slip occurred, despite the small size of the end cross section. The range of the vertical transducers was 0-100 mm, positioned at the locations of the point loads, except for beam FFB 4, as shown in *Figure 5.11*. The displacement measurements are designated $D1$ to $D7$ and the strain measurements $S1$ to $S7$. The choice of locations of recorded strains included as a minimum the cross section with maximum bending moment effects and cross sections adjacent to the end anchorages (refer to *Figure 5.11*). The collected data was acquired in order to compare the experimental and theoretically obtained load-deflection and load-strain relations.

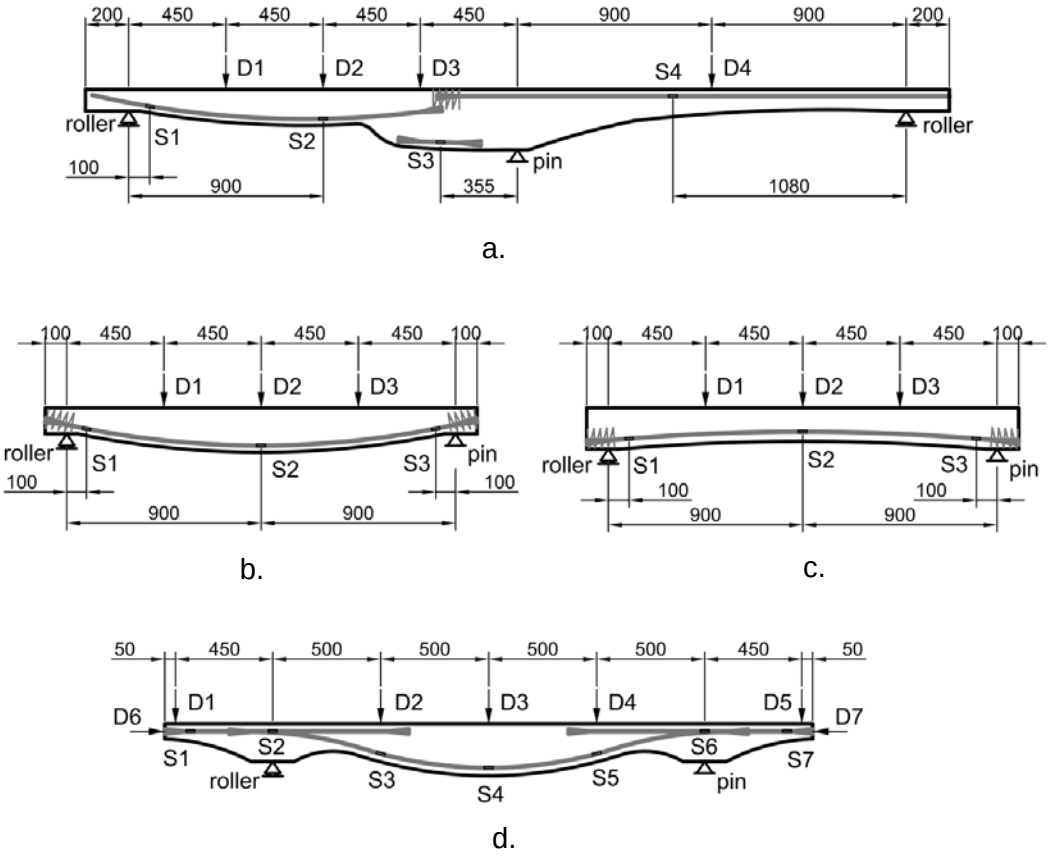

Figure 5.11. Test set-up (Series 1): (a) FFB 1, (b) FFB 2, (c) FFB 3 and (d) FFB 4 (all dimensions are in mm)

5.3. Construction of test specimens

5.3.1. Formwork details

During the design process it was assumed that all beam specimens would be cast in a freely hung fabric and both the horizontal and vertical cross-sectional dimensions would be allowed to vary along the length. In order to produce fabric-formed beams of varying geometries multiple times, a reusable supporting formwork table was designed. The table comprised replaceable top plates fixed onto the timber transverse frames, illustrated in *Figure 5.12*. The entire assembly, which could be up to 4 m in length, can be seen in *Figure 5.13*. The adjustable top beams of the transverse frames were bolted between two cover plates and supported an opening at the middle between 50 mm and 500 mm (*Figure 5.14*).

The top plywood sheets were cut out to match the design top breadth profile of the beam specimens. The possibility for multiple re-shaping of the sheets was limited due to the great variation of geometries; however, each plywood sheet was generally reused up to three times. A significant advantage of the developed fabric formwork table was its compact size when de-assembled, allowing easy storage and handling.

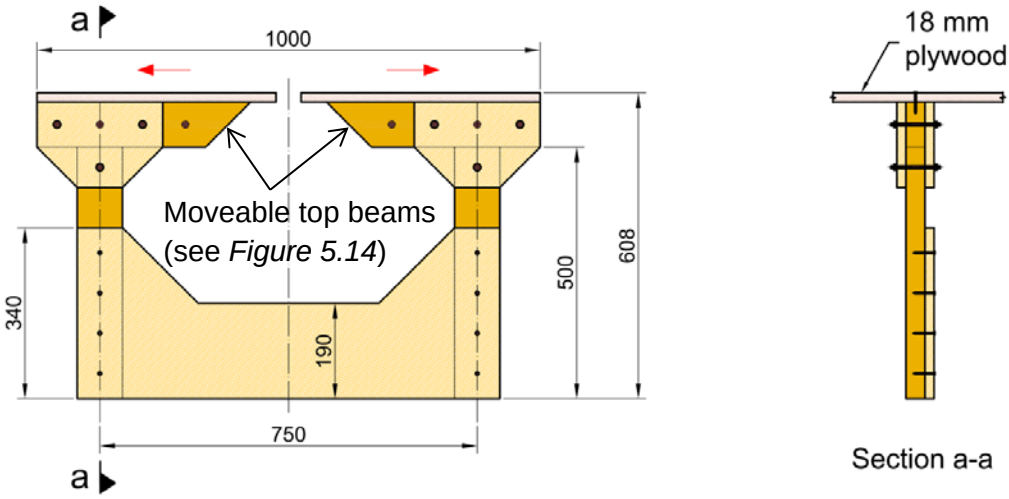

Figure 5.12. Adjustable transverse frames (all dimensions are in mm)

Figure 5.13. Fabric formwork reusable supporting table

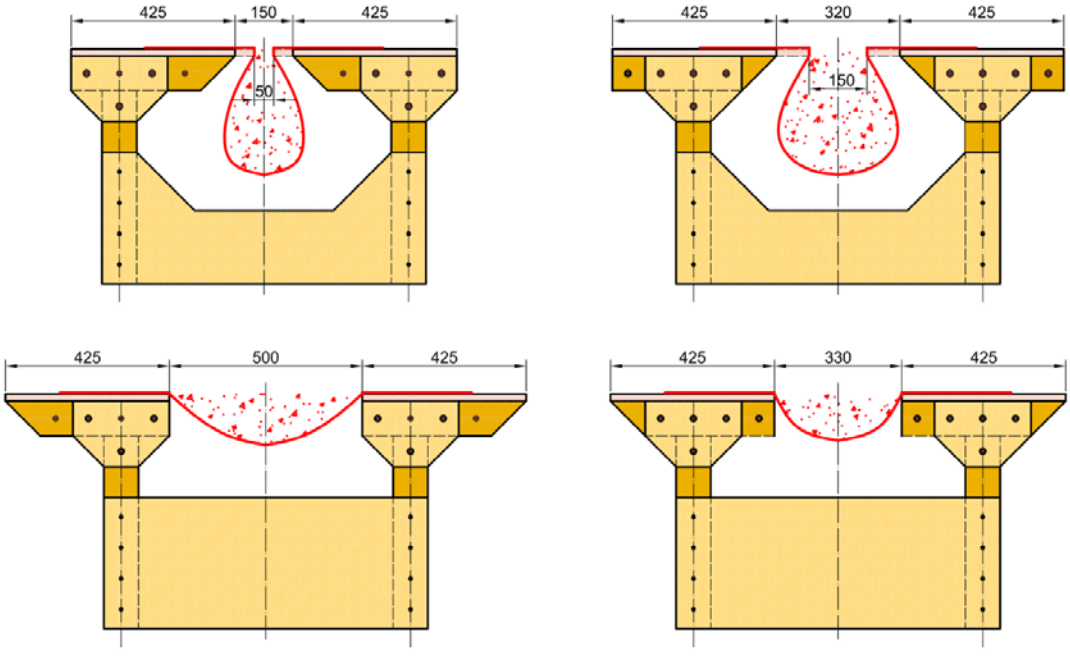

Figure 5.14. Maximum top opening for different arrangements of the transverse beams (all dimensions are in mm)

5.3.2. Construction parameters

The two main parameters required to construct a fabric-formed beam are the top breadth B, which is equal to the opening at the middle of the formwork table, and the hung perimeter P at each design cross section (refer to *Figure 4.36*). In addition, for sections formed in restrained fabric, the perimeter of the bottom bulb P_b, the width of the restrained part B_{web} and height of the web h_{web} are needed in order to install any ties and web formers in their correct position. For completeness, the parameters presented herein include the overall depth D and the depth of the bottom bulb of restrained sections D_b. Although not explicitly given as a construction parameter, the 18 mm thickness of the plywood top sheets was taken into account in determining h_{bulb} (refer to *Figure 4.12*).

Table 5.5 provides the parameters used to construct beam FFB 1, for cross sections positioned at a distance x_L from the end support of the first span. The last column in *Table 5.5* shows the predicted tension force in the fabric, required to calculate the extension at each section, which can then be added to the overall perimeter. However, the values for beam FFB 1 were found to be generally below 0.5 mm with a maximum of 1.6 mm at the cross sections near the internal support, demonstrating the negligible effect of fabric extension, as previously suggested. Therefore, the fabric extension was ignored.

Table 5.5. FFB 1 construction parameters

x_L	B	D	d_{eff}	B_{web}	D_b	h_{web}	P	P_b	T,
0	300	100	61	NOT USED	NOT USED	NOT USED	412	NOT USED	301
90	296	107	77				396		309
180	274	121	91				400		306
270	251	133	103				402		302
360	217	143	113				398		286
450	176	151	121				396		264
540	101	157	128				390		214
630	84	162	132				398		214
720	79	165	135				406		218
810	76	166	136				408		219
900	81	165	135				406		220
990	86	162	133				400		215
1080	98	158	128				390		214
1170	109	188	122				464		299
1260	119	267	114				660		573
1350	127	272	241				676		602
1440	134	276	244				684		624
1530	140	279	246				692		643
1620	145	280	249				696		652
1710	148	280	249				696		655
1800	150	280	249				802		657

1890	148	266	235				663		597
1980	146	237	206				588		486
2070	143	210	179				522		393
2160	141	186	155				464		319
2250	139	164	133				412		259
2340	137	145	113				368		218
2430	134	135	104				346		193
2520	132	121	89				314		163
2610	130	119	87				308		158
2700	128	114	58				296		147
2790	125	106	50				280		131
2880	123	102	44				268		123
2970	121	98	41				260		115
3060	119	96	39				254		111
3150	116	94	39				250		106
3240	114	94	42				248		105
3330	112	94	47				248		104
3420	110	96	54				250		106
3510	107	99	64				256		109
3600	105	100	69				352		109

All dimensions are in millimetres.

The construction parameters for beam FFB 2 are given in *Table 5.6*, where x_L is the distance measured from the left support. Only the maximum tension force is presented in the last column for all 'quilt-point' sections. Similarly to FFB 1, the calculated extension was low, being approximately 0.3 mm for the midspan cross-sections and up to 0.7 mm for the larger cross-sections near the supports, and was ignored.

Table 5.6. FFB 2 construction parameters

x_L	B	D	d_{eff}	B_{web}	D_b	h_{web}	P	P_b	T,
0	399	120	78			NOT USED	525		504
90	355	128	96				472		442
180	303	144	112				456		398
270	277	159	127				462		397
360	253	171	139				472		400
450	223	181	150				480		393
540	180	190	158				482		374
630	105	197	165	50	85		456	222	191
720	85	201	170	50	85		461	222	189
810	80	204	173	50	85		464	222	192
900	75	205	174	50	85		467	222	193
990	80	204	173	50	85		464	222	192
1080	85	201	170	50	85		461	222	189
1170	105	197	165	50	85		456	222	191
1260	180	190	158				482		374
1350	223	181	150				480		393
1440	253	171	139				472		400
1530	277	159	127				462		397

1620	303	144	112				456		398
1710	355	128	96				472		442
1800	399	120	78				525		504

All dimensions are in millimetres.

Beam FFB 3 represented the most practical design from a construction point of view. As indicated in *Table 5.7*, the only varying construction parameter which determines the final geometry is the hung perimeter of fabric and, therefore, the construction time required for preparation was expected to be considerably shorter than for the rest of the test beams. Due to the small specimen size the calculated maximum extension did not exceed 0.5 mm at any cross section and could be practically ignored. Again x_L again is the distance measured from the left support.

Table 5.7. FFB 3 construction parameters

x_L	B	D	d_{eff}	B_{web}	D_b	h_{web}	P	P_b	T, N/m
0	100	190	150	NOT USED	NOT USED	NOT USED	556	NOT USED	298
90	100	187	142				462		289
180	100	180	136				444		271
270	100	174	130				430		255
360	100	169	124				418		241
450	100	165	120				406		231
540	100	161	116				398		222
630	100	158	114				390		215
720	100	156	112				386		210
810	100	155	110				384		208
900	100	155	110				382		207
990	100	155	110				384		208
1080	100	156	112				386		210
1170	100	158	114				390		215
1260	100	161	116				398		222
1350	100	165	120				406		231
1440	100	169	124				418		241
1530	100	174	130				430		255
1620	100	180	136				444		271
1710	100	187	142				462		289
1800	100	190	150				556		298

All dimensions are in millimetres.

For the construction of beam FFB 4, the full set of parameters presented in *Table 5.8* was required. In this case, x_L is measured from the left end of the beam. The predicted extension of fabric was 1.27 mm at the supports and approximately 0.4 mm at midspan, considered sufficiently small to be ignored. The web formers were held with ties passing through the thickness of the beam at their mid height level. The exact position of each tie

was marked on the fabric, using the web formers as templates and, therefore did not need to be provided in advance. Although producing and attaching web formers to the fabric is a fairly complex construction process, it can be done prior to fixing the fabric to the formwork tables. This could be most advantageous for insitu concrete applications as greater material savings can be achieved in comparison with the rest of the studied methods without any additional work on site.

Table 5.8. FFB 4 construction parameters

x_L	B	D	d_{eff}	B_{web}	D_b	h_{web}	P	P_b	T, N/m
0	77	70	35				180		55
100	97	78	43				206		74
200	152	98	63				274		136
300	250	129	94				392		292
400	398	175	140				570		642
500	398	175	140				582		642
600	398	175	140				570		642
700	329	135	63				458		416
800	269	127	83				402		312
900	217	147	109				404		295
1000	174	176	139				446		328
1100	138	199	162	50	75	25	470	200	206
1200	110	217	180	50	75	43.11	494	200	191
1300	91	230	193	50	75	55.94	514	200	202
1400	79	237	201	50	75	63.6	527	200	209
1500	75	240	204	50	75	66.14	531	200	213
1600	79	237	201	50	75	63.6	527	200	209
1700	91	230	193	50	75	55.94	514	200	202
1800	110	217	180	50	75	43.11	494	200	191
1900	138	199	162	50	75	25	470	200	206
2000	174	176	139				446		328
2100	217	147	109				404		295
2200	269	127	83				402		312
2300	329	135	63				458		416
2400	398	175	140				570		642
2500	398	175	140				582		642
2600	398	175	140				570		642
2700	250	129	94				392		292
2800	152	98	63				274		136
2900	97	78	43				206		74
3000	77	70	35				180		55

All dimensions are in millimetres.

5.3.3. Fabric patterns

All fabric patterns were printed manually using a fine marker pen. The process required typically one hour for a two-metre beam. The top plates of the formwork table were also marked and the cross sections numbered to allow fast and accurate fitting of the fabric.

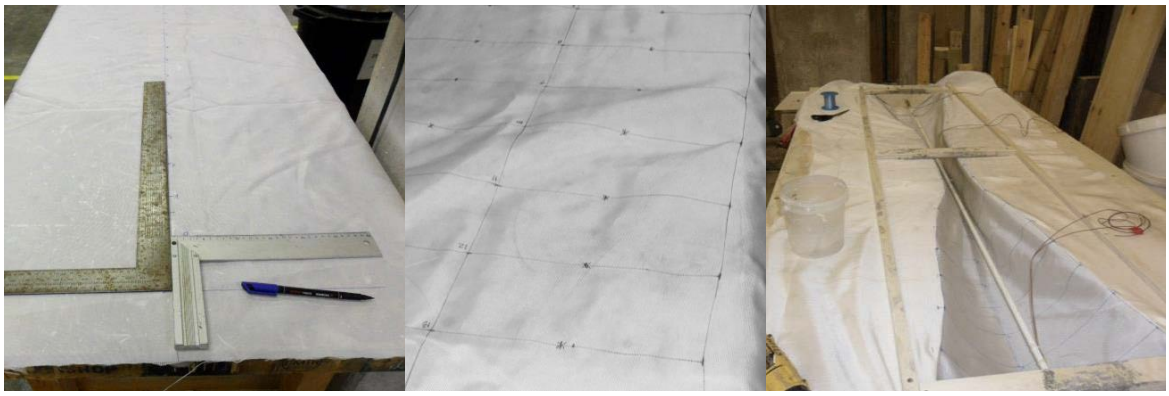

Figure 5.15. Fabric patterns and installation

The marked-up fabric was stapled directly onto the top plates as shown in *Figure 5.15*. In the case of restrained fabric, the 'quilt-point' ties or the web formers were attached before fixing the fabric to the formwork table. *Figure 5.16* illustrates the web formers used for constructing beam FFB 4. The web formers were cut out from plywood sheets and connected with formwork ties, made of 4 mm threaded steel bars and installed inside protective plastic sleeves. In order to prevent unravelling of fabric, the holes for the steel bars were formed by heat cutting. As a result, the fabric sheets could not be re-used for casting of other shapes. The use of strong plastic wire for discrete ties for beam FFB 2, however, did not compromise the reusability of fabric.

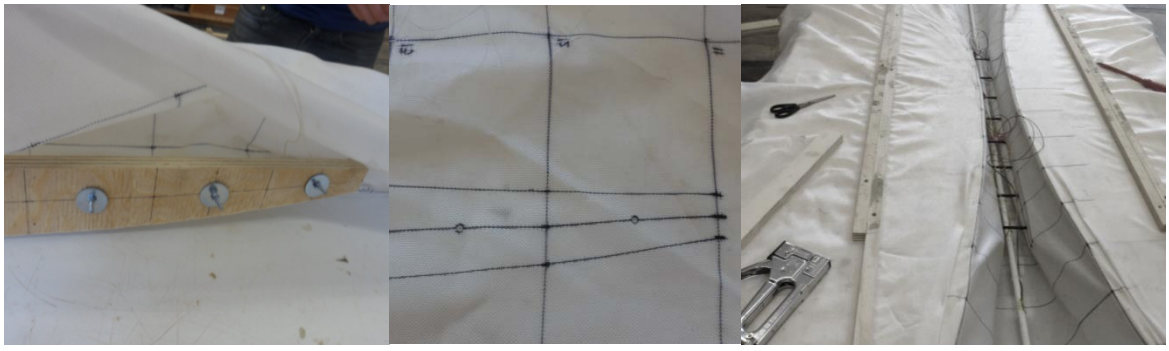

Figure 5.16. Installation of web formers

5.3.4. Reinforcement preparation and installation

All specimens comprised straight FRP bars, field-bent to suit the design beam profile. Two methods for reinforcement installation were considered. The first method required external

fixings for the FRP bars. Typically, this would include a ‘pull-down’ support at midspan and ‘pull-up’ supports at the ends of a beam, as highlighted in *Figure 5.17*. The lack of a physical connection between the reinforcing bars and the fabric, however, could pose a significant risk of displacement of the bars during the concrete pour.

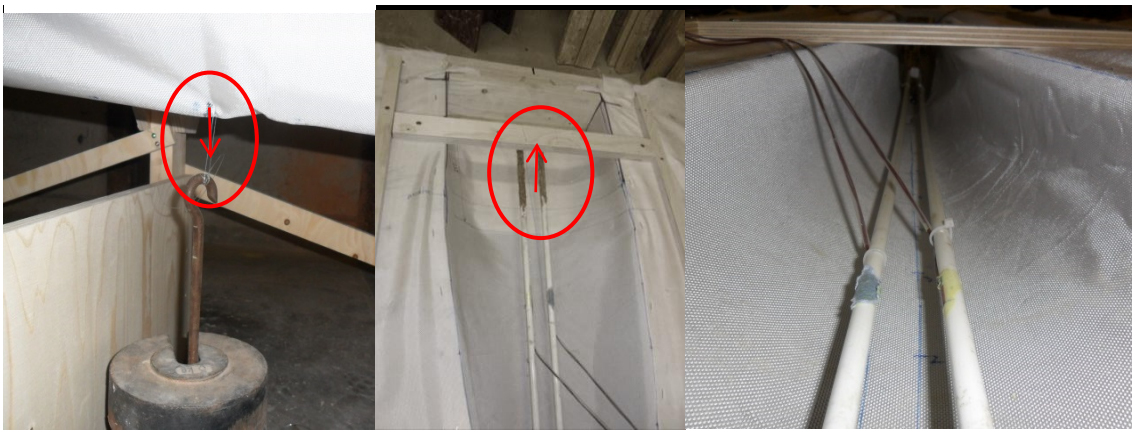

Figure 5.17. Externally fixed GFRP bars

An alternative method for installation of flexible FRP bars inside fabric formwork using internal ties was developed. The method was applied to beam FFB 2 and beam FFB 4. A number of discrete plastic ties were fixed along the length of the reinforcing bars and tied to the fabric itself. The selfweight of the wet concrete was then relied upon to provide a ‘pull-down’ support. As can be seen in *Figure 5.18*, the length of the ties provides the concrete cover to the reinforcement and can easily be varied. The ends of the FRP bars were still tied to ‘pull-up’ supports fastened to the formwork table, as illustrated in *Figure 5.19*. Prior to installation, the end anchorages were prepared, following the methods, described in § 3. Polystyrene plugs were also cast-in to provide access for monitoring of the end slip during load testing.

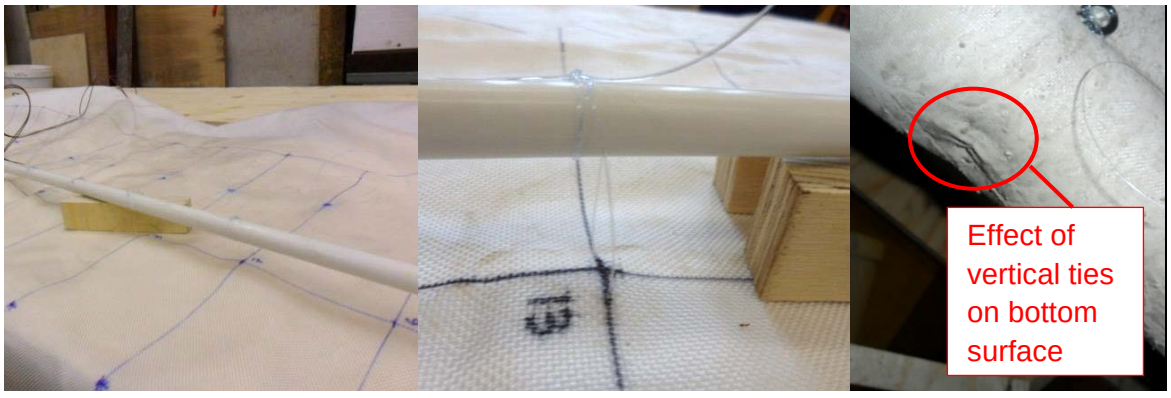

Figure 5.18. Vertical ties for internally fixed GFRP bars

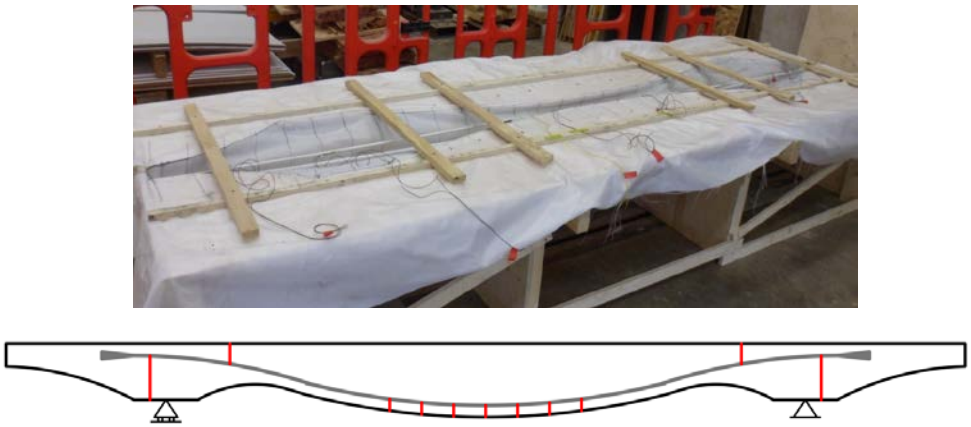

Figure 5.19. Internally fixed bars along beam length

5.3.5. Concrete casting and forming of supports

The test specimens were cast consecutively to allow re-use of the formwork table. Beams FFB 2 and FFB 3 were cast at the same time, while FFB 1 and FFB 4 were cast separately. The concrete volume of the specimens cast at once was limited to two concrete batches. *Figure 5.20* shows the concreting of FFB 1 and the level of fresh concrete before laying the second batch. The time between the two batches was used for compaction of concrete, using both needle vibrator and external compaction by hand.

Figure 5.20. FFB 1 concrete casting

Achieving correct levels and flatness at the supports can be problematic for fabric-formed beams cast in a freely hung fabric. Therefore, flat supporting surfaces were provided at the location of the beam supports during concreting. *Figure 5.21* demonstrates that the bottom surfaces formed in this way did not require additional levelling, however as described earlier, they resulted in unnecessarily large cross-sections due to the design approach. The supports for FFB 2 and FFB 3 were formed in a similar manner.

Following the successful trial ‘quilt-point’ construction, plastic ties were used at the midspan length of beam FFB 2. Easy to install and to remove, the ties also create a beautiful pattern shown in *Figure 5.22*.

a.

b.

c.

Figure 5.21. FFB 1: (a) internal support, (b) first span end support and (c) second span end support

Figure 5.22. FFB 2 'quilt-point' construction

Beam FFB 4, shown in *Figure 5.23*, was cast with the help of delegates who were participating in a conference workshop. In this case the beam was cast on supports independent from the formwork frames. This allowed a complete removal of the fabric formwork and the supporting table without lifting the beam in order to provide an early access for examination within the duration of the conference. As can be seen, the flat bottom surfaces were successfully formed using the method illustrated in *Figure 5.7*.

Figure 5.23. Beam FFB 4 construction

5.3.6. As-built geometry

5.3.6.1. Survey of as-built geometry

Recording the as-built geometry of fabric-formed elements is a challenging task. The dimensions that can be checked include the top breadth, the overall depth and the perimeter of each design cross section. However, in order to confirm the ability of the form-finding algorithm to accurately predict entire shapes, it is necessary to obtain the full cross-sectional profile of sections under consideration. In addition, the position of the reinforcing bars is needed to assess the actual stiffness and load capacity of a fabric-formed beam.

The top breadth of the as-built sections is equal to the opening across the formwork table. Therefore, its accuracy depends on the quality of workmanship and can be controlled prior

to filling the fabric with concrete. In contrast, the overall cross-sectional depth can only be measured once the section has attained its final shape. *Figure 5.24* illustrates two methods for manual measurement of depth, using a large size vernier calliper or two spirit levels. *Figure 5.24a* suggests the calliper could provide a high accuracy measurement for sections with a perfectly flat top surface, however, any unevenness of the actual hand-trowelled surfaces could affect the depth measurement, as indicated in *Figure 5.24b.* Furthermore, the jaws of the vernier calliper could not reach the centreline of wider cross sections and another method was required. By fixing two spirit levels in the horizontal direction above and below the cross section it was possible to measure the perpendicular distance between the outermost top and bottom points (*Figure 5.24c)*. A combination of the two methods was also used by attaching a spirit level to the top jaw of the calliper. Nevertheless, positioning the spirit levels required considerably more time and was applied only when the first method was found not to be suitable.

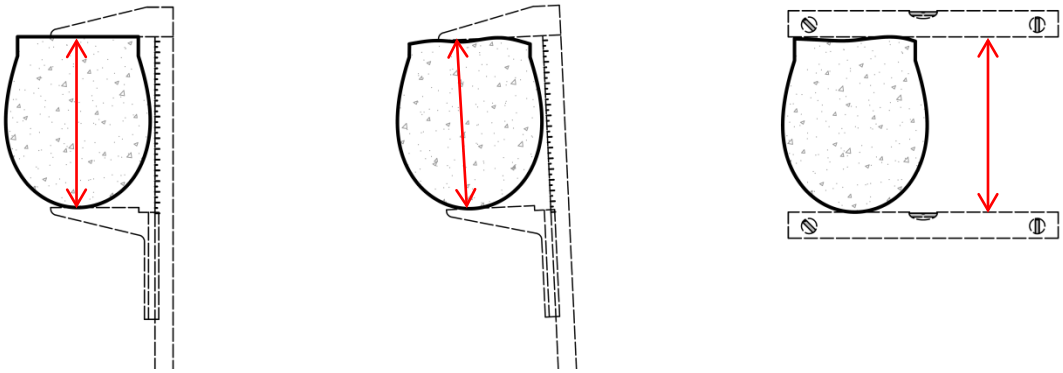

a. b. c.

Figure 5.24.Depth measurement: (a) using Vernier calliper for flat top surface, (b) using Vernier calliper for actual top surface (c) using two spirit levels

3-D scanning of fabric-formed as-built shapes was also investigated in collaboration with another research project studying the application of Microsoft Xbox Kinect as a low-cost 3-D scanner for engineering applications (Smith, 2012). The estimated depth accuracy of the Kinect of +/- 2-3 mm was considered appropriate for the purpose of the current study. Broken parts of the tested beam specimens were positioned at the closest possible distance from the scanner of approximately 1.5 m, as shown in *Figure 5.25a*, in order to minimise the error of Kinect. The beam objects were then scanned on both sides along their longitudinal axis. The process required only a few minutes per side. Cross-sectional profiles were extracted from the recorded point cloud data, graphically presented in *Figure 5.25b*. However, the extent of the point cloud on each side was not always found sufficient to describe the full curved profile of a cross-section, as illustrated in *Figure 5.26*. Furthermore, it was expected that any following beam specimens would be scanned in full

prior to destructive testing, which would make the scanning of the bottom part of a curved cross-sectional profile particularly difficult. In addition, the as-built location of reinforcing bars inside the cross sections could not be determined by measuring the surface geometry. For this reason, more intrusive methods, such as physical slicing of beams into sections, were considered and the application of Kinect was not pursued further.

a.

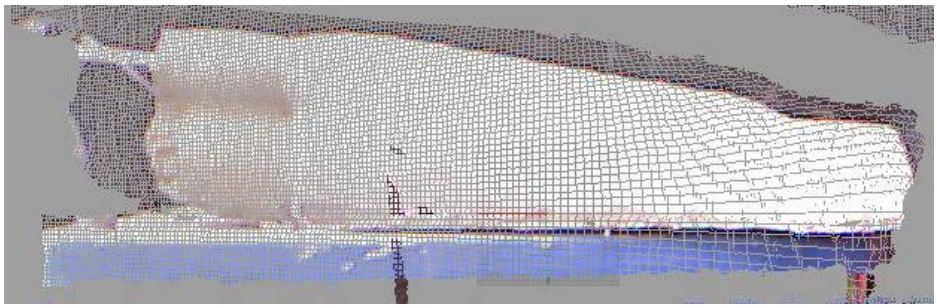

b.

Figure 5.25. Xbox Kinect: (a) 3-D scanning of a fabric-formed beam and (b) recorded data

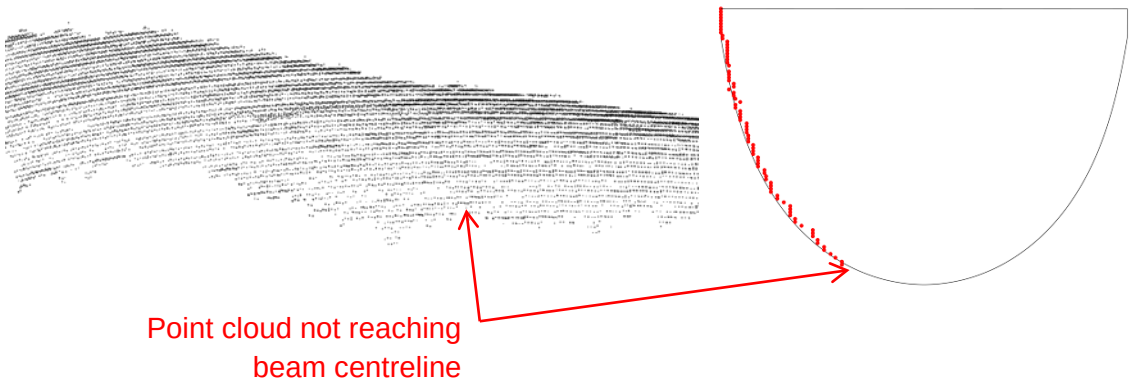

a. b.

Figure 5.26. Insufficient 3-D point cloud data: (a) top view and (b) cross section

5.3.6.2. Beam FFB 1

Figure 5.27 presents the as-built dimensions of beam FFB 1. The measurements include only the top breadth and the overall depth. As can be seen, the as-built longitudinal profile generally follows closely the design shape at midspans. It should be noted that at locations with sudden changes in the cross section the fabric could not be fitted to the top of the formwork tables and remained locally detached during construction resulting in significant displacements (see *Figure 5.28).* As indicated, the maximum deviations from the design geometry reached values greater than 30 mm. This demonstrated some of the limitations of casting complex 3-D concrete shapes in flat fabrics.

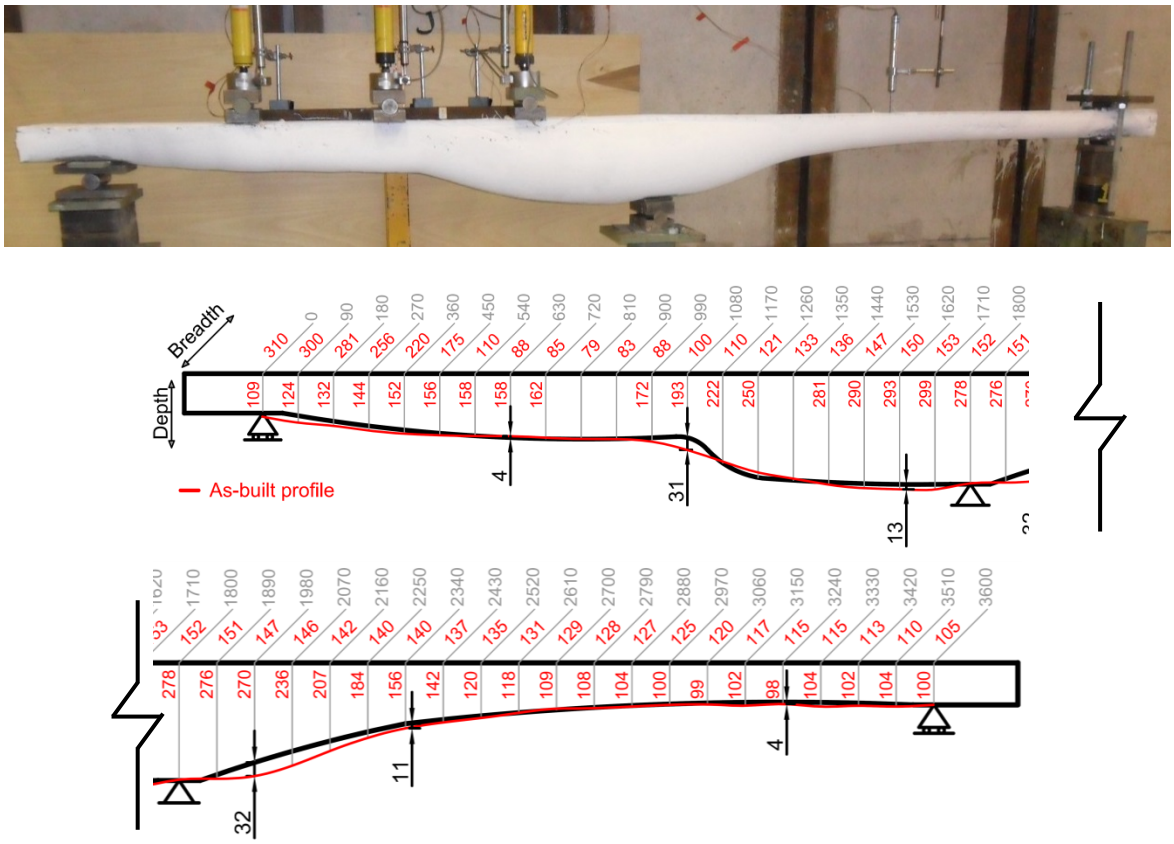

Figure 5.27. FFB 1 as-built measurements (all dimensions are in millimetres)

Figure 5.28. FFB 1 detached fabric during construction

Figure 5.29 shows the deviations in both dimensions along the beam length. As can be seen the varying top breadth was achieved within 10 mm tolerance, which was practically the tolerance in cutting the table tops in the required shape. The as-built position of the reinforcement was also not satisfactory, as *Figure 5.30* suggests. The bars were displaced from their design position and the concrete cover was reduced to approximately 15 mm. The measured effective depth, averaged between the two bars, was 146 mm.

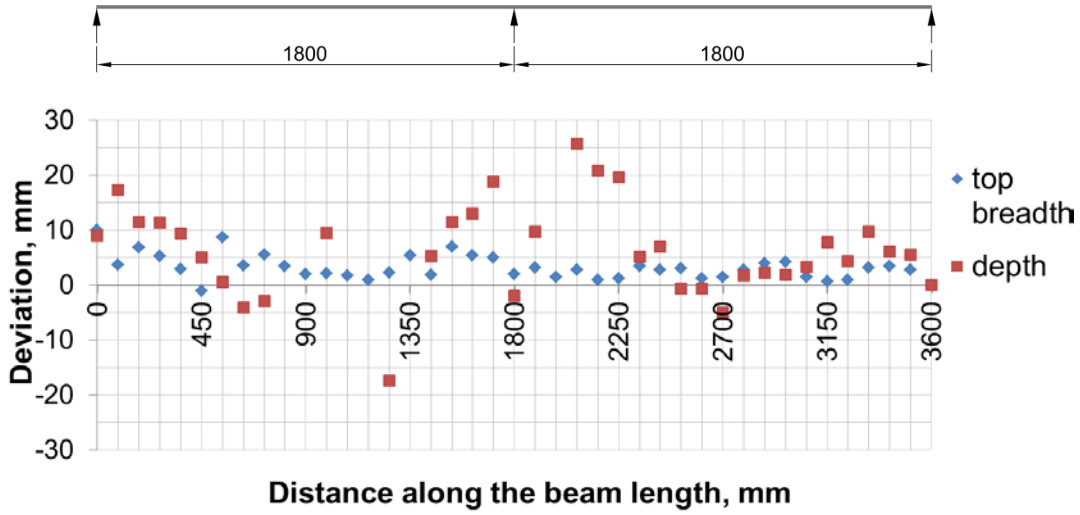

Figure 5.29. FFB 1 deviation from design geometry

a. b.

Figure 5.30. As-built position of reinforcing bars at failed section: (a) right side and (b) left side

5.3.6.3. Beam FFB 2

Similarly to FFB 1, the as-built dimensions of cross sections near the midspan of beam FFB 2 were found to be very close to their design values with practically no deviation at the centre section (see *Figure 5.31*). The adopted method for reinforcement installation by attaching GFRP bars to the fabric was also successful. The post-mortem examination of beam FFB 2 confirmed that the reinforcing bars were fixed in their design position (refer to *Figure 5.32*), unlike the externally tied bars in beam FFB 1. Similarly to FFB 1, beam FFB 2 was found to be up to 32 mm deeper near the supports. The tolerance in the top

breadth was also generally about 10 mm, except at the rounded corners of the bell shaped top plate, due to imperfect fabrication. However, practically no deviation was recorded at midspan, as indicated in *Figure 5.33*.

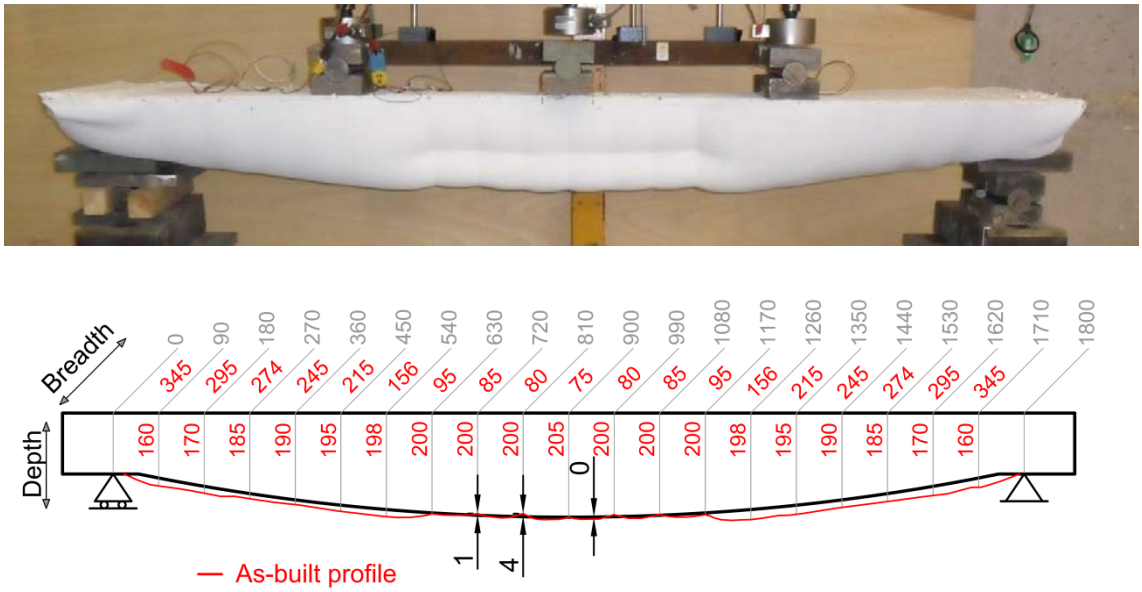

Figure 5.31. FFB 2 as-built measurements (all dimensions are in millimetres)

Figure 5.32. As-built position of reinforcing bar

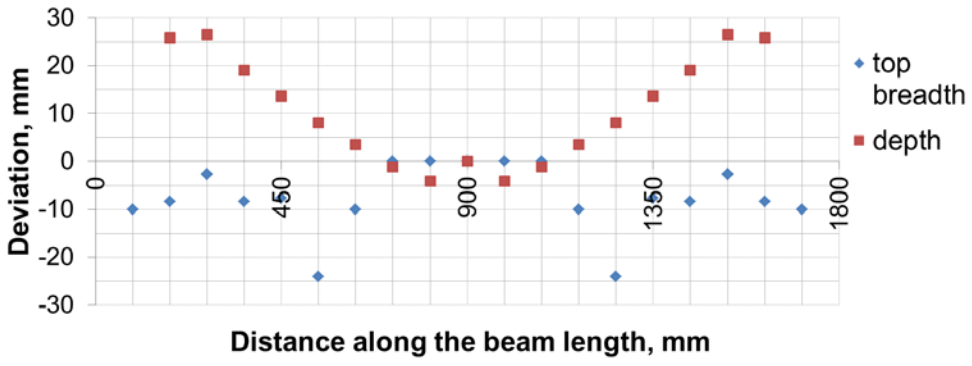

Figure 5.33. FFB 2 deviation from design geometry

5.3.6.4. Beam FFB 3

Less deviation from the design geometry was observed for beam FFB 3, most likely due to its fairly simple shape. The uniform top breadth of 100 mm was confirmed by tape measurement, while the results of the depth measurement are presented in *Figure 5.34*. The average tolerance in the depth along the beam length was 10 mm (see *Figure 5.35*). The as-built position of the reinforcing bars was also found to be accurate at the failed cross section.

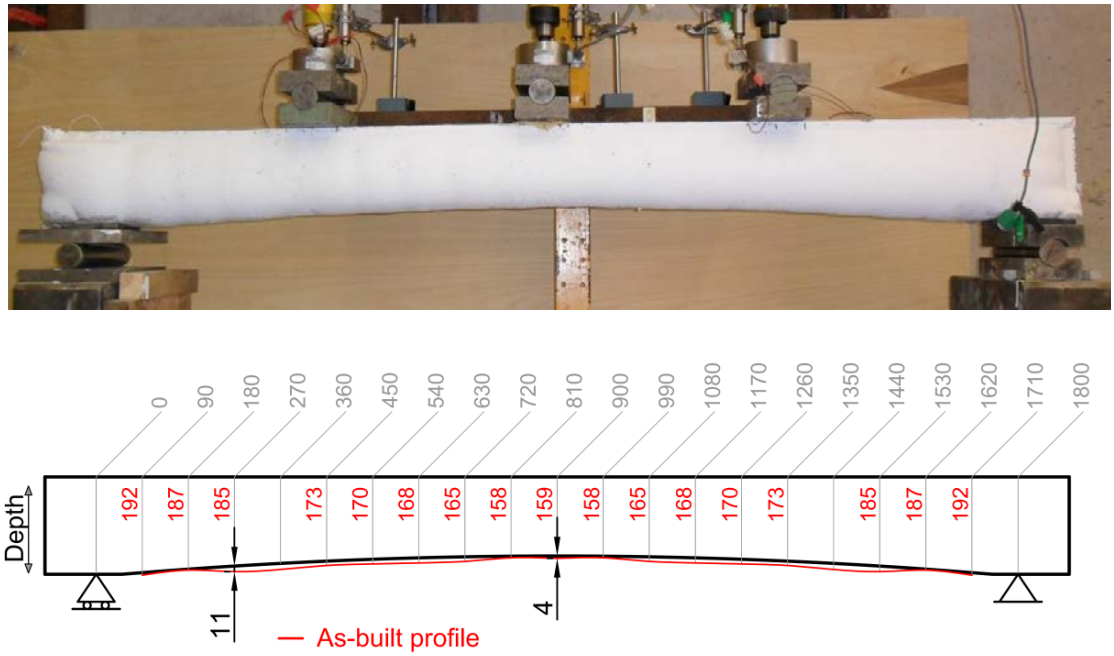

Figure 5.34. FFB 3 as-built measurements (all dimensions are in millimetres)

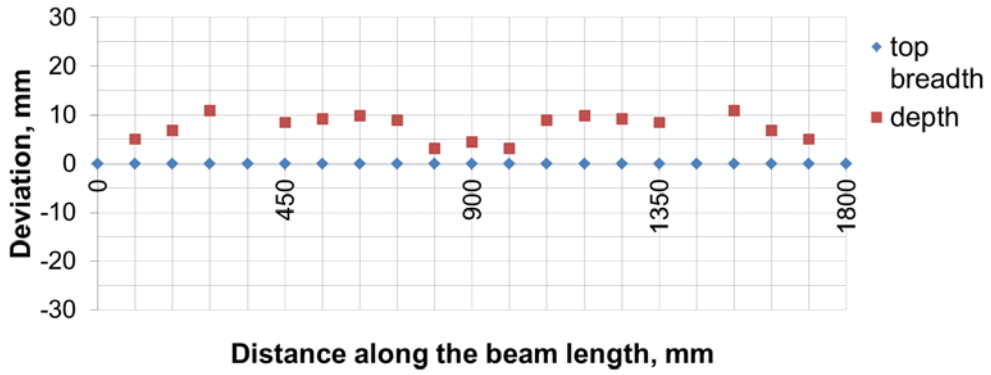

Figure 5.35. FFB 3 deviation from design geometry

5.3.6.5. Beam FFB 4

Figure 5.36 illustrates the measurement data for beam FFB 4. In this case, a flexible tape measure was also used to check the perimeter of each section. The full curved profiles

and the actual effective depths were determined for a number of cross sections, directly cut from the tested beam specimen, as shown in *Figure 5.37*.

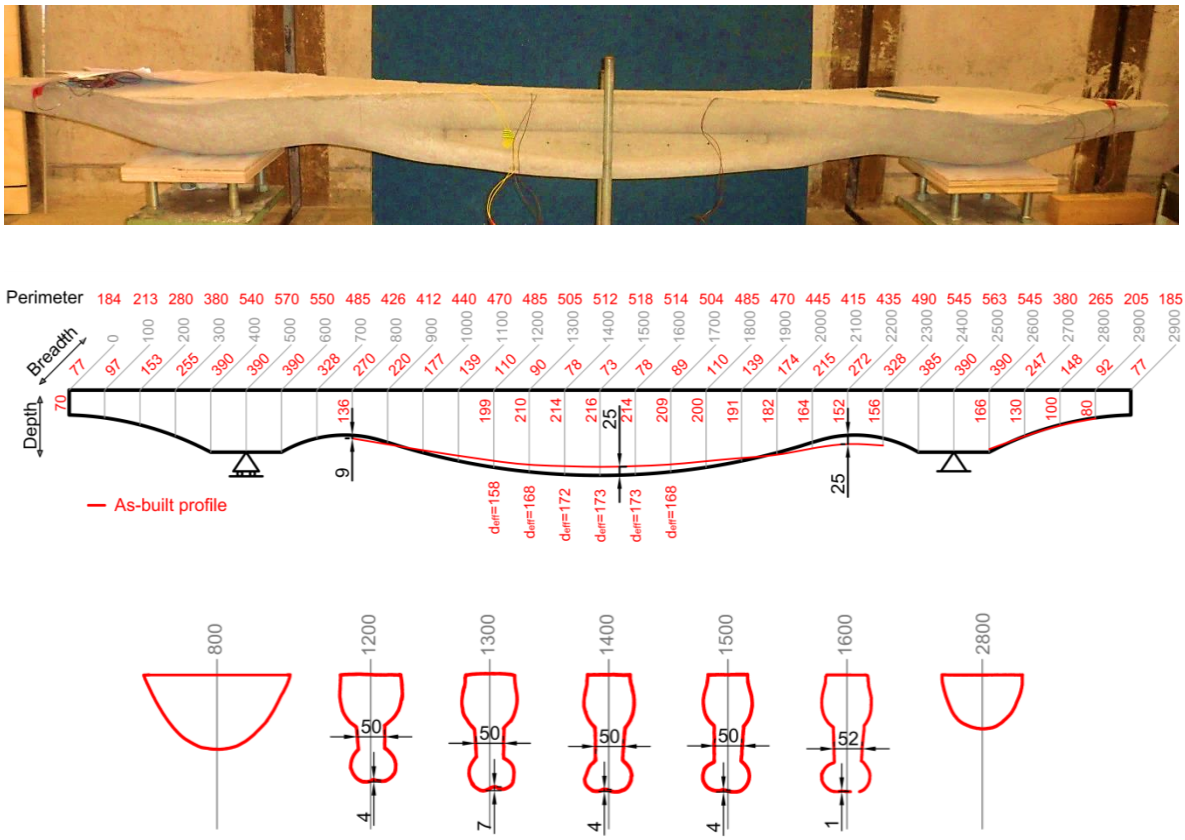

Figure 5.36. FFB 4 as-built measurements (all dimensions are in millimetres)

Figure 5.37. FFB 4 'key-hole' section

As can be seen the 'key-hole' midspan sections had generally unsymmetrical shapes, mainly due to inadequate hand compaction. A finger print visible on the concrete surface, shown in *Figure 5.37*, also affected the cross-sectional shape. Nevertheless, it was successfully demonstrated that the web formers can be restrained internally avoiding the need of additional side supports used previously for the construction of 'key-hole' fabric-

formed beams (Garbett, 2009). The specified concrete cover to the internally tied reinforcing bar was also achieved, demonstrating again the effectiveness of the proposed method.

The measured cross-sectional perimeters of beam FFB 4 followed closely the design values, except near the supports, as can be seen in *Figure 5.38*. However, the differences at these locations can also be attributed to inaccurate measurement of the curved profile, formed by wrinkling at the top of the cross-sections. The tolerance in the top breadth at midspan was only 2 mm, reaching larger values of about 10 mm over the supports. The overall depth differences are presented in *Figure 5.39*, which shows the outlines of sliced cross sections compared with theoretical predictions, produced by the MATLAB programme, not available at the time of the design. In this case, the vertical ties caused a significant change in the overall depth at midspan. This highlighted the importance of being able to predict the shape of vertically restrained fabric under the forces, required to bend the reinforcing bars into their design curved profiles, as discussed in detail in § 6.

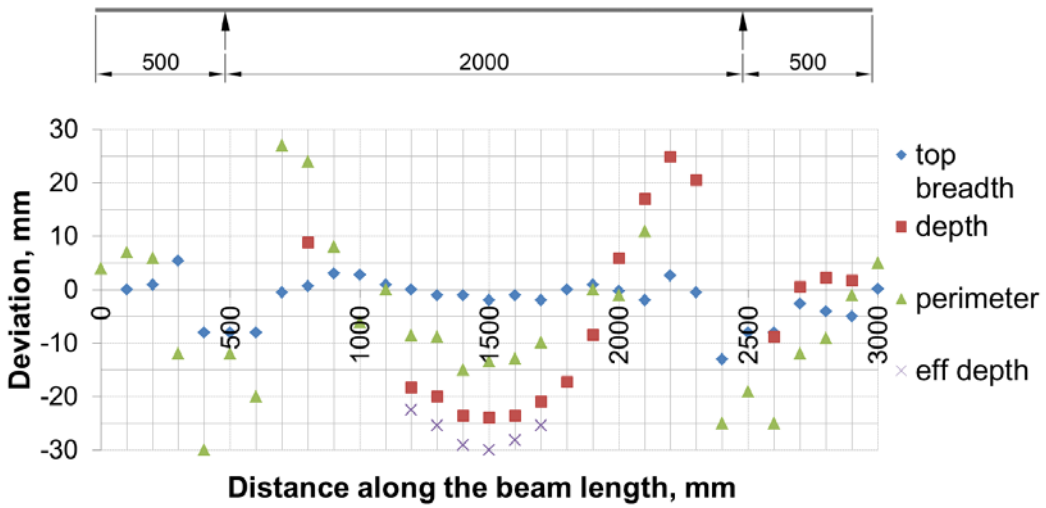

Figure 5.38. FFB 4 deviation from design geometry

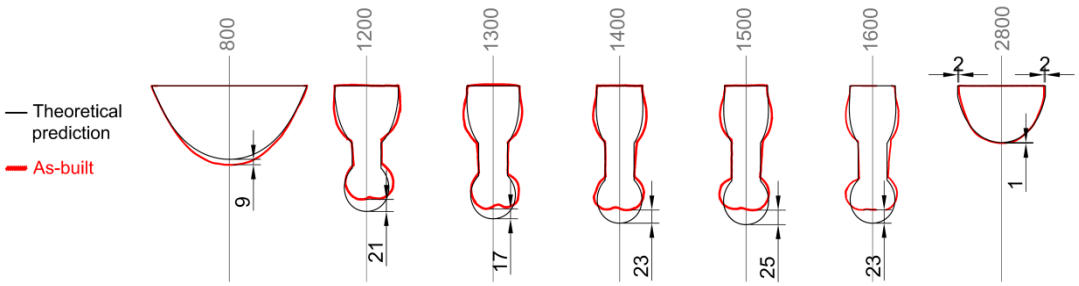

Figure 5.39. FFB 4 as-built cross sections (all dimensions are in millimetres)

5.4. Test results

5.4.1. Material testing

The number of concrete batches used per specimen and the measured concrete strengths are presented in *Table 5.9*. Only concrete cubes were tested, while the cylinder strengths were calculated by multiplying the cube compressive strengths by 0.8. Furthermore the cubes were cast in standard moulds and no enhancement due to the permeability of fabric formwork was taken into account. A considerable difference can be noticed between the compressive concrete strengths of the two batches produced for FFB 1, which may be due to a weighing error during the preparation of the mix. In addition, the strengths of FFB 2 and FFB 3 mixes were far below the target of 16 MPa. The first three specimens were cast during the winter season and a possible reason for the great variation in the strength may also be the unpredictable and unevenly distributed moisture content of aggregates stored outside. For comparison, beam FFB 4 was cast in July and achieved its design strength fairly accurately, as confirmed by the results in *Table 5.9*. The design of concrete mixes in accordance with Teychenné et al. (1997) assumes surface dry aggregates and, consequently, measures for reducing the extra moisture content in aggregates have been considered for the following specimens cast in winter conditions, as described in § 6.

Table 5.9. Compressive concrete strengths (Series 1)

Beam ID	Date cast	Date tested	Average Batch I, MPa	Average Batch II, MPa	Average cube strength, MPa	Predicted cylinder strength, MPa
FFB 1	20/01/2012	25/01/2012	18.3	40.6	29.4	23.6
FFB 2	26/01/2012	01/02/2012	8.9	N/A	8.9	7.1
FFB 3	26/01/2012	01/02/2012	11.5	N/A	11.5	9.2
FFB 4	27/06/2012	06/07/2012	21.4	18.4	19.9	15.9

The elastic moduli of the different types of FRP bars, presented in *Table 5.3* and experimentally confirmed by the results in *Figure 3.32*, were used for theoretical load-deflection analysis of the experimental beams.

5.4.2. Failure modes and failure loads

All beam specimens failed in flexure, developing large cracks in the tensile zone prior to concrete failure in compression. *Figure 5.40* shows the failed section of beam FFB 1. As can be seen, following the failure of concrete in compression, the low-strength 10 mm GFRP bars in the first span snapped and the beam split into two in a very brittle manner. However, a large crack was also formed in the second span leading to significant rotation,

highlighted in *Figure 5.41*. The failure loads, indicated in *Figure 5.41*, were very close to the predicted ultimate design values.

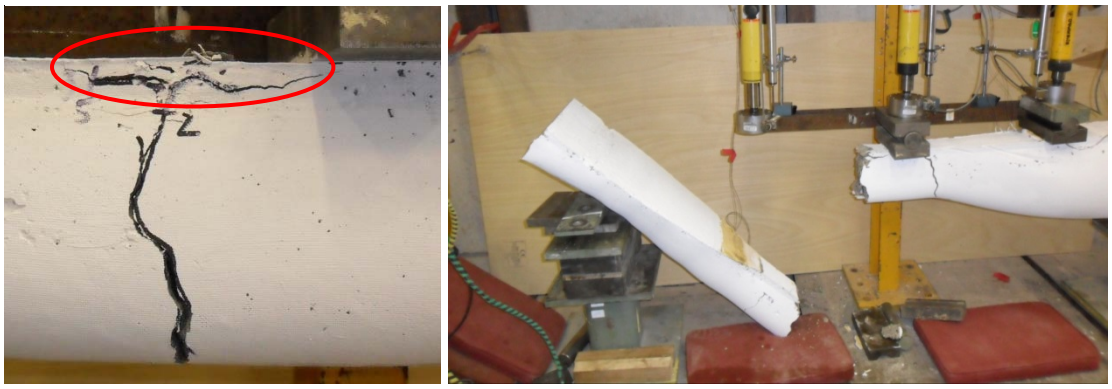

Figure 5.40. FFB1 concrete compression failure followed by snapping of the GFRP bars

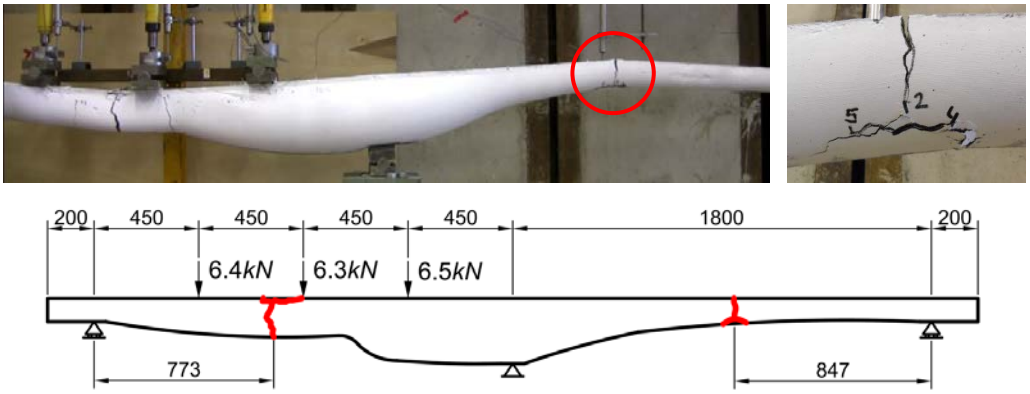

Figure 5.41. FFB 1 failure loads (all dimensions are in millimetres)

Beams FFB 2 and FFB 3 exhibited similar type of failure, as shown in *Figure 5.42* and *Figure 5.43*. The failure loads were lower than the predicted ultimate values, as indicated in *Figure 5.44*, which was expected due to the as-built concrete strengths being lower than the assumed design strength. No slip was observed at the ends of the reinforcing bars.

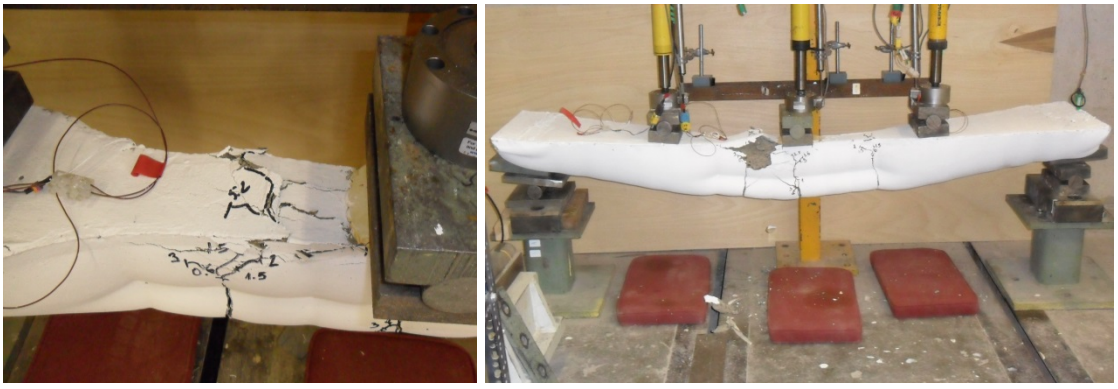

Figure 5.42. FFB 2 failure by concrete crushing in the compression zone

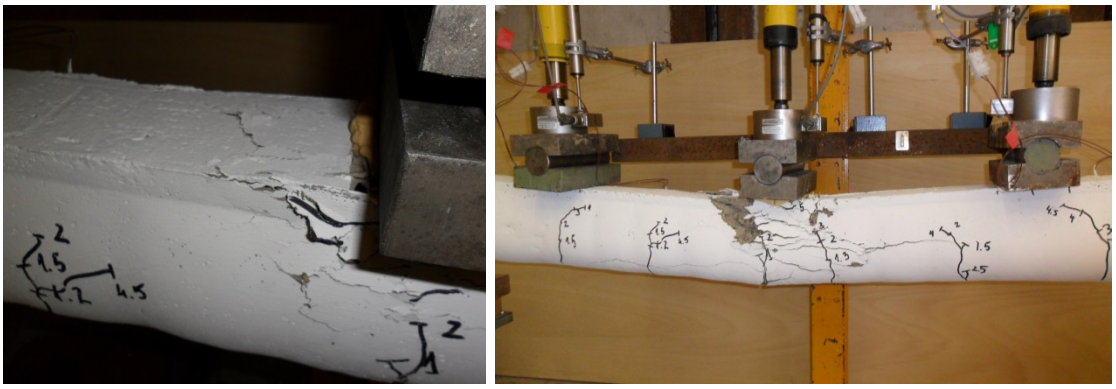

Figure 5.43. FFB 3 failure by concrete crushing in the compression zone

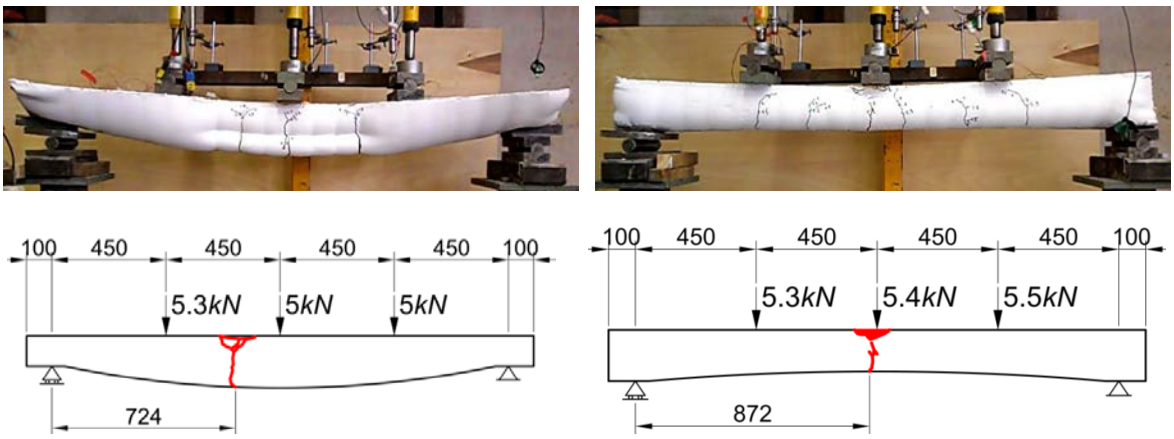

a. b.

Figure 5.44. Failure loads: (a) FFB 2 and (b) FFB 3 (all dimensions are in millimetres)

Beam FFB 4 failed near the middle left point at loads similar to the predicted ultimate design values, as illustrated in *Figure 5.45* and *Figure 5.46*. Only two major tensile cracks were observed. This was most likely due to the low bond strength of the reinforcing bars. The horizontal transducers did not record any slip at the ends of the top bars.

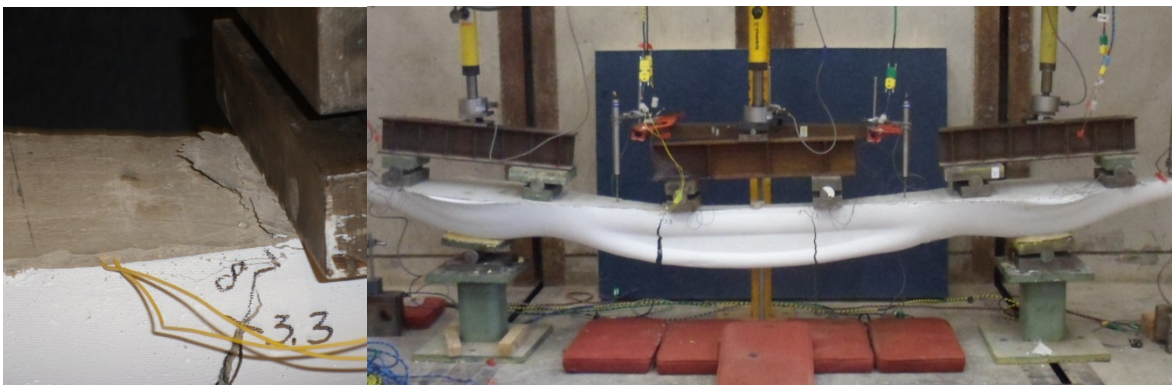

Figure 5.45. FFB 4 failure by concrete crushing in the compression zone

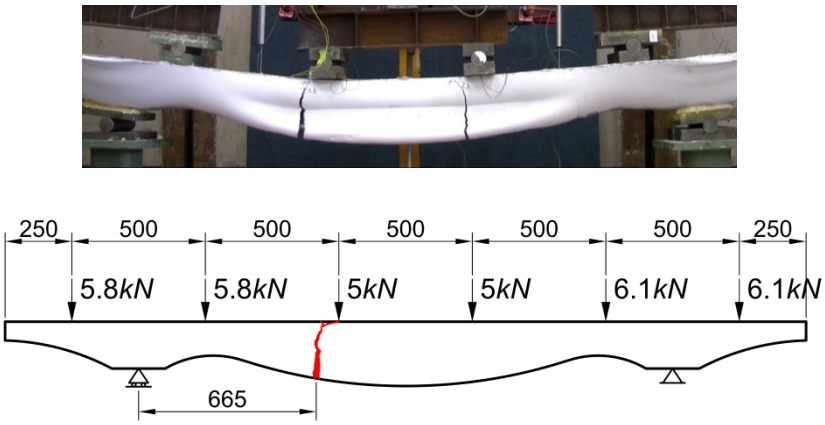

Figure 5.46. FFB 4 failure loads (all dimensions are in millimetres)

5.4.3. Load-deflection relations

The experimental load-deflection curves were recorded at the midspan and quarter-points of all loaded spans. In addition, measurements were taken along the second span of beam FFB 1 and the end cantilevers of beam FFB 4. The results presented in *Figure 5.47* to *Figure 5.50* show the obtained load-deflection relations for the total vertical load applied to each specimen.

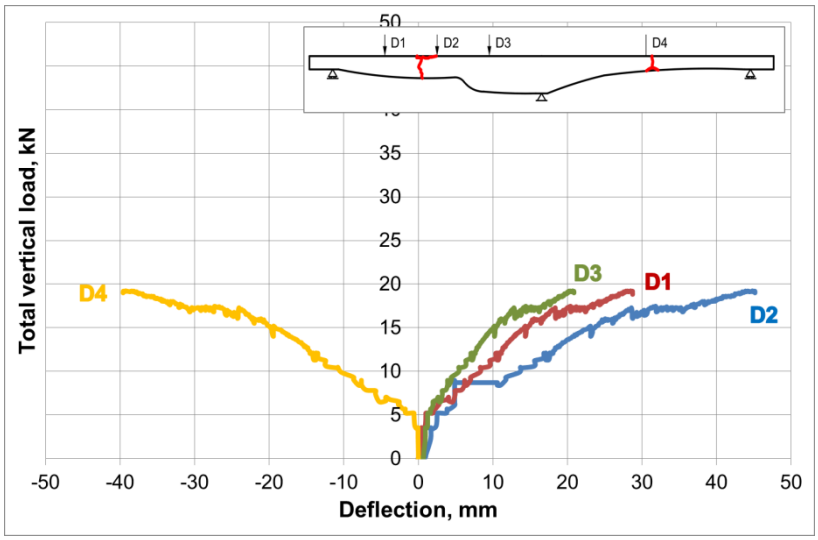

Figure 5.47. FFB 1 experimental load-deflection relations

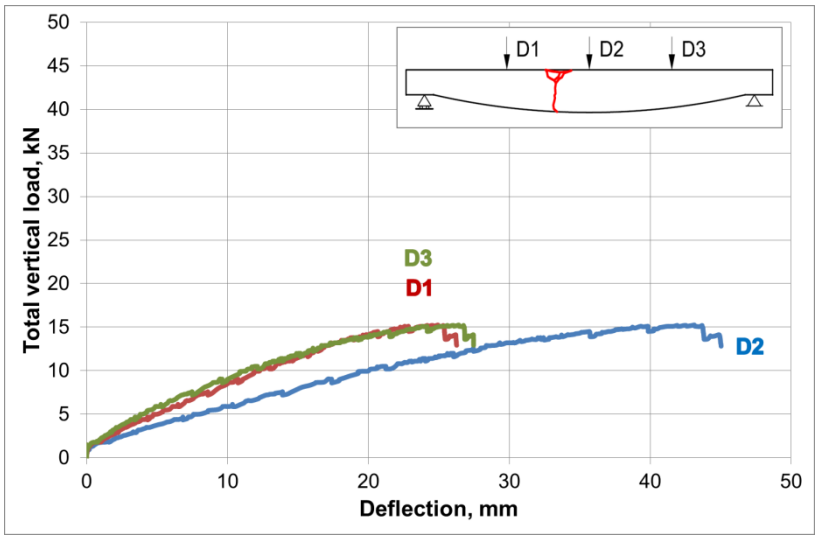

Figure 5.48. FFB 2 experimental load-deflection relations

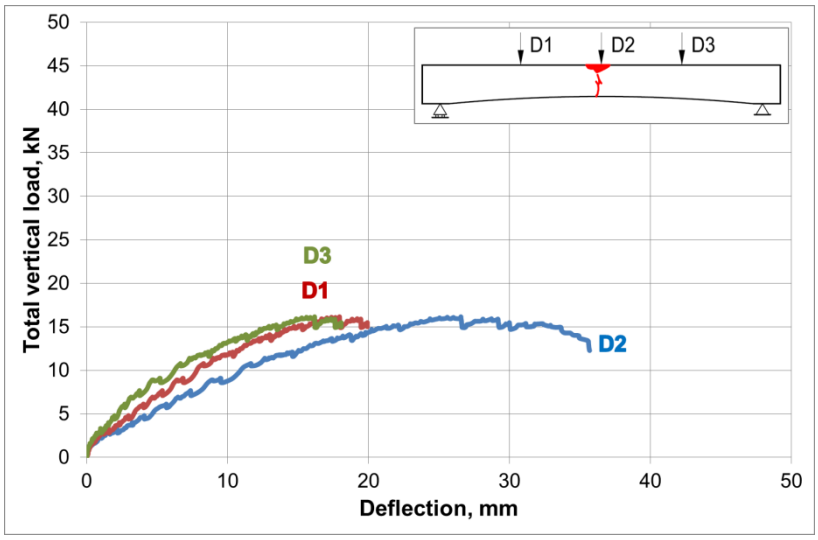

Figure 5.49. FFB 3 experimental load-deflection relations

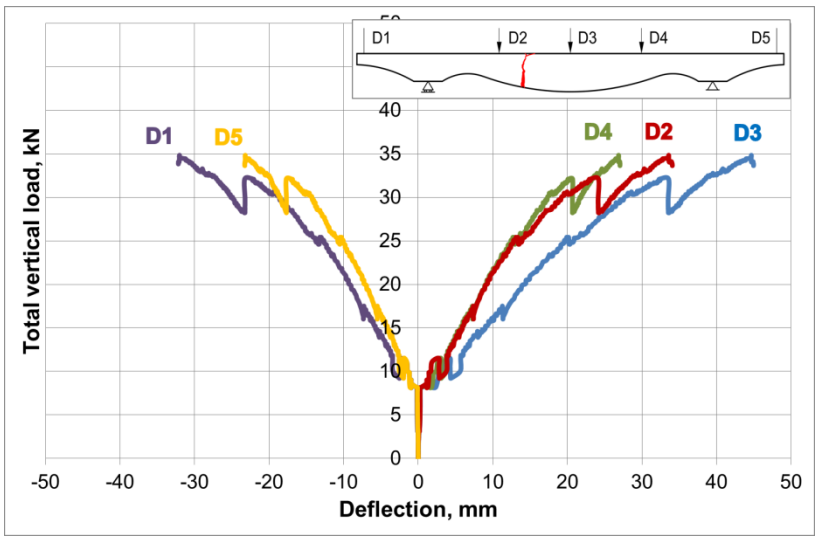

Figure 5.50. FFB 4 experimental load-deflection relations

5.4.4. Load-strain relations

The load-strain plots, presented in *Figure 5.51* to *Figure 5.54* are based on the average strains in the reinforcing bars, measured at the effective depth level by means of strain gauges, attached to the two sides of each bar. The exact location of the measurements in the longitudinal direction is indicated on the beam sketches, accompanying each plot. As can be seen from *Figure 5.54*, the control gauges near the anchorage zones for beam FFB 4 recorded practically zero strains, which could be expected for bottom reinforcement in the hogging zone and the tip of the cantilevers.

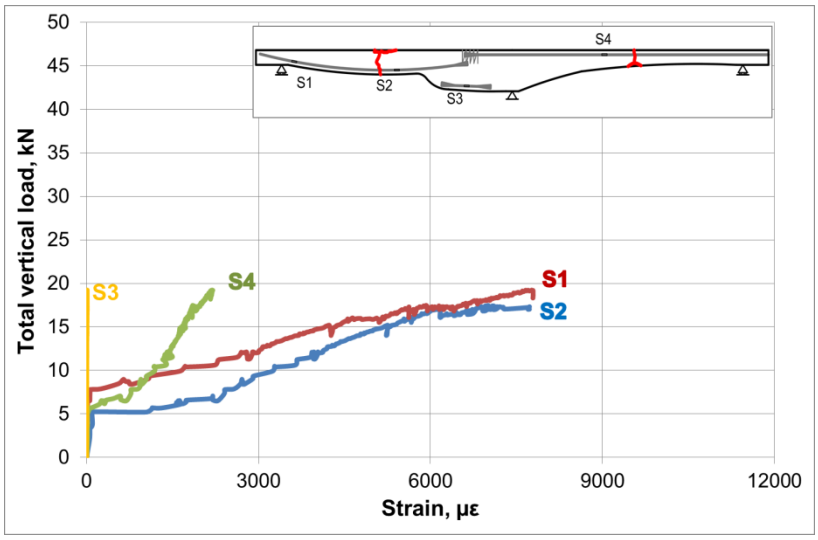

Figure 5.51. FFB 1 experimental load-strain relations

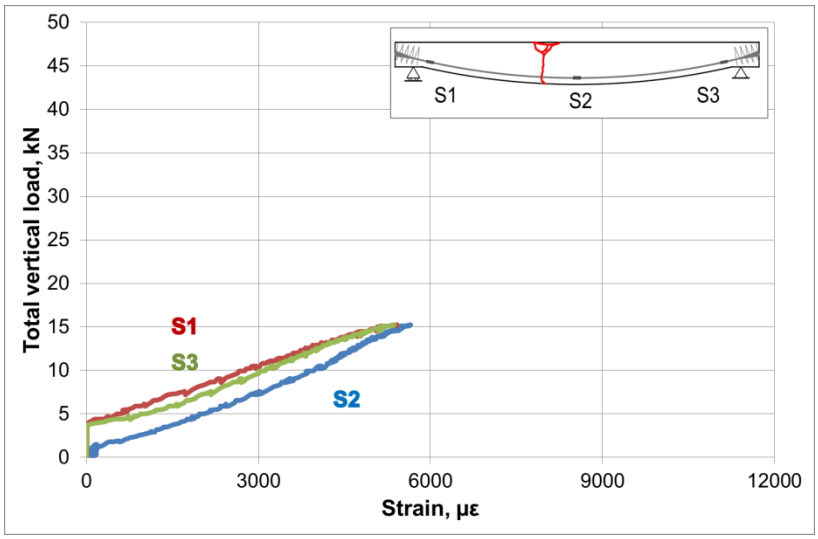

Figure 5.52. FFB 2 experimental load-strain relations

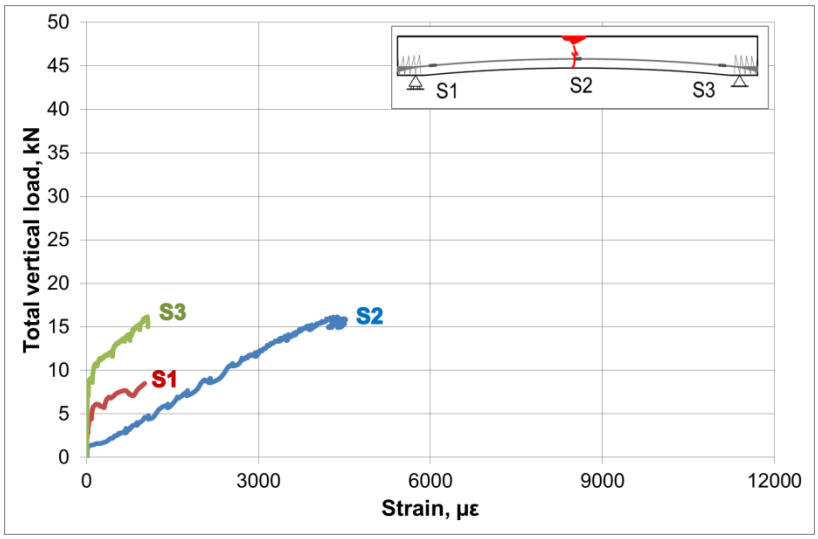

Figure 5.53. FFB 3 experimental load-strain relations

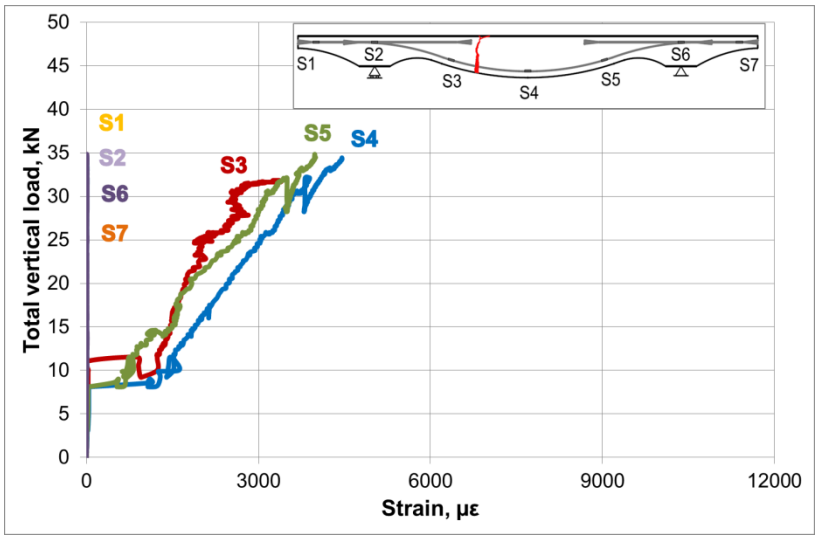

Figure 5.54. FFB 4 experimental load-strain relations

5.5. Discussion of results

5.5.1. Comparison of experimental and predicted capacities

The bending moment and shear force capacities are re-calculated based on the actual concrete compressive strengths for both the design and the as-built geometries. *Figure 5.55* presents a comparison of the calculated capacities and the applied maximum load effects for all cross sections along the length of beam FFB 1. The plot indicates that the second span should have failed in flexure first. However, it is likely that the compressive strength of concrete on the compression side, in this case, was significantly increased due to the permeability of fabric formwork, and the actual capacity exceeded the prediction based on the measured concrete strength, given in *Table 5.9*. Furthermore,

the moment in the first span could have been increased by moment redistribution. Nevertheless, a major conclusion that could be derived from the comparison is that the difference between the theoretical capacities, calculated for the design and as-built geometries, respectively, is not significant, particularly at the critical sections.

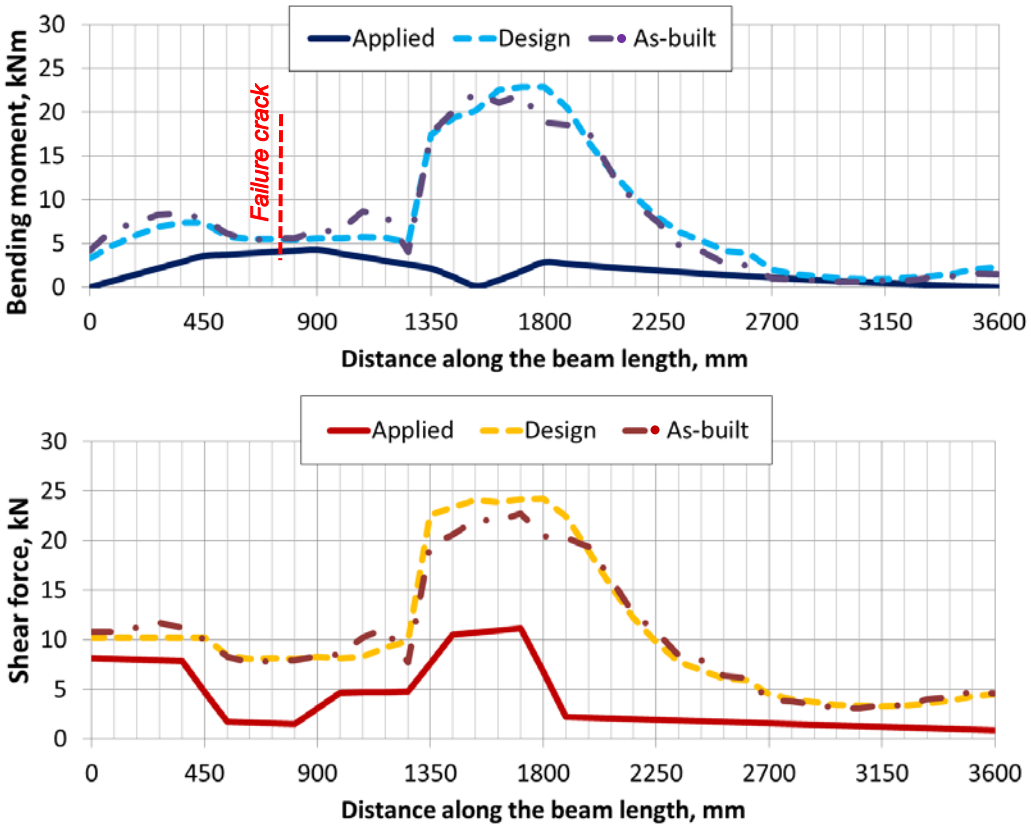

Figure 5.55. FFB 1 maximum load effects vs section capacities for design and as-built conditions

Figure 5.56 and *Figure 5.57* present the results for FFB 2 and FFB 3, respectively. Similarly to the results for beam FFB 1, the capacities based on design and on as-built geometries indicate the same expected failure type and critical sections. Therefore, the first three specimens have demonstrated that it is possible to design fabric-formed beams with reasonably predictable failure mechanisms and load capacities.

Beam FFB 4 is the only example where the as-built geometry had an effect in terms of clearly reducing the beam capacity. As the actual mean concrete strength was only 0.3% lower than the design strength, the reduction of the bending moment capacity at midspan, in *Figure 5.58*, is due only to the reduced effective depths during construction.

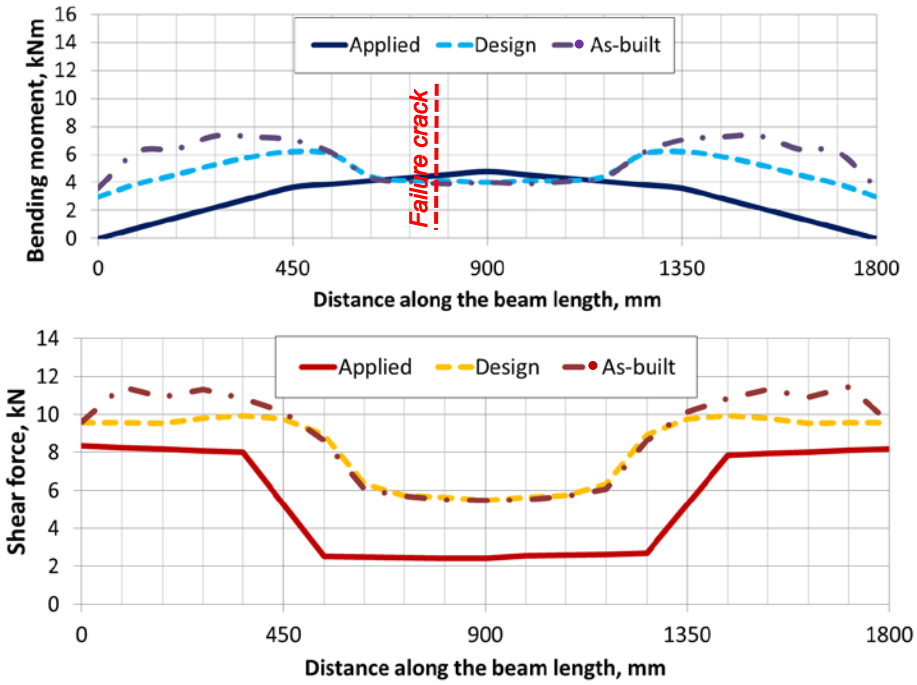

Figure 5.56. FFB 2 maximum load effects vs section capacities for design and as-built conditions

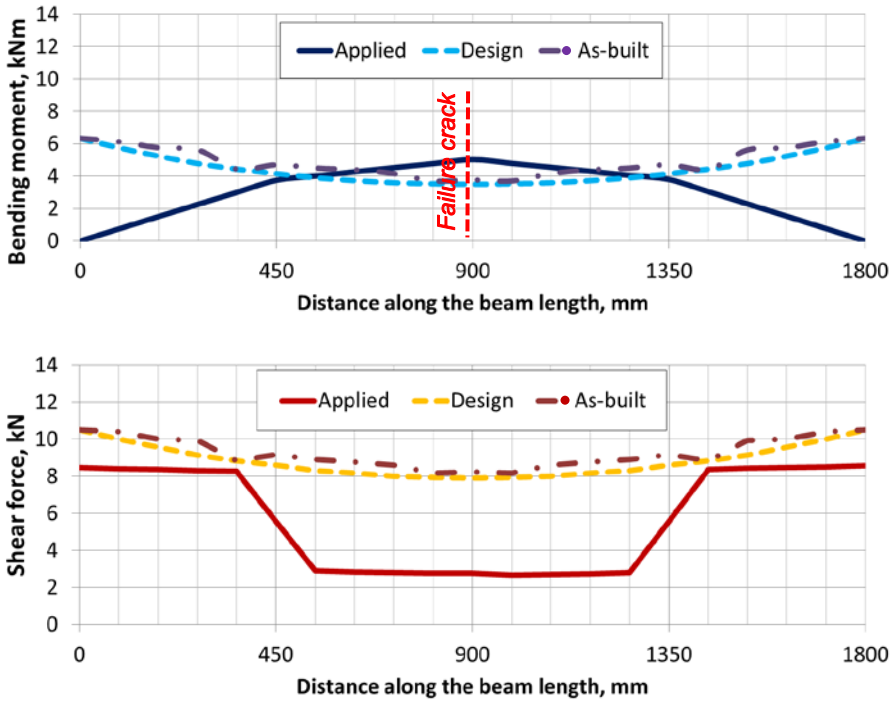

Figure 5.57. FFB 3 maximum load effects vs section capacities for design and as-built conditions

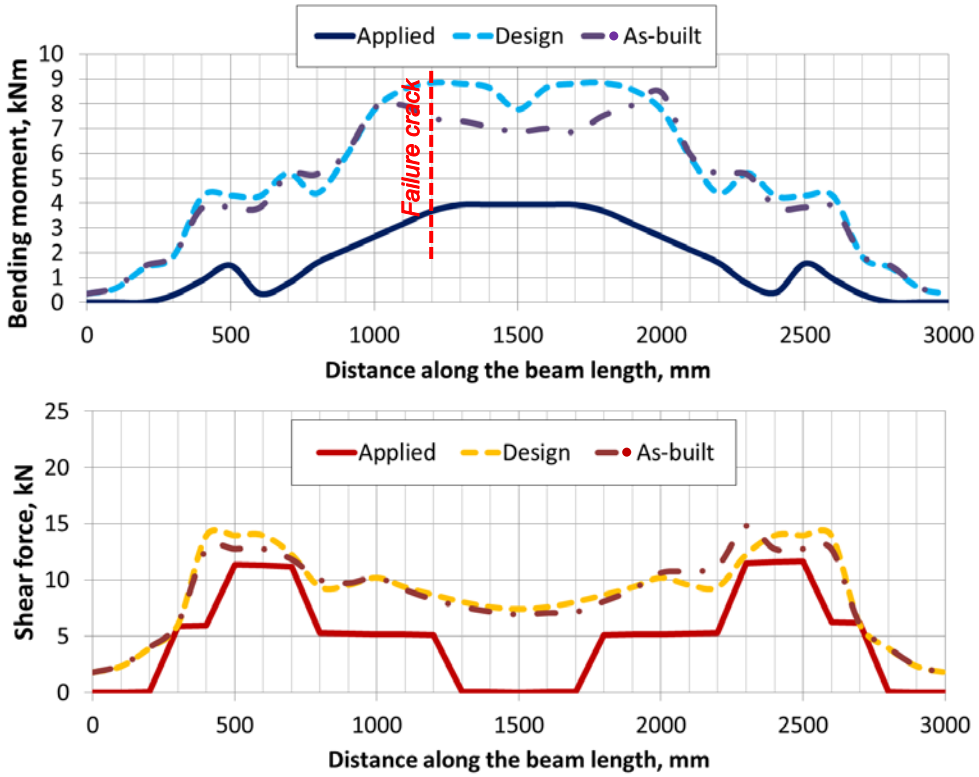

Figure 5.58. FFB 4 max load effects vs section capacities for design and as-built conditions

5.5.2. Experimental and predicted load-deflection behaviour

The theoretical load-deflection curves are obtained through double integration of curvature using the MATLAB program (not used for the design of the specimens), described in § 4. The initial sag of the beams under selfweight was not recorded and, therefore, the part of the theoretical curves corresponding to the selfweight is excluded from the presented results, as schematically explained in *Figure 5.59*. Again the predictions are based on the actual concrete compressive strengths for both the design and the as-built geometries.

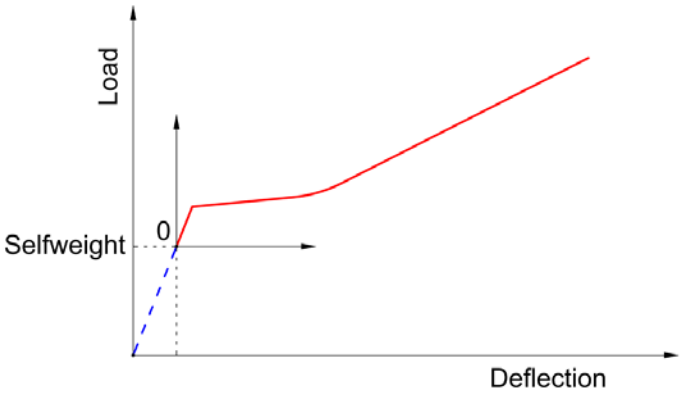

Figure 5.59. Theoretical load-deflection curve excluding selfweight

The theoretical results for beam FFB 1, presented in *Figure 5.60*, show a fairly good correlation with the experimental curves up to more than 50% of the failure load, which is satisfactory for predicting serviceability deflections. Thus, the experimental results can be used for assessing the stiffness of FRP reinforced optimised beams under serviceability loads. Considering a load partial safety factor of 1.5 for variable actions at ultimate limit states, in accordance with BS EN 1990:2002+A1:2005, applied to the factored design capacity of the beam, based on a material partial safety factor of 1.5, the design serviceability load for beam FFB 1 would be 7.6 kN. Following the results in *Figure 5.60a*, the corresponding deflection of 6.5 mm is less than the limit of span/250 (7.2 mm) in accordance with BS EN 1992-1-1:2004. A more detailed approach to evaluation of realistic serviceability loads is provided in § 6. The predicted curves based on as-built geometry follow the experimental curves more accurately. However, at early load stages the differences with the theoretical curves based on design geometry are fairly small.

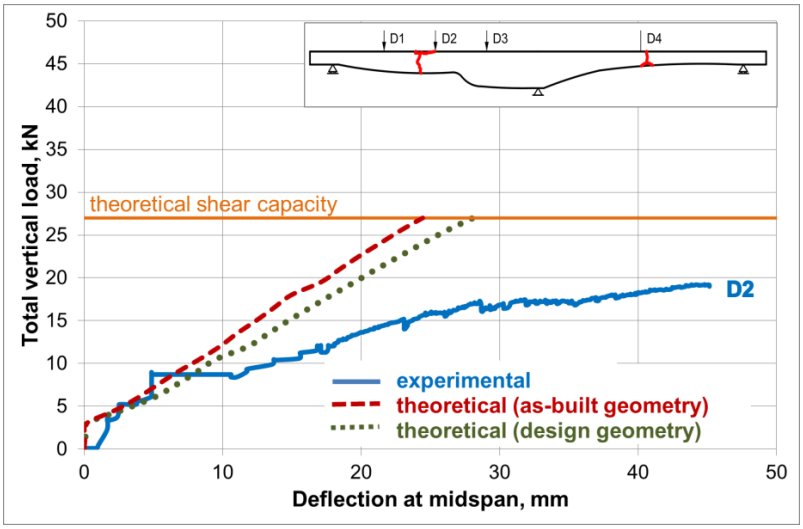

a.

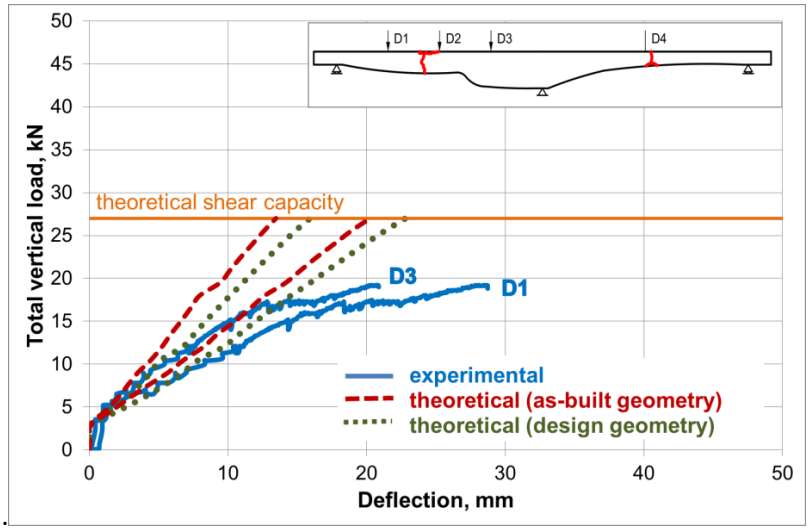

b.

Figure 5.60. FFB 1 Load-deflection relation: (a) at midspan and (b) at quarter span

The prediction of the load-deflection behaviour of beam FFB 2 is less successful, as can be seen in *Figure 5.61*. The stiffness is significantly overestimated, which could be due to local slip of the reinforcing bar inside the concrete, due to its very low bond characteristics. Furthermore, the serviceability deflections of beam FFB 2 would exceed the BS 1992-1-1:2004 limit by 40% following the described approach for defining the serviceability load. The predictions for beam FFB 3, which contained a sand-coated CFRP bar with higher bond strength, agree well with the experimental results, presented in *Figure 5.62*. The beam also has adequate stiffness, as could be expected, due to the stiffer CFRP reinforcement. The differences between the predicted curves based on as-built geometry and on design geometry are reasonably small for both beams, FFB 2 and FFB 3.

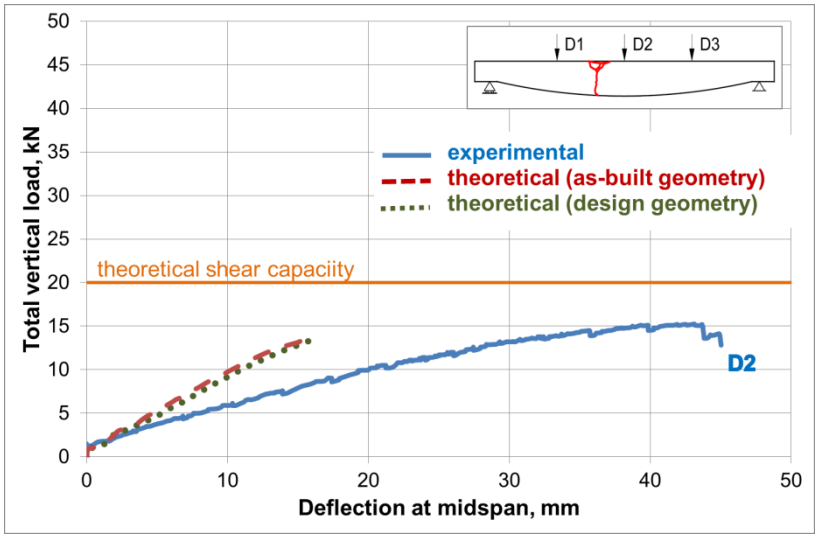

a.

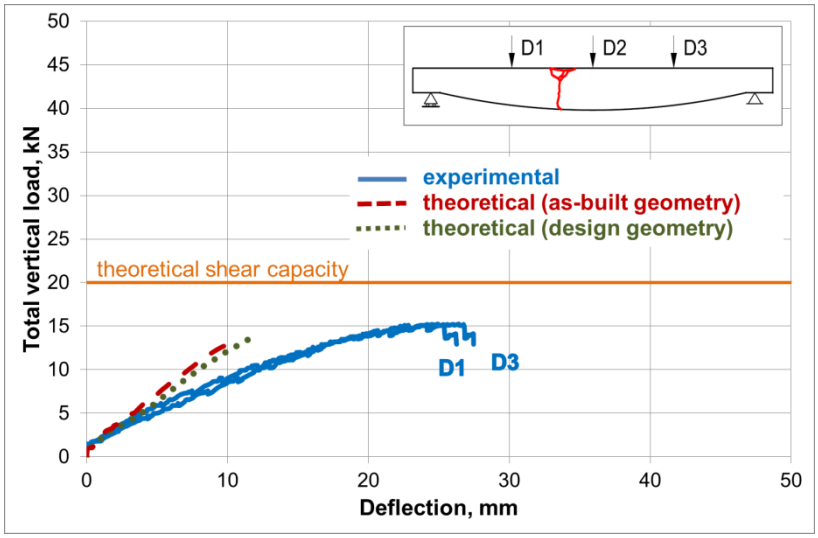

b.

Figure 5.61. FFB 2 Load-deflection relation: (a) at midspan and (b) at quarter span

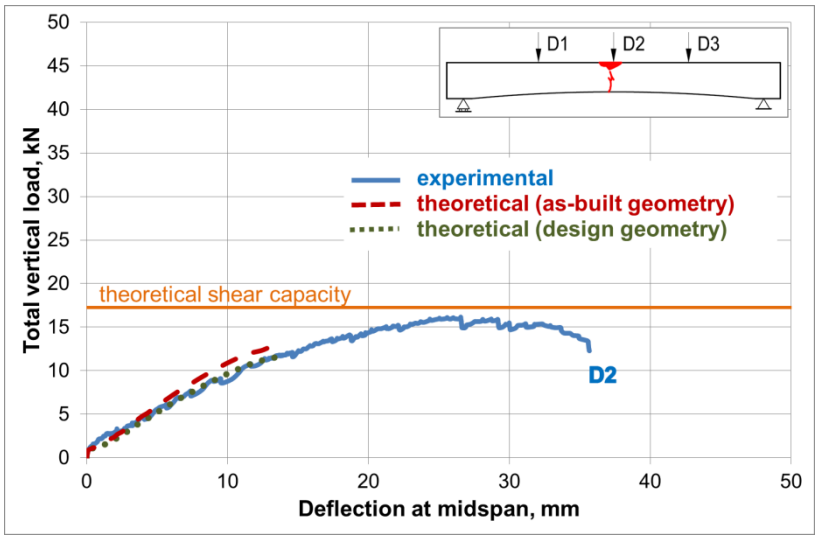

a.

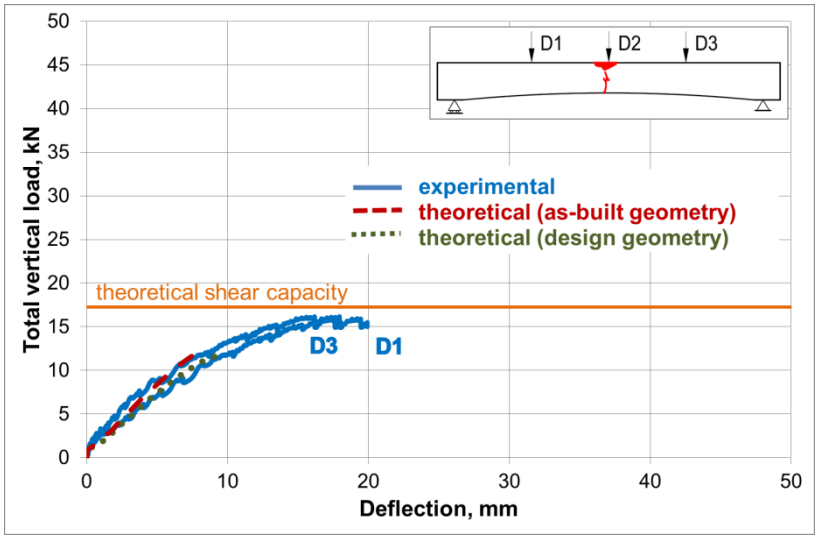

b.

Figure 5.62. FFB 3 Load-deflection relation: (a) at midspan and (b) at quarter span

Figure 5.63 shows the experimental and predicted plots for beam FFB 4. Similarly to the results for beam FFB 2, the predictions considerably overestimate the beam stiffness. Furthermore, the deflection at midspan at serviceability loads would exceed the acceptable limits. Both beams were reinforced with smooth FRP bars, which appears to be inappropriate for the adopted theoretical model, based on the assumption of perfect bond. Therefore, sand-coated bars are considered for the further investigations of the load-deflection behaviour of fabric-formed beams, presented in § 6 and § 7. The differences between the predicted curves based on as-built geometry and on design geometry again appears to be adequately small at the early load stages.

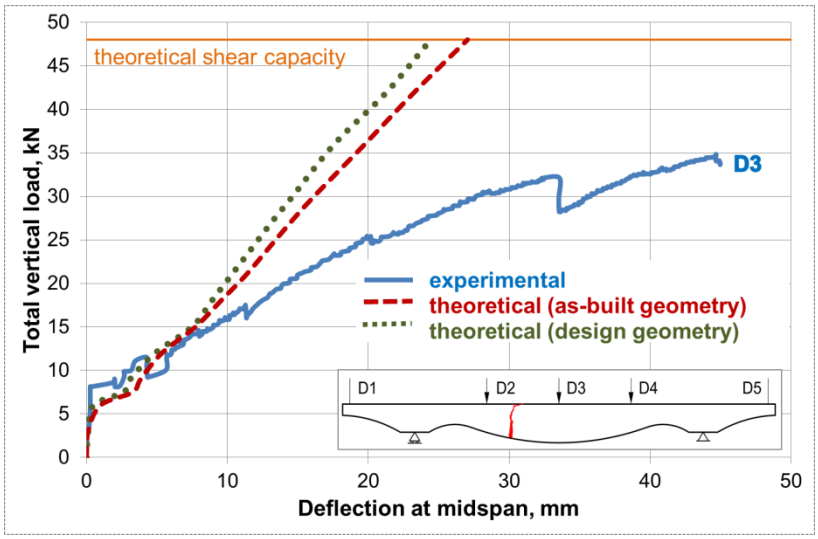

a.

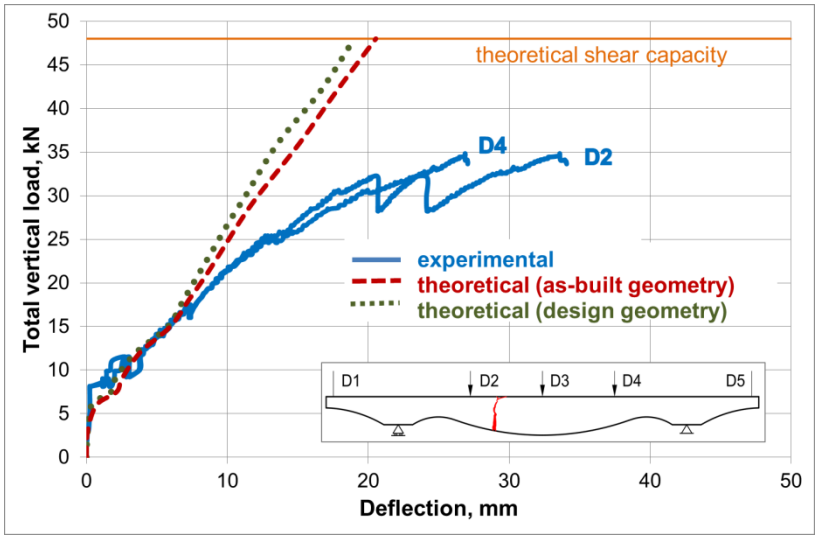

b.

Figure 5.63. FFB 4 Load-deflection relation: (a) at midspan and (b) at quarter span

5.5.3. Experimental and predicted load-strain behaviour of FRP reinforcement

The load-strain plots shown in *Figure 5.64* to *Figure 5.67* compare the experimental and predicted behaviour of FRP bars at the midspan section of each beam. The predictions are based on the actual concrete strength, again presented for both, the design and the as-built geometry, for sections under consideration. The first three beams show a good correlation between the experimental results and the theoretical predictions. This may suggest that the overestimation of the beam stiffness in *Figure 5.61a* could not be fully explained only by the low bond of the reinforcing bar. Nevertheless, the use of smooth bars is generally not recommended in the design codes and it is unlikely such bars will be specified for permanent structures in practice.

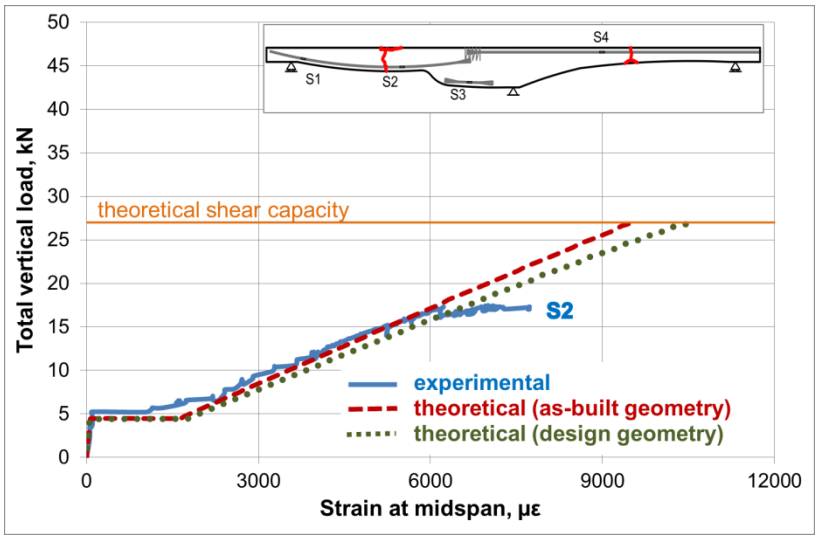

Figure 5.64. FFB 1 load-strain relation at midspan section

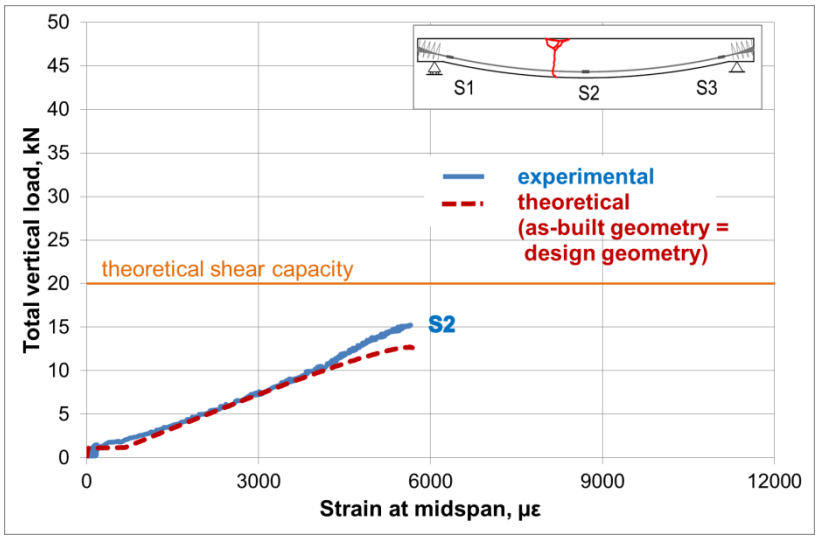

Figure 5.65. FFB 2 load-strain relation at midspan section

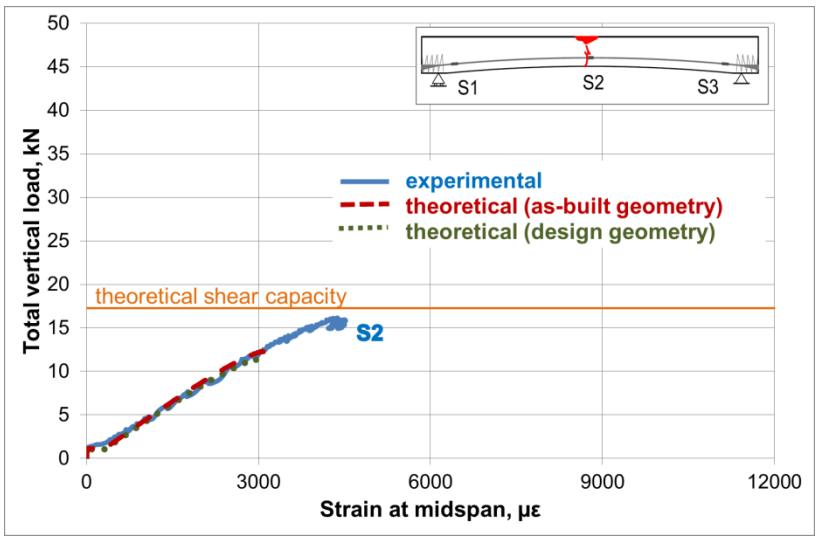

Figure 5.66. FFB 3 load-strain relation at midspan section

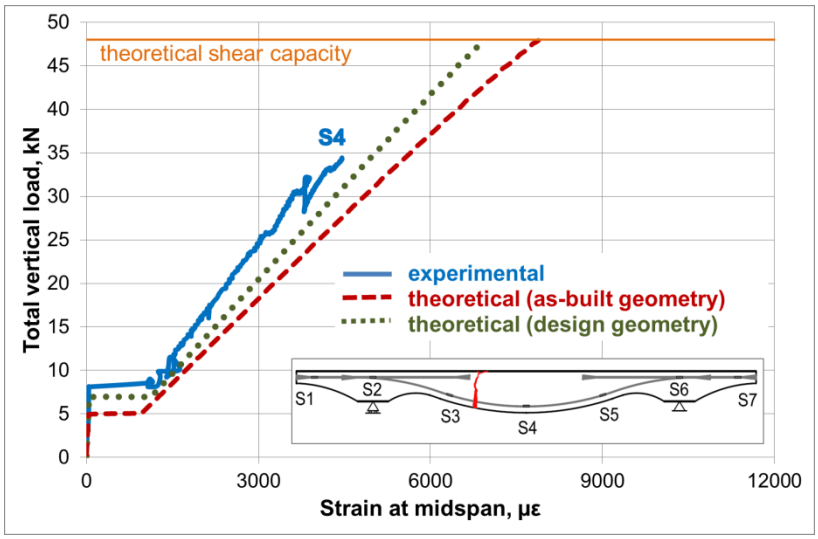

Figure 5.67. FFB 4 load-strain relation at midspan section

The load-strain curves for beam FFB 4 in *Figure 5.67* indicate a more significant difference between predicted and measured strains. Furthermore, as could be expected in this case, the reduced effective depths near midspan during construction had affected the strains in the reinforcing bars, resulting in a larger difference between the predictions based on as-built and on design geometry.

5.6. Concluding remarks

The study presented in this chapter explored mainly the relationship between constructability and possibilities for optimised design of fabric-formed beams. The effect of construction choices on the efficiency of design has been demonstrated. Methods for producing efficient cross sections through the use of internal restraints, which limit unnecessary bulging of concrete inside a freely hung fabric, have been developed. Realistic material savings between 40% and 60% have been achieved. Different methods for installation of FRP reinforcement inside flexible formwork have also been considered. It has been successfully demonstrated that it is possible to field bend straight GFRP bars, attached to the fabric, using the self-weight of the fresh concrete. An adequate method for forming ‘flat-bottom’ sections, however, has not been established. Although the approach used for beam FFB 4 increased the cross-sectional efficiency, it was difficult to ensure the correct size of the flat surface footprint of concrete cast in a freely hung fabric, and a different method is proposed in § 6.

Methods for surveying of as-built fabric-formed concrete geometries have been discussed. The potential of using Xbox Kinect has been investigated for its advantages as a fast and inexpensive 3-D scanner with acceptable accuracy. However, for the purpose of the current research, it was found most useful to physically slice cross sections through saw-

cutting. The initial findings show promising results in terms of achieving satisfactory construction accuracy for the critical design sections, and reasonably small differences between the predicted load capacities and load-deflection behaviour for as-built and design geometries. Nevertheless, the large local deviations from design dimensions due to poor construction make the initial results to some extent inconclusive. In addition, although the load tests data suggest that higher concrete strengths may have been reached due to permeability of fabric formwork, only cubes cast in standard moulds have been tested and the actual strength enhancement was not available. A further and more extensive investigation of the effect of as-built geometry on the structural behaviour of fabric-formed beams, including the effect of concrete strength enhancement, is presented in § 6.

As discussed, the size of the beam specimens has been chosen based on the capacity of the laboratory space and equipment. However, the presented construction approach can be fully adopted for building large-scale elements. It has been shown that the type of fabric used to cast the experimental beams would indeed be suitable for cross sections of up to 1000 mm breadth and 2500 mm depth. It can also be argued that the absolute values of the tolerances due to construction errors would remain similar. Therefore, two-metre span test beams have been used for the rest of the experimental work as well.

6. Effect of Construction Tolerances on Structural Behaviour

6.1. Introduction

The initial study on constructability has helped to develop methods for fabric formwork construction, including reinforcement installation, of reinforced with FRP bars. These methods have been incorporated in the design computer program developed in MATLAB and described in § 4. The experimental investigation included in this chapter aims to provide data for validation of the computer program results and to examine in greater detail the overall effect of construction tolerances on the structural behaviour of fabric-formed beams.

6.2. Design of test specimens

Four test beams (Series 2) were included in this study. All specimens had simply supported spans of equal lengths, as shown in *Table 6.1*. The optimised beam designs, including form-finding, were carried out with the help of the MATLAB program. The beams did not contain shear reinforcement. No partial safety factors were applied to the materials.

Table 6.1. Test beam design parameters (Series 2)

Beam ID	No of spans	Span, m	Total length, m	Flexural reinforcement	Concrete cylinder strength, MPa
FFB 5	1	1.8	2	1 No GFRP bar	20
FFB 6	1	1.8	2	1 No CFRP bar	20
FFB 7	1	1.8	2	1 No GFRP bar	20
FFB 8	1	1.8	2	1 No GFRP bar	20

6.2.1. Materials

6.2.1.1. Concrete

The workability of concrete appeared to be inadequate during the construction of the initial test beams, despite the chosen high water-to-cement ratios and the assessment of trial mixes. For this reason, self-compacting concrete was considered as a viable alternative for producing complex concrete geometries (see *Table 6.2*). Self-compacting concrete (SCC) relies on specially adapted superplasticizers, in combination with a higher-than-conventional concrete fines content, to produce increased fluidity and inherent compactability. Binder fillers, such as limestone powder and blast furnace slag, are also added to the SSC mixes in order to limit the heat generation and to enhance the cohesiveness and fluidity of concrete.

The selected superplasticiser for the current study was Sika ViscoCrete 20RM, a liquid admixture for concrete with recommended dosage 1.0 - 2.0% by weight of cement for special applications such as self-compacting concrete. The concrete mix design was

adjusted in accordance with the recommendations provided in the supplier's concrete handbook. The proportions of the fine and coarse aggregates were set to 60% and 40%, respectively. The water content, dependent on the required concrete quality, was taken between 180 and 200 l/m^3 for achieving a standard quality. The binder was initially composed of 60% CEM-I cement and 40% GGBS and used to cast beams FFB 5 and FFB 6. However, due to slower than expected early strength development, the GGBS content was consequently reduced to 20% for beams FFB 7 and FFB 8. Furthermore, all specimens were cast in winter conditions so that measures, such as storing the aggregates indoors 18 to 24 hours before adding them to the concrete mix, were taken to reduce the excess moisture content in the aggregates.

Table 6.2. Self-compacting concrete mix (Series 2)

Water	Binder	W/C ratio	Fine aggregates	Coarse aggregates
190 l/m^3	320 kg/m^3	0.59	1150 kg/m^3	770 kg/m^3

6.2.1.2. Reinforcement

The reinforcement characteristics and sizes, summarised in *Table 6.3*, indicate that the same types of reinforcing bars as for Series 1 tests were used. However the bond properties of the 12 mm GFRP bars were improved by manual sand-coating, using the method shown earlier in § 3, *Figure 3.33*.

Table 6.3. Reinforcing bars properties (Series 2)

	10 mm	12 mm	12 mm
Material	glass	glass	carbon
Tensile strength, MPa	550	<1000	2300
Nominal cross-sectional area, mm^2	71.3	126.7	113
Modulus of elasticity, Gpa	30	40	130
Tensile strain, %	>3	>3	1.8
Surface treatment	smooth	sand	sand
Minimum allowable radius, mm	1300	1693	620

6.2.1.3. Fabric formwork

Twin-layer polypropylene fabric, supplied by Proserve Ltd, was used as main formwork material in order to further minimise the effect of fabric extension on the final concrete shapes. As the name suggests, this fabric consists of two identical layers, which are intermittently stitched. The properties of each layer are provided in *Table 5.4*.

6.2.2. Geometry details

Four cases of geometry optimisation under the same loading arrangement were designed with the aim to provide a quantitative comparison of the concrete material savings, which

could be achieved for each option. The reinforcement details for each beam are shown in § 6.2.3, while more detailed dimensions of cross sections taken along the beam lengths are provided in § 6.3.2.

6.2.2.1. Beam FFB 5

The first test beam, FFB 5, had a uniform top breadth dimension of 100 mm and an optimised varying longitudinal profile. Although the beam would appear to be similar to beam FFB 3, included in the initial investigation of constructability presented in § 5, FFB 5 was reinforced with a more flexible 10 mm GFRP bar to allow a greater variation of geometry than the CFRP reinforcement used previously. Furthermore, all cross sections with B/D ratios less than 0.8 were formed by 'quilt-point' ties, as illustrated in *Figure 6.1*.

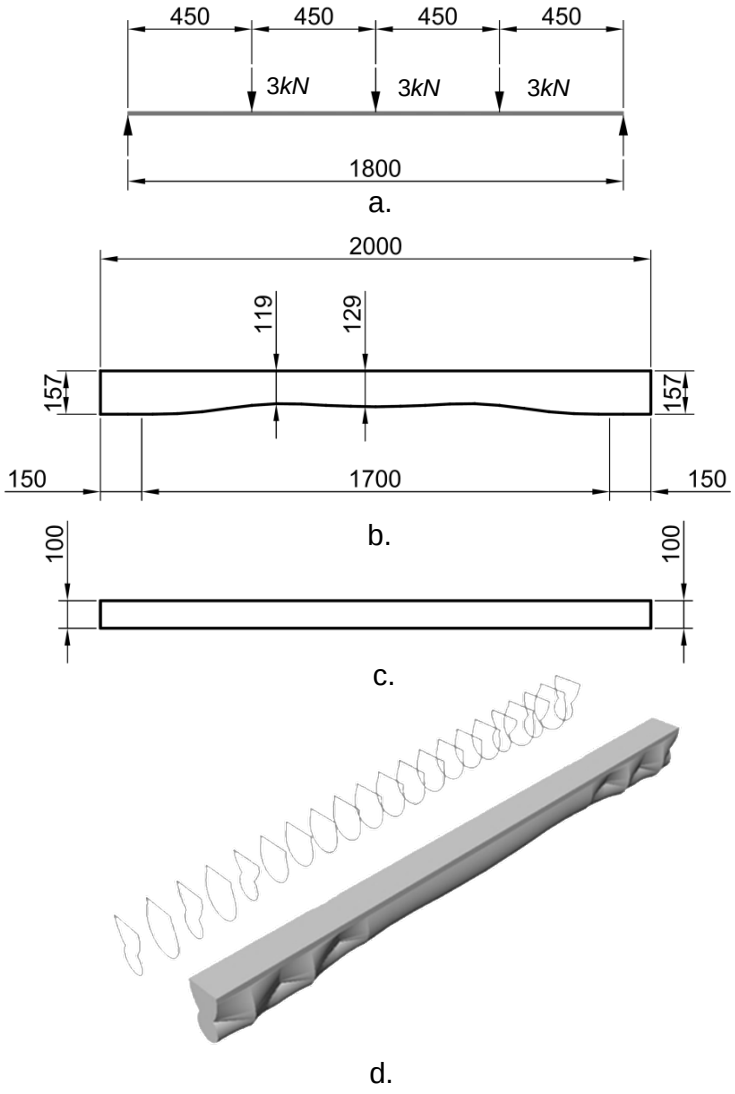

Figure 6.1. Beam FFB 5 geometry details: (a) loading arrangement, (b) elevation, (c) plan and (d) perspective view (all dimensions are in mm)

For design purposes the beam was divided into 20 segments. An optimisation algorithm including functions, previously described in *Table 4.2*, for minimising the depth profile for the envelopes of design bending moment and shear force, assuming a fixed B-profile, was applied. The algorithm was implemented twice, once to obtain the optimised cross sections cast in unrestrained fabric and the second time to allow for 'quilt-point' restraints, where required. The final shape was checked against the requirement for a minimum bend radius of the reinforcing bar. The total ultimate design load was chosen to be 9 kN.

6.2.2.2. Beam FFB 6

For the purpose of this study, an optimisation for uniform depth and varying top breadth was considered as well. The overall depth was fixed to 200 mm along the length of beam FFB 6, as can be seen in *Figure 6.2*. '

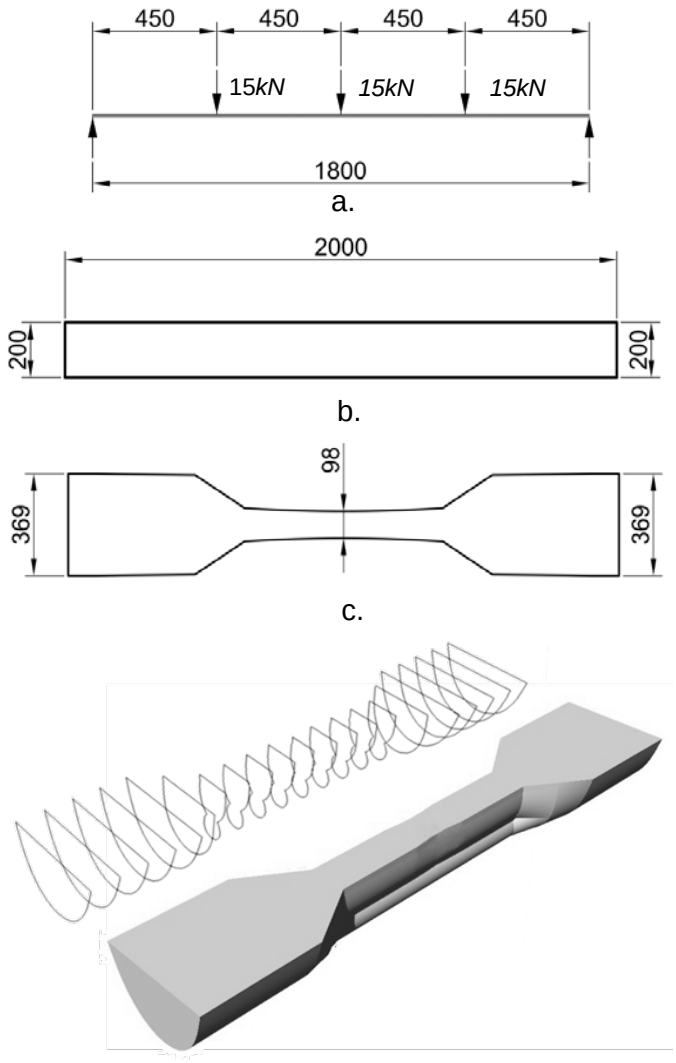

Figure 6.2. Beam FFB 6 geometry details: (a) loading arrangement, (b) elevation, (c) plan and (d) perspective view (all dimensions are in mm)

Quilt-point' cross sections were designed at midspan, where the B/D ratio was found to be less than 0.8. The optimisation algorithm and design procedure were similar to the optimisation procedure for a uniform top breadth. The beam was divided into 20 segments and B was optimised for the applied bending moments and shear forces, assuming a fixed D-profile. However, no check for bending radius limits was required since the reinforcement profile was straight. The total ultimate design load was 45 kN.

6.2.2.3. Beam FFB 7

Beam specimen FFB 7, shown in *Figure 6.3*, had a 'key-hole' shape at midspan with both a varying overall depth and top breadth, and was built using the construction method developed for the demonstration beam FFB 4, presented in § 5.

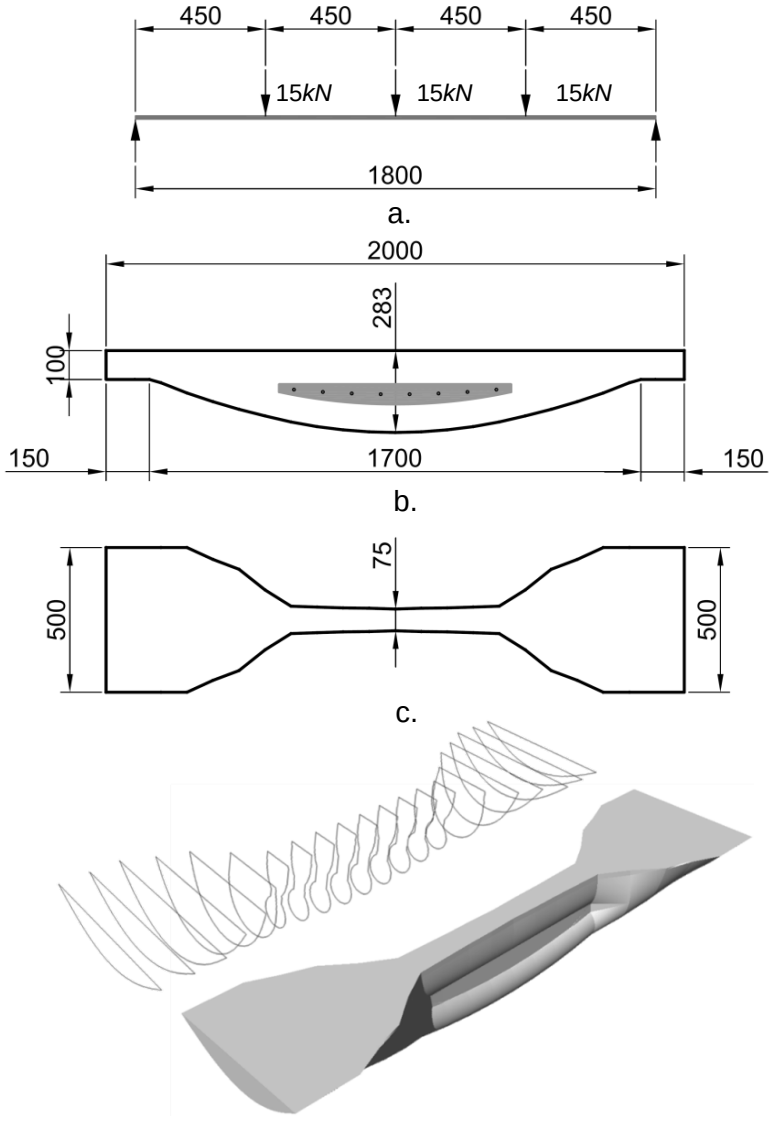

Figure 6.3. Beam FFB 7 geometry details: (a) loading arrangement, (b) elevation, (c) plan and (d) perspective view (all dimensions are in mm)

The optimisation algorithm combined the optimisation of D for the applied bending moments, assuming constant B-profile, and the optimisation of B for the applied shear forces, assuming fixed D-profile, determined in the previous step. The top breadth was initially set to a minimum of 75 mm and allowed to vary up to 500 mm. Similarly, the beam was divided into 20 segments and the algorithm was executed twice to obtain the dimensions of the 'key-hole' sections. The curvature of the longitudinal profile was checked against the limits in *Table 6.3* for buildabilty. The total ultimate design load was chosen to be 45 kN.

6.2.2.4. Beam FFB 8

The design of beam FFB 8, shown in *Figure 6.4*, was based on limiting the cross-sectional B/D ratio in order to produce efficient shapes, cast in unrestrained freely hung fabric.

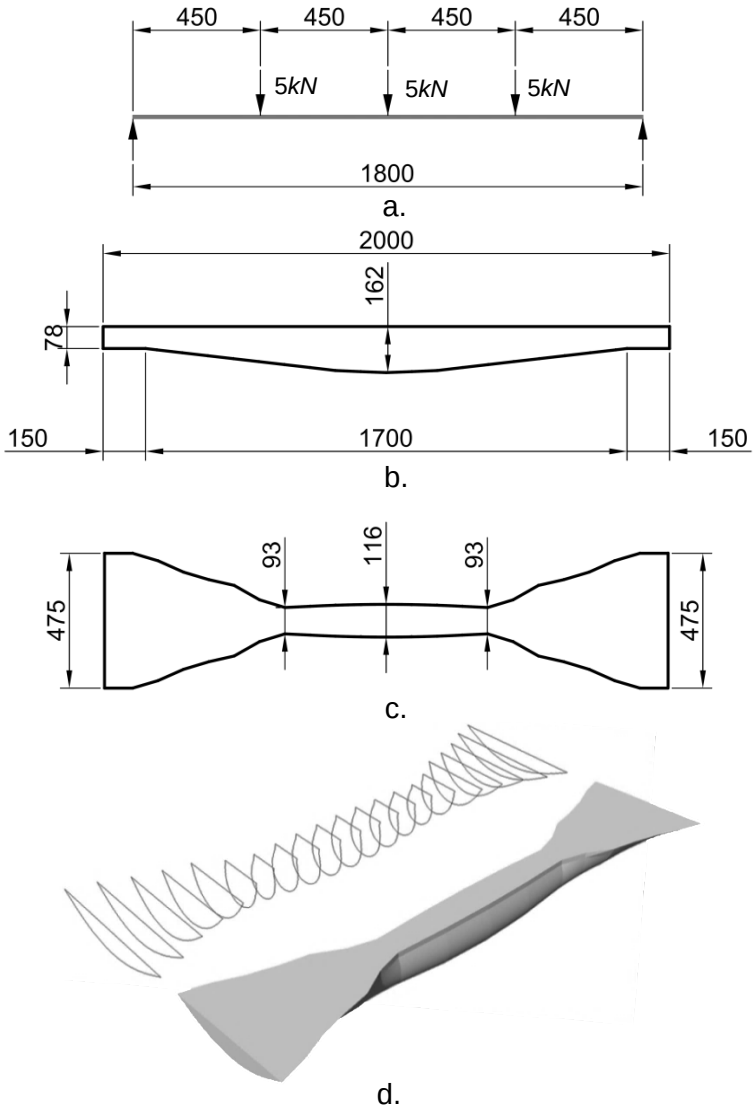

Figure 6.4. Beam FFB 8 geometry details: (a) loading arrangement, (b) elevation, (c) plan and (d) perspective view (all dimensions are in mm)

While maintaining simplicity of the construction process, this approach allowed the fastest optimisation as no adjustments were required for bulging cross sections. Furthermore, the resulting longitudinal curvatures were unlikely to exceed the limits for field bending of straight FRP bars. The optimised geometry of the beam divided into 20 segments was found by fixing the B/D ratio to 0.8 for bending moment and adjusting the top breadth for shear forces, thereby ensuring a B/D ratio greater than 0.8 for all sections. The total ultimate design load in this case was chosen to be 15 kN.

6.2.3. Reinforcement details

Single splayed anchored FRP bars were used as the main reinforcement for all test specimens (refer to *Figure 6.5*). No shear reinforcement was provided and the minimum concrete cover was 30 mm. The minimum bar bend radius for the 10 mm GFRP bar FFB 5 was 1792 mm at the concave parts and 4667 mm at midspan, well above the permissible limit of 1300 mm (*Table 6.3*). The 12 mm GFRP bars were bent at a radius of 1762 mm for FFB 7 and 2606 mm for FFB 8, compared with the minimum permissible radius of 1693 mm (*Table 6.3*).

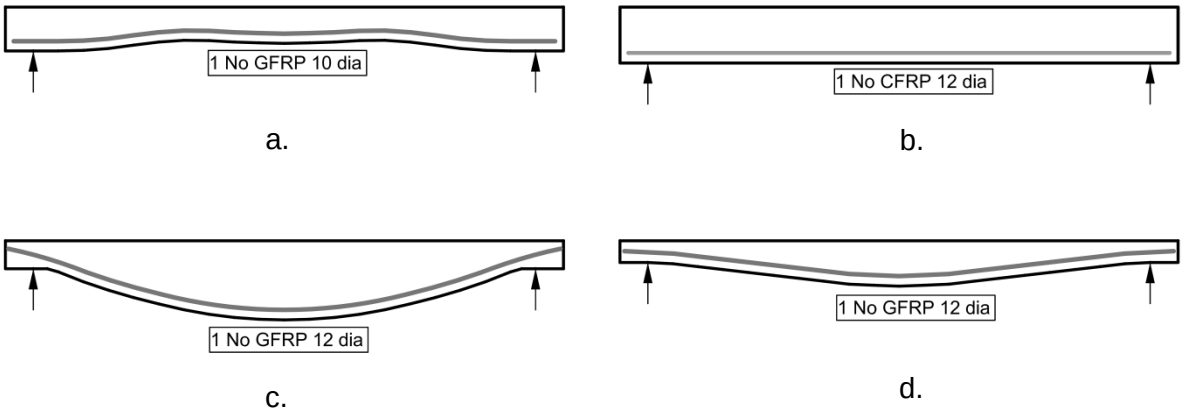

Figure 6.5. Reinforcement details (Series 2): (a) FFB 5, (b) FFB 6, (c) FFB 7 and (d) FFB 8

6.2.4. Utilisation and material savings

The utilisation of shear and moment capacities varied for the different test beams, as can be seen in *Figure 6.6*. The concrete savings, based on equivalent uniform rectangular sections are summarised in *Table 6.4*. The approach for finding the equivalent rectangular sections again aims to follow closely the adopted design procedure and construction constraints for the purpose of comparison.

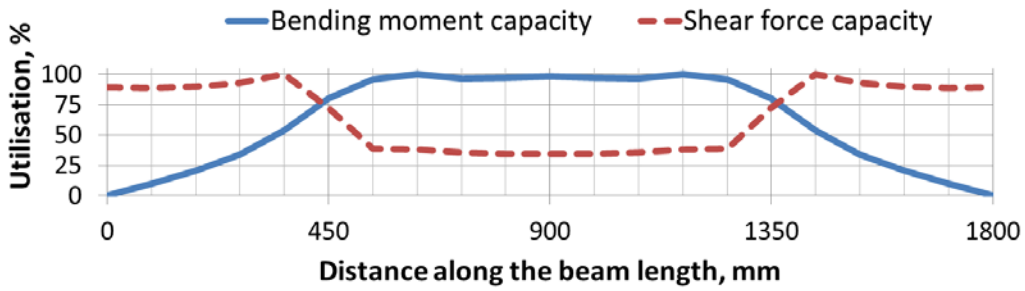

a.

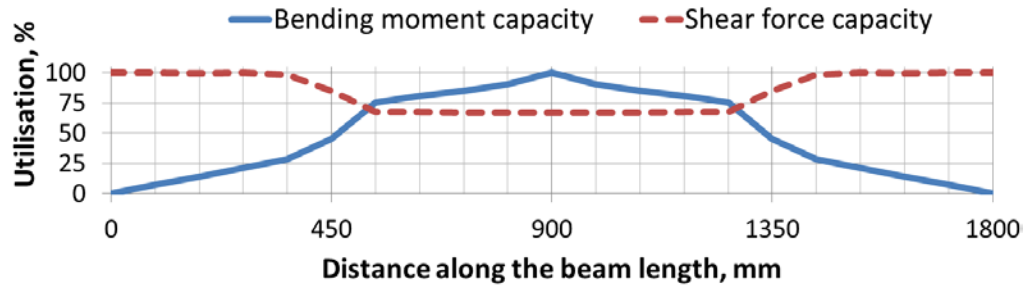

b.

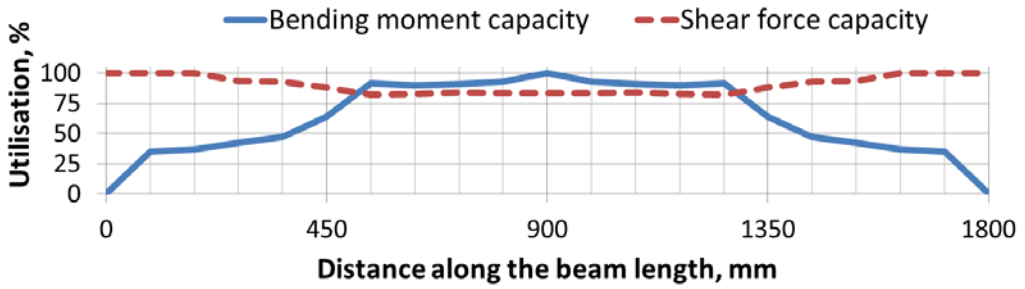

c.

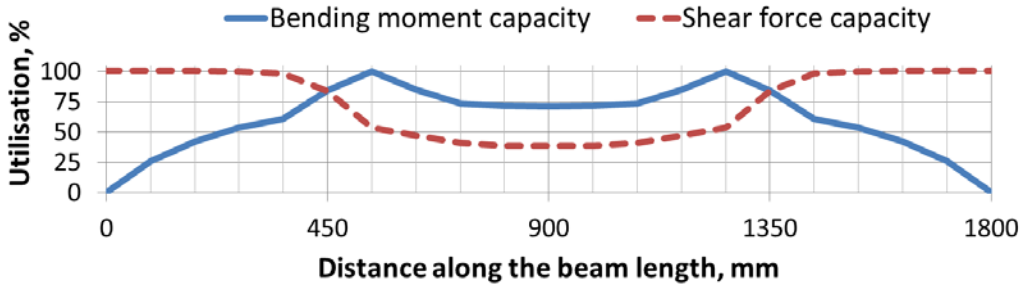

d.

Figure 6.6. Capacity utilisation: (a) FFB 5, (b) FFB 6, (c) FFB 7 and (d) FFB 8

The equivalent sections for beam FFB 5 (B=100 mm and D=152 mm) and beam FFB 6 (B=343 mm and D=200 mm) are based on a fixed breadth of 100 mm and a fixed depth of 200 mm, respectively. The equivalent section for beam FFB 7 can also be found fairly straightforwardly by calculating the required overall depth for the minimum breadth of 75 mm and the maximum bending moment. The breadth is then determined from the required shear force capacity and the final rectangular dimensions are B=239 mm and D=291 mm. This approach is less well defined for beam FFB 8 and in this case the

equivalent section is based on the average top breadth. The resulting section is B=229 mm and D=136 mm. The concrete savings, presented in *Table 6.4*, are expressed as:

$$\frac{volume\ of\ equivalent\ prismatic\ beam - volume\ of\ fabric\text{-}formed\ beam}{volume\ of\ equivalent\ prismatic\ beam} * 100\ \% \quad (6.1)$$

As previously discussed, the concrete savings for optimised simply supported concrete beams without shear reinforcement may not be high due to the non-coinciding bending moment and shear force effects. In fact, as can be seen in *Table 6.4*, more savings were achieved for a beam of a uniform depth compared to a beam of a uniform breadth. This is not surprising as a significant proportion of the concrete savings is due to the efficiency of the cross-sectional shapes.

The values in the last column of *Table 6.4* correspond to the difference in the concrete volumes of tapered prismatic beams and fabric-formed beams, having the same depth profile and strength capacities at each section along the length. This allows excluding the effect of depth optimisation. As can be seen, for the majority of the cases more than 50% of the material savings are as a result of the difference in the cross-sectional areas of fabric-formed and equivalent rectangular sections. Therefore, it can be concluded that fabric formwork construction may offer an opportunity for more efficient structural designs even without a significant change in the longitudinal profile.

Table 6.4. Concrete material savings in comparison with prismatic beams (Series 2)

Beam ID	Main optimisation constraints	Equivalent prismatic beams (uniform depth) %	Equivalent prismatic beams (optimised tapered profile) %
FFB 5	B=100 mm	18	5
FFB 6	D=200 mm	50	28
FFB 7	75mm ≤ B ≤ 500 mm	50	29
FFB 8	B/D≥0.8	39	25

6.2.5. Instrumentation and test set-up

All specimens were tested under 5-point bending. The test equipment and measurement techniques were as described in § 5. The positions of displacement transducers, designated *D1* to *D3*, and strain gauges on the reinforcing bars, *S1* to *S3*, are indicated in *Figure 6.7*.

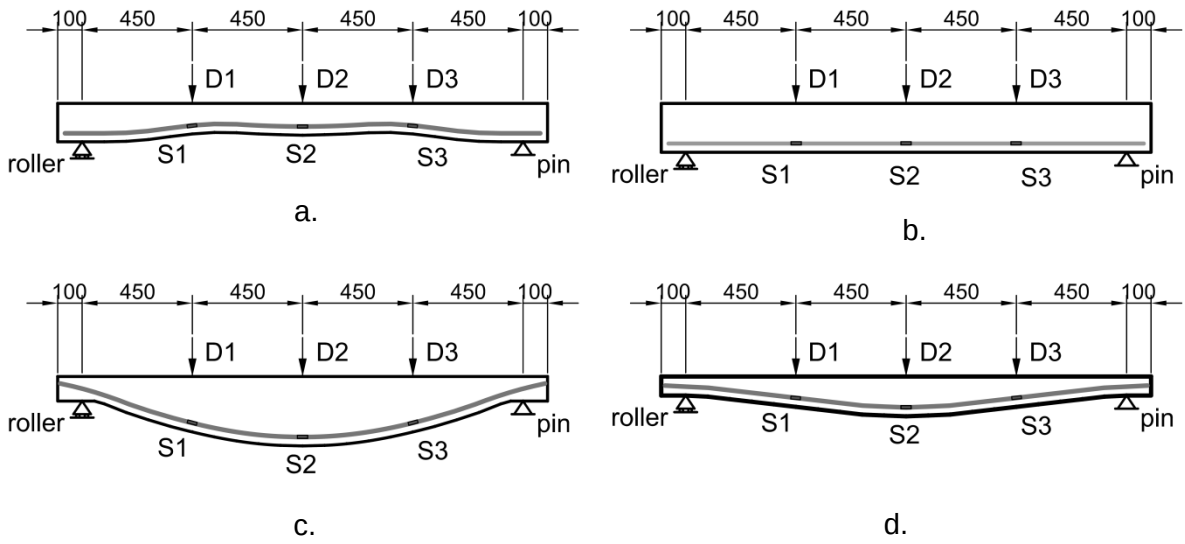

Figure 6.7. Test set-up (Series 2): (a) FFB 5, (b) FFB 6, (c) FFB 7 and (d) FFB 8

6.3. Construction of test specimens

6.3.1. Formwork details

The manually marked-up fabric was attached to the supporting formwork table, described in § 5. The transverse timber frames were fully reused, while the top plates were made by cutting new plywood sheets into the desired shape of the top openings. Details of the formwork ties and web former installation and formwork de-assembling procedure can be seen in *Figure 6.8*.

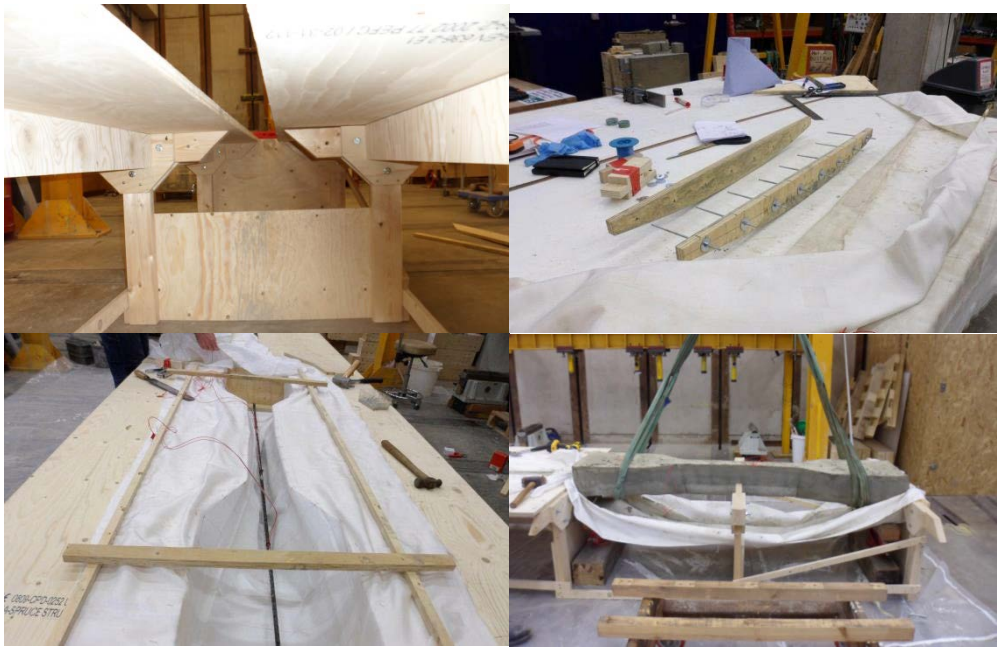

Figure 6.8. Formwork set up and removal

6.3.2. Construction parameters

The construction parameters, provided in *Table 6.5* to *Table 6.7*, have been defined in § 5.3.2. The distance x_L is measured from the left support, and the thickness of the plywood top sheets, included in the design input, is 18 mm. The maximum calculated extension of fabric was 0.82 mm for the end parts of beam FFB 7. However, for the majority of cross sections the values did not exceed 0.5 mm and was ignored for in the calculation of the construction perimeters. Hence, any significant deviations from the intended geometry could be considered due to construction or design errors.

Table 6.5. FFB 5 construction parameters

x_L	B	D	d_{eff}	B_{web}	D_b	h_{web}	P	P_b	T, N/m
0	100	157	122	50	75	NOT USED	374	198	139
90	100	157	122				388		213
180	100	155	120	50	75		370	198	137
270	100	148	113				366		192
360	100	136	101	50	75		332	196	123
450	100	125	90				312		146
540	100	119	84				298		135
630	100	120	85				300		137
720	100	125	90				312		146
810	100	128	93				318		151
900	100	130	95				322		155
990	100	128	93				318		151
1080	100	125	90				312		146
1170	100	120	85				300		137
1260	100	119	84				298		135
1350	100	125	90				312		146
1440	100	136	101	50	75		332	196	123
1530	100	148	113				366		192
1620	100	155	120	50	75		370	198	137
1710	100	157	122				388		213
1800	100	157	122	50	75		374	198	139

All dimensions are in millimetres.

Table 6.6. FFB 6 construction parameters

x_L	B	D	d_{eff}	B_{web}	D_b	h_{web}	P	P_b	T, N/m
0	369	200	164			NOT USED	594		668
90	367	200	164				592		664
180	365	200	164				590		659
270	363	200	164				590		657
360	361	200	164				588		653
450	242	200	164				526		474

540	121	200	164	50	75		470	200	213
630	121	200	164	50	75		470	200	213
720	120	200	164	50	75		470	200	213
810	119	200	164	50	75		470	200	212
900	98	200	164	50	75		466	200	196
990	119	200	164	50	75		470	200	212
1080	120	200	164	50	75		470	200	213
1170	121	200	164	50	75		470	200	213
1260	121	200	164	50	75		470	200	213
1350	242	200	164				526		474
1440	361	200	164				588		653
1530	363	200	164				590		657
1620	365	200	164				590		659
1710	367	200	164				592		664
1800	369	200	164				594		668

All dimensions are in millimetres.

Table 6.7. FFB 7 construction parameters

x_L	B	D	d_{eff}	B_{web}	D_b	h_{web}	P	P_b	T, N/m
0	500	100	39				570		839
90	500	111	75				578		841
180	500	147	111				614		877
270	418	177	140				588		729
360	350	203	167				588		662
450	207	226	190				572		515
540	95	247	211	50	98	32	569	260	261
630	89	263	227	50	99	47	602	266	285
720	83	274	238	50	100	58	623	268	300
810	81	281	245	50	100	64	638	268	308
900	75	283	247	50	100	66	642	268	311
990	81	281	245	50	100	64	638	268	308
1080	83	274	238	50	100	58	623	268	300
1170	89	263	227	50	99	47	602	266	285
1260	95	247	211	50	98	32	569	260	261
1350	207	226	190				572		515
1440	350	203	167				588		662
1530	418	177	140				588		729
1620	500	147	111				614		877
1710	500	111	75				578		841
1800	500	100	39				570		839

All dimensions are in millimetres.

Table 6.8. FFB 8 construction parameters

x_L	B	D	d_{eff}	B_{web}	D_b	h_{web}	P	P_b	T, N/m
0	475	78	41				528		590

90	422	82	46	NOT USED	NOT USED	NOT USED	482	NOT USED	486
180	343	93	56				418		356
270	289	103	67				384		292
360	249	113	77				366		258
450	147	124	87				324		180
540	93	134	98				332		159
630	101	144	108				358		185
720	110	155	119				384		215
810	113	159	123				394		227
900	116	162	126				402		237
990	113	159	123				394		227
1080	110	155	119				384		215
1170	101	144	108				358		185
1260	93	134	98				332		159
1350	147	124	87				324		180
1440	249	113	77				366		258
1530	289	103	67				384		292
1620	343	93	56				418		356
1710	422	82	46				482		486
1800	475	78	41				528		590

All dimensions are in millimetres.

6.3.3. Reinforcement preparation and installation

All reinforcing bars were prepared using the methods for forming of splayed anchorages and manual sand-coating, presented in § 3. Following the successful installation of flexible GFRP bars by attaching them to the fabric formwork, as described in § 5, the approach was applied to all beams containing GFRP reinforcement. The straight CFRP bar, used to reinforce beam FFB 6, was suspended from the top of the formwork table as well as connected to the fabric sheet at selected points. However, as revealed by the post-mortem examination, this could not provide any restraint against the lateral displacement of the bar, which remains a challenge for the installation of straight or pre-bent bars inside fabric formwork.

6.3.4. Concrete casting and forming of supports

The size of the formwork table and the requirement for manual mixing and placing of concrete allowed up to two test specimens to be cast at the same time. Beams FFB 5 and FFB 6 were cast first, which provided an opportunity to improve the concrete mix design for beams FFB 7 and FFB 8, as highlighted in § 6.2.1. A trial mix was produced to assess the workability of the self-compacting concrete mix and the required quantity of superplasticiser. However, in order to avoid the need for further tests of the fresh mixes, the concrete was compacted using needle vibrators and external hand compaction. The

pictures presented in *Figure 6.9* show the consistency of the fresh concrete and its ability to form hydrostatic shapes.

Figure 6.9. Fresh self-compacting concrete

Following the problematic design of flat bottom sections, new approaches for forming cross sections at the beam supports were explored. The first approach, applied to beams FFB 5 and FFB 6, used flat bottom plates positioned inside the fabric and fastened to the sides of the formwork table, as illustrated in *Figure 6.10*.

Figure 6.10. Forming of supports by plates positioned inside fabric formwork

The method could potentially provide the most precise dimensions and level of the support. However the plates formed a step in the beam's longitudinal profile, which may need to be avoided in future for structural or aesthetical reasons. The second approach, applied to beams FFB 7 and FFB 8, resulted in a less accurately defined shape, created by stapling the fabric on the top of a supporting plate. Nevertheless, the method was found to be adequate to ensure the correct position of the flat bottom surfaces and the

stability of a beam during load testing. Both methods rely on light prestressing of the fabric to limit the lateral deflections and reduce the area of the end cross sections.

6.3.5. As-built geometry

6.3.5.1. Survey of as-built geometry

The methods for measuring the overall dimensions of the constructed test specimens described in § 5 were applied. As previously demonstrated, the most effective method for survey of the as-built profiles of fabric-formed cross sections and the reinforcement depths can be achieved by wet saw-cutting of a beam into segments replicating the design sections. The outline of each cross section can then be transferred into CAD format for comparison with the predicted profiles and extraction of input data required for structural analysis. An alternative method for non-destructive measurement of complex shapes using profile gauges was also applied. As schematically presented in *Figure 6.11*, in this case the profile has to be measured in several steps allowing for sufficient overlap of the parts of the curve between two consecutive steps in order to describe the full section. The exact position of each design cross section was easily identified by the imprints on the concrete surface left from the fabric marker pen lines. For this reason only the front face of the specimens was painted for marking cracks during the load testing.

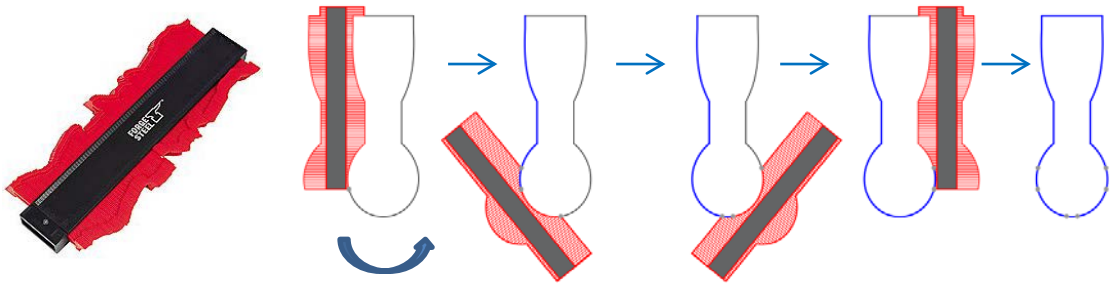

Figure 6.11. Measurement using a profile gauge

6.3.5.2. Beam FFB 5

The depth and breadth of all cross sections were measured before the destructive load testing. Subsequently, the beam was saw-cut at ten locations, indicated in *Figure 6.12*. The presented values include also the measured effective depths and perimeters. The minimum measured cover was 28 mm. The depth measurements in brackets refer to the minimum overall depth at points where the fabric was tied vertically to the reinforcing bars.

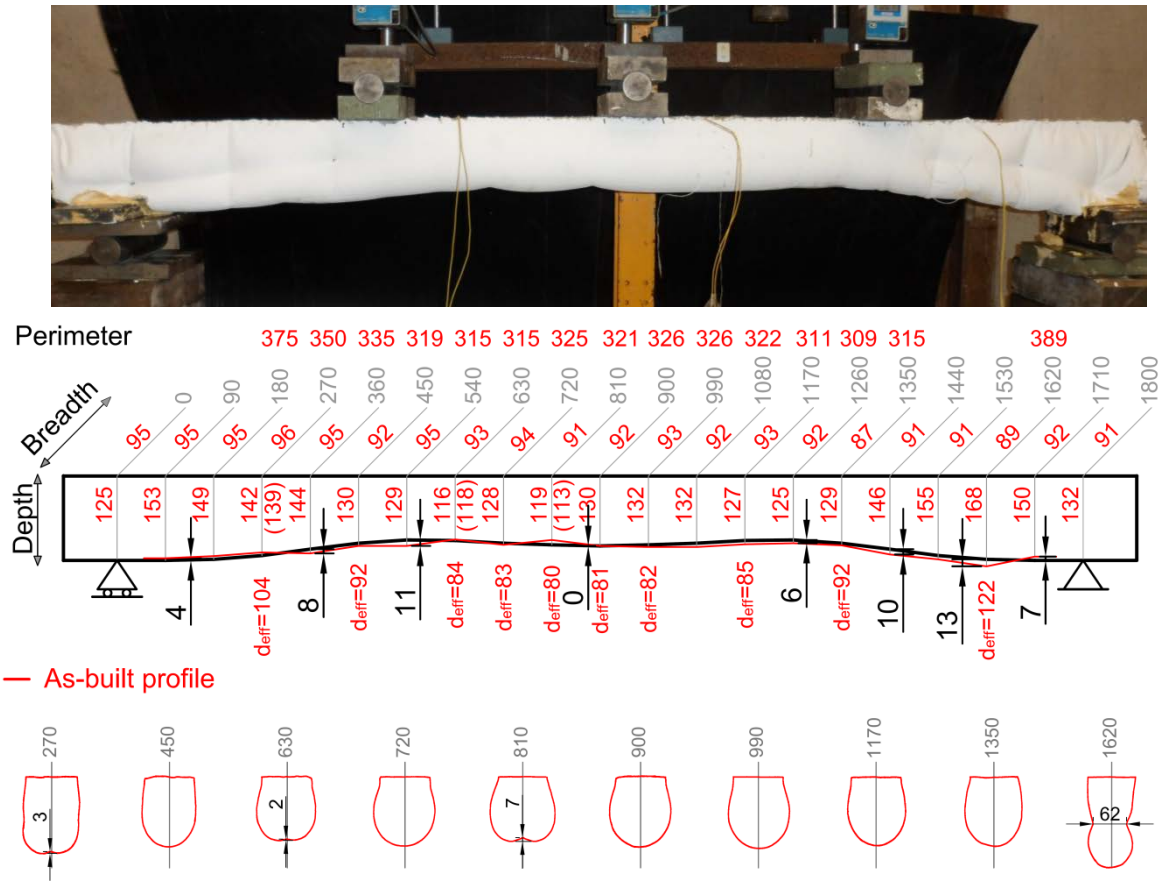

Figure 6.12. FFB 5 as-built measurements (all dimensions are in millimetres)

As can be seen from the photograph in *Figure 6.12*, the longitudinal depth profile does not appear to be fully symmetrical due to a missing vertical tie at section 990. This resulted in an increased concrete cover; however, the reinforcing bar remained on the vertical centreline of the cross section (*Figure 6.13*). *Figure 6.13* also shows a typical section located between two horizontally restrained sections, the shape of which cannot be predicted directly by the adopted 2-D form-finding approach unless the restraining effect of the adjacent horizontal ties is taken into account.

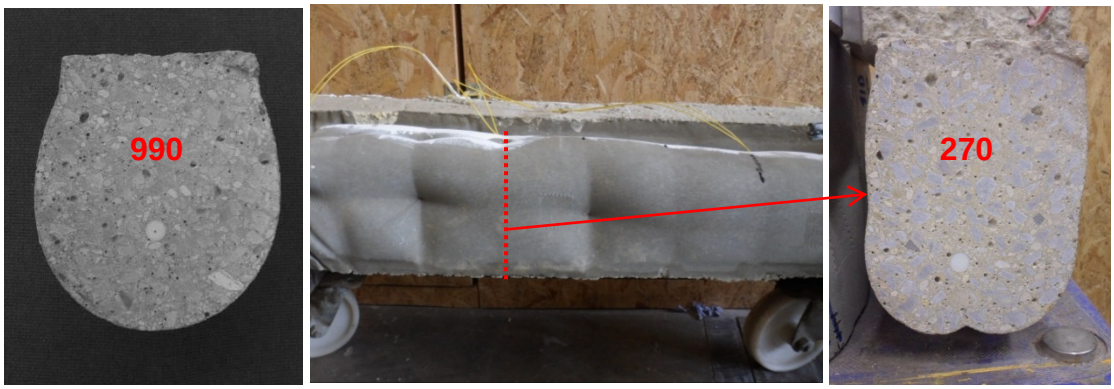

Figure 6.13. FFB 5 as-built cross sections

The deviation from predicted geometry is plotted in *Figure 6.14* for all cross sections, measured along the beam length. As can be expected for most locations with reduced top breadth, the overall depth was increased with the exception of sections containing vertical ties. The effect of the vertical restraints was not taken into account in the design. However, an additional form-finding algorithm, presented in § 4, has been developed in order to compare the theoretical predictions and the as-built profiles.

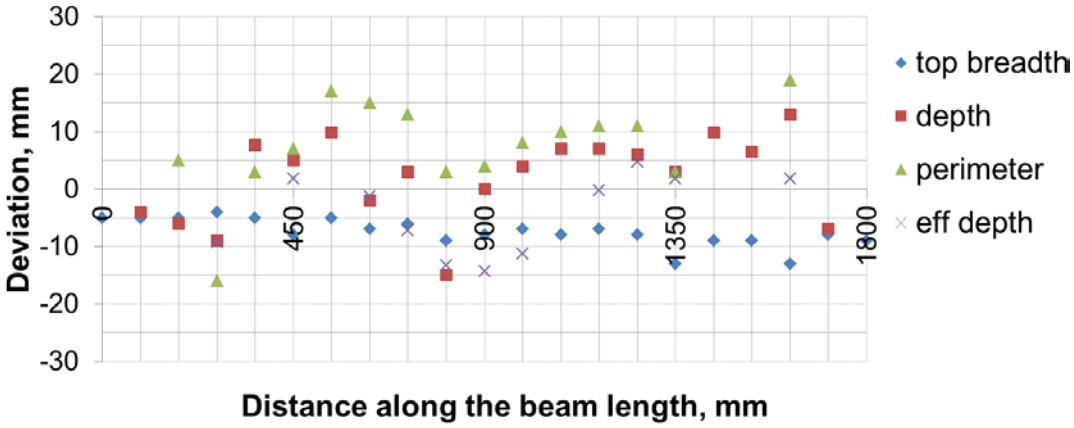

Figure 6.14. FFB 5 deviation from design geometry

Two sets of theoretical predictions are presented. The as-built profiles in *Figure 6.15* are compared with the predicted cross sections, as originally designed. The predictions are then revisited for the actual top breadth and overall depth in order to examine the accuracy of the predicted full profiles.

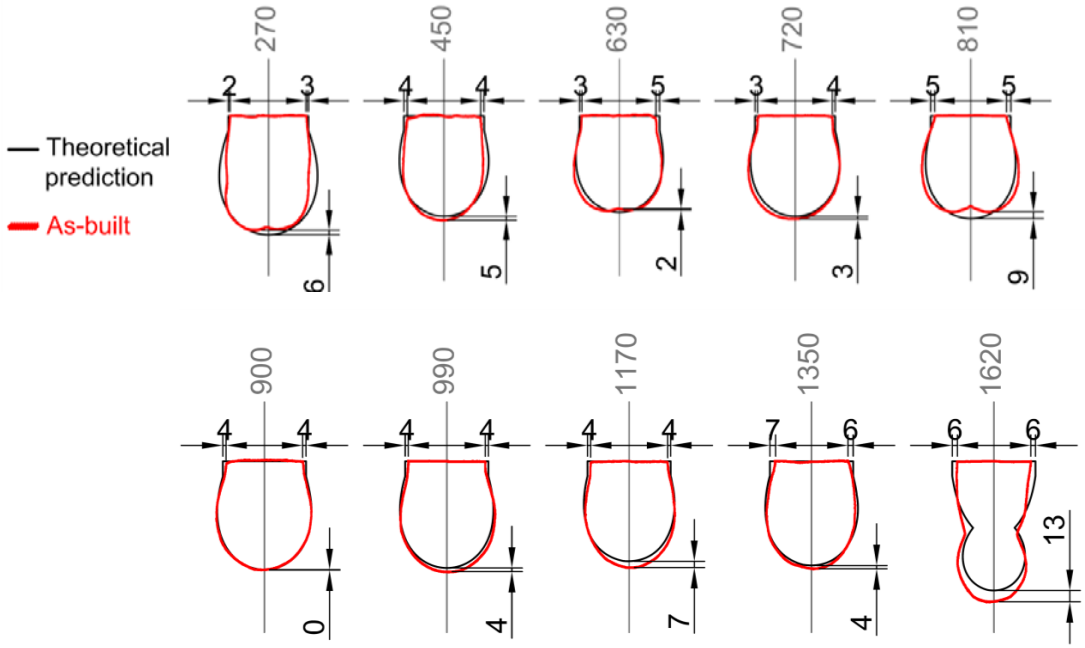

Figure 6.15. FFB 5 comparison of as-built profiles and theoretical predictions (design) (all dimensions are in millimetres)

The cross-sectional profiles restrained by vertical ties were predicted using the maximum and minimum as-built depth measurements. The final shape was obtained by iteration of the pull-out force until the actual difference between the minimum and maximum depth was reached. The close-up views in *Figure 6.16* highlight the zones of largest differences over a 1 mm x 1 mm grid. As can be observed, despite some local deviations, the form-finding algorithm is able to predict fairly accurately the overall shapes.

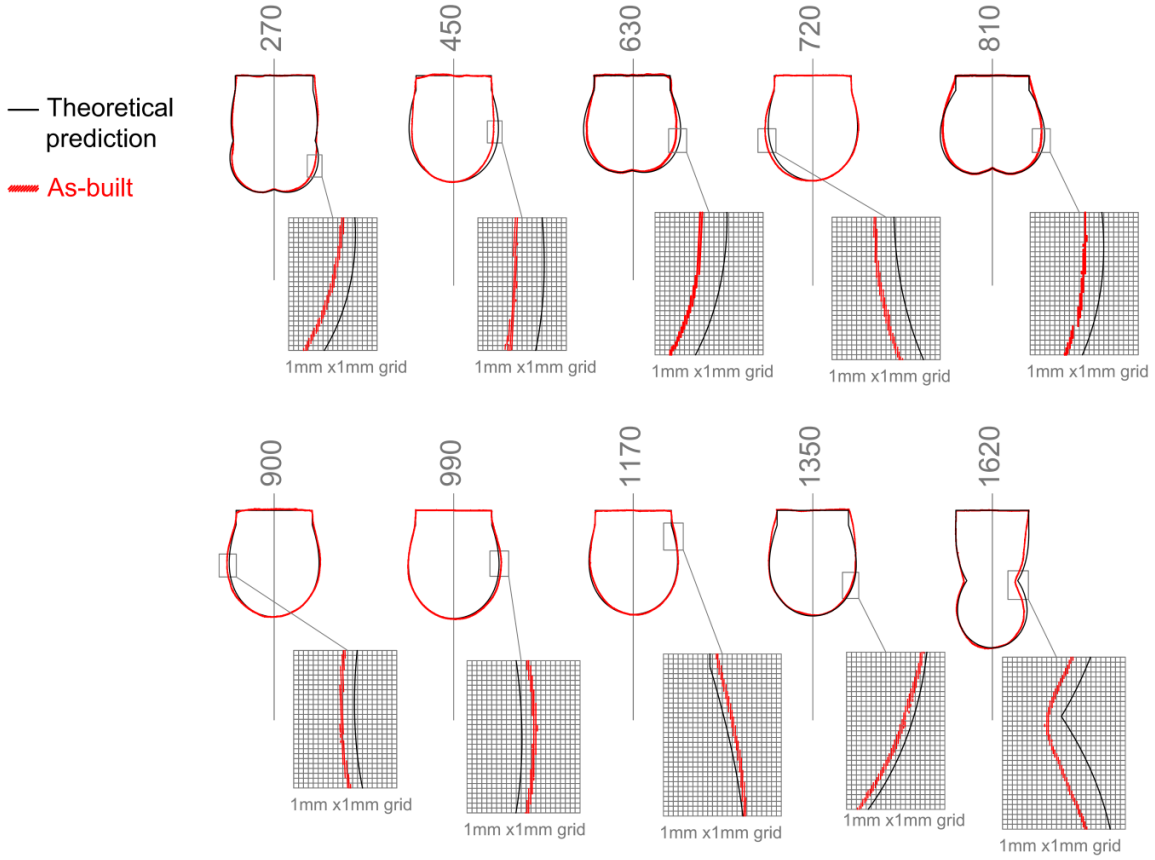

Figure 6.16. FFB5 comparison of as-built profiles and theoretical predictions (revisited for actual overall dimensions)

6.3.5.3. Beam FFB 6

The as-built measurements for beam FFB 6 are presented in the same format as for beam FFB 5 (see *Figure 6.17*). However, the size of the cross sections near the beam ends was found to be too large for saw-cutting and only sections located near the midspan were examined in detail. In addition, the overall depths near the supports were not successfully measured by non-destructive methods. It should also be noted that the horizontal flexible ties did not provide a uniform breadth at the restraint points, as intended in the design. This can be attributed to an inadequacy for manual installation and may be overcome by use of rigid ties or more effective fixing techniques.

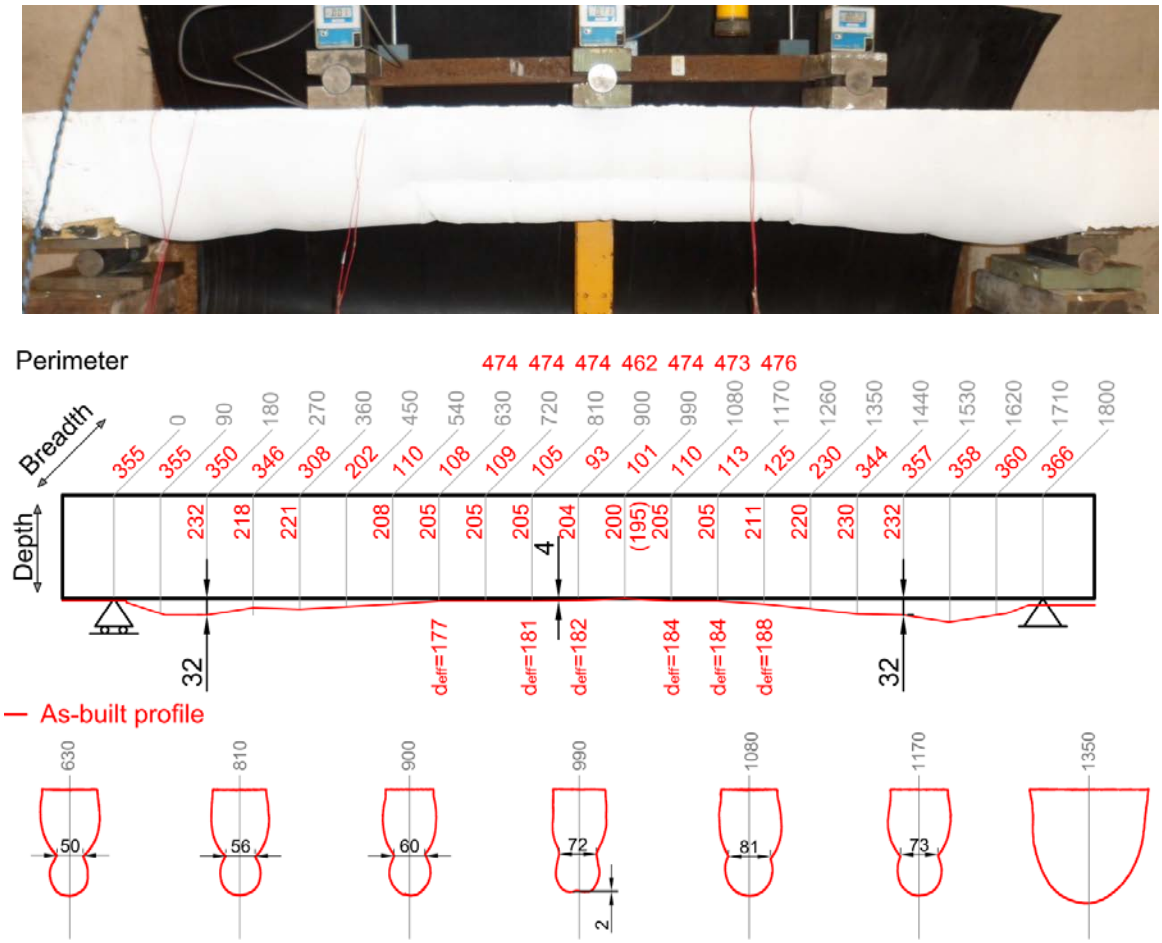

Figure 6.17. FFB 6 as-built measurements (all dimensions are in millimetres)

Overall, two major problems, illustrated in *Figure 6.18*, were identified. Firstly, large wrinkles were formed at the transition zone between horizontally restrained and unrestrained fabric could lead to a significantly reduced cross-sectional depth locally. Although it is not considered necessary to avoid wrinkles in fabric-formed concrete surfaces, the 2-D design approach is unable to predict the effects of sudden changes in the cross-sectional shape, which can result in such undesirable wrinkling or difficulties in fitting the edge of the fabric to the formwork table, as already experienced during the construction of beam FFB 1. The second problem, highlighted in *Figure 6.18b*, was the lateral displacement of the reinforcing bar during construction. The position of the bar was also found to be generally lower than its design position, reaching up to a deviation of 23 mm (refer to *Figure 6.19*), while the minimum measured concrete cover was 14 mm, approximately half of the design value.

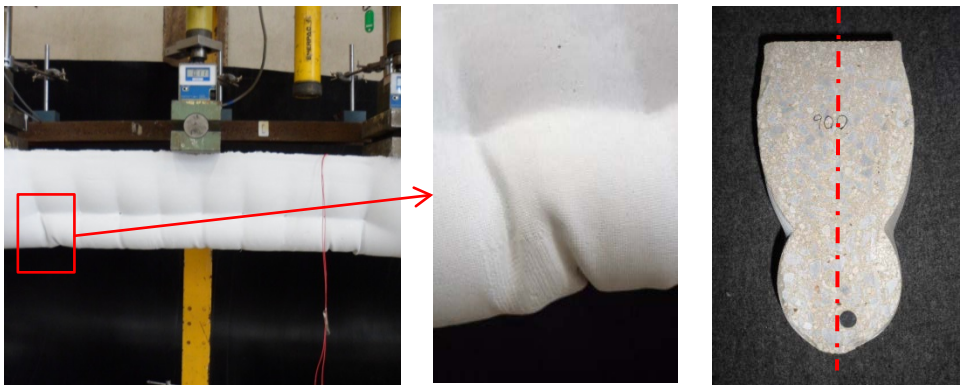

a. b.

Figure 6.18. As-built survey: (a) excessive wrinkling and (b) displaced reinforcement

The differences between the as-built and predicted cross-sectional profiles near midspan, presented in *Figure 6.19* and *Figure 6.20*, are fairly small. Despite the fairly large tolerance in top breadth reached during construction, the overall depth was not increased by more than 5 mm at midspan. However, towards the supports the as-built cross-sections are noticeably deeper, which suggests a construction or design error.

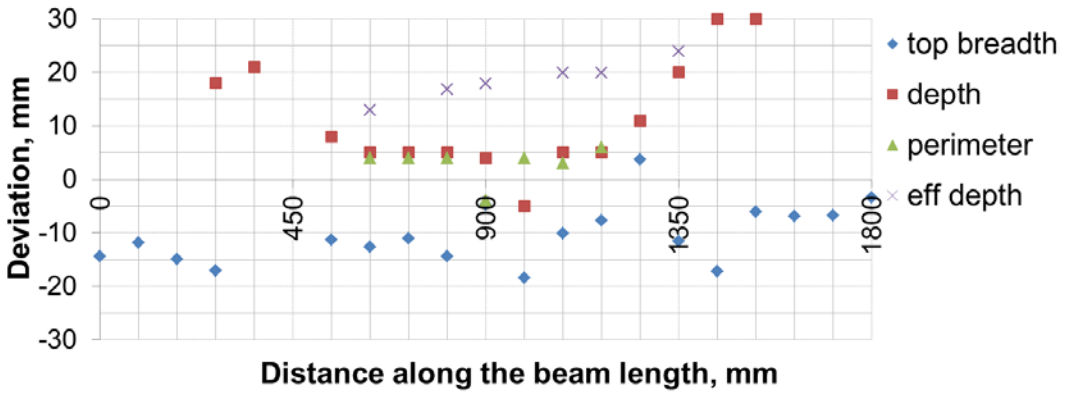

Figure 6.19. FFB 6 deviation from design geometry

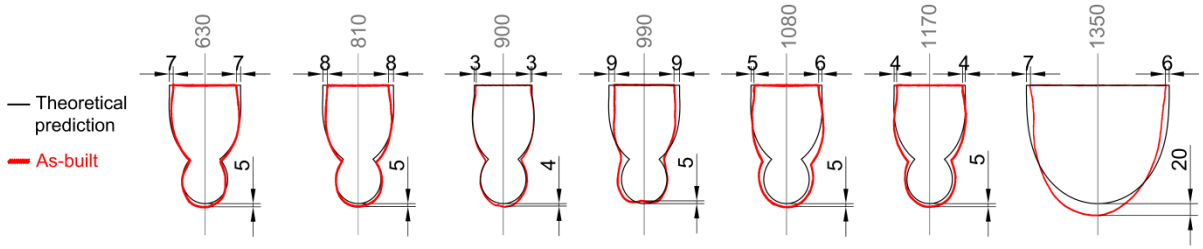

Figure 6.20. FFB 6 comparison of as-built profiles and theoretical predictions (design) (all dimensions are in millimetres)

The revised theoretical profiles in *Figure 6.21* again follow closely the shapes of the as-built profiles. The larger difference for section 1350 is most likely due to the 3-D effect from the horizontal restraint installed at the adjacent section.

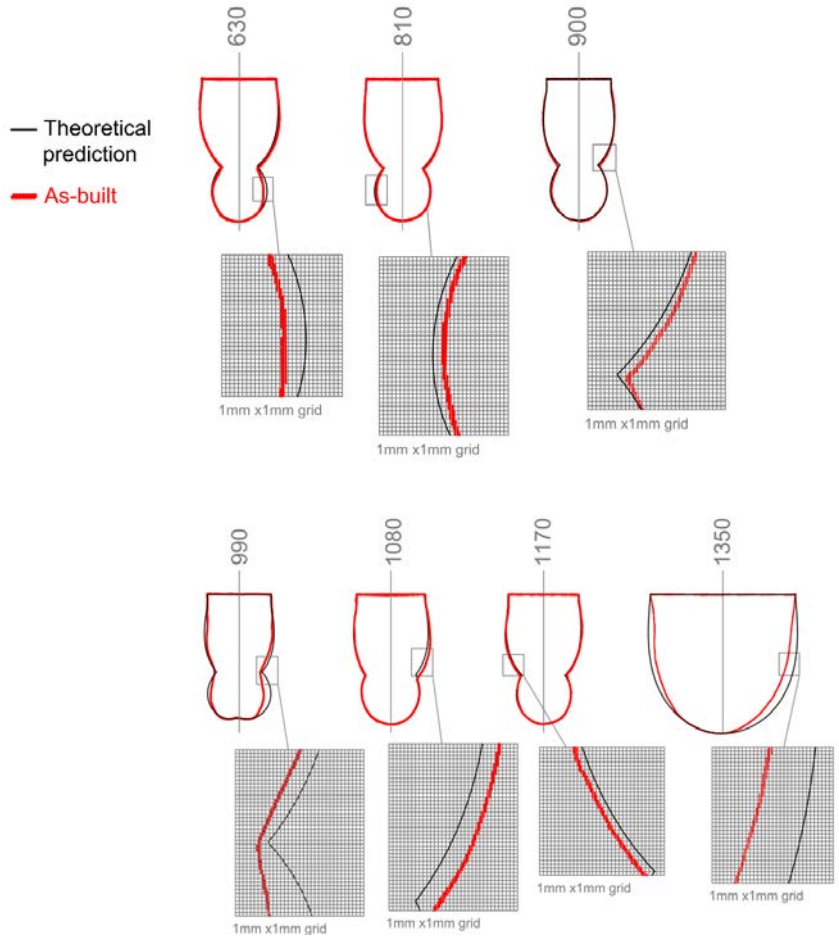

Figure 6.21. FFB 6 comparison of as-built profiles and theoretical predictions (revisited for actual overall dimensions)

6.3.5.4. Beam FFB 7

Slicing of beam FFB 7 into segments was relatively difficult due to the size of the specimen and the large extent of flexural cracks near midspan. Therefore, the majority of the cross-sectional profiles, presented in *Figure 6.22*, were obtained by the use of profile gauges. Following the load testing, the beam was surveyed at a number of sections and was subsequently broken down into smaller parts in order to measure the as-built depth of the reinforcing bar, as shown in *Figure 6.23*. The plot of the deviations from design geometry along the beam length in *Figure 6.24* indicates that the as-built overall depths near supports were significantly larger, up to 30 mm, than the design values. Although this might have been caused by the reduced top breadth, which leads to an increased depth for shallow sections of the same perimeter, the overlapped profiles in *Figure 6.25* also reveal a problem with the shape prediction of sections 270 and 360, due to an error in the form-finding algorithm (fixed later).

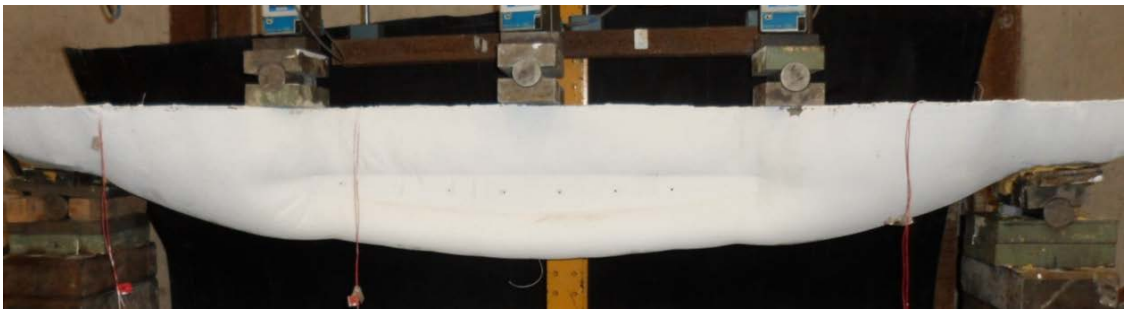

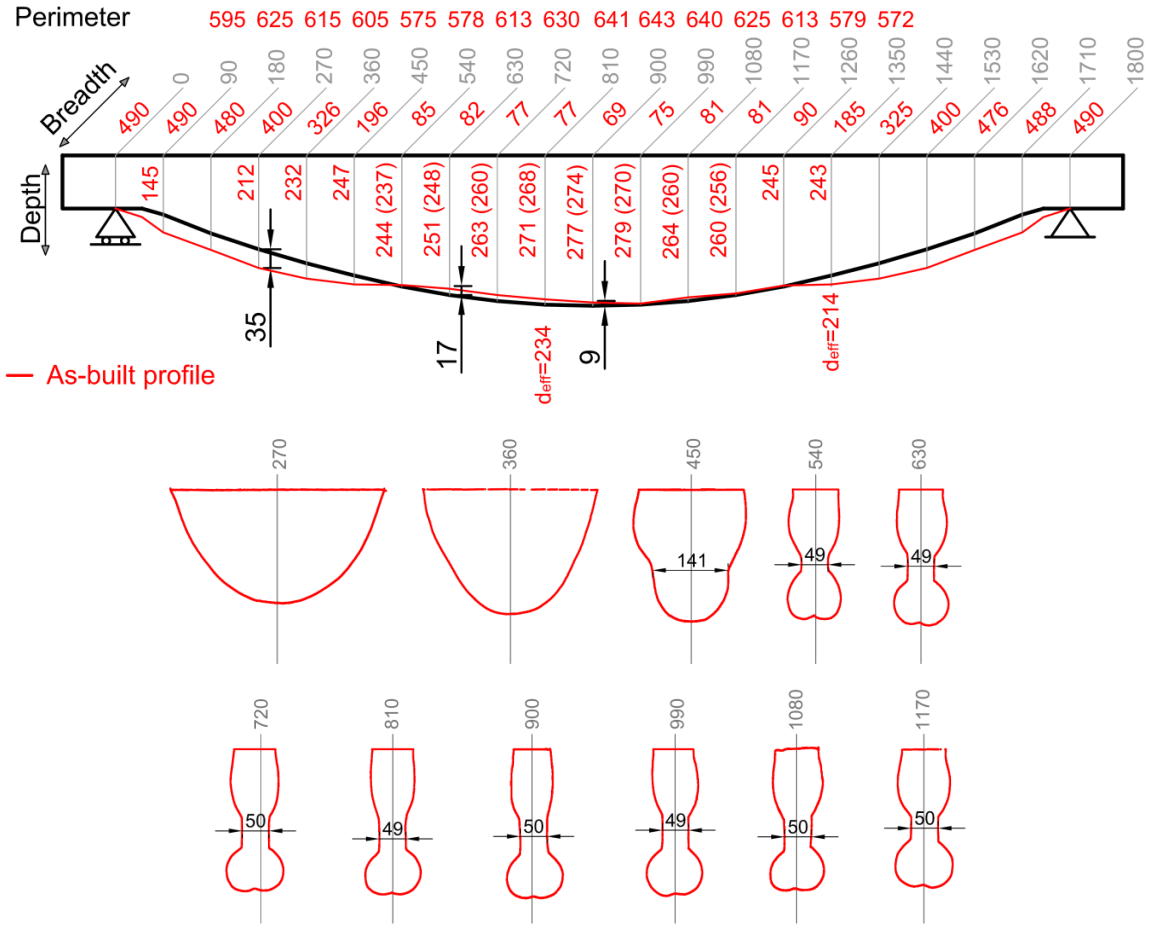

Figure 6.22. FFB 7 as-built measurements (all dimensions are in millimetres)

Figure 6.23. FFB 7 as-built survey

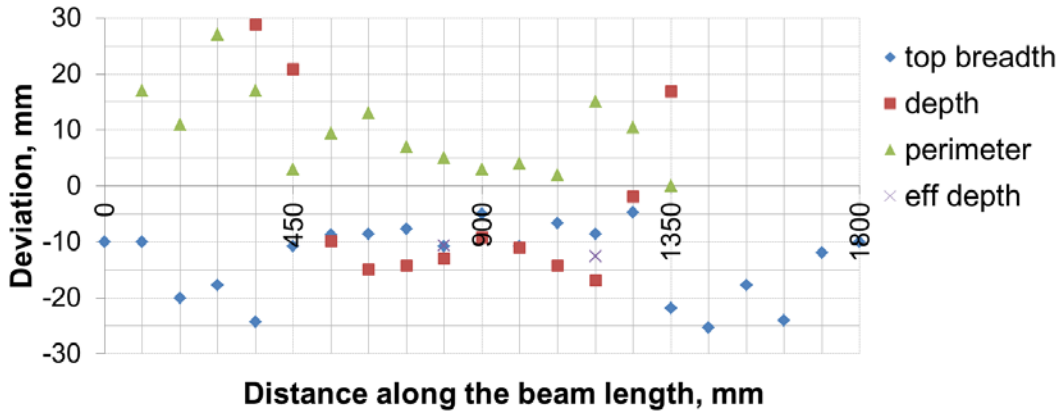

Figure 6.24. FFB 7 deviation from design geometry

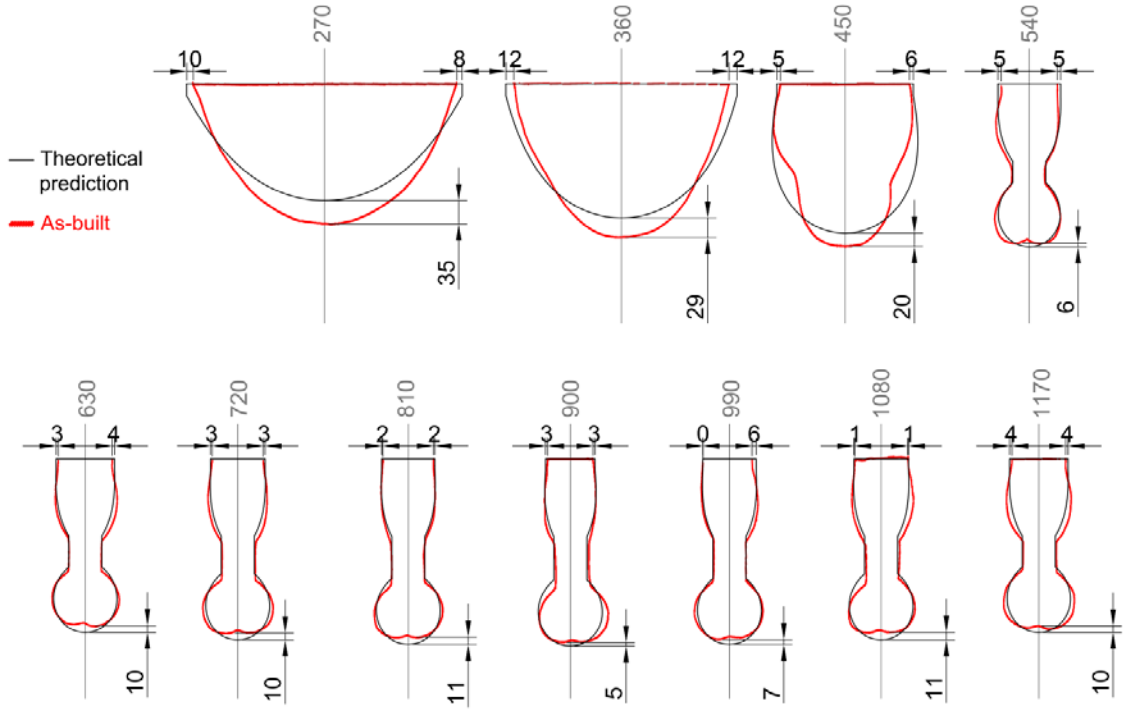

Figure 6.25. FFB 7 comparison of as-built profiles and theoretical predictions (design) (all dimensions are in millimetres)

It was found that the applied form-finding algorithm was not able to predict the shape of wide and shallow sections, at which the fabric moves away from the edge of the formwork table top plate, i.e. in situations where the angle of the top straight segment of the curve profile with the horizontal axis is greater than 90 degrees (for example section 270). This may also explain the differences between the design and measured depths for beam FFB 6. As the curvatures of the cross-sectional profiles depend entirely on the top breadth-to-depth ratio, a fairly easy solution was implemented by defining the input parameters according to the breadth-to-depth ratio for each section. It can be demonstrated that the hung perimeter is perpendicular to the top plane at a ratio of approximately 1.2. Therefore, for sections with higher breadth-to-depth ratios the overall

depth should be taken as equal to the hydrostatic depth regardless of the top plate thickness. The revised theoretical predictions based on the as-built measurements and redefined input for different breadth-to-depth ratios, presented in *Figure 6.26*, are in good agreement with the as-built profiles, including the sections with vertical ties. Although there are local deviations, the accuracy of the as-built cross sections is significantly improved in comparison with the results for beam FFB 4, described in § 5. A typical problem of the 'key-hole' sections, however, is the unsymmetrical shape, resulting in one side bulging more than the other. The effect is more pronounced at the top part of the sections and may be dictated by the construction tolerance of fixing the side web plates to the fabric sheet. Furthermore, the profile of section 360 is affected by the horizontal restraint at section 540 and, as previously discussed, is not predictable by the 2-D design approach.

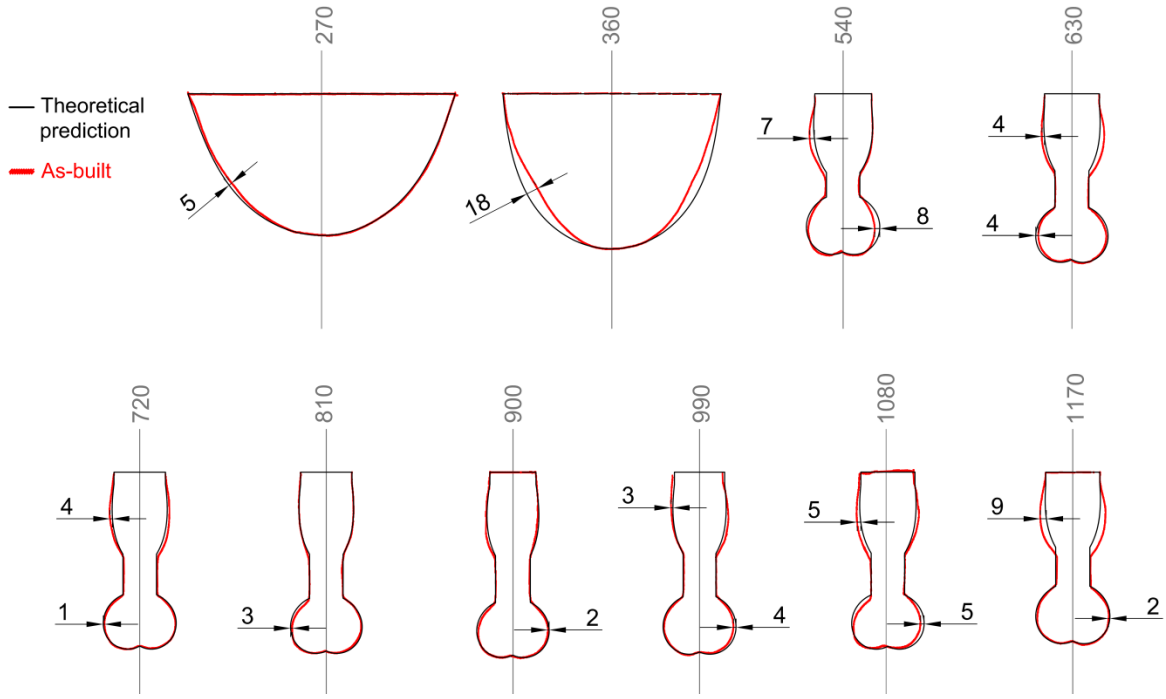

Figure 6.26. FFB 7 comparison of as-built profiles and theoretical predictions (revisited for actual overall dimensions) (all dimensions are in millimetres)

6.3.5.5. Beam FFB 8

The use of profile gauges was more extensively exploited for obtaining all cross-sectional profiles shown in *Figure 6.27*, in order to study the as-built geometry of beam FFB 8. While faster and safer, this method also allows for more precise location of the design cross sections avoiding the loss of concrete removed by the saw blade when slicing a beam.

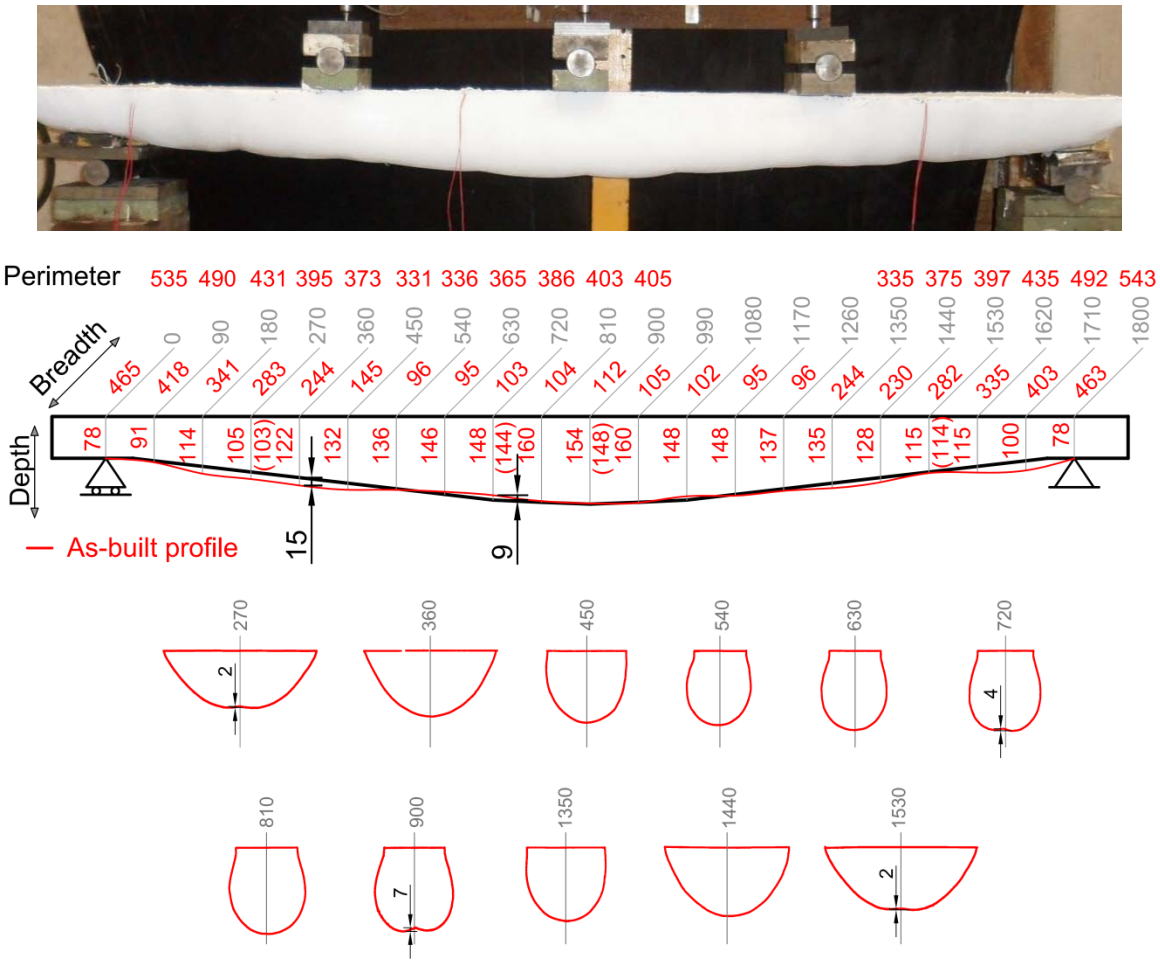

Figure 6.27. FFB 8 as-built measurements (all dimensions are in millimetres)

The cover to the reinforcing bar was checked by breaking the concrete around the bar. The photographs in *Figure 6.28* show the bottom side of the constructed beam and the exposed reinforcement after the removal of concrete near midspan. The minimum concrete cover was 28 mm, measured at the point of restraint for sections with vertical ties and corresponding to the minimum overall depth values provided in brackets in *Figure 6.27*. The effective depth profile was adjusted accordingly in order to reflect the as-built position of the reinforcing bar when calculating the actual capacity and load-deflection response.

Figure 6.28. FFB 8 as-built survey

The plots in *Figure 6.29* present the deviations from the design dimensions along the length of beam FFB 8. As discussed, the large differences between the constructed and design depths near the beam supports can be attributed to an error in the definition of the form-finding input parameters. The reduced overall depths near midspan correspond to the positions of the vertical ties connecting the fabric and the reinforcement. The results suggest that the vertical pull-out forces due to the stiffness of the reinforcing bar can alter the cross-sectional profile significantly. Therefore, such effects should be considered in the design and the perimeter of sections with vertical restraints accurately predicted in order to avoid undesirable reduction of the effective depths, which has been subsequently added to the MATLAB programme.

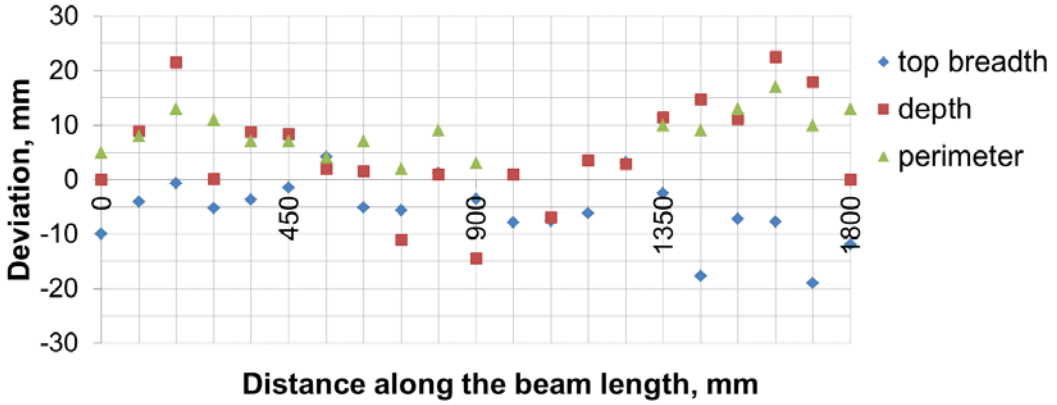

Figure 6.29. FFB 8 deviation from design geometry

The theoretical predictions in *Figure 6.30* and *Figure 6.31* represent the design profiles and the profiles based on as-built overall dimensions, respectively.

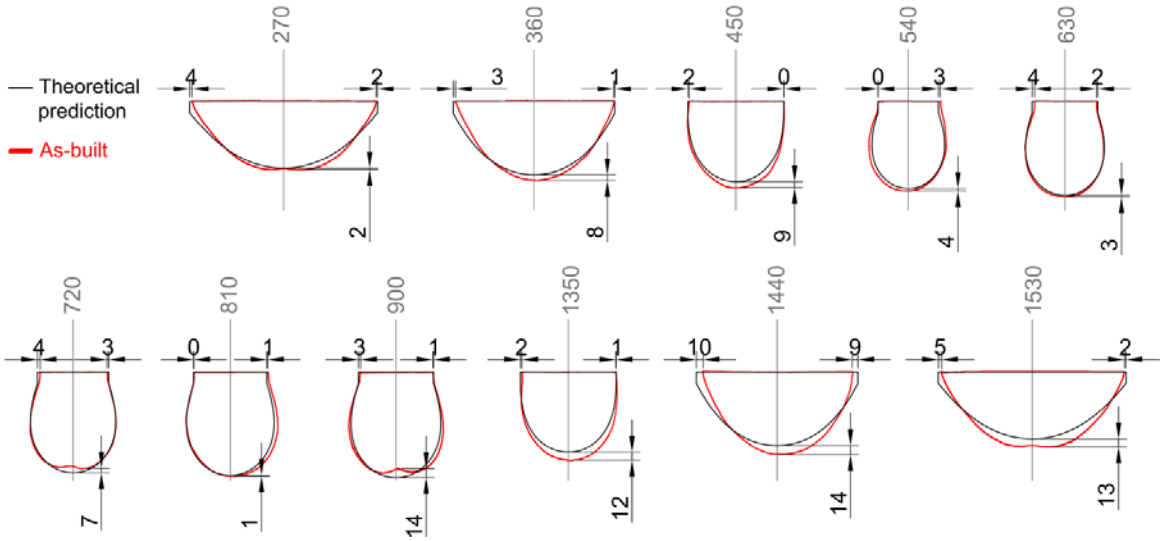

Figure 6.30. FFB 8 comparison of as-built profiles and theoretical predictions (design) (all dimensions are in millimetres)

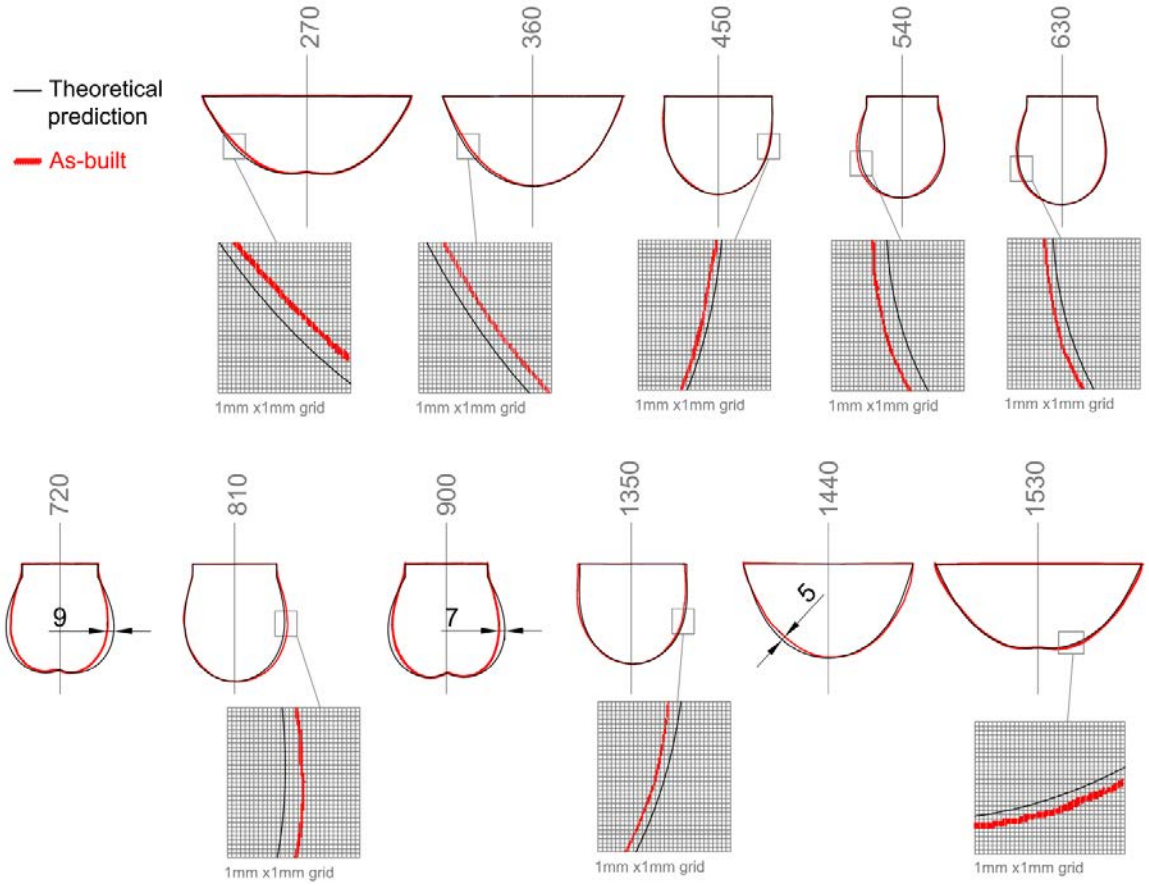

Figure 6.31. FFB 8 comparison of as-built profiles and theoretical predictions (revisited for actual overall dimensions) (all dimensions are in millimetres)

The theoretical predictions for cross sections cast in unrestrained fabric remain better, and for a number of sections near midspan are very close to their design shapes (see *Figure 6.30*). The corrected form-finding procedure also predicts accurately the profiles of the shallower sections near the support, as demonstrated by the comparison presented in *Figure 6.31*.

6.3.6. As-built position of reinforcement attached to the fabric

As demonstrated by the survey of the as-built geometry, the stiffness of the longitudinal bars attached to the fabric can change significantly the cross-sectional profiles, thereby reducing the effective depth of reinforcement. An algorithm capable of predicting such profiles has been developed and tested for describing the as-built shapes with known height of the vertical lift in the fabric sheet (not available at the time of design of the beam specimens). The design problem, however, requires determining the uplift forces, based on the stiffness of the reinforcing bars and the points of attachment. Therefore, it is necessary to demonstrate that the theoretical forces required to pull down straight reinforcing bars into their as-built positions are equal to the uplift forces in the ties required

to form the as-built profiles. The results for beam FFB7, which present the most complete set of data of sections with vertical ties, would be used to provide this comparison.

Two sets of uplift forces were calculated (see *Figure 6.32)*. The first set contains forces obtained from the form-finding algorithm and the as-built data. The forces corresponding to the actual uplift are expressed in N/m and then multiplied by the spacing between the ties in order to be converted to N. The sketch in *Figure 6.32* indicates the positions of the forces and provides a table with their values. The flexural stiffness of the GFRP reinforcing bar, based on 12.7 mm effective diameter and 40 GPa modulus of elasticity, is used to calculate the forces corresponding to the maximum measured deflection, assuming equal distribution among all ties. As can be seen, the difference between the two sets of forces is within +/-10 % of their values.

The deflections of the bar along the length of the beam comprising vertical ties was also calculated for the two sets of forces and is presented in *Figure 6.33*. The curve based on the maximum deflection of the bar agrees well with the experimental deflected shape, which suggests that the applied method for determining the forces in the ties and form-finding of the resulting cross-sectional shapes is appropriate. A further discussion and a case study illustrating the design procedure can be found in § 8.

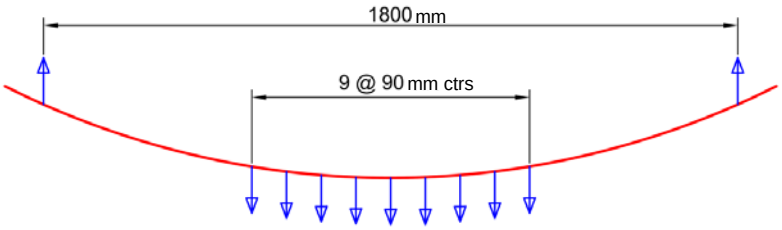

a.

Forces based on actual uplift of fabric

N/m	118	97	106	97	102	95	104	97	118
N	10.6	8.73	9.54	8.73	9.18	8.55	9.36	8.73	10.6

b.

Forces based on flexural stiffness of reinforcement

N	9.74	9.74	9.74	9.74	9.74	9.74	9.74	9.74	9.74

c.

Figure 6.32. FFB7 design compared with as-built: (a) attachment points, (b) forces in the ties based on the as-built geometry and (c) forces in the ties based on actual maximum deflection of the reinforcing bar

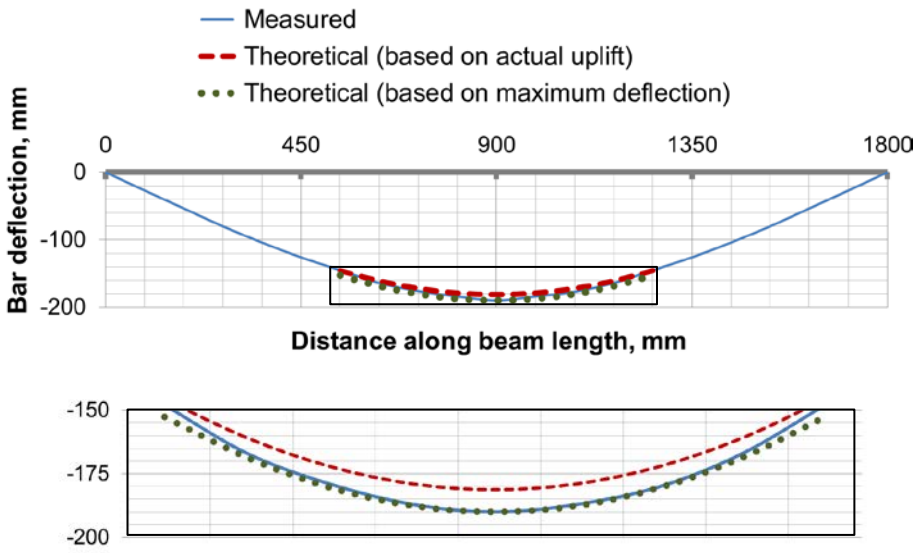

(Zoomed in view)

Figure 6.33. FFB 7 deflection of reinforcing bar

6.4. Test results

6.4.1. Material testing

Beams FFB 5 and FFB 6 were cast together due to the larger volume of FFB 6, which exceeded the capacity of a single concrete batch of 200 kg, while FFB 5 required only 75 kg of concrete. Similarly, FFB 7 had to be cast together with FFB 8 to allow for efficient use of the concrete mixer capacity. Both concrete cube and cylinder samples were tested in order to gauge the compressive strength of concrete. The cubes were also used to monitor the 28-day development of strength. The number of cylinder samples was limited and provided results only for the concrete age during load testing. The average ratio of the cylinder and cube strengths for the results presented in *Table 6.9* and *Table 6.10* is approximately 0.8, which agrees with the theoretical value used in § 5.

Table 6.9. Concrete cube compressive strengths (Series 2)

Beam ID	Date cast	Date tested	Average Mix I, MPa	Average Mix II, MPa	Average strength, MPa
FFB 5 & 6	01/02/2013	05/02/2013	17.3	15.2	16.2
FFB 7 & 8	07/02/2013	11/02/2013	27.9	24.9	26.0

Table 6.10. Concrete cylinder compressive strengths (Series 2)

Beam ID	Date cast	Date tested	Mix I, MPa	Mix II, MPa	Cylinder strength, MPa
FFB 5 & 6	01/02/2013	05/02/2013	12.7	12.1	12.4
FFB 7 & 8	07/02/2013	11/02/2013	23.2	20.7	22.0

In addition to the standard cylinder samples formed in plastic moulds, fabric-formed cylinders were also tested for the FFB 5 and FFB 6 concrete mixes. The samples were cut from a long concrete cylinder cast in a fabric sock, provided by the fabric formwork supplier and shown in *Figure 6.34*. Only two samples were produced per mix, which may be the reason for the great variation in the enhancement of concrete strength, due to the permeability of fabric formwork, between the two tested mixes (see *Table 6.11*).

Figure 6.34. Fabric-formed cylinder samples

Table 6.11. Enhancement of compressive cylinder strength (FFB 5 and FFB 6)

Mix	Normal cast	Fabric-formed	Enhancement
I	12.7	15.0	18 %
II	12.1	13.1	9 %

As discussed in § 6.2.1, the addition of GGBS to the self-compacting concrete mix had an unexpectedly high adverse effect on the early compressive strength of concrete. *Figure 6.35* shows a comparison between the recorded early cube strengths for beams FFB 5 and FFB 6 and theoretical predictions, calculated in accordance with BS EN 1992-1-1:2004. Reducing the amount of GGBS by half helped to achieve the theoretical early cube strength of 26 MPa for beams FFB 7 and FFB 8, as demonstrated by the results in *Table 6.9*.

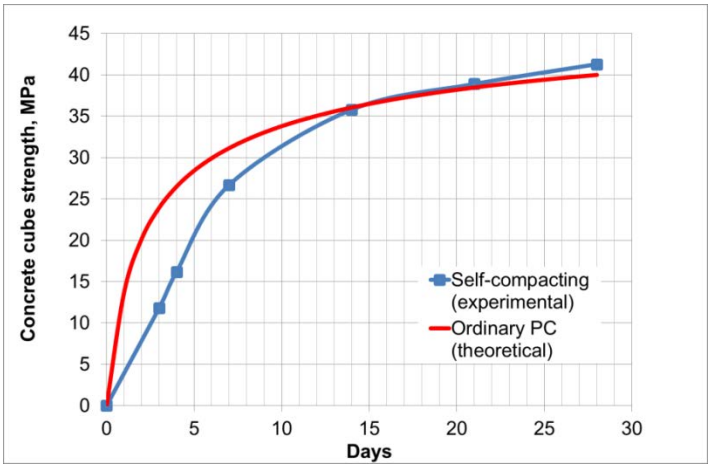

Figure 6.35. Comparison of early concrete strength development between theoretical and self-compacting mix for beams FFB 5 and FFB 6

6.4.2. Failure modes and failure loads

The photographs in *Figure 6.36* to *Figure 6.39* show the test beams at failure. Beams FFB 5 and FFB 8 both failed in flexure by crushing of the concrete in the compression zone. However, beam FFB 8 developed significant flexural cracking before reaching its ultimate capacity, while FFB 5 failed under a single crack near the middle point load. Furthermore, the failure of beam FFB 5 was extremely brittle due to snapping of the 10 mm smooth GFRP bar immediately after the concrete in compression had failed, as illustrated in *Figure 6.36*.

A large shear crack was formed near the left support of beam FFB 6, as shown in *Figure 6.37*. However, the beam was able to sustain the maximum applied loads before reaching ultimate failure, accompanied by a simultaneous splitting of concrete near the anchorage zone. The major reasons for the concrete splitting could be the lack of sufficient bond cover and the low as-built strength of concrete. Beam FFB 7 also failed in a brittle manner, as can be seen in *Figure 6.38*.

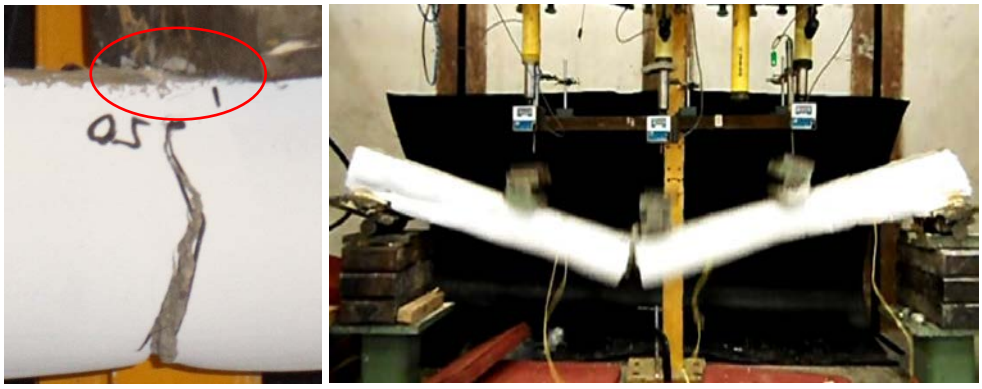

Figure 6.36. FFB 5 failure of concrete in compression, followed by snapping of the GFRP bar

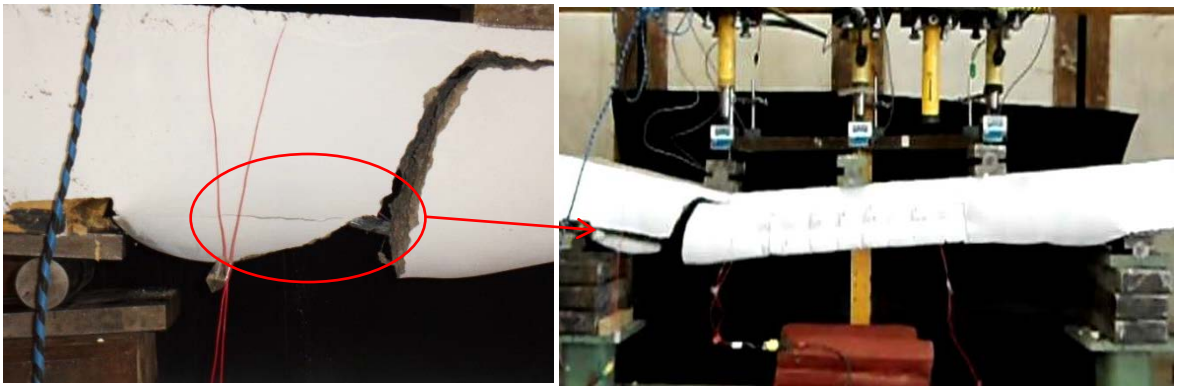

Figure 6.37. FFB 6 shear failure and concrete splitting near the end anchorage

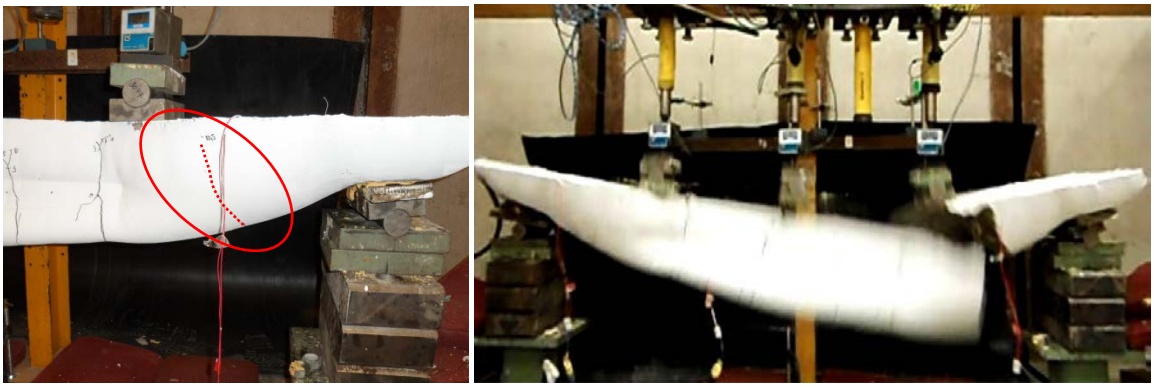

Figure 6.38. FFB 7 sudden failure in quarter span

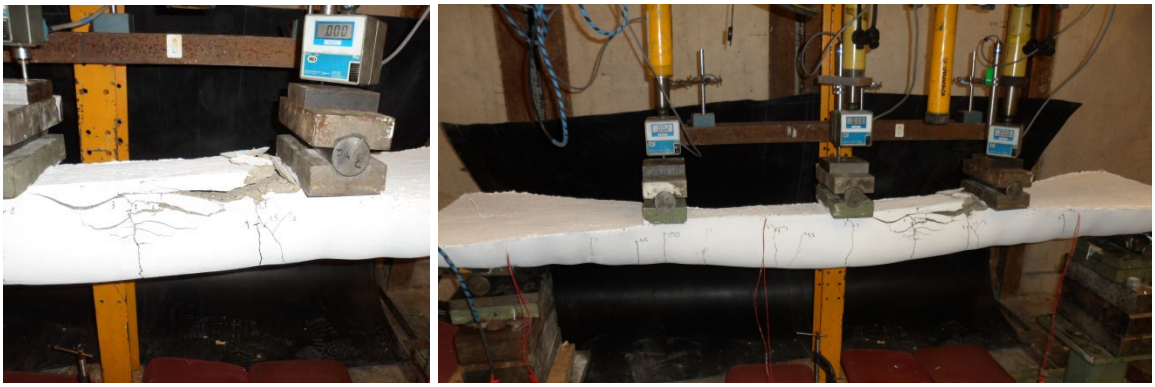

Figure 6.39. FFB 8 failure of concrete in compression

The maximum point loads reached at failure for each specimen are indicated in *Figure 6.40*. Beams FFB 5 and FFB 6 failed at loads significantly lower than the values used for design of the beams, partially due to lower than expected concrete strengths at testing. On the other hand, the recorded cylinder compressive strength of concrete for beams FFB 7 and FFB 8 was slightly higher than the design strength, and their capacity exceeded the design loads.

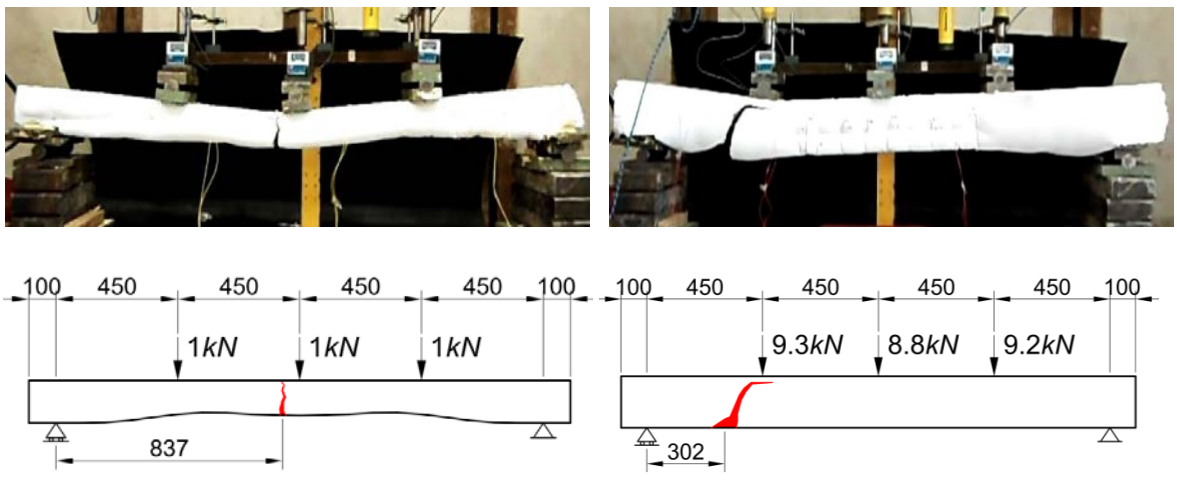

a. b.

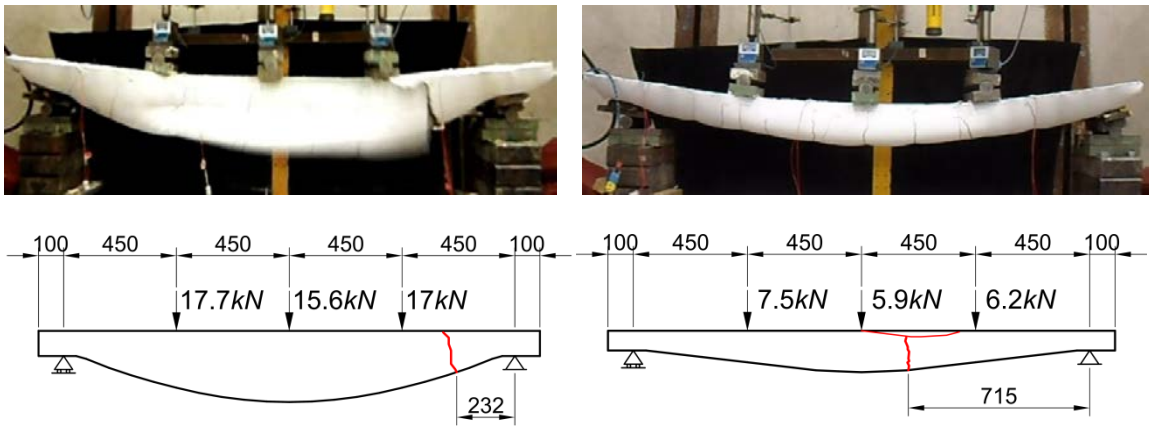

c. d.

Figure 6.40. Failure loads: (a) FFB 5, (b) FFB 6, (c) FFB 7 and (b) FFB 8 (all dimensions are in millimetres)

6.4.3. Load-deflection relations

The load-deflection curves in *Figure 6.41* to *Figure 6.44* represent the deflections measured at the position of each point load plotted against the total vertical load for the four test beams. Most of the results demonstrate the typical brittle behaviour of FRP reinforced concrete beams, with the exception of beam FFB 6, which exhibited a degree of ductility, most likely governed by slip of the end anchorage prior to concrete splitting failure.

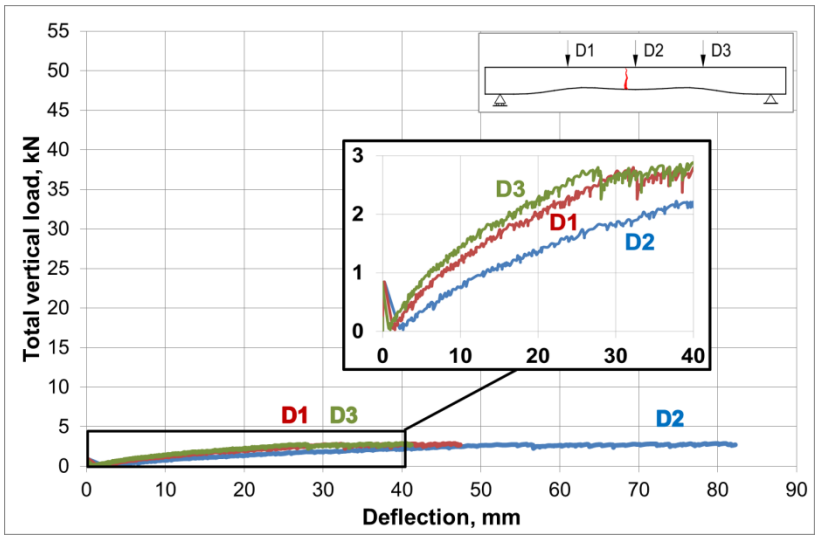

Figure 6.41. FFB 5 experimental load-deflection relations

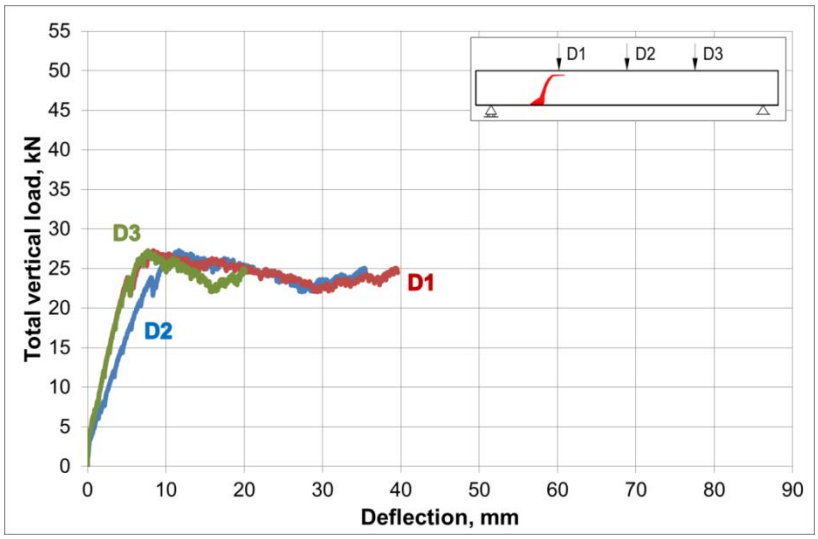

Figure 6.42. FFB 6 experimental load-deflection relations

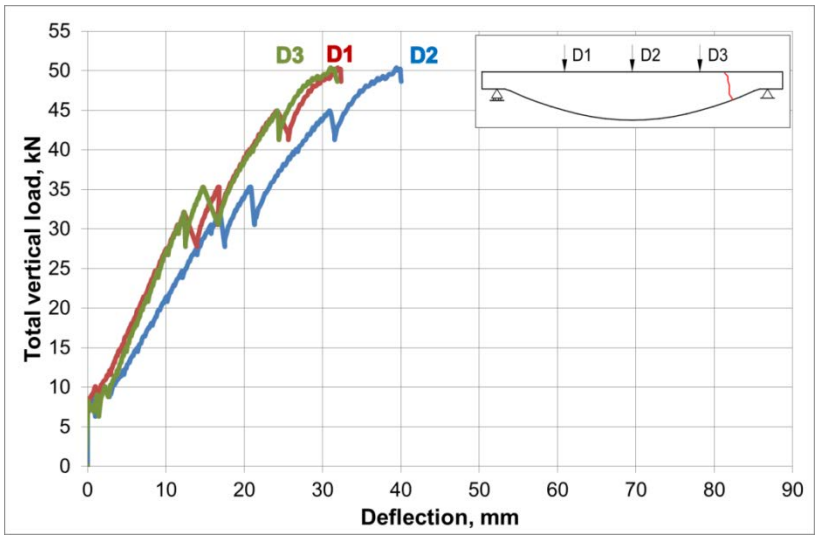

Figure 6.43. FFB 7 experimental load-deflection relations

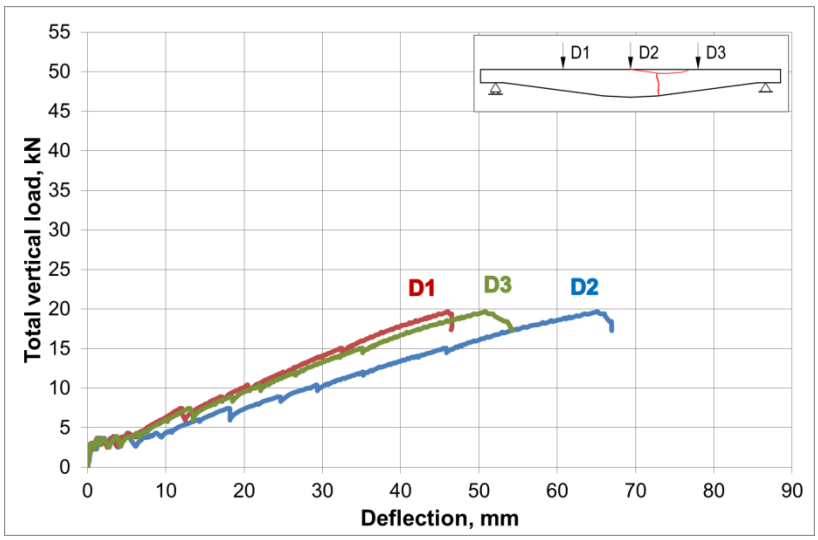

Figure 6.44. FFB 8 experimental load-deflection relations

6.4.4. Load-strain relations

The strains in the reinforcing bars were measured along the sides of each bar approximately at the point load locations. The results, presented in *Figure 6.45* to *Figure 6.48* correspond well to the utilisation plots in *Figure 6.6*, indicating the level of utilisation of each bar along its length. For all beams with varying depth profile, the bars were almost equally stressed at each measured location, while for beam FFB 6 the stress decreases away from midspan, which would be typical for beams with uniform sections. Although the reinforcing bar in beam FFB 5 snapped, the recorded strains during the test were relatively low, which could be explained with the fact that the strains were measured near the neutral axis of the bar and, therefore, the maximum strain at the extreme fibre due to excessive bending of the bar after concrete crushing at the top, was not available.

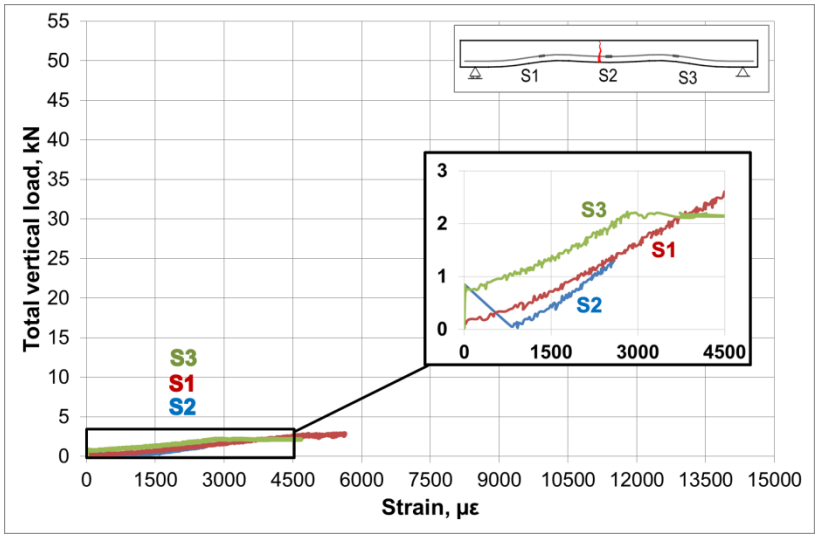

Figure 6.45. FFB 5 experimental load-strain relations

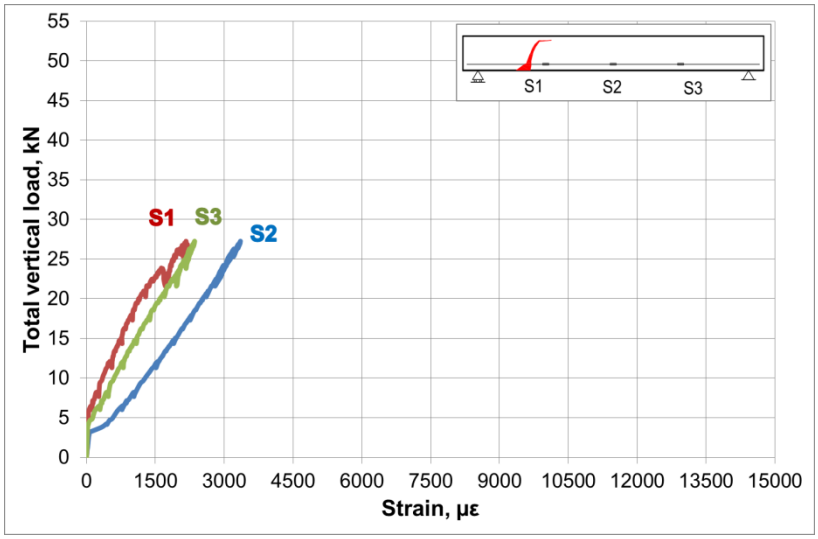

Figure 6.46. FFB 6 experimental load-strain relations

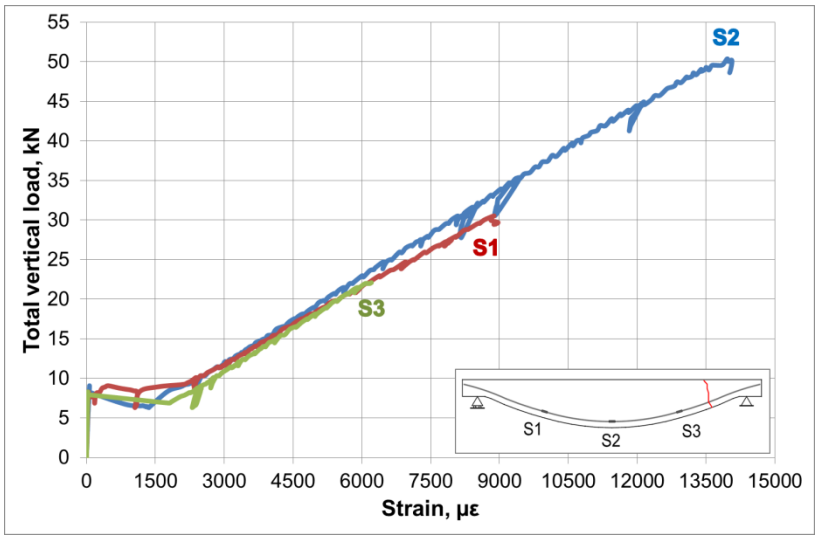

Figure 6.47. FFB 7 experimental load-strain relations

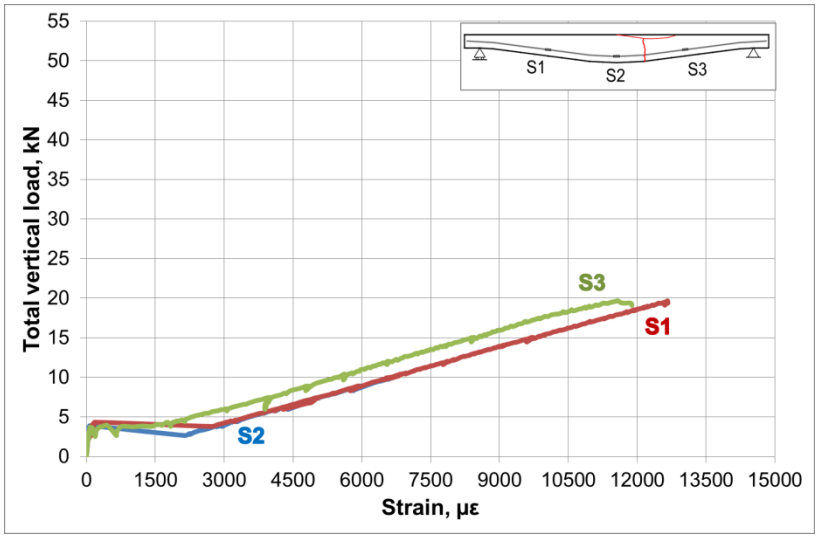

Figure 6.48. FFB 8 experimental load-strain relations

6.5. Discussion of results

The experimental results are compared with theoretical predictions in order to validate the proposed design method and to assess the effect of construction inaccuracies. Accordingly, two sets of theoretical predictions are presented, the first based on the design geometry and the second on the as-built data. The as-built data comprises measured overall dimensions and full as-built profiles for a number of cross sections. The developed MATLAB program allows the combination of both input types for a single beam, as described in § 4. The full profiles are directly input as coordinates, extracted from the CAD model at a pre-defined step for the vertical coordinate. The rest of the cross-sectional profiles are obtained through form-finding using the as-built dimensions. The comparison is provided in terms of cross-sectional capacities and load-deflection response.

6.5.1. Comparison of experimental and predicted capacities

The predicted capacities are calculated for the as-built concrete strengths and compared with the maximum load effects, corresponding to the failure loads indicated in *Figure 6.40*. Predictions based on the tested enhanced fabric-formed concrete strength are presented for beams FFB 5 and FFB 6. The enhanced cylinder strength of beams FFB 7 and FFB 8 was taken as 26 MPa, assuming 18% enhancement, based on the experimental results for beams FFB 5 and FFB 6..

Beam FFB 5 and FFB 6 both failed below their predicted capacities. The plots in *Figure 6.49* indicate that the minimum predicted moment capacity was 42% higher than the maximum applied bending moment at midspan. The behaviour of beam FFB 5, however, may have been partially influenced by the low bond strength of the reinforcing bar, invalidating the assumption for perfect bond. Although beam FFB 6 was reinforced with a sand-coated CFRP bar, the predicted moment capacity exceeds the applied moment by approximately 20% at midspan (see *Figure 6.50*). In this case, the difference could be attributed to a premature failure, governed by the slip of the end anchorage. Although the slip was not monitored, the observed horizontal cracks confirmed the loss of bond in the anchorage zone, resulting in a loss of concrete below the reinforcing bar, prior to ultimate failure.

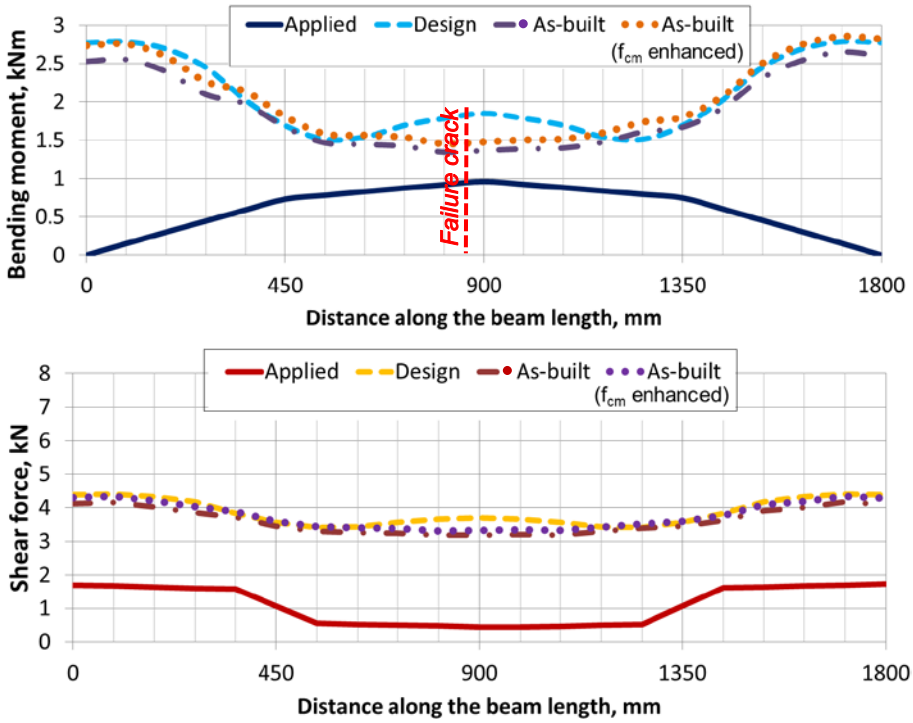

Figure 6.49. FFB 5 maximum load effects vs section capacities for design and as-built geometry

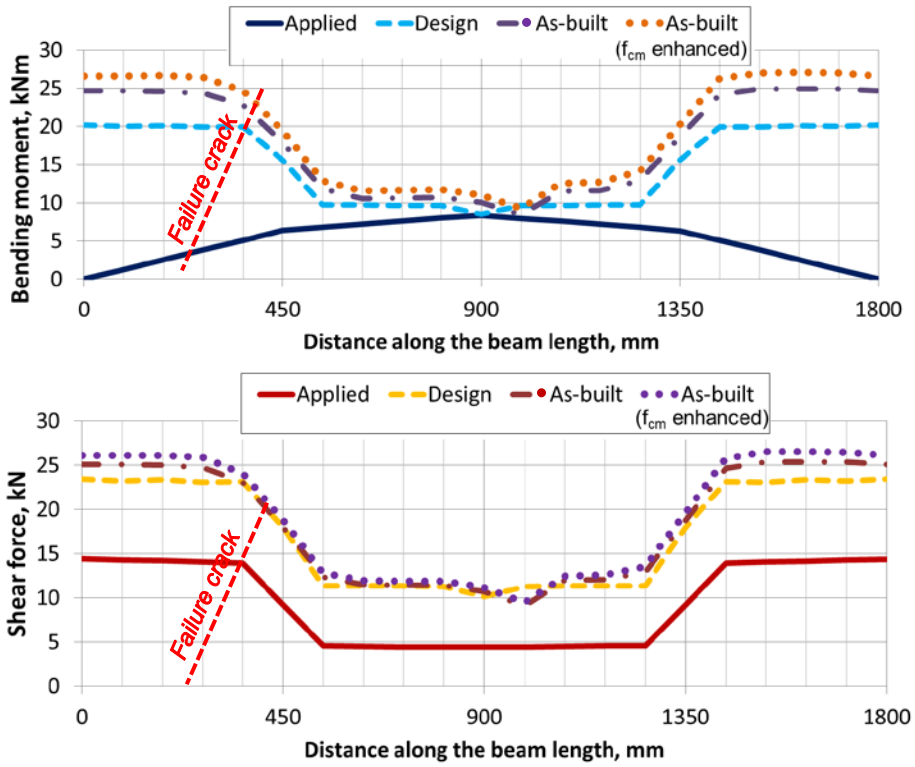

Figure 6.50. FFB 6 maximum load effects vs section capacities for design and as-built geometry

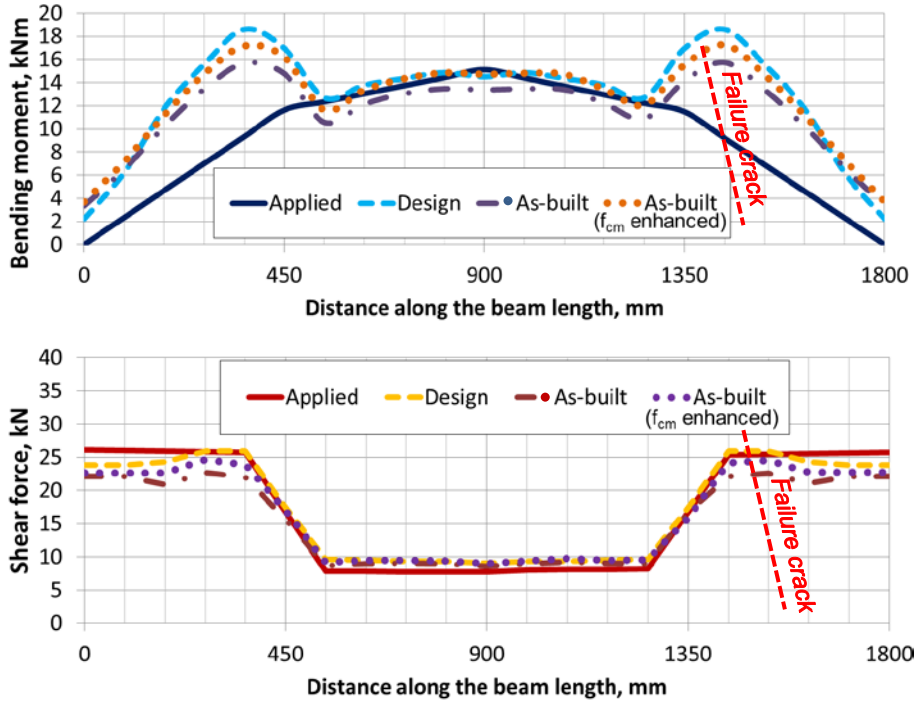

Figure 6.51. FFB 7 maximum load effects vs section capacities for design and as-built geometry

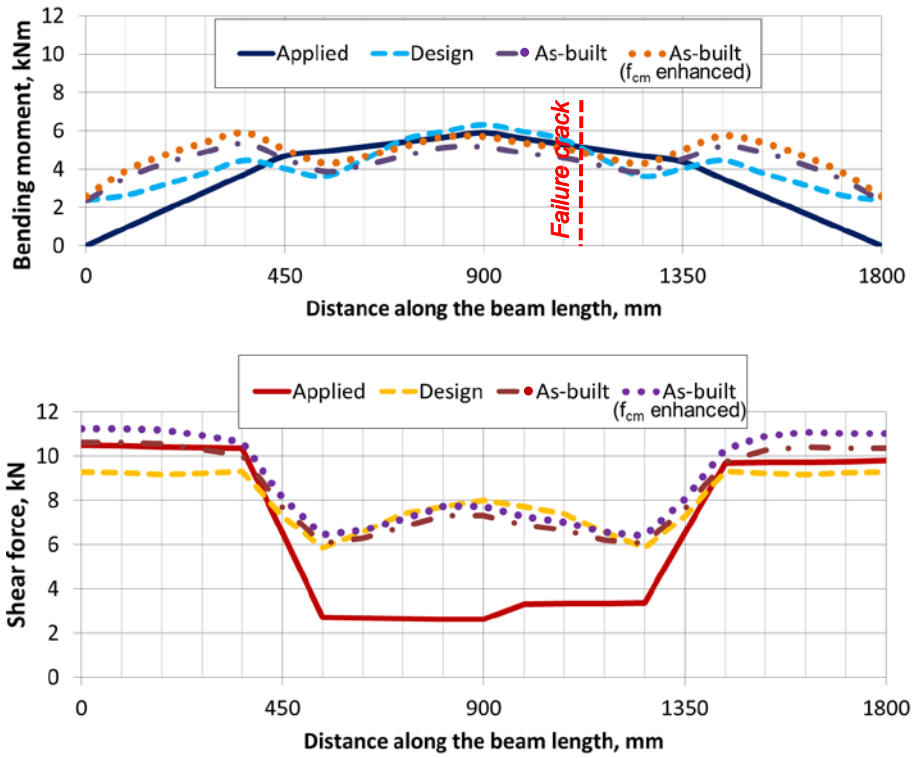

Figure 6.52. FFB 8 maximum load effects vs section capacities for design and as-built geometry

The theoretical predictions for beams FFB 7 and FFB 8 are exceeded by the actual strength capacities. The maximum applied bending moment at the midspan of beam FFB 7 is 3% higher than the predicted capacity, while the maximum applied shear is 12% higher than the capacity at section 1620, indicating the shear failure at this location (see *Figure 6.51*). Similarly, the 'as-built' capacity predictions for beam FFB 8 clearly indicate flexural failure between the point loads, as can be seen in *Figure 6.52*.

6.5.2. Experimental and predicted load-deflection behaviour

The experimental load-deflection curves are compared with theoretical predictions, excluding the initial beam deflections under selfweight, as described in § 5. The plots in *Figure 6.53* to *Figure 6.56* are based on the as-built concrete strengths. Again two sets of geometry inputs, design and as-built, are analysed in order to assess the effect of the construction inaccuracies on the structural behaviour of fabric-formed beams. For clarity, the results presented for the deflections at the centre and at the quarter points are presented separately. The theoretical maximum shear capacities, expressed in terms of the total vertical load are also indicated on the graphs.

The theoretical curves for beam FFB 5, presented in *Figure 6.53*, significantly overestimate the beam stiffness, providing close predictions up to 40% of the ultimate

load capacity, which corresponds to the previous findings for beams reinforced with smooth GFRP bars, presented in § 5. The difference between the different theoretical curves below 40% of the ultimate load is negligibly small, suggesting that the measured deviations from the design geometry (refer to *Figure 6.12*) may be acceptable for the initial loading stages. The maximum difference between the predicted deflections for the as-built and design geometries reaches 19%, equal to 6.5 mm in this case. The increased strength of concrete results in a higher cracking moment and ultimate moment capacity, however the slope of the predicted curve after the first crack is fairly similar to the slope of the theoretical curve based on as-built geometry without enhancement of the concrete strength, showing less than 1 mm difference against the predicted deflections.

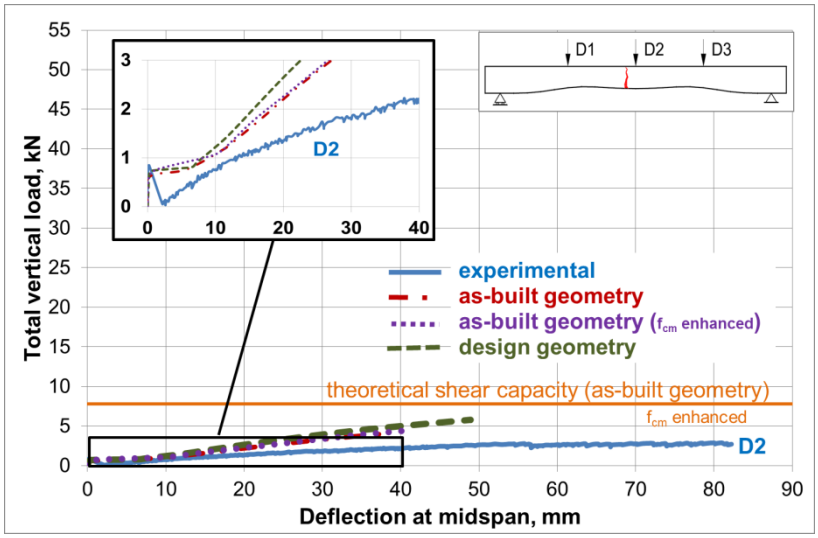

a.

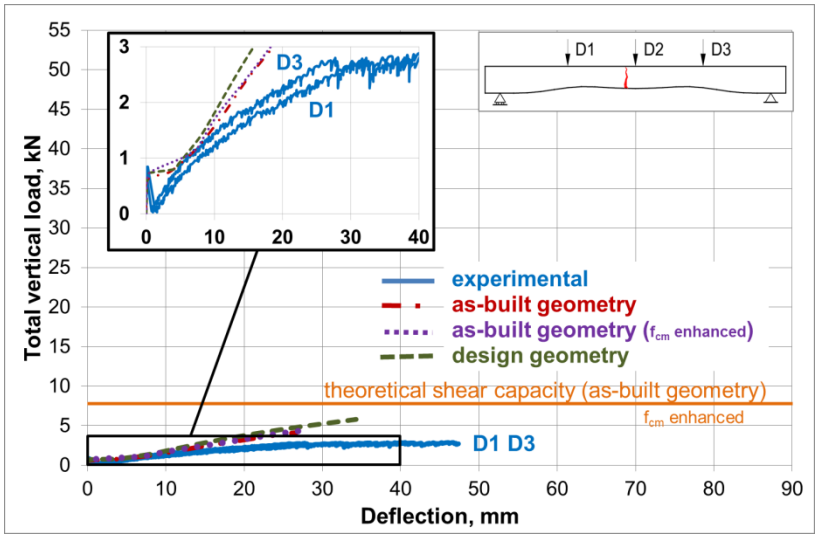

b.

Figure 6.53. FFB 5 Load-deflection relation: (a) at midspan and (b) at quarter span

The 'as-built' theoretical curve for beam FFB 6 describes fairly well the experimental behaviour of the beam up to approximately 60% of the maximum load, predicted for

concrete strength enhancement, as demonstrated in *Figure 6.54*. However, beyond this point the load-deflection behaviour of beam FFB 6 appears to be governed by the anchorage slip and cannot be predicted by the adopted approach for analysis. Furthermore, the enhancement of the concrete strength has insignificant effect below 60% of the maximum load, reaching only up to 0.1 mm difference between the predicted 'as-built' deflections. The difference between the 'as-built' and 'design' deflections has a maximum value of 23%, corresponding to 2.7 mm for concrete strength without enhancement.

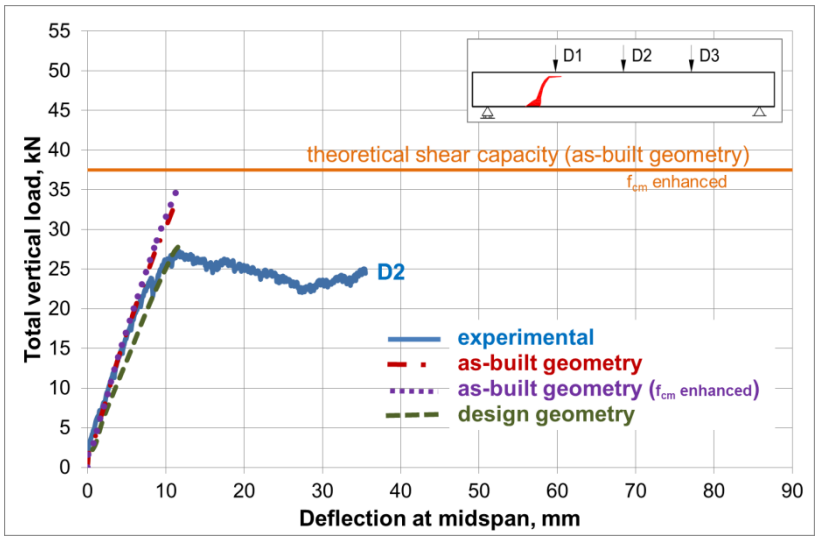

a.

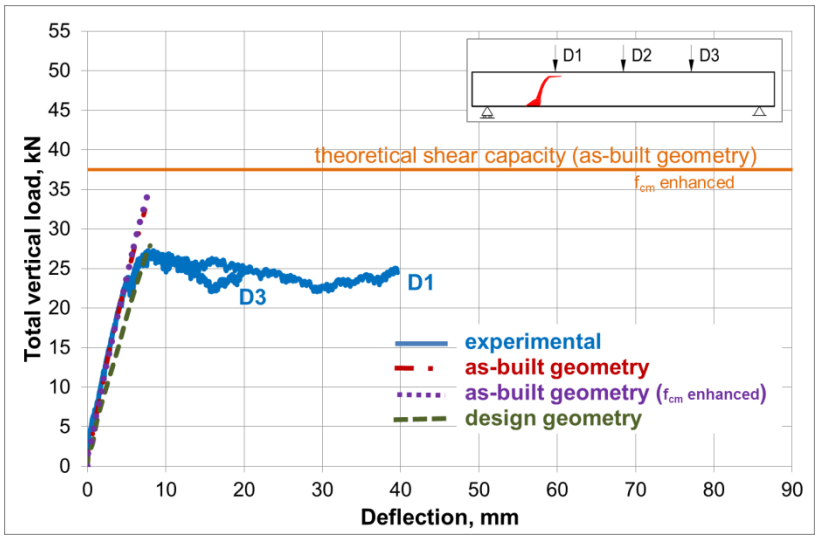

b.

Figure 6.54. FFB 6 Load-deflection relation: (a) at midspan and (b) at quarter span

The predicted curve, based on the as-built geometry for beam FFB 7 appears to follow closely the experimental curve, shown in *Figure 6.55*. Again the difference between the two 'as-built' theoretical plots, based on concrete strength with and without enhancement

due the fabric formwork, appears to be insignificant. The deflections calculated for the design geometry input are up to 14%, or 4 mm, higher than the deflections, calculated for as-built geometry without concrete strength enhancement. However, the difference between the two theoretical curves becomes pronounced only above 60% of the predicted maximum load, suggesting that the achieved construction tolerances could be acceptable for assessing the beam behaviour under serviceability loads.

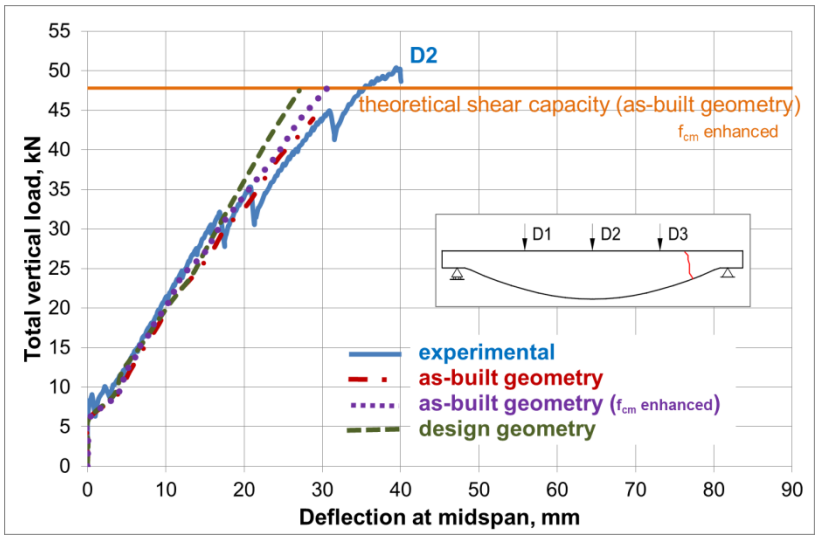

a.

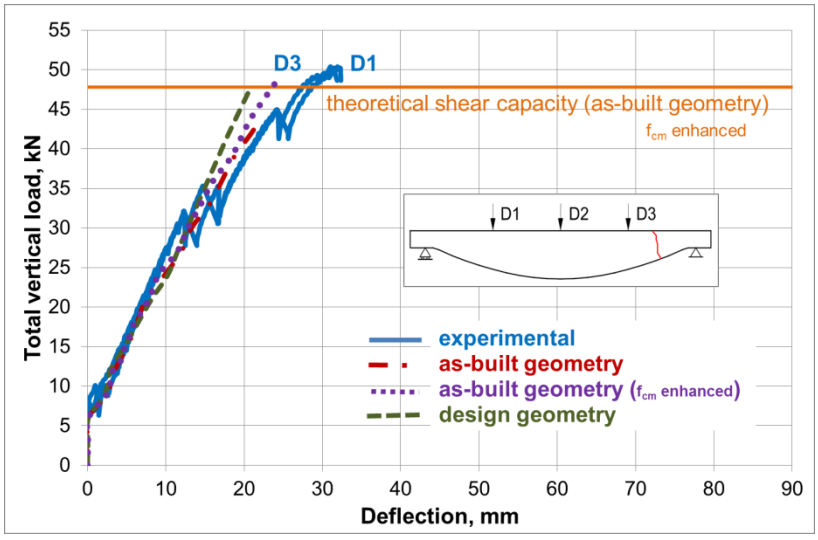

b.

Figure 6.55. FFB 7 Load-deflection relation: (a) at midspan and (b) at quarter span

All theoretical curves for beam FFB 8, presented in *Figure 6.56*, predict a fairly similar load-deflection response, particularly at midspan, with a major variation only in the calculated ultimate capacities. Nevertheless, the theoretical curves overestimate the beam stiffness for loads above approximately 40% of the maximum load and would not be appropriate to predict deflections for higher serviceability loads.

Overall, it can be concluded that the proposed load-deflection analysis shows reasonably successful results for determining the deflections of fabric-formed beams under serviceability conditions, which was the main objective defined in § 4. However, as demonstrated in § 5 the shape-optimised beams are more flexible compared with uniform rectangular beams of the same strength and, in fact, can be less efficient in terms of material use than rectangular beams of equivalent stiffness. Therefore, it would be more appropriate to demonstrate that fabric-formed beams designed for ultimate strength capacity can still satisfy the standard serviceability criteria for deflections.

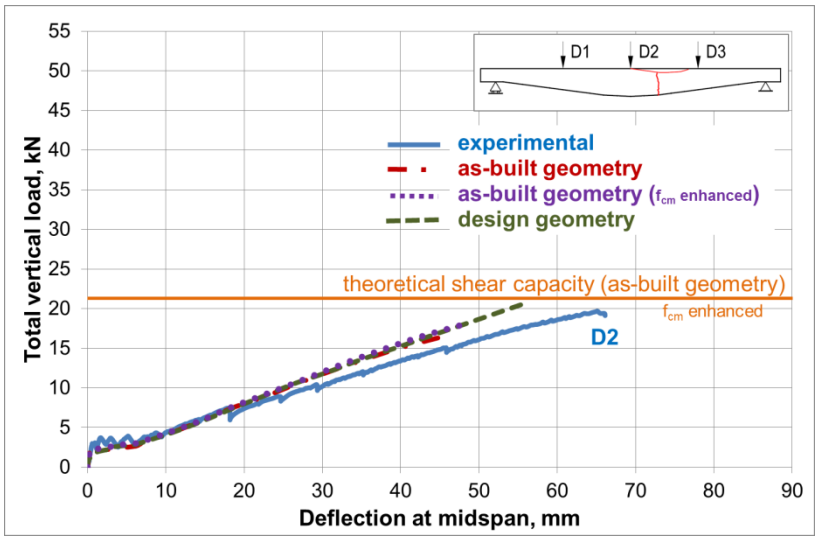

a.

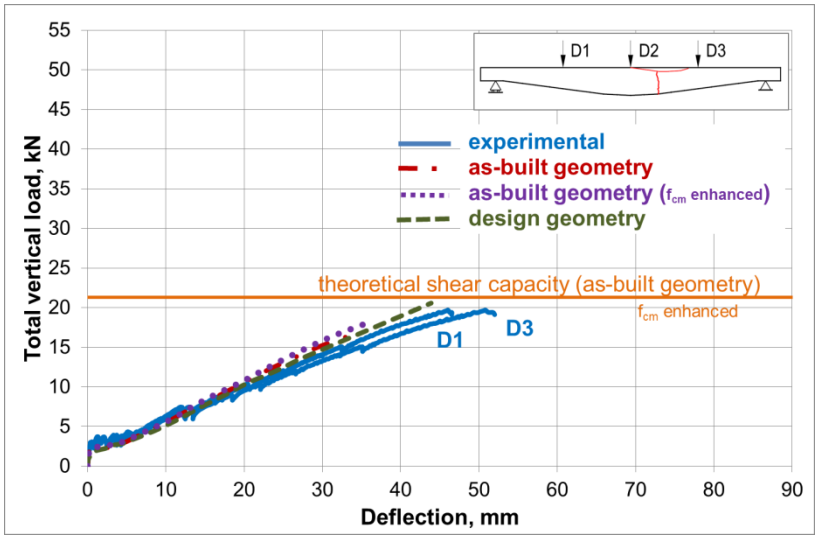

b.

Figure 6.56. FFB 8 Load-deflection relation: (a) at midspan and (b) at quarter span

The deflections of the test beams have been checked against the limits provided in the Eurocodes. In accordance with BS EN 1992-1-1:2004, the deflection of a beam subjected to quasi-permanent loads should not exceed span/250 limit for appearance and general

utility of structures. Thus, in order to obtain the deflection values from the theoretical and experimental curves for each specimen, it is required to determine the ratio of the quasi-permanent load to the maximum load, corresponding to the ultimate capacity of the beam under consideration. The maximum load at ULS (Ultimate Limit States), in accordance with BS EN 1990:2002+A1:2005, can be taken as:

$$1.35G + 1.5Q \tag{6.2}$$

where G is the characteristic value of the permanent action and Q is the characteristic value of the leading variable action, defined according to the category of the building in line with BS EN 1991-1-1:2002. The quasi-permanent combination is given by:

$$G + \psi_2 Q \tag{6.3}$$

where ψ_2 is the factor for quasi-permanent value of a variable action, again dependent on the category of the building and specified in BS EN 1990:2002+A1:2005.

Four categories of buildings are considered, namely A, B, C and D. Categories A and B represent residential and office buildings and have a ψ_2 factor of 0.3. The characteristic value of the free variable action is equal to the imposed load, assumed to be 3 kN/m^2. The ψ_2 factor for categories C and D is 0.6, applicable to congregation and shopping areas for an assumed average value of the imposed load of 5 kN/m^2. Furthermore, a superimposed load of 1.5 kN/m^2 is added to the permanent actions in order to provide a realistic assessment of the total ratio between variable and permanent actions. A summary of the loads, broken down into three components, comprising the load due to selfweight, the additional permanent and the variable loads, is shown in *Table 6.12*.

Table 6.12. Breakdown of the total ULS load into variable and permanent actions

			Category A & B		**Category C & D**	
Beam ID	Total ULS, kN	Selfweight, kN	Permanent, kN*	Variable, kN*	Permanent, kN*	Variable, kN*
FFB 5	4.5	0.60	0.85	1.70	0.58	1.94
FFB 6	35.2	1.62	7.59	15.2	5.20	17.3
FFB 7	48.2	1.66	10.6	21.1	7.24	24.1
FFB 8	18.8	0.91	4.04	8.08	2.67	8.90

* Unfactored loads

For design of beams at ULS, compliant with BS EN 1991-2-1-1:2004, in addition to the load factors in *Equation 6.2*, a material factor of 1.5 would be applied to the concrete strength. Therefore, the final ratios of the quasi-permanent and the ULS loads, presented in *Table 6.13*, are reduced by the ratio of the factored and unfactored strength capacities of each test beam. The deflection due to selfweight δ_{sw} is added to the total deflection δ_{total}, calculated for the different categories combined in two groups.

The results in *Table 6.13* indicate that only beam FFB 6 meets the deflection limits for all considered categories, which can be explained by the high stiffness of the contained CFRP reinforcing bar. The GFRP-reinforced beams are characterised in general with considerably larger vertical displacements. Nevertheless, the deflection of beam FFB 7 is well below the limit for Categories A and B, while still providing 50% material savings. This could be considered as a promising result, demonstrating the benefits of constructing a beam with 'key-hole' cross sections.

Beams FFB 5 and FFB 8 fail to satisfy the deflection criteria for the assumed distribution of permanent and variable actions. Whilst the behaviour of beam FFB 5 was found generally unsatisfactory and less predictable, beam FFB 8 is a competitive alternative to beam FFB 7 with the advantage of avoiding complex construction processes. However, the imposed limit on the top breadth-depth ratio for beam FFB 8 affects further the flexural stiffness of the beam and, as demonstrated by the results in *Table 6.13*, cannot ensure that a ULS design would satisfy the serviceability criteria.

Table 6.13. Beam deflections for quasi-permanent loads

		Category A & B			**Category C & D**		
Beam ID	δ_{sw}, mm	Q-P load/ ULS load	δ_{total}, mm	Span/ δ_{total}	Q-P load/ ULS load	δ_{total}, mm	Span/ δ_{total}
FFB 5	0.13	0.33	9.73	185	0.40	12.6	143
FFB 6	0.06	0.29	2.56	703	0.36	3.25	553
FFB 7	0.03	0.30	5.85	308	0.38	8.04	224
FFB 8	0.09	0.31	12.2	148	0.38	15.3	118

6.5.3. Experimental and predicted load-strain behaviour of FRP reinforcement

In addition to the load-deflection analysis, the load-strain relations are plotted for all midspan cross sections and compared with experimental curves. The results are presented in a format similar to the load-deflection plots, including the three types of theoretical predictions, according to the input geometry data and concrete strength, as shown in *Figure 6.57* to *Figure 6.60*. Overall, the extent of agreement between the experimental and analytical results confirms the conclusions from the load-deflection comparisons. In addition, as can be seen from the plots for beams FFB 6 and FFB 8, the cracking moment is more accurately predicted by the theoretical curves which are based on the enhanced concrete strength.

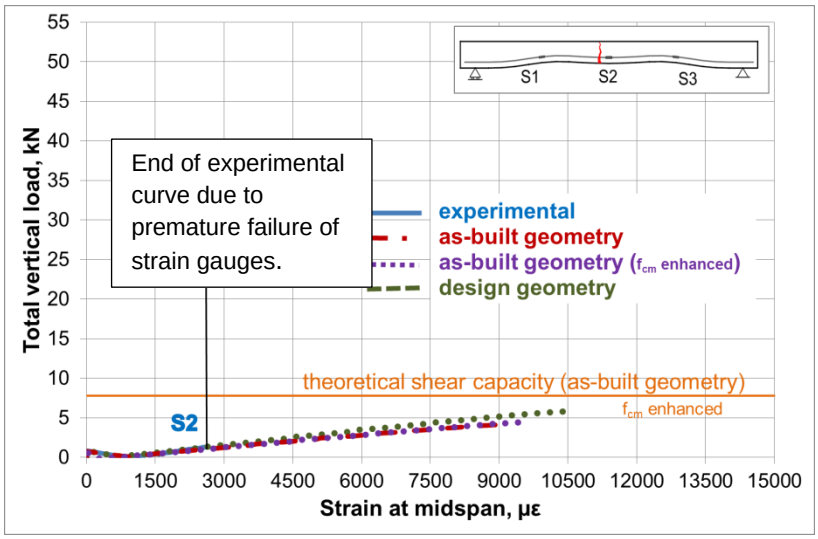

Figure 6.57. FFB 5 Load-strain relation at midspan section

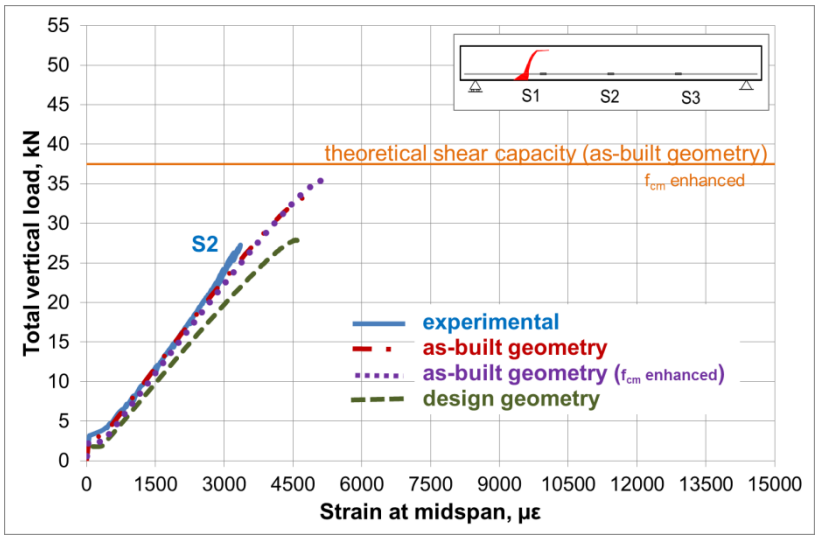

Figure 6.58. FFB 6 Load-strain relation at midspan section

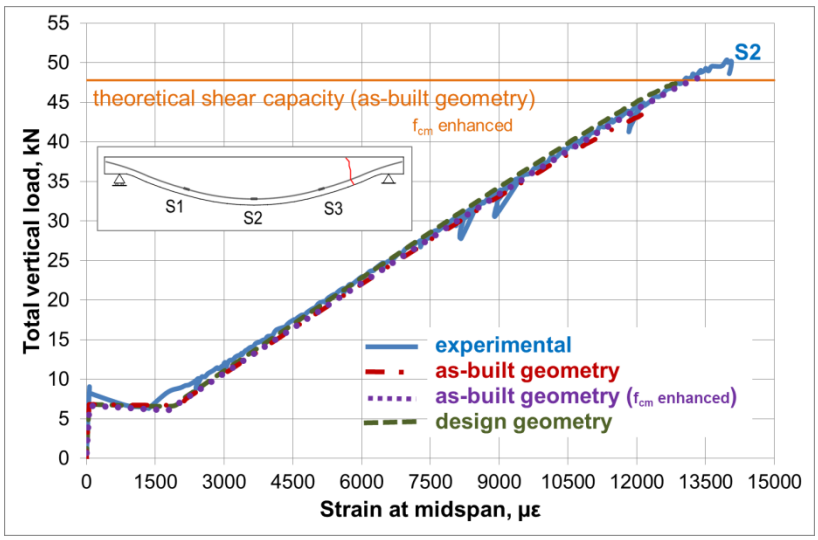

Figure 6.59. FFB 7 Load-strain relation at midspan section

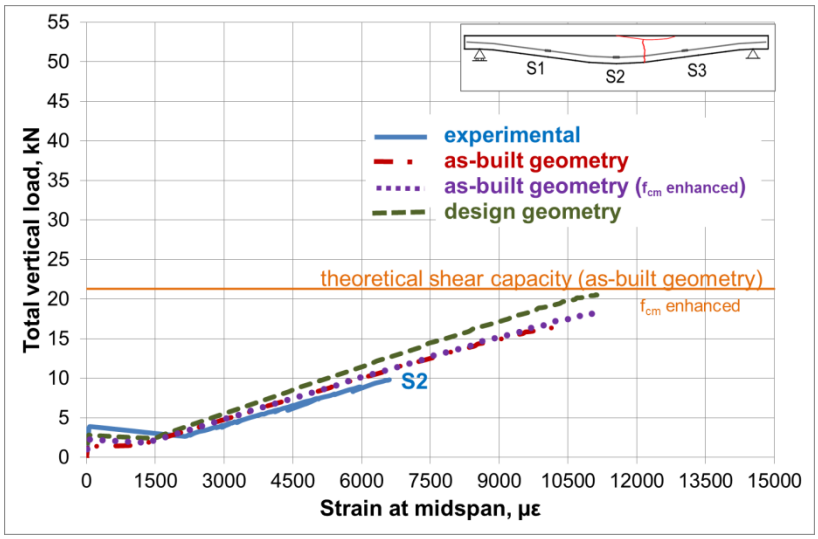

Figure 6.60. FFB 8 Load-strain relation at midspan section

6.6. Concluding remarks

This chapter has presented the findings of a study focused on investigation of the achievable construction tolerances and their effect on the structural performance of fabric-formed beams. The experimental results have also been used to validate and further enhance the outputs of the computer program, developed for the design and analysis of fabric-formed beams. The experimental investigation considered four examples of optimised test beams cast in fabric formwork. The first two designs followed a simple optimisation approach based on a single variable, such as the depth or the top breadth dimension. The remaining two cases proposed design approaches for creating most efficient forms or providing most efficient construction.

It has been demonstrated that in most cases the form-finding algorithm can successfully predict the as-built hydrostatic shapes, based on the measured overall dimensions. However, the recorded differences between the design and as-built cross-sectional profiles have been found to be significant at a number of locations. The main reason for these differences was an identified error in the form-finding input, which has been corrected and verified against the experimental results. Nevertheless, the final shapes remain highly dependent on the construction tolerances in the top breadth and the fabric hung perimeter, which naturally influence the constructed depth. Further complication arises for beams, which contain GFRP bars attached to the fabric. Although it has been shown that the shapes of cross-sections cast in a vertically restrained fabric are predictable, incorporating the additional form-finding algorithm in the design process requires a potentially complex analysis for determining the tension forces in the vertical ties. Such a design approach is proposed for the second case study, presented in § 8. It should be noted that the recorded deviations from design geometry include the inherited

inaccuracy of the adopted measurement methods, which present an additional challenge and could be a subject of future research. Furthermore, the automation of manual construction process, such as printing of fabric patterns and cutting of the top opening, could offer significant improvements and reduce the tolerances.

The limitation of using flat fabric sheets for creating complex varying shapes has also been demonstrated. In most cases, wrinkles in fabrics form interesting architectural features, however, undesirable effects such as weakening of cross sections due to excessive wrinkling should be avoided. Potentially, such effects may be predicted by specially developed software (Veenendaal and Block, 2012). Furthermore, the use of stitched flat patterns can offer greater freedom in producing complex forms and may be explored for cases where flat sheets are inappropriate. Examples of columns cast in stitched fabric are presented in § 9.

The experimental results have demonstrated a predictable load-deflection response of the fabric-formed beams up to serviceability loads, influenced to a lesser extent than expected by the deviations from the design geometry. The enhancement of the concrete strength due to the permeability of the fabric formwork has also been considered. Although it provided more accurate results for the cracking and ultimate bending moments, it had little effect on the flexural stiffness. Moreover, for beams with concrete in compression at the top, ignoring the compressive strength enhancement would be reasonable in the design for ultimate load capacity.

The assessment of the beam deflections at serviceability loads has demonstrated that fabric formwork construction utilising horizontal restraints could lead to substantial material savings without exceeding the acceptable limits for certain types of structures and applied loads. Crack widths have not been discussed in relation to serviceability criteria as it can be argued that due to the high durability of FRP reinforcement, FRP-reinforced concrete elements may be allowed to develop larger cracks than elements reinforced with steel. Nevertheless, crack widths would often also be limited for aesthetic reasons. In such cases, the shear spiral reinforcement developed and described in § 7 could provide an appropriate option for crack control reinforcement.

Finally, although the objectives of the presented study have been met to a great extent, the brittle behaviour exhibited by FRP-reinforced concrete beams remains a major disadvantage for practical applications. Therefore, the experimental investigation described in § 7 is focused on improving the ductility of FRP-reinforced fabric-formed beams through confinement of concrete in the compression zones. Methods for producing various types of spiral FRP confining and shear reinforcement are also proposed.

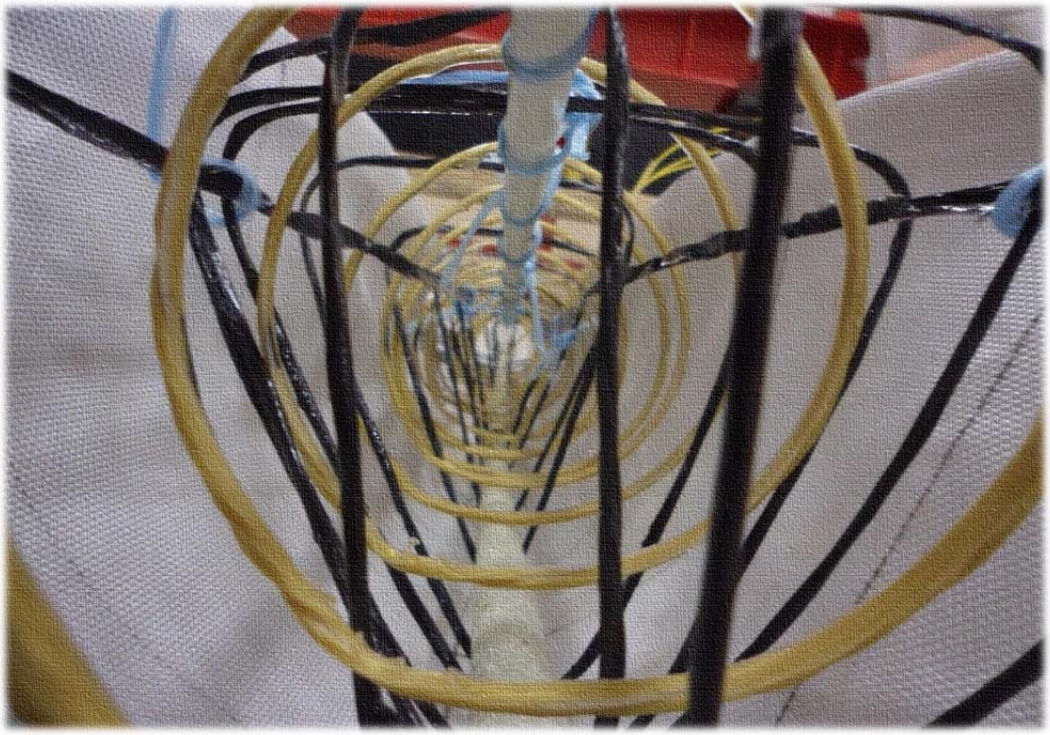

7. Improving Ductility of FRP-reinforced Fabric-formed Beams

7.1. Introduction

Developing design tools and building FRP-reinforced fabric-formed beams with predictable geometry and behaviour was a major step in demonstrating the feasibility of fabric formwork construction. However, the lack of ductility of FRP reinforcement materials remains a challenge for all practical applications. As discussed in § 2, the behaviour of FRP-reinforced beams relies on the capability of concrete to exhibit a certain degree of ductility, which can be improved considerably by means of confining reinforcement installed in the concrete compression zone. Whilst the proposed method has been successfully applied to rectangular concrete beams, no test data is available for fabric-formed beams. Therefore, the experimental investigation presented in this chapter has been undertaken in order to study the construction possibilities and provide results for theoretical analysis of fabric-formed beams, which contain confining reinforcement in the form of AFRP helices, produced by winding resin-impregnated fibres around a tube section. Further winding techniques have been investigated in order to create continuous spiral shear reinforcement fitting complex fabric-formed shapes.

7.2. Design of test specimens

Eight test specimens (Series 3) were included in the presented study (refer to *Table 7.1*). These comprised four reference beams and four test beams including confining and/or shear reinforcement. Each reference beam, denoted with R, had the same geometry and longitudinal reinforcement as the corresponding test beam.

The first pair of beams, FFB 9 and FFB 9R, was designed in order to investigate the effect of concrete confinement on the flexural behaviour of beam FFB 9. However, confining the compression zone of sections resisting the maximum bending moment effects resulted unsurprisingly in brittle shear failure near the supports, even though the specimens had been overdesigned for the shear force effects. This failure emphasised the need for provision of shear reinforcement and led to the development of two types of CFRP spiral reinforcement cages, illustrated in *Figure 7.1*. The configuration of Type A cage showed insignificant contribution to the shear capacity of specimen FFB 10 and, therefore, was further developed to create Type B cage, which could then be used in combination with confining reinforcement. Both beams FFB 11 and FFB 11R were reinforced with Type B cage in order to isolate the effect of the AFRP confining helix. Finally, test beams FFB 12 and FFB 12 R were included in the study to investigate the additional shear capacity provided by the Type B reinforcement cage.

Table 7.1. Test beam design parameters (Series 3)

Beam ID	Span, m	Total length, m	Reinforcement			Concrete cylinder strength, MPa
			GFRP flexural	CFRP shear	AFRP confining	
FFB 9R	1.8	2	1 No 12 dia (#4)	No	No	25
FFB 9					Yes	
FFB 10R	1.8	2	2 No 16 dia (#5)	No	No	16
FFB 10				Type A		
FFB 11R	1.8	2	1 No 10 dia (#3)	Type B	No	16
FFB 11					Yes	
FFB 12R	1.8	2	1 No 12 dia (#4)	No	No	16
FFB 12				Type B		

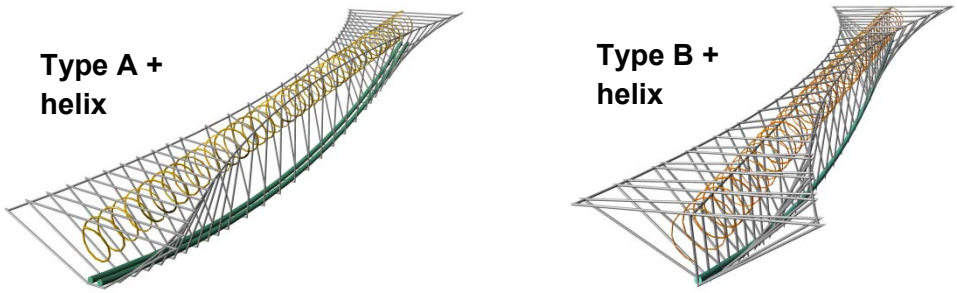

a.

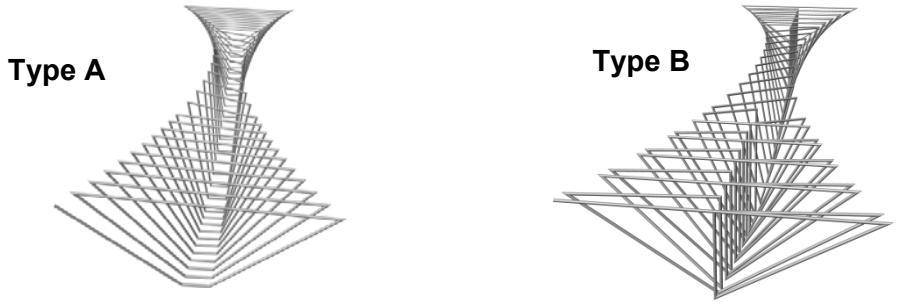

b.

Figure 7.1. Reinforcement cage types: (a) full cage and (b) shear spiral alone

7.2.1. Materials

7.2.1.1. Concrete

The concrete mix design followed the procedure described in § 5, using the same aggregate materials and cement type. However, the workability of the concrete mixes was increased by the addition of superplactiser, when required. All mixes in *Table 7.2* were based on the same free water content. The 16 MPa concrete mix was redesigned for the last four specimens to allow for increased proportion of the fine aggregates and improved flow through the dense reinforcing cages.

Table 7.2. Concrete mixes (Series 3)

Beam ID	Water	Cement	W/C ratio	Fine aggregates	Coarse aggregates
FFB 9R & 9	205 l/m^3	402 kg/m^3	0.51	811 kg/m^3	992 kg/m^3
FFB 10R & 10	205 l/m^3	387 kg/m^3	0.53	873 kg/m^3	945 kg/m^3
FFB 11, 11R, 12 &12R	205 l/m^3	383 kg/m^3	0.57	923 kg/m^3	922 kg/m^3

7.2.1.2. Reinforcement

Three types of reinforcement were used. The longitudinal reinforcement consisted of commercially available GFRP sand-coated V-Rod HM bars, produced by Pultrall Inc (Pultrall, 2011). The manufacturer's data, as well as the measured moduli of elasticity, are presented in *Table 7.3*. The minimum allowable radii for field-bending of straight bars are based on the limit of 20% sustained stress recommended in ACI 440.1R-06. The confining reinforcement was made of manually impregnated-with-resin aramid fibres, wound and set in a helical shape of 90 mm diameter and 30 mm pitch. A stress-strain diagram corresponding to the concrete confined by this type of reinforcement and based on previous research results, is proposed in § 4.

Table 7.3. Reinforcing GFRP V-Rod bars properties (Series 3)

	10 mm (#3)	12 mm (#4)	16 mm (#5)
Tensile strength, MPa	1372	1312	1184
Tensile modulus of elasticity, GPa	65.1±2.5	65.6±2.5	62.6±2.5
Tensile strain, %	2.11	2	1.89
Nominal cross-sectional area, mm^2	71.3	126.7	197.9
Nominal diameter, mm	9.53	12.7	15.99
Minimum allowable radius, mm	900	1497	2034
Measured tensile modulus, GPa	78.5	69.2	n/a

The shear reinforcement was produced in a similar manner, using carbon fibre tow Sigrafil C Type from SGL Group. Nevertheless, the resulting shapes were more complex than that of the confining helices, and are referred to more generally as spiral shear reinforcement or spiral cages. The ultimate strength of the impregnated fibre was tested by Walkin (2013), which for a single tow was found to be 2672 MPa, based on a diameter of 1.065 mm, determined by weighing a sample of known length and density. The calculated ultimate strain at failure was 1.3% (Walkin, 2013).

7.2.1.3. Fabric formwork

All test beams were cast in a single layer fabric (refer to *Table 5.4*), following the construction methods described in § 5 and § 6.

7.2.2. Geometry details

The geometry of each pair of test beams was determined by optimisation for pre-defined construction constraints and load effects from pre-defined loads, similarly to the previous test series and using the developed MATLAB program. Furthermore, the specimens were designed to fail in a particular mode and, therefore, factors of safety were applied to the design resistances which were not anticipated to govern the failure. The overall dimensions of all beam specimens are presented below, while detailed dimensions defining the design sections along the length can be found in § 7.3.2. The reinforcement details are provided in § 7.2.3.

7.2.2.1. Beams FFB 9R and FFB 9

The design of beams FFB 9R and FFB 9 aimed to provide a comparison between the ultimate bending moment resistances and load-deflection behaviour of beams with unconfined and confined concrete in compression, respectively. Therefore, it was decided to test the beams under three-point bending, as indicated in *Figure 7.2*. The depth profile of the beams was optimised for the bending moment effects based on the unconfined concrete model. A factor of safety of 1.25 was applied to the required shear resistances and used to optimise the top breadth profile. The design load corresponding to the optimised geometry was 17 kN.

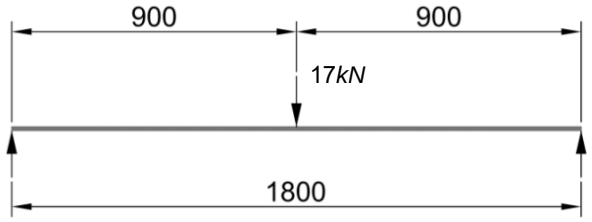

a.

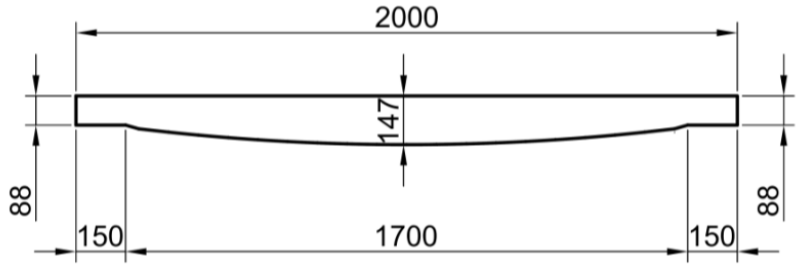

b.

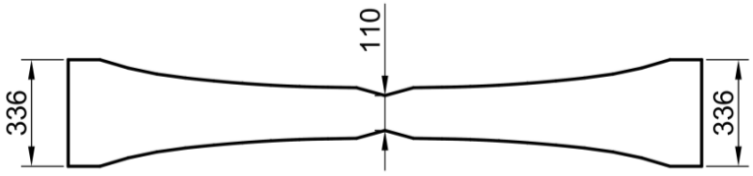

c.

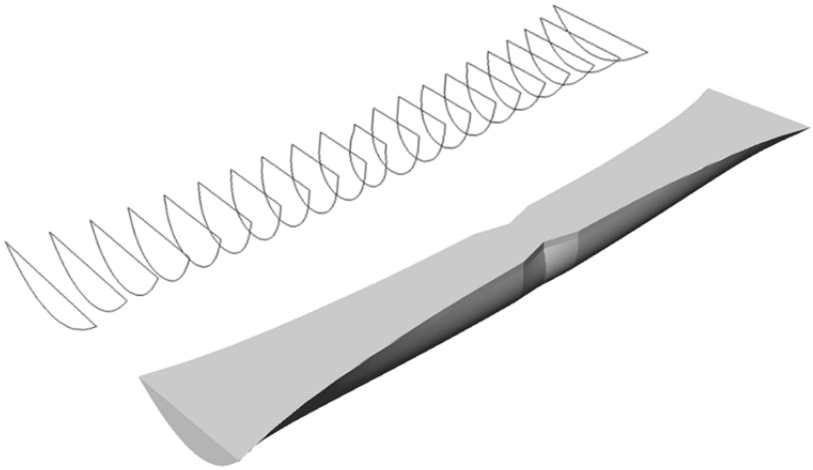

d.

Figure 7.2. FFB 9R and FFB 9 geometry details: (a) loading arrangement, (b) elevation, (c) plan and (d) perspective view (all dimensions are in mm)

7.2.2.2. Beams FFB 10R and FFB 10

The next pair of beams FFB 10R and FFB 10, shown in *Figure 7.3*, was designed to determine the efficacy of the proposed spiral shear reinforcement to be used in combination with confining reinforcement for test beam FFB 11, discussed later. The shear reinforcement was required to provide additional shear resistance and to ensure flexural failure without designing unreasonably large sections near the beam supports. The loading arrangement was changed to the typical five-point bending used for the previous experiments. Furthermore, the geometry of the shear spans of beams FFB 10R and FFB 10 was set to be the same as for beams FFB 11R and FFB 11. This could allow the direct addition of the measured contribution of shear reinforcement to the design strength of beam FFB 11.

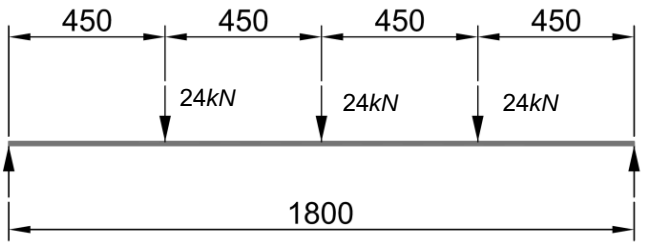

a.

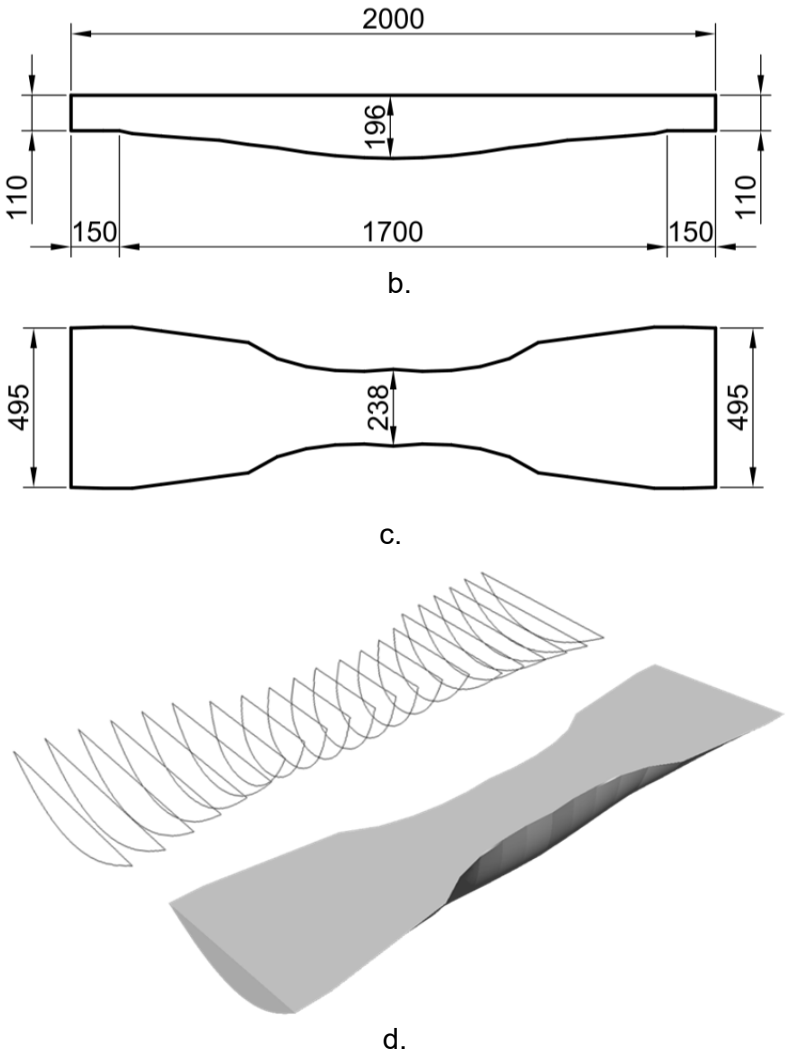

Figure 7.3. FFB 10R and FFB 10 geometry details: (a) loading arrangement, (b) elevation, (c) plan and (d) perspective view (all dimensions are in mm)

The concrete shear resistance of beams FFB 10R and FFB 10 was found to be approximately 13.5 kN, based on 16 MPa cylinder concrete strength and two CFRP longitudinal bars of 16 mm dimeter (#5). The bending moment resistance was then factored by 1.8 to allow for up to 80% increase in the ultimate shear resistance due to shear reinforcement, predicted by theoretical calculations. Therefore, the design loads indicated in *Figure 7.3* refer to the loads used to design and optimise the middle half of the beams for bending moment effects in order to ensure shear failure. The test results, however, were not satisfactory (as will be discussed later) and a different type of spiral cage was used to reinforce beams FFB 11R and FFB 11 in shear.

7.2.2.3. Beams FFB 11R and FFB 11

The geometry of beams FFB 11R and FFB 11 (see *Figure 7.4*) was determined by optimisation for bending moment effects, based on the unconfined concrete model,

followed by optimisation for shear force effects similarly to the design of beams FFB 9 and FFB 9R. The concrete shear resistance was again designed for a factor of safety of 1.25. However, it was expected that the addition of the shear reinforcement would further ensure a flexural failure mode, required to study the effect of concrete confinement on the flexural behaviour of test beam FFB 11.

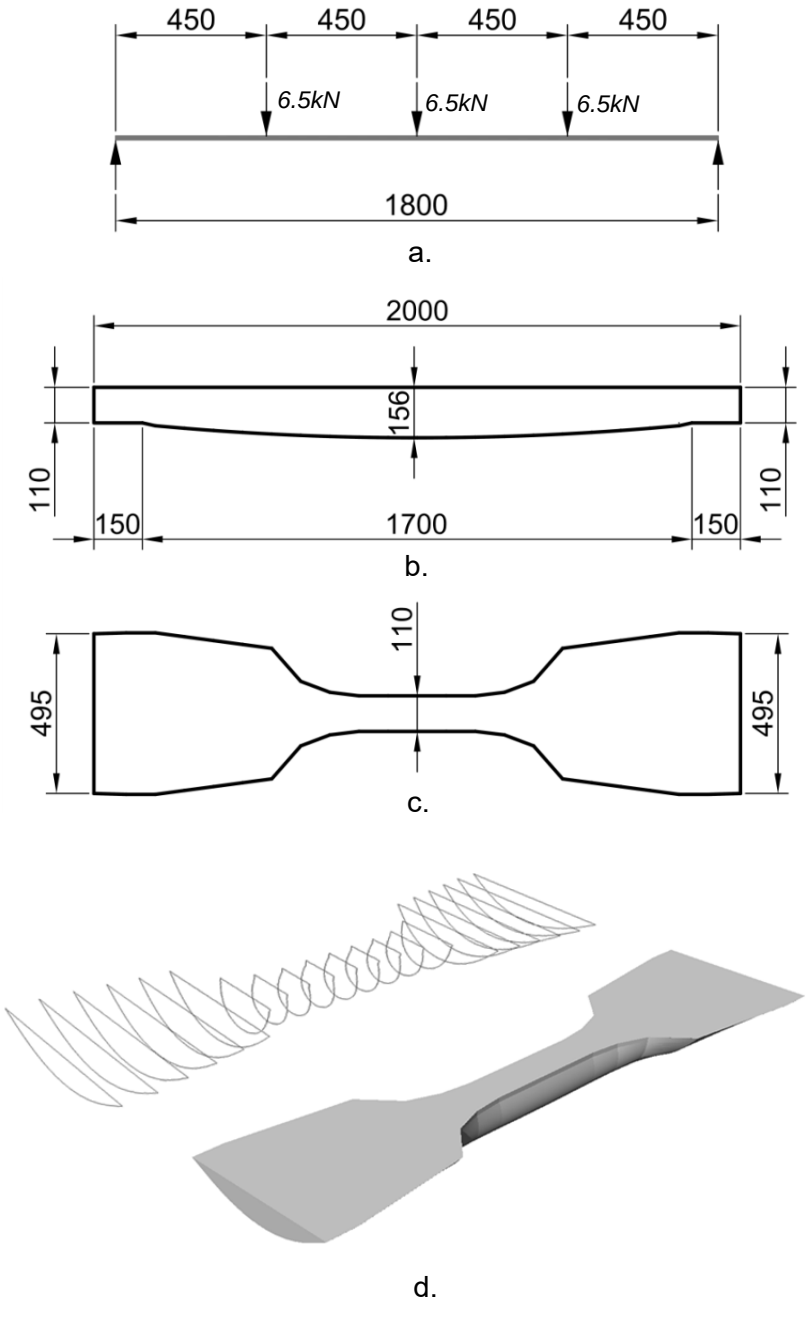

Figure 7.4. FFB 11R and FFB 11 geometry details: (a) loading arrangement, (b) elevation, (c) plan and (d) perspective view (all dimensions are in mm)

7.2.2.4. Beams FFB 12R and FFB 12

As predicted, both beams FFB 11R and FFB 11 failed in flexure near midspan. Therefore, it was not possible to determine the actual contribution of Type B spiral shear

reinforcement to the shear capacity of the beams. For completeness of the study, beams FFB 12R and FFB 12 were designed to compare the ultimate shear resistances of a beam containing no shear reinforcement and a beam reinforced with Type B spiral. The shape of the beams was fully dictated by the bending moment diagram under the design loads, shown in *Figure 7.5*. The ratio of the bending moment and the concrete shear resistances was approximately 4. The ratio of the bending moment resistance against the ultimate shear capacity, including the predicted contribution of shear reinforcement was 1.5. Therefore, it was expected that both test specimens would fail in shear.

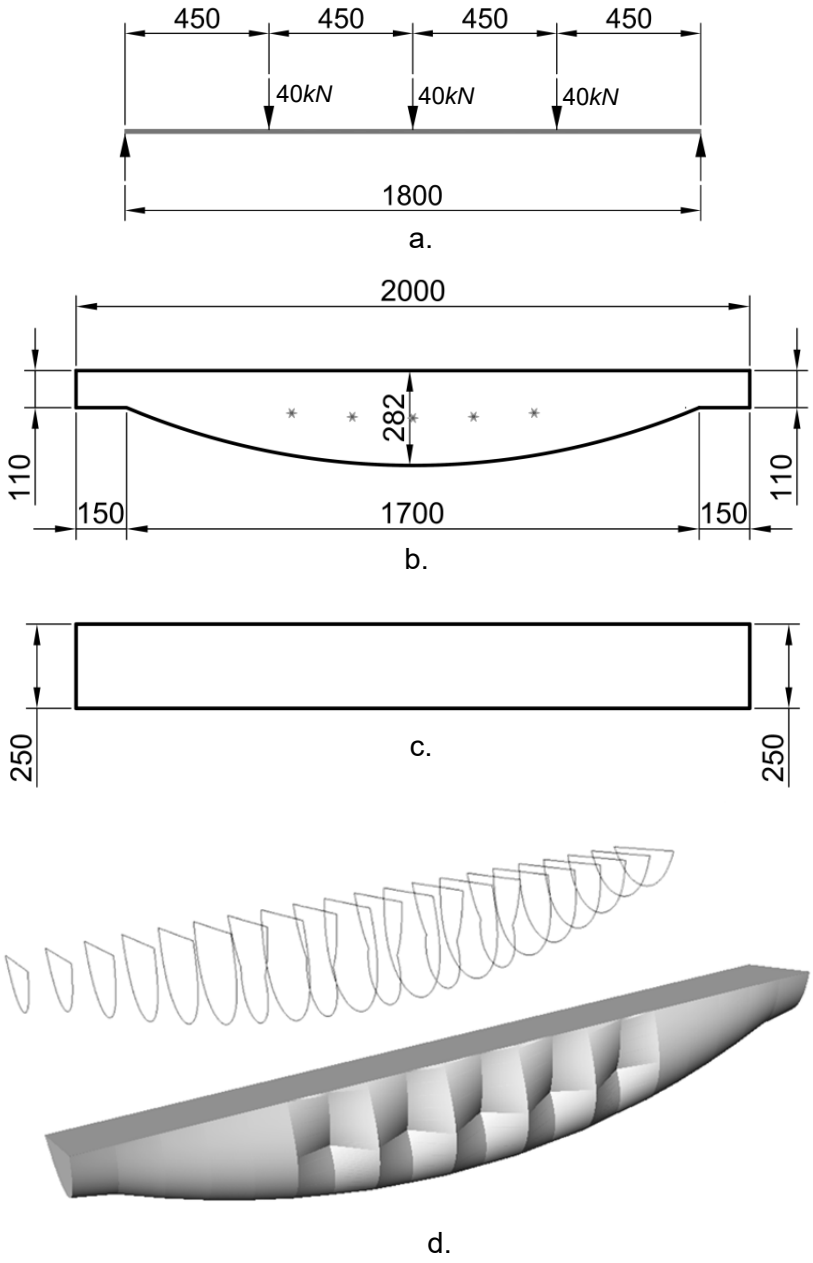

Figure 7.5. FFB 12R and FFB 12 geometry details: (a) loading arrangement, (b) elevation, (c) plan and (d) perspective view (all dimensions are in mm)

7.2.3. Reinforcement details

The reinforcement details, presented in *Figure 7.6*, combined the three types of reinforcement, namely longitudinal, confining helix and shear spirals. The main longitudinal reinforcement comprised various sizes of commercially available GFRP sand-coated rods. In addition to being more cost effective, the straight GFRP bars could be installed more easily in curved shapes than CFRP bars, as demonstrated previously. Small size GFRP or CFRP leftover bars, the compressive strength of which was ignored, were used as top reinforcement for fixing the cages.

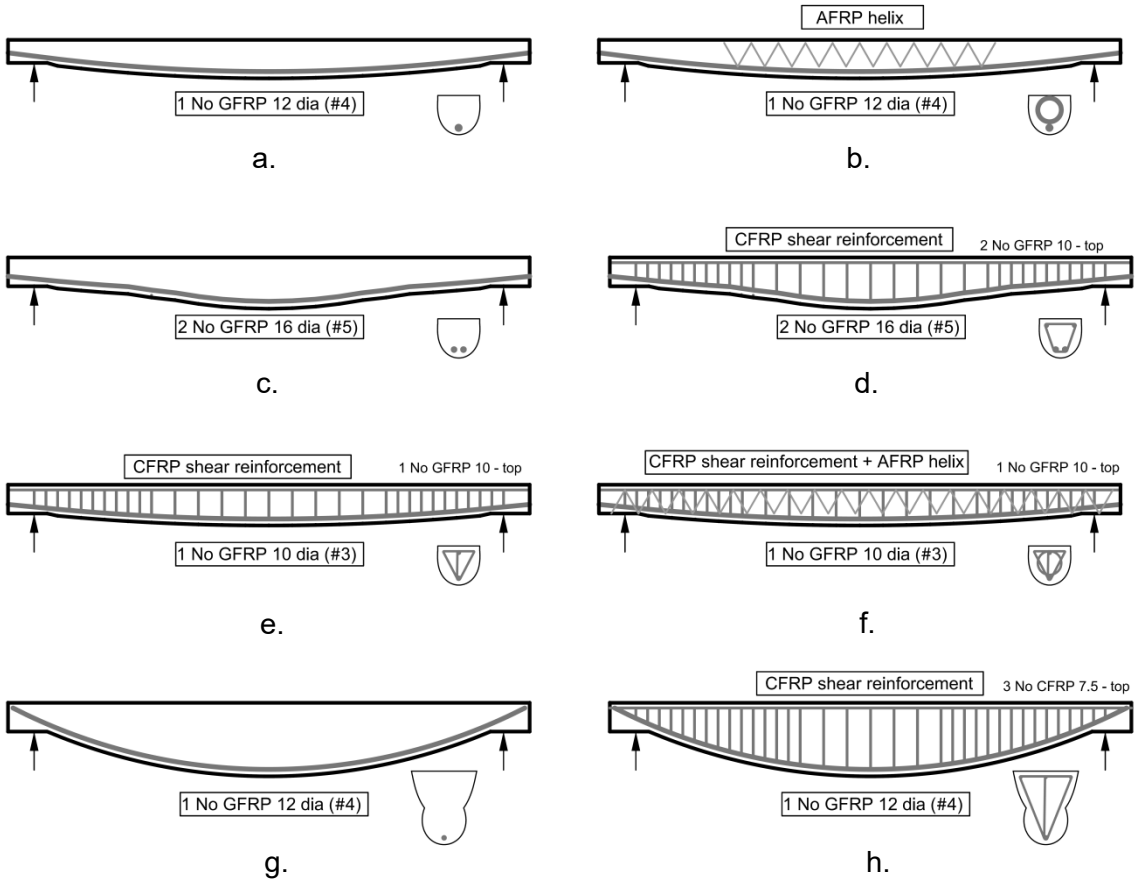

Figure 7.6. Reinforcement details (Series 3): (a) FFB 9R, (b) FFB 9, (c) FFB 10R, (d) FFB 10, (e) FFB 11R, (f) FFB 11, (g) FFB 12R and (h) FFB 12

The AFRP confining reinforcement was produced from aramid fibres using the already established method, presented in § 3. Moreover, the available stress-strain relations for concrete confined by the same type of reinforcement could be used for theoretical analysis without the need of further testing. Similarly, the choice of CFRP shear reinforcement was related to a parallel research project studying rectangular spiral reinforcement for prismatic beams (Walkin, 2013). As well as using the readily available

material test results, the CFRP spiral cages made of thin fibre tow offered the benefit of low material consumption and fast production of unique shapes.

The design concrete cover to the longitudinal reinforcement was typically 20 mm. Only the first pair of beams FFB 9R and FFB 9 used internal ties for attaching the bars to the fabric. For the rest of the specimens the final reinforcement shapes were formed prior to pouring of the fresh concrete by means of externally attached ties (as previously shown in *Figure 5.17*). The minimum bend radii of the main longitudinal reinforcement for the four pairs of test beams, in the order given in *Figure 7.6*, were: 7019 mm, 2147 mm, 8982 mm and 2165 mm, which were below the limits, specified in *Table 7.3*.

The CFRP spiral cages for beams FFB 10R and FFB 10 were made of a single carbon fibre tow, which provided little enhancement of the ultimate shear resistance. Therefore, it was decided to increase the thickness of the fibre by using a double fibre tow for the rest of the specimens. Construction details of the two type of cages are presented in § 7.3.

7.2.4. Utilisation

The geometry of the reference beams was optimised for the applied load effects and used for both beams in each pair. The distribution of concrete material and the final shapes of the specimens were also influenced by the factors of safety applied to the design resistances in order to ensure a particular type of failure, as explained. Therefore, the utilisation plots in *Figure 7.7* include the spare shear or bending moment capacities along the length of each reference beam.

The material savings for each reference beam were calculated using *Equation 6.1*, based on comparison with ‘equivalent strength’ rectangular beams. The dimensions of the rectangular sections were determined for fixed depths equal to the maximum overall depths of the fabric-formed beams with the exception of beam FFB 12R, which had a uniform top breadth. As can be seen from the results presented in *Table 7.4*, the concrete savings varied between 23% and 45%. This could be attributed to the different applied factors of safety as well as the different loading arrangement for beam FFB 9R.

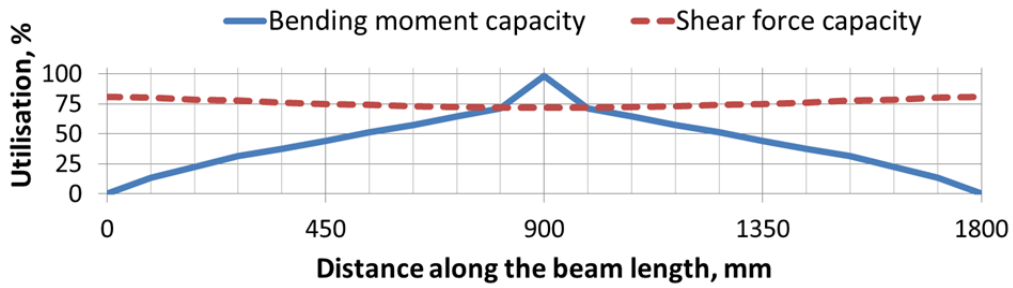

a.

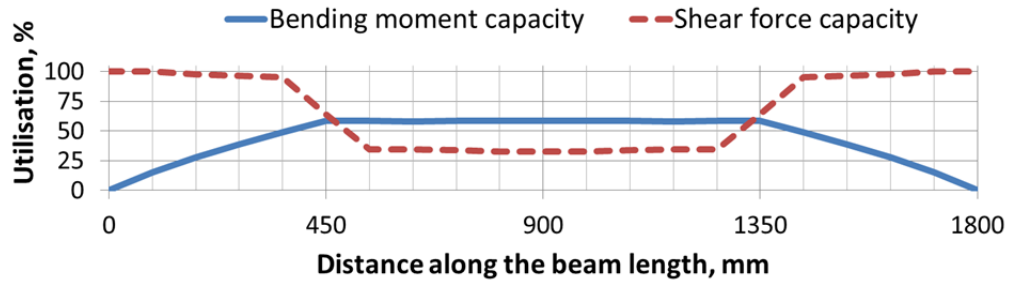

b.

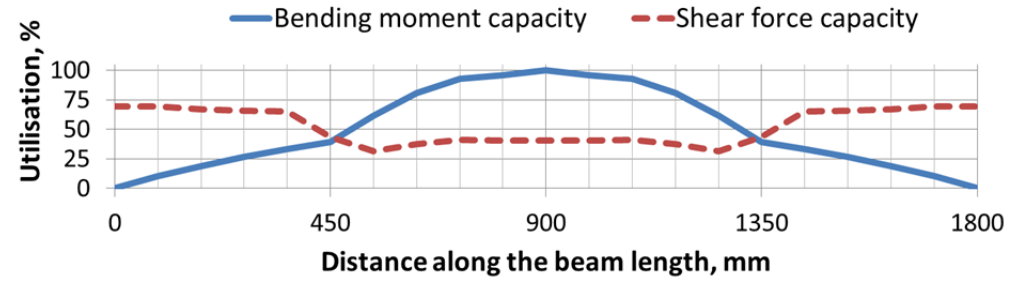

c.

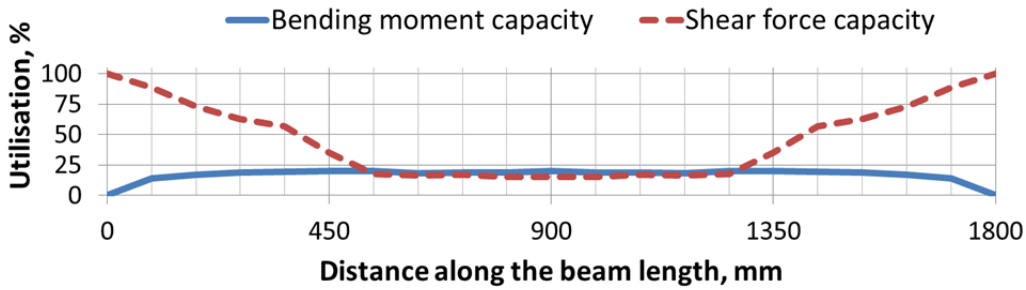

d.

Figure 7.7. Capacity utilisation: (a) FFB 9R, (b) FFB 10R, (c) FFB 11R and (d) FFB 12R

Table 7.4. Concrete material savings

Beam ID	Equivalent strength rectangular beam	Material savings
FFB 9R	B=170 mm, D=147 mm	23 %
FFB 10R	B=253 mm, D=196 mm	24 %
FFB 11R	B=361 mm, D=156 mm	45 %
FFB 12R	B=250 mm, D=284 mm	41 %

7.2.5. Instrumentation and test set-up

The vertical displacements were measured at midspan and at the quarter points during the load testing of each beam. The strains in the FRP bars were measured at the same positions, as shown in *Figure 7.8*, with the exception of beams FFB 10R and FFB 10, which were designed to determine the shear resistance of Type A spiral cages by a direct comparison of the ultimate shear capacities so that no strains were recorded. Additional gauges were used to record the strains in the anchorages (*Figure 7.8a* and *Figure 7.8d*) for beams where significant stresses could be expected, such as FFB 12R and FFB12.

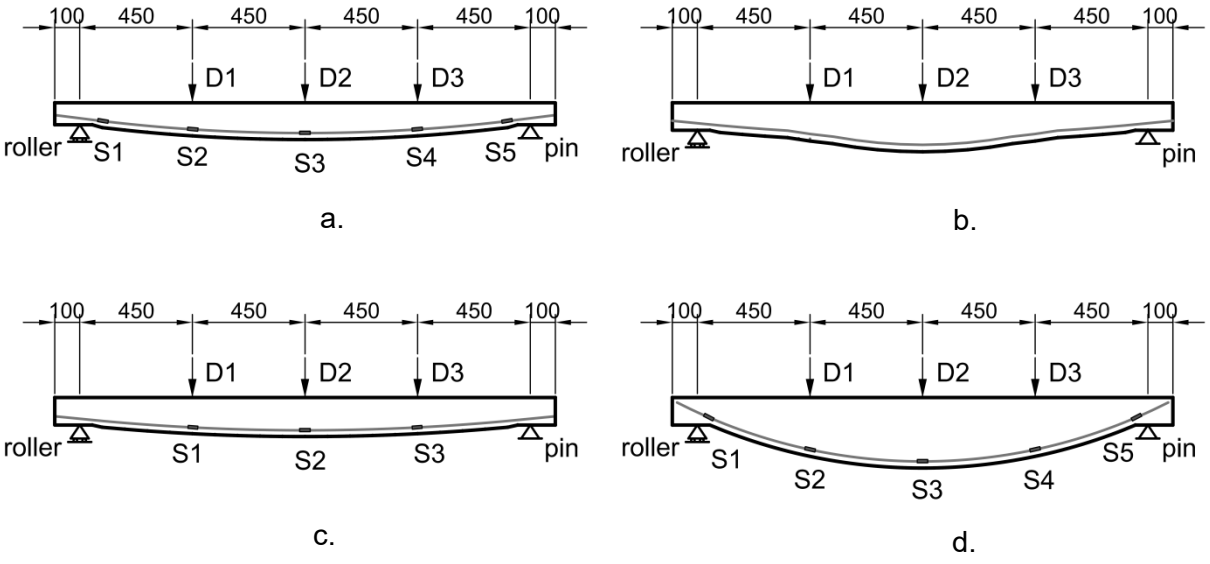

Figure 7.8. Test set-up (Series 3): (a) FFB 9R and FFB 9, (b) FFB 10R and FFB 10, (c) FFB 11R and FFB 11 and (d) FFB 12R and FFB 12

7.3. Construction of test specimens

7.3.1. Formwork details

The specimens were cast in pairs, such that each pair comprised a test beam and its corresponding reference beam. The formwork was assembled from new table top plates fixed onto the existing frame supports, described in § 5 (see *Figure 7.9*). The single layer fabric was stapled along the top plate edges and to the plates forming the flat bottom surfaces at the supports. Timber spacers were used to maintain the lateral distance between the two reinforcing bars in beams FFB 10R and FFB 10. In addition to the vertical ties, standard plastic cover formers were also attached to the reinforcing bars to secure their position against rigid surfaces, such as the end plates, shown in *Figure 7.9*.

Despite the dense reinforcement in many specimens, the concrete was easily compacted through the fabric externally.

Figure 7.9. Formwork set-up (Series 3)

7.3.2. Construction parameters

The construction parameters, previously described in § 5.3.2, for each pair of test beams are presented in *Table 7.5* to *Table 7.8*. The distance x_L, measured from the left support, is later used to identify the location of as-built sections along the longitudinal axis of a beam.

Table 7.5. FFB 9R and FFB 9 construction parameters

x_L	B	D	d_{eff}	B_{web}	D_b	h_{web}	P	P_b	T, N/m
0	336	88	62	NOT USED	NOT USED	NOT USED	388	NOT USED	336
90	283	99	73				360		277
180	245	109	83				350		247
270	221	118	92				348		236
360	202	126	100				354		232
450	188	132	106				360		232
540	175	138	112				366		233
630	167	142	116				370		234

720	162	145	119				374		236
810	159	146	120				378		237
900	110	147	121				364		197
990	159	146	120				378		237
1080	162	145	119				374		236
1170	167	142	116				370		234
1260	175	138	112				366		233
1350	188	132	106				360		232
1440	202	126	100				354		232
1530	221	118	92				348		236
1620	245	109	83				350		247
1710	283	99	73				360		277
1800	336	88	62				388		336

All dimensions are in millimetres.

Table 7.6. FFB 10R and FFB 10 construction parameters

x_L	B	D	d_{eff}	B_{web}	D_b	h_{web}	P	P_b	T, N/m
0	500	110	82	NOT USED	NOT USED	NOT USED	556	NOT USED	702
90	500	119	91				566		721
180	476	127	99				554		682
270	452	133	105				542		644
360	428	139	111				530		607
450	404	145	117				520		570
540	304	163	135				482		448
630	255	178	150				484		421
720	231	188	160				494		422
810	225	194	166				506		434
900	238	196	168				514		456
990	225	194	166				506		434
1080	231	188	160				494		422
1170	255	178	150				484		421
1260	304	163	135				482		448
1350	404	145	117				520		570
1440	428	139	111				530		607
1530	452	133	105				542		644
1620	476	127	99				554		682
1710	500	119	91				566		721
1800	500	110	82				556		702

All dimensions are in millimetres.

Table 7.7. FFB 11R and FFB 11 construction parameters

x_L	B	D	d_{eff}	B_{web}	D_b	h_{web}	P	P_b	T, N/m
0	500	110	84	NOT USED	NOT USED	NOT USED	556	NOT USED	702
90	500	119	93				566		721
180	476	127	101				554		682

270	452	133	107				542		644
360	428	139	113				530		607
450	404	145	119				520		570
540	200	149	123				398		281
630	132	152	126				382		225
720	110	154	128				382		213
810	110	156	130				384		216
900	110	156	130				386		217
990	110	156	130				384		216
1080	110	154	128				382		213
1170	132	152	126				382		225
1260	200	149	123				398		281
1350	404	145	119				520		570
1440	428	139	113				530		607
1530	452	133	107				542		644
1620	476	127	101				554		682
1710	500	119	93				566		721
1800	500	110	84				556		702

All dimensions are in millimetres..

Table 7.8. FFB 12R and FFB 12 construction parameters

x_L	B	D	d_{eff}	B_{web}	D_b	h_{web}	P	P_b	T, N/m
0	250	110	84			NOT USED	354		253
90	250	126	100				382		286
180	250	160	133				446		366
270	250	189	163				506		449
360	250	214	187				558		531
450	250	235	208				606		606
540	250	252	225	150	126		614	342	526
630	250	265	238				674		726
720	250	274	248	150	137		662	368	579
810	250	280	253				708		790
900	250	282	255	150	141		678	376	597
990	250	280	253				708		790
1080	250	274	248	150	137		662	368	579
1170	250	265	238				674		726
1260	250	252	225	150	126		614	342	526
1350	250	235	208				606		606
1440	250	214	187				558		531
1530	250	189	163				506		449
1620	250	160	133				446		366
1710	250	126	100				382		286
1800	250	110	84				354		253

All dimensions are in millimetres.

7.3.3. Reinforcement preparation and installation

The longitudinal bars were sand-coated by the manufacturer and required only preparation of the end splayed anchorages, formed by resin-glued 100 mm 2˚ carbon fibre wedge plates (see *Figure 7.10*). The bars were then strain-gauged and positioned inside the fabric formwork alone or as part of the reinforcing cages.

The method of installation of the helical AFRP reinforcement depended on whether the final shape of the longitudinal bars was pre-set or formed under the weight of the fresh concrete. In the former case, relevant to the construction of beam FFB 11, the helix was simply tied to the CFRP reinforcement cage before the concrete was cast. The construction of beam FFB 9, which represented the latter case, required fixing the AFRP helix only after the weight of the poured concrete was sufficient to pull down the longitudinal bar below the position of the confining reinforcement. Although the procedure was easily managed in laboratory conditions, it was recognised that it would be unsuitable for practical applications.

a. b.

Figure 7.10. Splayed anchored V-Rod bars: (a) side elevation and (b) end section

Several ideas for producing CFRP spiral reinforcement for fabric-formed beams were considered. These included dividing the continuous spiral into a number of overlapping tapered spirals of straight lengths, producing continuous spiral to be tied to the longitudinal bars and winding freshly impregnated carbon fibre directly onto the longitudinal bars. The last two methods were applied for the production of Type A and Type B cages. Type A spiral was formed separately onto a fixed frame. As can be seen in *Figure 7.11*, it had a trapezoidal cross-sectional shape, uniform top and bottom width, and varying depth. The pitch of the spiral was 45 mm over the end quarters of the beam and 90 mm near midspan. The spiral was fixed to the longitudinal bars using plastic zip ties. Type B spiral had the same pitch and was produced in a similar manner to Type A for beams FFB 11R and FFB 11. The major difference between the two reinforcement types was the vertical leg of Type B, which made the spiral suitable for triangular shapes, comprising a single longitudinal bar in tension (see *Figure 7.12*). Furthermore, for Type B

spiral, the plastic zip ties were replaced with softer hand-tied plastic strings in order to avoid possible damage to the impregnated carbon fibre.

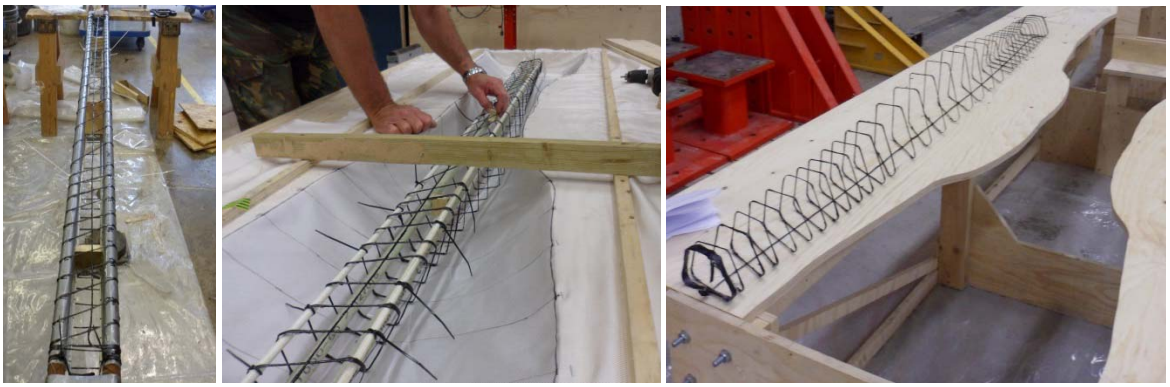

Figure 7.11. Type A CFRP spiral reinforcement

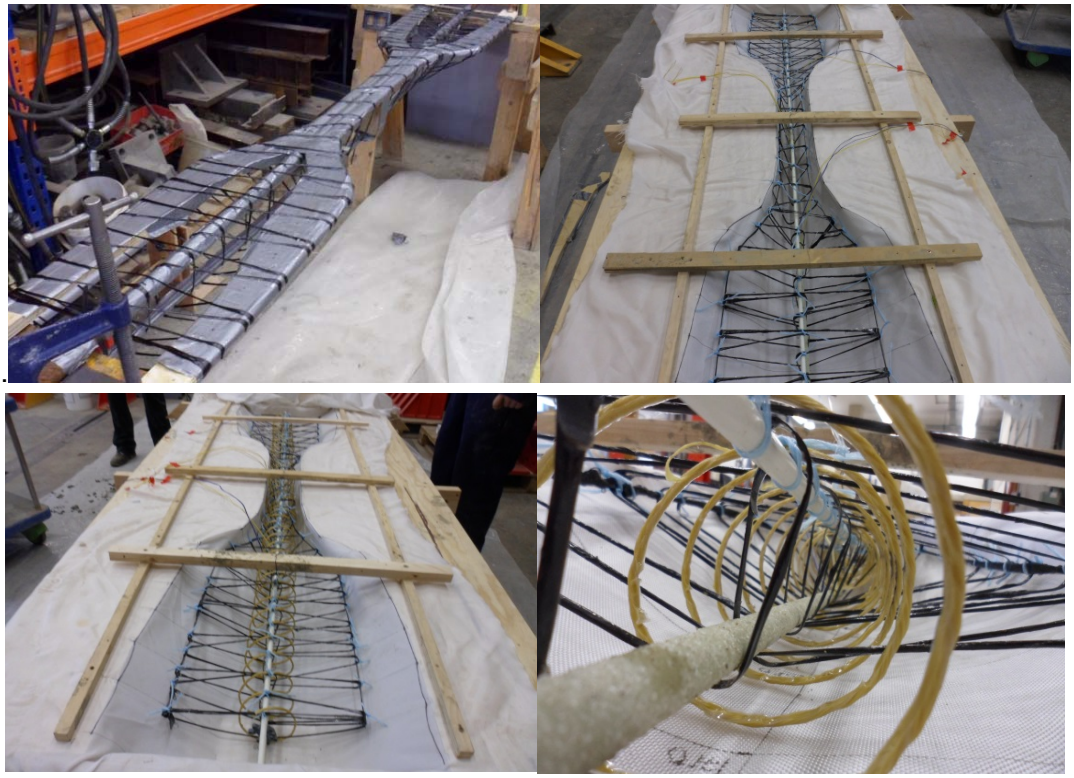

Figure 7.12. Type B CFRP spiral reinforcement and AFRP helix

A further development of Type B spiral reinforcement involved winding the fibre tow directly onto the longitudinal bars, set into their final shape. However, this method would not be practical for field bent straight longitudinal bars. Although it was used to produce the reinforcing cage for beam FFB 12, handling and transporting the ready cage required a temporary timber support system, in order to maintain the profile of the GFRP bars, before the cage was installed inside the fabric formwork and the position of the longitudinal bars secured (see *Figure 7.13*). Once the cage was installed and the GFRP

bars tied down to external weights, the temporary support system was removed. The position of the cage was further adjusted by top cover formers.

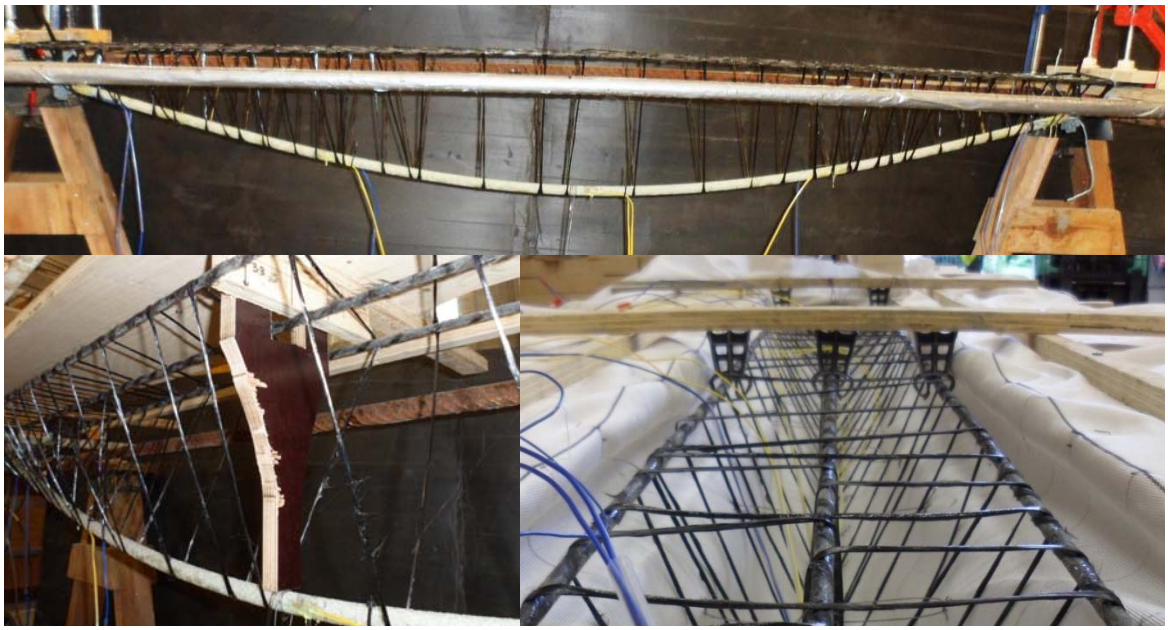

Figure 7.13. Type B CFRP spiral reinforcement wound onto the longitudinal bars

The presented methods for production of CFRP spiral cages could be improved significantly by automated manufacturing processes. Moreover, manufacturing the longitudinal bars with curved profiles could allow the creation of any complex shape without the need for additional winding frames.

7.3.4. As-built geometry

Profile gauges and saw-cutting after testing were used to obtain the profiles of selected cross-sections. The top breadth and overall depth of all other sections were measured by a tape measure and a large size vernier caliper, as described in § 5. The as-built dimensions of the specimens are presented in the following sections.

7.3.4.1. Beam FFB 9R and FFB 9

The as-built measurements of beam FFB 9R are shown in *Figure 7.14*. The dimensions in brackets indicate the minimum depths at sections with vertical ties between the fabric and the longitudinal bars. The effective depths for use in analysis were adjusted according to the measured cover at the cracked sections and the overall depths.

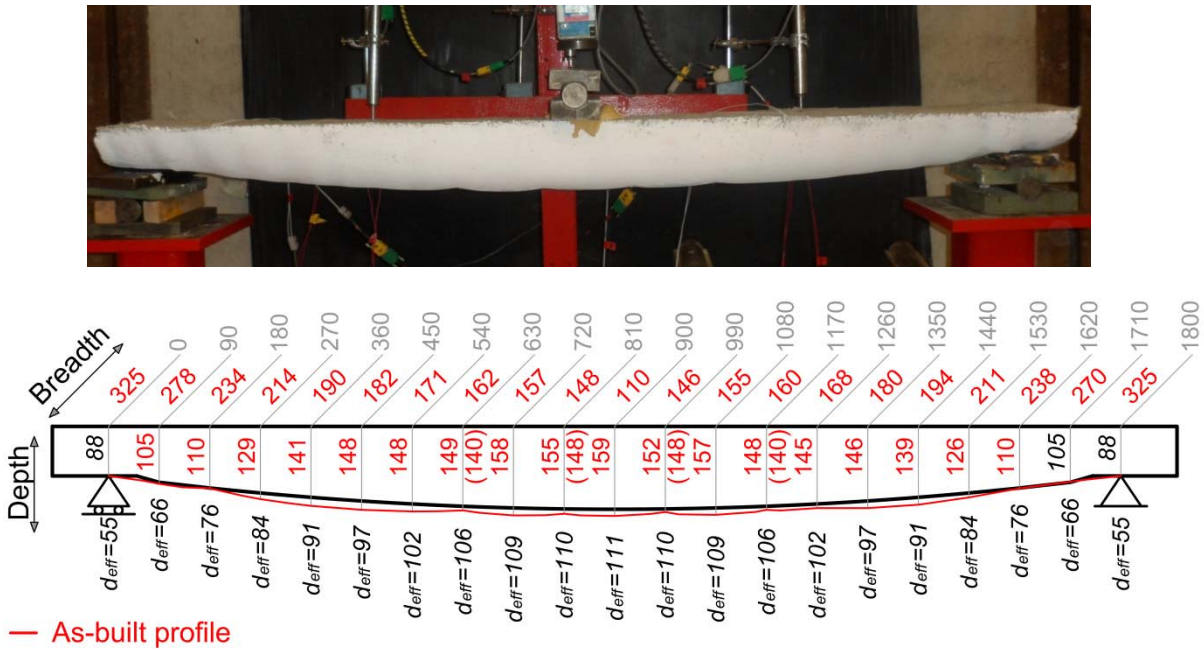

Figure 7.14. FFB 9R as-built measurements (all dimensions are in millimetres)

Figure 7.15 presents the difference between the as-built and design dimensions at each section. The average construction tolerance in the top breadth is approximately 8 mm in total or 4 mm each side, which could be considered a reasonable tolerance for manual cutting, compared to previous experiment. The reduced top breadth resulted in increased overall depth, as can be seen from the plot. However, at locations where the fabric was attached to the longitudinal bar, the difference was compensated by the lift of the fabric and the final depths were close to their design values.

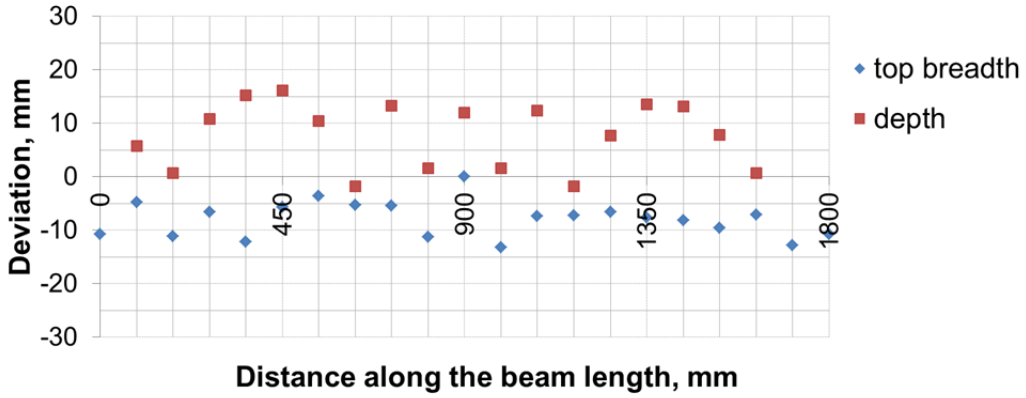

Figure 7.15. FFB 9R deviation from design geometry

The as-built dimensions of beam FFB9 are presented in a similar format in Figure 7.16. As-built cross-sectional profiles are also available and compared with the predicted design geometry in Figure 7.17. The construction accuracy of the top breadth is slightly improved in comparison with beam FFB 9R, resulting in a maximum tolerance in the depth of +/-10 mm (see *Figure 7.18*).

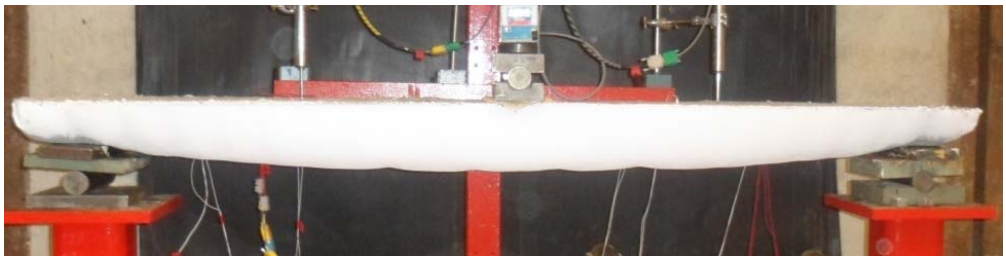

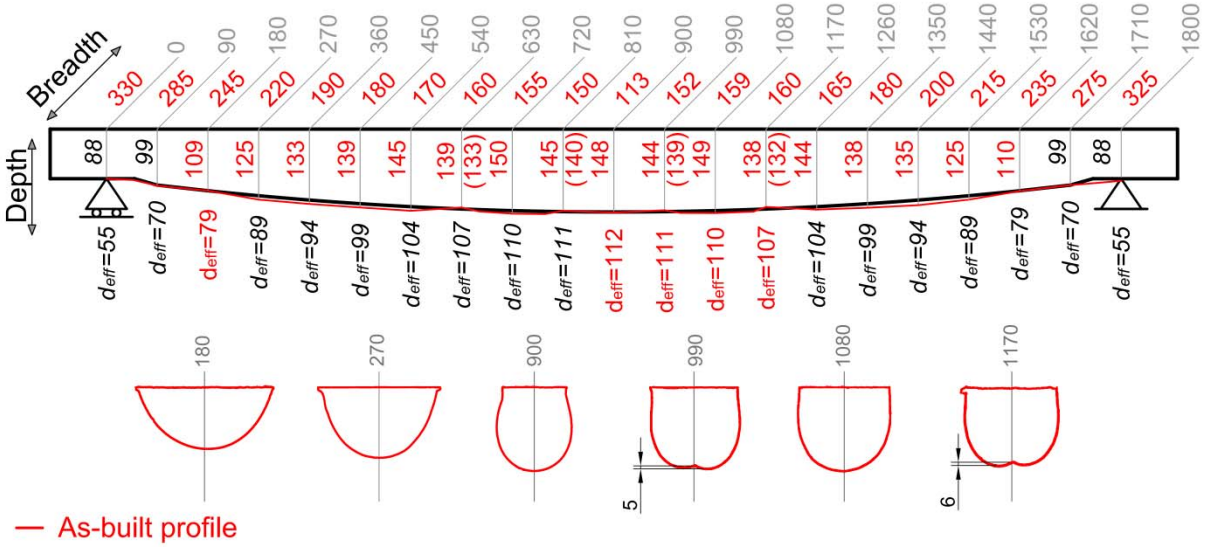

Figure 7.16. FFB 9 as-built measurements (all dimensions are in millimetres)

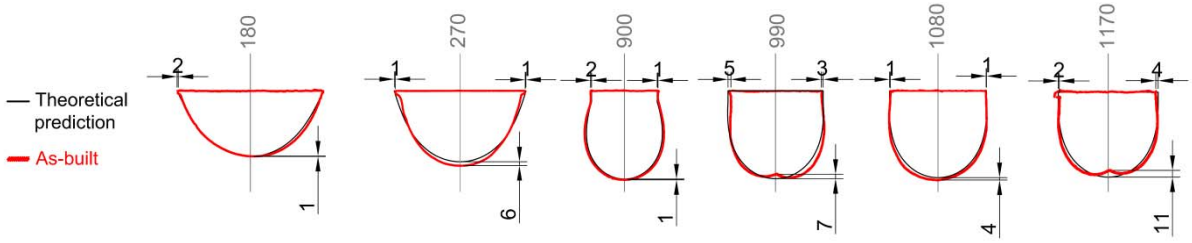

Figure 7.17. FFB 9 comparison of as-built profiles and theoretical predictions (design) (all dimensions are in millimetres)

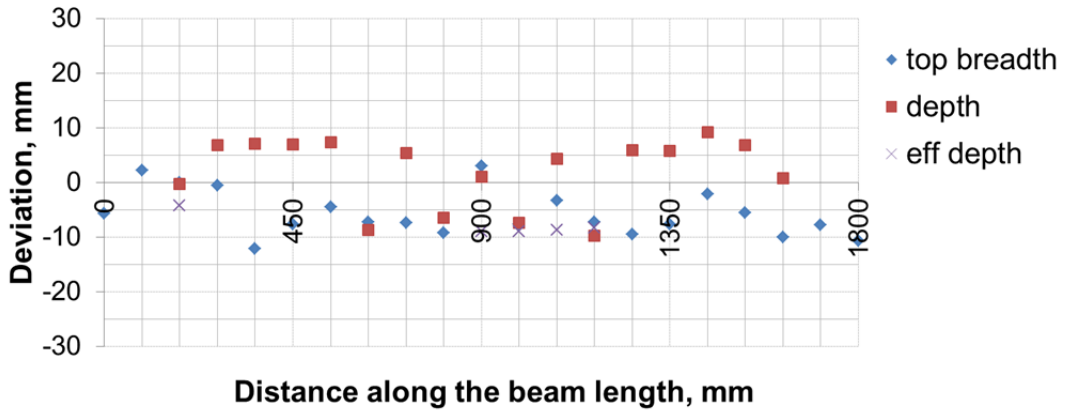

Figure 7.18. FFB 9 deviation from design geometry

The predicted cross-sectional profiles based on the measured overall dimensions are compared with the as-built profiles in *Figure 7.19*. As can be seen, the differences are relatively small.

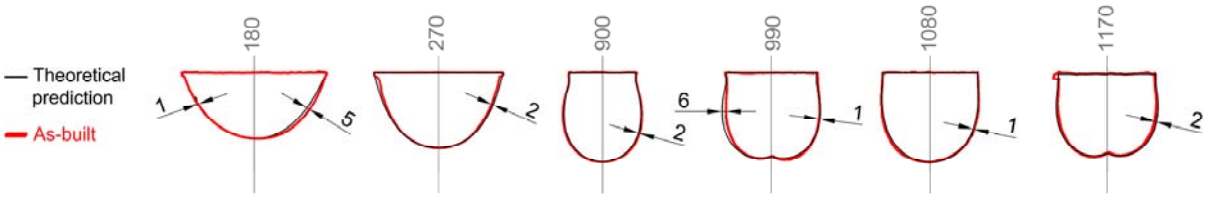

Figure 7.19. FFB 9 comparison of as-built profiles and theoretical predictions (revisited for actual overall dimensions) (all dimensions are in millimetres)

The as-built positions of the longitudinal and helical reinforcement were confirmed by examining the saw-cut sections (refer to *Figure 7.20*). As can be seen in *Figure 7.20a*, the helix remained well inside the concrete and relatively close to its design position. The top cover to the helix was 10 mm.

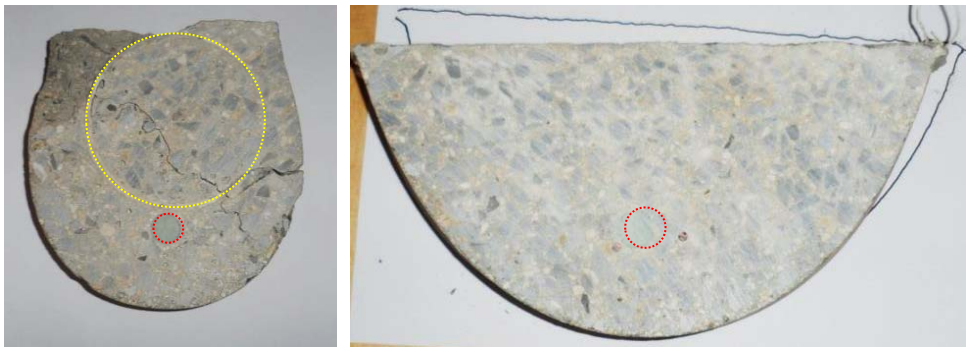

a. b.

Figure 7.20. FFB 9 as-built position of reinforcement: (a) Section 900 and (b) Section 270

7.3.4.2. Beam FFB 10R and FFB 10

The as-built geometry of beams FFB 10R and FFB10 was not surveyed in detail due to the unsatisfactory test results. However the effective depths and the concrete cover were confirmed at the failed sections, which can be seen in Figure 7.35, and the position of the longitudinal bars adjusted accordingly at each section. The measured cover was 29 mm for beam FFB 10R and 32 mm for beam FFB 10.

7.3.4.3. Beam FFB 11R and FFB 11

The as-built dimensions of beam FFB 11R are presented in *Figure 7.21*. The values shown in italics represent the depths of the beam profile adjusted for the measured depths and concrete cover to the longitudinal bar. The design dimensions near midspan were achieved with a good accuracy, as confirmed by the plots in *Figure 7.22*. The deviation

from the design position of the tension longitudinal bar was less than 5 mm. However, the reduced top breadth under the quarter point loads affected the shape of the beam, causing local increase in depth, as can be seen from the photograph in *Figure 7.21*.

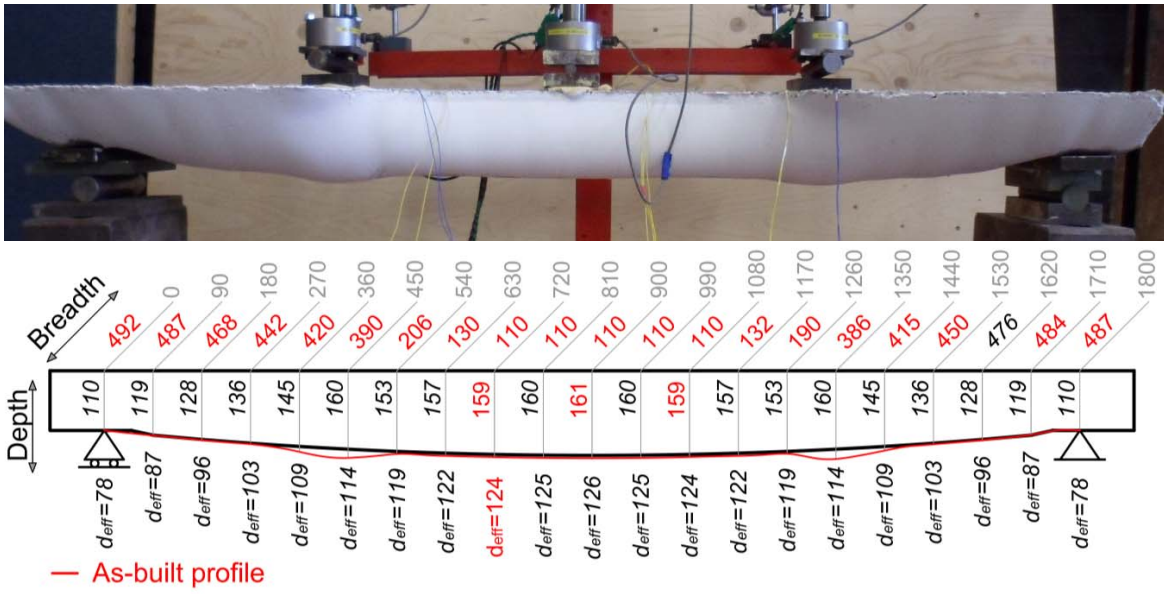

Figure 7.21. FFB 11R as-built measurements (all dimensions are in millimetres)

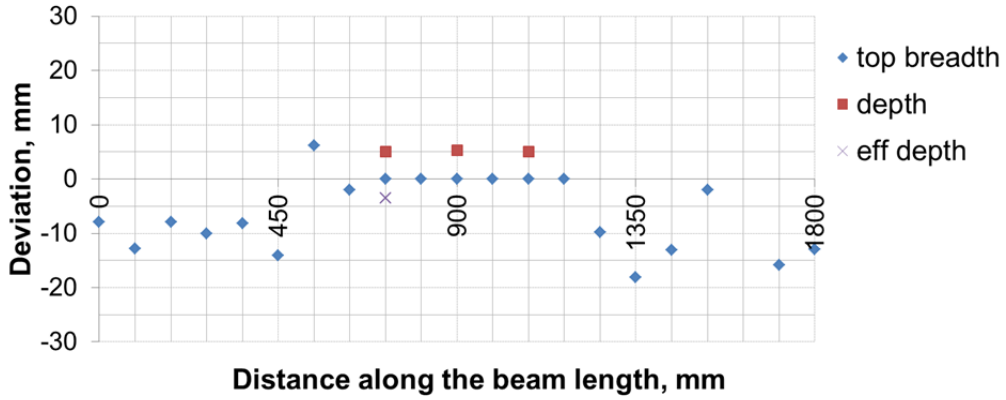

Figure 7.22. FFB 11R deviation from design geometry

The as-built dimensions of beam FFB 11, presented in *Figure 7.23*, deviated slightly more from their design values near midspan in comparison with the reference beam, as suggested by the plots in *Figure 7.24*. However, the differences did not exceed 10 mm. The top cover to the confining reinforcement was measured after the load testing (see *Figure 7.25*). The measurements varied between 26 mm and 30 mm. For the purpose of the analytical predictions a uniform value of 30 mm was assumed along the whole length of the beam.

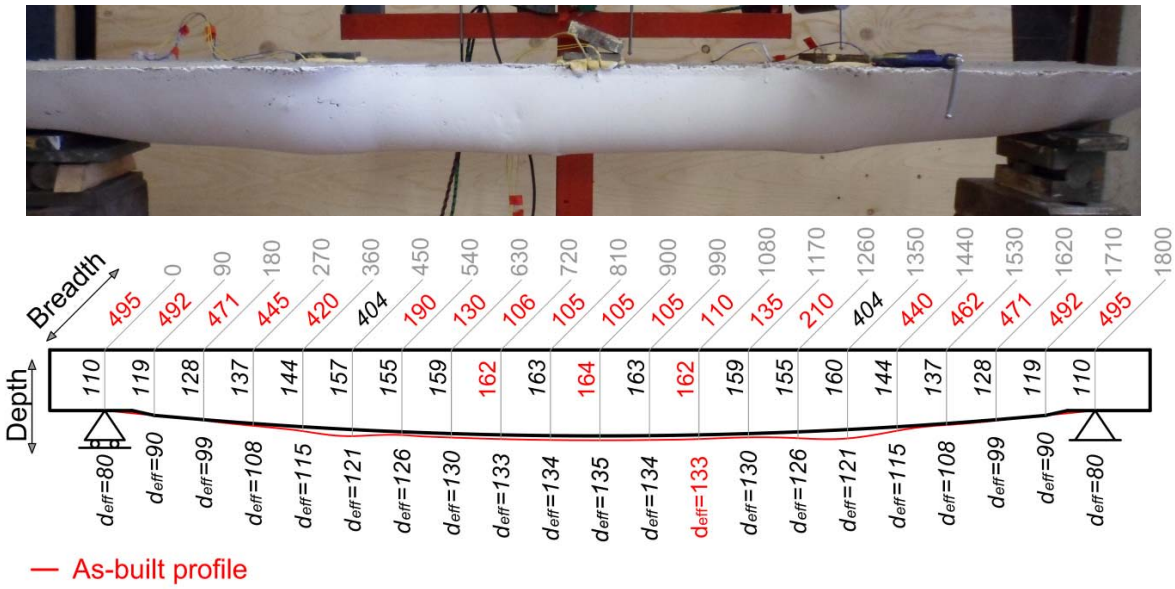

Figure 7.23. FFB 11 as-built measurements (all dimensions are in millimetres)

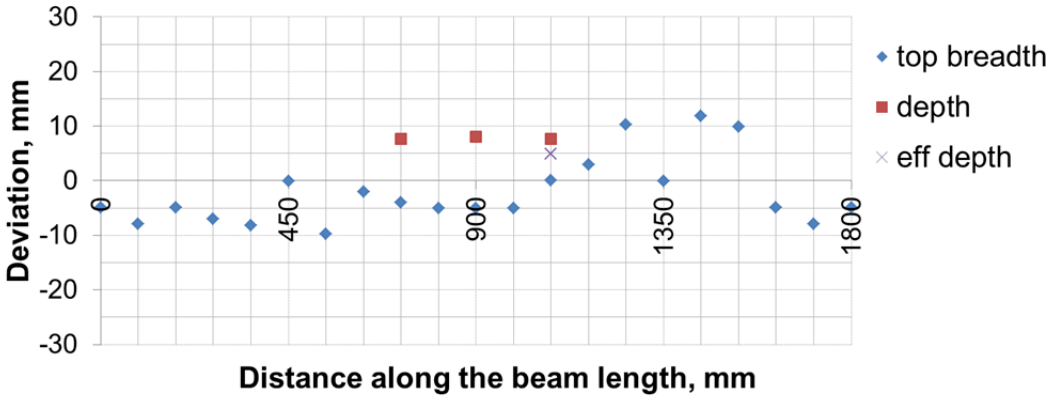

Figure 7.24. FFB 11 deviation from design geometry

Figure 7.25. FFB 11 concrete confined by the helical reinforcement

7.3.4.4. Beams FFB 12R and FFB 12

The top breadth dimension for the last pair of beams was confirmed by tape measurement at each design cross-section. The as-built dimensions of each beam are presented in

Figure 7.26 and *Figure 7.28*, respectively. The concrete cover to the tension reinforcement and the effective depth were checked at the failed sections, while the rest of the dimensions were adjusted, as indicated in italics.

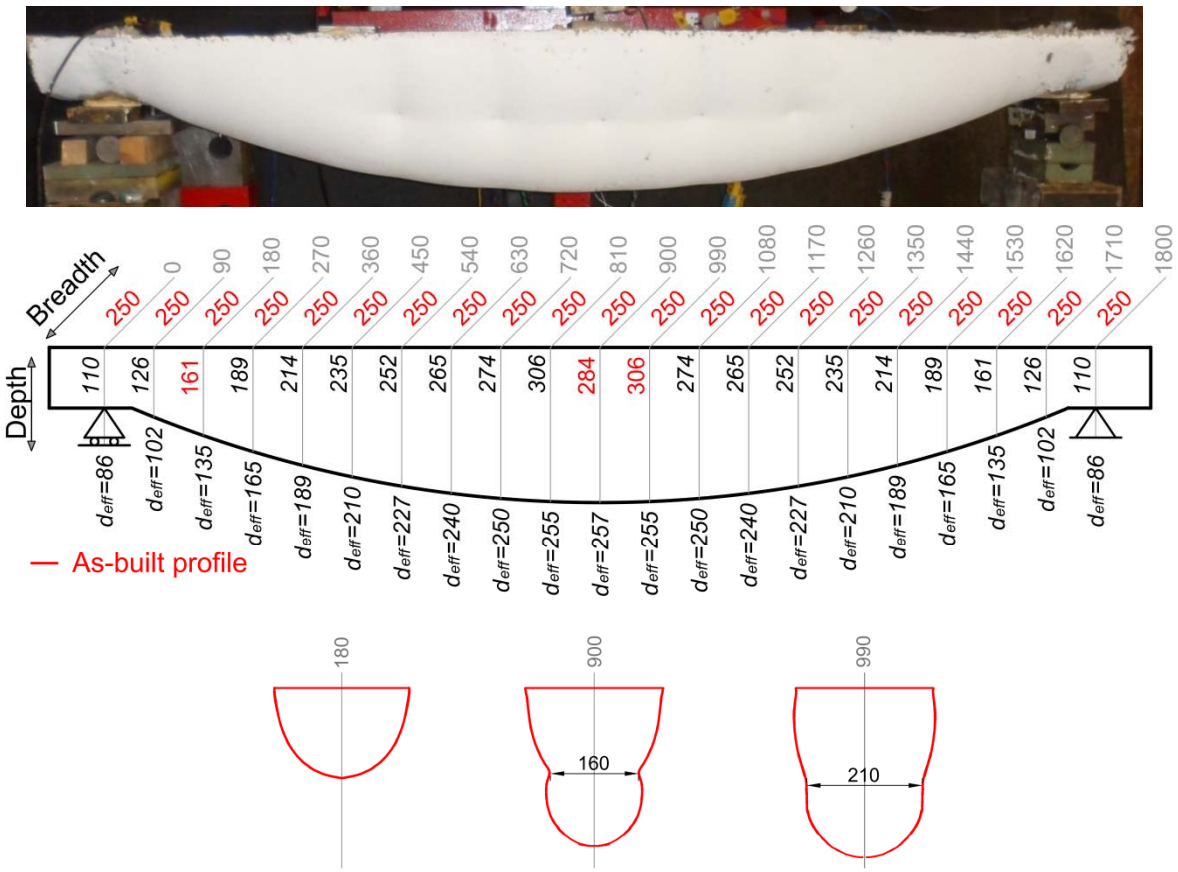

Figure 7.26. FFB 12R as-built measurements (all dimensions are in millimetres)

The profiles of the two typical sections, a section through point of horizontal restraint and a section between two points of restraint, were obtained by profile gauges for both specimens. In addition, a section near a support was also taken for beam FFB 12R (see *Figure 7.26*). The as-built profiles were compared with the theoretical predictions and the differences in the depth dimensions are indicated in *Figure 7.27* and *Figure 7.29*.

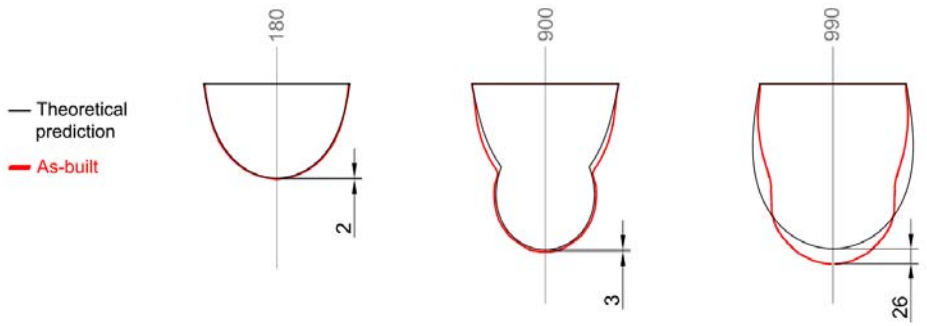

Figure 7.27. FFB 15 comparison of as-built profiles and theoretical predictions (design) (all dimensions are in millimetres)

As can be seen, the slight increase in the overall depth for sections through the points of horizontal restraints was due to a variation in the restrained width, the accuracy of which was compromised by the use of manually fixed plastic ties. While this could suggest that the applied method may be inappropriate for construction, the actual deviation from the design values was within 5 mm. The differences for the sections between restraints, however, are significant, which can be explained by the incapability of the form-finding algorithm to calculate any interaction between restraints in the longitudinal direction. This could be solved by using more advanced software for three-dimensional analysis or by obtaining the profile of fabric in the plane of the horizontal restraints separately and applying the restrained breadths as input to the two-dimensional algorithm.

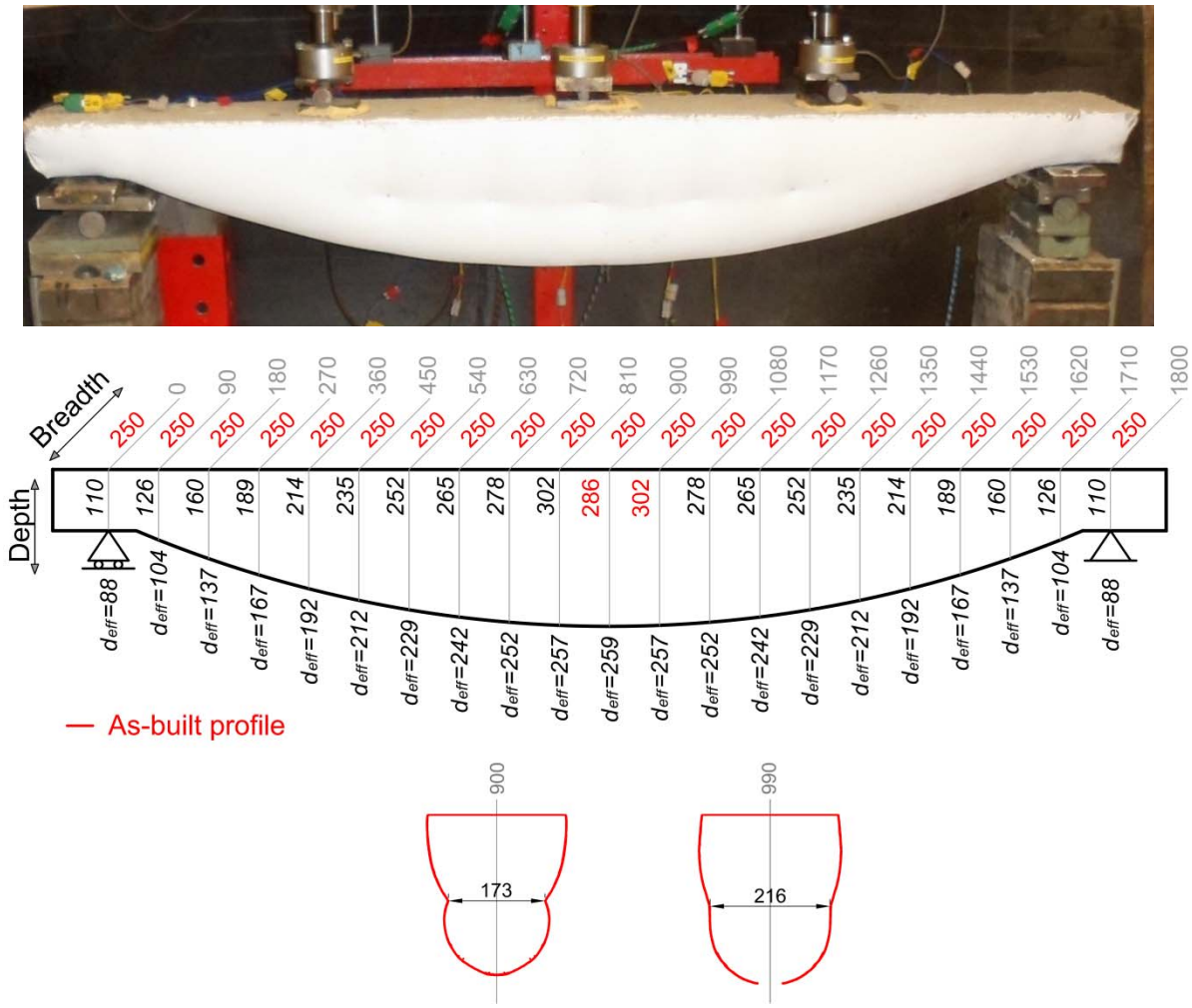

Figure 7.28. FFB 12 as-built measurements (all dimensions are in millimetres)

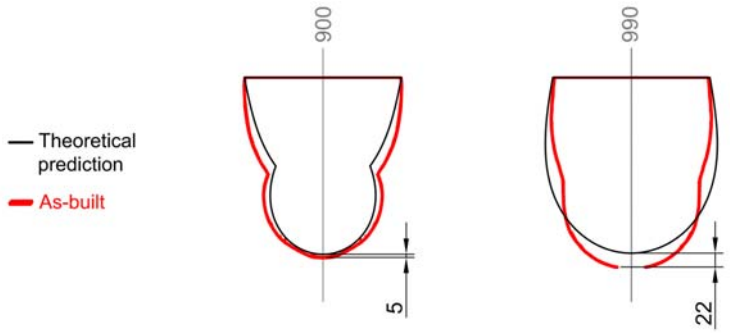

Figure 7.29. FFB12 comparison of as-built profiles and theoretical predictions (design) (all dimensions are in millimetres)

7.3.5. As-built position of reinforcement attached to the fabric

The importance of predicting the position of straight reinforcing bars attached to the fabric and pulled down by the weight of the fresh concrete during construction has already been discussed in § 6. A method for determining the forces in the ties, connecting the fabric and the bars, as well as the resulting hydrostatic shapes has been proposed and verified against experimental data. A further verification based on the experimental results for beam FFB 9 is presented here.

Figure 7.30 summarises the forces in the vertical ties, theoretically obtained for the as-built data. The uplift concentrated forces required to create the as-built cross-sectional shapes correspond well to the assumed equally distributed forces required to bend the bar. The flexural stiffness of the bar is obtained for an effective diameter of 12.7 mm and modulus of elasticity of 69.2 GPa, according to the manufacturer's data. Furthermore, the deflected shape of the bar for both sets of forces, plotted in *Figure 7.31* over a length defined by the extent of the vertical ties, shows a good agreement with the actual deflection. A detailed design procedure, taking into account the interaction between the connected fabric and reinforcing bars during construction, is proposed for the second case study described in § 8.

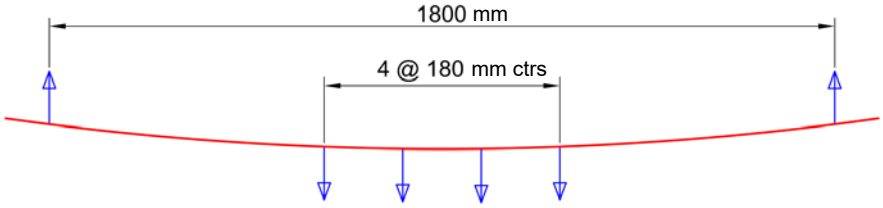

a.

Forces based on actual uplift of fabric

N/m	61	65	65	61
N	11	11.7	11.7	11

b.

Forces based on flexural stiffness of reinforcement

N	11.2	11.2	11.2	11.2

c.

Figure 7.30. FFB9 design compared with as-built: (a) attachment points, (b) forces in the ties based on the as-built geometry and (c) forces in the ties based on actual maximum deflection of the reinforcing bar

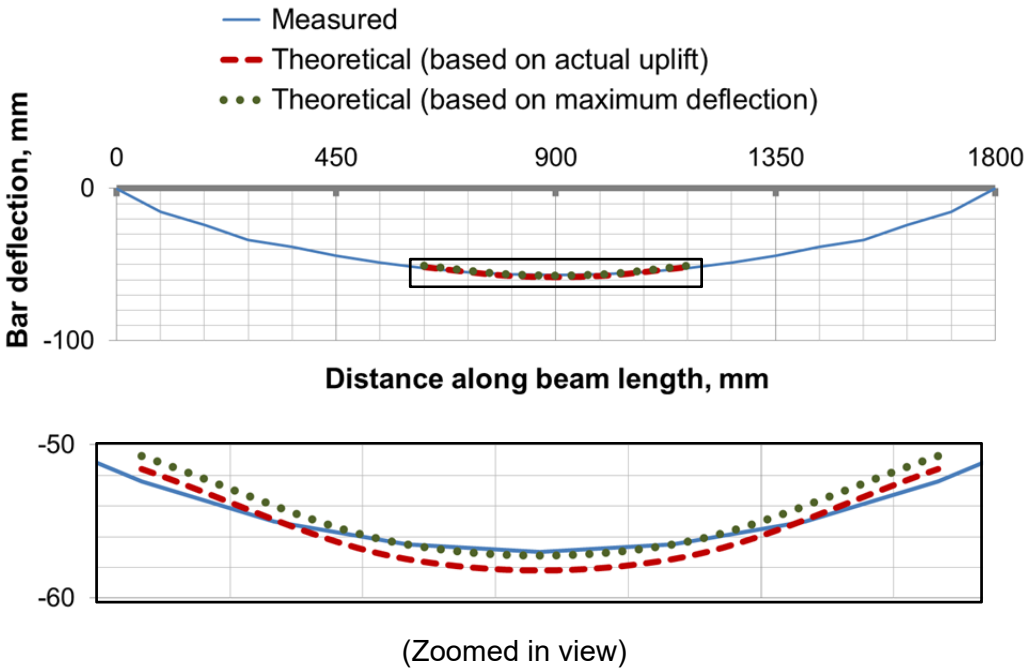

Figure 7.31. FFB9 deflection of reinforcing bar

7.4. Test results

7.4.1. Material testing

The concrete compressive strength for each specimen at the time of load testing was determined from cube samples. The results presented in *Table 7.9* include the measured cube strength for every concrete batch and the average cube strength for every beam, if more than one batch was used. In addition, the cube strength is converted to cylinder strength, based on a theoretical ratio of 0.8. In general, the differences between the concrete strengths of the reference and their relevant test beams can be considered reasonably small.

Table 7.9. Concrete compressive strength (Series 3)

Beam ID	Date cast	Date tested	Average Batch I, MPa	Average Batch II, MPa	Cube strength, MPa	Cylinder strength, MPa
FFB 9R	01/02/2013	05/02/2013	35.3	N/A	35.3	28.2
FFB 9	01/02/2013	05/02/2013	42.0	N/A	42.0	33.6
FFB 10R	07/02/2013	11/02/2013	25.2	25.8	25.5	20.4
FFB 10	07/02/2013	11/02/2013	25.8	24.1	24.9	19.9
FFB 11R	21/06/2013	02/07/2013	20.1	N/A	20.1	16.1
FFB 11	21/06/2013	02/07/2013	20.9	N/A	20.9	16.7
FFB 12R	29/07/2013	05/08/2013	21.1	20.8	21.0	16.8
FFB 12	29/07/2013	05/08/2013	23.3	21.1	22.2	17.8

7.4.2. Failure modes and failure loads

Each pair of beams was designed to fail in a particular mode. Beams FFB 9R, FFB 9, FFB 11R and FFB 11 were anticipated to fail in flexure, while a shear failure mode was anticipated for the rest of the test specimens. All beams, except FFB 9, exhibited their predicted behaviour at failure. The crack patterns and the maximum failure loads for every test beam can be seen in *Figure 7.32* to *Figure 7.40*.

Beams FFB 9R and FFB 9 failed at similar loads, shown in *Figure 7.33*, in a brittle manner. Although the reference beam reached flexural failure based on concrete crushing in the compression zone near midspan, shear failure in beam FFB 9 occurred near the support beyond the extents of the confining reinforcement (see *Figure 7.32*). Therefore, the test results could not provide useful information regarding the flexural behaviour of fabric-formed beams with confined concrete in compression, other than a marginal increase in flexural capacity was achieved through the addition of confining helices, although the concrete strength was also higher.

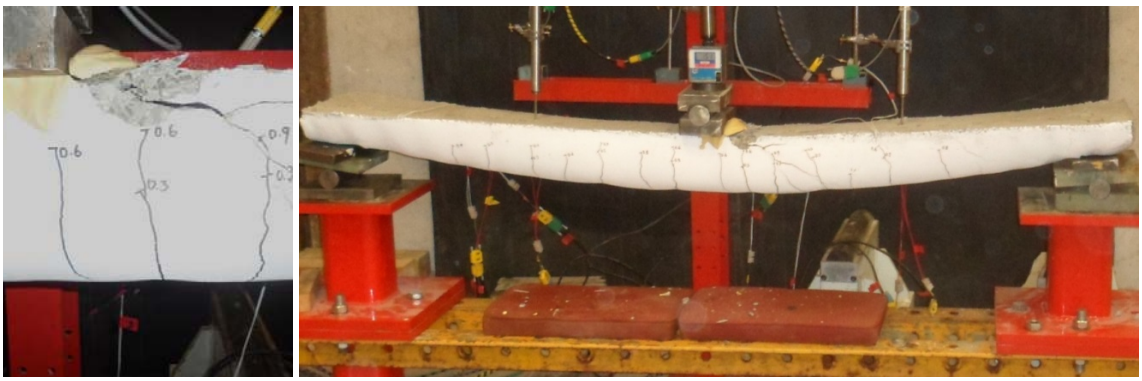

a.

b.

Figure 7.32. Failure modes: (a) FFB 9R and (b) FFB 9

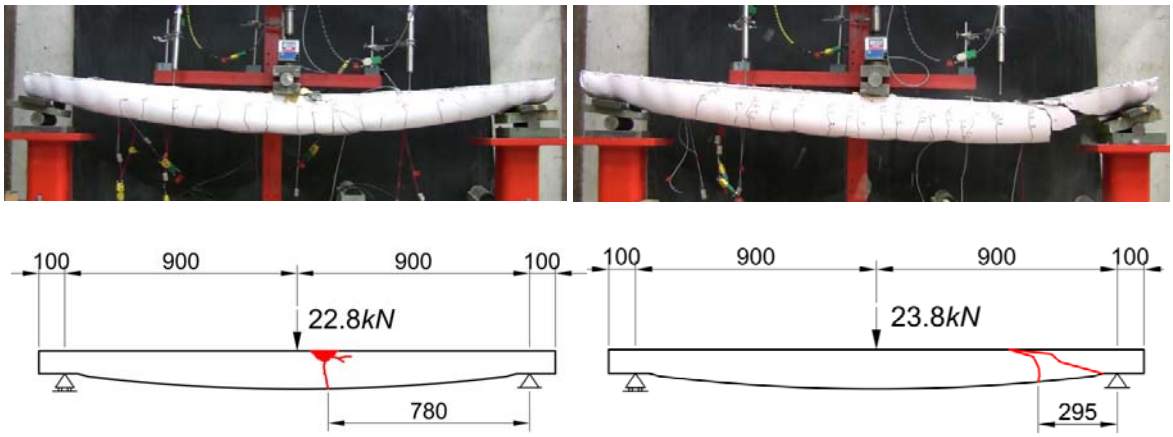

a. b.

Figure 7.33. Failure loads: (a) FFB 9R and (b) FFB 9 (all dimensions are in millimetres)

Beams FFB 10R and FFB 10 failed in shear as expected (see *Figure 7.34*). However, there was a considerable difference between their load-deflection behaviours. The failure of the reference beam, unreinforced in shear, was sudden and catastrophic, while beam FFB 10, reinforced with Type A cage, was able to sustain a modest post-peak load. Nevertheless, no significant increase in the maximum load capacity was observed, as indicated in *Figure 7.35*.

The carbon fibre spiral reinforcement failed at the bends (see *Figure 7.34b*), a typical failure previously observed by Walkin (2013), caused by stress concentration and weakening due to fibre tow fanning.

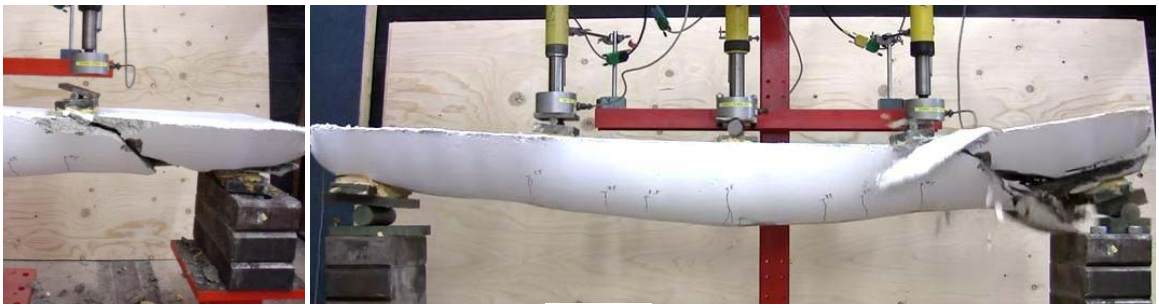

a.

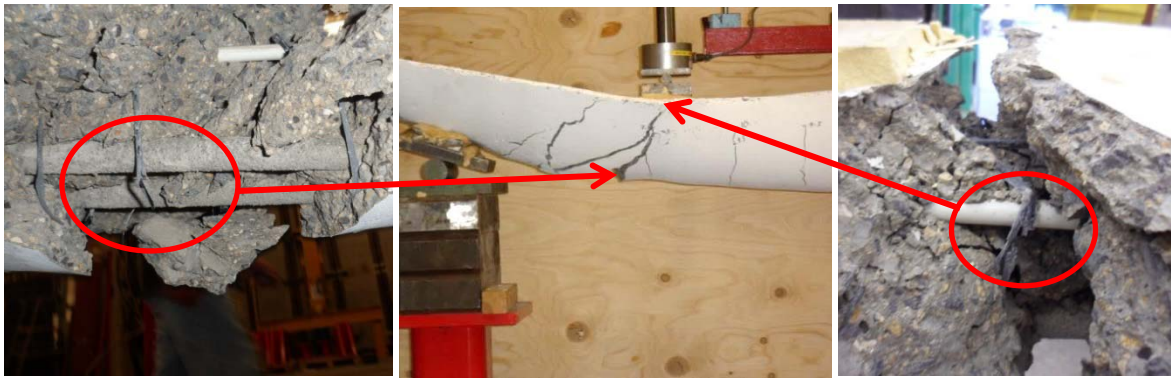

b.

Figure 7.34. Failure loads: (a) FFB 10R and (b) FFB 10

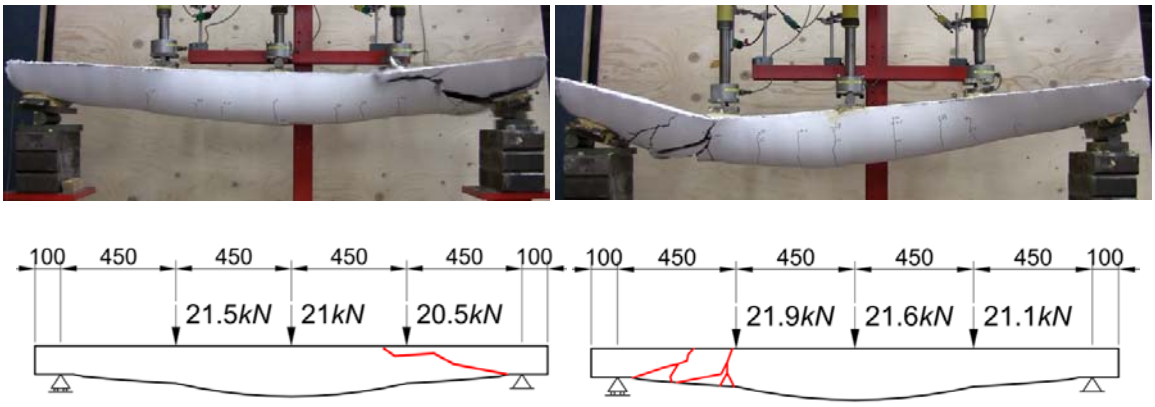

a. b.

Figure 7.35. Failure loads: (a) FFB 10R and (b) FFB 10 (all dimensions are in millimetres)

The next pair of beams, FFB 11R and FFB 11, both contained CFRP spiral shear reinforcement and both failed in flexure, as expected (see *Figure 7.36*). The reference beam, which had no confining reinforcement in the concrete compression zone, exhibited brittle failure, typical for FRP-reinforced concrete beams. The integrity of concrete was lost rapidly, as can be seen in *Figure 7.36a,* and the beam was not able to sustain any further load.

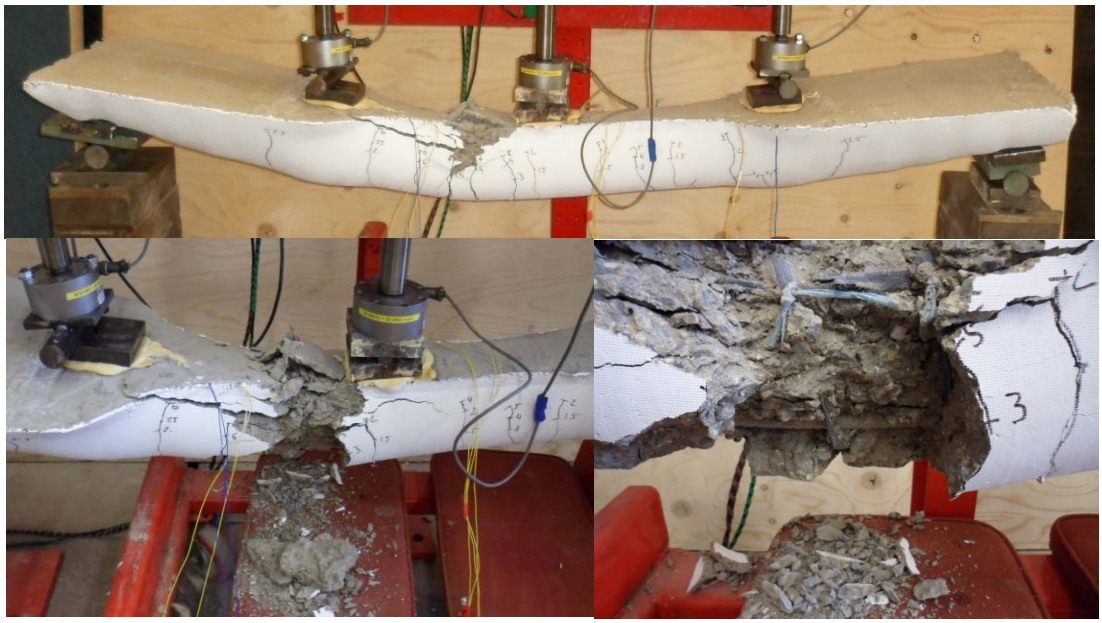

a.

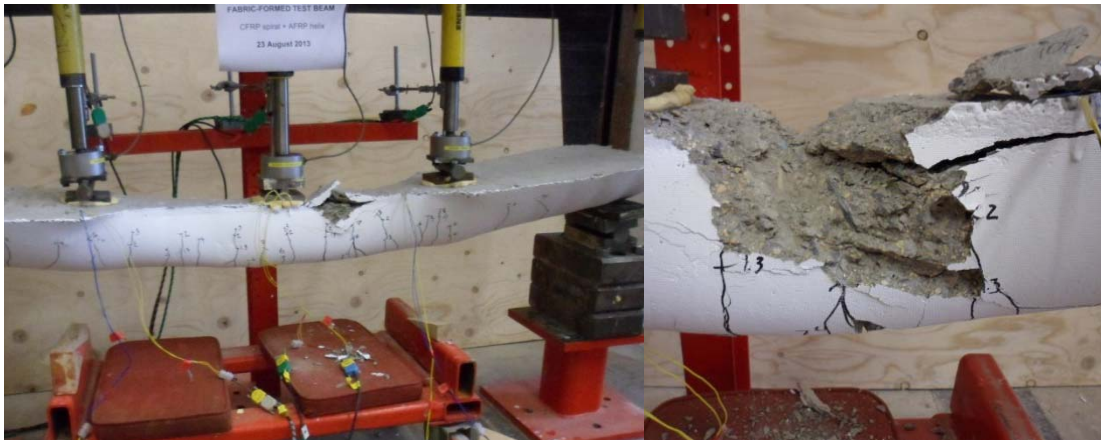

b.

Figure 7.36. Failure modes: (a) FFB 11R and (b) FFB 11

Beam FFB 11, shown in *Figure 7.36b*, exhibited behaviour similar to the reference beam until the peak load was reached. However, the confined concrete remained in place and provided a more ductile response of the beam thereafter. The load testing continued until the top concrete surrounding the AFRP helix was completely lost, sustaining a fairly constant load. The peak loads resisted by the two beams are given in *Figure 7.37*. As can be seen, the failure zones were almost symmetrical about the midspan and the loads were similar in value. This confirms the proposed confined concrete model, described in § 4, which assumed no increase in the concrete strength due to confinement for the adopted type and configuration of confining reinforcement.

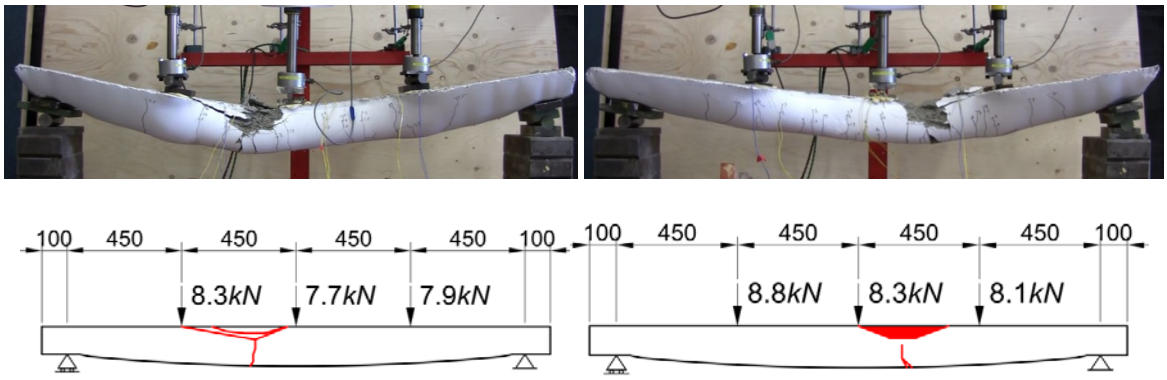

a. b.

Figure 7.37. Failure loads: (a) FFB 11R and (b) FFB 11 (all dimensions are in millimetres)

The last two beams failed in shear, as expected, at nearly the same location with slightly different crack patterns, as can be seen in *Figure 7.38*. The reference beam, however, reached only half of the maximum load of the beam containing Type B CFRP spiral cage (see *Figure 7.40*). This was a major improvement in comparison with the Type A cage test. The spiral reinforcement again snapped at the bend portions, as indicated in *Figure 7.39*.

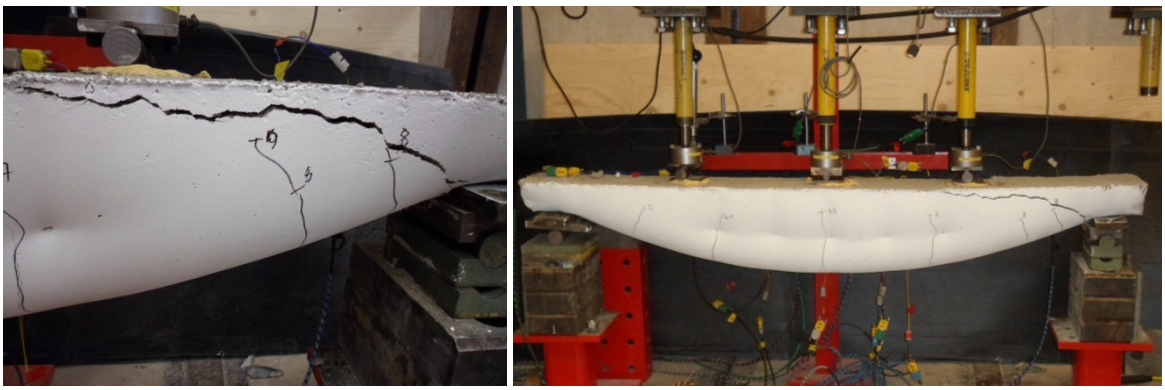

a.

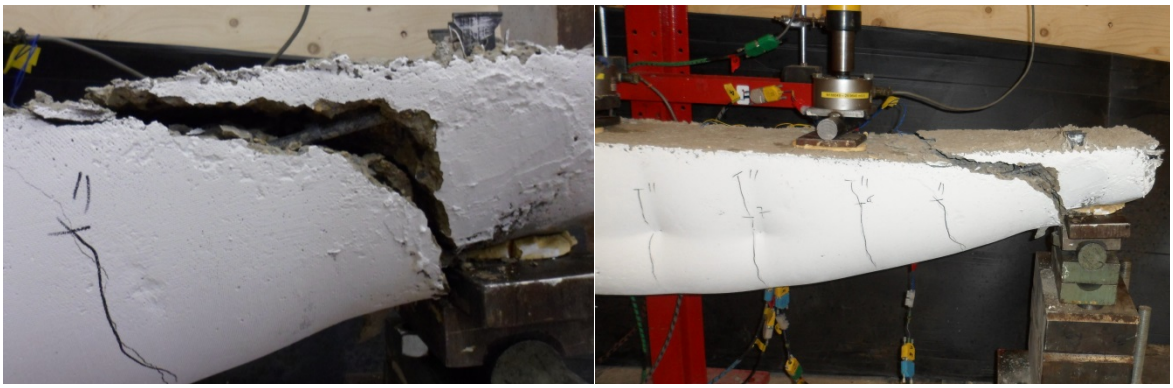

b.

Figure 7.38. Failure modes: (a) FFB 12R and (b) FFB 12

Figure 7.39. FFB 12 failure of the carbon spiral reinforcement

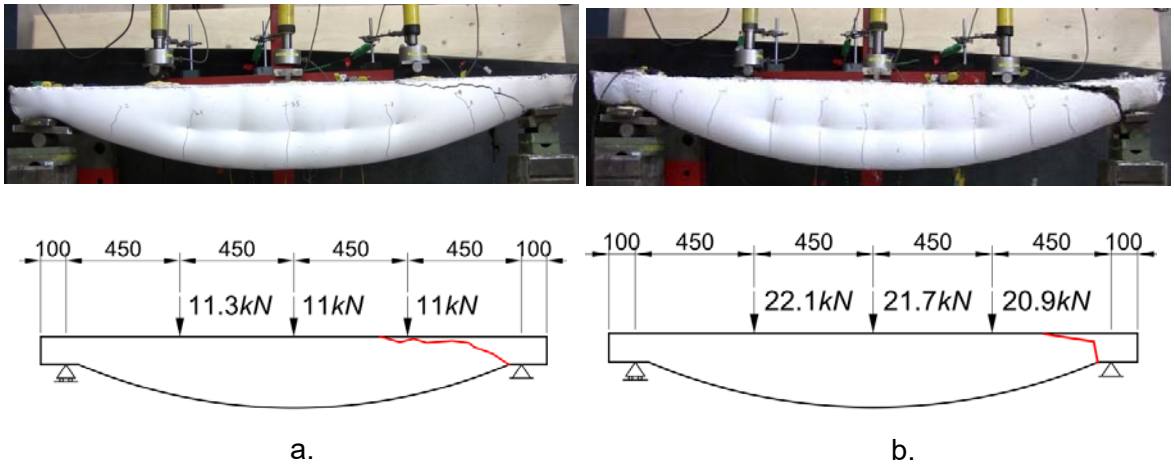

Figure 7.40. Failure loads: (a) FFB 12R and (b) FFB 12 (all dimensions are in millimetres)

7.4.3. Load-deflection relations

The load-deflection responses at each measured location, for all test beams, are presented in *Figure 7.41* to *Figure 7.48*. Due to an instrumentation failure, the displacements at midspan for beams FFB 11 and FFB 12R were not recorded successfully and are not included in the presented results. Nevertheless, the post-peak behaviour of beam FFB 11 can still be studied from the plots in *Figure 7.46*.

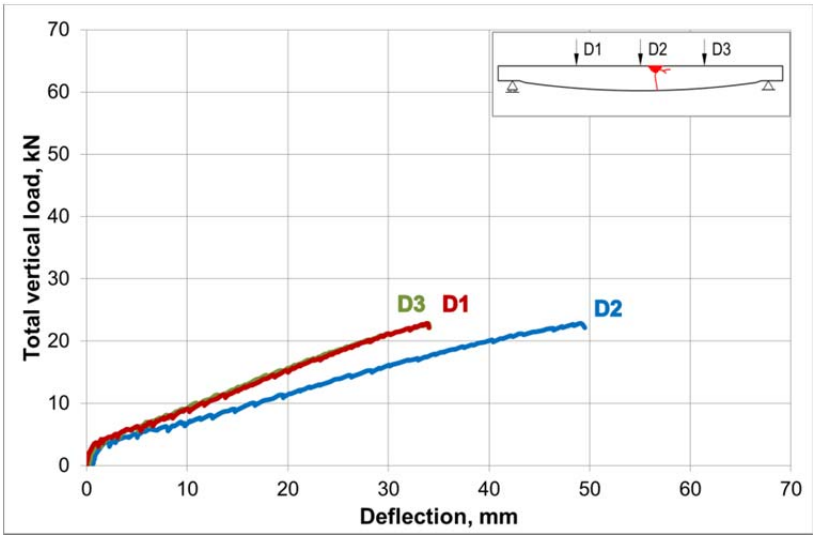

Figure 7.41. FFB 9R experimental load-deflection relations

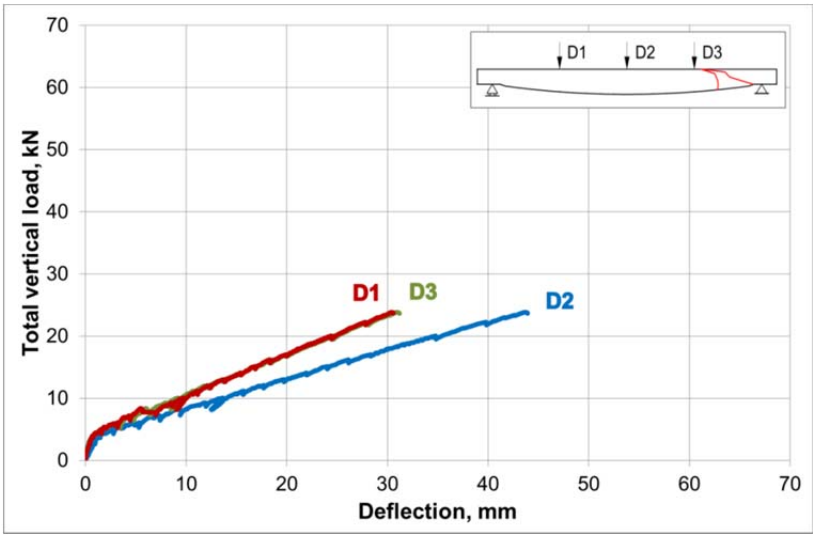

Figure 7.42. FFB9 experimental load-deflection relations

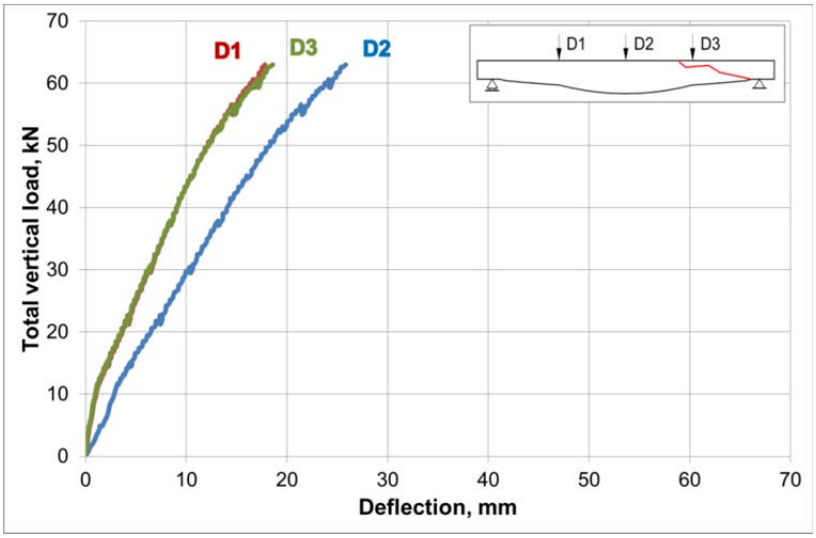

Figure 7.43. FFB10R experimental load-deflection relations

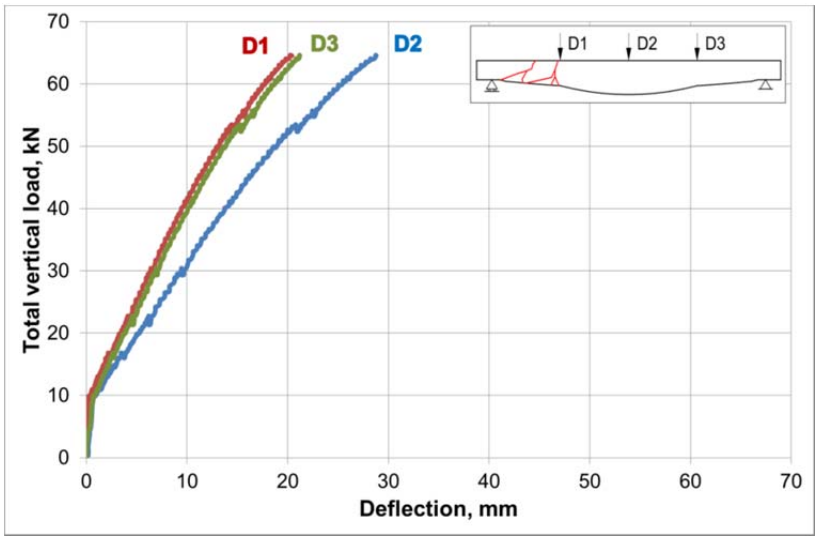

Figure 7.44. FFB10 experimental load-deflection relations

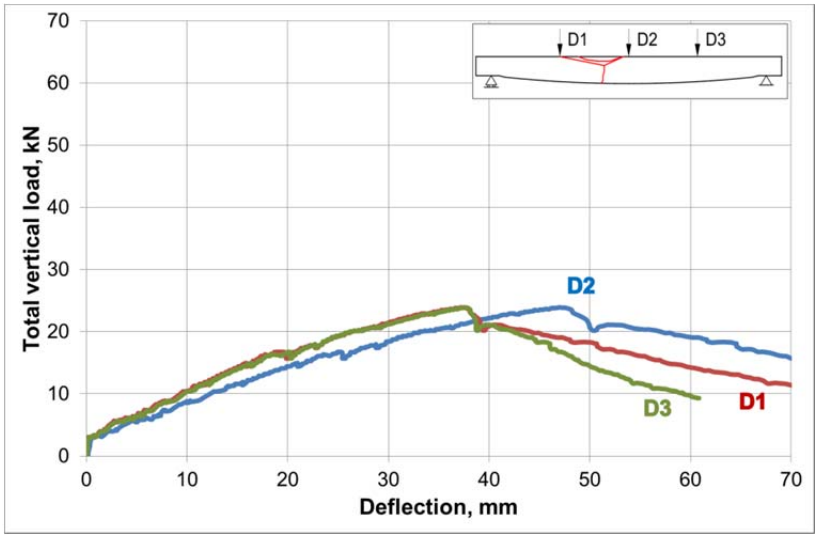

Figure 7.45. FFB11R experimental load-deflection relations

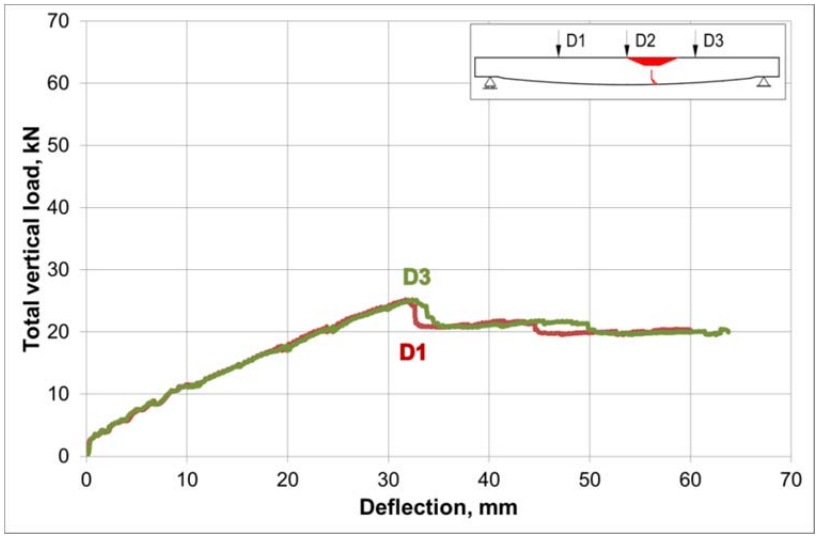

Figure 7.46. FFB11 experimental load-deflection relations

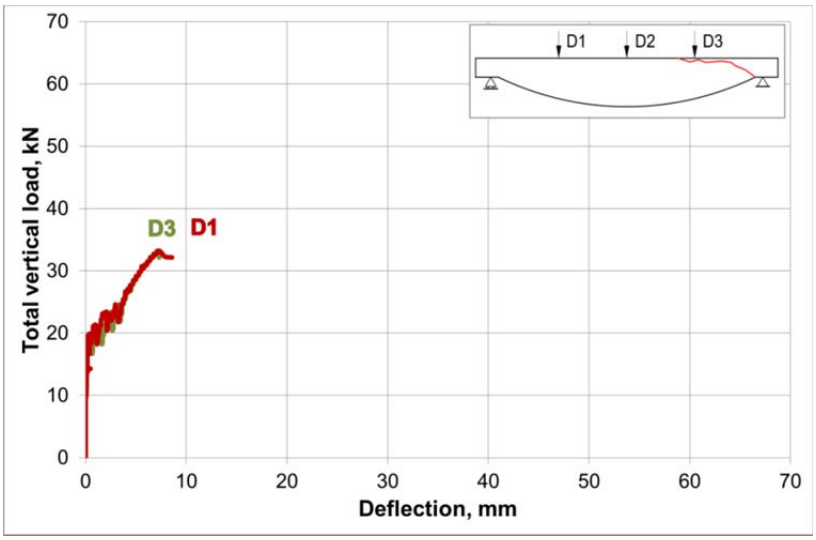

Figure 7.47. FFB12R experimental load-deflection relations

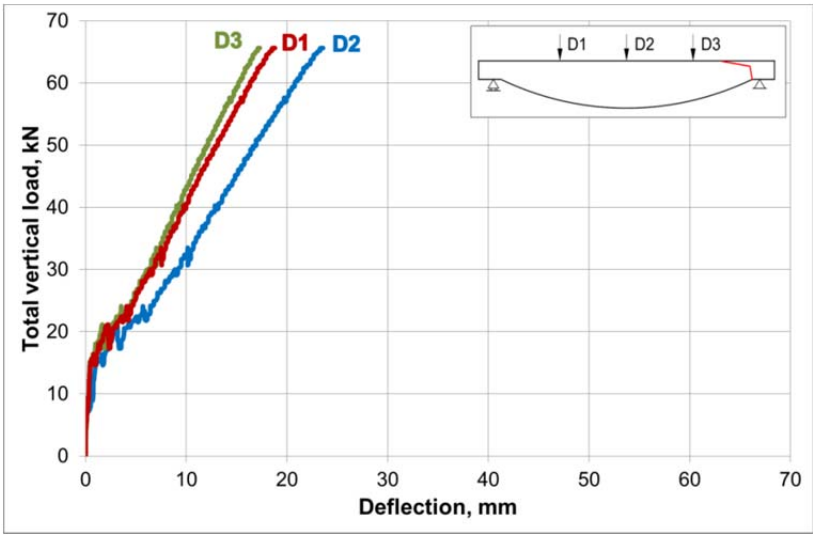

Figure 7.48. FFB12 experimental load-deflection relations

7.4.4. Load-strain relations

The load-strain relations, presented in *Figure 7.49* to *Figure 7.54*, are based on the average readings of two strain gauges installed at each of the indicated locations on the reinforcing bars (at the level of the effective depth). Most of the recorded strains appear valid with the exception of the relation at midspan for beam FFB 12R, which could have been expected to have been similar to the plot for FFB 12 in the early stages of loading and may be assumed to be an error (see *Figure 7.53*). The rest of the results demonstrate a fairly consistent distribution of the strains along the length of the reinforcing bars.

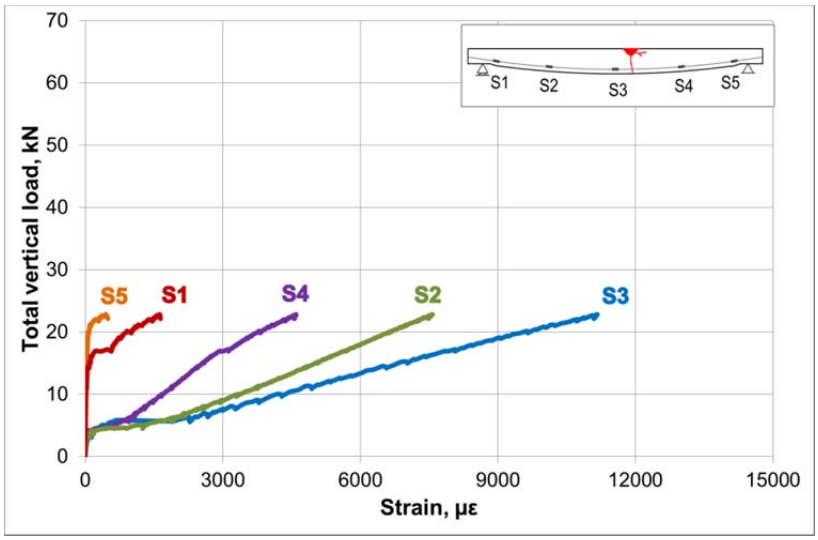

Figure 7.49. FFB 9R experimental load-strain relations

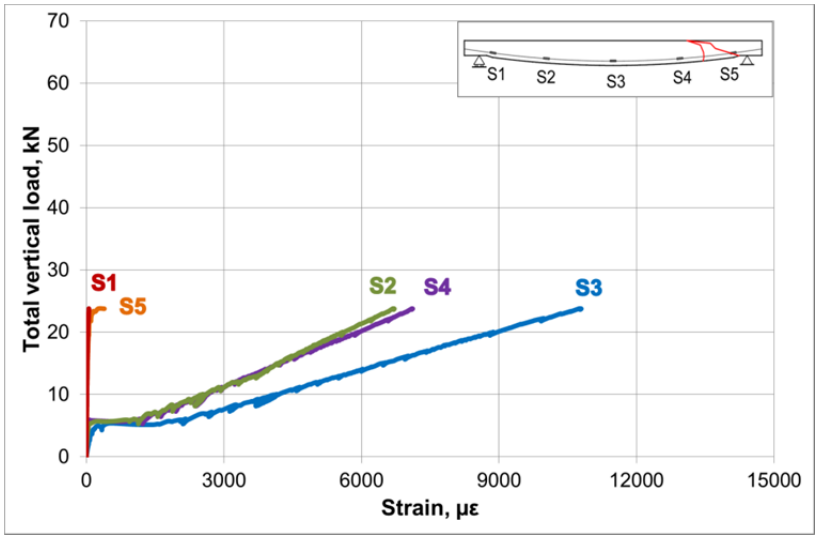

Figure 7.50. FFB 9 experimental load-strain relations

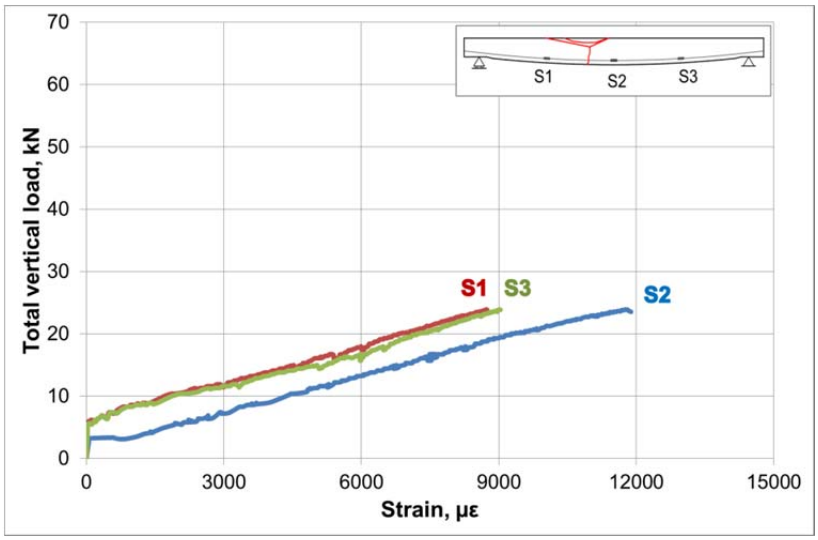

Figure 7.51. FFB 11R experimental load-strain relations

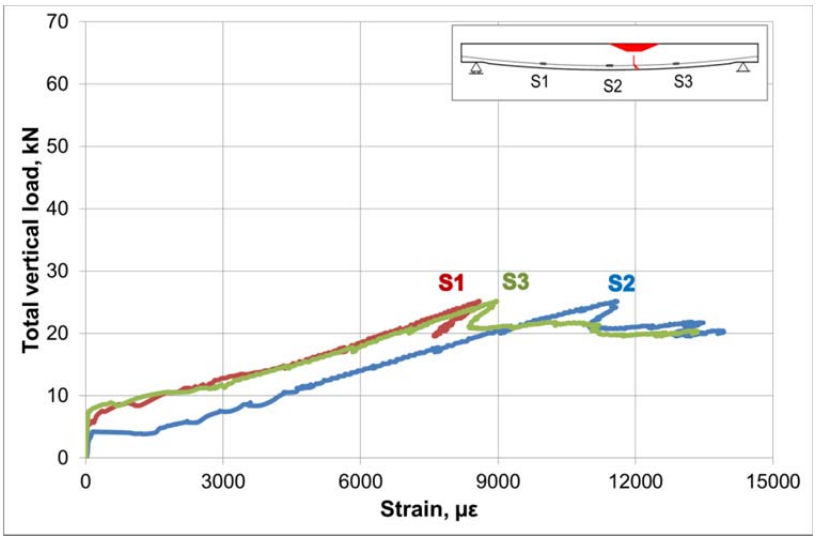

Figure 7.52. FFB 11 experimental load-strain relations

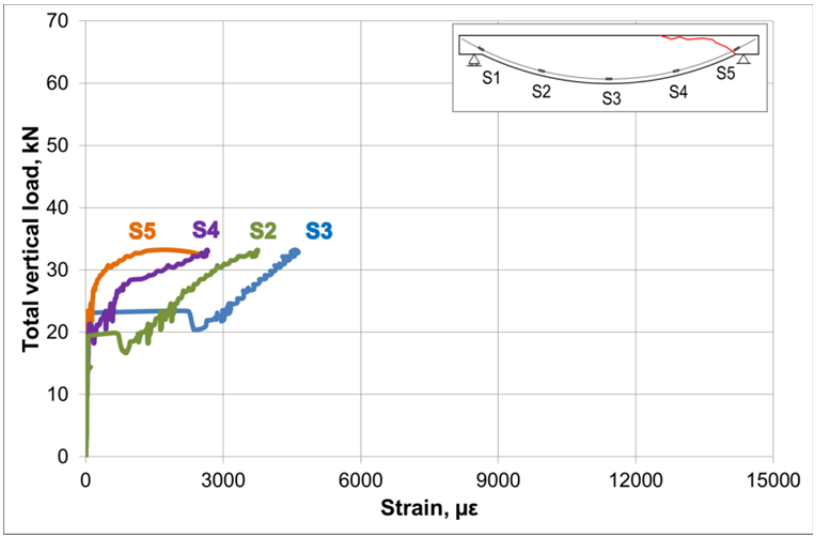

Figure 7.53. FFB 12R experimental load-strain relations

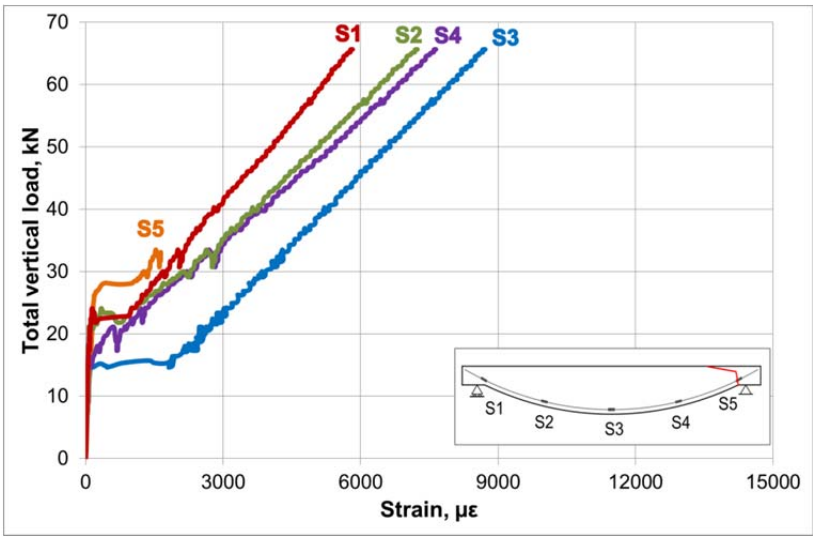

Figure 7.54. FFB 12 experimental load-strain relations

7.5. Discussion of results

7.5.1. Comparison of experimental and predicted capacities

The bending moment and shear force diagrams, calculated for the maximum test loads, are compared with the cross-sectional capacities along the length of each beam in *Figure 7.55* to *Figure 7.62*. The flexural and shear capacities are based on the actual concrete strengths presented separately for the design and the as-built geometry of the test beams. In addition, a theoretical enhancement of 18% is applied to the concrete strength to allow for the effect of fabric formwork construction. The assumed value corresponds to the maximum experimentally confirmed enhancement in § 6.

The comparison of predicted capacities and applied load effects for beam FFB 9R confirms the location of the failed section in flexure. However, the predictions underestimate the actual capacity at midspan, which results in applied shear forces along the beam length close to the predicted capacities (see *Figure 7.55*). A similar underestimation of the ultimate moment of resistance could explain the shear failure of beam FFB 9 (see *Figure 7.56*), where the confinement of concrete near midspan may have additionally prevented flexural failure. As previously discussed, this emphasised the need for providing shear reinforcement in order to achieve adequate behaviour of beams containing confinement reinforcement in the compression zone.

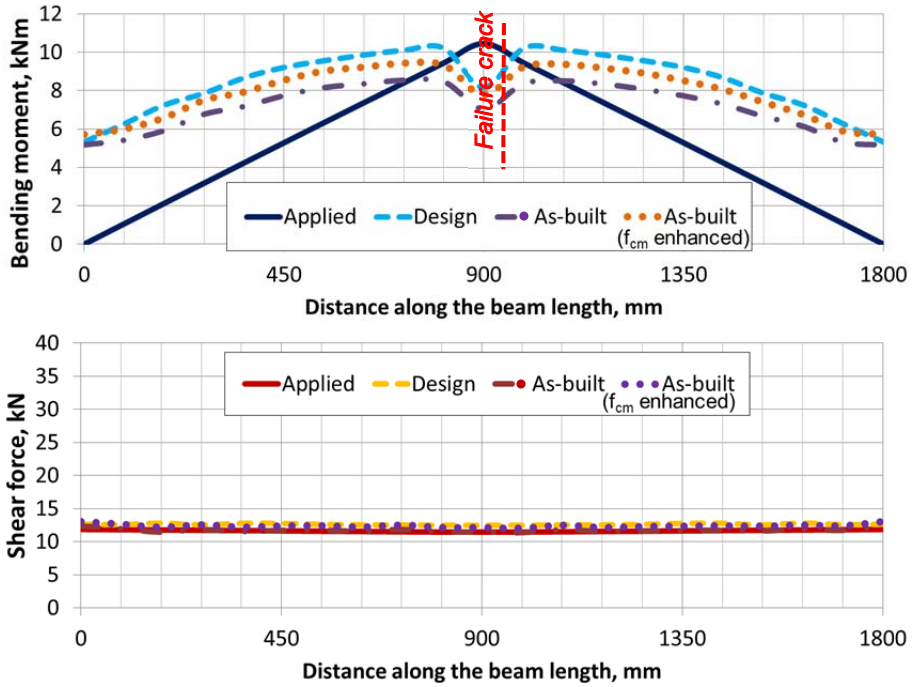

Figure 7.55. FFB 9R maximum load effects vs section capacities for design and as-built geometry

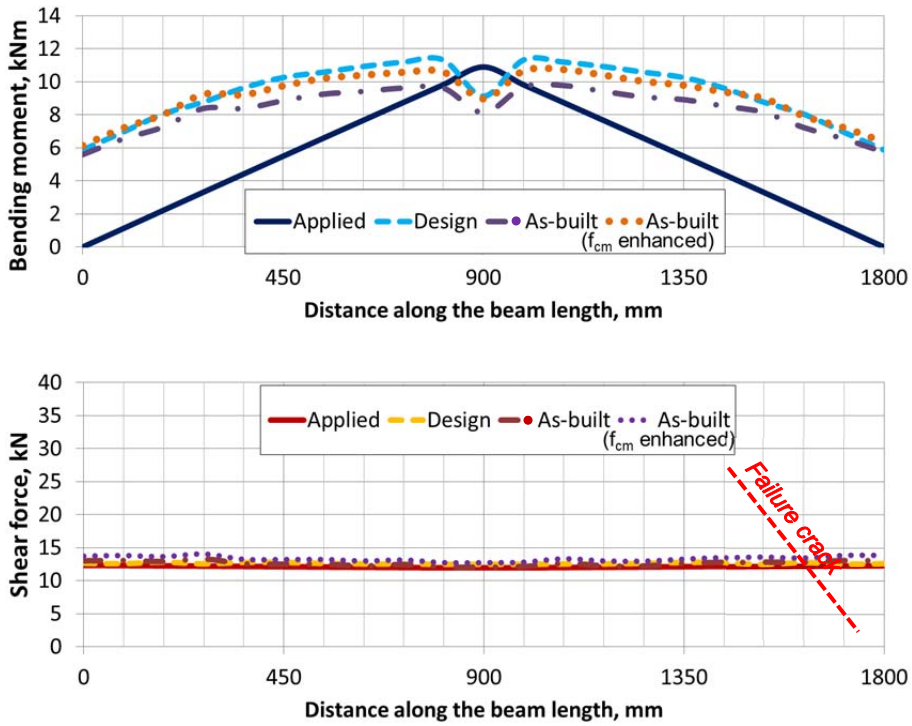

Figure 7.56. FFB 9 maximum load effects vs section capacities for design and as-built geometry

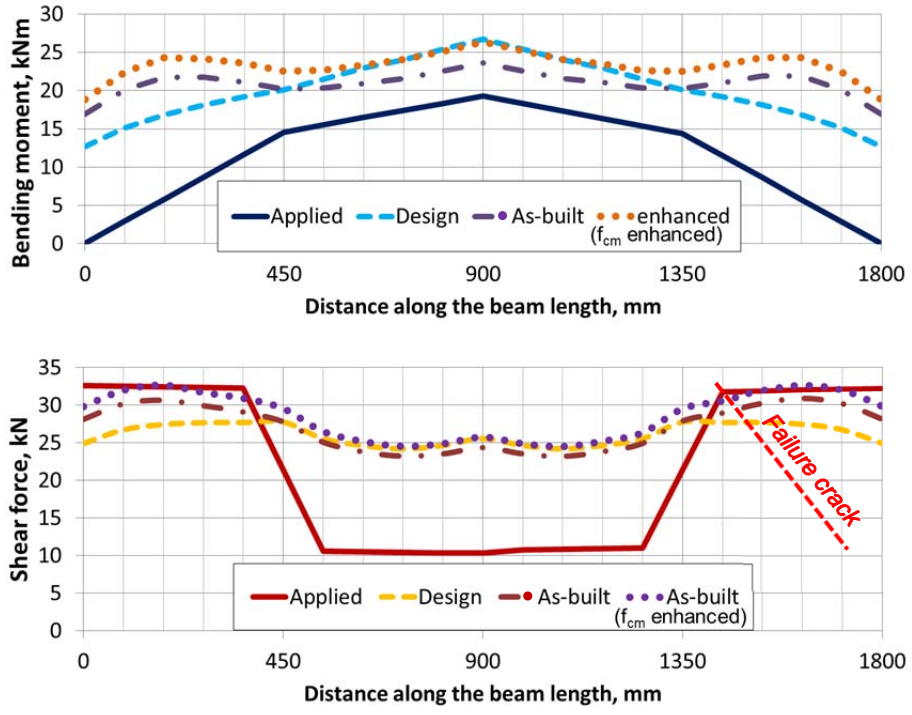

Figure 7.57. FFB 10R maximum load effects vs section capacities for design and as-built geometry

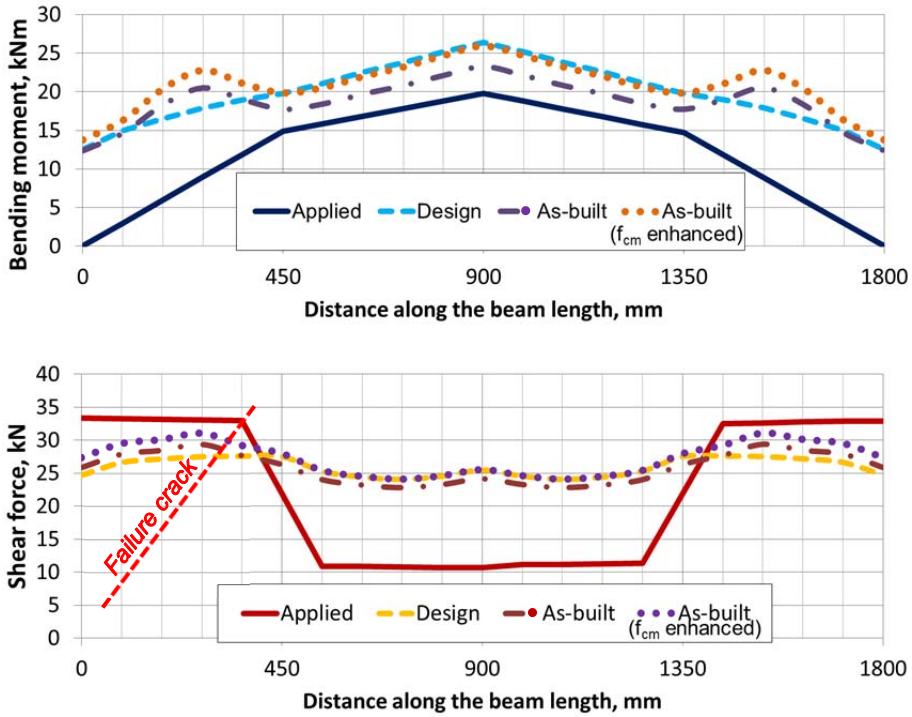

Figure 7.58. FFB 10 maximum load effects vs section capacities for design and as-built geometry

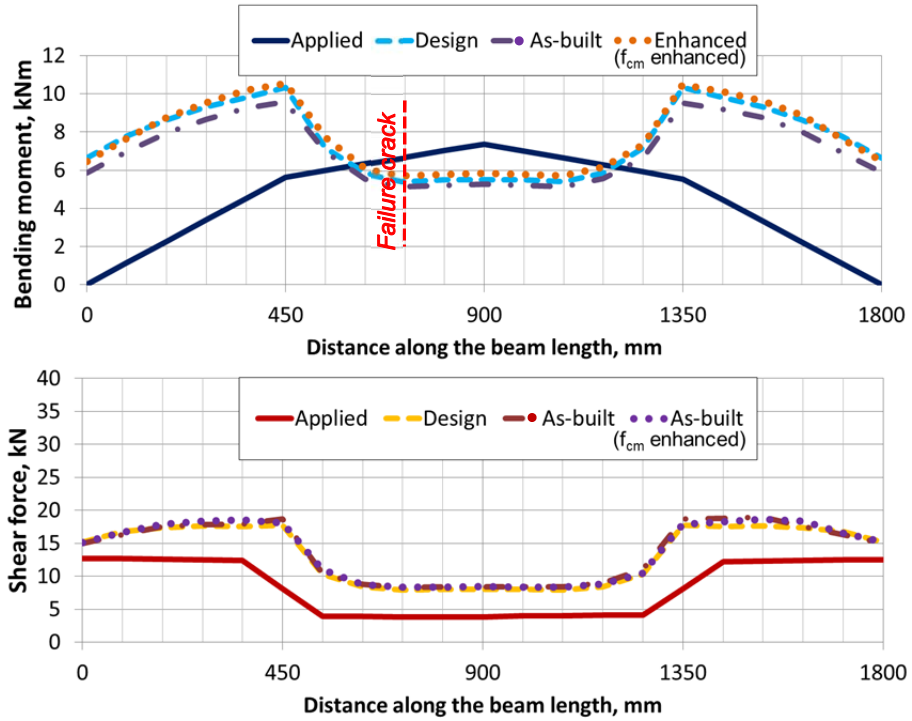

Figure 7.59. FFB 11R maximum load effects vs section capacities for design and as-built geometry

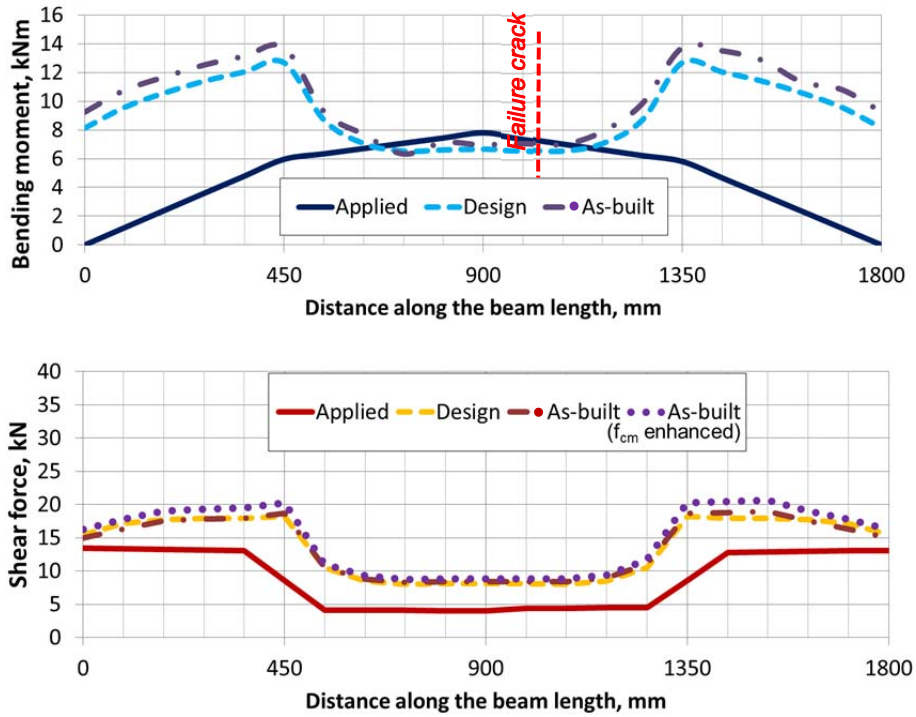

Figure 7.60. FFB 11 maximum load effects vs section capacities for design and as-built geometry

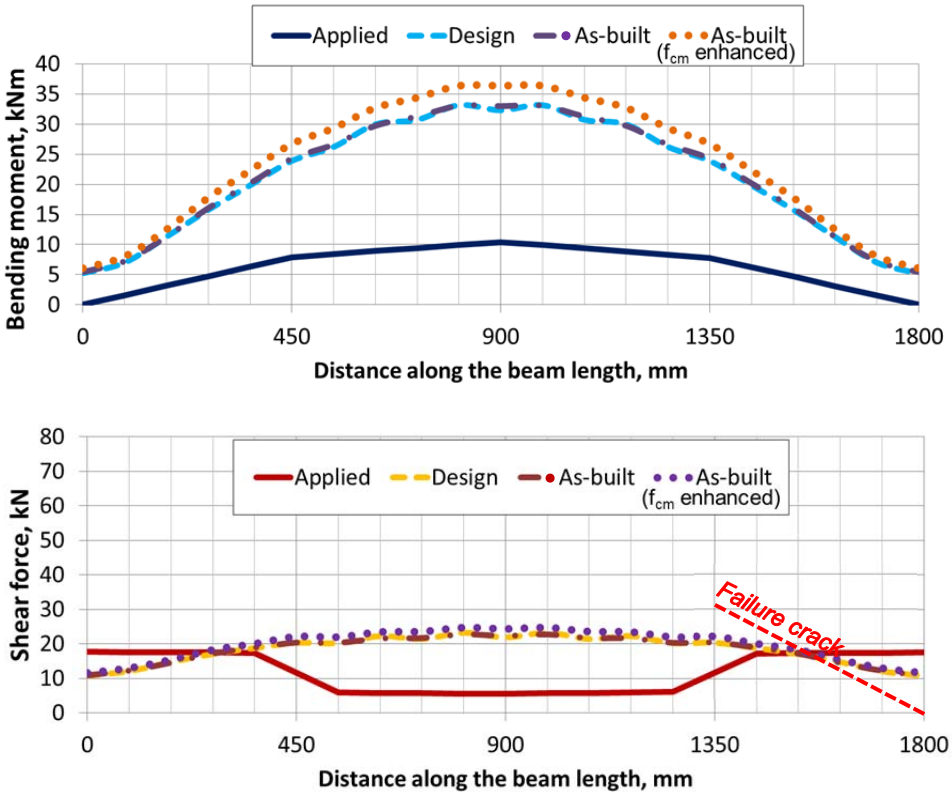

Figure 7.61. FFB 12R maximum load effects vs section capacities for design and as-built geometry

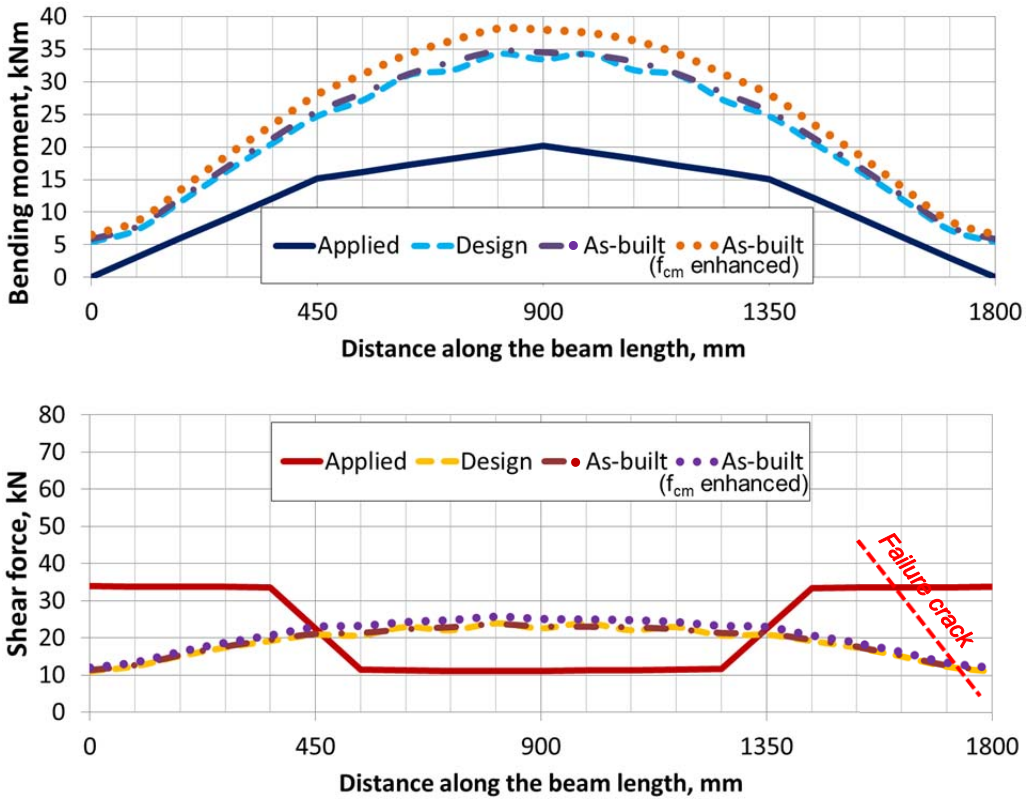

Figure 7.62. FFB 12 maximum load effects vs section capacities for design and as-built geometry

The presented results show only the predicted concrete shear capacities. The increase in the total shear capacity, provided by the CFRP spiral reinforcement, by comparing beams FFB 10R and FFB 10 is approximately 1.55 kN (see *Figure 7.57* and *Figure 7.58*). An additional increase of 0.6 kN, due to the difference in the measured concrete strengths, could add up to 2.15 kN, which still appears to be very low compared with a theoretically calculated contribution of 17.1 kN, based on two inclined legs at 45 mm centres. However, a single impregnated carbon tow has a tensile strength of 2.38 kN, reduced to 2.12 kN for a maximum inclination of the shear leg of 26°. This could lead to a conclusion that in this case the failure of the spiral was governed by snapping at a single point.

The contribution of shear reinforcement to beam FFB 12 is significant, as a comparison between the shear force plots in *Figure 7.61* and *Figure 7.62* suggests. A further analysis, based on the enhanced concrete strength and including only the vertical legs of the shear spiral, is presented in *Figure 7.63*. The total shear capacity is calculated for the ultimate failure strain of 1.3% and for the permissible 0.4% strain in accordance with ACI 440.1R-06. The spiral had vertical legs (spaced at 45 mm) only at the end quarters of the span and, therefore, no contribution is added over the centre half-span length. As can be seen, in this case the continuous CFRP spiral provided capacity close to the theoretical predictions and failed at higher than apparently permissible design strain levels.

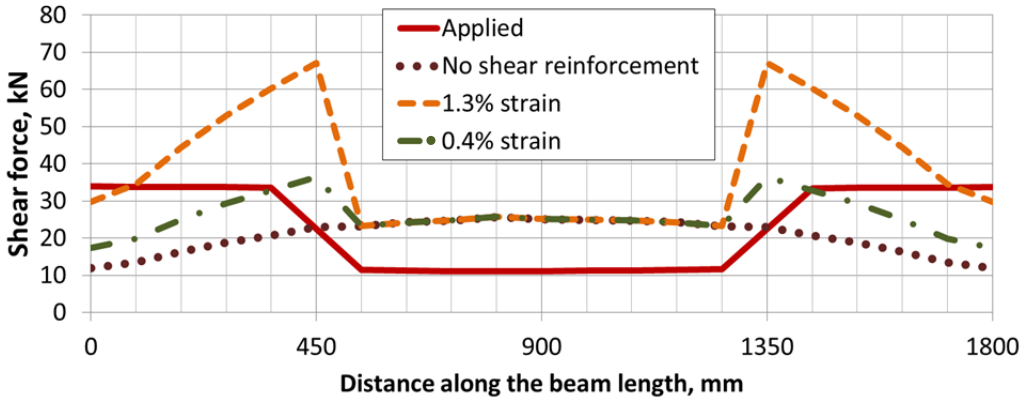

Figure 7.63. FFB 12 maximum shear forces vs section capacities including shear reinforcement

7.5.2. Experimental and predicted load-deflection behaviour

The load-deflection response of each test beam is calculated for the design and the as-built geometries. The analysis is based on the actual concrete strengths for both sets of geometry data, while the as-built geometry is also analysed for the theoretically enhanced strength, as described in the previous section. The concrete shear capacities are calculated only for the combination of enhanced concrete strength and as-built geometry.

The first pair of beams shows a similar load-deflection behaviour, with a slight difference between the deflections at failure (see *Figure 7.64*), which may have been influenced by the concrete strength and the different failure modes. The comparisons between the experimental and theoretical load-deflection curves for both beams are presented in *Figure 7.65* and *Figure 7.66*, respectively.

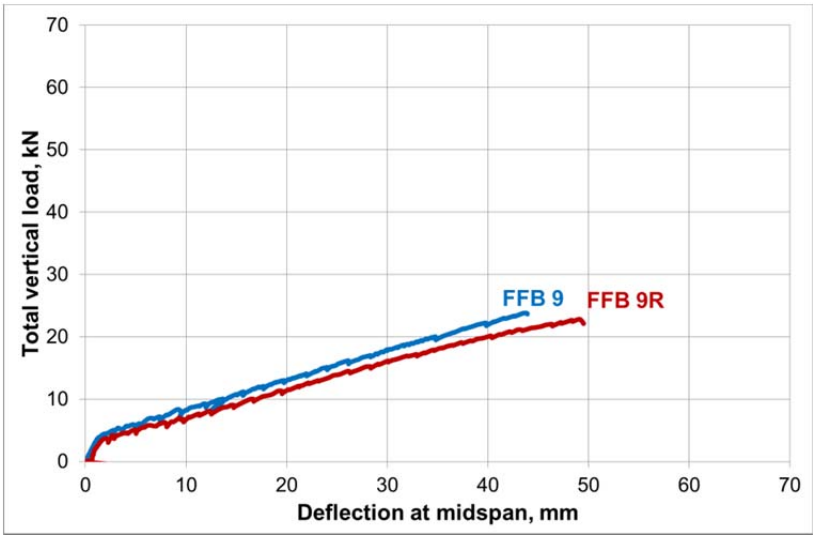

Figure 7.64. Experimental load-deflection curves for FFB 9 and FFB9R

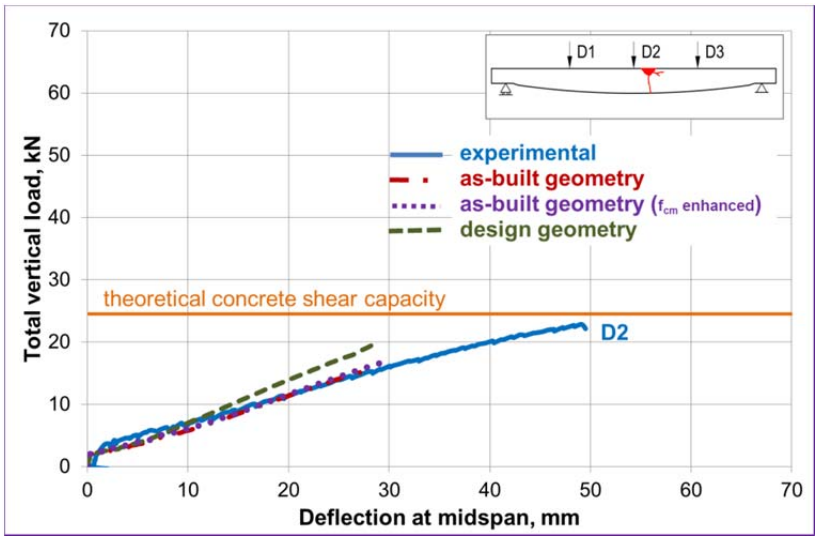

a.

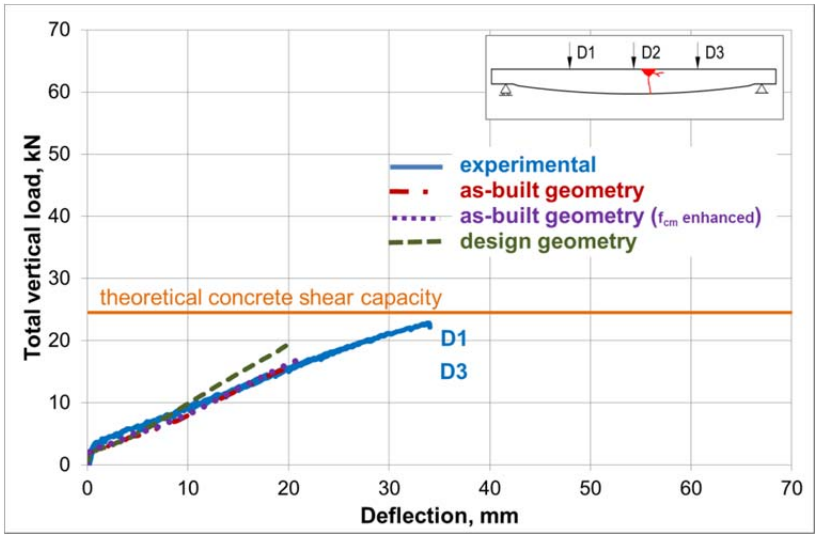

b.

Figure 7.65. FFB 9R Load-deflection relation: (a) at midspan and (b) at quarter span

Overall, all predictions based on the as-built geometry and the assumed concrete strength enhancement show better agreement with the test results, although in all cases the ultimate load capacity is underestimated. This may suggest that a higher increase of the concrete strength is possible, which can be further confirmed by examining the load-strain relations, later.

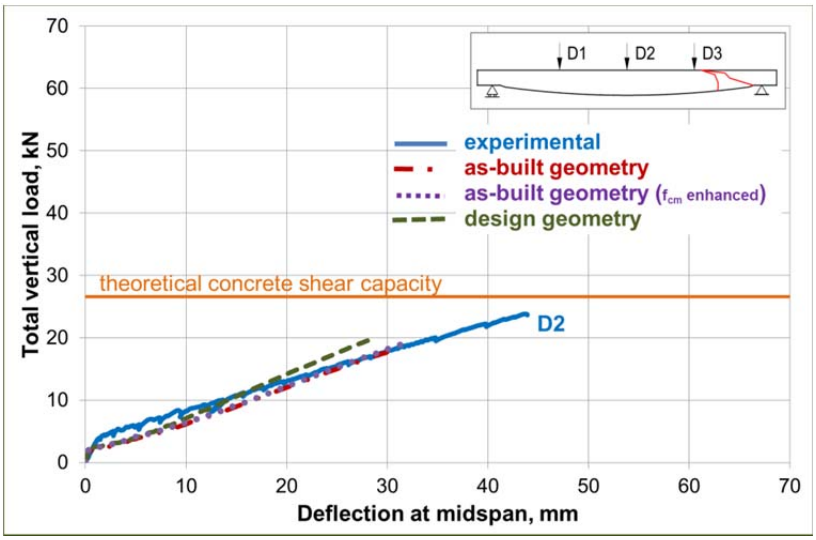

a.

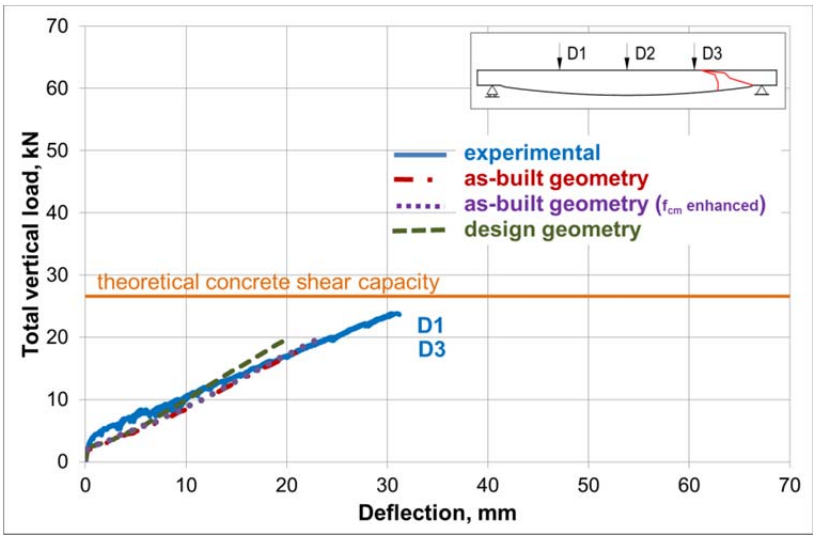

b.

Figure 7.66. FFB 9 Load-deflection relation: (a) at midspan and (b) at quarter span

The experimental load-deflection curves for beams FFB 10R and FFB 10 are compared in *Figure 7.67*. Again the ascending part of the two curves is similar although the initial stiffness of beam FFB 10R appears to be lower than the stiffness of beam FFB 10 (see *Figure 7.67a*). The post-peak load sustained by beam FFB 10 was approximately 20% of the maximum load before the loss of the roller support, caused by an excessive rotation.

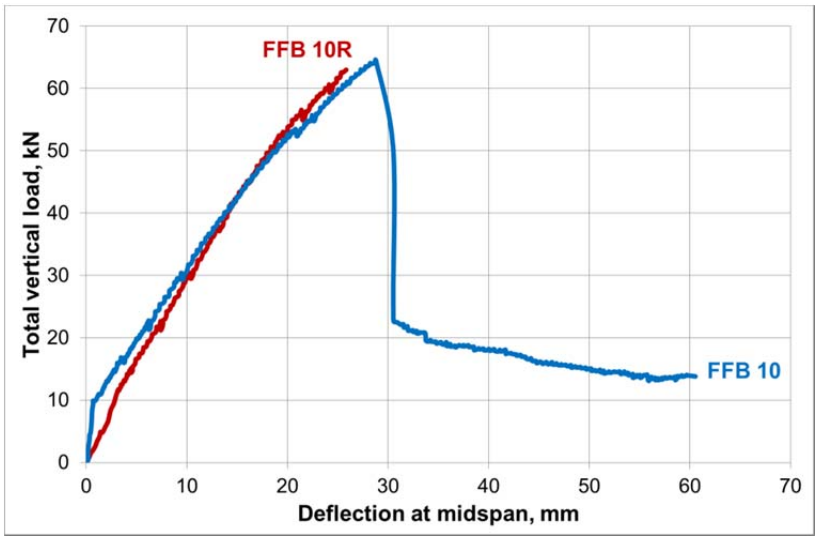

a.

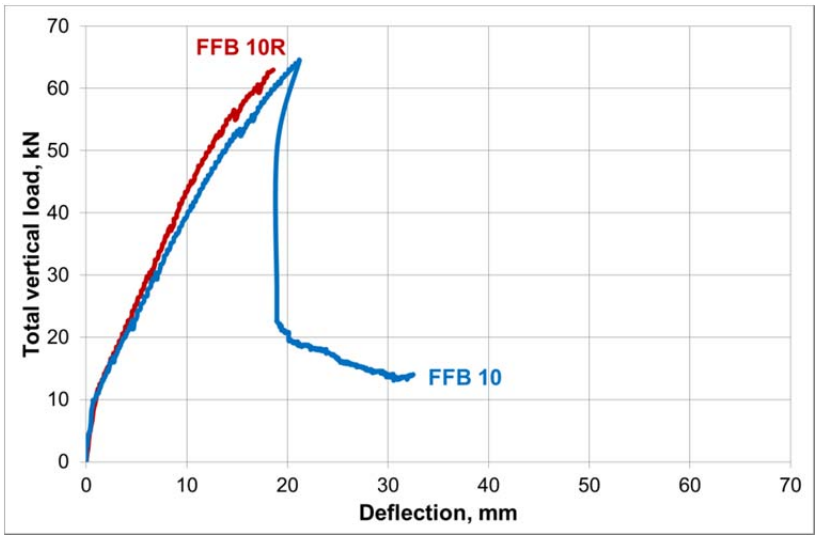

b.

Figure 7.67. Experimental load-deflection curves for FFB 10R and FFB10: (a) at midspan and (b) at quarter span

Figure 7.68 shows the experimental and theoretical results for the reference beam FFB 10R. In this case, the predictions overstimate the beam stiffness near the failure load, which is consistent with the previous findings of this research. Based on the load-deflection curves in *Figure 7.68b*, the proposed method of analysis produces adequate results up to a minimum of 50% of the theoretical ultimate flexural load capacity. The results at midspan predict less accurately the measured response.

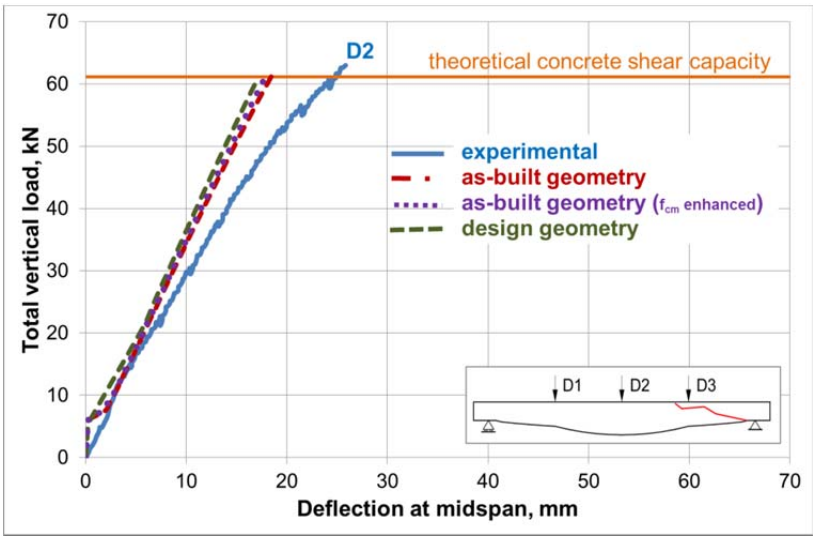

a.

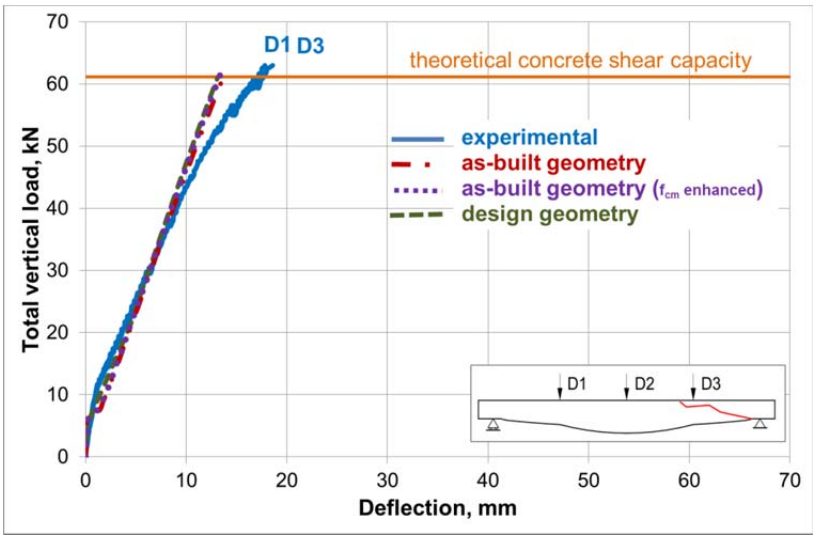

b.

Figure 7.68. FFB 10R Load-deflection relation: (a) at midspan and (b) at quarter span

Only the ascending branch of the load-deflection curve for beam FFB 10 is theoretically predicted, as can be seen in *Figure 7.69*. In general, a slightly better correlation between the theoretical and experimental results can be observed in comparison with beam FFB 10R. Nevertheless, the beam stiffness is also overestimated beyond approximately 50% of the predicted ultimate load. Based on the detailed investigation presented in § 6, the ratio of the quasi-permanent to ultimate loads was found to be in the range of 0.3 to 0.4, which implies that the theoretical curves could still be adequate for predicting serviceability deflections, which is in agreement with the previous findings.

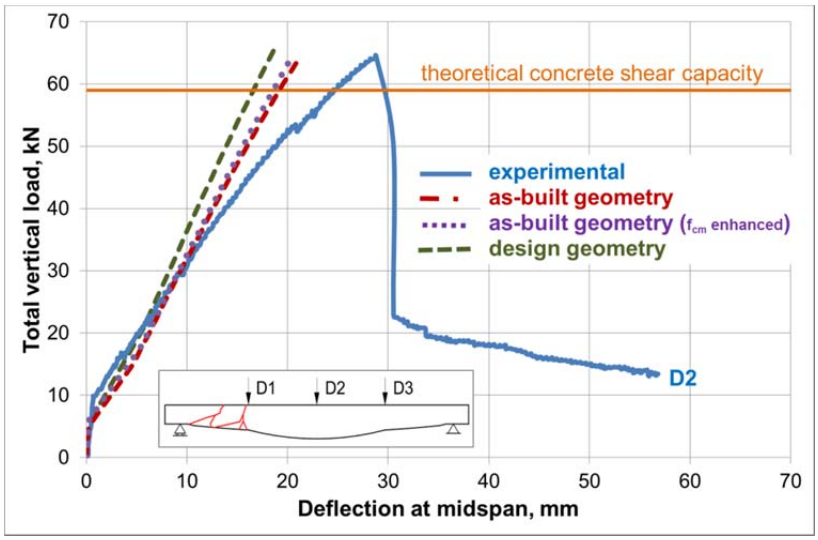

a.

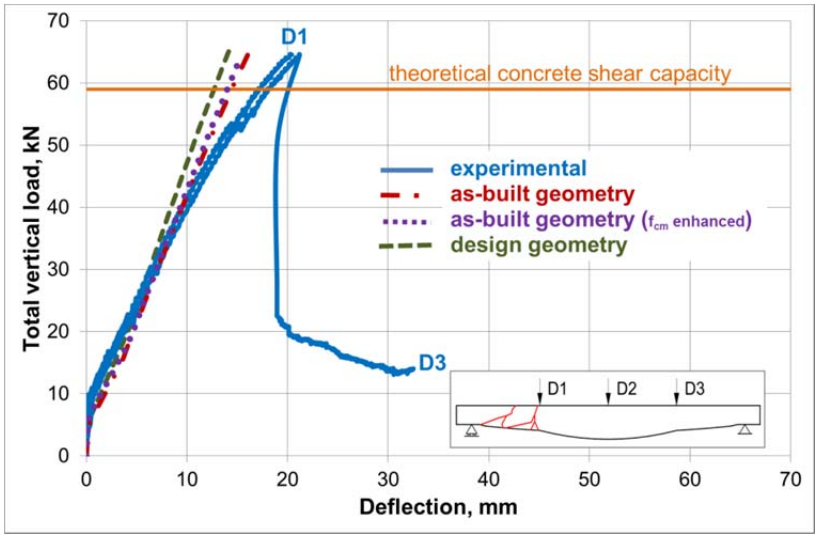

b.

Figure 7.69. FFB 10 Load-deflection relation: (a) at midspan and (b) at quarter span

The difference between the load-deflection relations for beams FFB 11R and FFB 11, presented in *Figure 7.70*, mainly concerns the post-peak behaviour of the two beams. Beam FFB 11 sustained high post-peak load, following the loss of concrete in the cover zone, which surrounded the confining reinforcement. However, the theoretical predictions in *Figure 7.71* and *Figure 7.72* are focused only on the ascending branch of the curves. As can be seen, the major problem, similarly to beams FFB 9R and FFB 9R, appears to be the predictability of the ultimate load capacity, as well as the load corresponding to the cracking moment. This suggests again the possibility to consider higher concrete strength enhancement.

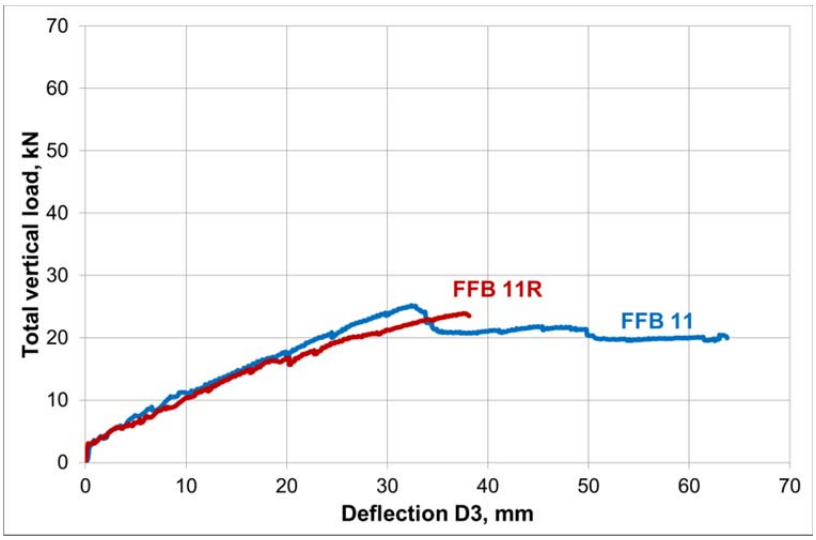

Figure 7.70. FFB 11R and FFB 11 Load-deflection relation at quarter span

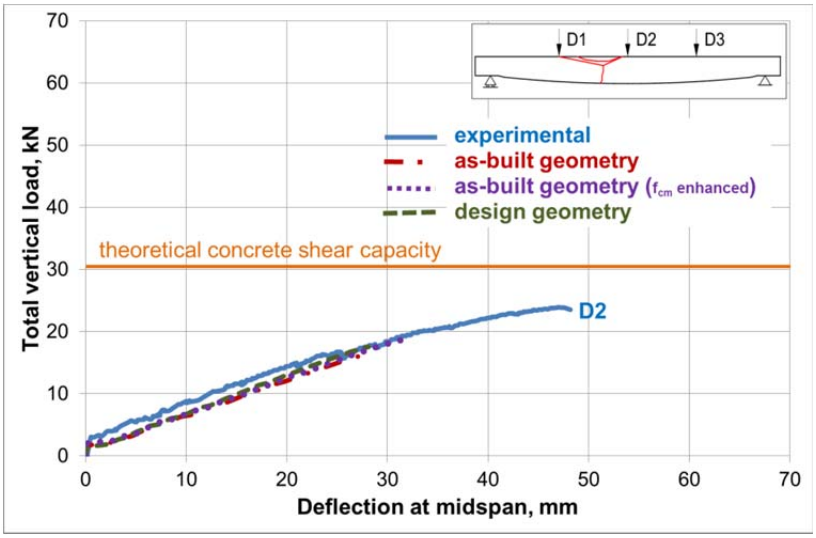

a.

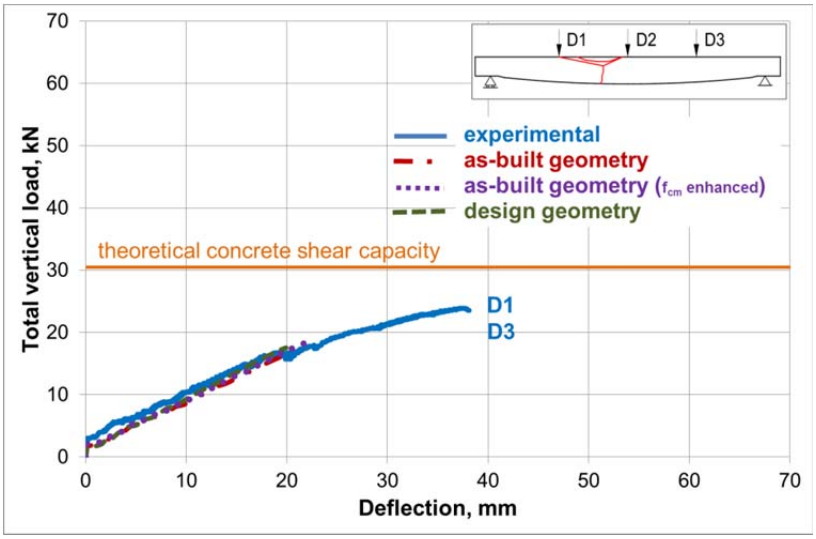

b.

Figure 7.71. FFB 11R Load-deflection relation: (a) at midspan and (b) at quarter span

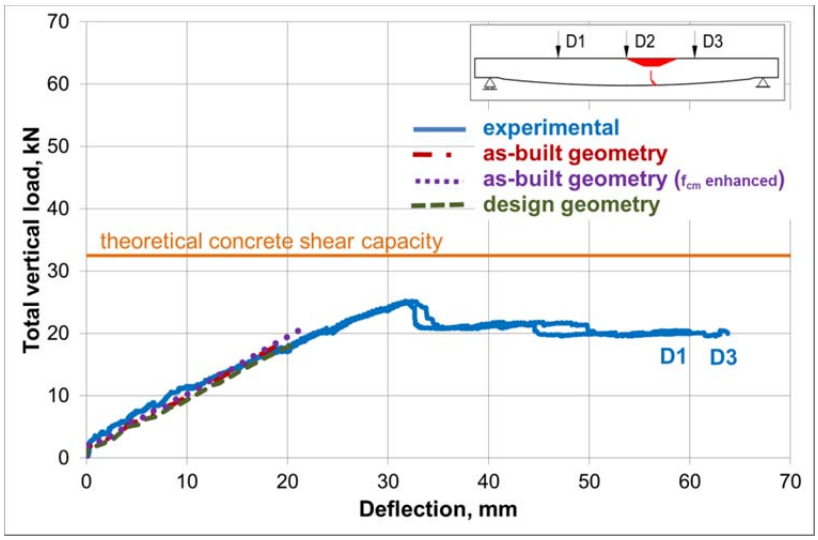

Figure 7.72. FFB 11 Load-deflection relation at end quarter points

The final pair of beams, FFB 12 and FFB 12R, also exhibit similar load-deflection behaviour until the failure of the reference beam, as can be seen in *Figure 7.73*. The predicted load-deflection curves do not fully match the experimental results in *Figure 7.74* and *Figure 7.75*. Nevertheless, the differences could be acceptable for loads corresponding to serviceability levels. Beyond that load stage, the theoretical analysis significantly overestimates the stiffness of beam FFB 12, which could be expected for high reinforcement ratios, as demonstrated by the examples studied in § 4.

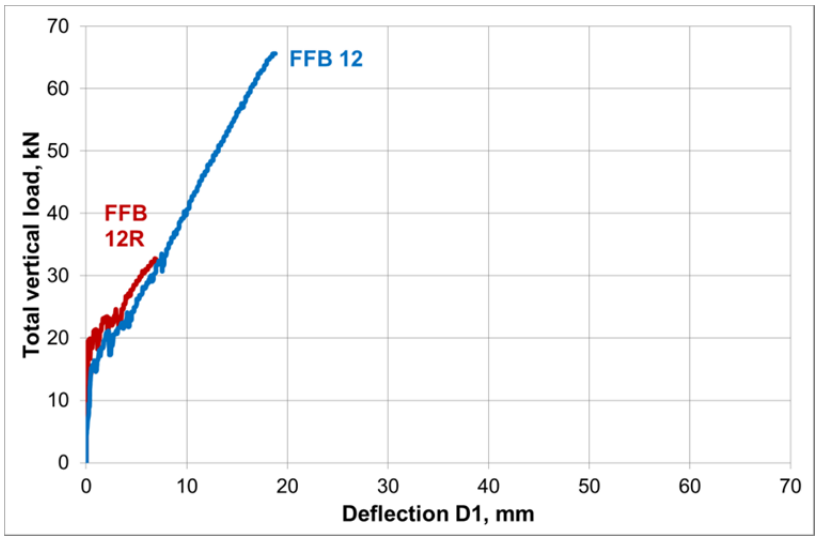

Figure 7.73. FFB 12R and FFB 12 Load-deflection relation at quarter span

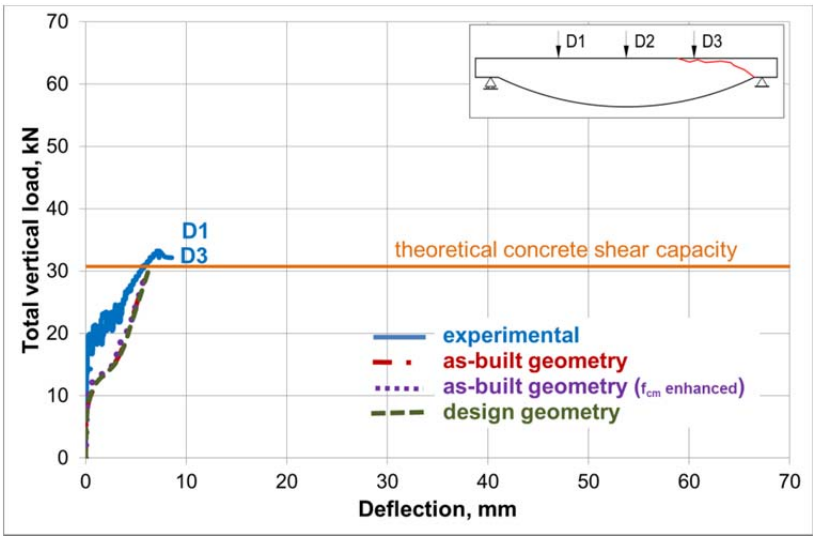

Figure 7.74. FFB 12R Load-deflection relation at end quarter points

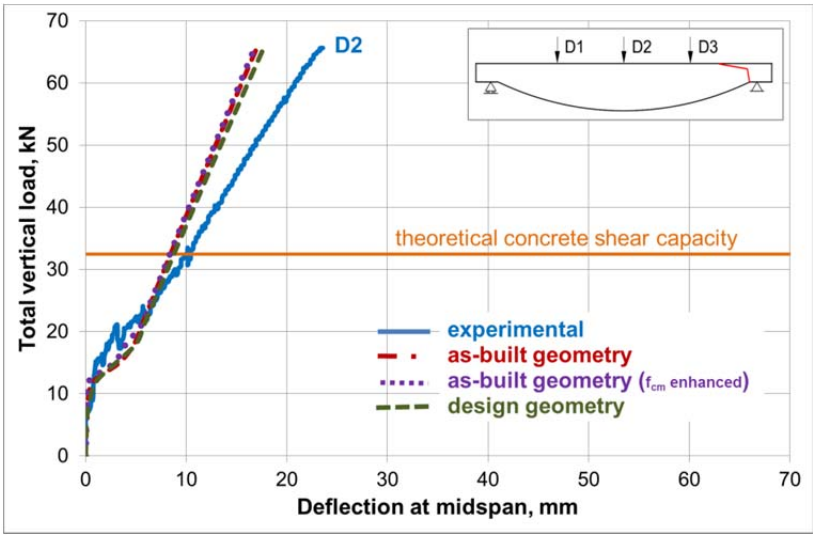

a.

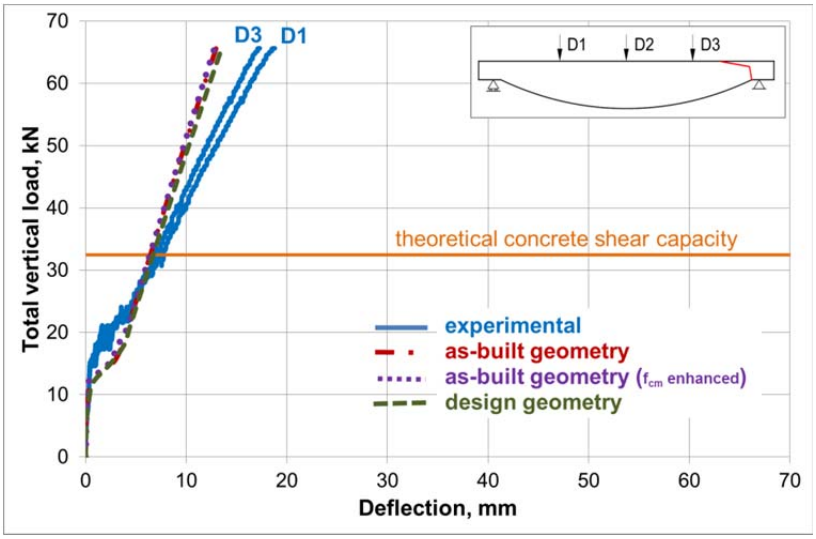

b.

Figure 7.75. FFB 12 Load-deflection relation: (a) at midspan and (b) at quarter span

7.5.3. Experimental and predicted load-strain behaviour of FRP reinforcement

The load-strain plots shown in *Figure 7.76* to *Figure 7.81* compare the experimental and predicted behaviour of FRP bars at the midspan section of each beam. The predicted relations follow fairly accurately the slope of the experimental curves. While this may indicate that the position and the stiffness of the reinforcing bars were correctly defined, the typically lower predicted cracking and ultimate bending moments may be explained with underestimated concrete strength, as suggested earlier.

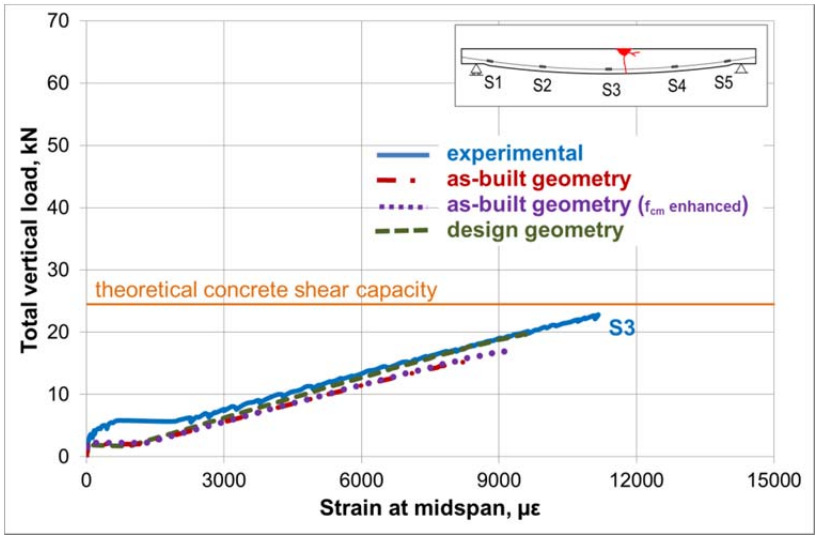

Figure 7.76. FFB 9R Load-strain relation at midspan section

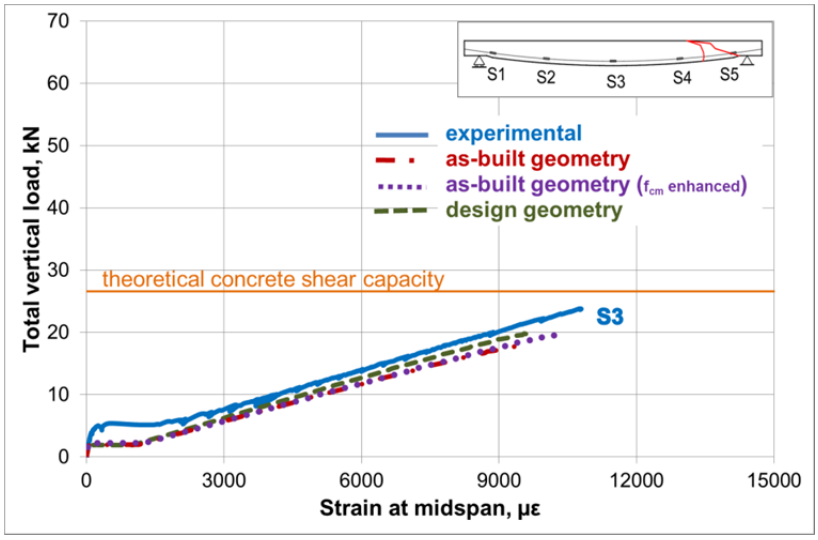

Figure 7.77. FFB 9 Load-strain relation at midspan section

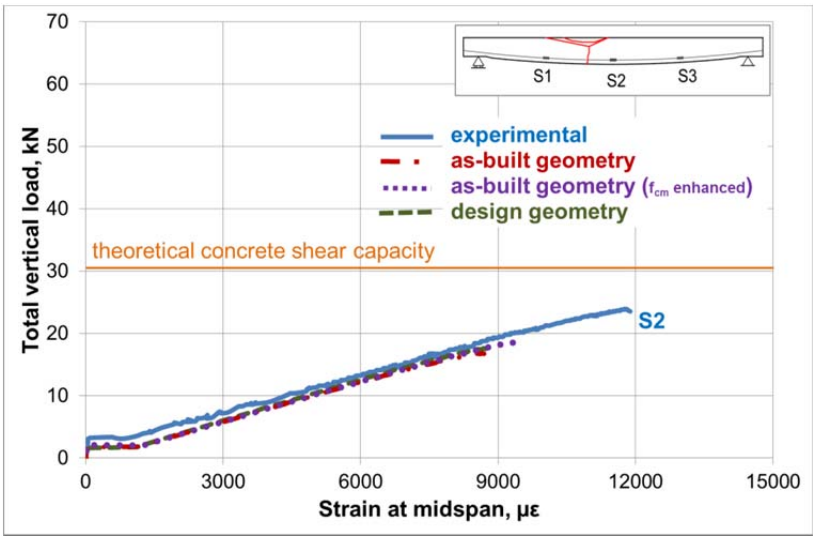

Figure 7.78. FFB 11R Load-strain relation at midspan section

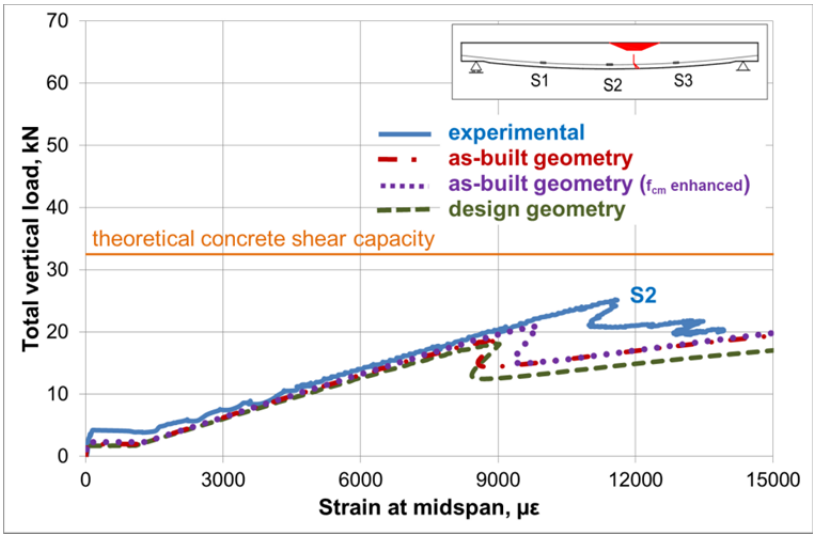

Figure 7.79. FFB 11 Load-strain relation at midspan section

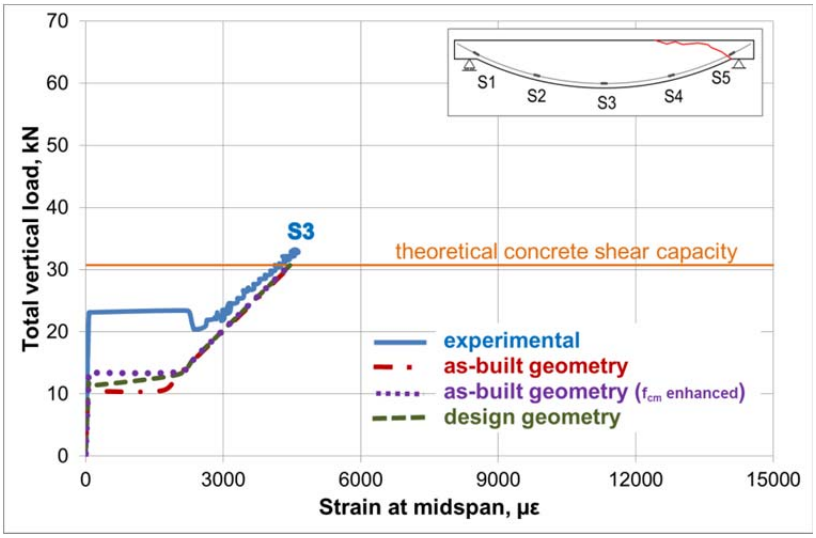

Figure 7.80. FFB 12R Load-strain relation at midspan section

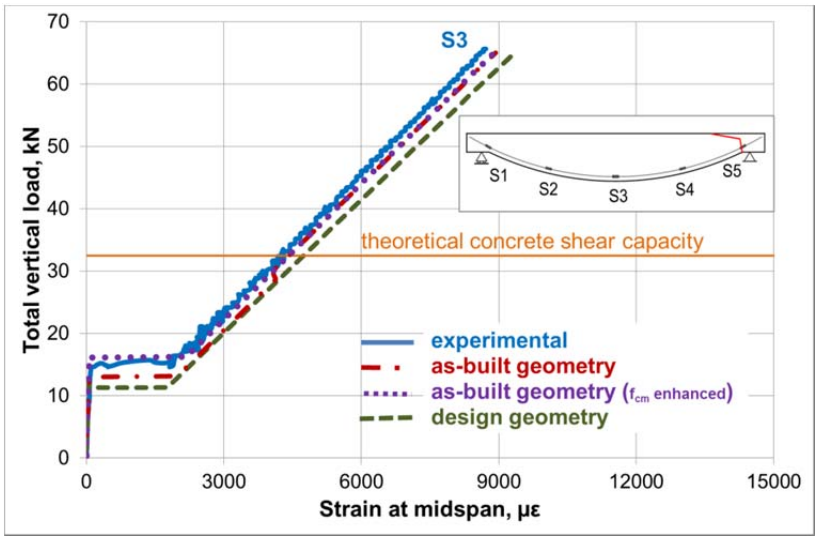

Figure 7.81. FFB 12 Load-strain relation at midspan section

7.5.4. Influence of concrete cover on post-peak strength of beams, which contain confining reinforcement

Beam FFB 11 provided good results demonstrating the possibility to improve the ductility of FRP-reinforced beams through confinement of concrete in compression, the main objective of this chapter. However, the difference between the maximum capacity and post-peak load sustained by the test beam was fairly large, approximately 25%. It is expected that this difference depends mainly on the concrete cover above the helical reinforcement. Therefore, it could be possible to control the step in the load-deflection curve by determining an appropriate cover, as confirmed by the parametric study presented below.

For the purpose of this study, the theoretical load-strain curve for beam FFB 11, shown in *Figure 7.82*, is fitted to match the experimental curve by increasing the enhancement of concrete strength, based on the conclusions from comparison of the predicted and experimental load-deflection curves for all test beams. The fitted concrete strength is 26.7 MPa, which predicts accurately the maximum load and the load corresponding to the cracking moment. The post-peak part of the curve also describes relatively well the experimental data recorded until 1.4% strain in the GFRP reinforcement. The test was stopped in order to avoid a potential damage of the loading jacks due to the lateral bending caused by the rotation of the test beam. Although the final failure was not observed, the theoretically obtained strain at the top extreme fibre of the confined concrete is 0.8%, indicating that concrete had reached nearly 1% without failing, as expected

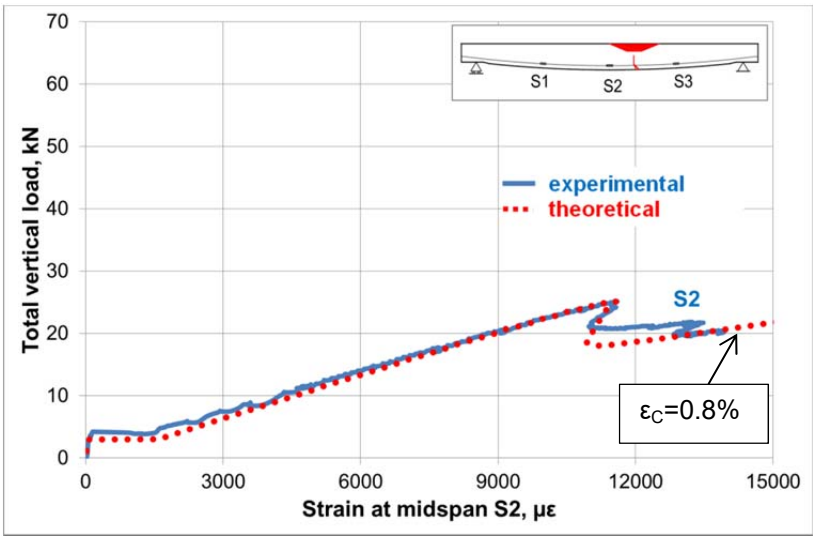

Figure 7.82. FFB 11 Fitted load-strain relation

Using the adjusted concrete strength, the load-strain relation for beam FFB 11 is re-calculated for different adequate values of the concrete cover above the AFRP helix, assuming the same overall depth. The results presented in *Figure 7.83* could suggest that, in this case, 10 mm cover would have been appropriate to practically sustain the maximum load.

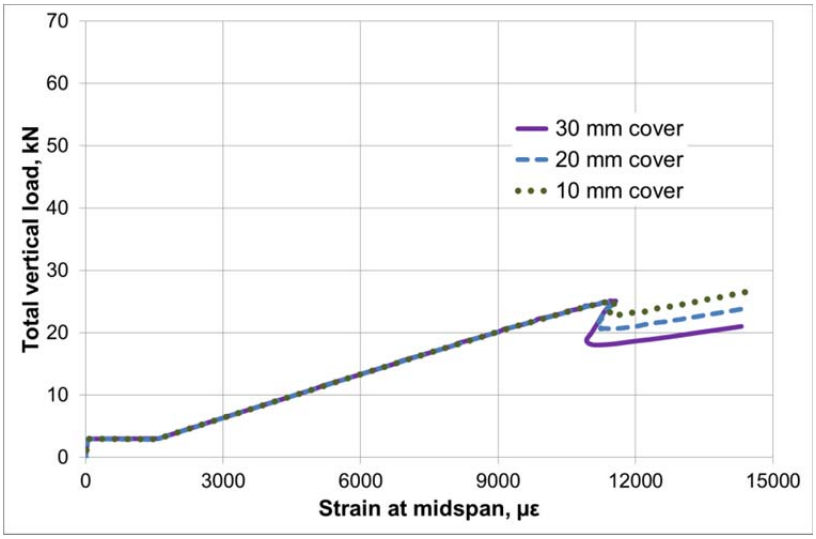

Figure 7.83. FFB 11 load-strain relation for different top cover to confined zone

7.6. Concluding remarks

The main objective of the experimental study presented in this chapter was to provide an effective method for the design and construction of FRP-reinforced fabric-formed concrete beams with improved ductility through confinement of concrete in the compression zone. The possibility to produce complete FRP reinforcement cages, containing both confining and shear reinforcement of complex shapes, has also been investigated and successfully demonstrated.

The major challenge for providing FRP reinforcement cages is their production and installation. The most economical and accurate manufacturing method, avoiding fiddly reinforcement assembly, would involve winding freshly impregnated continuous fibres directly onto the longitudinal bars. The longitudinal bars, however, need to be produced in their design curved shape.

The load test data and the theoretical analysis presented in this chapter confirmed the potential ductile behaviour of fabric-formed beams by relying on confined concrete. It also confirmed the predictability of the results for beams reinforced with FRP materials. However, the comparison of experimental and predicted load-deflection relations posed a question over the actual strength of concrete cast in fabric formwork. Although a major increase of the concrete strength can be expected near the fabric-cast faces due to the loss of excessive free water, a similar enhancement was observed for the top concrete. This could be explained with the relatively small size of the test specimens. A potential implication in a design situation would be the need to check the strains in the longitudinal FRP reinforcement for higher concrete strengths at ULS failure in order to avoid rupture of the FRP bars. However, the flexural resistance of the design member should be conservatively determined for normally cast concrete strength.

The position of the confining helix can have a significant effect on the post-peak response of a beam, resulting in a large step in the load-deflection curve. However, it has been demonstrated that the effect is fully predictable and could be controlled, while still ensuring adequate bond cover to the helical reinforcement.

Finally, the predictability of the shear resistance of beams reinforced using CFRP spiral cages has also been demonstrated. Two types of CFRP spiral cages have been developed and tested. The first type resembled the rectangular spiral reinforcement used for prismatic beams with uniform sections. Although the cage prevented a catastrophic failure, the beam’s additional shear resistance provided by the CFRP spiral was curtailed by tensile rupture at a single location. This is most likely related to the small size of the spiral near the supports, resulting in insufficient anchorage of the legs crossing the shear cracks. Furthermore, the first type of spiral cage would not be suitable for beam cross sections with nearly triangular shapes. The second type benefited from a vertical central leg and provided shear resistance close to the theoretical predictions. In addition, the applied winding technique for the second spiral can be applied to both trapezoidal and triangular cross-sectional reinforcement configurations.

In summary, it has been shown that by using suitable shear spiral reinforcement in combination with a confining helix, it is possible to enhance the shear capacity and the ductility response of FRP-reinforced fabric-formed concrete beams.

8. Case Studies

8.1. Introduction

The design and construction methods for fabric-formed beams proposed in the current research have been developed through several series of experimental tests focused on different problems. This chapter aims to collate all research findings by demonstrating a step-by-step design procedure, including constructability considerations. For this purpose two case studies of beam designs are presented. The first beam contains confining helices and shear spiral reinforcement for improved ductility. The second case study relates to the design of a beam with a 'key-hole' cross section and field-bent reinforcement, attached to fabric during construction. The examples do not aim necessarily to represent real beams but to demonstrate the extents of applicability, particularly in meeting serviceability criteria.

8.2. Design of a ductile FRP-reinforced fabric-formed beam

8.2.1. Design parameters

The first design example is based on a two-metre simply supported beam. A uniformly distributed live load of 30 kN/m is applied with a load factor 1.5 over the whole length of the beam, as shown in *Figure 8.1*. The load factor on the load due to beam selfweight is 1.35.

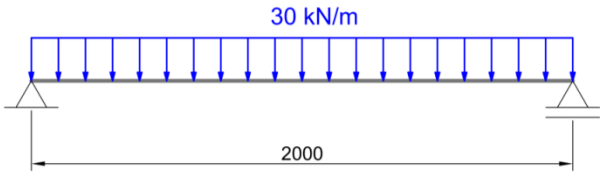

Figure 8.1. Case study 1 applied loads (all dimensions are in millimetres)

The concrete grade is C40/50, while the assumed tension reinforcement has a Young's modulus of 60 GPa and an ultimate tensile strength of 1300 MPa, corresponding closely to manufacturer's data for GFRP bars. The partial material safety factor for concrete is 1.5, in accordance with BS EN 1992-1-1:2004. The stress-strain curve for concrete, confined by AFRP helical reinforcement with 90 mm diameter and 30 mm pitch as adopted for the experimental investigation, is used (see § 4). The properties of the CFRP shear spiral reinforcement are also taken from the experimental studies for Type B cage (refer to § 7) and the design strain is limited to 0.4% in accordance with ACI 440.1R-06.

The assumed geometrical constraints include a fixed top breadth of 110 mm, required to accommodate a 90 mm diameter helix with 10 mm side cover, a minimum breadth of 80 mm, and a maximum depth of 250 mm. In addition, 200 mm length is allowed for

forming flat bottom surfaces over each support, as described in § 5, § 6 and § 7, adding up to an overall length of 2.2 m. The concrete cover is 25 mm to the tension reinforcement and 10 mm to the top of confined concrete.

8.2.2. Design procedure

8.2.2.1. Design load effects

The load effect diagrams for the factored loads are presented in *Figure 8.2*. The load effects due to selfweight are initially assumed for a preliminary sized constant cross section and automatically updated during the geometry optimisation process.

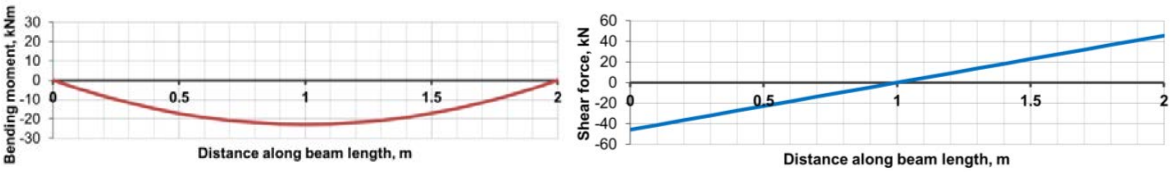

Figure 8.2. Case study 1 total factored bending moment and shear force diagrams at ULS

8.2.2.2. Design options

The design is initiated by determining the required tension reinforcement for a rectangular cross section, subjected to the maximum bending moment effects. In this case, a single 16 mm diameter bar would be adequate for a section of 250 mm maximum overall depth. The choice of the shear reinforcement strength, however, can have a significant effect on the final geometry, as illustrated in *Figure 8.3*. The three presented options are designed for shear spiral reinforcement, made of two, three and four carbon fibre tow thicknesses, respectively, and a minimum of 50 mm spacing between the vertical legs. The design takes into account the shear enhancement near the supports and includes horizontal restraints, preventing the bulging of deep sections. The pinched breadth, which is formed by the horizontal ties, is equal to the minimum defined breadth of 80 mm and is positioned at mid-depth or at 110 mm from the top concrete surface in order to accommodate the helix in the top bulb.

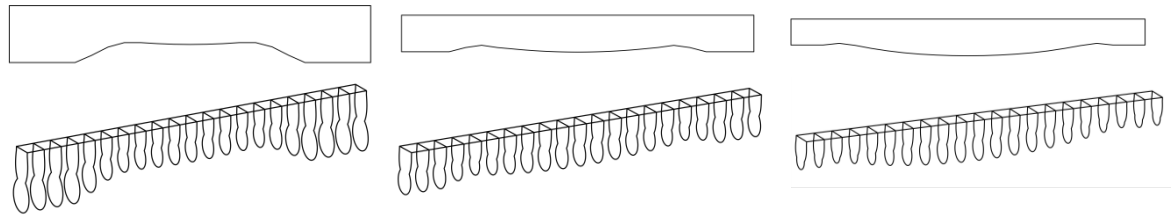

Figure 8.3. Case study 1 beam profile for different diameter of the shear spiral: (a) Option 1 (two fibre tows), (b) Option 2 (three fibre tows) and (c) Option 3 (four fibre tows)

The utilisation of the bending moment and shear force capacities for each option can be seen in *Figure 8.4*. The corresponding concrete material savings are also calculated and are 22%, 23% and 34%, respectively, in comparison with an equivalent uniform rectangular section.

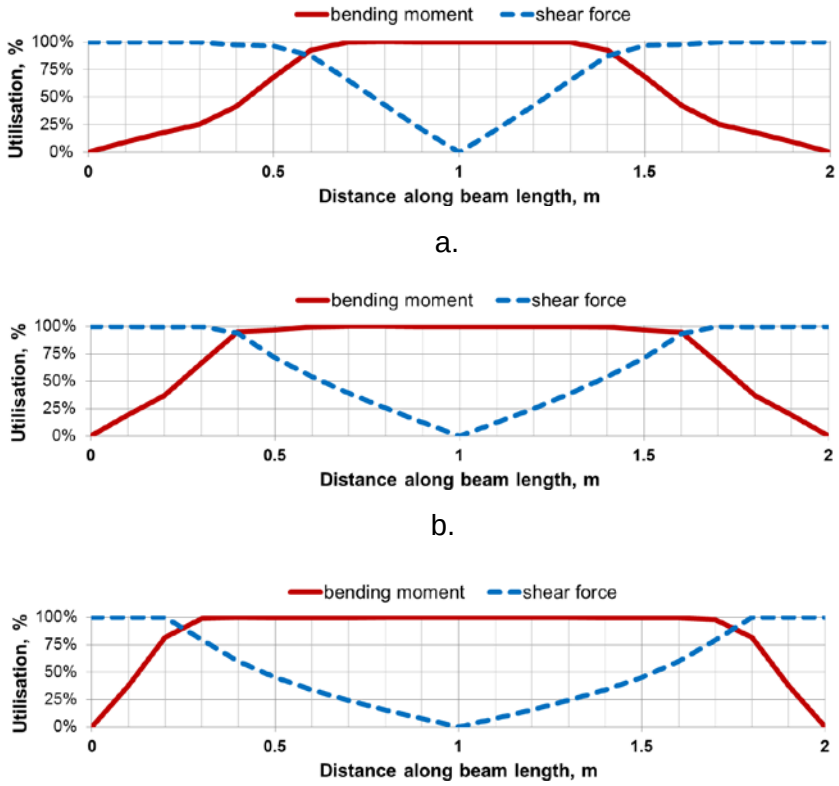

Figure 8.4. Case study 1 capacity utilisation: (a) Option 1 (two fibre tows), (b) Option 2 (three fibre tows) and (c) Option 3 (four fibre tows)

Finally, the three options are assessed against the serviceability criteria for vertical deflection. The deflected shapes, presented in *Figure 8.5,* are obtained for a quasi-permanent value of the live load, assuming a ψ_2 factor of 0.3. As can be seen, the beams become more flexible with the reduction of the concrete material. However, the maximum deflection at midspan remains below the span/250 limit of 8 mm for all options.

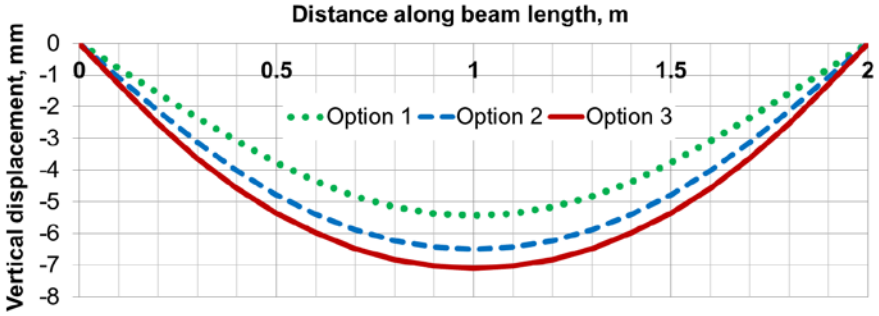

Figure 8.5. Case study 1 deflected shapes at SLS for all options, presented in Figure 8.3

8.2.2.3. Geometry and reinforcement details

The last of the three presented options offers the greatest concrete savings within the acceptable limits for vertical displacement and, therefore, is selected for further analysis and for calculation of the parameters needed for construction. The longitudinal profile of the beam is slightly adjusted to form a smooth curve of the FRP reinforcement, as shown with the dashed line in *Figure 8.6*. The spacing between the vertical legs of the shear spiral is varied in order to increase the design efficiency.

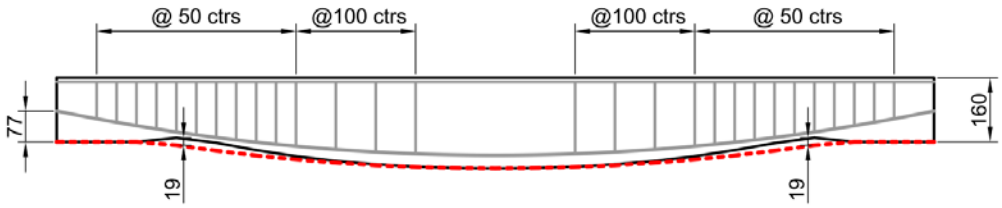

Figure 8.6. Case study 1 revised beam profile for Option 3 (all dimensions are in millimetres)

8.2.2.4. Utilisation and material savings

The capacity utilisation for the adjusted geometry and reinforcement details of the final design is shown in *Figure 8.7*. The utilisation of the shear force capacity is significantly improved by variation of the spiral pitch, which would also save carbon fibre material. The reduction of the concrete material savings due to the deepening of cross sections near the supports, indicated in *Figure 8.6,* is fairly small, leading to final savings of 31%.

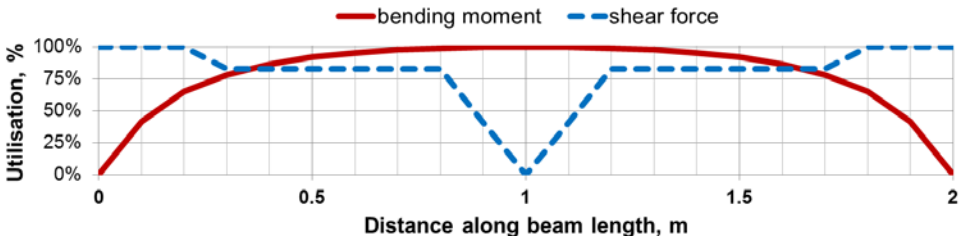

Figure 8.7. Case study 1 revised capacity utilisation for final beam design

8.2.2.5. Vertical deflections and strains in FRP bar

Figure 8.8 provides both the predicted moment-strain and predicted moment-deflection relations at midspan for the final beam design. The curves in *Figure 8.8a* are plotted up to 1% strain at the top extreme fibre of the confined concrete zone for two values of cover to the confined concrete, the adopted 10 mm and an increased value of 20 mm. In this case, the plots may suggest that concrete cover of 20 mm could also be adequate. It should also be noted that the strain in the GFRP bar at failure, calculated for 1% strain in

concrete, increases with the reduction of the cover and an appropriate safety factor should be applied to the stress, corresponding to this strain.

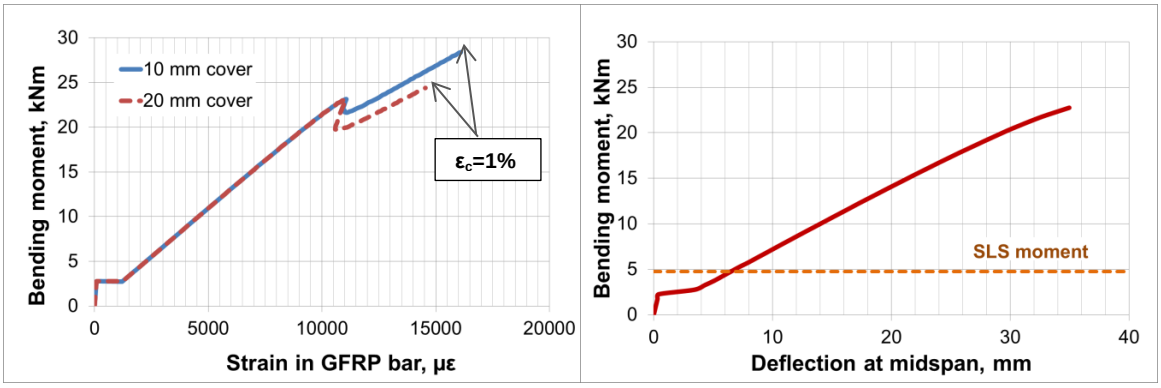

a. b.

Figure 8.8. Case study 1 final beam design: (a) predicted moment-strain and (b) predicted moment-deflection relations

8.2.2.6. End anchorage design

Figure 8.9 illustrates the distribution of the tensile force along the length of the GFRP bar, including the additional force due to shear. Splayed ends are designed for the maximum force in the bar, based on the proposed force-slip expressions in § 3. It has previously been demonstrated that these expressions successfully describe the actual pull-out behaviour of splayed anchorage up to approximately 0.3 mm end slip, which can be accepted as a safe design criterion.

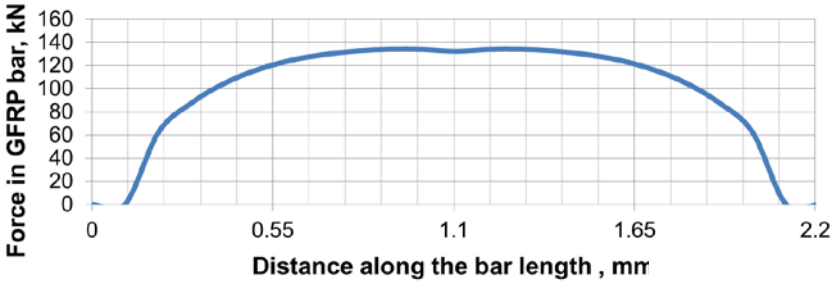

Figure 8.9. Case study 1 force in tension reinforcement at ULS

The assumed bond-slip curves for determining the surface bond for the bar and wedge plate area are presented in *Figure 8.10a*. The bond stresses in the straight bar correspond to the typical values for sand-coated GFRP reinforcement. The bond-slip relation for the wedge area, which highly depends on the method of preparation, is conservatively taken to be similar to the bond strength of smooth bars, as recommended in § 3. *Equation 3.27* is then applied, and the results plotted in *Figure 8.10b* indicate that a 100 mm 4° wedge would provide adequate resistance, which is twice as high as the pull-out resistance of a 100 mm straight anchorage length. In addition, providing helical reinforcement around the

splayed anchorage would prevent brittle failure of the surrounding concrete at increased slip levels, and help to maintain the overall ductile behaviour of the beam.

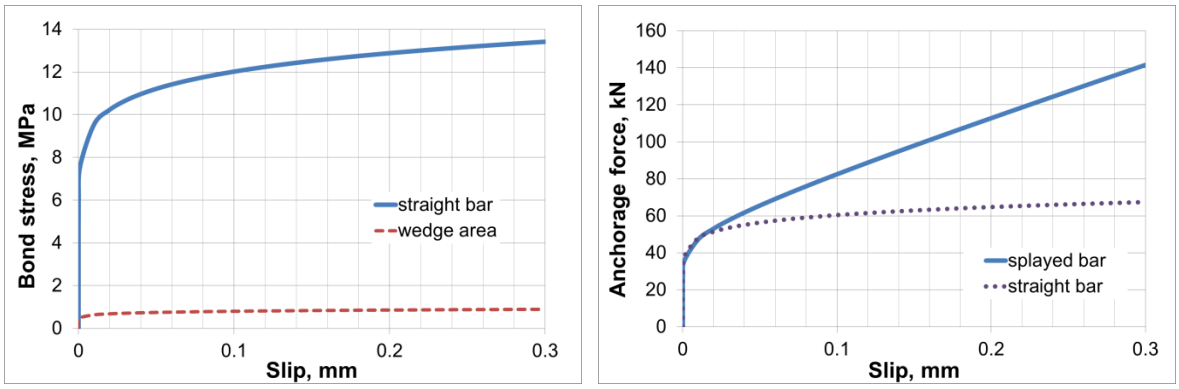

a. b.

Figure 8.10. Case study 1: (a) bond-slip relation for the different surface treatments of the GFRP bar and the wedge area and (b) force-slip relation for straight end and 100mm 4° wedge

8.2.3. Construction parameters

The parameters required for construction are determined for the final design geometry and reinforcement details, illustrated in *Figure 8.11* and *Figure 8.12*. Based on the limitation of stresses in the bends of FRP reinforcement in accordance with ACI 440.1R-06, a bend radius of 3 mm would be adequate for the CFRP spiral. Therefore, three top reinforcing bars of minimum diameter 6 mm are specified to hold the CFRP cage. However, the diameter of the middle bar is increased to 10 mm to improve the verticality of the middle leg, indicated on cross sections 1-1 and 2-2 in *Figure 8.12*.

The position of the horizontal formwork ties is defined by the perimeter of the bottom bulb, and shown on the fabric pattern in *Figure 8.11d.* The restrained breadth, as defined, is 80 mm. *Table 8.1* summarises all parameters for cross sections positioned at a distance x_L from the left support. Only half of the beam length is presented due to symmetry. A constant thickness of 20 mm is assumed for the top plate of the formwork table. The total perimeter, P, and the perimeter of the bottom bulb, P_b, are automatically obtained from the form-finding algorithm. However, the perimeter of the sections at the supports needs to be increased to allow creation of a flat bottom surface by fixing the fabric to a rigid plate, explained in *Figure 8.13*.

The final construction perimeters, P* and P_b*, also take into account the extension of the fabric during construction, due to the tensile forces in the bottom and top bulbs, T_1 and T_2.

As can be seen, in this case the values of the total extension are fairly small and have negligible effect on the lengths of the cross-sectional perimeters.

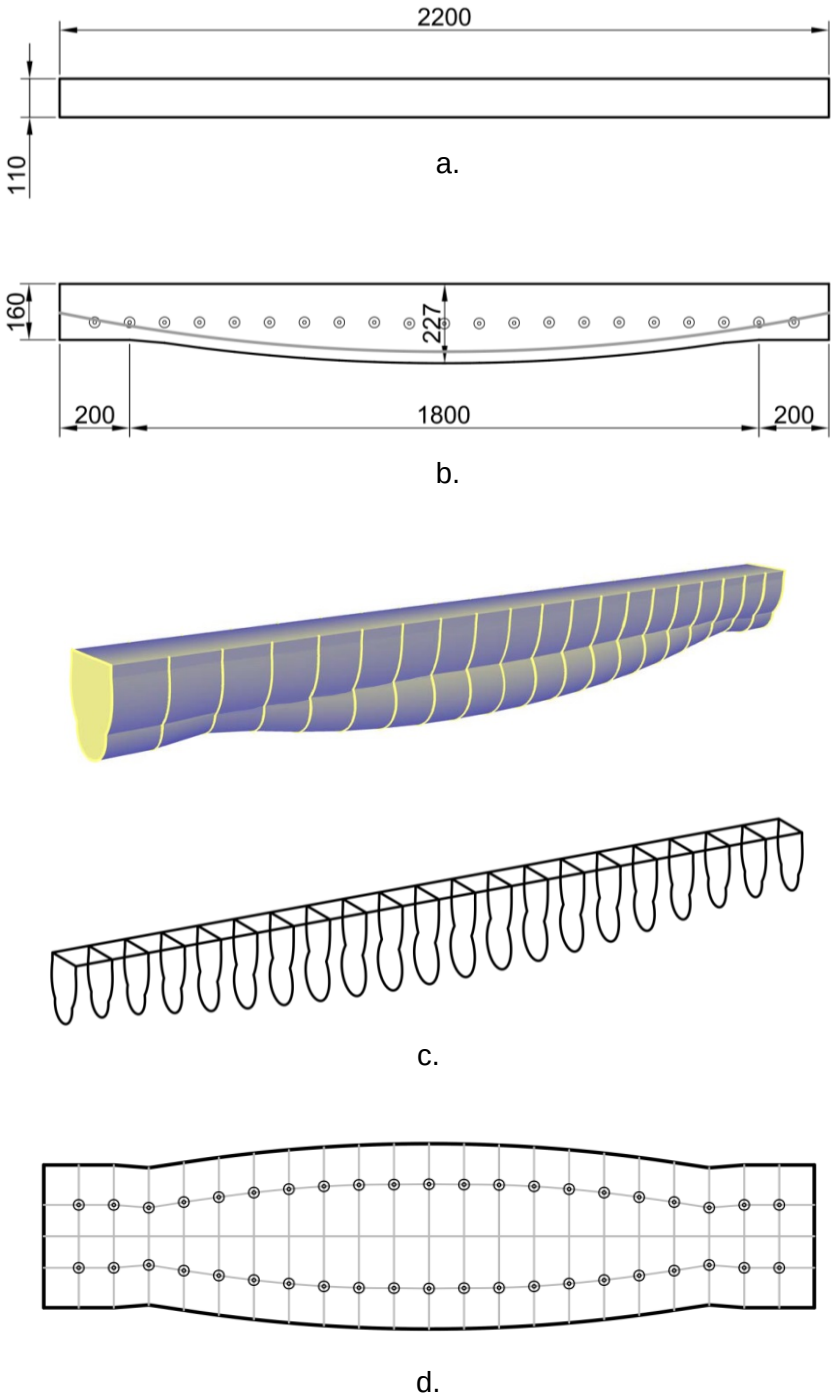

Figure 8.11. Case study 1 geometry details: (a) plan, (b) elevation, (c) 3-D view of cross sections and (d) fabric pattern (all dimensions are in millimetres)

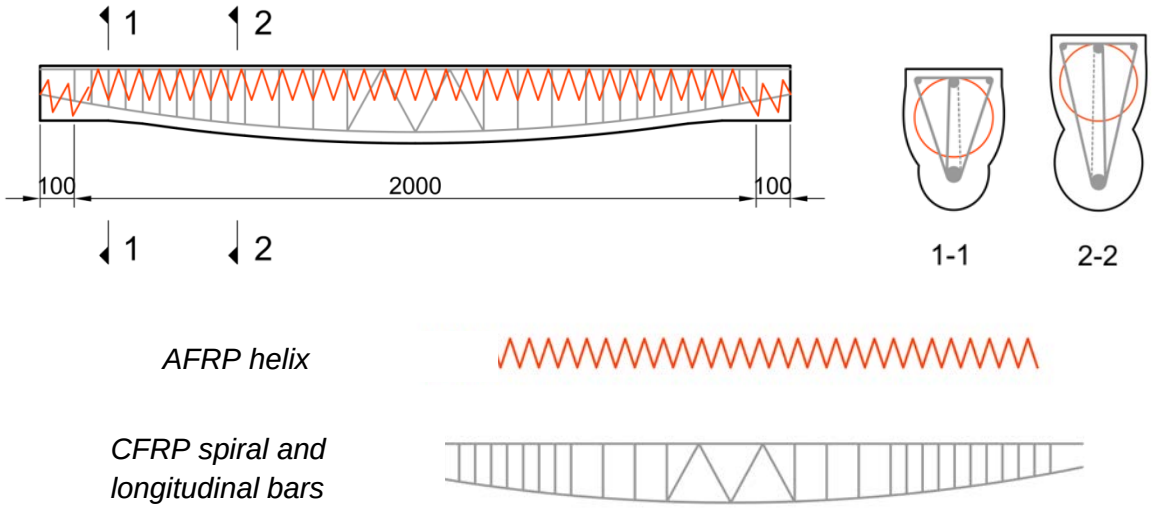

Figure 8.12. Case study 1 reinforcement details (all dimensions are in millimetres)

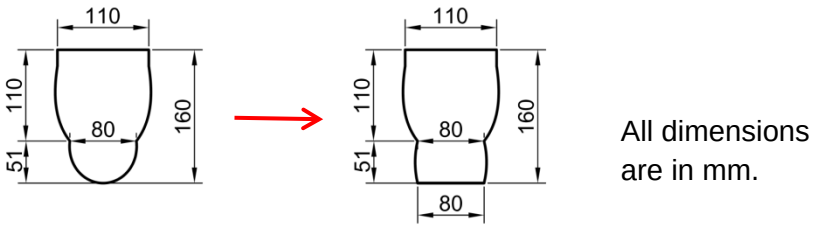

Figure 8.13. Case study 1 adjusted shapes at supports (following the method in § 7)

Table 8.1. Construction parameters (Case study 1)

x_L	B	P	P_b	T_1, N/m	T_2, N/m	extension	P*	P_b*
0	110	374	180	144	180	0.2	408	180
100	110	374	180	144	180	0.2	408	180
200	110	392	164	156	188	0.2	392	164
300	110	422	196	182	203	0.3	422	196
400	110	450	224	207	218	0.3	450	224
500	110	474	250	232	232	0.4	474	250
600	110	494	270	253	244	0.4	494	270
700	110	510	286	270	255	0.5	510	286
800	110	522	294	281	262	0.5	522	294
900	110	528	296	286	266	0.5	529	296
1000	110	530	298	288	268	0.5	531	298

All dimensions are in millimetres.

8.3. Design of a ‘key-hole’ cross-section beam

8.3.1. Design parameters

The second example represents a simply supported beam with end cantilevers, subjected to more complex loading, including superimposed load of 5 kN/m, 10 kN/m live load positioned over the cantilevers and a single concentrated load of 10 kN moving between the supports, as illustrated in *Figure 8.14*. Again a load safety factor of 1.5 is applied to the live load, while the superimposed load and load due to selfweight are multiplied by a safety factor of 1.35.

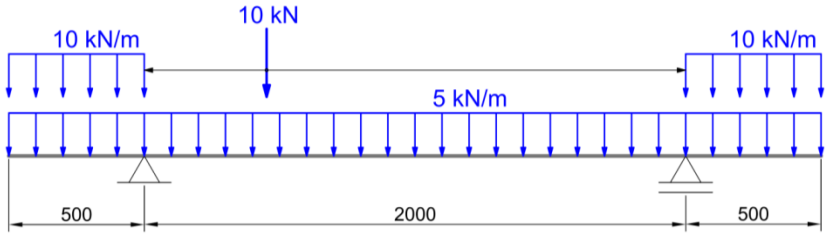

Figure 8.14. Case study 2 applied loads (all dimensions are in millimetres)

The partial material safety factors, concrete grade and tension reinforcement properties are assumed to be similar to those of the first example. The top breadth is allowed to vary between 80 mm and 400 mm. The minimum overall depth is set to 75 mm, largely based on 25 mm cover to the tension reinforcement, while a maximum depth of 350 mm is defined, based on preliminary sizing of a rectangular section. Again a 200 mm flat length is required at the supports. In this case, bulging of deep sections is to be restrained by web formers, creating ‘key-hole’ shaped cross sections. The height of the top bulb, the height of the bottom bulb and the thickness of the web are all set to 75 mm.

8.3.2. Design procedure

8.3.2.1. Design load effects

The total design load effects in terms of bending moment and shear force diagrams, presented in *Figure 8.15*, are a combination of the factored permanent load effects and the envelope of the factored live load effects. Again the load effects due to selfweight are re-calculated at each step of the geometry optimisation process.

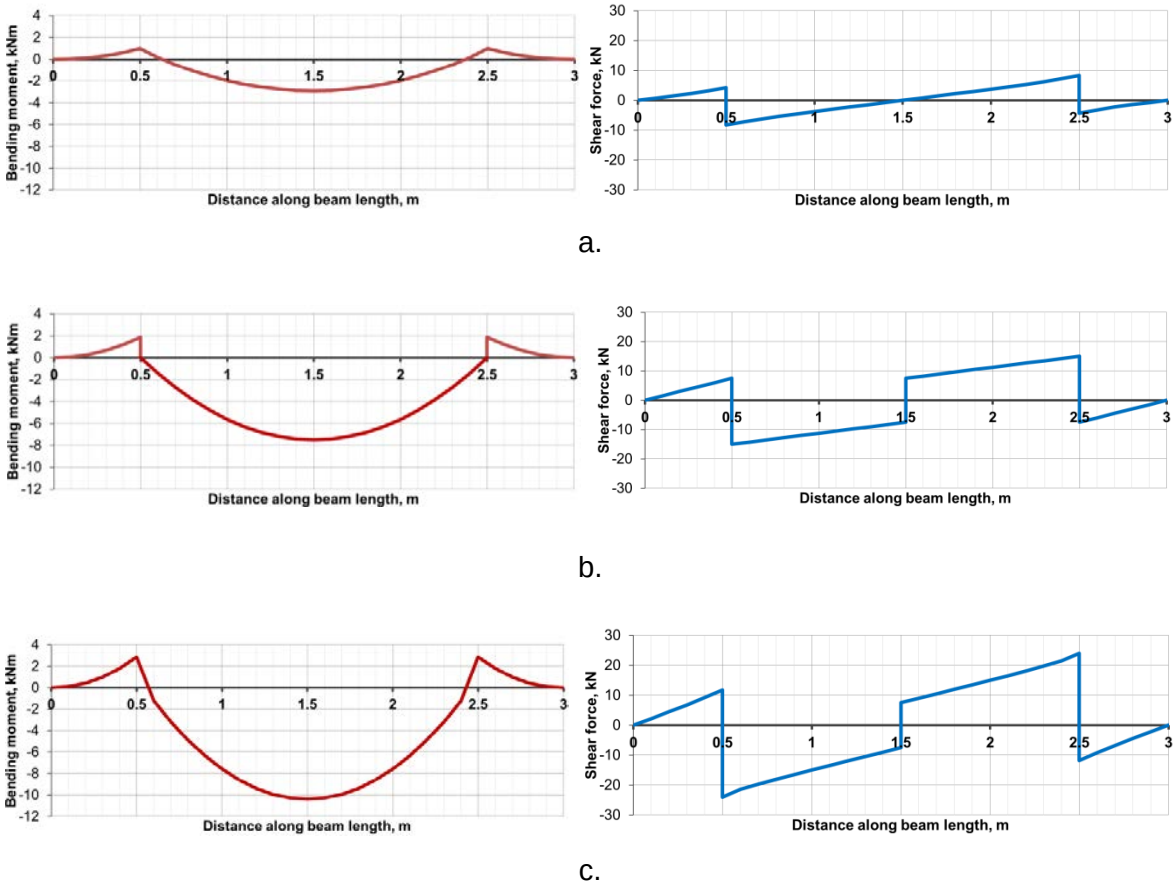

Figure 8.15. Bending moment and shear force diagrams due to: (a) permanent loads, (b) live load envelopes and (c) combination of all loads

8.3.2.2. Geometry and reinforcement details

In this example, the reinforcement comprises straight GFRP bars, which will be bent into their design curve during construction. Therefore, a more flexible reinforcement of 12 mm nominal size diameter is chosen. The geometry optimisation is initiated for a cross section with total depth of 350 mm and a top breadth of 80 mm. The results from the optimisation process, developed in § 4, are presented in *Figure 8.16a*. However, the obtained longitudinal profile is not suitable for achieving adequate anchorage at the ends of the central reinforcing bar, as highlighted on the elevation drawing. Therefore, the profile is slightly straightened to ensure that the ends of the bar are positioned well inside the concrete. The sharp corners near the supports are also replaced with smooth curves for improved buildability and the flat length over the supports is extended to 200 mm. Although all dimensions are defined at this stage, the exact shape of the reinforcement profile still depends on the proposed method for installation using vertical ties. In this case, the bar is attached to the fabric at 11 cross sections, as shown in *Figure 8.17*. The resulting deflected shape is then used for a final adjustment of the depth profile, which

requires final optimisation of the top breadth profile, both indicated with dashed lines in *Figure 8.16b*.

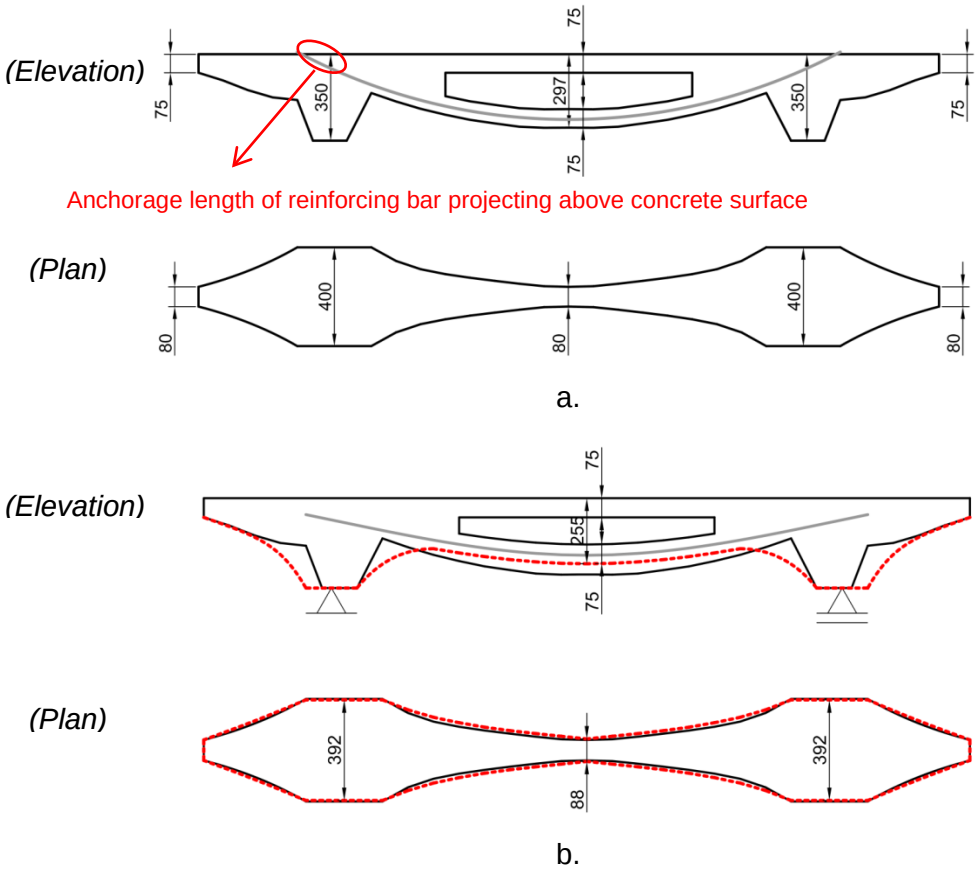

Figure 8.16. Case study 2 beam geometry: (a) optimised beam design and (b) adjusted longitudinal profile (all dimensions are in millimetres)

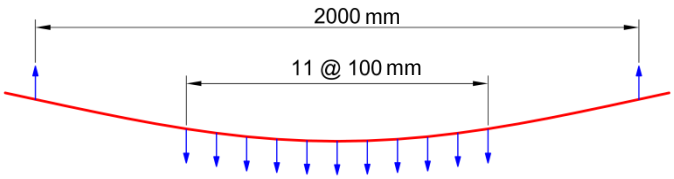

Figure 8.17. Case study 2 position of vertical ties

The radius of the reinforcement curve of the bottom tension bar also needs to be checked against the minimum allowable radius for field bending. For the assumed properties of the GFRP bar, i.e. 60 GPa modulus of elasticity and 1300 MPa ultimate tensile strength, and limiting the sustained stresses to 20% according to the recommendations provided in ACI 440.1R-06, a minimum bend radius of 1465 mm would be required. The actual curve radius is greater than 3900 mm, which is well above the limit.

The analysis of the deflected shape of the reinforcing bar also provides the forces in the vertical ties, required to determine the cross-sectional profiles at each point of attachment.

For the vertical tie arrangement in *Figure 8.17*, the calculated force in each tie is 6.5 N, equal to 65 N/m for 100 mm spacing between the ties. The shapes of all affected cross sections are shown in *Figure 8.18* (the identical sections due to symmetry are omitted). As can be seen, the uplift is fairly small and leads to only 6% increase in the cross-sectional area in comparison with the initially unrestrained sections.

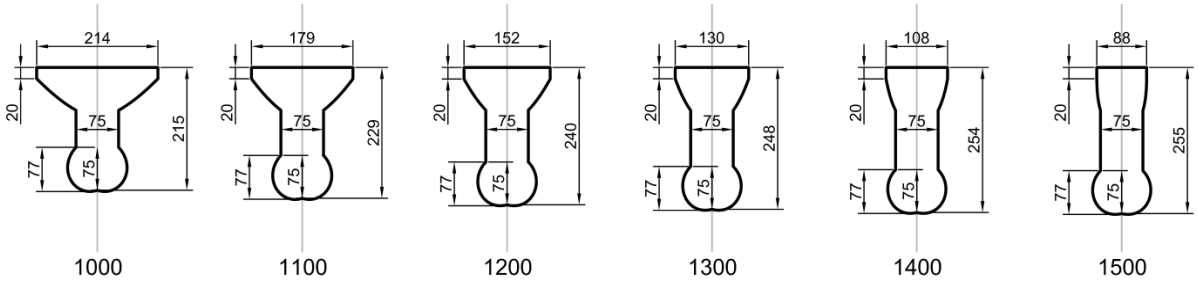

All dimensions are in mm.

Figure 8.18. Case study 2 vertically restrained cross sections (location of sections measured from the left beam end)

8.3.2.3. Utilisation and material savings

The graph, presented in *Figure 8.19*, shows a high utilisation in shear over the whole length of the beam, except for the locations where the beam depth has been increased to provide a smooth curve to the profile. The concrete material savings, calculated for the final geometry, are 32%, or very close to the saving achieved in the first case study design.

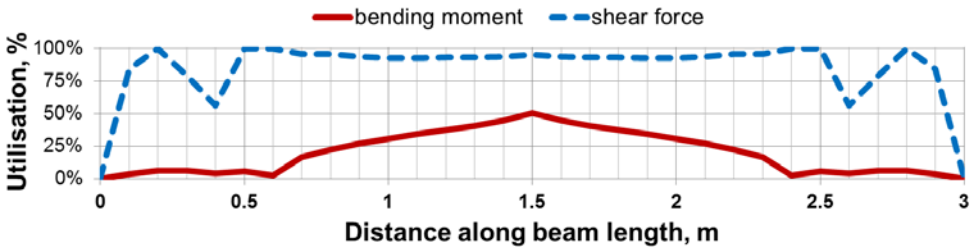

Figure 8.19. Case study 2 capacity utilisation

8.3.2.4. Vertical deflections and strains in FRP bar

The low utilisation of bending moment capacity results in a high actual factor of safety for the GFRP bar in this case, as can be seen in *Figure 8.20a*. The moment-deflection analysis, presented in *Figure 8.20b*, indicates that the deflections under serviceability loads, assuming again a ψ_2 factor of 0.3 on the live load, would be acceptable. The contribution of the permanent and live loads are further examined in *Figure 8.21*.

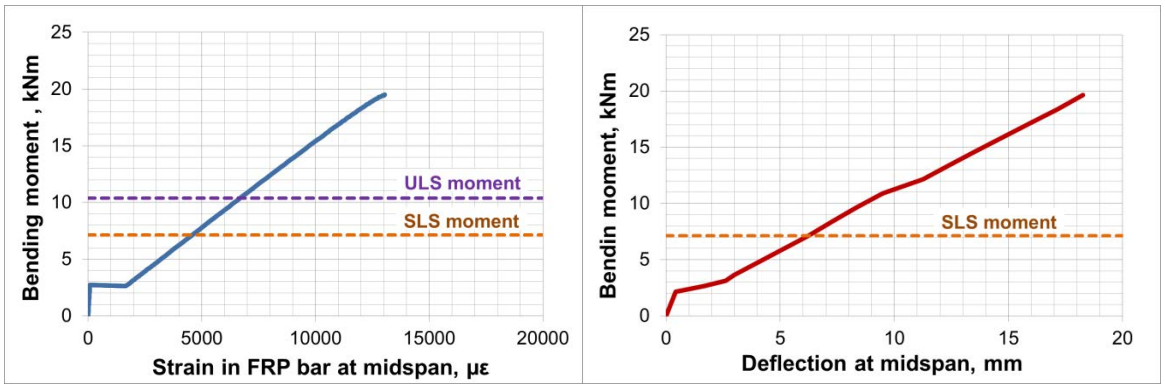

a. b.

Figure 8.20. Case study 2 beam: (a) moment-strain and (b) moment-deflection relations at midspan

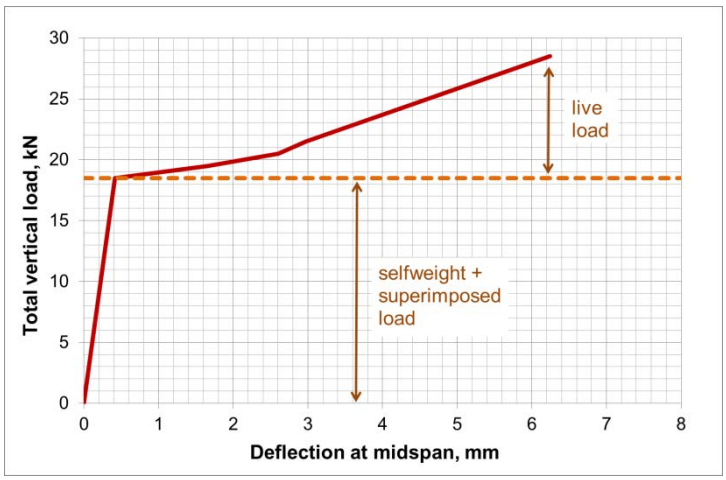

Figure 8.21. Case study 2 load-deflection relation showing the applied SLS loads

8.3.2.5. End anchorage design

Splayed bars, confined by helical reinforcement, are designed following the procedure described for Case study 1. However, the reinforcing bars do not require high anchorage resistance due to lower forces in this case. As demonstrated by the plots in *Figure 8.22* and *Figure 8.23*, even a straight anchorage end may be sufficient for the bar at the main span. Adding a 100 mm 1° wedge, however, would prevent the sudden loss of bond which can occur for straight sand-coated bars, as demonstrated by the experimental results provided in § 3. The forces in the reinforcing bars at the cantilever spans are even lower and, therefore, the same type of splayed anchorage would be adequate.

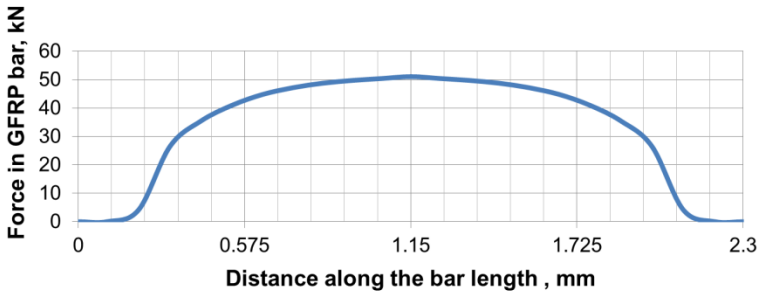

Figure 8.22. Case study 2 force in the bottom tension reinforcement

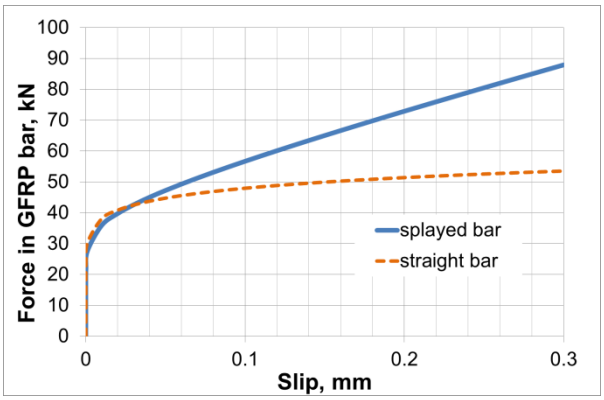

Figure 8.23. Case study 2 force-slip relation for a straight end and for a 100 mm 1° wedge

8.3.3. Construction parameters

The final geometry and reinforcement details for the current case study are shown in *Figure 8.24*. The construction parameters needed to produce the fabric pattern, in this case, include the total hung perimeter P at each design cross section, the perimeter of the bottom bulb P_b and height of the web h_{web}. The position of the formwork ties connecting the web plates also needs to be indicated on the fabric pattern, as illustrated in *Figure 8.24d*. Again the calculated perimeters allow for 20 mm thick top plate of the formwork table.

All construction parameters are provided for half of the beam length at sections positioned at a distance x_L from the left beam end face in *Table 8.2*. The extension of the fabric during construction, presented as the total value due to the tensile forces in the top and bottom bulbs, exceeds 4 mm for the large sections over the supports, leading to a reduced final construction perimeter P*. However, the reduction is less than 0.5% and may be considered practically negligible. Furthermore, the sections over the supports may usually be formed by pre-stressing the fabric between the top and bottom plate supports, as proposed previously in § 7.

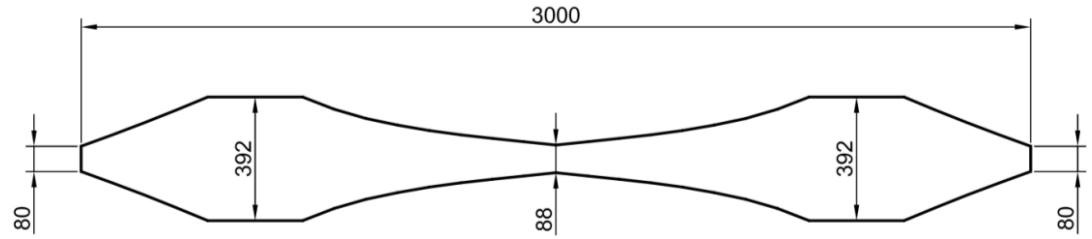

a.

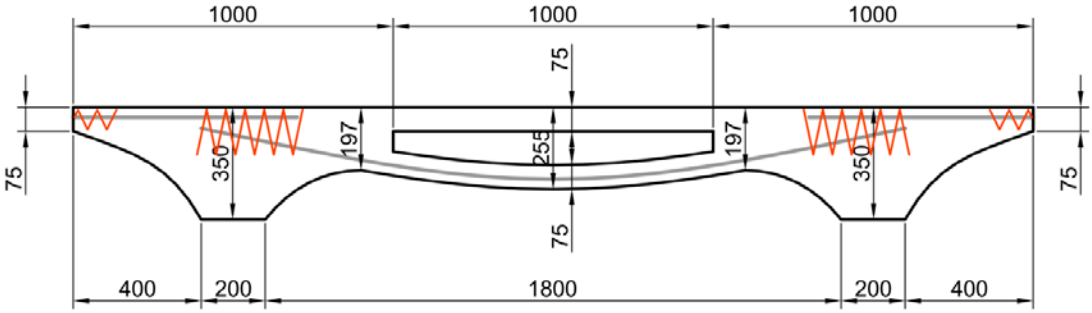

b.

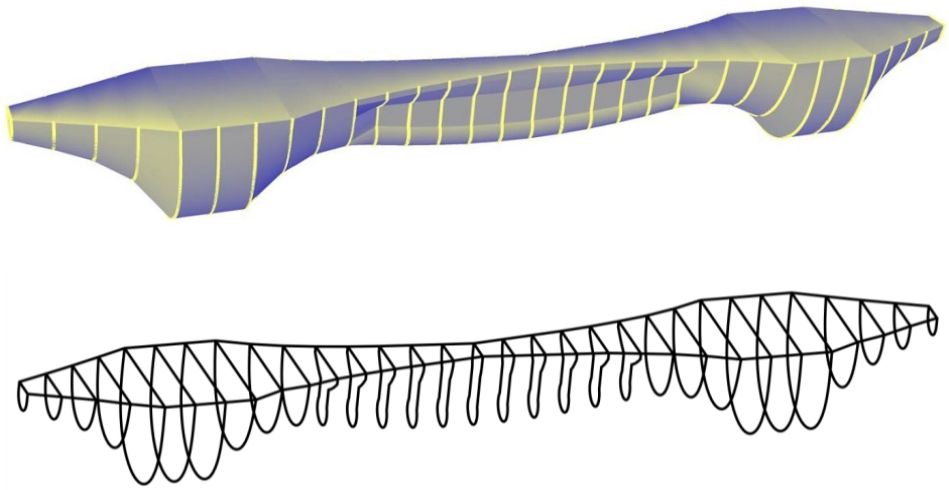

c.

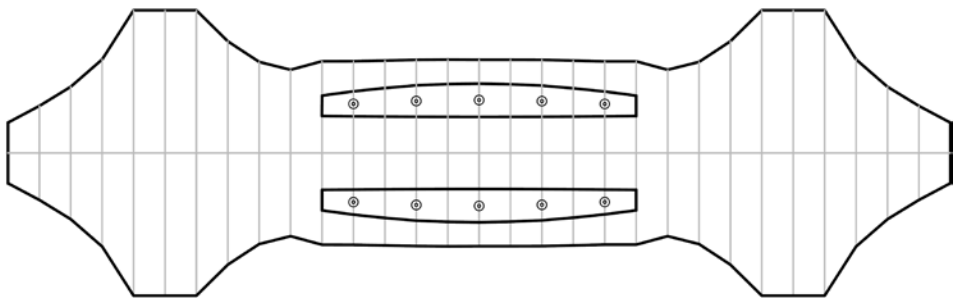

d.

Figure 8.24. Case study 2 geometry details: (a) plan, (b) elevation, (c) 3-D view of cross sections and (d) fabric pattern (all dimensions are in millimetres)

Table 8.2. Construction parameters (Case study 2)

x_L	B	P	h_{web}	P_b	T_1, N/m	T_2, N/m	extension	P*	P_b*
0	80	192			61		0.0	192	
100	153	298			159		0.2	298	
200	229	420			321		0.5	420	
300	309	594			634		1.3	593	
400	392	908			1381		4.2	904	
500	392	908			1381		4.2	904	
600	392	908			1381		4.2	904	
700	392	710			925		2.3	708	
800	314	578			610		1.2	577	
900	256	524			481		0.9	523	
1000	214	582	65	234	214	384	0.4	581	234
1100	179	582	79	232	230	329	0.3	582	232
1200	152	585	91	230	242	294	0.3	585	230
1300	130	590	99	230	228	269	0.3	590	230
1400	108	592	104	228	232	248	0.3	592	228
1500	88	591	106	228	234	234	0.3	591	228

All dimensions are in millimetres.

8.4. Concluding remarks

Two beam design case studies have been presented in this chapter with the objective to demonstrate how constructability can be considered in the design of fabric-formed beams, based on the findings of the current research. A typical design process has been presented for assumed design parameters and geometrical constraints in order to provide a step-by-step guidance and to illustrate the effect of the different design decisions required during the process.

Three main conclusions may be drawn from the presented case studies. The first conclusion is that optimisation forms only a part of the design process. Finding a practical and efficient design solution depends on a variety of design parameters other than the concrete geometry alone. The second conclusion is that realistic concrete material savings above 30% can be achieved for design, including constructability considerations. The final conclusion is that it may be possible to satisfy serviceability deflection criteria for ultimate limit state governed design of optimised fabric-formed beams.

9. Construction of Fabric-formed Elements Cast in Sewn Fabrics

9.1. Introduction

The construction of all experimental fabric-formed beams, described in § 5, § 6 and § 7 was carried out using single flat fabric sheets. Although various design shapes have been produced with repeated success, selected specimens with abrupt changes in the cross-sectional profiles of adjacent sections have demonstrated the limits of using flat sheets. Apart from the problems associated with fixing fabric to the supporting structure in such cases, the examples showing excessive creasing of the fabric during construction have highlighted the risk associated with creating weak zones and reducing the cover at the locations of deep wrinkles, which may cause an adverse effect on the structural performance of a reinforced concrete element. However, these limitations can be overcome by using sewn fabrics.

Sewn fabrics can be used not only to reduce wrinkling. They can make possible the creation of more intricate and unusual concrete forms. Furthermore, sewing fabrics may help to improve the construction accuracy of complex shapes by reducing the installation works required on site. Current industrial application of sewn fabrics in the marine construction, as well as sewn corners and T-junctions used for Fastfoot® installation referred to in § 2, have already demonstrated the feasibility and practicality of the method. Ultimately, sewn fabrics may also have the potential of becoming an entirely new area of investigation in terms of construction techniques and offer a more complete formwork system, particularly useful for creating closed-section vertical forms.

A major motivation for using flat fabrics, however, is the reusability of the fabric sheets. While sewn fabrics would often require cutting fabric sheets into a number of flat patterns fitting a particular three-dimensional surface, it may be possible to use folds sewn in place, which can be undone without compromising the reusability of fabric. This chapter presents an experimental construction investigation of the application of sewn fabrics for vertical elements, such as columns and walls. The size of the built specimens has been limited to allow easy handling and moving in laboratory conditions. However, the presented construction principles and ideas would be appropriate for larger scale elements.

9.2. Fabric-formed wall demonstration workshop

Wall construction is among the most practical applications of fabric-formwork, resembling closely known construction methods with the added benefit of lighter formwork frame supports and reduced transportation requirements, as discussed in § 2. In addition, stitching the two layers of fabric, forming the faces of a wall, offers a practical method for

creating openings of any shape and position. This method may further be applied to construct frames or branched vertical structures.

The advantages of fabric-formed construction were demonstrated at a practical workshop for Engineers Without Borders at the University of Bath. The purpose of the workshop was to introduce fabric formwork to student volunteers as an appropriate construction method requiring low skills and technology. A brief description and construction details of the built wall panels are presented herein.

9.2.1. Construction ideas

Two wall panels were constructed for demonstration purposes. The first panel represented a small-scale example of the well-established ‘quilt-point’ method, developed by the Japanese architect Kenzo Unno, presented in § 2. The second wall panel had large arch openings created by sewing two fabric sheets. No reinforcement was installed due to the small size of the panels.

9.2.2. Construction details

In both cases the fabric was stapled to self-standing timber frames, which were then clamped together in a vertical position. The first panel was cast between two layers of fabric, laterally restrained by small-size formwork ties, made of threaded bars and fixed with nuts and bolts at the ends, as can be seen from the photographs shown in *Figure 9.1*. The threaded bars were isolated from concrete by sleeves, cut from plastic round tubes.

Figure 9.1. ‘Quilt-point’ wall panel construction

The two layers of fabric used for the second panel construction, illustrated in *Figure 9.2*, were sewn in advance. Therefore, the installation process required considerably less effort and time. The concrete was placed by hand and compacted by means of a needle vibrator. The final 'as-built' shapes of the two walls panels are shown in *Figure 9.3*.

Figure 9.2. Wall panel construction using sewn fabric for creating openings

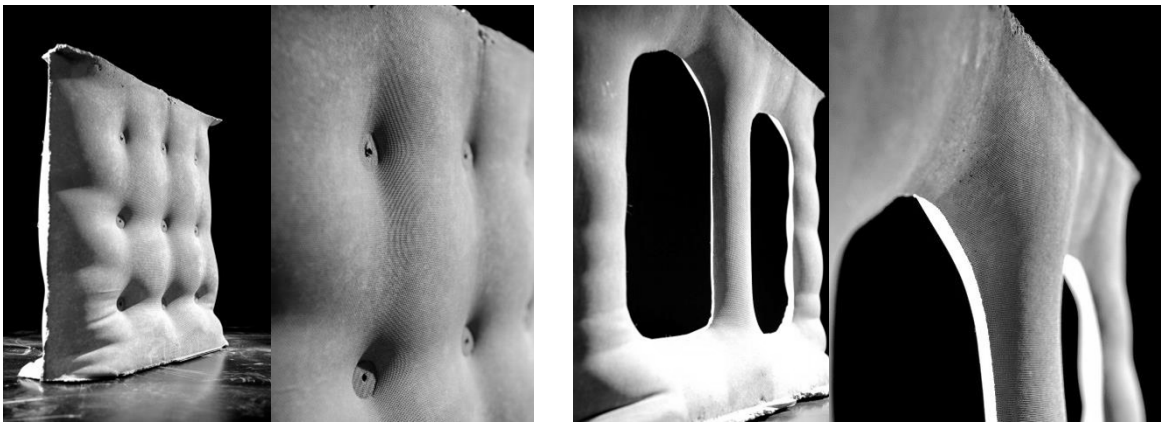

a. b.

Figure 9.3. Demoulded wall panels: (a) 'quilt-point' panel and (b) panel with openings

9.3. Fabric-formed columns cast in sewn fabrics

Five columns in total were constructed in order to explore the possibilities of using sewn fabrics for vertically cast elements. Although columns can be cast horizontally and lifted into a vertical position, the hydrostatic pressure applied to a vertical fabric sheet with a closed cross-sectional perimeter would create easily predictable and more structurally efficient symmetrical forms.

9.3.1. Construction ideas

The construction ideas considered for this experimental study were based on sewn fabrics with closed cross-sectional perimeters, stretched vertically and temporarily supported at both ends. A typical formwork installation process of the ready sewn fabrics is explained in *Figure 9.4*. The top and bottom plates in this case are supported by timber columns and split in two halves for easy removal. The fabric can be attached to the plates prior to installation on site and transported in a flat form, as indicated *Figure 9.4a*. The design of the temporary supports would depend on the size of the concrete columns and could vary for different projects and site constraints.

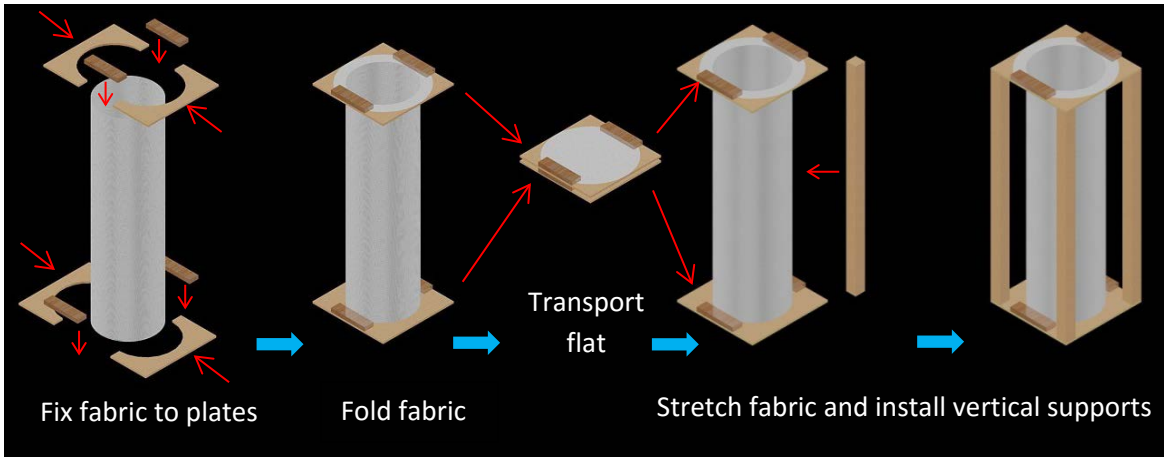

a.

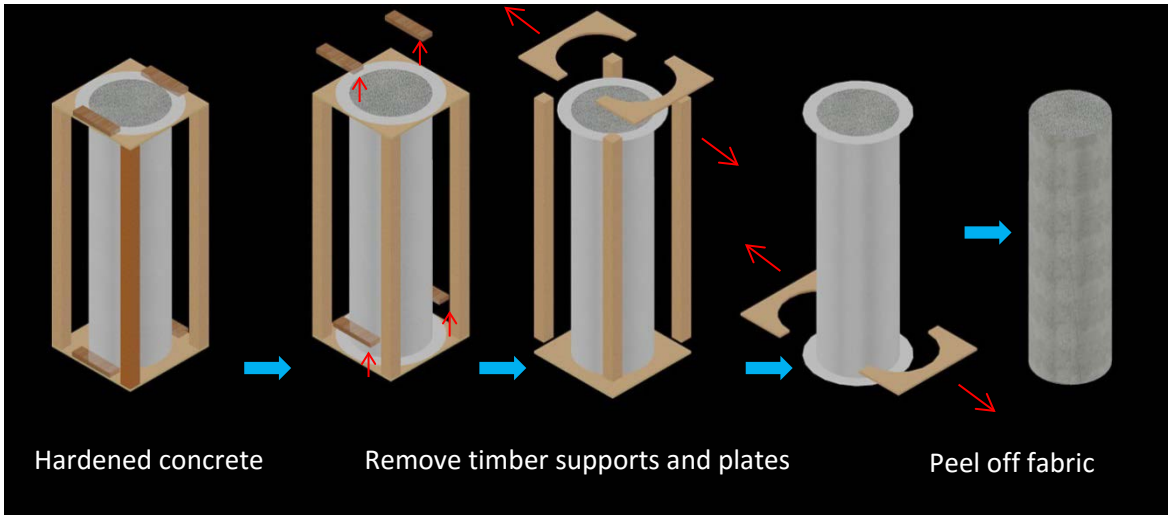

b.

Figure 9.4. Fabric-formed column construction: (a) installation and (b) removal of formwork

Two initial ideas explored methods for construction of circular hollow section columns, cast between two layers of fabric. The first method proposed forming a void inside the

concrete by filling the volume enclosed by the inner fabric layer with a suitable material. The second idea developed around the 'quilt-point' method. However, the bolted formwork ties were replaced with flexible plastic ties, used to attach and pull down reinforcing bars, as described in § 5, which can easily be removed from outside once the concrete has hardened. The construction details and the resulting shapes are presented in the next section.

Three further conceptual column designs were developed using the proposed method for temporary support of fabric. The first conceptual design, presented in *Figure 9.5*, comprised a solid column with varying cross section, achieved by stitching four identical flat patterns, indicated in *Figure 9.6a*. The resulting circular section column, illustrated in *Figure 9.5a*, was transformed into a column of a 'four-leaf' cross section along a part of the total height, formed by pinching the fabric with steel wires tied across the section (*Figure 9.6b*).

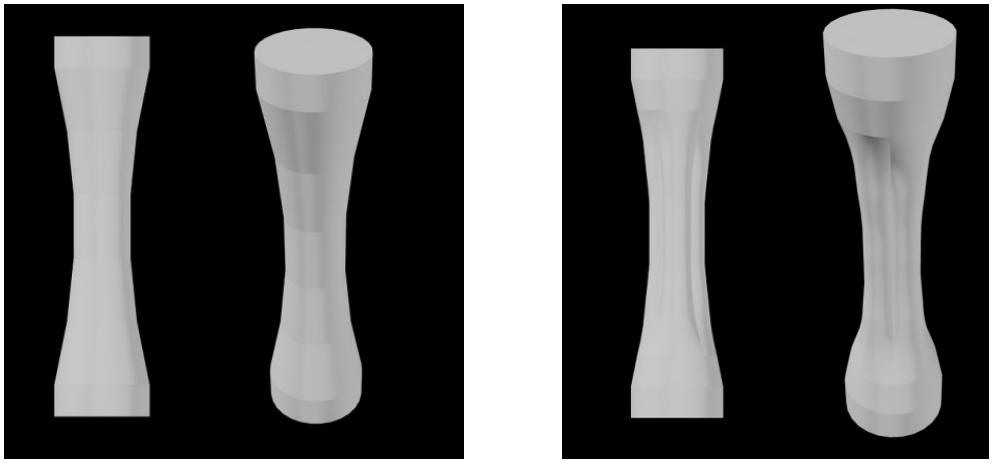

Front view *Perspective* *Front view* *Perspective*

a. b.

Figure 9.5. Conceptual design 1: (a) circular and (b) pinched 'four-leaf' cross sections

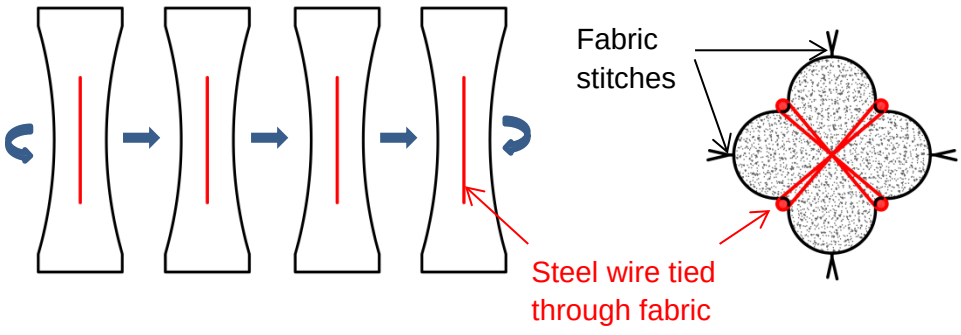

a. b.

Figure 9.6. Conceptual design 1: (a) flat patterns and (b) 'four-leaf' cross section

The second conceptual design represented a hollow section column with three openings, as illustrated indicatively by the three-dimensional models in *Figure 9.7*. The initial 'tall' column design was modified to allow production of a size, manageable for laboratory construction, and the model presented in *Figure 9.7b* was built. In this case, the fabric was not cut into separate patterns. Single rectangular sheets were used to cast the inner and outer surface of the column. The voids were created by stitching the sheets along the perimeter of the areas, indicated in *Figure 9.8*, while other changes of geometry were achieved by tucks. The form-finding of the shapes in this case was based on linear transition between the circular section of each leg at mid-height the top and bottom bases, assuming sufficient prestress in fabric.

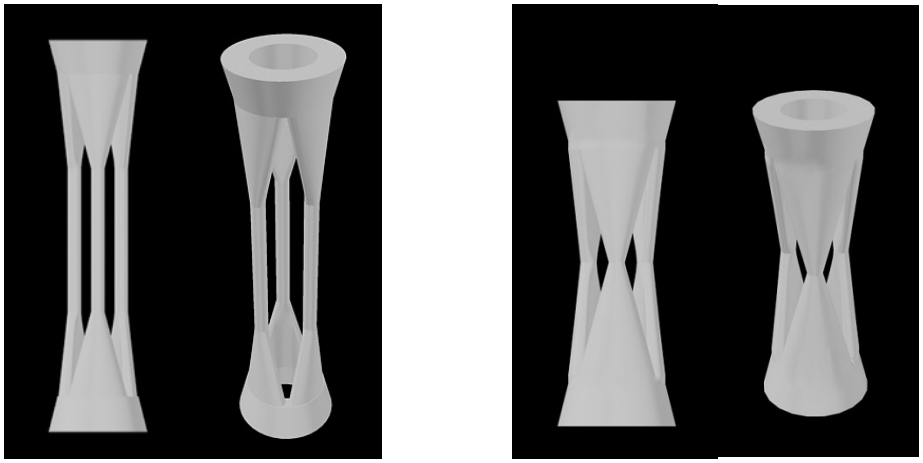

Front view *Perspective* *Front view* *Perspective*

a. b.

Figure 9.7. Conceptual design 2: (a) 'tall' and (b) 'short' version

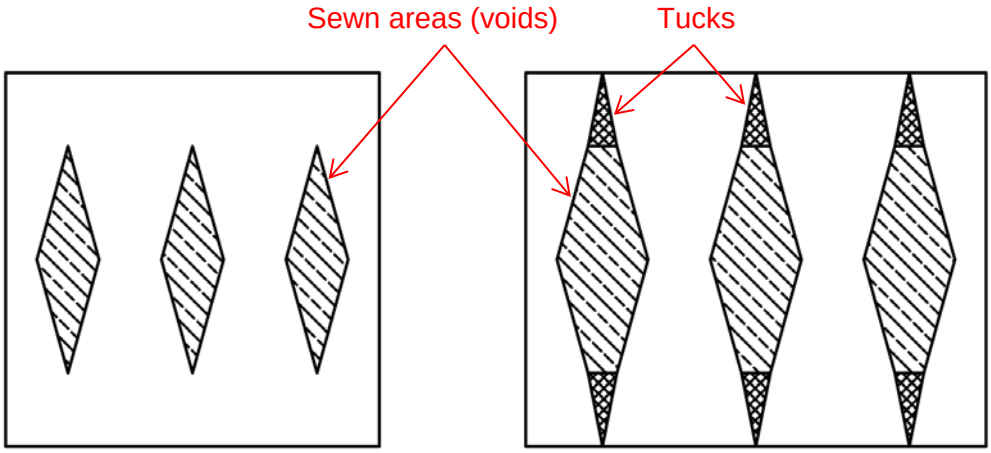

a. b.

Figure 9.8. Conceptual design 2 fabric patterns: (a) inner and (b) outer fabric layers

The final column design aimed to create an easily identifiable, but not typical for concrete construction, form in order to demonstrate how far the limits of sewn fabric formwork could be stretched using the simple installation process, described in *Figure 9.4*. The proposed column comprised a concrete double helix cross section, as illustrated in *Figure 9.9*. For demonstration purposes only a segment of the total column height, including a wider base, was built (see *Figure 9.9b*).

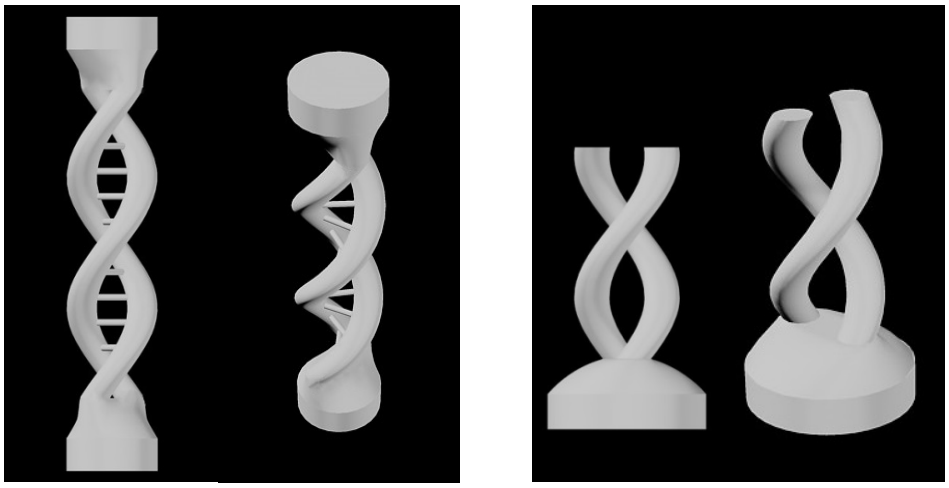

Front view *Perspective* a. *Front view* *Perspective* b.

Figure 9.9. Conceptual design 3: (a) 'tall' and (b) 'segment' version

9.3.2. Construction details

The construction details of the first two circular hollow section columns are presented in *Figure 9.10*. As can be seen, in this case the fabric was fixed to top plates clamped onto reusable trestle supports, which determined the actual height of the columns. The material used to form the void in the first column was sand. Alternative options may include replacing the inner fabric layer with inflatable bags or use of water as a filling material. However, the construction principle would remain the same.

The second hollow section column, identifiable by the mattress-looking outer surface, was slightly less successful in terms of construction. The inner fabric layer remained trapped at the 'quilt-point' locations, while the thickness of the concrete was increased due to the bulging of concrete inwards. This can be controlled by reducing the spacing of the ties. However, the construction method would be more appropriate for larger diameter columns.

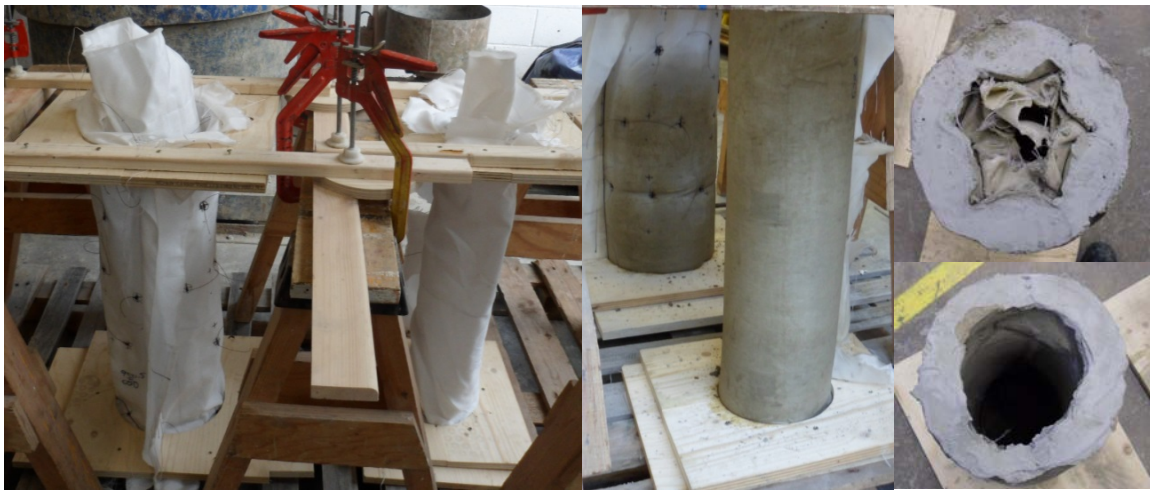

a. b. c.

Figure 9.10. Hollow section columns: (a) formwork installation, (b) concrete casting and (c) 'as-built' cross sections

The three presented conceptual designs were adapted for the construction of small-scale demonstration columns. The height of the columns was limited to 1 m for the reasons stated earlier. It was attempted to install reinforcing cages for some of the specimens. However, it was difficult to achieve a free flow of concrete through the thinnest cross-sections and the reinforcement was removed.

Figure 9.11 shows the formwork details for the column based on conceptual design 1. The installation and the formwork supports followed the procedure suggested in *Figure 9.4*. As can be seen from *Figure 9.12*, the fabric was stripped off by cutting along one of the stitches. The fabric remained undamaged and could be re-sewn and re-used. It should be noted that use of tucks instead of separate patterns was also possible. The final shape, presented in *Figure 9.13*, carried the architectural features of the stitching details and the steel wire imprints.

Figure 9.11. Conceptual design 1 fabric formwork preparation and installation

Figure 9.12. Conceptual design 1 concrete casting and fabric formwork removal

Figure 9.13. Conceptual design 1 final shape

The construction process for the column, based on conceptual design 2 is illustrated by the photographs shown in *Figure 9.14* and *Figure 9.15*, and the final constructed shape is presented in *Figure 9.16*.

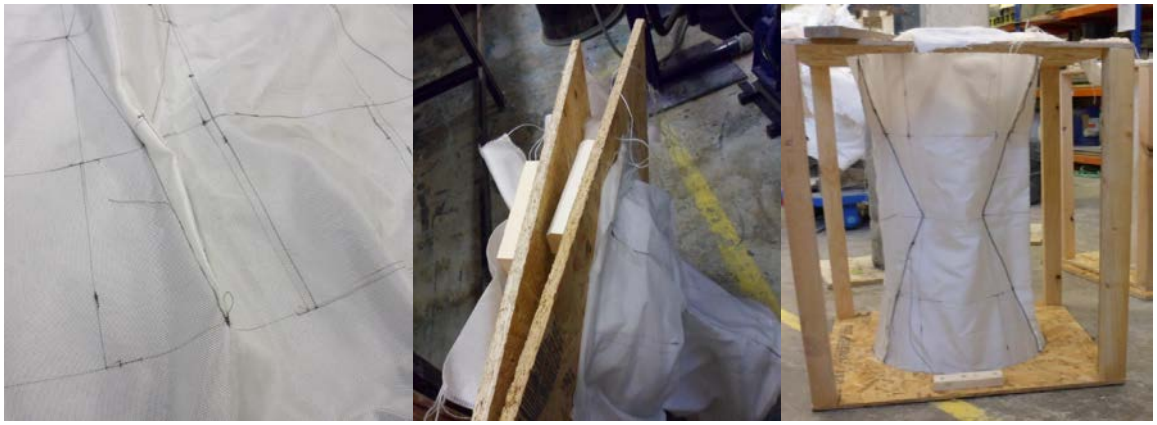

a. b. c.

Figure 9.14. Conceptual design 2 fabric formwork: (a) pattern, showing a tuck detail, (b) folded for transportation and (b) ready for concreting

Figure 9.15. Conceptual design 2 concrete casting and fabric formwork removal

Figure 9.16. Conceptual design 2 final shape

Despite the significant differences between the final shapes of the last two specimens, the only major variation in the construction process was the pattern design. The construction of the final column aimed to demonstrate that this would apply to even more complex forms. Although a more skilful and elaborate preparation of the sewn fabric shown in *Figure 9.17* was required, the formwork installation was not different from that for a simpler form. Furthermore, improvements such as automated pattern printing and cutting could speed up the process considerably.

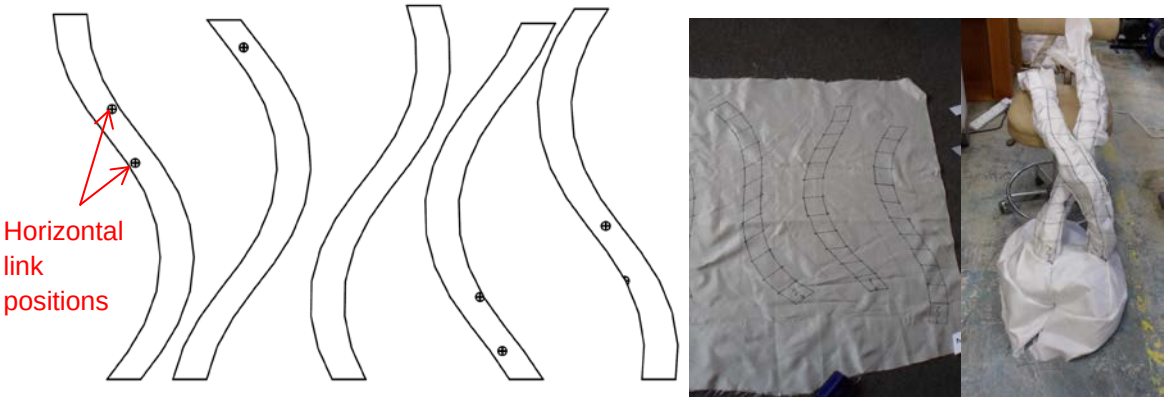

Figure 9.17. Conceptual design 3 fabric patterns

The photographs presented in *Figure 9.18* illustrate the construction and the achieved concrete form for the final column. Short-length sand-coated GFRP bars were utilised as horizontal links between the two helical branches, adding to the architectural appearance of the column. The bars were simply inserted through heat-cut holes in the fabric, at the positions indicated in *Figure 9.17*, and cast in the concrete.

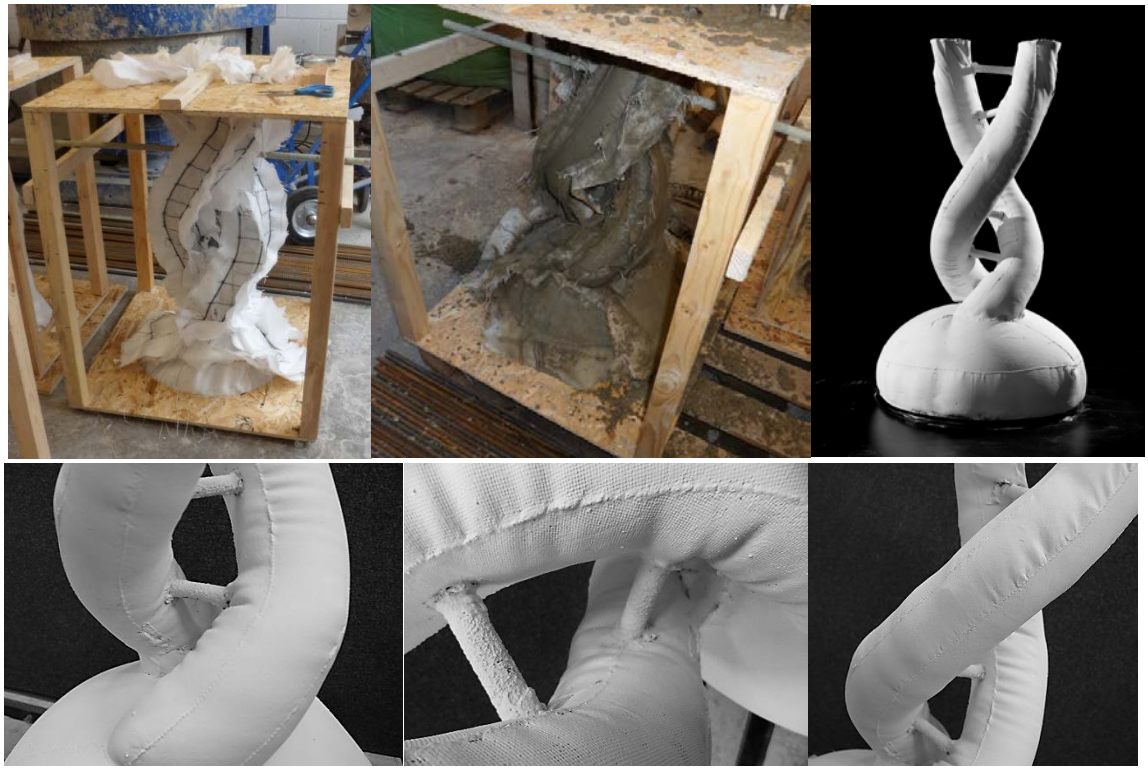

Figure 9.18. Conceptual design 3 construction and final shape

9.4. Concluding remarks

The work presented in this chapter has been entirely focused on demonstrating the opportunities of using sewn fabrics for the construction of fabric-formed elements and

motivating further research in this area. While the structural design of such elements has not been discussed, it has been demonstrated that the built forms could vary from simple circular-section columns, designed by standard methods, to complex slender branched structures, requiring more advanced analysis.

The experimental construction has helped to demonstrate the simplicity and accessibility of fabric formwork as a construction method. In addition, the use of sewn fabrics could allow the creation of forms of varying complexity without affecting the construction process on site. Although the preparation of sewn fabrics requires certain skills and technology, it would still provide a considerably more practical and economical option than producing rigid 3-D moulds. Moreover, sewing techniques for fabric formwork have already been developed in industry, while software products for creating flat patterns of 3-D surfaces are also readily available.

The experimental investigation of the proposed construction methods has been limited by the size of the built specimens. However, many of the presented ideas and conceptual designs would be applicable to realistic sized elements. Possible size limits may be related to the strength of the stitches or the formwork supporting structures, which need to be designed for construction loads arising from the weight and compaction of fresh concrete. Furthermore, as discussed, the reusability of sewn fabric sheets may not be feasible in many cases. Nevertheless, this may not be regarded as a disadvantage and might motivate future research into stay-in-place sewn fabric formwork systems, potentially used as reinforcement.

10. Conclusions

This research project has involved a wide range of activities related to the design and constructability of fabric-formed elements. The main focus of the presented work has been the investigation of FRP materials as an alternative to steel for reinforcing concrete elements cast in flexible formwork, in order to resolve the major durability problem related to ensuring adequate protective cover to steel bars. Existing methods for building ductile FRP-reinforced beams have been adapted and further developed to suit fabric formwork construction. Other constructability problems have been addressed as well, including provision of end anchorage and shear reinforcement. New methods for installation of reinforcement in fabric, specific for FRP bars, have been introduced. Overall, the following objectives have been achieved, slightly exceeding the extent of the originally defined objectives in § 1:

- Design methodology and guidance, including finding of the final concrete shape and structural optimisation, for fabric-formed elements have been developed and verified through experimental investigation. It has been demonstrated that fabric-formed concrete elements can be form-found in a predictable manner by measuring the as-built concrete geometry for a series of test beams. The strength and stiffness of fabric-formed beams have also been predicted accurately, using the developed design tool.
- It has been demonstrated that FRP bars, which do not rely on concrete cover for protection against corrosion, can successfully replace steel reinforcement, offering further advantages to fabric formwork construction, such as low weight and the possibility to form curved reinforcement profiles under the selfweight of concrete. Furthermore, FRP helical reinforcement has been incorporated into the compression zone of concrete, in order to increase the concrete strain capacity and ensure ductile behaviour of FRP-reinforced beams.
- A novel splayed anchorage system, based on a technique invented at the University of Bath, has been developed and fully tested to provide a rational design approach to anchoring reinforcing bars in concrete elements with relatively small optimised end cross sections.
- FRP spiral reinforcement with varying geometry has been produced and tested to demonstrate its effectiveness in providing adequate shear capacity to fabric-formed beams.

Furthermore, the use of low carbon cements in FRP-reinforced concrete structures has been discussed for their benefit on the durability of glass FRP bars. Unlike steel bars, which need to be encased in a high-alkaline environment, glass fibres are susceptible to alkaline degradation. Therefore, while low carbon cements typically lower the pH of

concrete and, therefore, cannot provide effective protection against corrosion for steel bars, they offer a viable option for building low-carbon and durable FRP-reinforced structures.

The next two sections present the conclusions derived for each of the main investigated areas, whereas the last section discusses possible directions for future research.

10.1. Constructability

A major part of the current research work has been focused on the constructability of fabric-formed elements, aiming not only to solve existing issues but also to offer new possibilities and ideas for construction. The following areas have been studied:

10.1.1. Methods for restraining of fabric during construction

A number of methods have been tested for forming ‘flat-bottom’ cross sections at beam supports and reducing the bulging ‘tear-drop’ effect in sections with narrow top breadth and large depth. It has been demonstrated that the fabric shape can easily be controlled by the use of internal ties to produce fully-predictable structurally efficient shapes. Both standard formwork ties and innovative flexible ties, made of plastic wire, have been applied. While the standard ties have been found to be suitable for connecting rigid web-former plates along a continuous length of a beam, the flexible ties provide a time-saving method for restraining fabric at discrete points. Their easy removal and the possibility to be pre-attached to fabric in factory conditions could make the flexible ties particularly useful for insitu applications.

10.1.2. Forming curved GFRP bar profiles

The flexibility of GFRP bars allows for their bending into large-radius curves on site. This could be utilised in the production of fabric-formed elements since the concrete shape is also formed during the construction process. It has been demonstrated that GFRP bars can be positioned at their correct level by being attached to fabric prior to concreting, using internal flexible ties. The method also helps to ensure accurate minimum bond concrete cover, defined by length of the ties. A potential drawback, however, is the pinching effect on fabric at the position of each tie, which reduces the minimum depth and, if not considered in the design, may reduce considerably the capacity of a structural element. Therefore, a method for form-finding of sections with such vertical ties has been developed and verified against the test data to demonstrate the feasibility of the proposed construction approach.

10.1.3. FRP spiral reinforcement

The need to produce shear reinforcement matching complex fabric-formed concrete shapes could present a major drawback in fabric formwork construction. Through this project it has been demonstrated that shear spirals made of impregnated carbon fibres can be produced in the desired shapes, or directly wound around the longitudinal bars, to act as shear reinforcement, providing adequate contribution to the shear resistance of structural elements. Two types of CFRP shear spirals have been investigated. The first type, produced in a similar manner as rectangular spirals for uniform beams, has proven to be ineffective for nearly triangular cross sections with decreasing depth towards the end supports. Therefore, a second, improved, spiral type has been introduced, which includes vertical central legs, irrespective of the concrete cross-sectional outline. The experimental results for the second spiral type have not only demonstrated a considerable enhancement in the shear strength but also agreed well with theoretical predictions. Furthermore, placing a confining FRP helix in the compression zone of a fabric-formed beam, in combination with a CFRP shear spiral, has helped to completely avert brittle failure, otherwise typical for FRP-reinforced flexural concrete elements.

10.1.4. End anchorage

Splaying the ends of a reinforcing bar to create wedge anchors, named splayed anchorages, is a novel method for providing effective pull-out resistance without the need to bend bars over their anchorage lengths. The constructability and the load-slip behaviour of splayed bars have been investigated through a series of hinged-beam bond tests. Carbon fibre wedge plates have been glued inside the slots of splayed bars to maintain the geometric stability of the anchorage. The experimental results have shown that the preparation of a wedge and the glue type may have a significant effect on the adhesion between the anchorage and the surrounding concrete and, therefore, can help to enhance the total pull-out resistance. It has been demonstrated that fully sand-coated wedges are most effective, although they require additional treatment possibly not suitable for preparation on site. However, sand-coating could easily be incorporated in the manufacturing process of pre-fabricated splayed FRP bars to improve their performance. Based on the test observations, it has been recommended that FRP confining helices should be placed around the anchorages to prevent brittle failure of concrete due to splitting cracks. The wedging action could also play an important role in preventing brittle surface bond failure, which may occur for straight bars, as revealed by the experiments.

10.1.5. Sewn fabric formwork methods

Despite the versatility of flat fabric sheets for creating a variety of shapes, their use is limited, particularly in cases where the complexity of forms leads to excessive wrinkling affecting the structural performance of an element, as demonstrated by the experimental construction of fabric-formed beams in § 6. This research has touched to some extent on the advantages and opportunities of using sewn fabrics, which can provide economically viable methods to cast highly complex forms without the need to produce custom-made rigid 3-D moulds. Experimental construction methods accenting on the simplicity of the construction process on site, once the fabric formwork has been sewn, have been developed for column-like forms of varying complexity. In addition, it has been demonstrated that the required flat fabric patterns are fairly simple to create, compared with the capabilities of readily available software and technology in other industries.

10.2. Design

The design of fabric-formed elements involves a number of steps not normally performed in conventional reinforced concrete design. In addition, the incorporation of FRP materials challenges fundamental design concepts related to steel reinforcement, as discussed, by relying on the limited ductility of concrete to ensure a safe failure mode. The three major components of the design process, including form-finding, sectional analysis and optimisation of geometry, have been implemented through a computational program, written in MATLAB and experimentally verified. The serviceability performance, end anchorage and shear reinforcement design have also been considered. Furthermore, two case study beams have been designed to illustrate the full design approach and provide a step-by-step guidance.

10.2.1. Form-finding

A form-finding iterative method has been proposed, based on finding a single constant, which uniquely identifies every curve between two points of restraint for given overall dimensions of a two-dimensional fabric-formed cross section. The method is suitable for horizontally cast elements in freely hung fabric, with or without internal restraints, and although it is not fully capable of predicting 3-D effects between successive cross sections, provides a practical tool for the design of linear elements, such as beams. The experimental investigation of as-built geometries has helped to identify and correct any errors in the form-finding algorithm, demonstrating that in most cases the final concrete shapes can be accurately predicted. Nevertheless, the construction tolerances in the top breadth and the hung perimeter of fabric affect the depth of fabric-formed sections and

alter the design geometry. This may not necessarily affect the structural performance, as proven by the load test results. However, it presents an area for further improvement.

10.2.2. Lifting forces from bending of reinforcing bars

The proposed form-finding algorithm allows for shape prediction of concrete-filled fabric cross sections, containing vertical ties attached to the reinforcing bars. The algorithm requires that the forces in the ties are known, as well as the minimum depth required by design. Finding these forces can be defined as a separate task, which depends on the flexural stiffness and the design longitudinal curvature of the reinforcing bars. It has been shown that the forces can be calculated for different numbers of restraint points, and the resulting sections have been compared with experimental results, demonstrating the predictability of such sections. Since the effect of the vertical ties changes the final concrete profile only on the tension side of a cross section, they do not need to be taken into account during the optimisation process based on ultimate strength capacity, when concrete in tension is ignored. Only once the final reinforcement profile is determined, should the vertical ties be added to the form-finding input parameters in order to calculate the extra length of fabric perimeter to be allowed around pinching points.

10.2.3. ULS design

The output data from the form-finding algorithm can be directly used for conventional two-dimensional sectional analysis at a number of pre-defined sections along the length of a beam. Methods for flexural and shear design of FRP-reinforced concrete, containing confining and shear spiral reinforcement, have been adapted and verified against the load test data. It has been demonstrated that theoretical analysis based on stress-strain curves for confined concrete, taken from the literature for spiral reinforcement of the same type and size, can predict the actual behaviour, while the permissible strain levels in the shear reinforcement in accordance with ACI 440.1R-06 were found to be a safe limit for shear design.

The enhancement of compressive concrete strength due to the permeability of fabric formwork has been studied for a limited number of beams by testing fabric-formed cylinders. It has been found that in many cases the enhanced strength provided marginally more accurate prediction of the ultimate load capacity, even when used for concrete near the top surface. A possible explanation of this finding is the small size of the test beams, which has resulted in overall reduction in the water-to-cement ratio. It has been recommended that strength enhancement should be ignored for design at ULS, but

the force in FRP reinforcement may be checked for higher concrete strength to guarantee over-reinforced design.

10.2.4. Serviceability criteria

The theoretical analysis and the load test results have demonstrated that it is possible to satisfy serviceability deflection criteria for fabric-formed beams designed at ULS, based on safety factors and applied loads in accordance with Eurocodes. Neither the recorded deviations from design geometry nor the enhancement of concrete strength have shown a significant effect on the theoretical load-deflection behaviour of the test beams, which generally agreed well with the experimental results for loads not exceeding the serviceability levels.

10.2.5. Optimisation

It has been demonstrated that the geometry of fabric-formed beams can be optimised by minimising the section depth or the top breadth, or both, at each section along the length of a beam element, leading to minimum concrete material savings of 30%. It has been recognised that the construction possibilities for manipulation of the concrete shapes have a significant effect on the achievable material savings. For this reason, the use of internal restraints has been proposed to limit unnecessary bulging effects on a freely hung fabric, which has helped to reach material savings of up to 60%.

10.2.6. Splayed anchorage design

The practical application of splayed anchorage requires design capabilities for determining the pull-out force that can be resisted by a wedge of a defined type and size. An anchorage model able to predict the initial force-slip behaviour of splayed FRP bars has been developed, which could potentially be applied for any type of reinforcing bar with a known local bond-slip law. It has been shown that the model is valid up to 0.3 mm slip, assumed to be the limit below which the slip is governed by the transverse elastic deformation of the wedge/concrete interface. Therefore, an expression for the design resistance of splayed anchorage, based on 0.3 mm slip failure criterion, has been derived.

10.3. Future work

The current project has helped to demonstrate that the concept of fabric formwork is viable technically and economically. However, many of the explored areas need further improvement and may form the basis of future research, the possible directions of which are suggested below.

10.3.1. Improvement of construction tolerances

The adopted manual methods for marking of fabric and cutting the top plates of the supporting tables have inevitably led to some locally large deviations from the design geometry, which may be an important area for improvement in industrial fabrication. Automated pattern printing and cutting could help to achieve smaller tolerances in the construction process. Similarly, the accuracy of the adopted methods for measurement of the as-built concrete profiles has had an effect on the presented results, which could be improved by using more advanced surface scanning techniques.

10.3.2. Splayed anchorage model

The developed splayed anchorage model has been calibrated for FRP bars and, therefore, is not directly applicable to steel reinforcement, which may become a subject of further research. Furthermore, the current experimental work has not provided sufficient data to study the influence of different concrete grades. Although the proposed model mainly depends on transverse stiffness of the bars, more research is required to confirm its validity for different concrete strengths. Another potential area of further research could be the behaviour of a three-dimensional wedge, created by cutting two perpendicular slots, which may provide increased pull-out resistance for FRP bars with diameter larger than the maximum tested diameter of 12 mm, while maintaining the wedge angle within safe limits to avoid longitudinal splitting of the splayed bars.

10.3.3. Shear reinforcement

The use of spiral FRP shear reinforcement has shown promising results as a feasible method for reinforcing fabric-formed beams of varying cross section. However, the number of tested beams was very limited and collectively could only be regarded as an initial investigation. The combined shear and confining reinforcement can be pre-fabricated as a complete reinforcement cage, containing longitudinal bars, which may also be attached to the fabric. However, in this case the longitudinal bars would have to be produced in curved shapes as well. Due to the light weight of FRP reinforcement, the lateral stability of such cages during concreting may present a problem to be resolved by further research. This could be done by generating tension in vertical ties through allowing for a larger perimeter of fabric or by using internal horizontal ties balancing the concrete section on both sides of the spiral. Moreover, the spiral reinforcement presents only one possibility. There is still a large scope for adopting new materials such as advanced textiles incorporating reinforcement, or stay-in-place fabric formwork acting as shear reinforcement alone or as shear and flexural reinforcement.

10.3.4. Serviceability performance

The current research work has been focused on determining the adequacy of the test beam performance under serviceability loads. Although the results have been fairly satisfactory, prestressing of fabric-formed beams presents a logical next step for improvement of the flexural stiffness of such beams as a subject of future research.

10.3.5. New areas of application

Other areas, such as natural ventilation, acoustics and thermal performance, may also benefit from designing and forming appropriate concrete shapes using fabric formwork. Such opportunities could be explored through collaboration projects between different disciplines in future. Another strand of research would involve collaboration between universities and contractors for building prototype fabric-formed structures to assess the realistic construction costs and time. New research at University of Bath, which explores the collection and analysis of big data, has indicated that fabric could also play an important role for integration of sensing systems. Nevertheless, it should not be forgotten that the greatest advantages of fabric formwork lie in its simplicity and low technological requirements, as well as the possibility to use materials other than concrete such as rammed earth, which makes fabric formwork suitable for fast construction in disaster relief engineering as another area of application and research.

References

A

Abdalla H.A., 2002. Evaluation of deflection in concrete members reinforced with fibre reinforced polymer (FRP) bars, *Composite Structures*, 56, pp. 63–71.

Abdegader, H., West, M. and Gorski, J., 2008. State-of-the-Art Report on Fabric Formwork. *In Proceedings of International Conference on Construction and Building Technology 2008 (ICCBT 2008)*, 16 - 20 June 2008, Kuala Lumpur, pp. 93-106.

Achintha, M., Alami, F. and Bloodworth, A., 2015. CFRP fabrics as internal reinforcement in concrete beams. *In Proceedings of Advanced Composites in Construction conference (ACIC 2015)*, 09 - 11 September 2015, Cambridge.

ACI, 2006. *440.1R-06: Guide for the Design and Construction of Structural Concrete Reinforced with FRP Bars*. ACI.

ACI, 2008. Building code requirements for structural concrete (ACI 318M-08) and commentary. Farmington Hills, Mich.

Ahmed, E.A. and Benmokrane, B., 2009. *Technical report on characterization and strength evaluation of the headed GFRP bars" Pultrall Inc.* Quebec: Thetford Mines, Available from: http://www.trancels-pultrall.com [Accessed 21 December 2013].

Ahmed, E.A., El-Sayed, A.K., El-Salakawy, E. and Benmokrane, B., 2010. Bend strength of FRP stirrups: comparison and evaluation of testing methods. *Journal of Composites for Construction*, 14 (1), pp.3-10. doi: 10.1061/(ASCE)CC.1943-5614.0000050.

Al-Janabi A.I.M, Ahmed S.A. and Safi A.R., 2008. Behaviour of RC beams strengthened with CFRP plates using the finite element modelling. *In Proceedings of Fourth International Conference on FRP Composites in Civil Engineering (CICE 2008)*, 22-24 July 2008, Zurich, Switzerland.

Al Awwadi Ghaib, M. & Gorsky, J. 2001. Mechanical properties of concrete cast in fabric formworks. *Cement and Concrete Research*, 31, pp. 1459-1465. doi: 10.1016/S0008-8846(01)00568-3.

B

Bailiss, J., 2006. Fabric-formed concrete beams design and analysis. MEng Dissertation, University of Bath.

Bak, A., Shepherd, P. and Richens, P., 2012. Intuitive interactive form finding of optimised fabric-cast concrete. *In Proceedings of 2nd International Conference on Flexible Formwork (icff 2012)*, 27 - 29 June 2012, Bath, pp. 46-53.

Bakis, C. E., Bank, L. C., Brown, V. L., Cosenza, E., Davalos, J. F., Lesko, J. J., Machida, A., Rizkalla, S. H. and Triantafillou, T. C., 2002. Fiber-reinforced polymer composites for construction - state-of-the-art review. *ASCE Journal of Composites for Construction*, 6 (2), pp. 73–87. doi: 10.1061/(ASCE)1090-0268(2002)6:2(73).

Ball, D.M.J., Liska, M. and Hewlett, P., 2013. *Cementitious binders, activators and methods for making concrete*. WO patent application WO2013179065A1. 2013-12-05.

Bank, L., Puterman, M. and Katz, A., 1998. The effect of material degradation on bond properties of fiber reinforced plastic reinforcing bars in concrete. *ACI Materials Journal*, 95, pp. 232-243.

Belton S., 2012.Digital form finding. *In Proceedings of 2nd International Conference on Flexible Formwork (icff 2012)*, 27 - 29 June 2012, Bath, pp. 54-62.

Benmokrane, B., Chaallal, O. and Masmoudi, R., 1996. Flexural response of concrete beams reinforced with FRP reinforcing bars. *ACI Structural Journal*, 93(1), pp. 46-55.

Bhooshan S. and El Sayed M., 2012. Sub-division surfaces in architectural form finding and fabric forming. *In Proceedings of 2nd International Conference on Flexible Formwork (icff 2012)*, 27 - 29 June 2012, Bath, pp. 64-74.

Böer, P., Holliday, L. and Kang, T.H.-K., 2013. Independent environmental effects on durability of fiber-reinforced polymer wraps in civil applications: A review. *Construction and Building Materials*, 48, pp. 360–370. doi: 10.1016/j.conbuildmat.2013.06.077.

Brennan J., Pedreschi R., Walker P. and Ansell M., 2013. The potential of advanced textiles for fabric formwork*. In Proceedings of the Institution of Civil Engineers: Construction Materials*, 166 (CM4), pp. 229–237. doi: 10.1680/coma.12.00052.

BS EN 10080:2005. *Steel for the reinforcement of concrete. Weldable reinforcing steel. General*. BSI.

BS EN 12390-3:2009-3. *Testing hardened concrete. Part 3: Compressive strength of test specimens.* BSI.

BS EN 12390-3:2009-6. *Testing hardened concrete. Part 6: Tensile splitting strength of test specimens.* BSI.

BS EN 1990: 2002+A1:2005. *Basis of structural design*. BSI.

BS EN 1991-1-1:2004. *Actions on structures - Part 1-1: General actions — Densities, self-weight, imposed loads for buildings*. BSI.

BS EN 1992-1-1:2004. *Design of concrete structures - Part 1-1: General rules and rules for buildings*. BSI.

Buckhouse, E.R., 1997. External Flexural Reinforcement of Existing Reinforced Concrete Beams Using Bolted Steel Channels, Master’s Thesis, Marquette University, Milwaukee, Wisconsin.

Burgoyne C.J., 1993. Should FRP tendons be bonded to Concrete?. *Chapter in Non-metallic reinforcement and prestressing*, *American Concrete Institute*, SP 138-23, pp. 367-380.

Burgoyne, C. J., 2001. Rational use of advanced composites in concrete. *In Proceedings of the ICE - Structures and Buildings*, 146 (3), pp. 253 –262. doi: 10.1680/stbu.2001.146.3.253.

C

C.A.S.T., 2007. *Construction* [Online]. Available from: http://www.umanitoba.ca/cast_building/assets/downloads/PDFS/Fabric_Formwork/CAST_Booklet_SMALL.pdf. [Last accessed 14 June 2015].

Chandler, A and Keable, R., 2009. Achieving carbon neutral structures through pure tension: using a fabric formwork to construct rammed earth columns and walls. *In Proceedings of the 11th International Conference on Non-conventional Materials and Technologies (NOCMAT 2009)*, 6 - 9 September 2009, Bath.

Chandler, A. and Pedreschi, R., ed., 2007. *Fabric Formwork*. London: RIBA Publishing.

Chawla, A., 2010. Fabric-formed beams using splayed bars. MEng Dissertation, University of Bath.

Climate Change Act 2008. (c.27). London: The Stationery Office.

Condie, C., 1911. *Revetment-Mattress*. United States Patent Office patent application US984121A. 1911-02-14.

Conroy, A.,Halliwell, S. and Reynolds, T., 2006. Composite recycling in the construction industry. *Composites Part A: Applied Science and Manufacturing*, 37 (8), pp. 1216–1222. doi:10.1016/j.compositesa.2005.05.031

Cosenza, E., Manfredi, G. and Realfonzo, R., 1997. Behavior and modeling of bond of FRP rebars to concrete. *Journal of composites for construction*, 1 (40), pp. 40–51. doi: 10.1061/(ASCE)1090-0268(1997)1:2(40).

Cosenza, E., Manfredi, G. and Realfonzo, R., 2002. Development length of FRP straight rebars. *Composites: Part B*, 33, pp. 493–504.

Cripps, A., Harris, B. and Ibell, T., 2002. *C564 Fibre-reinforced polymer composites in construction*. London: CIRIA.

Crossett, P., Taylor,S., Robinson, D., Sonebi, M. and Garcia-Taengua, M., 2015. The flexural behaviour of SCC beams pre-stressed with BFRP. *In Proceedings of Advanced Composites in Construction conference (ACIC 2015)*, 09 - 11 September 2015, Cambridge.

Cullen, J.M., Carruth, M.A., Moynihan, M., Allwood, J. M. and Epstein, D., 2011. *Reducing embodied carbon through efficient design*. Learning legacy: Lessons learned from the London 2012 Games construction project. [Online]. Available from: http://learninglegacy.independent.gov.uk/publications/reducing-embodied-carbon-through-efficient-design.php [Last accessed 12 October 2015].

D

Darby, A.P., Ibell, T.J., Tallis, S. and Winkle, C., 2007. End Anchorage technique for internal FRP reinforcement. *In Proceedings of 8th International Symposium on Fiber Reinforced Polymer Reinforcement for Concrete Structures (FRPRCS-8),* July 2007, Patras.

Darwin, D., McCabe, S.L., Idun, E.K.and Schoenekase,S.P., 1992. Development length criteria: bars not confined by transverse reinforcement. *ACI Structural Journal*, 89, pp. 709-722.

Debaiky, S. Y. and Elniema, E. I., 1982. Behavior and strength of reinforced concrete haunched beams in shear. *ACI Journal Proceedings,* 79, pp. 184-194.

Department of Energy and Climate Change, 2009. Carbon Valuation in UK Policy Appraisal: A Revised Approach. [Online]. Available from: https://www.gov.uk/government/publications/carbon-valuation-in-uk-policy-appraisal-a-revised-approach [Last accessed 12 October 2015].

Department of Energy and Climate Change, 2014. Updated short-term traded carbon values for policy appraisal. [Online]. Available from: https://www.gov.uk/search?q=Updated+short-term+traded+carbon+values+for+policy+appraisal [Last accessed 12 October 2015].

E

Edinburgh College of Art, 2010. *Single cast fabric formwork*. Disruptive technologies workshop, The University of Edinburgh [Online]. Available from: https://richardbush.wordpress.com/2010/12/03/single-cast-fabric-formwork/ [Last accessed 02 August 2015].

Eligehausen, R., Popov, E.P. and Bertero, V.V., 1982. Local bond stress-slip relationships of deformed bars under generalized excitations. *In Proceedings of the 7th European Conference on Earthquake Engineering*, Athens: Techn. Chamber of Greece, 4, pp. 69-80.

Engineered Composites. Solid round rods. [Online]. Available from: http://www.engineered-composites.co.uk/our-products/grp-rods-and-tubes/solid-round-rods. [Last accessed 11 June 2013].

F

Faruqi, M.A., Roy, S. and Salem, A., 2012. Elevated temperature deflection behavior of concrete members reinforced with FRP bars. *Journal of Fire Protection Engineering*, 22 (3), pp.183-196. doi: 10.1177/1042391512447045.

Fastfoot® [Online]. Available from: http://www.fab-form.com/fastfoot/ [Last accessed 02 August 2015].

Fast-Tube™ [Online]. Available from: http://www.fab-form.com/fast-tube/ [Last accessed 02 August 2015].

fib, 2007. Bulletin No.40: FRP reinforcement in RC structures. Lausanne, Switzerland: International Federation for Structural Concrete (fib).

Flower, D. J. M., and Sanjayan, J. G., 2007. Greenhouse gas emissions due to concrete manufacture. *The International Journal of Life Cycle Assessment*, 12 (5), pp. 282-288. doi: 10.1065/lca2007.05.327.

Focacci, F., Nanni, A. and Bakis, C., 2000. Local bond-slip relationship for FRP reinforcement in concrete. *Journal of composites for construction*, 4, pp. 24-31. doi: 10.1061/(ASCE)1090-0268(2000)4:1(24).

Foster, R., 2010. Form finding and analysis of fabric-formed concrete beams. MEng Dissertation, University of Bath.

Fourne, F., 1999. *Synthetic Fibers - Machines and Equipment Manufacture, Properties*. Munich. Hanser Publishers.

G

Garbett, J., 2008. Bone growth analogy for optimising flexibly formed concrete beams. MEng Dissertation, University of Bath.

Garbett, J., Darby, A. P. and Ibell, T. J., 2010. Optimised beam design using innovative fabric-formed concrete. *Advances in Structural Engineering*, 13 (5), pp. 849-860. doi:10.1260/1369-4332.13.5.849.

Grammatikos, S.A., Evernden, M. and Ball, R.J., 2015. Effects of hygrothermal aging on pultruded glass fibre reinforced polymers: a complimentary study. *In Proceedings of Advanced Composites in Construction conference (ACIC 2015)*, 09 - 11 September 2015, Cambridge.

Grant, W., 2013. Shear capacity of concrete beams reinforced with continuous rectangular CFRP spirals. MSc. Thesis. University of Bath.

H

Hall, C., Chen, J.-F. and Hollaway, L., ed., 2010. *Polymers and polymer fibre composites: ICE manual of construction materials*. London: Thomas Telford Ltd.

Harajli, M.H., Hamad, B.S. and Rteil, A.A., 2004. Effect of Confinement on Bond Strength between Steel Bars and Concrete. *ACI Structural Journal*, 101, pp. 595-603.

Harrison, T. 1991. Introducing controlled permeability formwork. *Concrete International*, pp. 198-202.

Hasaballa, M.H. and El-Salakawy, E.F., 2012. Influence of joint-shear stress on seismic behaviour of exterior beam-column joints reinforced with GFRP bars and stirrups, *In Proceedings of 6th International Conference on Advanced Composite Materials in Bridges and Structures (ACMBS-VI)*, 22-25 May 2012 Kingston. CD-ROM.

Hawkswood, M., 2012. Fabric Formwork Systems used in Marine Construction. *In Proceedings of 2nd International Conference on Flexible Formwork (icff 2012)*, 27 - 29 June 2012, Bath, pp. 140-152.

HM Government, 2013. Industrial Strategy: government and industry in partnership. Construction 2025. [Online]. Available from: https://www.gov.uk/government/publications/construction-2025-strategy [Last accessed 12 October 2015].

Hobbs, M., 2015. *Lecture on fully polymeric structures.* FRP internal training, Tony Gee and Partners, 27 August 2015, Esher.

Hughes Brothers, 2011. Glass Fiber Reinforced Polymer (GFRP) Rebar - Aslan™ 100 series FIBERGLASS REBAR. Available online: http://www.aslanfrp.com/Media/Aslan100.pdf.

I

Ibell, T., Darby, A. and Denton, S., 2009. Research issues related to the appropriate use of FRP in concrete structures. *Construction and building materials*, 23, pp. 1521-1528. doi: 10.1016/j.conbuildmat.2008.05.011.

Ibell, T. and Burgoyne, C., 1999. Use of fiber-reinforced plastics versus steel for shear reinforcement of concrete. *ACI Structural Journal*, 96, pp. 997-1003.

Institute for Computational Design, 2012. ICD/ITKE Research Pavilion 2012. [Online]. Available from: http://icd.uni-stuttgart.de/?p=8807. [Last accessed 02 August 2015].

Ioannou S, 2013. An assessment of the performance of calcium sulfoaluminate and supersulfated cements for use in concrete. PhD Thesis. University of Bath.

Iosilevskii, G., 2010. Shape of a soft container under hydrostatic load. *Journal of Applied Mechanics*, 77, pp. 014501/1-3.

J

Juenger, M.C.G., Winnefeld, F., Provis, J.L. and Ideker J.H., 2011. Advances in alternative cementitious binders. *Cement and Concrete Research*, 41 (12), pp. 1232-1243. doi: 10.1016/j.cemconres.2010.11.012.

K

Karayannis, C. G. , Chalioris, C. E. and Mavroeidis, P. D., 2005. Shear capacity of RC rectangular beams with continuous spiral transversal reinforcement. *WIT Transactions on Modelling and Simulation*, 41, pp. 379-386.

Karbhari, V. M., Murphy, K. and Zhang, S., 2002. Effect of Concrete Based Alkali Solutions on Short-Term Durability of E-Glass/Vinylester Composites, *Journal of Composite Materials*, 36 (17). doi: 10.1177/0021998302036017977

Katz, A. M., 1999. Bond mechanism of FRP rebars to concrete, *Materials and Structures/Matériaux et Constructions*, 32, pp. 761-768. doi: 10.1007/BF02905073.

Kiari, M., Triantafyllidou, E., Grosu, S., Stratford,T. and Bisby, L., 2013. Design of an FRP-Reinforced Concrete Beam System for Fire Performance. *In Proceedings of Advanced Composites in Construction conference (ACIC 2013)*, 10 - 12 September 2013, Belfast.

Kostova K.Z., Ibell T.J., Darby A.P. and Evernden M.C., 2013. Sustainable concrete construction using fabric formwork, *In Proceedings of FutureBuild 2013*, 4 - 6 September 2013, Bath.

L

Lamberton, B., 1968a. *Method of forming concrete bodies*. United States Patent Office patent application US3396545A. 1968-08-13.

Lamberton, B. A., 1968b. *Method and arrangements for protecting shorelines*. United States Patent Office patent application US3396542A. 1968-08-13.

Lamberton, B. A., 1969. *Fabric forms for concrete structures*. United States Patent Office patent application US3425228A. 1969-02-04.

Lamberton B.A., 1980. Fabric forms for erosion control and pile jacketing: Innovative uses of fabric forms where soil meets water and for repair of existing coastal structures. *Concrete construction*. Publication #C800395, The Aberdeen Group.

Lamberton, B. 1989. Fabric forms for Concrete. *Concrete International*, 11 (12), pp. 59-67.

Lee, D. S.-H., 2010. Study of construction methodology and structural behaviour of fabric-formed form-efficient reinforced concrete beam. PhD Thesis, The University of Edinburgh.

Lee, H.W., 2012. Enhancement in surface quality of concrete when cast in fabric. MEng Dissertation. University of Bath.

Lees, J. M. and Burgoyne, C. J., 2000. Analysis of concrete beams with partially bonded composite reinforcement. *ACI Structural Journal*, 97, pp. 252-260.

Leung, H.Y., Balendran R.V., Maqsood T., Nadeem A., Rana T.M. and Tang, W.C., 2003. Fibre reinforced polymer materials for prestressed concrete structures. *Structural Survey*, 21 (2), pp. 95-101. doi: 10.1108/02630800310479098

Leung, H.Y. and Burgoyne, C.J., 2001a. Compressive Behaviour of Concrete Confined by Aramid Fibre Spirals. *Structural engineering, mechanics and computation*, 2, pp.1357-1364.

Leung, H.Y. and Burgoyne, C.J., 2001b. Analysis of FRP-reinforced concrete beam with aramid spirals as compression confinement. *Structural engineering, mechanics and computation*, 1, pp. 335-342.

Leung, H.Y and Burgoyne, C.J., 2005.Uniaxial Stress-Strain Relationship of Spirally Confined Concrete. *ACI Materials Journal*, 102, pp. 445-453. ISSN 0889-325X.

Lilienthal, L. W. G., 1899. *Fireproof ceiling*. United States Patent Office patent application US619769A. 1899-02-21.

M

MacLeod, I. A. and Houmsi, A., 1994. Shear strength of haunched beams without shear reinforcement. *ACI Structural Journal*, 91 (1), pp. 79-89.

Maji, A. and Orozco, A.L., 2005. Prediction of bond failure and deflection of carbon fiber-reinforced plastic reinforced concrete beams. *Society for Experimental Mechanic,* 45 (1), pp. 35-41. doi: 10.1007/BF02428988.

Malvar, L.J., 1994. *Bond stress-slip characteristics of FRP rebars.,* California: Naval Facilities Engineering Service Center, Port Hueneme, (TR-2013-SHR).

Manelius, A. 2012. *Fabric formwork for concrete: Investigations into formwork tectonics and stereogenity in architectural constructions*. Doctoral Thesis. Royal Danish Academy of Fine Arts.

Micelli, F. and Nanni, A., 2004. Durability of FRP rods for concrete structures. *Construction and Building Materials*, 18, pp. 491–503. doi: 10.1016/j.conbuildmat.2004.04.012

Monti, G. & Spacone, E., 2000. Reinforced concrete fiber beam element with bond-slip. *Journal of Structural Engineering*, 126 (6), pp. 654-661. doi: 10.1061/(ASCE)0733-9445(2000)126:6(654)

N

Nanni, A., 2003. North American design guidelines for concrete reinforcement and strengthening using FRP: principles, applications and unresolved issues. *Construction and building materials*, 17 (6-7), pp. 439-446. doi:10.1016/S0950-0618(03)00042-4

Nanni, A., Bakis, C. & Boothby, T. 1995. Test methods for FRP-concrete systems subjected to mechanical loads: State of the art review. *Journal of reinforced plastics and composites*, 14, pp. 524-558. doi: 10.1177/073168449501400601.

Ngo, M. D. Ferrier, E. and Michel, L., 2015. Experimental Study on the Shear Behaviour of RC Beams Reinforced by Natural Composite Materials (Linen Fibres). *In Proceedings of Advanced Composites in Construction conference (ACIC 2015)*, 09 - 11 September 2015, Cambridge.

O

Oehlers, D. J., Visintin, P., Chen, J. F. and Ibell, T. J., 2014. Simulating reinforced concrete members. Part 2: Displacementbased analyses*. In Proceedings of the Institution of Civil Engineers-Structures and Buildings*, 167 (12). pp. 718-727. doi: 10.1680/stbu.13.00072

Oehlers, D. J., Visintin, P., Haskett, M. and Sebastian, W.M., 2013. Flexural ductility fundamental mechanisms governing all RC members in particular FRP RC. *Construction and Building Materials*, 49, pp. 985–997. doi: 10.1016/j.conbuildmat.2013.02.018.

Olivier, J.G.J., Janssens-Maenhout, G., Muntean, M. and Peters J.A.H.W, 2012. *Trends in global CO_2 emissions*. The Hague/Bilthoven: PBL Netherlands Environmental Assessment Agency, (publication number: 500114022).

Orangun C., Jirsa, J. and Breen, J., 1977. A reevaluation of test data on development length and splices. *ACI Journal*, 74, pp. 114-122.

Orr, J.J., 2012. Flexible formwork for concrete structures, PhD dissertation, University of Bath.

Orr, J., Darby, A.P., Ibell, T.J. and Evernden, M., 2010. Innovative reinforcement for fabric formed concrete structures. *In Proceedings of 10th International Symposium on Fiber Reinforced Polymer Reinforcement for Concrete Structures (FRPRCS-10)*, 2-4 April 2011, Tampa, CD-ROM.

Orr, J., Darby, A., Ibell, T. and Evernden, M., 2013. Durability enhancements using fabric formwork. *Magazine of Concrete Research*, 65 (20), pp. 1236-1245.

Orr, J. J., Darby, A., Ibell, T. and Evernden, M., 2014. Design methods for flexibly formed concrete beams. *Proceedings of the Institution of Civil Engineers-Structures and Buildings*, 167 (11), pp. 654-666. doi: 10.1680/stbu.13.00061.

Orr, J. J., Ibell, T. J., Darby, A. P. and Evernden, M., 2014. Shear behaviour of non-prismatic steel reinforced concrete beams. *Engineering Structures*, 71, pp. 48-59.

P

Pade, C and Guimaraes, M., 2007. The CO_2 uptake of concrete in a 100 year perspective. *Cement and Concrete Research*, 37 (9), pp. 1348–1356. doi: 10.1016/j.cemconres.2007.06.009

Paglietti, A. and Carta, G., 2009. Remarks on the Current Theory of Shear Strength of Variable Depth Beams. *The Open Civil Engineering Journal*, 3, pp. 28-33.

Portnov, G., Bakis, C. E., Lackey, E. and Kulakov, V., 2013. FRP reinforcing bars-designs and methods of manufacture (review of patents). *Mechanics of composite materials*, 49 (4), pp. 381-400.

Price, W.F., 2000. *Controlled permeability formwork*. CIRIA Report No. C511. London.

Pultrall, 2011. V-ROD - Specifications HM. [Online]. Available from: http://www.pultrall.com [Last accessed 11 June 2013].

Q

R

Rafi, M. M. and Nadjai A., 2011. A suggested model for European code to calculate deflection of FRP reinforced concrete beams, *Magazine of Concrete Research* , 63 (3), pp. 197–214, doi: 10.1680/macr.9.00085.

S

Schmitz, R., 2006. Fabric-Formed Concrete Panel Design. *In Proceedings of Structures Congress 2006: 17th Analysis and Computation Specialty Conference*, 18 – 21 May 2006 pp. 1-16. doi: 10.1061/40878(202)25.

Sharma, B., Gatóo, A. and Ramage, M., 2015. Natural fibre composites: engineered bamboo for construction. *In Proceedings of Advanced Composites in Construction conference (ACIC 2015)*, 09 - 11 September 2015, Cambridge.

Shima, H., Chou, L. L. and Okamura, H., 1987. Micro and macro models for bond in reinforced concrete. *Journal of the Faculty of Engineering*, 39, pp. 133-94.

Sireg, 2011. *Geotechnical solutions*. Italy. Graficart – Biassono.

Smith, S., 2012.Technical Potential of 3D Scanning for Engineering Applications using Microsoft Kinect. BEng Dissertation. University of Bath. Bath.

Soong, W.H., Raghavan, J. and Rizkalla, S.H., 2011. Fundamental mechanisms of bonding of glass fiber reinforced polymer reinforcement to concrete. *Construction and Building Materials*, 25, pp. 2813–2821. doi: 10.1155/2013/631216.

Sprung, S. 2008. *Cement. Ullmann's Encyclopedia of Industrial Chemistry*. Wiley-VCH Verlag GmbH & Co. KGaA. doi: 10.1002/14356007.a05_489.pub2.

Sridharan, R., 2004. From lintearia to lemniscate 1, *Resonance*, 9 (4), pp. 21-29.

Stefanou G. D., 1983. Shear resistance of reinforced concrete beams with non-prismatic sections. *Engineering Fracture Mechanics*. 18 (3), pp. 613-666. doi: 10.1016/0013-7944(83)90057-7.

Stratford, T.J. and Burgoyne, C.J., 2001. Shear analysis of concrete with brittle reinforcement. *In Proceedings of the 5th International Conference on Fibre-Reinforced Plastics for Reinforced Concrete Structures (FRPRCS-5),* 16-18 July 2001, Cambridge, vol. 2, pp. 939-948.

Sturgeon K. A., Holzwart C. and Raczkowski K., 2010. Fatty shell (v 01). Dezeen magazine. [Online]. Available from: http://www.dezeen.com/2010/05/19/fattyshell-v-01-by-kyle-a-sturgeon-chris-holzwart-and-kelly-raczkowski/ [Last accessed 02 August 2015].

T

Tallis, S., 2005. Novel Anchorage of Internal FRP Reinforcement. MEng Dissertation. The University of Bath, Bath.

Tepfers, R. and De Lorenzis, L., 2003. Bond of FRP reinforcement in concrete – a challenge, *Mechanics of Composite Materials,* 39b (4), pp. 315-328. doi: 10.1023/A:1025642411103

Teychenné, D. C. Franklin, R. E. and Erntroy, H. C., 1997*. Report 331: Design of normal concrete mixes – second edition*. BRE

Thirion, C., 2010. Putting the material in the right place: the role of material-efficiency in reducing the environmental impact of building structures. MRes. University College London.

Tighiouart B., Benmokrane B. and Gao, D., 1998. Investigation of bond in concrete member with fibre reinforced polymer (FRP) bars. *Construction and Building Materials*, 12, pp. 453-462. doi: 10.1016/S0950-0618(98)00027-0.

Tena-Colungaa, A., Archundia-Arandaa, H.I. and Gonzalez-Cuevasa O.M., 2008. Behaviour of reinforced concrete haunched beams subjected to static shear loading. *Engineering Structures*, 30, pp. 478–492. doi: 10.1016/j.engstruct.2007.04.017.

Torres, Ll., Miàs, C.,Turon, A. and Baena, M., 2012. A rational method to predict long-term deflections of FRP reinforced concrete members. Engineering Structures, 40, pp. 230–239. doi:10.1016/j.engstruct.2012.02.021.

Trancels-Pultrall Canada Inc., 2011. Why V-Rod composite rebar. Available from: http://www.trancels-pultrall.com [Accessed 21 December 2013].

Trejo, D., Gardoni, P. and Kim, J.J., 2011. Long-Term Performance of Glass Fiber Reinforced Polymer Reinforcement Embedded in Concrete. *ACI Materials Journal*, 108 (6), pp. 605-613.

Tysmans, T., Adriaenssens S. and Wastiels J., 2011. Form finding methodology for force-modelled anticlastic shells in glass fibre textile reinforced cement composites. *Engineering Structures*, 33, pp. 2603–2611. doi: 10.1016/j.engstruct.2011.05.007.

Tysmans T., Belkassem B., Adriaenssens S., Wastiels J. and Cauberghell N., 2009. Elements of architectural concrete using fabric formwork – Part B: Case study. *In Proceedings of FRPRCS-9*, 13 - 15 July 2009, Sydney.

U

Umi Architectural Atelier. *URC (fabric formwork)* [Online]. Available from: http://www.umi-aa.com/urc-gallery/ [Last accessed 14 June 2015].

V

Van Mele, T. and Block, P., 2010. A novel form finding method for fabric formwork for concrete shells. *In Proceedings of the International Association for Shell and Spatial Structures (IASS) Symposium 2010,* 08 – 12 Nov 2010, Shanghai.

Veenendaal, D., 2008. *Evolutionary Optimization of Fabric Formed Structural Elements: Bridging the gap between computational optimization and manufacturability*. Master's Thesis, Delft University of Technology.

Veenendaal, D. and Block, P., 2012. Computational form-finding of fabric formworks: an overview and discussion. *In Proceedings of 2nd International Conference on Flexible Formwork*, 27 - 29 June 2012, Bath, pp. 368-378.

Veenendaal, D. and Block, P., 2014. Design process for prototype concrete shells using a hybrid cable-net and fabric formwork. *Engineering Structures*, 75, pp. 39-50. doi: 10.1016/j.engstruct.2014.05.036.

Veenendaal, D., Coenders, J., Vambersky, J., and West, M., 2011a. Design and optimization of fabric-formed beams and trusses: evolutionary algorithms and form-finding. *Structural Concrete*, 12 (4), pp. 241-254. doi: 10.1002/suco.201100020.

Veenendaal, D., West, M. and Block, P., 2011b. History and overview of fabric formwork: using fabrics for concrete casting. *Structural Concrete*, 12 (3), pp. 164-177. doi: 10.1002/suco.201100014.

W

Waller, W., 1934. *Method of building with cementitious material applied to vegetable fabrics*. United States Patent Office patent application US1955716A. 1934-04-17.

Wambeke, B.W. and Shield C.K, 2006. Development length of glass fiber-reinforced polymer bars in concrete. *ACI Structural Journal*, 103, pp. 11-17.

West M., 2009. Thin-Shell Concrete from Fabric Moulds [Online]. Available:http://www.umanitoba.ca/cast_building/assets/downloads/PDFS/Fabric_For

mwork/Thin-Shell_Concrete_From_Fabric_Forms_SCREEN.pdf [Accessed 1 August 2011].

West, M., 2010a. *Kenzo Unno: Fabric Formed Walls* [Online]. Available from: http://www.umanitoba.ca/cast_building/assets/downloads/PDFS/Fabric_Formwork/Kenzo_Unno_Article.pdf [Last accessed 14 June 2015].

West, M.,2010 b. *Fabric-formed concrete structures* [Online]. Available from: http://www.umanitoba.ca/cast_building/assets/downloads/PDFS/Fabric_Formwork/Fab-Form_conc_structs.pdf [Last accessed 14 June 2015].

West, M., 2010c. *Fabric-formed concrete columns for casa dent in Culebra Puerto Rico* [Online]. Available from: http://www.umanitoba.ca/cast_building/assets/downloads/PDFS/Fabric_Formwork/Casa_Dent.pdf [Last accessed 14 June 2015].

West, M. and Araya, R., 2012. Recent Fabric Formwork Construction Projects. *In Proceedings of 2nd International Conference on Flexible Formwork*, 27 - 29 June 2012, Bath, pp. 390-397.

Whitehead, P. A., 2002. *Shear Strength of Concrete containing Fibre- Reinforced-Plastic Reinforcement*. PhD Thesis, University of Bath.

Whitehead, P.A. and Ibell, T. J., 2004. Deformability and ductility in over-reinforced concrete structures. *Magazine of Concrete Research*, 56 (3), pp. 167–177. doi: 10.1680/macr.2004.56.3.167.

Williams, C.J.K., 2012. Meshfree peridynamic computer modelling of concrete in three dimensions using randomly positioned particles. *In Proceedings of 2nd International Conference on Flexible Formwork (icff 2012)*, 27 - 29 June 2012, Bath, pp. 398-403.

Winkle, C. 2005. Anchorage of Fibre-Reinforced-Polymer (FRP) Bars. MEng Dissertation, The University of Bath, Bath.

Wolanski A.J., 2004. Flexural Behaviour of RC and Pre-stressed Concrete Beams Using FE Analysis. Master's Thesis, Dept. of Civil Engineering, Marqutte University, Milwaukee, Wisconsin.

X

Y

Yang, Y., Orr, J., Ibell, T. and Darby, A., 2015. Shear strength theories for beams of variable depth. *In Proceedings of IASS2015 Annual International Symposium on Future Visions IASS/ISOFF*, 16-20 August 2015, Amsterdam.

Yazdanbakhsh, A. and Bank L.C., 2014. A critical review of research on reuse of mechanically recycled FRP production and end-of-life waste for construction. *Polymers*, 6 (6), pp. 1810-1826. doi: 10.3390/polym6061810.

Z

Appendix A

A.1. Introduction

The hinged-beam test results presented in § 3 are based on measurement of strains in the test bars taken near the bonded splayed ends. While this has helped to determine the actual pull-out force resisted by the anchorages, theoretical prediction of the forces was not possible. However, strain measurements were also taken at mid-length of the test bars in order to assess the loss of tension along the length of the bar and to provide data for comparison with theoretically calculated forces. For a standard hinged-beam test, the force at the middle of a test bar is equal to the applied bending moment at midspan divided by the lever arm, defined by the distance between the centre of the bar and the hinge. The standard test, however, has been modified, as described in § 3, and a new method for theoretical prediction is required to allow for the change in the lever arm during the load test.

A.2. Theoretical calculation of tension force

The modifications to the standard hinged-beam test, aimed to improve the results for splayed FRP bars by casting polystyrene 100 mm 4° wedges on the top of the bars at midspan, resulted in a non-constant lever arm between the tensile force in the FRP bars and the compression force in the top reinforcement. It can be shown that the lever arm, determined by the position of points *A*, *D*, *A'* and *D'* indicated in *Figure A.1*., depends on the rotational angle φ, which can be found from *Equations A.1* and *A.2*, where v and $v1$ are the vertical displacements, defined in *Figure A.2*. The tension force at the middle of the test bar is then calculated by dividing the applied moment by the lever arm and can be represented as a force-deflection curve.

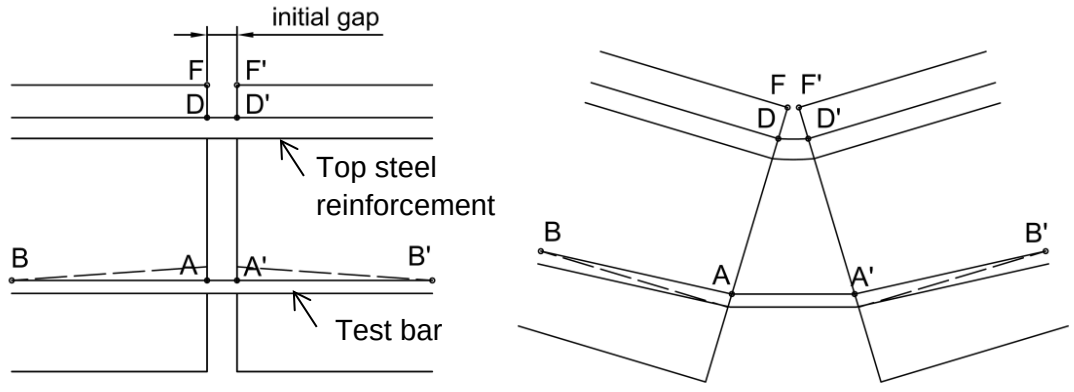

Figure A.1. Change of lever arm during hinged-beam test (experimentally confirmed)

$$tan\varphi = \frac{v1 + v}{400} \tag{A.1}$$

$$cos\varphi = \frac{220}{220 + v1} \tag{A.2}$$

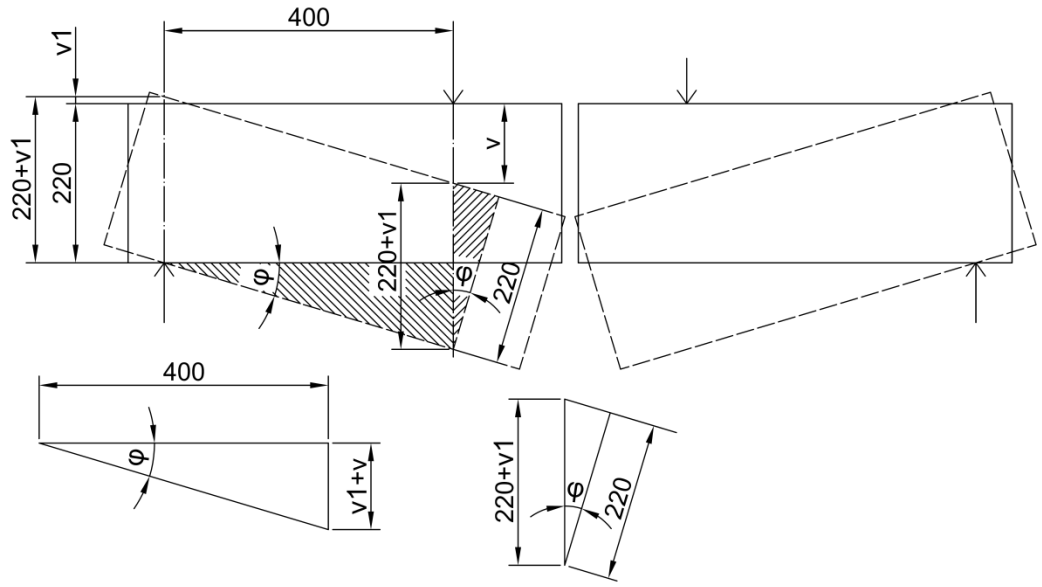

Figure A.2. Relation between vertical displacement and rotation of hinged-beam blocks

A.3. Comparison of theoretical and experimental results

The theoretical and experimental results are compared in *Figure A.3*. The solid lines represent the predicted force-deflection response, while the dotted lines correspond to the forces obtained from the control gauges on the FRP bars. The strains were measured horizontally, parallel to the centreline, on both sides of each test bar. The predicted force takes into account the reduction of the applied bending moment due to the plastic moment of resistance of the top bars. The size of the initial gap and the position of the top bars were measured prior to each load test. As can be seen, taking the average strain from two side gauges can provide reliable results close to the theoretically calculated forces. Therefore, it may be concluded that the similar measurement of strains near splayed ends was appropriate for obtaining realistic forces in the anchorages, used for development of the splayed anchorage model in § 3.

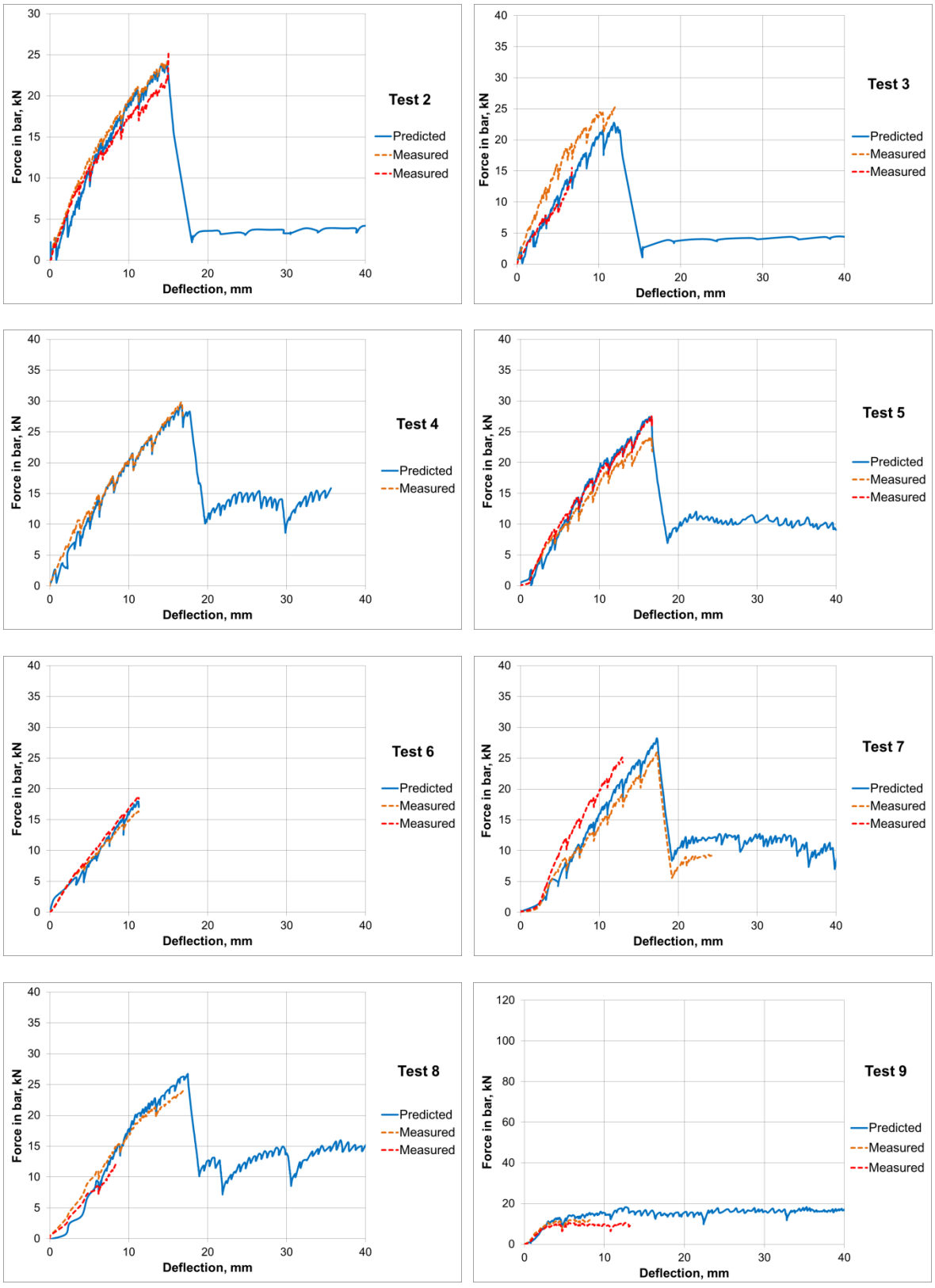

Figure A.3. Predicted and experimental vertical load-deflection curves at hinged-beam midspan

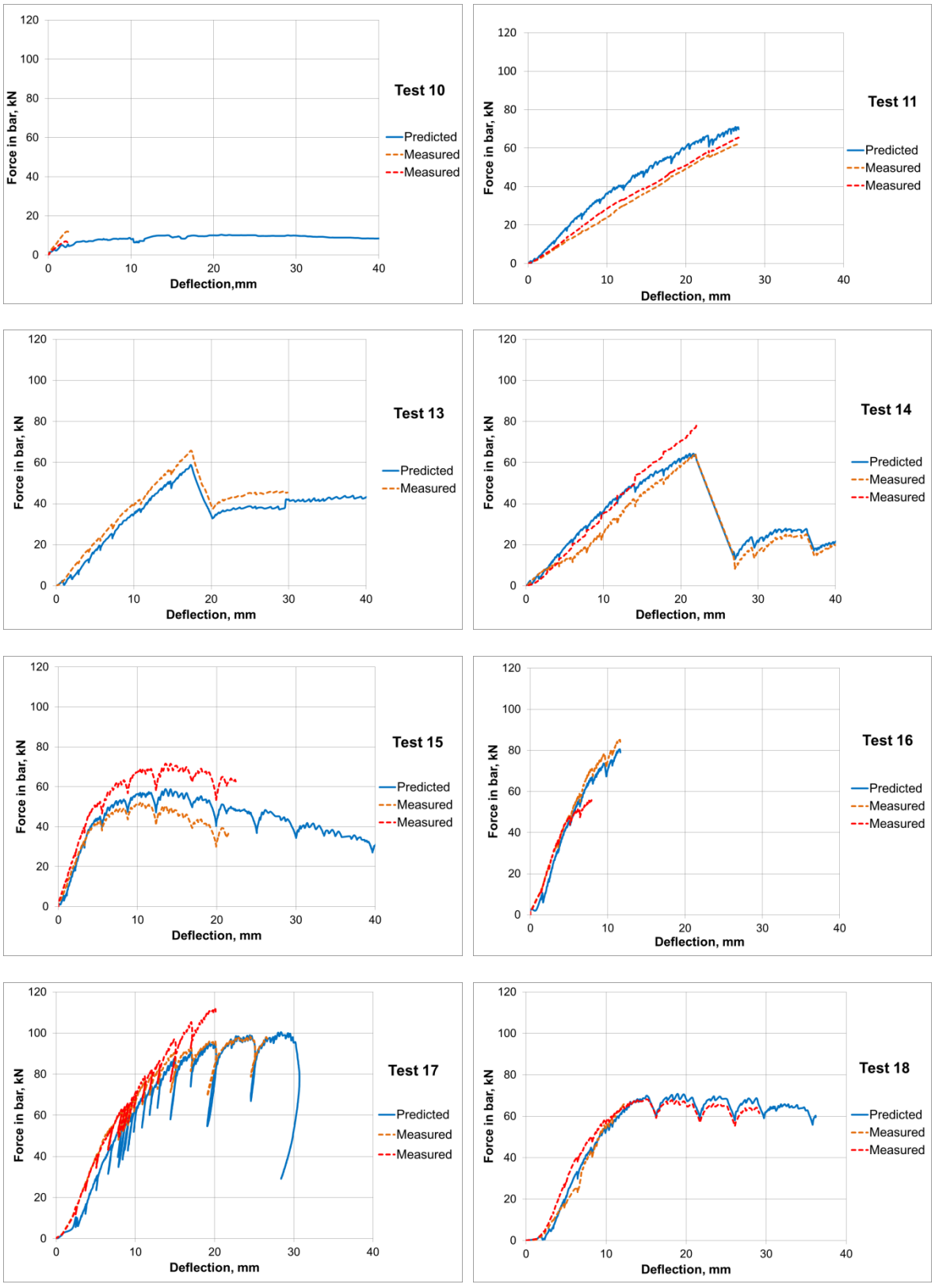

Figure A.3. Predicted and experimental vertical load-deflection curves at hinged-beam midspan (continued)

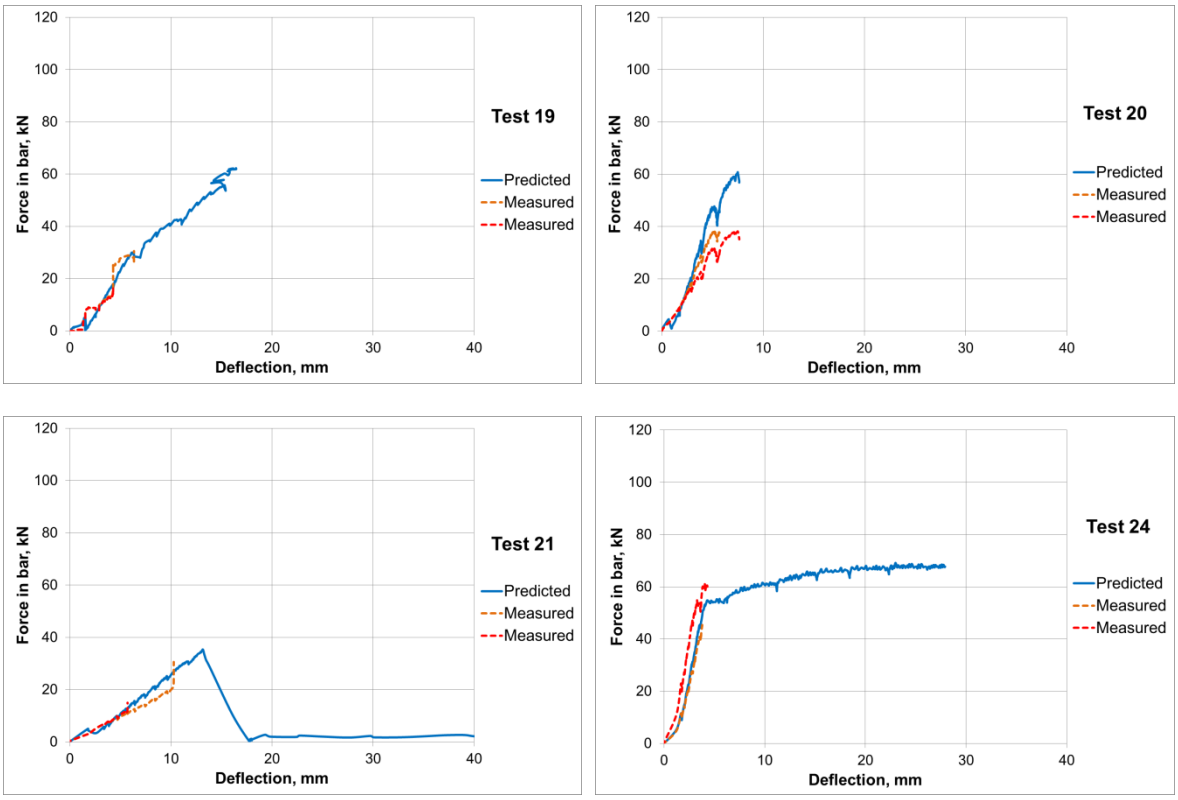

Figure A.3. Predicted and experimental vertical load-deflection curves at hinged-beam midspan (continued)